

*Framing the Chalcogen-Bonding Interaction in the  
Supramolecular Toolbox for Solid-State  
Applications*

*Thesis presented by*

Nicolas BIOT

*Under the supervision of Davide Bonifazi*

*For the degree of Doctor of Philosophy (Chemistry)*

**Cardiff University 2019**







À mon Papa, à ma Maman,

Avec une infinie gratitude











### **Acknowledgements**

First, I would like to thank Professor *Davide Bonifazi* for giving me the opportunity to do my PhD under his supervision. This work has been the result of our fruitful collaboration and mutual trust. You have considerably widened my vision of science along the years through discussions about various topics. Thanks also for the chance you gave me to meet, listen to and speak with quality scientists from across Europe. Your enthusiasm and willpower have always motivated me. For everything we have achieved in and beyond those pages, I am deeply grateful.

Many thanks to Dr. *Benson Kariuki* for having taught me the technique of crystallography from data collection, to solution and refinement of X-ray structures. This work would not have been the same without you and I am extremely grateful of the knowledge you have transmitted to me.

Thanks to Prof. *Scott Cockroft* and Prof. *Thomas Wirth* for accepting the role of examiners of this thesis.

I would like to thank Cardiff University and Infusion for funding this thesis and promoting mobility.

To the students I had the chance to supervise during those last years, I am thankful for your work. I know I haven't given you an easy time, but I took every opportunity to teach you and I hope you have learned from this experience. To *Sam* and *Tooba*, I wish you all the best for the future. Particularly, *Deborah*, you have been my first student and I had the pleasure to watch you grow during those years. You have done a long way since we met. I am deeply grateful to you for having been there for me in good and hard moment. I am happy for having been part of the 'Chalcogen Team' with you.

I also would like to thank the people I have collaborated with inside the Bonifazi Lab. Particularly, *Andrey*, *Andrea F.*, *Tanja*, *Cataldo*, *Jacopo*, *Oliwia*, *Maria*, *Francesco*, *Alexandre* and *Dmytro*. I have been happy to solve and refine crystal structures and perform calculations for you. I hope my help has been useful.

This thesis would not have been possible without the support of the analytical service of Cardiff University. I would like to give a special thanks to *Rob*, *Robin*, *Tom* and *Simon*. With you, the work has always been fast and precise. The same goes to the workshop team, *Steve*, *Lee*, *Julian* and *Alun*. A special thanks goes to *James* and *Simon*, who always tried to find the best reasonable way to solve our problems.

Thanks to the ARCCA for providing the computational resources that helped me during these four years. Thanks to Dr. *Jamie Platts* and Prof. *Stefano Leoni* for your patience and the discussions we had about theoretical calculations.

## Acknowledgements

---

I would like to give a particular thanks to the organising comity of the MASC meetings. Those conferences have always been inspiring and allowed me to meet many quality scientists from all around UK and beyond.

I am grateful to the past members of the COMS, *Adrian, Jonathan, Florent, Daphné, Rosaria, Hamid, Federica, Laure-Elie*. They have inspired me on the path I am today and showed me primordial quality to have in a research lab.

I also would like to thank the past and present members of the Bonifazi lab in Cardiff, *Andrey, Andrea F., Antoine, Grazia, Tanja, Tommaso, Dmytro, Jacopo, Francesco, Jack, Oliwia, Lou, Deborah, Alexandre, Melina, Andrea S., André, Rodolfo, Cataldo, Alexandra* and *Diem*.

Thanks to Dr. *Tanja Miletić* for the proofreading of the manuscript. I know those last months have not been easy for you, thank you for having found the time. I would like also to thank you for the three years we have spent together and for having been there in bad times.

To my friend *Antoine*, I thank you for everything. During the last six years, we have shared scientific achievements as well as life moments, good or bad. The first trip from Namur to Cardiff will always stay in my memories. We have also shared many circles of friend, from our time at the 'acoustique' with *Audrey* and *Alex* to the PoGo community of Cardiff.

A particular shout out to *Carol, Scott, Dino, Phil, Rich, Ash, Rich, Renato, Rich, Terry, Page* and *Rachel*. You helped me to change my mind when I needed it the most.

To *Max* and *Alex*, thanks for having made those helmets flying more than often. Now, prepare for more handsome adventures!

Thanks to Browne's, Morill's and Wirth's group members, particularly, to *Florence, Christiane, James, Joey* and *Filipa*. Special thanks to *Micol*, our working schedule did not allow us to party as often as we wanted but each time has been intense.

The final thanks go to my family. A ma Maman, pour ta gentillesse et ton amour infini, ton support durant toutes ces années a été ma plus grande motivation. A mon Papa, j'aurais aimé que tu puisses lire ces quelques lignes. De là-haut, je suis sûr que tu es fier de moi. Tous les deux, vous m'avez donné la patience, le gout du travail bien fait, le souci des autres et de la communauté. Je vous remercie d'avoir donné, à mon frère et moi, la chance de nous développer et nous accomplir dans foyer aimant. Merci pour tout!

<b>Abbreviations.....</b>	<b>V</b>
<b>Summary.....</b>	<b>VIII</b>
<b>Chapter I Introduction.....</b>	<b>1</b>
<b>I – 1 Introduction .....</b>	<b>2</b>
I – 1.1 THE SUPRAMOLECULAR TOOLBOX.....	2
I – 1.2 HALOGEN-BONDING.....	4
<b>I – 2 Chalcogen bonding: nature of the interaction .....</b>	<b>6</b>
I – 2.1 ORIGIN OF CHALCOGEN-BONDING INTERACTION .....	6
I – 2.2 CHALCOGEN BONDING DOMINATED BY ELECTROSTATIC CONTRIBUTION .....	7
I – 2.3 CHALCOGEN BONDING DOMINATED BY ORBITAL CONTRIBUTION .....	8
I – 2.4 CHALCOGEN-BONDING DOMINATED BY DISPERSION CONTRIBUTION .....	9
<b>I – 3 Chalcogen bonding at work: applications in solution .....</b>	<b>10</b>
I – 3.1 ANION RECOGNITION.....	10
<i>I – 3.1.1 Anion binding involving single chalcogen bond.....</i>	<i>10</i>
<i>I – 3.1.2 Anion binding involving two chalcogen bonds: confocal approach.....</i>	<i>13</i>
I – 3.2 CATALYSIS .....	15
<i>I – 3.2.1 Hydrogenation transfer reactions.....</i>	<i>15</i>
<i>I – 3.2.2 Halide abstraction reactions.....</i>	<i>16</i>
<i>I – 3.2.3 Ring formation.....</i>	<i>17</i>
I – 3.3 SELF-ASSEMBLY IN SOLUTION .....	18
<i>I – 3.3.1 Micellar structures in water.....</i>	<i>18</i>
<i>I – 3.3.2 Supramolecular capsules .....</i>	<i>19</i>
<b>I – 4 Chalcogen-bonding at work: applications at the solid state .....</b>	<b>20</b>
I – 4.1 CHALCOGENADIAZOLE: INFINITE RIBBON VS DISCRETE ASSEMBLY .....	20
I – 4.2 1,2-CHALCOGENAZOLE N-OXIDE: DISCRETE MACROCYCLIC ASSEMBLY .....	25
I – 4.3 CHALCOGEN-BONDING MEETING HALOGEN-BONDING .....	27
I – 4.4 POROUS ARCHITECTURE FORMATION THROUGH CHALCOGEN-CHALCOGEN INTERACTIONS.....	29
I – 4.5 SELF-ASSEMBLED FIBRES FOR OPTOELECTRONIC APPLICATIONS CONTROLLED BY CHALCOGEN-BONDING INTERACTIONS	30
I – 4.6 WIRE-LIKE STRUCTURES FORMED BY BENZO-1,3-CHALCOGENAZOLE .....	31
<b>I – 5 Outline of the dissertation.....</b>	<b>33</b>
<b>I – 6 Bibliography .....</b>	<b>34</b>
<b>Chapter II Programming Recognition Array Through Double Chalcogen-Bonding Interactions.....</b>	<b>41</b>
<b>II – 1 Introduction .....</b>	<b>42</b>
<b>II – 2 Design.....</b>	<b>43</b>

*Table of Content*

---

<b>II – 3 Synthesis</b> .....	<b>46</b>
<b>II – 4 Solid-state analysis</b> .....	<b>49</b>
II – 4.1 RECOGNITION AT WORK – TELLURIUM CONTAINING DERIVATIVES .....	49
II – 4.2 STRENGTHENING OF THE INTERACTION – TELLURIUM CONTAINING DERIVATIVES .....	52
II – 4.3 THE CASE OF SELENIUM .....	55
II – 4.4 STRENGTHENING OF THE INTERACTION – EFFECT OF EWG .....	58
<b>II – 5 Synthesis of symmetric ditopic derivatives</b> .....	<b>60</b>
<b>II – 6 Inclusion of the CGP motif in functional system: towards chalcogen-bonded soft materials</b> .....	<b>62</b>
II – 6.1 GEL DESIGN: PROGRAMMING “ACRYLAMIDE” POLYMER WITH EB INTERACTIONS .....	62
II – 6.2 DITOPIC DERIVATIVES WITH AN ALKYL SPACER: SUPRAMOLECULAR POLYMERS .....	64
<b>II – 7 Chalcogen-bonding vs <math>\pi</math>-<math>\pi</math> stacking interactions: from dimers to semi-conductor materials</b> .....	<b>65</b>
II – 7.1 INTRODUCTION .....	65
II – 7.1.1 <i>Organic semiconductors</i> .....	65
II – 7.1.2 <i>Charge mobility through Space-Charge Limited Current experiments</i> .....	67
II – 7.2 DESIGN OF THE PYRENE-BASED MOLECULAR BUILDING BLOCKS .....	68
II – 7.3 SYNTHESIS .....	70
II – 7.4 FRONTIER ORBITAL CHARACTERISATION .....	70
7.4.2 <i>Electrochemical properties</i> .....	72
7.4.3 <i>Energy diagram of pyrene derivatives II-39<sub>E</sub> and II-40<sub>E</sub></i> .....	74
7.4.4 <i>Computed molecular orbitals and energy diagram of pyrene derivatives II-39<sub>E</sub> and II-40<sub>E</sub></i> .....	75
II – 7.5 SOLID-STATE ORGANISATION .....	77
II – 7.6 CHARGE MOBILITY MEASUREMENTS.....	80
<b>II – 8 Conclusion</b> .....	<b>83</b>
<b>II – 9 Bibliography</b> .....	<b>84</b>
<b>Chapter III Synergy between Chalcogen and Halogen Bonding</b> .....	<b>89</b>
<b>III – 1 Introduction</b> .....	<b>90</b>
III – 1.1 THE PRINCIPLE OF ORTHOGONALITY IN SUPRAMOLECULAR CHEMISTRY .....	90
III – 1.2 ORTHOGONAL FUNCTIONALISATION OF MACROMOLECULAR BACKBONES.....	91
III – 1.3 SUPRAMOLECULAR POLYMERS THROUGH ORTHOGONAL NON-COVALENT INTERACTIONS .....	92
<b>III – 2 Design of multi-component orthogonal supramolecular polymers</b> .....	<b>94</b>
<b>III – 3 Crystal structure analysis</b> .....	<b>98</b>
III – 3.1 CO-CRYSTAL PREPARATION .....	98
III – 3.2 CO-CRYSTALS: TELLURIUM CONTAINING CGP BEARING A HALOGEN-BOND ACCEPTOR.....	100
III – 3.3 CO-CRYSTALS: SELENIUM CONTAINING CGP BEARING HALOGEN BOND ACCEPTOR .....	107

III – 3.4 CO-CRYSTALS: CGP BEARING HALOGEN BOND DONOR .....	111
<b>III – 4 Conclusion .....</b>	<b>115</b>
<b>III – 5 Bibliography .....</b>	<b>116</b>
<b>Chapter IV Blending Chalcogen and Hydrogen Bonding: Multipoint Recognition Motifs .....</b>	<b>119</b>
<b>IV – 1 Introduction .....</b>	<b>120</b>
IV – 1.1 CHALCOGEN- AND HYDROGEN-BONDING INTERACTIONS .....	120
IV – 1.2 MULTIVALENT HYDROGEN-BONDED SYSTEM .....	121
<b>IV – 2 Strategy: Introduction of a substituent in the 5-position of the CGP scaffold .....</b>	<b>124</b>
<b>IV – 3 Synthesis .....</b>	<b>125</b>
IV – 3.1 SYNTHESIS OF METHYL 5-SUBSTITUTED CGP .....	125
IV – 3.2 SYNTHESIS OF HALOGEN 5-SUBSTITUTED CGP .....	128
<b>IV – 4 Solid-state analysis .....</b>	<b>129</b>
IV – 4.1 ELECTROSTATIC SURFACE POTENTIAL .....	129
IV – 4.2 SINGLE COMPONENT CRYSTALS.....	131
IV – 4.2.1 <i>CF<sub>3</sub> substituted derivatives: face-to-face dimer vs head-to-tail ribbon</i> .....	131
IV – 4.2.2 <i>Phenyl and thiophenyl substituted derivatives: wire-like structures</i> .....	133
<b>IV – 5 En route to a homo-molecular self-recognition system through tetra-chalcogen-bonding interactions.....</b>	<b>135</b>
IV – 5.1 HEAD-TO-TAIL VS FACE-TO-FACE: FROM RIBBON TO DIMER .....	135
IV – 5.2 RETROSYNTHETIC ANALYSIS .....	138
IV – 5.3 SYNTHESIS: OXIDATIVE CYCLISATION PATHWAY.....	138
IV – 5.4 SYNTHESIS: CROSS-COUPLED PATHWAY .....	139
IV – 5.5 X-RAY ANALYSIS .....	140
<b>IV – 6 Heteromolecular recognition through multi-type interactions .....</b>	<b>142</b>
IV – 6.1 DESIGN .....	142
IV – 6.2 CO-CRYSTALS X-RAY ANALYSIS.....	143
<b>IV – 7 Conclusion .....</b>	<b>145</b>
<b>IV – 8 Bibliography .....</b>	<b>146</b>
<b>Chapter V Conclusion and Outlooks .....</b>	<b>149</b>
<b>Chapter VI Experimental Section .....</b>	<b>155</b>
<b>VI – 1 General remarks.....</b>	<b>156</b>
VI – 1.1 INSTRUMENTATION.....	156

*Table of Content*

---

VI – 1.2 MATERIALS AND METHODS.....	157
<b>VI – 2 Synthetic procedure and spectral data.....</b>	<b>159</b>
<b>VI – 3 <sup>1</sup>H, <sup>13</sup>C and <sup>19</sup>F spectra .....</b>	<b>206</b>
<b>VI – 4 Calculations.....</b>	<b>283</b>
VI – 4.1 GENERAL REMARKS.....	283
VI – 4.2 ELECTROSTATIC SURFACE POTENTIAL .....	283
VI – 4.3 FRONTIER ORBITALS .....	285
<b>VI – 5 Crystal data and structure refinement .....</b>	<b>289</b>
<b>VI – 6 References .....</b>	<b>337</b>

## Abbreviations

°	degree
°C	degree Celsius
1D	one-dimensional
2D	two-dimensional
Å	angstrom (1 Å = 10 <sup>-10</sup> m)
aq.	aqueous
Ar	aryl
Bu	butyl
Calc.	calculated
CCDC	Cambridge Crystallographic Data Centre
CGP	chalcogenazopyridine
CMC	critical micellar concentration
δ	chemical shift (NMR)
Δ	difference
d	doublet (NMR)
DCC	dynamic covalent chemistry
DFT	density functional theory
DIPEA	diisopropylethylamine
DMF	<i>N,N</i> -dimethylformamide
DMSO	dimethylsulfoxide
ε	extinction coefficient (M <sup>-1</sup> cm <sup>-1</sup> )
εε <sub>0</sub>	relative permittivity
E	potential
E <sup>1/2</sup>	half-wave potential
E <sup>e</sup>	edge potential
ΔE <sub>op</sub>	optical bandgap
ΔE <sub>el</sub>	bandgap calculated by CV
ΔE <sub>cal</sub>	bandgap calculated by DFT
EB	chalcogen bond
<i>e.g.</i>	<i>exempli gratia</i> (latin) – for example
EI	electron impact
eq.	equivalent
ESI	electrospray ionisation
ESP	electrostatic surface potential
Et <sub>2</sub> O	diethyl ether
EtOAc	ethyl acetate
EtOH	ethanol
eV	electron Volt
EWG	electron withdrawing group
Fc	ferrocene
Fc <sup>+</sup>	ferricenium
g	gram
G	Gibbs energy/free enthalpy
h	hour
HB	hydrogen bond
HOMO	highest occupied molecular orbital
HR	high resolution
Hz	Hertz (s <sup>-1</sup> )
<i>I</i>	current (CV)
IC <sub>50</sub>	half maximal inhibitory concentration

## Abbreviations

---

i.e.	<i>id est</i> (latin) – that is to say
IR	infra-red (spectroscopy)
ITC	isothermal titration calorimetry
ITO	Indium Tin Oxide
IUPAC	International Union of Pure and Applied Chemistry
<i>J</i>	density of current (SCLC) or coupling constant (NMR)
K	kelvin
k	kilo (10 <sup>3</sup> )
K <sub>a</sub>	association constant
λ	wavelength
<i>L</i>	thickness (SCLC)
L	litre
LUMO	lowest unoccupied molecular orbital
μ	charge mobility
μ	micro (10 <sup>-6</sup> )
m	milli (10 <sup>-3</sup> ) or multiplet (NMR)
M	molar (mol L <sup>-1</sup> )
MALDI	matrix assisted laser desorption-ionization
Me	methyl
MeOH	methanol
MHz	megahertz (10 <sup>6</sup> Hz)
min.	minute
mol	mole
m.p.	melting point
MS	mass spectrometry
m/z	mass over charge ratio
NBS	<i>N</i> -bromosuccinimide
NLO	nonlinear optics
NMR	nuclear magnetic resonance
OFET	organic field effect transistors
OLED	organic light emitting diode
OSCs	organic solar cells
ox	oxidation
PAH	polycyclic hydrocarbon
Ph	phenyl
q	quartet (NMR)
<i>R</i>	R-factor
tol	toluene
ppm	parts per million
r.t.	room temperature
red	reduction
s	second or singlet (NMR)
SAXS	small angle X-ray scattering
SCE	standard calomel electrode
SEM	scanning electron microscopy
SiO <sub>2</sub>	silica gel
t	triplet (NMR)
T	temperature
TEM	transmission electron microscopy
THF	tetrahydrofuran
TLC	thin layer chromatography

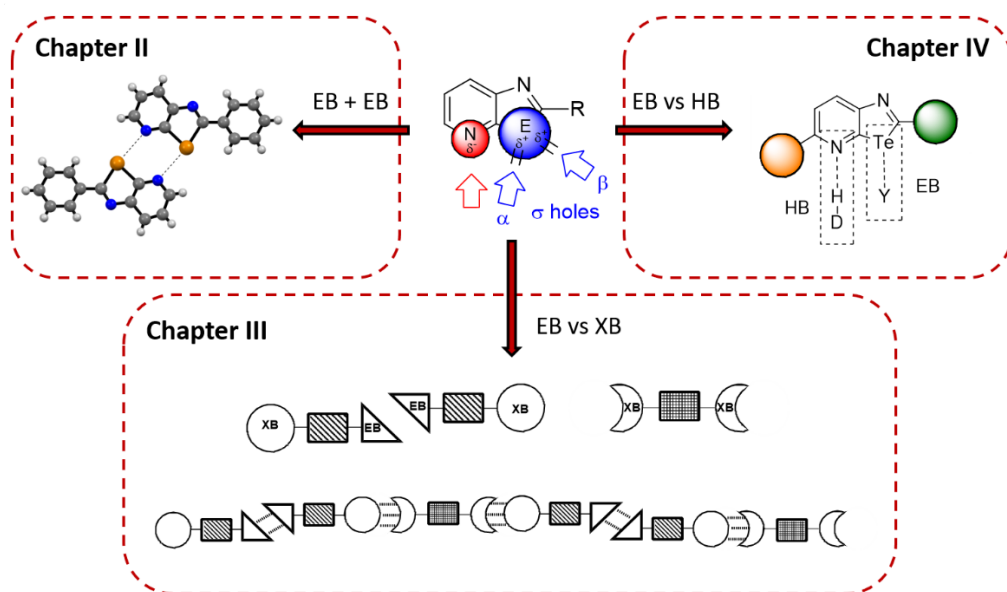
## *Abbreviations*

---

UV	ultraviolet
V	potential
V	Volt
Vis	visible
vdW	van der Waals
X	halogen
XB	halogen bond

## Summary

Out of the supramolecular toolbox, Secondary Bonding Interactions (SBIs) have been a topic of growing interest from the scientific community during the last decades, particularly halogen- and chalcogen-bonding. Those interactions are composed of orbital mixing, electrostatic and dispersion components. Heavier halogen (X) and chalcogen (E) atoms bonded to organic molecules present an anisotropic charge distribution. Specifically, a region of positive potential called a  $\sigma$ -hole can be found co-linear but opposite to the C-X or C-E bonds. Chalcogen atoms are able to form two covalent bonds and thus, exhibit two  $\sigma$ -holes. This ability allows them to be inserted in aromatic cycles making the C-E bonds less reactive compared to that of C-X. Those advantages make the chalcogen-bonding an interaction of choice to build new supramolecular architectures. However, the field still lacks a recognition motif showing fidelity and stability (*chapter I*). In consequence, this work presents the synthesis of a recognition motif bearing Se and Te atoms and showing a strong recognition persistence at the solid-state, namely the CGP array (*chapter II*). This building block can be easily substituted in 2-positions by various functional groups leading to a strengthening of the interaction or to the introduction of valuable properties. For instance, 1-pyrenyl derivatives have been synthesised showing that organic semi-conductor material can be synthesised relying on EB and  $\pi$ - $\pi$  stacking interactions to organise in the solid-state (*chapter II*). Further functionalisation allowed us to build supramolecular polymers in the form of co-crystal showing an orthogonal behaviour of EB and XB interactions (*chapter III*). The CGP scaffold could also be functionalised in 5-position leading to the formation of unprecedented multi-type interactions recognition motifs (*chapter IV*). Exploiting the parallel use of HB and EB, we have synthesised ribbon, wire-like structures and hetero-molecular dimers.



---

# ***Chapter I***

## ***Introduction***

---

In this chapter, we aim to give the reader an overview of the context in which this manuscript takes its place. Firstly, a brief presentation of the supramolecular toolbox will be made with particular highlight on the nature, geometry and energy of the main non-covalent interactions. Chalcogen-bonding will be discussed in detail from its nature to its application in solution and the solid state.

This chapter is divided in five main sections. *Section I – 1* gives a brief introduction on supramolecular chemistry and the different non-covalent interactions out of the toolbox; *Section I – 2* covers the nature of the chalcogen-bonding interaction and discusses different experimental and theoretical studies on the fundamental component of EBs; *Section I – 3* focuses on the applications of chalcogen-bonding in solution, particularly on ion recognition, organo-catalysis and self-assembly; *Section I – 4* deals with the use of EB in the solid state going through the different recognition motifs, leading to applications such as non-linear optic, optoelectronic, crystal engineering and inclusion compounds; *Section I – 5* presents the outline of the dissertation by identifying the context in which this manuscript takes place and highlighting the objectives of this doctoral work.

## I – 1 Introduction

### I – 1.1 The supramolecular toolbox

In his Nobel lecture,<sup>[1]</sup> *Jean-Marie Lehn* defines supramolecular chemistry as the chemistry beyond the molecules, covering architectures and function of structures formed by association of molecular entities. At the centre of these association processes are recognition and complementarity based on non-covalent interactions. While molecular chemistry rules over the covalent bonds between atoms, the supramolecular chemistry covers the aspect of the interactions between molecules to form entities of higher complexity, supermolecules. Thus, supramolecular chemistry takes its root in the molecular structures that chemists, by the means of molecular chemistry, can program to store the recognition information into to achieve supramolecular architectures.

The recognition information stored into the supramolecular synthons is based on numerous non-covalent interactions out of the supramolecular toolbox (Figure I – 1). The interactions we will cover here are van der Waals interactions,  $\pi$ - $\pi$  interactions, hydrogen-bonding, metal coordination, ion pairing and Secondary Bonding Interactions (SBIs).

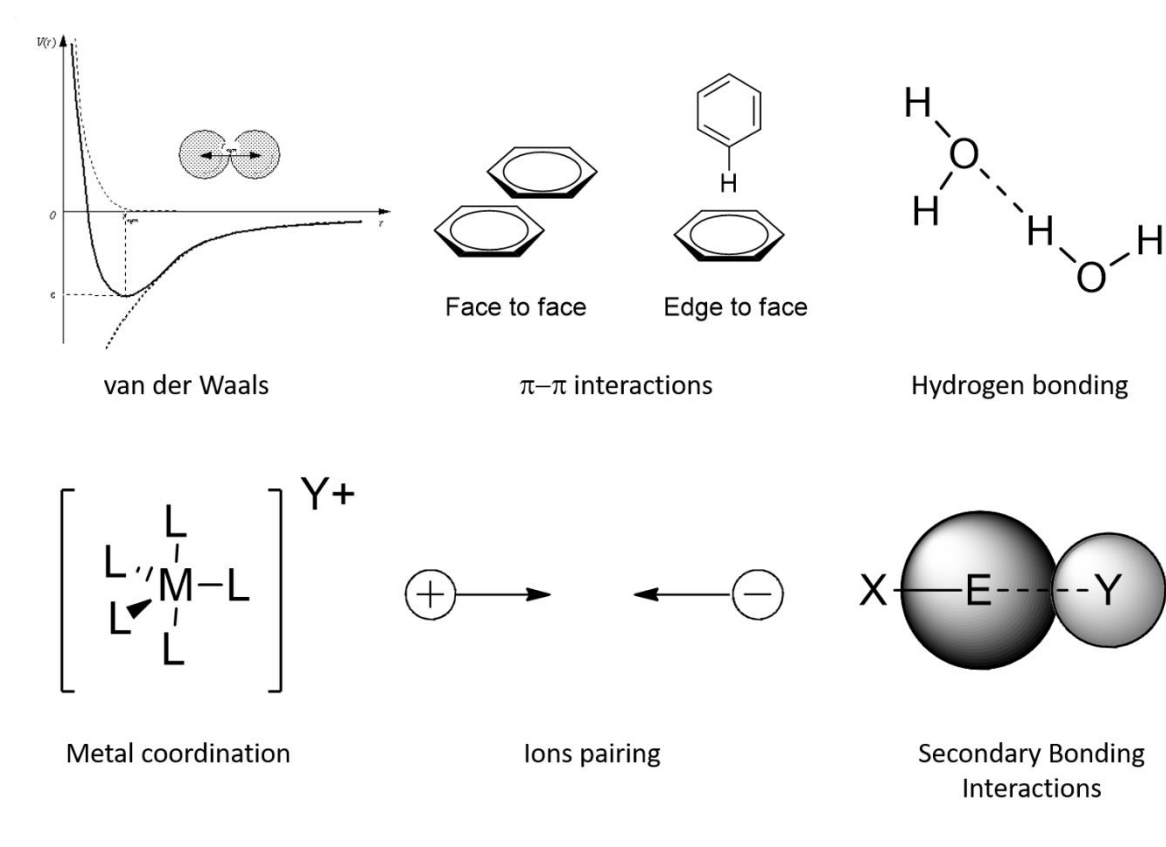


Figure I - 1: Supramolecular toolbox displaying van der Waals,  $\pi$ - $\pi$ , hydrogen-bonding interactions, metal coordination, ion pairing, acid-base Lewis adduct and secondary bonding interactions.

Van der Waals (vdW) interactions are ubiquitous in nature and chemical systems. These forces originate from electrostatic interactions between fluctuating electronic densities of molecules or atoms in close proximity. Originally, vdW interactions included forces between two permanent dipole moments (Debye), permanent dipole moment and induced moment (Keesom) and two induced moments (London). The term has evolved to refer to dispersion interactions.<sup>[2]</sup> Those forces take place at short range and follow the Lennard-Jones potential curve ( $V = A/r^6 - B/r^{12}$ ). The energy corresponding to this interaction range from 0.4 to 4 kJ mol<sup>-1</sup> at a distance of 0.3 to 0.6 nm.<sup>[3, 4]</sup>

Stacking between  $\pi$ -systems is governed by electrostatic and dispersion forces. Aromatic molecules such as benzene usually present a quadrupole behaviour, the  $\pi$ -electron cloud is negatively charged, and the outer rim of H atoms is positive. In a face-to-face complex, two aryls stacking are characterized by an off set. This displacement minimises the Coulomb repulsion between the negative charges and maximise the attractions between the parts of opposite potential. In an edge-to-face complex, the two aryls are perpendicular to each other and interact through CH $\cdots\pi$  contact. Also, the interaction originates mainly from the dispersion energy and the electrostatic contribution is small.<sup>[5-7]</sup> The energy of stacking interaction can rise up to 50 kJ mol<sup>-1</sup>.

Hydrogen-bonding is defined as an attractive interaction between a H atom from a molecule or a molecular fragment D-H (H-bond donor) in which D is more electronegative than H, and an atom or a group of atoms in the same or a different molecule, in which there is evidence of a bond formation.<sup>[8]</sup> Hydrogen-bonding interactions are mostly electrostatic with a H $\cdots$ A distance of 1.5 - 3.5 Å and a D-H $\cdots$ A angle between 90° to 180°. The energy of interaction ranges from 15 to 160 kJ mol<sup>-1</sup>.<sup>[9, 10]</sup> This interaction is not only omni-present in biological systems but has been used in many applications in chemistry and material science.<sup>[11]</sup>

Heteroatoms with a free electronic lone pair have the ability to form coordination complexes with transition metals presenting d orbitals. The strength of the resulting interaction (40 – 120 kJ mol<sup>-1</sup>) is intermediate between other non-covalent and covalent bonds. The metal coordination is thermally labile and features a greater specificity through annealing processes leading to the most thermodynamically favourable structures *via* self-correction. The complex geometry is dictated by the nature of the metal centre and the coordination strength of the ligand. This interaction has been applied to self-assembly in solution<sup>[12]</sup> or on surface,<sup>[13, 14]</sup> 1 and 2D polymeric materials,<sup>[15]</sup> and even in stimuli-responsive supramolecular cages.<sup>[16-21]</sup>

Ion pairing consists in the association of two charged species of opposite charge. This interaction is long range and decreases with the distance ( $r$ ) in a  $1/r$  fashion. The strength of interaction ranges

from 50 to 200 kJ mol<sup>-1</sup>. Ion pairs play a major role in supramolecular chemistry, particularly in aqueous environments. For example, this interaction can exercise a key role in the active centre of enzymes or drive the association of supramolecular capsules formed by macrocycles such as calixarenes.<sup>[6]</sup>

Secondary Bonding Interactions (SBIs) are a family of non-covalent bonds based on a concept first introduced by *Alcock* in 1972:

*“A number of recent crystal structure determinations on compounds of the non-metals have discovered intramolecular distances that are much longer than normal bonds and intermolecular distances that are much shorter than van der Waals distances. It [...] is sufficiently regular and understandable for the name **secondary bond to be appropriate.**”*<sup>[22]</sup>

Even though, the nature of such interaction was not clearly understood, this concept has attracted the interest of many research groups. Examples of SBIs are halogen, chalcogen and pnictogen bond (XB, EB, and PB respectively).<sup>[23-25]</sup> XB and EB interactions will be explored in further detail in the next sections.

## I – 1.2 Halogen-bonding

A particular case of SBI is halogen bonding (XB). This interaction involves a halogen atom (X) with a substituent (R) and a lone pair donor (Y) organised in a linear fashion (R-X...Y angle = 160-180°) with an energy of interaction ranging from 10 to 200 kJ mol<sup>-1</sup>. The nature of the interaction fundamentally resides in three components, the electrostatic, the orbital and the dispersion contributions.<sup>[26-33]</sup> The recommended IUPAC definition is the following:

*“A halogen bond occurs when there is evidence of a net attractive interaction between an electrophilic region associated with a halogen atom in a molecular entity and a nucleophilic region in another, or the same, molecular entity.”*<sup>[34]</sup>

The key part of this definition lies in the electrophilic nature of the halogen involved in the XB interaction. Indeed, contrary to ions in gas phase, the electronic density is anisotropically distributed around the atoms in molecules.<sup>[35]</sup> One can easily observe such behaviour when plotting the Electrostatic Surface Potential (ESP) map at the 0.001 electrons Bohr<sup>-3</sup> isodensity surface. More particularly, if the molecule contains halogen atoms a region of more positive potential appears (positive potential in red and negative in blue, Figure I – 2).<sup>[27]</sup> This region, which is co-linear but opposite to the  $\sigma$ -bond C-X, is called a  $\sigma$ -hole. Moving down the halogen family in the periodic table, the calculated potential becomes more positive (X = F < Cl < Br < I) inferring stronger halogen

bonds. Indeed, the more polarizable the atom, the more anisotropically distributed the charge around it leading to more important  $\sigma$ -hole and a more defined negative belt around the halogen atom. The electrophilic nature is attributed to the  $\sigma$ -hole and the nucleophilic to the negative belt.

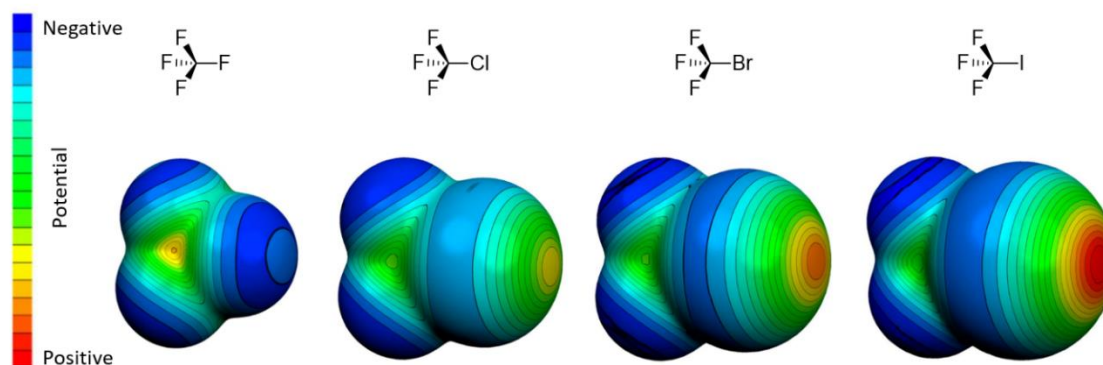


Figure I - 2: Electrostatic Surface Potential maps of  $CF_4$ ,  $CF_3Cl$ ,  $CF_3Br$ ,  $CF_3I$  at the 0.001 electrons Bohr<sup>-3</sup> isodensity surface. Reproduced with permission;<sup>[27]</sup> copyright 2007 Springer.

While looking at the ESP maps (Figure I – 2), one can easily anticipate the formation of an attractive interaction between a small electron rich atom and the positive  $\sigma$ -hole of the heavier halogen atoms. The co-crystal of 4,4'-bipyridyl (**biPy**) and diiodotetrafluorobenzene (**DITFB**) is a striking example of the application of halogen bonding in crystal engineering (Figure I – 3, a).<sup>[36]</sup> The two components assemble in a supramolecular polymer held together by XB interactions ( $d_{N...I} = 2.851$  Å, C-I...N angle = 177°). The ESP maps of the two molecules highlight the positive (in blue) and negative (in red) potential regions for **biPy** and **DITFB** (Figure I – 3, b).

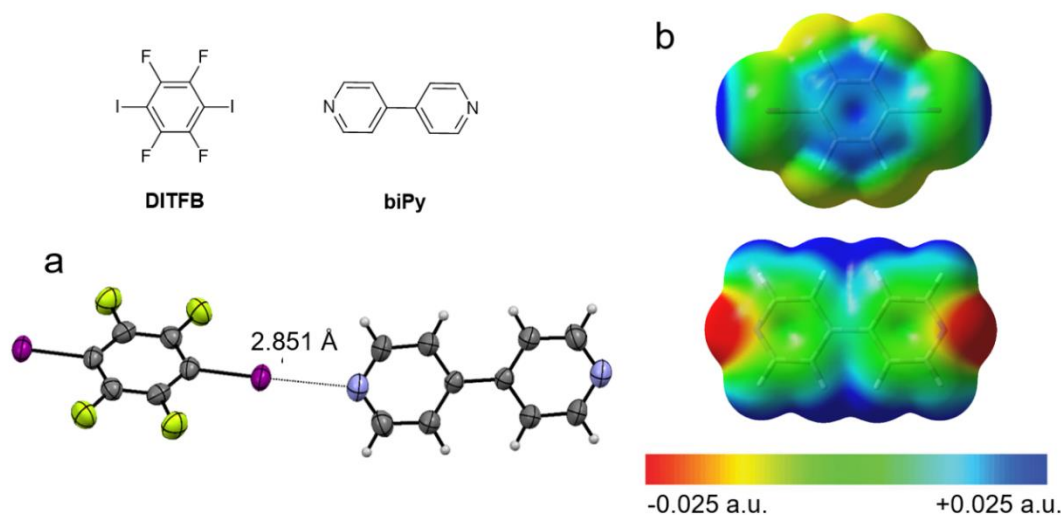


Figure I - 3: a) X-ray structure of co-crystal of **biPy**•**DITFB**;<sup>[36]</sup> b) ESP maps of **DITFB** and **biPy** at the 0.001 electrons Bohr<sup>-3</sup> isodensity surface. Level of theory: B97D3/Def2-TZVP using Gaussian09 including D01 revision.

However, the application of halogen-bonding interactions is limited due high geometrical demand and the high reactivity of the C-X bond (particularly the heavier halogen atoms) in the presence of transition metals. Those drawbacks must be overcome by careful design of the recognition motifs and synthetic planning, usually inserting the XB donor as final step. Therefore, attention has been drawn to the chalcogen family; their ability to form two covalent bonds allows easy insertion in aromatic rings making the resulting compound more stable.

## I – 2 Chalcogen bonding: nature of the interaction

### I – 2.1 Origin of chalcogen-bonding interaction

Chalcogen-bonding has recently attracted the interest of many research groups since its recognition in 2000.<sup>[37-42]</sup> However, a deep understanding of the nature of this SBIs is still required. Similarly to the halogen-bonding interaction, the chalcogen bond (EB) is composed of three energetic contributions: electrostatic, orbital mixing and dispersion. Chalcogen atoms being able to form two covalent bonds, feature two  $\sigma$ -holes as depicted by the ESP maps of 1,2,5-telluradiazole **I-2<sub>Te</sub>** (Figure I – 4).

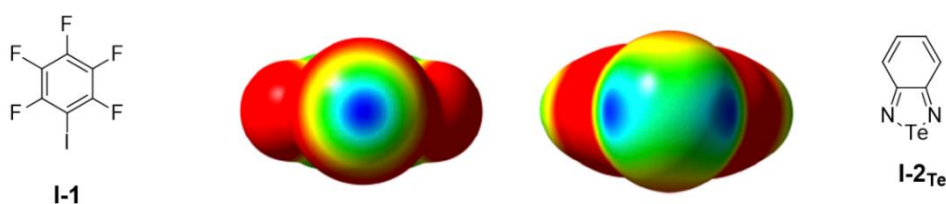


Figure I - 4: Iodopentafluorophenyl **I-1** and 1,2,5-telluradiazole **I-2<sub>Te</sub>** and their respective ESP maps. Level of theory: B97D3/Def2-TZVP. Adapted with permission;<sup>[43]</sup> Copyright 2015 American Chemical Society.

The most studied case of chalcogen bonding is 1,2,5-benzotelluradiazole **I-2<sub>Te</sub>**, which forms infinite ribbons at the solid state through double chalcogen bonding interactions ( $d_{\text{N-Te}} = 2.682\text{-}2.720 \text{ \AA}$ ) with an angle of  $134^\circ$  between the two EBs involving the same Te atom (Figure I – 5).<sup>[44]</sup>

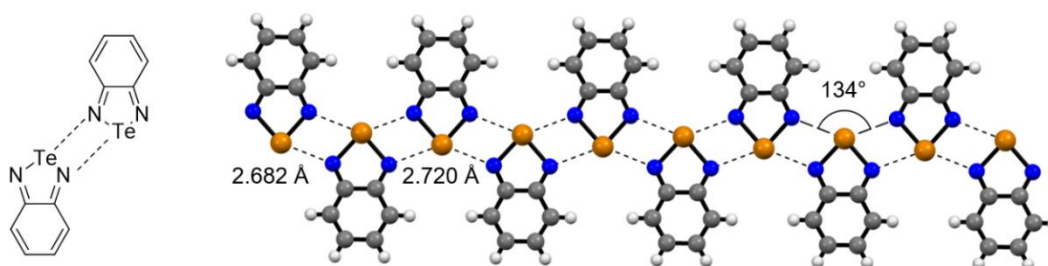
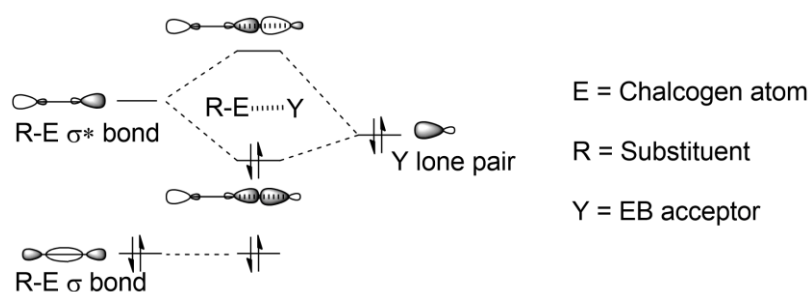


Figure I - 5: X-ray structure of 1,2,5-benzotelluradiazole **I-2<sub>Te</sub>** forming an infinite ribbon at the solid state.<sup>[44]</sup>

However, functionalisation of the benzo-ring often leads to a loss of the association properties in the solid state. This system is also moisture sensitive, addition of water leads to the opening of the telluradiazole moiety. Those drawbacks considerably limit the applications of this array in functional materials.<sup>[45]</sup>

Electrostatic surface potential is a handy tool to design supramolecular synthons based on halogen- and chalcogen-bonding interactions. However, ESP maps do not fully represent the interactions as they focus only on the electrostatic contribution. The second way to rationalise SBIs goes through the evaluation of molecular orbitals. The interaction takes place between R-E and Y (E being the chalcogen atom, R its substituent and Y a small electron rich atom) as the  $\sigma^*$  orbital of R-E overlaps with the  $n$  orbital of a lone pair donor (Scheme I – 1). This explanation accounts for the directionality of the interaction as the overlap is maximised when R, E and Y are perfectly aligned ( $180^\circ$ ).<sup>[46]</sup>



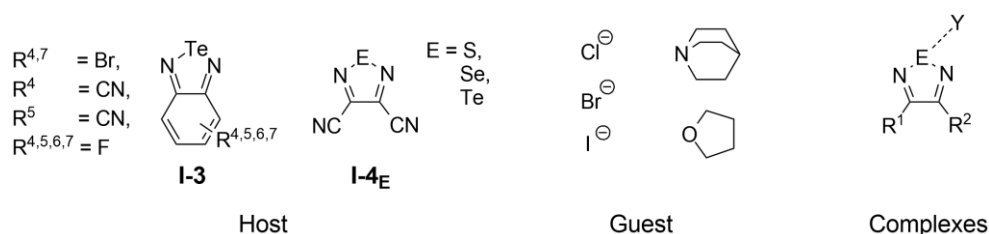
Scheme I - 1: Molecular orbital representation of the chalcogen-bonding interaction.<sup>[39]</sup>

From both bonding models, it is easily understandable that the more electron withdrawing the substituent at the chalcogen atom, the stronger the interaction. EWGs increase the positive potential of the  $\sigma$ -hole and lower the energy level of the LUMO containing the  $\sigma^*$  orbital.<sup>[47]</sup> In addition to two contributions, the omnipresent dispersion energy contributes to the interaction.<sup>[48, 49]</sup> Having in mind these three components, one can clearly understand the tendency of heavier atoms to lead to stronger chalcogen bonds (EB strength  $\text{Te} > \text{Se} > \text{S}$ ). The more polarizable the E atom, the more anisotropically distributed the charge around it (and thus “deeper” the  $\sigma$ -hole), the lower the energy level of the LUMO orbital of interest and the more favourable the dispersion contribution.

## I - 2.2 Chalcogen bonding dominated by electrostatic contribution

*De Vleeschouwer* and *De Proft* have investigated EB using high level computational tools.<sup>[50]</sup> Capitalising on the work of *Taylor, Seferos* and co-workers,<sup>[43]</sup> they decomposed the interaction energy of complexes formed by stoichiometric association of 1,2,5-chalcogenadiazoles (**I-3** and **I-4<sub>E</sub>**) and guests such as halogen anions, quinuclidine and THF (Scheme I – 2). Their results show an energy of interaction ranging from 40 to 200  $\text{kJ mol}^{-1}$  for those system with an angle of interaction

within the range 157-178°. The stronger chalcogen bonds were obtained for the heavier E atoms (E = Te > Se > S) and for more strongly charged EB acceptor (Cl<sup>-</sup> > Br<sup>-</sup> > I<sup>-</sup> > quinuclidine > THF). EBs involving anions are composed, in average, by 53% and 47% of electrostatic and orbital contributions, respectively with negligible dispersion energy. Those formed with neutral Lewis bases are composed, on average, by 57% of electrostatic contribution, 37% of orbital contribution and only 6% of dispersion. Therefore, the electrostatic component of the interaction is slightly favoured in the first cases and clearly dominates in the latter ones.<sup>[50]</sup>

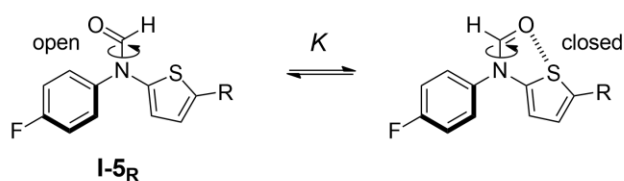


Scheme I - 2: Host-guest interaction through chalcogen-bonding interaction investigated in the computational study of De Vleeschouwer and De Proft.<sup>[50]</sup>

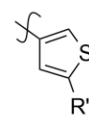
### I – 2.3 Chalcogen bonding dominated by orbital contribution

In order to investigate the origin of the chalcogen-bonding interaction, *Cockroft* and co-workers have engineered and synthesised molecular balances (Figure I – 6). Those are constituted of a thiophene or selenophene unit functionalised in  $\alpha$ - or  $\beta$ -position by a formamide or thioformamide group. Compound **I-5<sub>R</sub>**, **I-7** and **I-8<sub>R</sub>** present two stable conformations in solution exhibiting a chalcogen-bonding interaction (closed conformation) or not (open conformation). The population of the two energetically distinct conformations have been quantified by <sup>19</sup>F-NMR analysis in 13 different solvents leading to the conformational free energy difference,  $\Delta G_{\text{exp}} = -RT \ln(K)$ . Reference  $\beta$ -thiophenes compound **I-6<sub>R</sub>** and **I-9** were evaluated. All experimental data were backed up by DFT calculations at B3LYP/6-311G\*, M06-2X/6-311G\* and  $\omega$ B97X-D/6-311G\* levels of theory.<sup>[51]</sup> Compounds **I-5<sub>R</sub>** and **I-7** preferred the closed conformation in which chalcogen-bonding interactions were present involving O $\cdots$ S or O $\cdots$ Se contacts ( $\Delta G_{\text{exp}}$  ranging from -1 kJmol<sup>-1</sup> to -7.4 kJmol<sup>-1</sup>, detection limit of the method). Notably, the presence of EWG as substituent at the thiophene ring increased the strength of interaction (Me < Cl < COOMe < COMe < CHO) and the stronger EB was observed for the Se-analogue **I-7**.  $\beta$ -Thiophene references **I-6<sub>R</sub>** and **I-9** showed little preference for the closed conformation in which a weak hydrogen bond was observed instead of the chalcogen bond.

## Formamide balances

A  $\alpha$ -thiophenes

R = H, Me Cl, COMe, CHO, COOMe

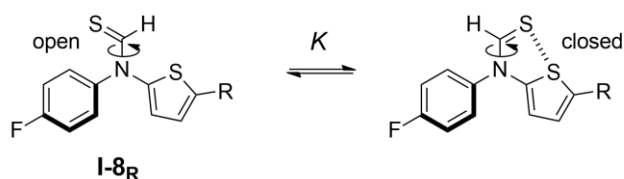
B  $\beta$ -thiophenes**I-6<sub>R'</sub>**

R' = H, Me, CHO

C selenophenes

**I-7**

## Thioformamide balances

D  $\alpha$ -thiophenes

R = H, Me Cl

E  $\beta$ -thiophenes**I-9**

Figure 1 - 6: Molecular balances used by Cockroft and co-workers to investigate chalcogen-chalcogen interactions. Reproduced with permission,<sup>[51]</sup> Copyright 2017 American Chemical Society.

The authors stated that the chalcogen-bonding interaction was found to be solvent independent, indicating no substantial contributions from electrostatic and solvophobic effects. The dispersion corrected calculations combined with this solvent independence showed that van der Waals dispersion forces did not significantly contribute to the trends observed in their study. However, variation in the computed bond lengths and NBO (natural bond orbital) analysis suggested the presence of an electron donation from the lone pair of the O/S atoms to the  $\sigma^*$  orbital of the adjacent chalcogenophenes. This led to the conclusion that the orbital contribution clearly dominates the chalcogen-bonding interactions in those thiophene based molecular balances.<sup>[51]</sup>

## I – 2.4 Chalcogen-bonding dominated by dispersion contribution

*Kumar and Chopra* and co-workers have studied experimentally and theoretically the unusual bifurcated  $E \cdots \pi$  double chalcogen-bonding interaction taking place in cryocrystals of biphenyl-selenide and telluride **I-10<sub>E</sub>**.<sup>[52]</sup> At room temperature, those compounds are yellow/orange liquid and their structure has been determined *via in-situ* cryocrystallisation. The structures are reported in Figure I – 7. Both Se- and Te-atom interact with two phenyl moieties through  $\pi-\sigma^*$  interaction ( $d_{C \cdots Se} = 3.627 \text{ \AA}$  and  $3.691 \text{ \AA}$  for **I-10<sub>Se</sub>** and  $d_{C \cdots Te} = 3.666 \text{ \AA}$  and  $3.732 \text{ \AA}$  for **I-10<sub>Te</sub>**), the aromatic rings giving electrons to the  $\sigma^*$  orbitals of the chalcogen atoms. Those structures have been computationally studied at M06-2X/cc-pVDZ-PP (for Se/Te) and 6-31G\*\* (for the other elements) level of theory using the energy decomposition analysis implemented in the GAMESS program.<sup>[53]</sup> The computational results reveals an energy of dimerization of  $-14.34 \text{ kJ mol}^{-1}$  for **I-10<sub>Se</sub>** and  $-15.26$

$\text{kJ mol}^{-1}$  for **I-10<sub>Te</sub>**. The contribution of the dispersion interactions to the stabilization is 70% and 67% in the Se- and Te-analogues, respectively. The electrostatic contribution is only 23% and 25%, respectively. NBO analysis revealed a contribution ranging between 0.8 and 3.5  $\text{kJ mol}^{-1}$  originating from the overlap of the  $\pi$  and  $\sigma^*$  orbitals (Figure I – 7, c and d). In this case, the dispersion contribution clearly dominates the chalcogen-bonding interaction.<sup>[52]</sup>

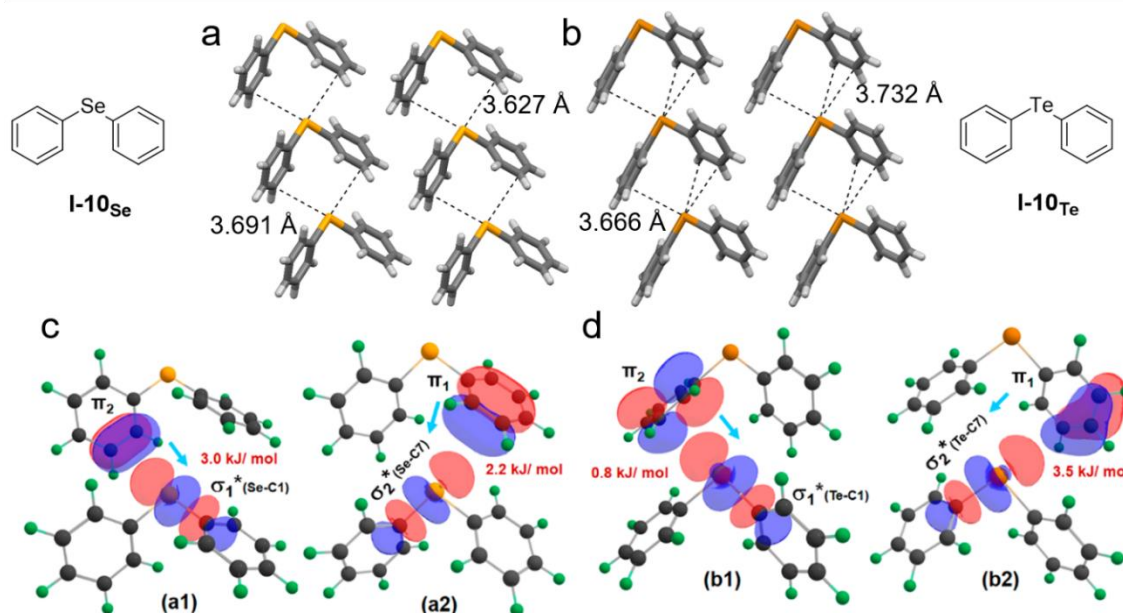


Figure I - 7: X-ray structure of a) diphenyl selenide **I-10<sub>Se</sub>** and b) diphenyl telluride **I-10<sub>Te</sub>**.<sup>[52]</sup> Space group:  $P2_1$ . NBO representation of the charge transfer between the  $\pi$  and  $\sigma^*$  orbitals for c) **I-10<sub>Se</sub>** and d) **I-10<sub>Te</sub>**. Adapted with permission;<sup>[52]</sup> copyright 2018 American Chemical Society.

Those studies clearly show the importance of the three contributions (electrostatic, orbital mixing and dispersion) to the chalcogen-bonding interaction. None of them should be excluded while engineering EB-based systems even though one can prevail over the other depending on the supramolecular structure.

## I – 3 Chalcogen bonding at work: applications in solution

### I – 3.1 Anion recognition

#### I – 3.1.1 Anion binding involving single chalcogen bond

In the recent literature, research on chalcogen-bonding interactions has been mainly focused on solution-state applications, particularly anion recognition.<sup>[37, 54]</sup> In this sub-section we present the most notable studies. The first example of anion recognition using an EB-based guest molecule was described by *Zhao* and *Gabbai* in 2010.<sup>[55]</sup> Using a polydentate Lewis acid, they report on the synthesis of naphthalene derivative **I-11** bearing telluronium and borane functionalities (Figure I – 8). A binding constant of  $750 \text{ M}^{-1}$  for  $\text{F}^-$  could be calculated by UV-vis titration of **I-11** with KF in

MeOH (Figure I – 8, b). The chalcogen-bonding interaction was further confirmed by  $^{19}\text{F}$ - and  $^{125}\text{Te}$ -NMR analysis displaying a coupling of those nuclei. However, treatment of **I-11** with other anion ( $\text{Cl}^-$ ,  $\text{Br}^-$ ,  $\text{I}^-$ ,  $\text{OAc}^-$ ,  $\text{NO}_3^-$ ,  $\text{H}_2\text{PO}_4^-$  and  $\text{HSO}_4^-$ ) did not produce any shift in the absorption spectrum showing a selectivity of the system for  $\text{F}^-$  binding. This study was further supported by X-ray structure of the resulting complex (Figure I – 8, b). The fluoride anion sits in between the Te and B atoms ( $d_{\text{F}\dots\text{Te}} = 2.506 \text{ \AA}$ ,  $\text{C-Te}\cdots\text{F}$  angle =  $174^\circ$  and  $d_{\text{F}\dots\text{B}} = 1.514 \text{ \AA}$ ). Similar structure could be obtained for the corresponding S-analogue even if no binding to  $\text{F}^-$  could be detected in solution by spectroscopy measurements.

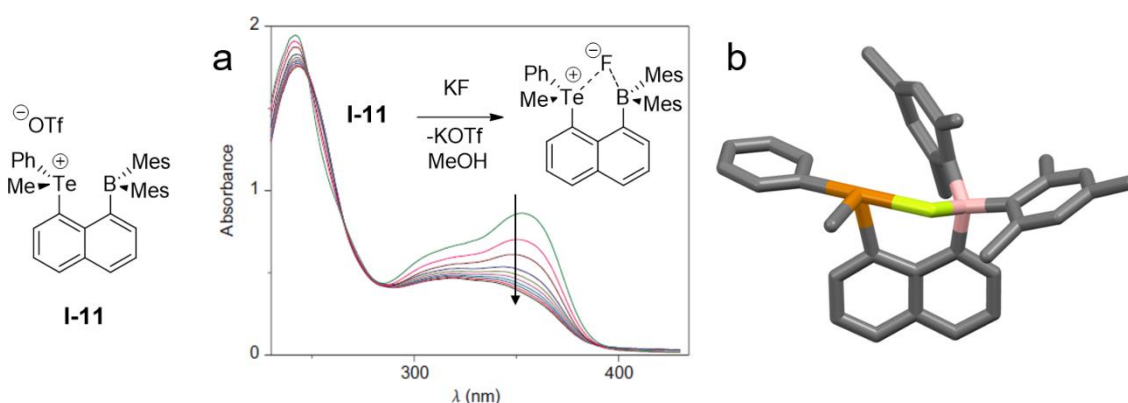


Figure I - 8: Naphthalene derivative **I-11** bearing telluronium and borane functionalities. a) UV-vis absorption spectra recorded during the titration of **I-11** with  $\text{KF}$  in  $\text{MeOH}$ ; b) X-ray structure of the complex structure with  $\text{F}^-$ . Adapted with permission,<sup>[55]</sup> copyright 2010 Springer Nature.

In 2011, Zibarev and co-workers published the first chalcogen bonding driven anion binding in solution with a neutral guest molecule.<sup>[56]</sup> In an attempt to synthesise chalcogen-nitrogen  $\pi$ -delocalised radical anions from 3,4-dicyano-1,2,5-selenadiazole **I-12** by reduction with thiophenolate, ‘hypercoordination’ complex **I-13** was formed (Figure I – 9, a). The chalcogen-bonding interaction was characterised in solution by UV-vis absorption and the free energy of association estimated in THF and MeCN to  $-27.6 \text{ kJ mol}^{-1}$  and  $-19.6 \text{ kJ mol}^{-1}$ , respectively. Complex **I-13** has been further characterised at the solid state by X-ray diffraction. The crystal structure (Figure I – 9, b) highlights the chalcogen-bonding interaction between thiophenolate and the selenadiazole derivatives ( $d_{\text{S}\dots\text{Se}} = 2.722 \text{ \AA}$ ,  $\text{C-Se}\cdots\text{S}$  angle =  $175^\circ$ ). This study has been expanded by the same group over the subsequent years.<sup>[57, 58]</sup>

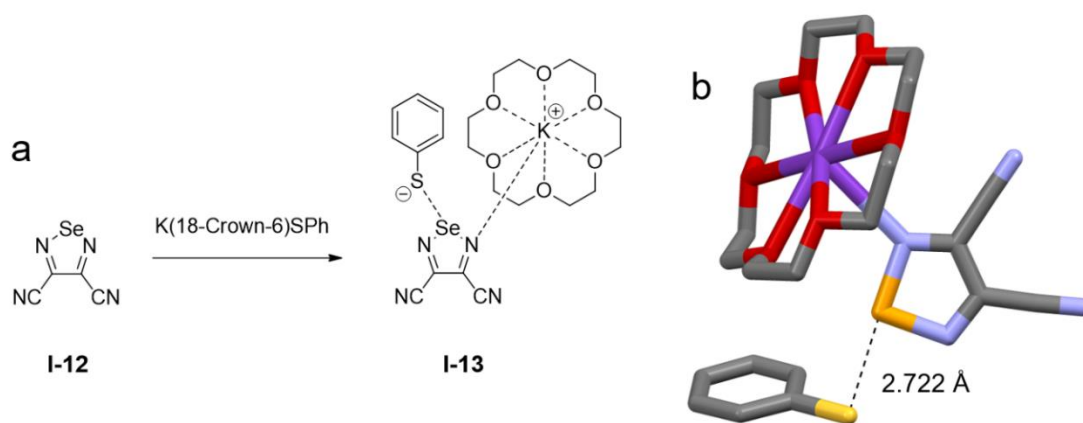


Figure I - 9: a) Formation of complex **I-13** from 3,4-dicyano-1,2,5-selenadiazole **I-12** upon addition of K(18-Crown-6)SPh; b) X-ray structure of complex **I-13**. Space group  $P2_1/n$ .

However, the first systematic and comprehensive study of anion binding through chalcogen-bonding interactions in solution was performed by Taylor, Seferos and co-workers only few years later.<sup>[43]</sup> The authors report on the synthesis of chalcogenadiazole units **I-2**, **I-3**, **I-4** and **I-14<sub>E</sub>** and their titration with anions in different organic solvents using UV-vis absorption method (Figure I – 10). Experimental association constant up to 130 000 M<sup>-1</sup> were measured. The data revealed to be in good agreement with the computational study carried out at B97-D3/def2-TVZP with the PCM model to account for solvent effects. The strongest chalcogen bonds have been observed for electron poor 1,2,5-telluradiazole derivatives **I-3<sub>F</sub>** ( $K_a = 130\ 000\ \text{M}^{-1}$  for Cl<sup>-</sup> and 9 800 M<sup>-1</sup> for Br<sup>-</sup>). Notably, association constant of 96 M<sup>-1</sup> with neutral host **I-3<sub>F</sub>** and quinuclidine as guest have been measured.<sup>[43]</sup>

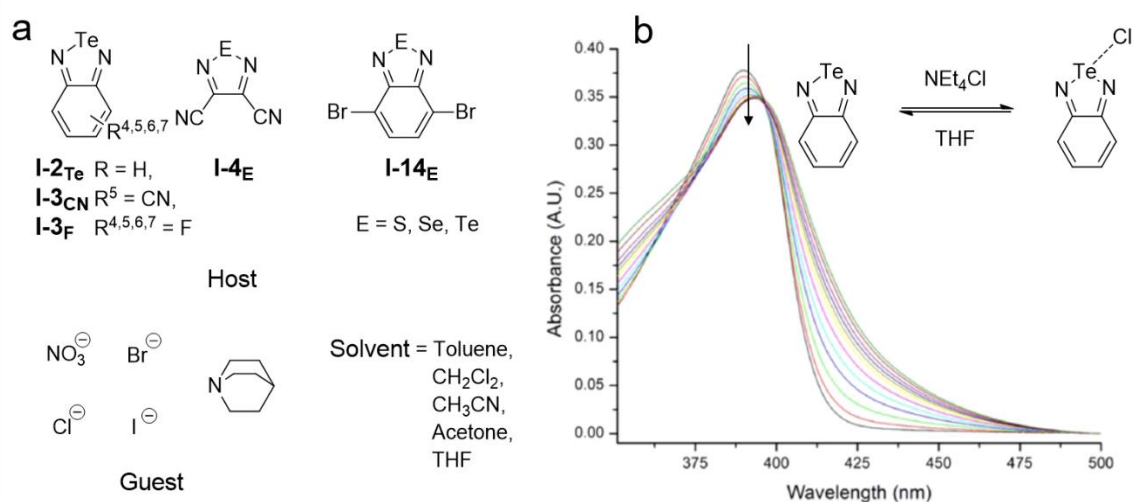


Figure I - 10: a) Host molecules **I-2**, **I-3**, **I-4<sub>E</sub>** and **I-14<sub>E</sub>** and anion guest used in titration experiment in different solvents performed by Taylor, Seferos and co-workers; b) UV-vis spectra acquired during the titration of **I-1<sub>H</sub>** with TBAC in THF. Adapted with permission,<sup>[43]</sup> copyright 2015 American Chemical Society.

## I – 3.1.2 Anion binding involving two chalcogen bonds: confocal approach

Capitalizing on a tellurophene motif, *Taylor, Seferos* and co-workers achieved anion recognition through multiple chalcogen-bonding interactions.<sup>[59]</sup> Molecule **I-16** was designed to bind halogen anions to both Te atoms in a pincer-like fashion (Figure I – 11, a). However, the association constant observed for Cl<sup>-</sup> was lower than that of monodentate **I-3<sub>F</sub>** ( $K_a = 2\,290\text{ M}^{-1}$  and  $130\,000\text{ M}^{-1}$ , respectively). Reference molecule **I-15**, which contains only one Te atom, show a lower binding ability ( $K_a = 310\text{ M}^{-1}$  for Cl<sup>-</sup>), roughly one order of magnitude lower compared to that of **I-16**.

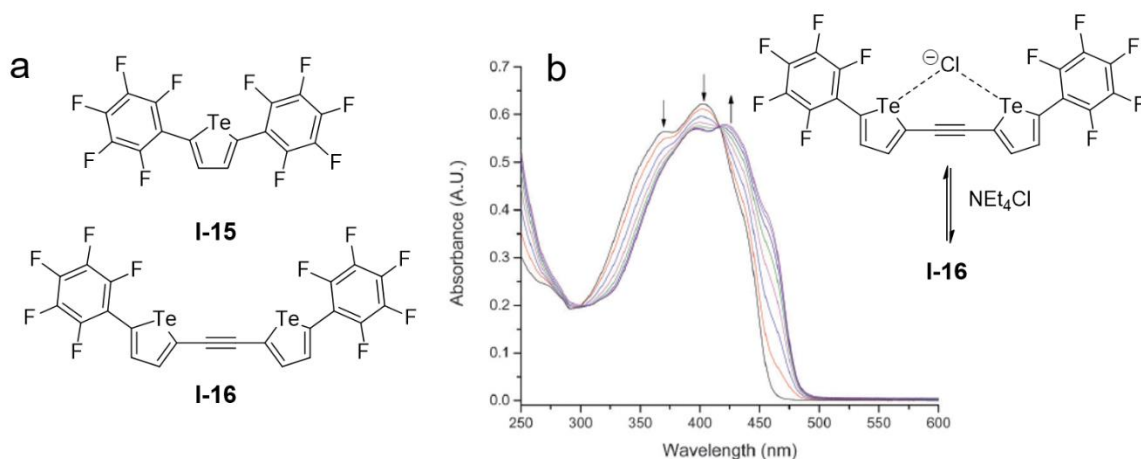
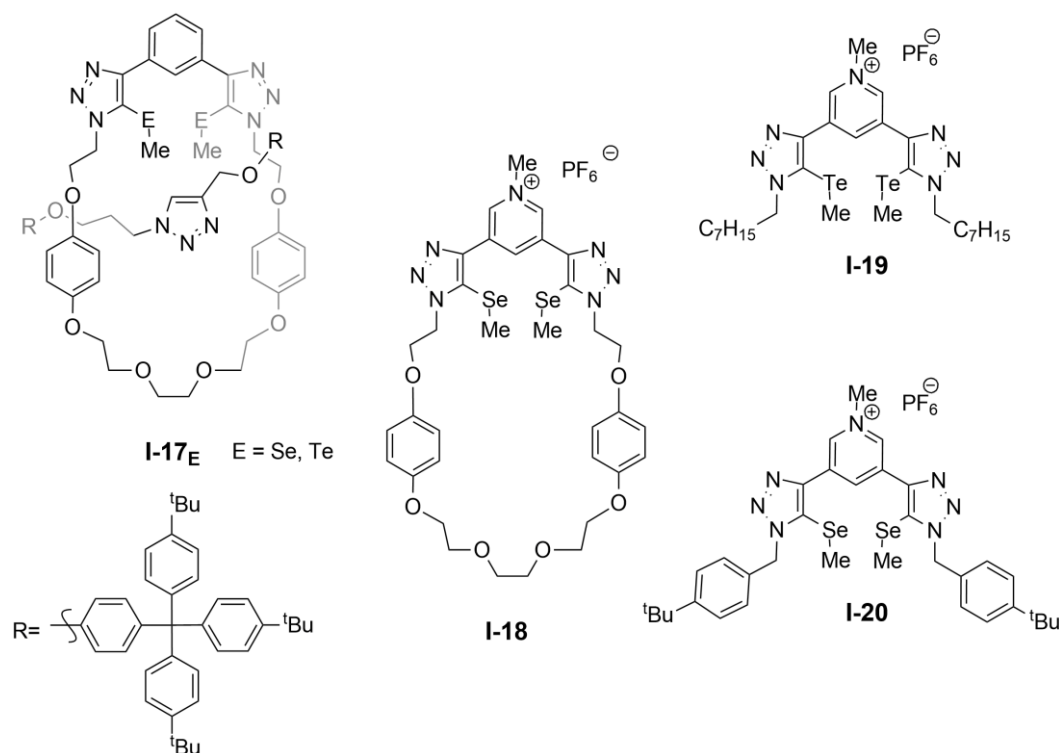


Figure I - 11: a) Tellurophene based chalcogen bond donor **I-15** and **I-16** developed by *Taylor, Seferos* and co-workers; b) UV-vis spectra acquired during the titration of **I-16** by TBAC.<sup>[59]</sup> – Published by The Royal Society of Chemistry.

*Beer* and co-workers reported on the synthesis of [2]rotaxanes **I-17<sub>E</sub>** bearing two 5-(methylchalcogeno)-1,2,3-triazole moieties (Scheme I – 3). Those supramolecules showed anion binding in solution. Particularly, **I-17<sub>Te</sub>** associate with SO<sub>4</sub><sup>2-</sup> with a constant of  $1\,130\text{ M}^{-1}$  in acetone. The Se-analogues could be methylated at the three triazole positions and the resulting salt showed a threefold enhancement of the association constant for SO<sub>4</sub><sup>2-</sup> in acetone ( $K_a = 3\,531\text{ M}^{-1}$ ).<sup>[60]</sup> To further understand the thermodynamics of anion binding by EB receptors, the same group synthesised the 5-(methylchalcogeno)-1,2,3-triazole based molecules **I-18**, **I-19** and **I-20** (Scheme I – 3). Those compounds showed association energies ( $\Delta G$ ) with different halides (Cl<sup>-</sup>, Br<sup>-</sup> and I<sup>-</sup>) in MeCN or acetone ranging from  $-12.9\text{ kJmol}^{-1}$  to  $-20.2\text{ kJmol}^{-1}$ . Interestingly, a strong enthalpic contribution for anion binding with **I-19** was observed in MeCN and gradually increases for larger halogens. Entropy is favourable to the association energy for Cl<sup>-</sup>, negligible for Br<sup>-</sup> and unfavourable for I<sup>-</sup>. In result of those two energetic components,  $\Delta G$  decreases for larger anions.<sup>[61]</sup>



Scheme I - 3: 5-(methylchalcogeno)-1,2,3-triazole based molecules **I-17<sub>E</sub>**, **I-18**, **I-19** and **I-20** used in the studies of Beer and co-workers. <sup>[60, 61]</sup>

Capitalising on the 5-(methylchalcogeno)-1,2,3-triazole motif, Beer and co-workers synthesised foldamers bearing four halogen/chalcogen-bonding sites per unit. Those molecules associate into dimeric structures, creating an interaction pocket presenting eight XB/EB acceptors and bind anions in water, with an extremely high I<sup>-</sup> affinity.<sup>[62]</sup> Recently, the same group reported the recognition of dicarboxylate isomer guest species by bi-naphthalene receptor molecules bearing HB, XB and EB binding sites. The complexes formed with different regio-isomers (phthalic and isophthalic acids) exhibit a diagnostic fluorescence response.<sup>[63]</sup>

Matile and co-workers conceptualised a confocal chalcogen-bonding approach in order to build anion binder molecules (Figure I – 12, b and c).<sup>[64]</sup> Molecules **I-21** has been engineered presenting a bithiophene unit functionalised with sulfone and two nitrile moieties as EWG enhancing the Lewis acidity of the S atoms (Figure I – 12, a). **I-21** showed a dissociation constant ( $K_D$ ) of 1.13 mM for the complex formed with Cl<sup>-</sup>. As application, the derivative was included in large unilamellar vesicles and the anion transport ability was assessed by measuring the acceleration of the dissipation of a pH gradient. The efficiency was quantified by the effective concentration required to reach 50% of the maximal activity ( $EC_{50} = 1.9 \mu\text{M}$  for **I-21**). Capitalising on those results, the same group synthesised molecule **I-22** (Figure I – 12, d), which features an  $EC_{50}$  of 0.28  $\mu\text{M}$ , one order of magnitude lower than that of **I-22**.<sup>[65]</sup> In a very recent work, they report that anion transport could

also been achieved through pnictogen bonding interactions and has been compared to XB and EB.<sup>[66]</sup>

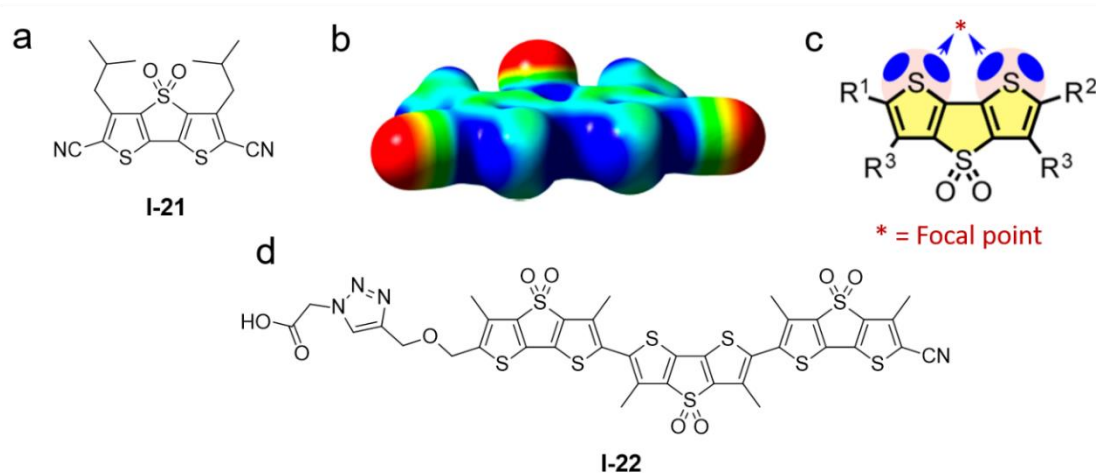


Figure I - 12: Molecule **I-21** used by Matile and co-workers in anion binding and anion transporting experiments; b) ESP map of **I-21**, level of theory: M062X/6-311G\*\*); c) representation of the confocal approach; Molecule **I-22** used in anion transporting experiments.<sup>[65]</sup> Adapted with permission;<sup>[64]</sup> copyright 2016 American Chemical society.

### I – 3.2 Catalysis

In the literature, a few examples of non-covalent catalysis using chalcogen-bonding interactions have been reported. In this section, we report the more recent works.

#### I – 3.2.1 Hydrogenation transfer reactions

Capitalising on the success of anion recognition and transport of the dithienothiophenes derivative **I-21**, Matile and co-workers envisaged the use of those compounds in organo-catalysis. A binding energy of  $-33.9 \text{ kJ mol}^{-1}$  was computed (level of theory: M062X/6-311G\*\*) for the association of **I-21** (displaying Me group in the place of *i*-Bu) and pyridine, which N atom sits at the focal point of  $\sigma$ -holes (Figure I – 13, a). Based on this prediction, the transfer hydrogenation of quinolines was envisaged. Different dithienothiophenes derivatives were synthesised and tested as catalyst for this transformation. Compound **I-23** (Figure I – 13, b) presents the highest rate enhancement for the reduction of quinoline and imine ( $k_{cat}/k_{unecat} = 1\ 290$  and  $335$ , respectively; Figure I – 13, d and e).<sup>[67]</sup> In a subsequent study, the same group developed benzodiselenazoles **I-24** as a stronger chalcogen bond donor, anticipating further augmentation of the catalytic activity. This compound was tested in the reduction of quinoline and showed a rate enhancement several orders of magnitude higher ( $k_{cat}/k_{unecat} = 1.5 \cdot 10^5$ ) compared to that of **I-23**.<sup>[68]</sup>

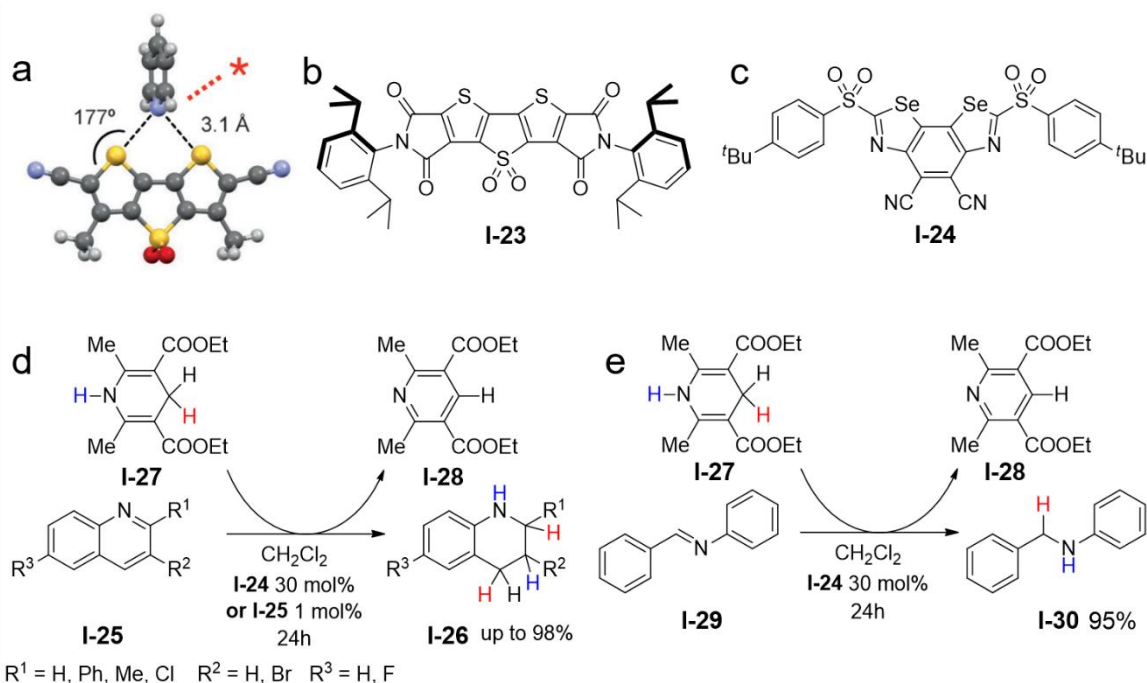
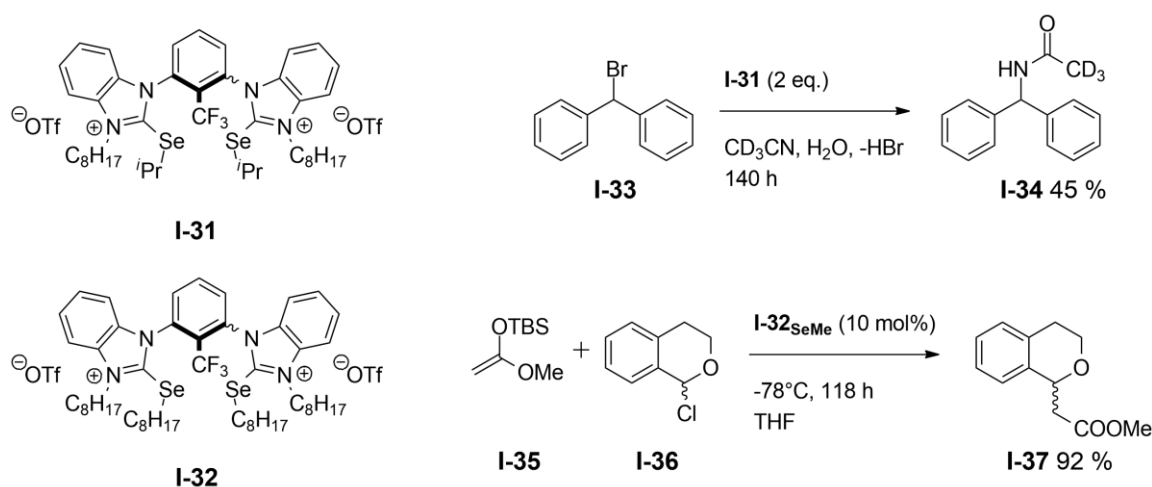


Figure I - 13: a) optimised geometry of the complex formed by pyridine and **I-21** (Me in place of *i*-Bu); b) structure of dithienothiophene based catalyst **I-23**; c) structure of benzodiselenazole based catalyst **I-24**; d) catalysed reduction of quinoline and e) imine.<sup>[67, 68]</sup> Adapted with permission;<sup>[67]</sup> copyright 2017 Willey-VCH Verlag GmbH & Co. KGaA, Weinheim.

### I – 3.2.2 Halide abstraction reactions

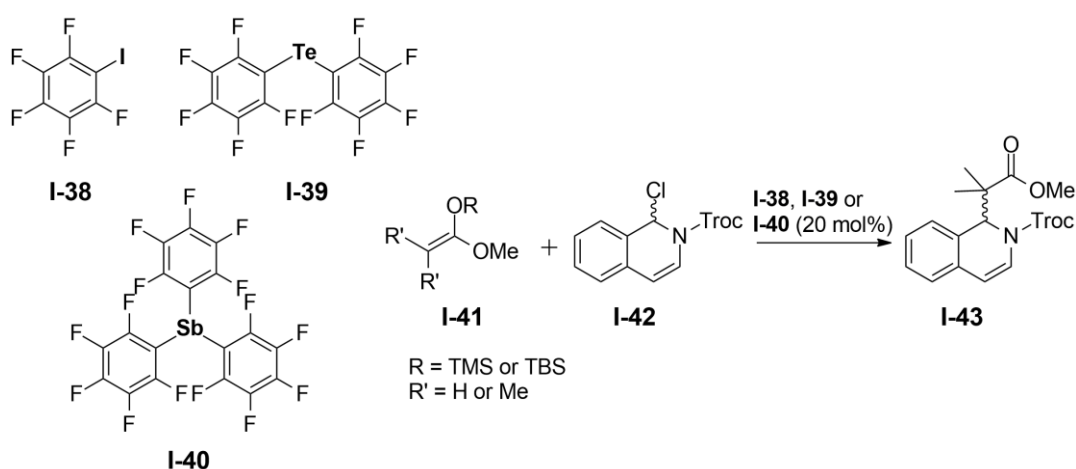
In 2017, *Huber* and co-workers also reported catalytic halide abstraction by Se-based chalcogen bond donors as Lewis acids.<sup>[69, 70]</sup> The design of the catalyst relies on a bis(benzimidazolium) scaffold exhibiting alkyl selenide (Scheme I – 4) follow a confocal approach for the recognition. In an early study, **I-33** could be transformed into **I-34** with a yield of 45% in the presence of two equivalent of **I-31** in *d*<sub>3</sub>-MeCN over 140h.<sup>[69]</sup>



Scheme I - 4: Catalyst **I-31** and **I-32** used by *Huber* in halide extraction reaction. <sup>[69, 70]</sup>

Afterward, chloro-compound **I-36** could undergo halide abstraction at  $-78^{\circ}\text{C}$  in the presence of **I-32** in 10 mol% and react with **I-35** to lead to the formation of **I-37** in 92% over a period of 118h.<sup>[70]</sup> However, both catalysts are outclassed by their halogen bond donor counterpart (I in the place of the alkyl selenide) in those reactions.<sup>[69, 70]</sup>

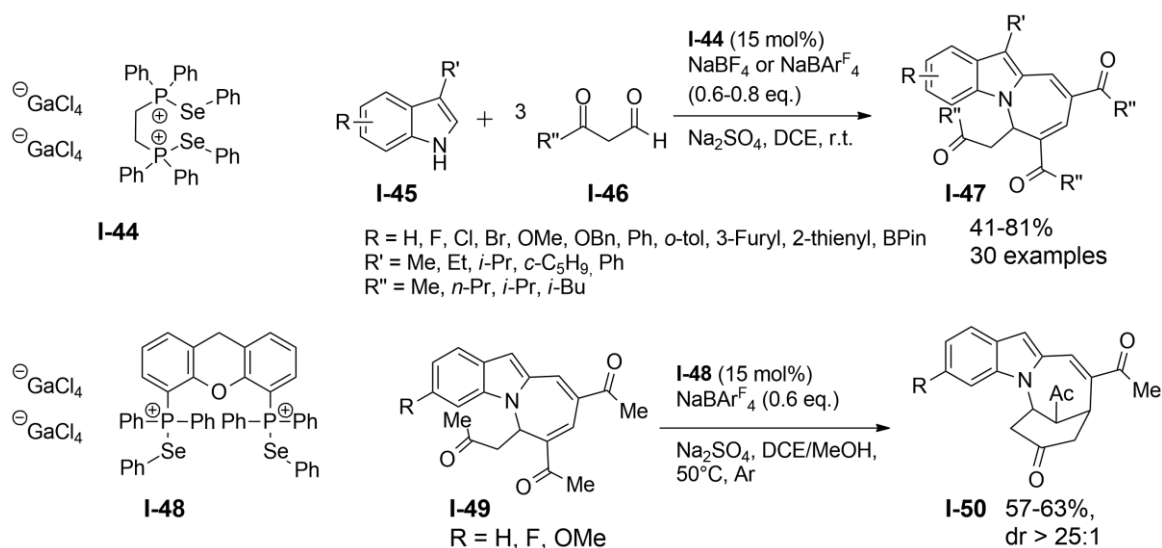
In a similar chloride abstraction reaction, *Matile* and co-workers compared halogen, chalcogen and pnictogen bonding based catalyst.<sup>[23]</sup> Molecules **I-38**, **I-39** and **I-40** substituted with pentafluorophenyl at the heavy atom have been synthesised and tested in the reaction between **I-41** and quinoline **I-42** (treated with Troc chloride). I- and Te- derivatives both increased the rate of the reaction of 50-fold ( $k_{\text{cat}}/k_{\text{uncat}} = 50$  and 52, respectively). On the opposite, Sb-compound **I-40** showed a much higher enhancement ( $k_{\text{cat}}/k_{\text{uncat}} = 4090$ ).<sup>[23]</sup>



Scheme I - 5: Catalysts **I-38**, **I-39** and **I-40** used by *Matile* and co-workers in the chloride abstraction reaction forming **I-43**.<sup>[23]</sup>

### I – 3.2.3 Ring formation

Very recently, *Wang* and co-workers reported on unprecedented reactivity triggered by chalcogen-bonding mediated catalysis.<sup>[71]</sup> Catalyst **I-44** was rationally designed and shown to activate linear ketones. The authors described the assembly of one indole and three  $\beta$ -ketoaldehydes molecules into seven-membered N-heterocycle **I-47** (Scheme I – 6). The reaction proceeds through sequential EB enabled additions and a final dehydration step. To further probe the reactivity of ketone activated by chalcogen-bonding interactions, the intramolecular cyclisation of compound **I-49** was triggered in the presence of **I-48** and formed **I-50** (Scheme I – 6). Catalyst **I-48** interact with a secondary ketone of **I-49** to form an enol that reacts with a double bond of the seven membered ring.<sup>[71]</sup>



Scheme 1 - 6: Catalysts **I-44** and **I-48** developed by Wang and co-workers and used to form **I-47** and **I-50**.<sup>[71]</sup>

### I – 3.3 Self-assembly in solution

#### I – 3.3.1 Micellar structures in water

Despite the power of chalcogen bonding revealed by anion binding and catalysis, no self-assembled complex architecture in solution were reported in the literature. It is only in 2018, that Yan and co-workers published the first supramolecular structure based on EB interaction in solution.<sup>[72]</sup>

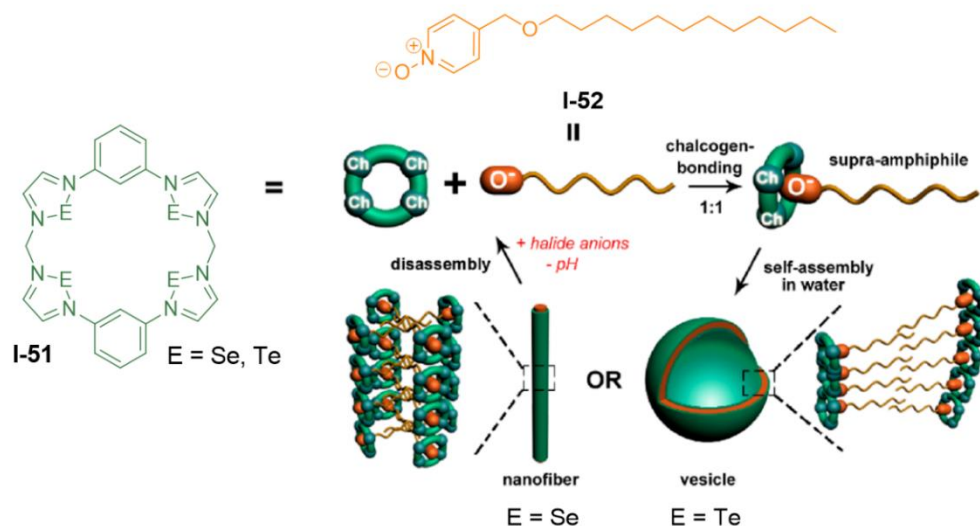


Figure I - 14: Quasi-calix[4]-chalcogenadiazole **I-51<sub>E</sub>** and surfactant **I-52** used by Yan and co-workers to build reversible nanofibers and spherical vesicle. Reproduced with permission;<sup>[72]</sup> copyright 2018 American Chemical Society.

Building on a quasi-calix[4]-chalcogenadiazole **I-51<sub>E</sub>** as multi-site chalcogen bond donor and pyridine *N*-oxide **I-52** bearing a 4-dodecyl chain as an acceptor, the two molecules associate to form

a supra-amphiphile. This supramolecule assembles into different structures in aqueous solution based on the strength of the chalcogen-bonding interactions. Compound **I-51<sub>Se</sub>** leads to the formation of nanofibers with a uniform radial diameter of 6.5 nm, observed by transmission electron microscopy (TEM). Te-analogue, **I-51<sub>Te</sub>** forms with **I-52** spherical micelles characterised by a critical micellar concentration (CMC) of 3.4  $\mu\text{M}$ . TEM imaging showed a size ranging from 40 to 130 nm for those micelles with a membrane thickness of 5.9 nm (obtained by SAXS measurement). The non-covalent interaction between **I-51<sub>E</sub>** and **I-52** was further confirmed by UV-vis, NMR and mass spectroscopy and isothermal titration calorimetry (ITC;  $K_a = 7.2 \cdot 10^5 \text{ M}^{-1}$  for **I-51<sub>Te</sub>** and  $1.4 \cdot 10^5 \text{ M}^{-1}$  for **I-51<sub>Se</sub>**).<sup>[72]</sup> Exploiting the reversibility of the chalcogen-bonding interaction, the spherical micelles could be disassembled by addition of halogen anions ( $\text{Cl}^-$  or  $\text{Br}^-$ ) or by decreasing the pH of the solution.

### I – 3.3.2 Supramolecular capsules

*Diederich* and co-workers have very recently published molecular capsules based on chalcogen-bonding interactions.<sup>[73]</sup> Those supramolecular arrangements are based on resorcin[4]arene cavitands containing telluradiazoles units (Figure I – 15, a) that dimerise through 16 EBs. The structure has been characterised in the solid state by X-ray diffraction analysis and in solution by variable-temperature NMR and quantitative electrospray ionisation mass analysis. The association constant for this structure has been calculated at  $2.9 \cdot 10^7 \text{ M}^{-1}$ .

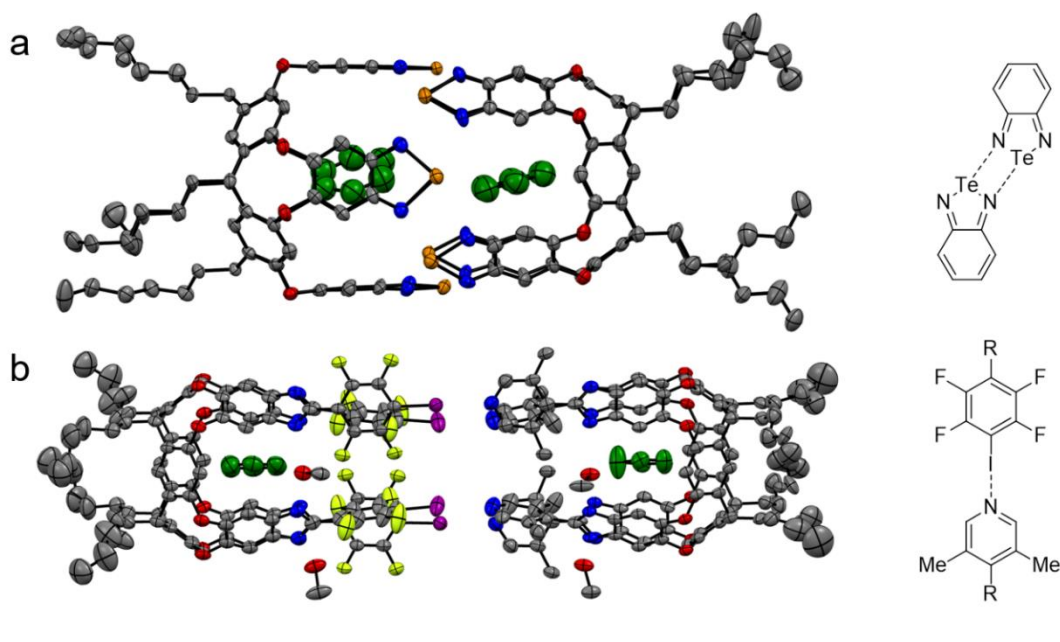


Figure I - 15: Molecular capsules by a) chalcogen-bonding and b) halogen-bonding interactions in ORTEP representation developed by *Diederich* and co-workers, H atoms are omitted for clarity.<sup>[73, 74]</sup> Space groups:  $C2/c$  and  $P2_1/c$ , respectively.

The crystal structure shows the two hemispheres hold together by means of strong chalcogen bonds ( $d_{N\dots Te} = 2.6 - 2.9 \text{ \AA}$ ) arranged in a circular array. Two benzene molecules are trapped inside the capsule. The S analogue has also been synthesised and crystallised. Weaker interactions are observed in solution ( $K_a = 786 \text{ M}^{-1}$ , determined by  $^1\text{H-NMR}$  analysis). Two different structures were obtained depending on the solvent of crystallisation. Benzene and toluene yielded a shifted capsule featuring 12 EBs ( $d_{N\dots S} = 3.0 - 3.5 \text{ \AA}$ ) and encapsulating two solvent molecules. Crystals obtained from  $\text{CH}_2\text{Cl}_2$  do not present the capsular assembly or any chalcogen bonds, instead the molecules arrange in an interlocked 1D polymeric assembly featuring  $\pi-\pi$  stacking interactions ( $d_{\pi-\pi} = 3.4 \text{ \AA}$ ).<sup>[73]</sup> The capsules based on halogen-bonding synthesised by the same group can be used as comparison point (Figure I – 15, b).<sup>[74, 75]</sup> Those features an association constant of  $5370 \text{ M}^{-1}$  in solution (determined by  $^1\text{H-NMR}$  analysis) for four cooperative XB interactions. The X-ray structure shows the hemisphere of the molecular capsule held together by halogen-bonding interactions ( $d_{N\dots I} = 2.82 \text{ \AA}$ ) and two solvent molecules.

## I – 4 Chalcogen-bonding at work: applications at the solid state

### I – 4.1 Chalcogenodiazole: infinite ribbon vs discrete assembly

The reference bonding motif for solid-state application and crystal engineering is 1,2,5-chalcogenodiazole. Unsubstituted benzotelluradiazoles **I-2<sub>Te</sub>** assembles in ribbon at the solid state (Figure I – 5).

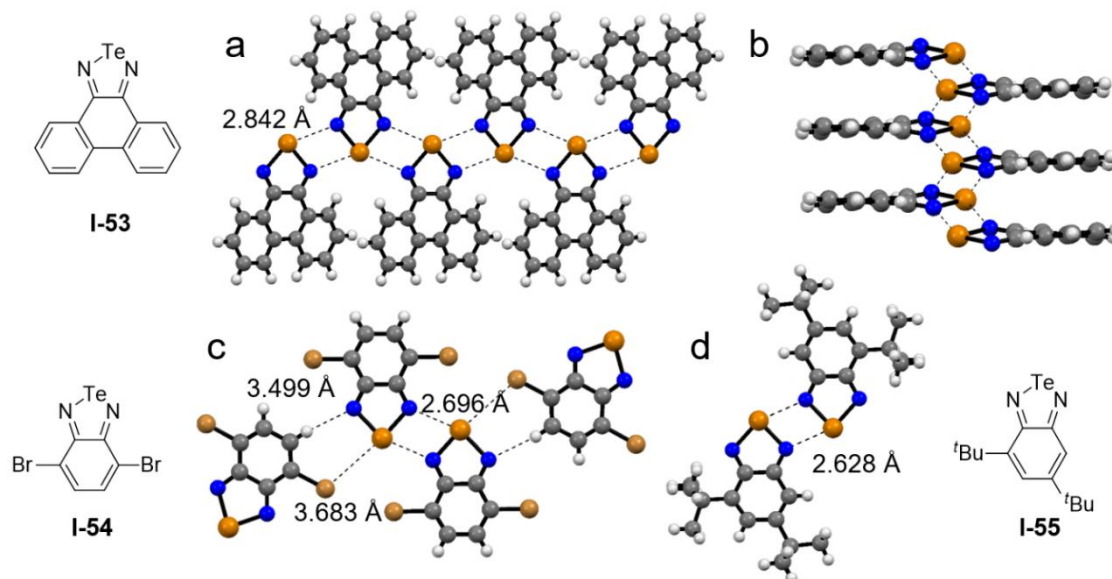


Figure I - 16: X-ray structure of 1,2,5-telluradiazole derivatives in ball and stick representation, a) top view of **I-53**;<sup>[76]</sup> b) side view of **I-53**; c) top view of **I-54**;<sup>[44]</sup> d) top view of **I-55**.<sup>[77]</sup> Space group:  $P\bar{1}$  (**I-53**),  $P2_1/c$  (**I-54**) and  $P2_1/n$  (**I-55**).

Over the years, this moiety has been derived in different structures, for example, phenanthro[9,10- $\gamma$ ][1,2,5]telluradiazole **I-53** synthesised by *Neidlein et al.*<sup>[76]</sup> fuses a phenanthro and a telluradiazole groups. The X-ray diffraction analysis (Figure I – 16, a) reveals the formation of a ribbon through multiple chalcogen-bonding interactions ( $d_{N\dots Te} = 2.842 \text{ \AA}$ ). However, the molecules do not lie in the same plane due to the bulk of the phenantro- moiety (Figure I – 16, b), this steric repulsion is offset by the strength of the EB interactions. On the contrary, di-bromo derivative **I-54** do not form a ribbon structure, but a dimer in the solid state (Figure I – 16, c) formed by double chalcogen bonds ( $d_{N\dots Te} = 2.696 \text{ \AA}$ ).<sup>[44]</sup> In this case, Br $\cdots$ Te short contacts are featured ( $d_{Br\dots Te} = 3.683 \text{ \AA}$ ) in addition of HBs ( $d_{N\dots C} = 3.499 \text{ \AA}$ ). Increasing the steric demand, di-tert-butyl derivative **I-55** arranges in discrete dimers at the solid state (Figure I -16, d) presenting a double EB interactions ( $d_{N\dots Te} = 2.628 \text{ \AA}$ ).<sup>[77]</sup>

Capitalizing of those results, *Vargas-Baca* and co-workers engineered non-centrosymmetric crystals, featuring non-linear optical (NLO) response, based on functionalised benzotelluradiazole unit.<sup>[78]</sup> Molecules of **I-56** arrange in a 1D flat ribbon at the solid state (Figure I – 17, a) through double chalcogen-bonding interactions ( $d_{N\dots Te} = 2.689 - 2.792 \text{ \AA}$ ). In a second dimension, HBs take place ( $d_{O\dots C} = 3.162 \text{ \AA}$ , C-H $\cdots$ O angle =  $119^\circ$ ), binding the ribbon together. The authors computed the optical properties of the resulting crystal highlighting NLO responses. Unsubstituted **I-2<sub>Te</sub>** show a static hyperpolarizability ( $\langle\beta\rangle$ ) of  $1.60 \text{ esu} \times 10^{30}$ , and **I-56**  $8.08 \text{ esu} \times 10^{30}$ , which is comparable to that found for *p*-nitroaniline ( $\langle\beta\rangle = 8.44 \text{ esu} \times 10^{30}$ ) used as reference material in this study.<sup>[78]</sup> One can foresee replacing the phenyl moiety with a chromophore to produce a functional material.

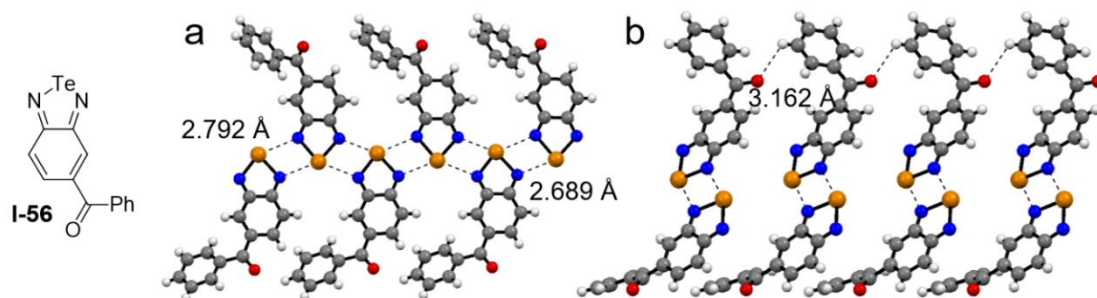


Figure I - 17: X-ray structure of **I-56**, a) top view; b) side view. Space group: *C2*.<sup>[78]</sup>

Despite the strength of the double EBs formed by the telluradiazole motif, which can overcome steric hindrance in certain cases, the main drawback of this recognition array lies in its moisture sensitivity. The more stable benzo-1,2,5-selenadiazole motif could be a viable alternative, however, this compound does not form a ribbon arrangement at the solid state (Figure I – 18). Instead, molecules of **I-2<sub>Se</sub>** arrange in trimeric clusters through chalcogen-bonding interactions ( $d_{N\dots Se} = 3.155 \text{ \AA}$ ) that bounds to the neighbouring molecules through hydrogen bonds ( $d_{N\dots C} = 3.417 \text{ \AA}$  and  $d_{Se\dots C} = 3.928 \text{ \AA}$ ).

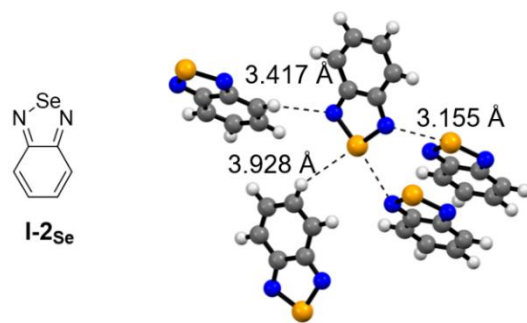


Figure I - 18: X-ray structure of **I-2<sub>Se</sub>**. Space group: *Pna2<sub>1</sub>*.

In 2014, Zade and co-workers reported on the synthesis of benzo-1,2,5-selenadiazole bearing different aryl moieties (Figure I -19) for optoelectronic applications.<sup>[79]</sup> Compounds **I-57** and **I-58** bearing phenyl and thiophenyl, respectively, associate in dimers at the solid state (Figure I – 19, a and b, respectively) through double chalcogen-bonding interactions ( $d_{N\dots Se} = 2.993 \text{ \AA}$  and  $3.424 \text{ \AA}$ , respectively).

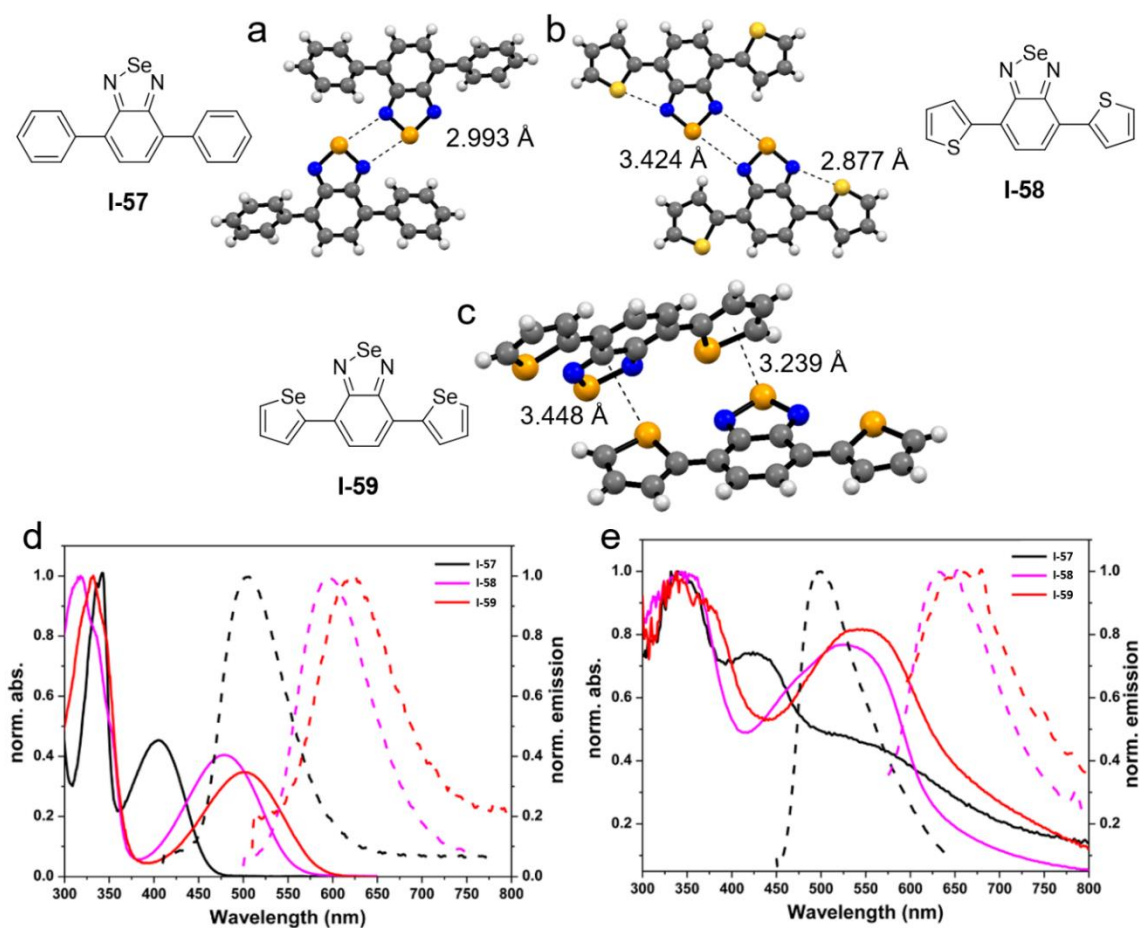


Figure I - 19: X-ray structure of a) **I-57**; b) **I-58** and c) **I-59**. Space group: *P21/c*, *Pca21* and *P21/c*, respectively. Uv-vis absorption-emission spectra d) in solution and e) of thin film on ITO coated glass. Adapted with permission;<sup>[79]</sup> copyright 2014 American Chemical Society.

On the contrary, molecules of **I-59** functionalised with selenophenyl form  $\pi$ - $\sigma^*$  interactions in the solid state (Figure I-19, c). Their optoelectronic properties have been evaluated in  $\text{CH}_2\text{Cl}_2$  solution by cyclic voltammetry (CV) and in benzene solution by UV-vis absorption-emission (Figure I – 19, d). Compounds **I-57**, **I-58** and **I-59** emit in the green, orange and red, respectively, under irradiation at 365 nm. The three compounds were deposited as thin film on ITO-coated glass and their UV-vis absorption-emission properties were evaluated (Figure I – 19, e). The resulting profiles show a bathochromic shift and a broadening of the peaks compared to those in benzene solution. The authors suggest that strong intermolecular interactions are responsible for this effect, those possibly being  $\pi$ -stacking or van der Waals interactions.<sup>[79]</sup> We would like to add that chalcogen bonds are also probably contributing to the optoelectronic properties of this material. Weak EBs, such as the one found in the dimer of selenadiazole, do not appear in solution but take place at the solid-state, thus impacting the resulting absorption-emission spectra. Since then, similar molecular scaffolds with different substituents have been reported for solution applications.<sup>[80]</sup>

To use the selenadiazole motif efficiently in solid-state applications, strategies to increase the strength of interaction using those building blocks have been investigated, one of them being the formation of a salt upon addition of a Bronsted acid. *Vargas-Baca* and co-workers reported in 2009 on the synthesis of various organic crystal based on selenadiazole.<sup>[81]</sup> Here we show the structure of **I-2<sub>Se</sub>•HCl** (Figure I – 20, a), which form a ribbon at the solid state through the combination of multiple chalcogen and hydrogen bonds ( $d_{\text{Cl}\dots\text{Se}} = 2.961 - 3.085 \text{ \AA}$ ,  $d_{\text{Cl}\dots\text{N}} = 3.087 \text{ \AA}$ ). While the Se-analogues leads to the formation of different products, only **I-2<sub>Te</sub>•(HCl)<sub>2</sub>** has been reported for the Te-containing derivative **I-2<sub>Te</sub>** (Figure I – 20, c). The compound arranges in ribbon through chalcogen and hydrogen-bonding interactions ( $d_{\text{Cl}\dots\text{Te}} = 2.773 \text{ \AA}$  and  $d_{\text{Cl}\dots\text{N}} = 3.245 \text{ \AA}$ ).

A second route to strengthen the SBIs involving benzo-1,2,5-selenadiazole consists in forming a salt by direct alkylation on the N position of the heterocycle. This has been achieved by *Berionni et al.*<sup>[82]</sup> and *Risto et al.*<sup>[83]</sup> under harsh conditions. *Vargas-Baca* and co-workers presented an alkylation method employing the milder MeI reagent as a rational strategy for EB strengthening in 2016.<sup>[84]</sup> In their study, different salts have been synthesised, specifically **I-60** and co-crystal **(I-60)<sub>2</sub>•I-2<sub>Se</sub>** (Figure I – 20, b and d, respectively). The former compound arranges in a discrete dimer at the solid state through four EBs involving the counter ion I<sup>-</sup> ( $d_{\text{I}\dots\text{Se}} = 3.176 - 3.610 \text{ \AA}$ ), whereas the latter in a trimeric arrangement featuring N $\cdots$ Se short contacts ( $d_{\text{N}\dots\text{Se}} = 2.573 - 2.937 \text{ \AA}$ ) and terminal I $\cdots$ Se EBs ( $d_{\text{I}\dots\text{Se}} = 3.528 \text{ \AA}$ ). Building on these results, the same authors recently reported on the preparation and characterisation of bridged dicationic derivatives.<sup>[85]</sup> Most of the structures shows chalcogen-bonding interactions between the selenadiazolium units and their counter ions at the exception of

**I-61** (Figure I – 20, e). For this compound a dimer through double EB of a length of interaction considerably shorter than that observed in the naked **I-2<sub>Se</sub>** ( $d_{N\dots Se} = 2.589 \text{ \AA}$  vs  $d_{N\dots Se} = 3.155 \text{ \AA}$ ).

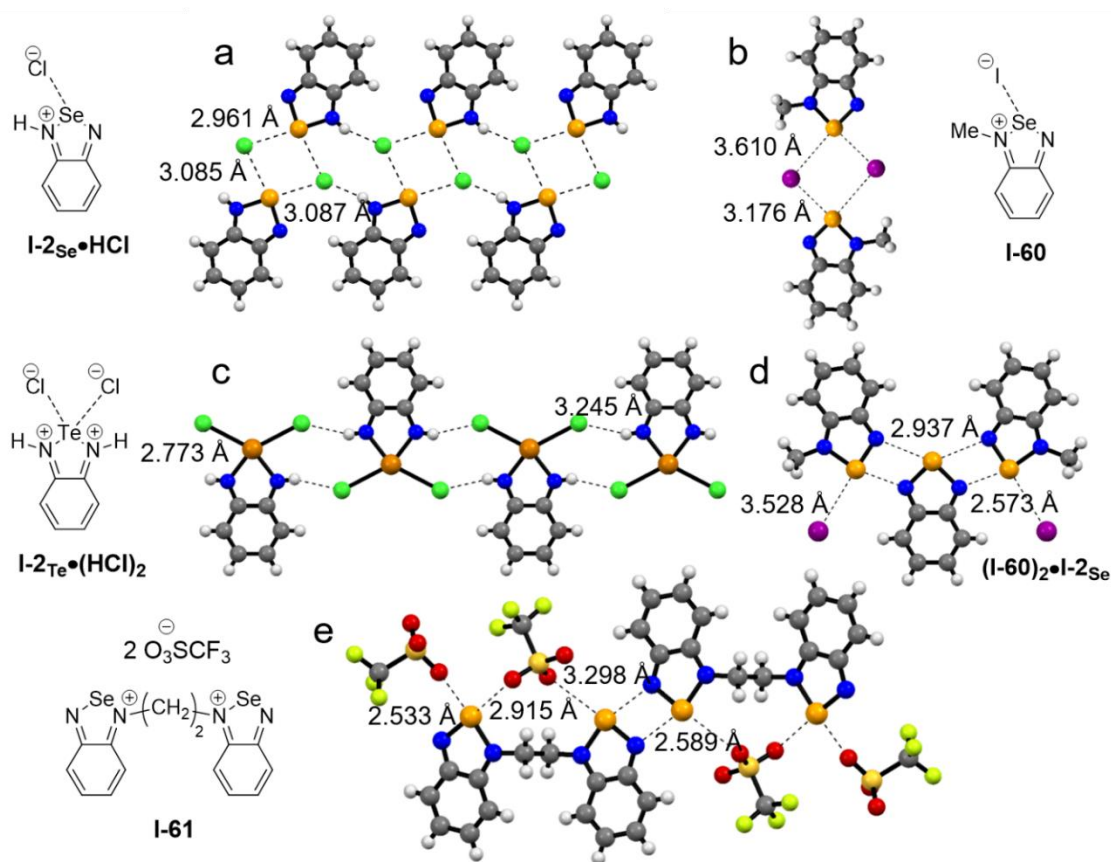


Figure I - 20: X-ray structure of chalcogenadiazolium salts in ball and stick representation, a) **I-2<sub>Se</sub>•HCl** ( $P\bar{1}$ );<sup>[81]</sup> b) **I-60** ( $P2_1/n$ );<sup>[84]</sup> c) **I-2<sub>Te</sub>•(HCl)<sub>2</sub>** ( $Pcca$ );<sup>[81]</sup> d) **(I-60)<sub>2</sub>•I-2<sub>Se</sub>** ( $C2/c$ );<sup>[84]</sup> e) **I-61** ( $P\bar{1}$ ).<sup>[85]</sup>

Further expanding this concept, the possibility to form chalcogen bonds in the presence of acid-base Lewis adducts has been also appraised by *Vargas-Baca* and co-workers.<sup>[86, 87]</sup> Upon addition of triphenylborane on **I-2<sub>Te</sub>**, neutral adducts bearing one and two Lewis acid molecules, respectively, have been identified in solution and crystallised. The 1:1 complex forms dimer through double EB interactions ( $d_{N\dots Te} = 2.578 \text{ \AA}$ ) in the solid-state (Figure I – 21, b). For each molecule **I-2<sub>Te</sub>**, one of the N atom is attached to the borane derivative while the second N atom engages in a chalcogen bond with the adjacent Te atom. The presence of the acid-base Lewis adduct strengthens the formation of the chalcogen bond. Moreover,  $\pi-\sigma^*$  interaction is observed between the phenyl moiety next to the Te atom. Adding a second equivalent of triphenyl borane lead to the formation of a trimeric structure (Figure I – 21, c). The crystal structure displays two N $\cdots$ B and two  $\pi-\sigma^*$  interactions. The steric hindrance of the phenyl moiety prevents the formation any further chalcogen bonds.

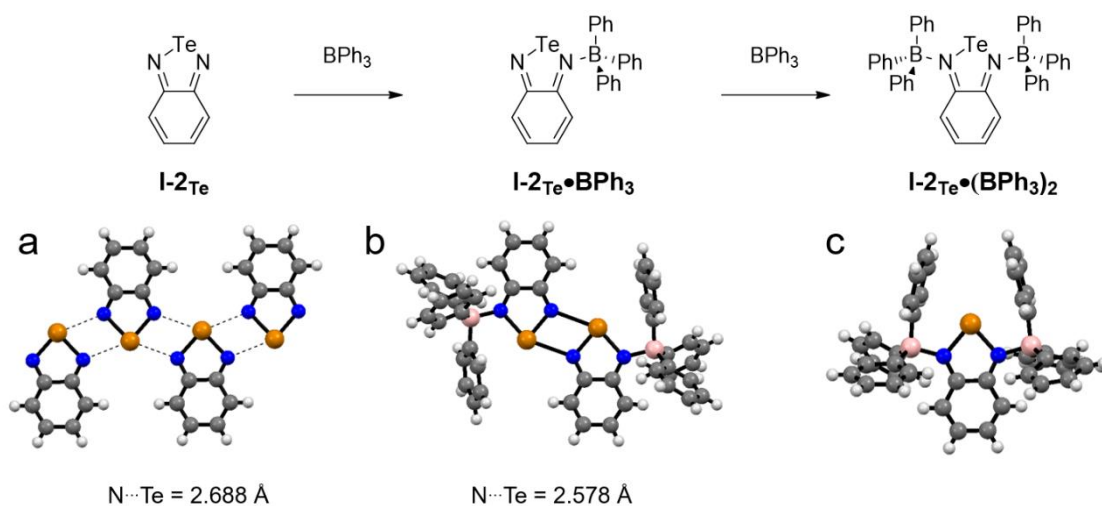


Figure I - 21: X-ray structure of a) **I-2<sub>Te</sub>** and the adducts formed upon addition of b) one and c) two  $\text{BPh}_3$  molecules, respectively. Space group  $C2/c$ ,  $P2_1/c$  and  $P2_1/n$ , respectively.<sup>[44, 86]</sup>

#### I – 4.2 1,2-Chalcogenazole N-oxide: discrete macrocyclic assembly

Despite the achievements met with the 1,2,5-chalcogenadiazole motif, well-defined supramolecular structures based on EB interaction remain scarce in the literature outside the classic ribbon association. In order to reach discrete cyclic architectures, *Vargas-Baca* and co-workers proposed the 1,2-chalcogenazole N-oxide motif. Specifically, they reported on the various arrangements of 3-methyl-5-phenyl-1,2-tellurazole N-oxide **I-62** connected by  $\text{N}\cdots\text{O}\cdots\text{Te}$  bridges.<sup>[88]</sup> Depending on the crystallisation method, one can control the supramolecular structure in the solid state. For instance, compound **I-62** forms chains through chalcogen-bonding interactions ( $d_{\text{O}\cdots\text{Te}} = 2.176 - 2.207 \text{ \AA}$ ) at the solid state after slow evaporation from a benzene solution (Figure I – 22, a). Cyclic tetramers (similarly to those of 3-methyl-5-(1,1-dimethylethyl)-Bu-1,2-tellurazole N-oxide)<sup>[89]</sup> can be formed ( $d_{\text{O}\cdots\text{Te}} = 2.203 - 2.241 \text{ \AA}$ ; Figure I – 22, b) from  $\text{CHCl}_3$  solution or slow diffusion of MeCN in  $\text{CH}_2\text{Cl}_2$  solution. The same MeCN/ $\text{CH}_2\text{Cl}_2$  solution mixed with  $[\text{Pd}(\text{NCMe})_4](\text{BF}_4)_2$  yields the complex  $[\text{Pd}(\text{I-62})_4](\text{BF}_4)_2$ , which was observed by X-ray diffraction analysis (Figure I – 22, c). Crystallisation of **I-62** from THF solution leads to the formation of an inclusion compound in which a cyclic hexamer hosts a THF molecule (Figure I – 22, d). On the other hand,  $\text{CH}_2\text{Cl}_2$  solution also yields the hexameric structure. In this crystal, the solvent sits outside the cavities that are partially filled by two Me groups from neighbouring molecules of **I-62**. Interestingly, the structure of the tetrameric assembly and  $[\text{Pd}(\text{I-62})_4](\text{BF}_4)_2$  could also be proven by NMR and absorption spectroscopy measurements, respectively. The authors reported that mixing **I-62** with  $\text{C}_{60}$  in  $\text{CHCl}_3$  yields a precipitate that could not be characterised in solution. However, crystals of the adduct  $(\text{I-62})_4\cdot\text{C}_{60}$  can be achieved by slow diffusion of fullerenes into a solution of **I-62** (Figure I – 22, e). In this structure, the tellurazole N-oxide entities arrange in a distorted boat conformation hosting the  $\text{C}_{60}$  molecules.

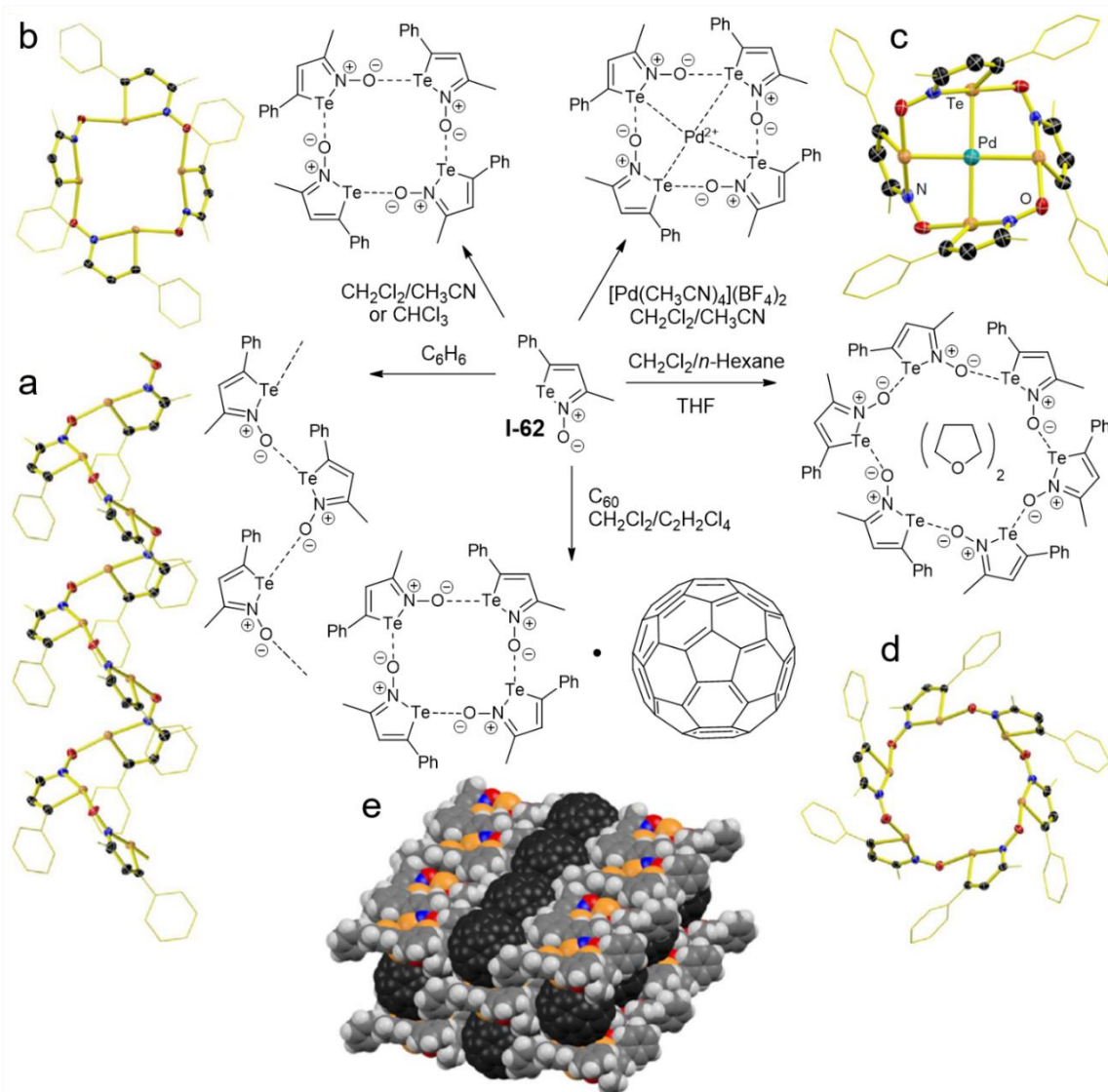


Figure I - 22: X-ray structure of **I-62** a) linear chain ( $P2_12_12_1$ ); b) cyclic tetramer ( $P\bar{1}$ ); c) adduct with Pd ( $I4_1/a$ ); cyclic hexamer ( $R\bar{3}$ ); inclusion of  $C_{60}$  ( $C2/c$ ).<sup>[88, 89]</sup> Adapted with permission,<sup>[88]</sup> copyright 2016 Springer Nature.

This unparalleled ability to form functional macrocycles through the self-association of simple building blocks shows the potential of 1,2-tellurazole *N*-oxide as reliable supramolecular synthons. Those molecules have an ambidentate nature that is expressed in their capability of forming defined structures able to bind transition-metal ions. Building on this idea, in 2019 the same group has reported on the preparation and characterisation of coordination complexes based on this principle. The macrocycles successfully bind Cu and Au cations in their tetrameric form while Ag cation has a preference for the hexameric one.<sup>[90]</sup>

Vargas-Baca and co-workers also reported the preparation of the annulated derivatives benzo-1,2-chalcogenazole *N*-oxide (Figure I -23). The authors aimed for a more easily functionalisable building block featuring the auto-association properties of **I-62** with a larger vdW surface that would enhance the intermolecular interactions due to dispersion forces. The crystal structures of **I-63<sub>E</sub>**

show similar tetrameric, hexameric and linear patterns than those obtained for **I-62**. Molecules of **I-63<sub>Te</sub>** arrange in a tetrameric (Figure I – 22, a) or hexameric (Figure I – 22, b) macrocycles while crystallised from CH<sub>2</sub>Cl<sub>2</sub>/pyridine solution. On the other hand, Se-derivative **I-60<sub>Se</sub>** forms linear chains at the solid state (Figure I – 22, c). Both **I-62** and **I-63<sub>Te</sub>** have shown the possibility to simultaneously associate at the crystalline state with Lewis acids (e.g. BF<sub>3</sub>) and bases (e.g. DMAP, MeCN, biPy, PPh<sub>3</sub> and carbene derivatives).<sup>[91]</sup>

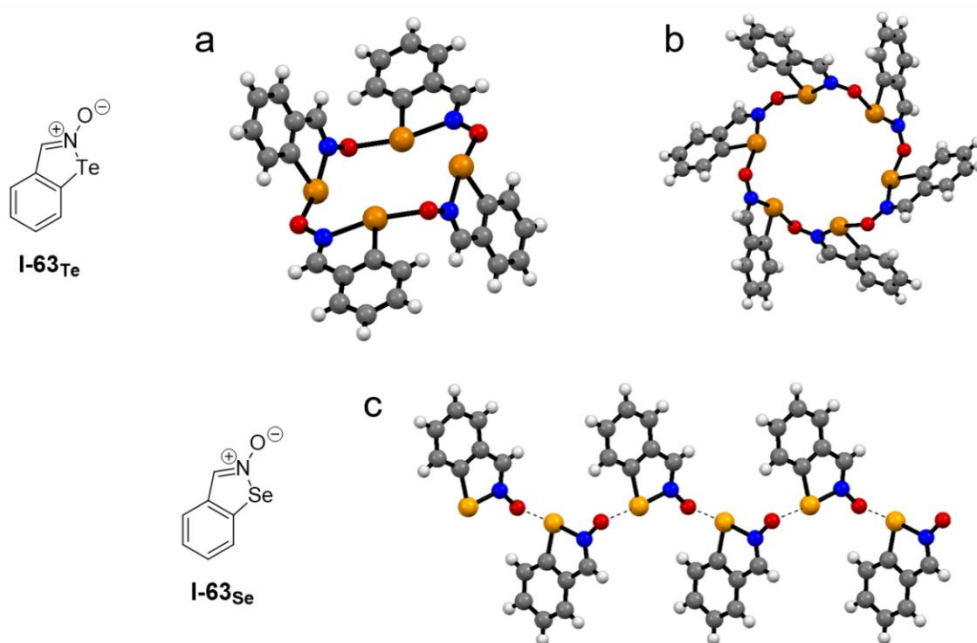


Figure I - 23: X-ray structure of **I-63<sub>Te</sub>**, a) cyclic tetramer of **I-63<sub>Te</sub>** ( $P\bar{1}$ ); b) cyclic hexamer of **I-63<sub>Te</sub>** ( $P3_1$ ); c) linear chains of **I-63<sub>Se</sub>** ( $P2_12_12_1$ ).<sup>[92]</sup>

#### I – 4.3 Chalcogen-bonding meeting halogen-bonding

Selenadiazole derivatives have also shown potential application in crystal engineering. Capitalizing on the basicity exhibited by the two N atoms of molecule **I-2<sub>Se</sub>**, co-crystals based on hydrogen- and halogen-bonding interactions meeting chalcogen bonds have been synthesised (Figure I – 24) by *Gdaniec, Polonski* and co-workers.<sup>[93]</sup> The main feature of those assembly lies in the formation of a dimeric (**I-2<sub>Se</sub>**)<sub>2</sub> structures engaging with a HB or XB donor. For example, co-crystal with perfluorobenzoic acid **I-61** show a tetrameric assembly (**I-2<sub>Se</sub>**)<sub>2</sub>•(**I-64**)<sub>2</sub> with four EBs ( $d_{O\dots Se} = 3.127$  Å,  $d_{N\dots Se} = 2.851$  Å) and two HBs ( $d_{N\dots O} = 2.641$  Å; Figure I – 24, a). In a similar fashion, **I-2<sub>Se</sub>** associate with perfluoriodobenzene **I-1** to form a tetramer (**I-2<sub>Se</sub>**)<sub>2</sub>•(**I-1**)<sub>2</sub> at the solid-state (Figure I – 24, b). Two units of **I-2<sub>Se</sub>** connect with each other through chalcogen-bonding interactions ( $d_{N\dots Se} = 2.972$  – 3.070 Å), while the free N atoms engage with two **I-1** in a halogen bond ( $d_{N\dots I} = 2.961$  – 3.073 Å). As a final selected example, dimer of **I-2<sub>Se</sub>** organises with the ditopic **DITFB** in a supramolecular

polymer (Figure I – 24, c) through simultaneous halogen- and chalcogen-bonding interactions ( $d_{N\dots I} = 3.025 - 3.104 \text{ \AA}$  and  $d_{N\dots Se} = 2.905 - 3.001 \text{ \AA}$ ).

The structures of  $(I-2_{Se})_2 \bullet (I-63)_2$ ,  $(I-2_{Se})_2 \bullet (I-1)_2$  and  $((I-2_{Se})_2 \bullet DITFB)_n$  show the potential application of the selenadiazole recognition motif in co-crystals built on simultaneous use of EB along with HB or XB interactions. However, as stated by the authors, the N binding sites of  $I-2_{Se}$  are identical, which may result in disruption of the dimers arrangement leading to a lack of control in supramolecular architectures of higher complexity.

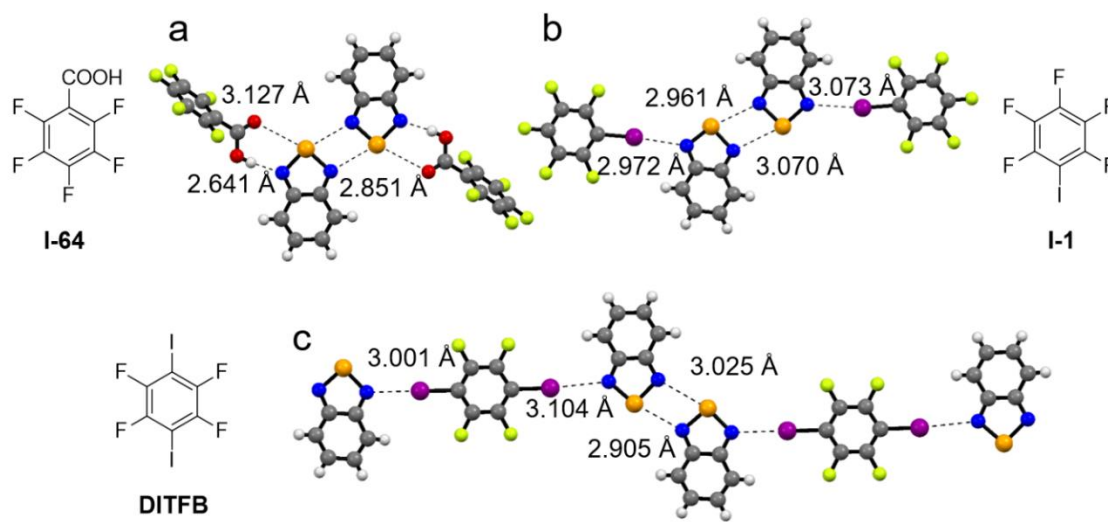


Figure I - 24: X-ray structure of co-crystal of a)  $I-2_{Se} \bullet I-64$ ; b)  $I-2_{Se} \bullet I-1$ ; c)  $I-2_{Se} \bullet DITFB$ . Space groups:  $P2_1/c$ ,  $P2_1/n$  and  $P2_1/c$ , respectively.<sup>[93]</sup>

Moving away from the 1,2,5-chalcogenadiazole motif, *Torubaev et al.* have successfully inserted **DITFB** in crystals of diphenyl dichalcogenide  $I-65_E$ .<sup>[94]</sup> At the solid state, pure  $I-65_{Te}$  arranges in columnar structures through  $\pi-\sigma^*$  interactions ( $d_{C\dots Te} = 3.604 - 3.646 \text{ \AA}$ ; Figure I – 25, a) and  $I-65_{Se}$  forms ribbons through Se $\cdots$ Se short contacts ( $d_{Se\dots Se} = 3.726 \text{ \AA}$ ; Figure I – 25, b). Co-crystallisation with **DITFB** leads to the insertion of the ditopic halogen-bond donor in the network of diphenyl chalcogenide. In the case of the Te-containing derivative, the columnar arrangements observed in the single component crystal are translated in the co-crystal with **DITFB** ( $d_{C\dots Te} = 3.453 \text{ \AA}$ ). The columnar structures connect with one another through halogen- and chalcogen-bonding interactions involving Te and I atoms ( $d_{Te\dots I} = 3.574 \text{ \AA}$  and  $d_{I\dots Te} = 4.031 \text{ \AA}$ ) with bridging **DITFB** molecule (Figure I – 25, c). For the co-crystal involving the Se-analogue, the ribbon structure is tightened up ( $d_{Se\dots Se} = 3.752 \text{ \AA}$  and  $3.606 \text{ \AA}$ ) and **DITFB** connects through  $\pi-\sigma^*$  interaction ( $d_{C\dots I} = 3.566 \text{ \AA}$ ; Figure I – 25, d). In both cases, the original connection between  $I-65_E$  molecules is kept identical while **DITFB** connects the columnar or ribbon structure showing a cooperative behaviour of the halogen- and chalcogen-bonding interactions at the solid state.

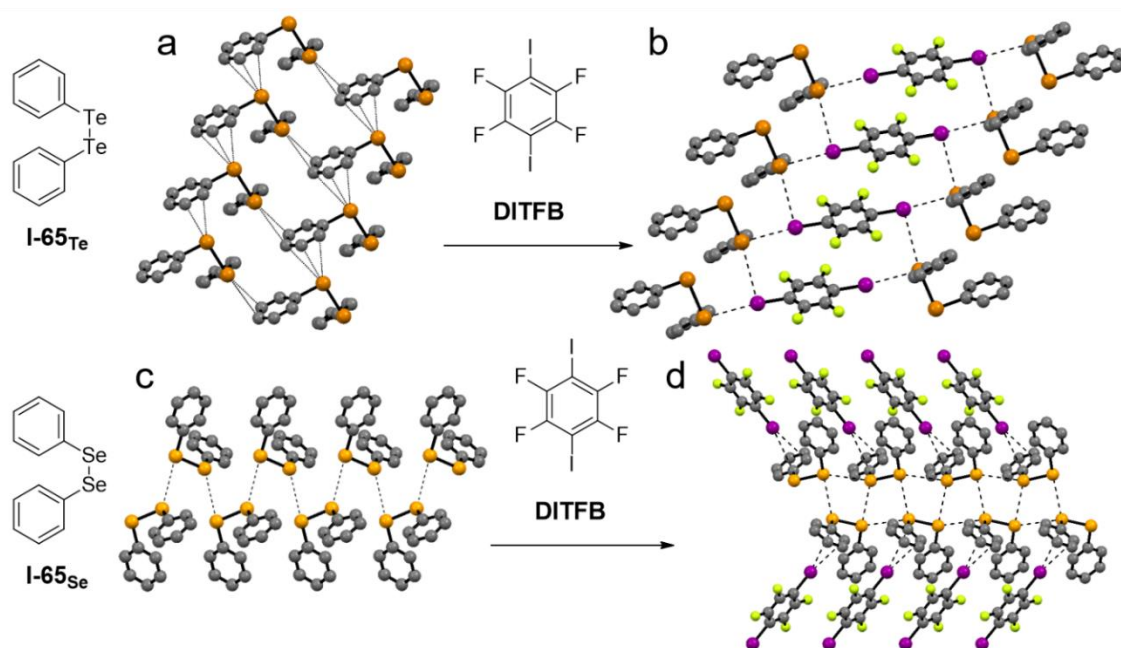


Figure I - 25: X-ray structure of **I-65<sub>E</sub>** and their respective co-crystal with **DITFB**. Space group:  $P2_12_12_1$  for **I-65<sub>Te</sub>**,  $P2_12_12_1$  for **I-65<sub>Se</sub>**,  $P2_1/n$  for **I-65<sub>Te</sub>•DITFB** and  $P2_1/c$  for **I-65<sub>Se</sub>•DITFB**.<sup>[94]</sup> H atoms are omitted for clarity.

#### I – 4.4 Porous architecture formation through chalcogen-chalcogen interactions

Another example of supramolecular structure in the solid state driven by chalcogen-bonding interactions is the formation of nanotubes by telluroethers reported by *Gleiter* and co-workers.<sup>[95]</sup> During their study they have synthesized a number of supramolecular tubular structures presenting cavities able to host small guest molecules such as toluene or *n*-hexane. This has been achieved by building architectures relying on chalcogen-chalcogen interactions. One of those being the helical structure of 1,4- bis(methyltellanyl)buta-1,3-diyne **I-66** presenting a square cavity (Figure I – 26, b and c). In this case each Te atom is involved in four EBs ( $d_{\text{Te-Te}} = 3.741 - 3.824 \text{ \AA}$ ), being simultaneously a chalcogen bond donor and an acceptor. When focused on the chalcogen atom as electron acceptor, the angle between the two EBs is  $110^\circ$  (Figure I -26, a). Similar behaviour has been observed with cyclophanes,<sup>[96]</sup> cyclic tetra- and hexaynes.<sup>[97]</sup> Chalcogen-chalcogen interactions have been also used to control face-to-face  $\pi$ - $\pi$  stacking of anthracene rings.<sup>[98]</sup> For a comprehensive review of those systems, we direct the interested reader to the recent paper of *Gleiter et al.*<sup>[99]</sup>

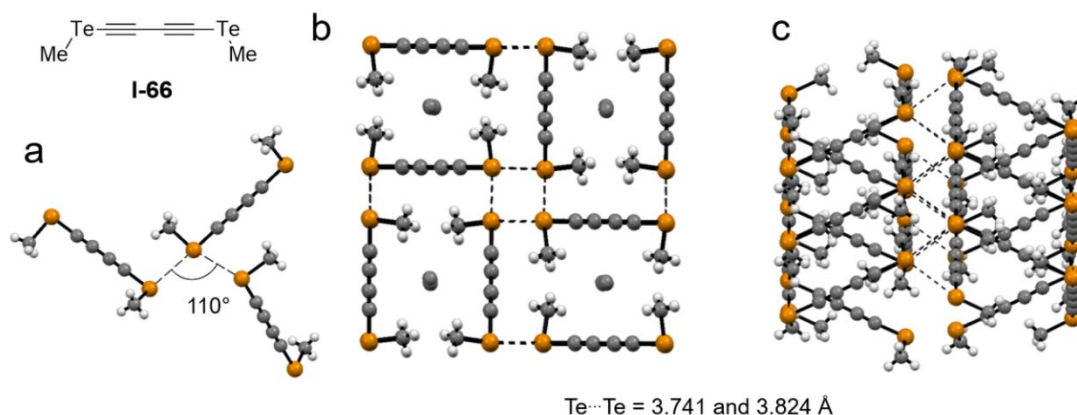


Figure I – 26: X-ray structure of 1,4-bis(methyltellanyl)buta-1,3-diyne.<sup>[95]</sup>

#### I – 4.5 Self-assembled fibres for optoelectronic applications controlled by chalcogen-bonding interactions

In 2011, *Barbarella* and co-workers successfully engineered functional supramolecular architectures through the self-assembly of a sulfur rich octatiophene bearing thioalkyl substituents (Figure I – 27).<sup>[100]</sup> In a bottom-up approach, the key design element lies in the addition of a S atom onto the  $\beta$ -carbon of the inner tetrameric core inducing an intramolecular chalcogen bond ( $d_{S...S} = 3.09 - 3.10$  Å; Figure I – 27, d). Compounds **I-67**, **I-68** and **I-69** have been synthesised and fibres have been grown on various surfaces (glass, ITO, silicon and gold) from toluene solution with slow diffusion of MeCN. The crystalline assemblies have been characterised by scanning electron microscopy (SEM; Figure I – 27, a – c) with a high aspect ratio (from 1:1 to 1:2 height *versus* width and length up to hundreds  $\mu\text{m}$ ). Compound **I-70** bearing hexyl chains (on the opposite of the S-hexyl for **I-67**) has been submitted to the same crystallisation conditions but only amorphous material was observed. This indicates the importance of the S atoms on the resulting structure.

The fibres of **I-67** and **I-68** present interesting optoelectronic properties such as an intense red fluorescence (observed by laser scanning confocal microscopy). The reduction and oxidation potential have been measured by cyclic voltammetry ( $E_{ox}^0 = 0.62$  V and 0.60 V vs SCE, respectively and  $E_{red}^0 = -1.45$  V and -1.52 V vs SCE, respectively). Particularly, the low value for the reduction process indicate a high electron affinity. The charge mobility has been measured at the nanoscale level by conductive atomic force microscopy (AFM) in contact mode. The fibres of **I-67** and **I-68** has been characterised by hole mobility values of  $9.8 \cdot 10^{-7}$  and  $5 \cdot 10^{-6} \text{ cm}^2 \text{ V}^{-1} \text{ s}^{-1}$ , respectively. Field effect transistor devices were built to measure the charge mobility along the fibres. Considering an effective coverage of 50% due to the fibrillar morphology, hole mobility has been calculated at 1

$10^{-5}$  and  $4 \cdot 10^{-4} \text{ cm}^2 \text{ V}^{-1} \text{ s}^{-1}$ , respectively, which is two orders of magnitude higher than the value observed for single fibres.

The fibres as a film have also been studied by small-angle reflection of X-ray and the authors proposed an arrangement of the molecules at the solid state. The octathiophenes, featuring a nearly flat conformation of the backbone, arrange in J-stacking type organisation. The chalcogen bonds between the S atoms impose an anti-orientation of the thiophenes rings (as shown by preliminary single crystal X-ray diffraction; Figure I – 27, d). The same principle was then applied using different capping functional group to the oligothiophene,<sup>[101]</sup> bulk-heterojunction materials,<sup>[102]</sup> and conjugated polymers.<sup>[103]</sup>

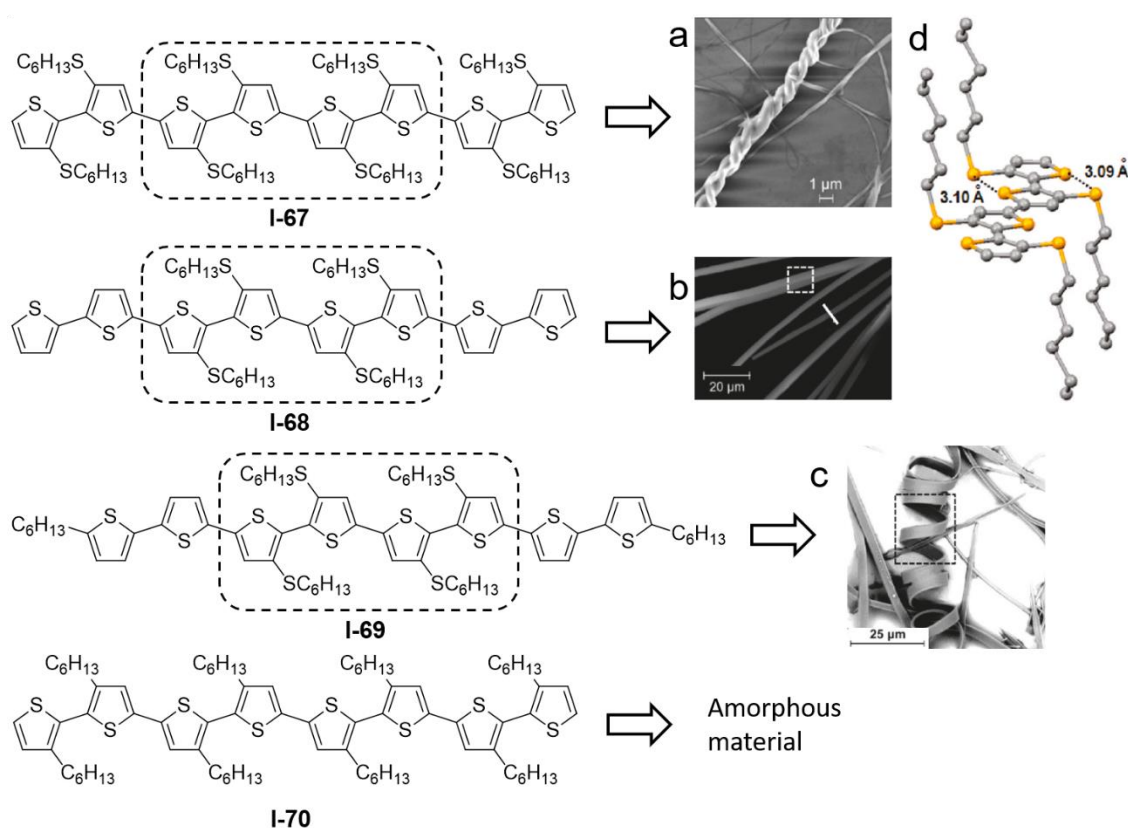


Figure I - 27: Oligothiophene **I-67**, **I-68**, **I-69** and **I-70** substituted with alkyl and thioalkyl chains, the inner tetrameric core is highlighted by dashed lines. SEM images of a) **I-68**; b) **I-69** and c) **I-70**; d) Preliminary X-ray structure of inner tetrameric core of the octamers. Adapted with permission,<sup>[100]</sup> copyright 2011 American Chemical Society.

#### I – 4.6 Wire-like structures formed by benzo-1,3-chalcogenazole

Finally, our group contributed to the topic by engineering wire-like structures through single chalcogen-bonding interactions.<sup>[104]</sup> The key element of this work was the improved synthesis of the benzo-1,3-selenazole motif over the reported procedures and its generalisation to the Te-containing heterocycle.<sup>[105-109]</sup> This functional group initially attracted our attention as potential application in organic phosphors. However, its easy derivatisation and solid-state arrangement led

us to engineer molecular structures with controlled association.<sup>[104, 105]</sup> Benzo-1,3-chalcogenazoles **I-71<sub>E</sub>** have been synthesised bearing different substituents (*e.g.* *i*-butyl, phenyl, furyl, thiophenyl, 2-pyridyl, 3-pyridyl, 4-pyridyl, styryl and ferrocenyl) in 2-position to control the supramolecular organisation in the solid state through chalcogen-bonding interactions (Figure I – 27). The EB usually takes place between the N atom of the chalcogenazole ring and the chalcogen atom of an adjacent molecule. The recognition properties at the chalcogen atom can be controlled by discriminating the two  $\sigma$ -holes ( $\alpha$ ) and ( $\beta$ ) (Figure I – 27, a and b). Particularly, the  $\sigma$ -hole ( $\beta$ ) can be blocked either by steric hindrance (steric tether) or involved in an intramolecular EB with a  $\sigma$ -hole stopper, leaving the  $\sigma$ -hole ( $\alpha$ ) free to engage with a lone pair donor atom.

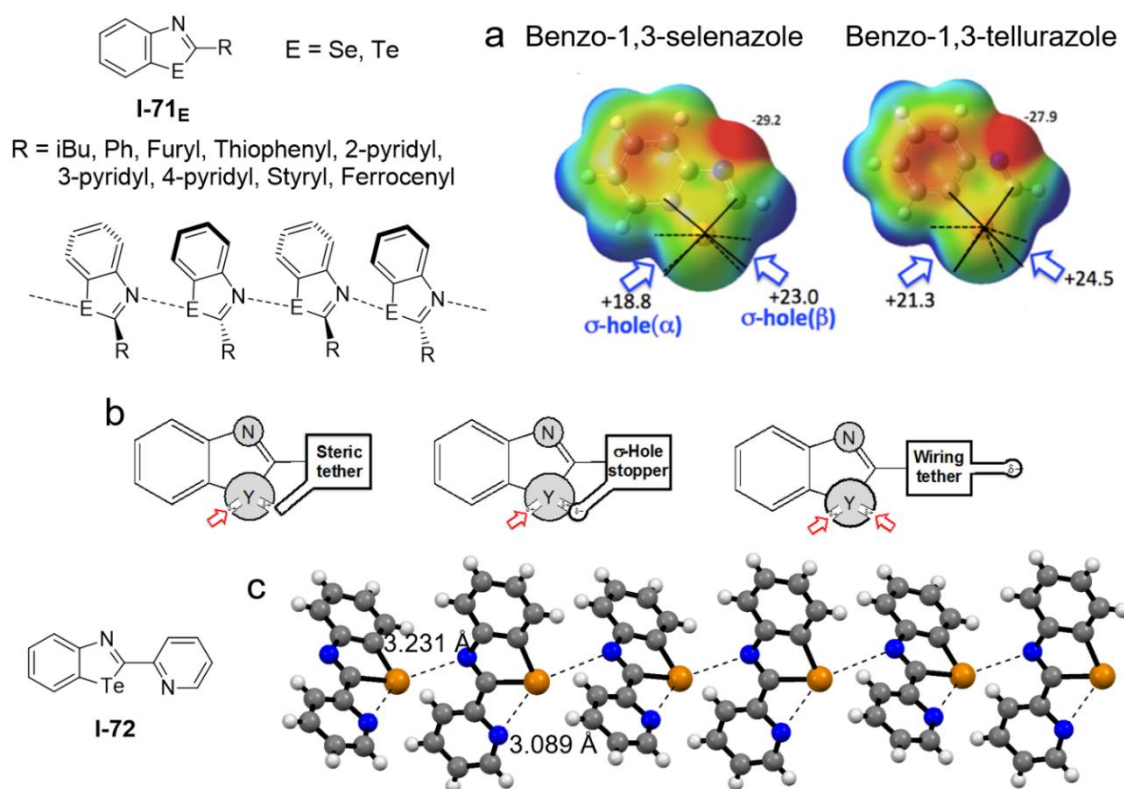


Figure I - 28: Benzo-1,3-chalcogenazole **I-71<sub>E</sub>** bearing different functionalisation in 2-position introduced by us to form wire-like structure through controlled single chalcogen-bonding interactions; a) ESP map of benzo-1,3-selenazole and benzo-1,3-tellurazole; b) Design of the molecular recognition of 2-substituted benzo-1,3-chalcogenazole; c) X-ray structure of **I-72**, space group: *Pca*2<sub>1</sub>. Adapted with permission;<sup>[104]</sup> Copyright 2016 Willey-VCH Verlag GmbH & Co. KGaA, Weinheim.

Substituents such as phenyl are sufficiently bulky to act as steric tether, and 2-furanyl and 2-pyridyl acts as  $\sigma$ -hole stoppers. The third strategy rely on 2-substituents bearing a more basic heteroatom than the N atom present in the chalcogenazole ring. The chalcogen-bonding interaction will thus take place between the more electron rich atom and the Se- or Te- atom. Substituents such as 3- and 4-pyridyl acts as wiring tether. For example, molecule **I-72** bears a  $\sigma$ -hole stopper in the 2-

pyridyl substituent which form an intramolecular EB ( $d_{N...Te} = 3.089 \text{ \AA}$ ) and form a wire-like assembly through intermolecular EB ( $d_{N...Te} = 3.231 \text{ \AA}$ ; Figure I – 27, c).

## I – 5 Outline of the dissertation

It is in this context of very recent and rapid expansion of the chalcogen-bonding topic in supramolecular chemistry that this doctoral work takes place. Despite the numerous achievements of chalcogen bonded systems in recent years, this field still lack of a versatile, reliable and stable supramolecular synthon for solid-state applications. It is this absence of persistent recognition systems that motivated us to design and synthesise a building block able to self-recognise and self-associate through double EB interactions involving Se or Te atoms (Figure I – 28). SBIs being stronger with larger atoms, we anticipate the strongest recognition persistence with the Te-congeners. Furthermore, defining the place of chalcogen-bonding among the other non-covalent interactions will also be considered as central point of this work. Indeed, only very few studies have conjectured the use of EB in multi-type interactions systems.

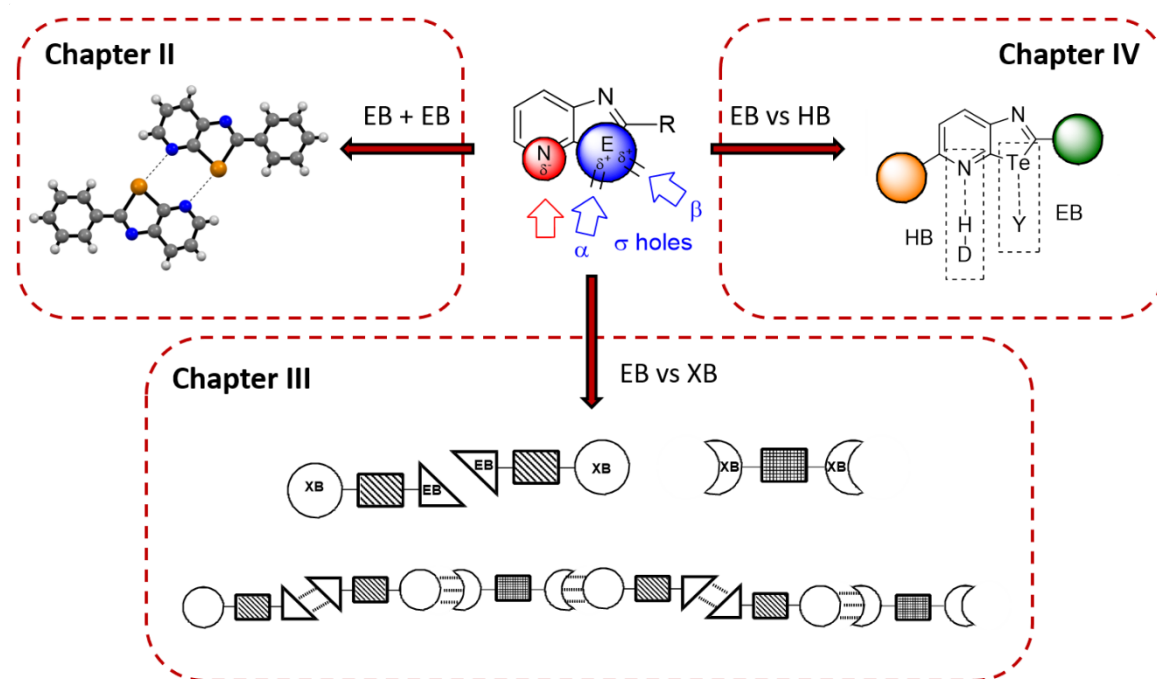


Figure I - 29: Schematic representation of the outline of this manuscript.

Thus, we will expand the functionalities of our recognition motif to include different interactions such as  $\pi$ - $\pi$  stacking, hydrogen- and halogen-bonding interactions to appraise their level of compatibility, orthogonality and/or competition. Accordingly, this work is divided in three main chapters (Figure I – 28).

*Chapter II* presents the design of the chalcogenazopyridine (CGP) motif and the synthesis of Se- and Te- containing molecules with various substituents to probe its recognition potential at the solid-state through double chalcogen-bonding interactions. The system is challenged through different applications such as crystal engineering, soft materials and organic semi-conductors. The latter requires the conjugation of the CGP array to polycyclic aromatics hydrocarbons leading to synergy between  $\pi$ - $\pi$  stacking and chalcogen-bonding interactions.

*Chapter III* addresses the potential orthogonality that exists between halogen- and chalcogen bonds through the design and synthesis of supramolecular polymers based on both interactions. Those materials are crystallised and analysed by X-ray diffraction experiments.

*Chapter IV* is dedicated to the expansion of the CGP array through the functionalisation of the 5-position. By preventing the face-to-face dimerization due to steric hindrance, this system opens the door to novel recognition arrays based on the simultaneous hydrogen- and chalcogen-bonding interactions. This self-assembly at the solid-state is extended to multicomponent crystals. The expansion of functionality in 5-positions also allowed us to design a potential tetra chalcogen bonded system.

## I – 6 Bibliography

- [1] J.-M. Lehn, 'Supramolecular Chemistry—Scope and Perspectives Molecules, Supermolecules, and Molecular Devices (Nobel Lecture)', *Angew. Chem. Int. Ed.* **1988**, *27*, 89-112.
- [2] J. Hermann, R. A. DiStasio, A. Tkatchenko, 'First-Principles Models for van der Waals Interactions in Molecules and Materials: Concepts, Theory, and Applications', *Chem. Rev.* **2017**, *117*, 4714-4758.
- [3] V. I. Minkin, 'Glossary of Terms Used in Theoretical Organic Chemistry', *Pure Appl. Chem.* **1999**, *71*, 1919-1981.
- [4] P. Atkins, J. De Paula, *Physical Chemistry Ninth Edition*, Oxford University Press, 2010.
- [5] C. A. Hunter, K. R. Lawson, J. Perkins, C. J. Urch, 'Aromatic Interactions', *J. Chem. Soc., Perkin Trans. 2* **2001**, 651-669.
- [6] H.-J. Schneider, 'Binding Mechanisms in Supramolecular Complexes', *Angew. Chem. Int. Ed.* **2009**, *48*, 3924-3977.
- [7] S. Tsuzuki, A. Fujii, 'Nature and Physical Origin of CH/ $\pi$  Interaction: Significant Difference from Conventional Hydrogen Bonds', *Phys. Chem. Chem. Phys.* **2008**, *10*, 2584-2594.
- [8] E. Arunan, R. Desiraju Gautam, A. Klein Roger, J. Sadlej, S. Scheiner, I. Alkorta, C. Clary David, H. Crabtree Robert, J. Dannenberg Joseph, P. Hobza, G. Kjaergaard Henrik, C. Legon Anthony, B. Mennucci, J. Nesbitt David, 'Definition of the Hydrogen Bond (IUPAC Recommendations 2011)', *Pure Appl. Chem.* **2011**, *83*, 1637-1641.
- [9] G. A. Jeffrey, *An Introduction to Hydrogen Bonding*, Oxford University Press, New York, 1997.
- [10] T. Steiner, 'The Hydrogen Bond in the Solid State', *Angew. Chem. Int. Ed.* **2002**, *41*, 48-76.
- [11] L. Zhan-Ting, W. Li-Zhu, *Hydrogen Bonded Supramolecular Materials, Vol. 88*, Springer, 2015.
- [12] C. M. Drain, J.-M. Lehn, 'Self-Assembly of Square Multiporphyrin Arrays by Metal Ion Coordination', *Chem. Commun.* **1994**, 2313-2315.

- [13] A. Semenov, J. P. Spatz, M. Möller, J.-M. Lehn, B. Sell, D. Schubert, C. H. Weidl, U. S. Schubert, 'Controlled Arrangement of Supramolecular Metal Coordination Arrays on Surfaces', *Angew. Chem. Int. Ed.* **1999**, *38*, 2547-2550.
- [14] M. Ruben, J.-M. Lehn, P. Müller, 'Addressing Metal Centres in Supramolecular Assemblies', *Chem. Soc. Rev.* **2006**, *35*, 1056-1067.
- [15] M. Ruben, J. Rojo, F. J. Romero-Salguero, L. H. Uppadine, J.-M. Lehn, 'Grid-Type Metal Ion Architectures: Functional Metallosupramolecular Arrays', *Angew. Chem. Int. Ed.* **2004**, *43*, 3644-3662.
- [16] R. J. Sarma, S. Otto, J. R. Nitschke, 'Disulfides, Imines, and Metal Coordination within a Single System: Interplay between Three Dynamic Equilibria', *Chem. Eur. J.* **2007**, *13*, 9542-9546.
- [17] A. J. McConnell, C. M. Aitchison, A. B. Grommet, J. R. Nitschke, 'Subcomponent Exchange Transforms an FeII4L4 Cage from High- to Low-Spin, Switching Guest Release in a Two-Cage System', *J. Am. Chem. Soc.* **2017**, *139*, 6294-6297.
- [18] J. L. Greenfield, E. W. Evans, D. Di Nuzzo, M. Di Antonio, R. H. Friend, J. R. Nitschke, 'Unraveling Mechanisms of Chiral Induction in Double-Helical Metallopolymers', *J. Am. Chem. Soc.* **2018**, *140*, 10344-10353.
- [19] A. B. Grommet, J. B. Hoffman, E. G. Percástegui, J. Mosquera, D. J. Howe, J. L. Bolliger, J. R. Nitschke, 'Anion Exchange Drives Reversible Phase Transfer of Coordination Cages and Their Cargoes', *J. Am. Chem. Soc.* **2018**, *140*, 14770-14776.
- [20] A. J. McConnell, C. J. E. Haynes, A. B. Grommet, C. M. Aitchison, J. Guilleme, S. Mikutis, J. R. Nitschke, 'Orthogonal Stimuli Trigger Self-Assembly and Phase Transfer of FeII4L4 Cages and Cargoes', *J. Am. Chem. Soc.* **2018**, *140*, 16952-16956.
- [21] D. Zhang, T. K. Ronson, J. R. Nitschke, 'Functional Capsules via Subcomponent Self-Assembly', *Acc. Chem. Res.* **2018**, *51*, 2423-2436.
- [22] N. W. Alcock, in *Advances in Inorganic Chemistry and Radiochemistry, Vol. 15* (Eds.: H. J. Emeléus, A. G. Sharpe), Academic Press, 1972, pp. 1-58.
- [23] S. Benz, A. I. Poblador-Bahamonde, N. Low-Ders, S. Matile, 'Catalysis with Pnictogen, Chalcogen, and Halogen Bonds', *Angew. Chem. Int. Ed.* **2018**, *57*, 5408-5412.
- [24] L. Brammer, 'Halogen Bonding, Chalcogen Bonding, Pnictogen Bonding, Tetrel Bonding: Origins, Current Status and Discussion', *Faraday Discuss.* **2017**, *203*, 485-507.
- [25] E. R. T. Tiekink, 'Supramolecular Assembly Based on "Emerging" Intermolecular Interactions of Particular Interest to Coordination Chemists', *Coord. Chem. Rev.* **2017**, *345*, 209-228.
- [26] P. Metrangolo, G. Resnati, 'Halogen Bonding: A Paradigm in Supramolecular Chemistry', *Chem. Eur. J.* **2001**, *7*, 2511-2519.
- [27] T. Clark, M. Hennemann, J. S. Murray, P. Politzer, 'Halogen Bonding: the  $\sigma$ -Hole', *J. Mol. Model.* **2007**, *13*, 291-296.
- [28] P. Metrangolo, F. Meyer, T. Pilati, G. Resnati, G. Terraneo, 'Halogen Bonding in Supramolecular Chemistry', *Angew. Chem. Int. Ed.* **2008**, *47*, 6114-6127.
- [29] M. Fourmigué, 'Halogen Bonding: Recent Advances', *Curr. Opin. Solid State Mater. Sci.* **2009**, *13*, 36-45.
- [30] M. Erdelyi, 'Halogen Bonding in Solution', *Chem. Soc. Rev.* **2012**, *41*, 3547-3557.
- [31] L. C. Gilday, S. W. Robinson, T. A. Barendt, M. J. Langton, B. R. Mullaney, P. D. Beer, 'Halogen Bonding in Supramolecular Chemistry', *Chem. Rev.* **2015**, *115*, 7118-7195.
- [32] G. A. Landrum, N. Goldberg, R. Hoffmann, 'Bonding in the Trihalides (X<sub>3</sub>-), Mixed Trihalides (X<sub>2</sub>Y-) and Hydrogen Bihalides (X<sub>2</sub>H-). The Connection Between Hypervalent, Electron-Rich Three-Center, Donor-Acceptor and Strong Hydrogen Bonding', *J. Chem. Soc., Dalton Trans.* **1997**, 3605-3613.
- [33] J. P. M. Lommerse, A. J. Stone, R. Taylor, F. H. Allen, 'The Nature and Geometry of Intermolecular Interactions between Halogens and Oxygen or Nitrogen', *J. Am. Chem. Soc.* **1996**, *118*, 3108-3116.

- [34] R. Desiraju Gautam, P. S. Ho, L. Kloo, C. Legon Anthony, R. Marquardt, P. Metrangolo, P. Politzer, G. Resnati, K. Rissanen, 'Definition of the Halogen Bond (IUPAC Recommendations 2013)', *Pure Appl. Chem.* **2013**, *85*, 1711-1713.
- [35] P. Politzer, J. S. Murray, M. C. Concha, ' $\sigma$ -Hole Bonding between like Atoms; a Fallacy of Atomic Charges', *J. Mol. Model.* **2008**, *14*, 659-665.
- [36] R. B. Walsh, C. W. Padgett, P. Metrangolo, G. Resnati, T. W. Hanks, W. T. Pennington, 'Crystal Engineering through Halogen Bonding: Complexes of Nitrogen Heterocycles with Organic Iodides', *Cryst. Growth Des.* **2001**, *1*, 165-175.
- [37] J. Y. C. Lim, P. D. Beer, 'Sigma-Hole Interactions in Anion Recognition', *Chem* **2018**, *4*, 731-783.
- [38] I. Vargas-Baca, T. Chivers, 'Weakly Bonding Interactions in Organochalcogen Chemistry', *Phosphorus Sulfur Silicon Relat. Elem.* **2000**, *164*, 207-227.
- [39] A. F. Cozzolino, P. J. W. Elder, I. Vargas-Baca, 'A Survey of Tellurium-Centered Secondary-Bonding Supramolecular Synthons', *Coord. Chem. Rev.* **2011**, *255*, 1426-1438.
- [40] A. F. Cozzolino, I. Vargas-Baca, 'Parametrization of a Force Field for Te-N Secondary Bonding Interactions and Its Application in the Design of Supramolecular Structures Based on Heterocyclic Building Blocks', *Cryst. Growth Des.* **2011**, *11*, 668-677.
- [41] A. Jolleys, W. Levason, G. Reid, 'Thioether Coordination to Divalent Selenium Halide Acceptors – Synthesis, Properties and Structures', *Dalton Trans.* **2013**, *42*, 2963-2972.
- [42] T. Chivers, R. S. Laitinen, 'Tellurium: a Maverick among the Chalcogens', *Chem. Soc. Rev.* **2015**, *44*, 1725-1739.
- [43] G. E. Garrett, G. L. Gibson, R. N. Straus, D. S. Seferos, M. S. Taylor, 'Chalcogen Bonding in Solution: Interactions of Benzotelluradiazoles with Anionic and Uncharged Lewis Bases', *J. Am. Chem. Soc.* **2015**, *137*, 4126-4133.
- [44] A. F. Cozzolino, J. F. Britten, I. Vargas-Baca, 'The Effect of Steric Hindrance on the Association of Telluradiazoles through Te-N Secondary Bonding Interactions', *Cryst. Growth Des.* **2006**, *6*, 181-186.
- [45] A. F. Cozzolino, I. Vargas-Baca, 'The Supramolecular Chemistry of 1,2,5-Chalcogenadiazoles', *J. Organomet. Chem.* **2007**, *692*, 2654-2657.
- [46] A. F. Cozzolino, I. Vargas-Baca, S. Mansour, A. H. Mahmoudkhani, 'The Nature of the Supramolecular Association of 1,2,5-Chalcogenadiazoles', *J. Am. Chem. Soc.* **2005**, *127*, 3184-3190.
- [47] P. L. Bora, M. Novák, J. Novotný, C. Foroutan-Nejad, R. Marek, 'Supramolecular Covalence in Bifurcated Chalcogen Bonding', *Chem. Eur. J.* **2017**, *23*, 7315-7323.
- [48] C. Bleiholder, R. Gleiter, D. B. Werz, H. Köppel, 'Theoretical Investigations on Heteronuclear Chalcogen-Chalcogen Interactions: On the Nature of Weak Bonds between Chalcogen Centers', *Inorg. Chem.* **2007**, *46*, 2249-2260.
- [49] C. Bleiholder, D. B. Werz, H. Köppel, R. Gleiter, 'Theoretical Investigations on Chalcogen-Chalcogen Interactions: What Makes These Nonbonded Interactions Bonding?', *J. Am. Chem. Soc.* **2006**, *128*, 2666-2674.
- [50] F. De Vleeschouwer, M. Denayer, B. Pinter, P. Geerlings, F. De Proft, 'Characterization of Chalcogen Bonding Interactions via an in-Depth Conceptual Quantum Chemical Analysis', *J. Comput. Chem.* **2018**, *39*, 557-572.
- [51] D. J. Pascoe, K. B. Ling, S. L. Cockroft, 'The Origin of Chalcogen-Bonding Interactions', *J. Am. Chem. Soc.* **2017**, *139*, 15160-15167.
- [52] S. Bhandary, A. Sirohiwal, R. Kadu, S. Kumar, D. Chopra, 'Dispersion Stabilized Se/Te $\cdots\pi$  Double Chalcogen Bonding Synthons in in Situ Cryocrystallized Divalent Organochalcogen Liquids', *Cryst. Growth Des.* **2018**, *18*, 3734-3739.
- [53] P. Su, H. Li, 'Energy Decomposition Analysis of Covalent Bonds and Intermolecular Interactions', *J. Chem. Phys.* **2009**, *131*, 014102.
- [54] L. Vogel, P. Wonner, S. M. Huber, 'Chalcogen Bonding: An Overview', *Angew. Chem. Int. Ed.* **2019**, *58*, 1880-1891.

- [55] H. Zhao, F. P. Gabbaï, 'A bidentate Lewis Acid with a Telluronium Ion as an Anion-Binding site', *Nat. Chem.* **2010**, *2*, 984-990.
- [56] E. A. Suturina, N. A. Semenov, A. V. Lonchakov, I. Y. Bagryanskaya, Y. V. Gatilov, I. G. Irtegov, N. V. Vasilieva, E. Lork, R. Mews, N. P. Gritsan, A. V. Zibarev, 'Interaction of 1,2,5-Chalcogenadiazole Derivatives with Thiophenolate: Hypercoordination with Formation of Interchalcogen Bond versus Reduction to Radical Anion', *J. Phys. Chem. A* **2011**, *115*, 4851-4860.
- [57] N. A. Semenov, N. A. Pushkarevsky, J. Beckmann, P. Finke, E. Lork, R. Mews, I. Y. Bagryanskaya, Y. V. Gatilov, S. N. Konchenko, V. G. Vasiliev, A. V. Zibarev, 'Tellurium–Nitrogen  $\pi$ -Heterocyclic Chemistry – Synthesis, Structure, and Reactivity Toward Halides and Pyridine of 3,4-Dicyano-1,2,5-telluradiazole', *Eur. J. Inorg. Chem.* **2012**, *2012*, 3693-3703.
- [58] N. A. Semenov, A. V. Lonchakov, N. A. Pushkarevsky, E. A. Suturina, V. V. Korolev, E. Lork, V. G. Vasiliev, S. N. Konchenko, J. Beckmann, N. P. Gritsan, A. V. Zibarev, 'Coordination of Halide and Chalcogenolate Anions to Heavier 1,2,5-Chalcogenadiazoles: Experiment and Theory', *Organomet.* **2014**, *33*, 4302-4314.
- [59] G. E. Garrett, E. I. Carrera, D. S. Seferos, M. S. Taylor, 'Anion Recognition by a Bidentate Chalcogen Bond Donor', *Chem. Commun.* **2016**, *52*, 9881-9884.
- [60] J. Y. C. Lim, I. Marques, A. L. Thompson, K. E. Christensen, V. Félix, P. D. Beer, 'Chalcogen Bonding Macrocycles and [2]Rotaxanes for Anion Recognition', *J. Am. Chem. Soc.* **2017**, *139*, 3122-3133.
- [61] J. Y. C. Lim, J. Y. Liew, P. D. Beer, 'Thermodynamics of Anion Binding by Chalcogen Bonding Receptors', *Chem. Eur. J.* **2018**, *24*, 14560-14566.
- [62] A. Borissov, I. Marques, J. Y. C. Lim, V. Félix, M. D. Smith, P. D. Beer, 'Anion Recognition in Water by Charge-Neutral Halogen and Chalcogen Bonding Foldamer Receptors', *J. Am. Chem. Soc.* **2019**, *141*, 4119-4129.
- [63] J. Y. C. Lim, I. Marques, V. Félix, P. D. Beer, 'Chiral Halogen and Chalcogen Bonding Receptors for Discrimination of Stereo- and Geometric Dicarboxylate Isomers in Aqueous Media', *Chem. Commun.* **2018**, *54*, 10851-10854.
- [64] S. Benz, M. Macchione, Q. Verolet, J. Mareda, N. Sakai, S. Matile, 'Anion Transport with Chalcogen Bonds', *J. Am. Chem. Soc.* **2016**, *138*, 9093-9096.
- [65] M. Macchione, M. Tsemperouli, A. Goujon, A. R. Mallia, N. Sakai, K. Sugihara, S. Matile, 'Mechanosensitive Oligodithienothiophenes: Transmembrane Anion Transport Along Chalcogen-Bonding Cascades', *Helv. Chim. Acta* **2018**, *101*, e1800014.
- [66] L. M. Lee, M. Tsemperouli, A. I. Poblador-Bahamonde, S. Benz, N. Sakai, K. Sugihara, S. Matile, 'Anion Transport with Pnictogen Bonds in Direct Comparison with Chalcogen and Halogen Bonds', *J. Am. Chem. Soc.* **2019**, *141*, 810-814.
- [67] S. Benz, J. López-Andarias, J. Mareda, N. Sakai, S. Matile, 'Catalysis with Chalcogen Bonds', *Angew. Chem. Int. Ed.* **2017**, *56*, 812-815.
- [68] S. Benz, J. Mareda, C. Besnard, N. Sakai, S. Matile, 'Catalysis with Chalcogen Bonds: Neutral Benzodiselenazole Scaffolds with High-Precision Selenium Donors of Variable Strength', *Chem. Sci.* **2017**, *8*, 8164-8169.
- [69] P. Wonner, L. Vogel, M. Düser, L. Gomes, F. Kniep, B. Mallick, D. B. Werz, S. M. Huber, 'Carbon–Halogen Bond Activation by Selenium-Based Chalcogen Bonding', *Angew. Chem. Int. Ed.* **2017**, *56*, 12009-12012.
- [70] P. Wonner, L. Vogel, F. Kniep, S. M. Huber, 'Catalytic Carbon–Chlorine Bond Activation by Selenium-Based Chalcogen Bond Donors', *Chem. Eur. J.* **2017**, *23*, 16972-16975.
- [71] W. Wang, H. Zhu, S. Liu, Z. Zhao, L. Zhang, J. Hao, Y. Wang, 'Chalcogen–Chalcogen Bonding Catalysis Enables Assembly of Discrete Molecules', *J. Am. Chem. Soc.* **2019**, *141*, 9175-9179.
- [72] L. Chen, J. Xiang, Y. Zhao, Q. Yan, 'Reversible Self-Assembly of Supramolecular Vesicles and Nanofibers Driven by Chalcogen-Bonding Interactions', *J. Am. Chem. Soc.* **2018**, *140*, 7079-7082.

- [73] L.-J. Riwar, N. Trapp, K. Root, R. Zenobi, F. Diederich, 'Supramolecular Capsules: Strong versus Weak Chalcogen Bonding', *Angew. Chem. Int. Ed.* **2018**, *57*, 17259-17264.
- [74] O. Dumele, B. Schreib, U. Warzok, N. Trapp, C. A. Schalley, F. Diederich, 'Halogen-Bonded Supramolecular Capsules in the Solid State, in Solution, and in the Gas Phase', *Angew. Chem. Int. Ed.* **2017**, *56*, 1152-1157.
- [75] O. Dumele, N. Trapp, F. Diederich, 'Halogen Bonding Molecular Capsules', *Angew. Chem. Int. Ed.* **2015**, *54*, 12339-12344.
- [76] R. Neidlein, D. Knecht, H. Endres, in *Zeitschrift für Naturforschung B*, Vol. 42, 1987, p. 84.
- [77] T. Chivers, X. Gao, M. Parvez, 'Preparation, Crystal Structures, and Isomerization of the Tellurium Diimide Dimers  $RNTe(\mu-NR')_2TeNR$  ( $R = R' = tBu$ ;  $R = PPh_2NSiMe_3$ ,  $R' = tBu$ ,  $tOct$ ): X-ray Structure of the Telluradiazole Dimer  $[tBu_2C_6H_2N_2Te]_2$ ', *Inorg. Chem.* **1996**, *35*, 9-15.
- [78] A. F. Cozzolino, Q. Yang, I. Vargas-Baca, 'Engineering Second-Order Nonlinear Optical Activity by Means of a Noncentrosymmetric Distortion of the  $[Te-N]_2$  Supramolecular Synthons', *Cryst. Growth Des.* **2010**, *10*, 4959-4964.
- [79] P. B. Pati, S. S. Zade, 'Benzoselenadiazole Containing Donor-Acceptor-Donor Small Molecules: Nonbonding Interactions, Packing Patterns, and Optoelectronic Properties', *Cryst. Growth Des.* **2014**, *14*, 1695-1700.
- [80] S. Mondal, M. Konda, B. Kauffmann, M. K. Manna, A. K. Das, 'Effects of Donor and Acceptor Units Attached with Benzoselenadiazole: Optoelectronic and Self-Assembling Patterns', *Cryst. Growth Des.* **2015**, *15*, 5548-5554.
- [81] L. M. Lee, P. J. W. Elder, A. F. Cozzolino, Q. Yang, I. Vargas-Baca, 'An Experimental and Computational Investigation of the Formation and Structures of N-hydro and N,N'-dihydrobenzo-2,1,3-chalcogenadiazolium Chloride', *Main Group Chem.* **2010**, *9*, 117-133.
- [82] G. Berionni, B. Pégot, J. Marrot, R. Goumont, 'Supramolecular Association of 1,2,5-Chalcogenadiazoles: an Unexpected Self-Assembled Dissymmetric  $[Se \cdots N]_2$  Four-Membered Ring', *Cryst. Eng. Comm.* **2009**, *11*, 986-988.
- [83] M. Risto, R. W. Reed, C. M. Robertson, R. Oilunkaniemi, R. S. Laitinen, R. T. Oakley, 'Self-association of the N-methyl Benzotellurodiazolium Cation: Implications for the Generation of Super-Heavy Atom Radicals', *Chem. Commun.* **2008**, 3278-3280.
- [84] L. M. Lee, V. B. Corless, M. Tran, H. Jenkins, J. F. Britten, I. Vargas-Baca, 'Synthetic, Structural, and Computational Investigations of N-alkyl benzo-2,1,3-selenadiazolium Iodides and their Supramolecular Aggregates', *Dalton Trans.* **2016**, *45*, 3285-3293.
- [85] L. M. Lee, V. Corless, H. Luu, A. He, H. Jenkins, J. F. Britten, F. Adam Pani, I. Vargas-Baca, 'Synthetic and Structural Investigations of Bis(N-alkyl-benzoselenadiazolium) Cations', *Dalton Trans.* **2019**, *48*, 12541-12548.
- [86] A. F. Cozzolino, A. D. Bain, S. Hanhan, I. Vargas-Baca, 'N-Triphenylboryl- and N,N'-bis(triphenylboryl)benzo-2,1,3-telluradiazole', *Chem. Commun.* **2009**, 4043-4045.
- [87] J. Lee, L. M. Lee, Z. Arnott, H. Jenkins, J. F. Britten, I. Vargas-Baca, 'Sigma-Hole Interactions in the Molecular and Crystal Structures of N-boryl benzo-2,1,3-selenadiazoles', *New J. Chem.* **2018**, *42*, 10555-10562.
- [88] P. C. Ho, P. Szydowski, J. Sinclair, P. J. W. Elder, J. Kubel, C. Gendy, L. M. Lee, H. Jenkins, J. F. Britten, D. R. Morim, I. Vargas-Baca, 'Supramolecular Macrocycles Reversibly Assembled by Te Center dot Center dot Center dot O Chalcogen Bonding', *Nat. Commun.* **2016**, *7*, 11299.
- [89] J. Kübel, P. J. W. Elder, H. A. Jenkins, I. Vargas-Baca, 'Structure and Formation of the First  $(-O-Te-N-)_4$  Ring', *Dalton Trans.* **2010**, *39*, 11126-11128.
- [90] J. Wang, P. C. Ho, J. F. Britten, V. Tomassetti, I. Vargas-Baca, 'Structural Diversity of the Complexes of Monovalent Metal d10 Ions with Macrocyclic Aggregates of Iso-tellurazole N-oxides', *New J. Chem.* **2019**.

- [91] P. C. Ho, H. A. Jenkins, J. F. Britten, I. Vargas-Baca, 'Building New Discrete Supramolecular Assemblies Through the Interaction of Iso-tellurazole N-oxides with Lewis Acids and Bases', *Faraday Discuss.* **2017**, *203*, 187-199.
- [92] P. C. Ho, J. Rafique, J. Lee, L. M. Lee, H. A. Jenkins, J. F. Britten, A. L. Braga, I. Vargas-Baca, 'Synthesis and Structural Characterisation of the Aggregates of Benzo-1,2-chalcogenazole 2-oxides', *Dalton Trans.* **2017**, *46*, 6570-6579.
- [93] K. Eichstaedt, A. Wasilewska, B. Wicher, M. Gdaniec, T. Połński, 'Supramolecular Synthesis Based on a Combination of Se...N Secondary Bonding Interactions with Hydrogen and Halogen Bonds', *Cryst. Growth Des.* **2016**, *16*, 1282-1293.
- [94] Y. V. Torubaev, D. K. Rai, I. V. Skabitsky, S. Pakhira, A. Dmitrienko, 'Energy Framework Approach to the Supramolecular Reactions: Interplay of the Secondary Bonding Interaction in Ph<sub>2</sub>E<sub>2</sub> (E = Se, Te)/p-I-C<sub>6</sub>F<sub>4</sub>-I co-crystals', *New J. Chem.* **2019**, *43*, 7941-7949.
- [95] D. B. Werz, R. Gleiter, F. Rominger, 'Nanotube Formation Favored by Chalcogen-Chalcogen Interactions', *J. Am. Chem. Soc.* **2002**, *124*, 10638-10639.
- [96] D. B. Werz, F. R. Fischer, S. C. Kornmayer, F. Rominger, R. Gleiter, 'Macrocyclic Cyclophanes with Two and Three  $\alpha,\omega$ -Dichalcogeno-1,4-diethynylaryl Units: Syntheses and Structural Properties', *J. Org. Chem.* **2008**, *73*, 8021-8029.
- [97] D. B. Werz, R. Gleiter, F. Rominger, 'Cyclic Tetra- and Hexayines Containing 1,4-Donor-Substituted Butadiyne Units: Synthesis and Supramolecular Organization', *J. Org. Chem.* **2004**, *69*, 2945-2952.
- [98] K. Kobayashi, H. Masu, A. Shuto, K. Yamaguchi, 'Control of Face-to-Face  $\pi$ - $\pi$  Stacked Packing Arrangement of Anthracene Rings via Chalcogen-Chalcogen Interaction: 9,10-Bis(methylchalcogeno)anthracenes', *Chem. Mater.* **2005**, *17*, 6666-6673.
- [99] R. Gleiter, G. Haberhauer, D. B. Werz, F. Rominger, C. Bleiholder, 'From Noncovalent Chalcogen-Chalcogen Interactions to Supramolecular Aggregates: Experiments and Calculations', *Chem. Rev.* **2018**, *118*, 2010-2041.
- [100] F. Di Maria, P. Olivelli, M. Gazzano, A. Zanelli, M. Biasiucci, G. Gigli, D. Gentili, P. D'Angelo, M. Cavallini, G. Barbarella, 'A Successful Chemical Strategy To Induce Oligothiophene Self-Assembly into Fibers with Tunable Shape and Function', *J. Am. Chem. Soc.* **2011**, *133*, 8654-8661.
- [101] F. Di Maria, M. Zangoli, M. Gazzano, E. Fabiano, D. Gentili, A. Zanelli, A. Fermi, G. Bergamini, D. Bonifazi, A. Perinot, M. Caironi, R. Mazzaro, V. Morandi, G. Gigli, A. Liscio, G. Barbarella, 'Controlling the Functional Properties of Oligothiophene Crystalline Nano/Microfibers via Tailoring of the Self-Assembling Molecular Precursors', *Adv. Funct. Mater.* **2018**, *28*, 1801946.
- [102] E. Salatelli, M. Marinelli, M. Lanzi, A. Zanelli, S. Dell'Elce, A. Liscio, M. Gazzano, F. Di Maria, 'Bulk Heterojunction Solar Cells: The Role of Alkyl Side Chain on Nanoscale Morphology of Sulfur Over-rich Regioregular Polythiophene/Fullerene Blends', *J. Phys. Chem. C* **2018**, *122*, 4156-4164.
- [103] R. Peng, H. Guo, J. Xiao, G. Wang, S. Tan, B. Zhao, X. Guo, Y. Li, 'Synergistic Effect of Fluorine Substitution and Thio-Alkylation on Photovoltaic Performances of Alternating Conjugated Polymers Based on Alkylthio-Substituted Benzothiadiazole-Quaterthiophene', *ACS Appl. Energy Mater.* **2018**, *1*, 2192-2199.
- [104] A. Kremer, A. Fermi, N. Biot, J. Wouters, D. Bonifazi, 'Supramolecular Wiring of Benzo-1,3-chalcogenazoles through Programmed Chalcogen Bonding Interactions', *Chem. Eur. J.* **2016**, *22*, 5665-5675.
- [105] A. Kremer, C. Aurisicchio, F. De Leo, B. Ventura, J. Wouters, N. Armaroli, A. Barbieri, D. Bonifazi, 'Walking Down the Chalcogenic Group of the Periodic Table: From Singlet to Triplet Organic Emitters', *Chem. Eur. J.* **2015**, *21*, 15377-15387.
- [106] M. Mbuyi, M. Evers, G. Tihange, A. Luxen, L. Christiaens, 'The 1,3-Benzotellurazole : A New Heterocyclic System', *Tetrahedron Lett.* **1983**, *24*, 5873-5876.

- [107] C. S. Radatz, D. Alves, P. H. Schneider, 'Direct Synthesis of 2-aryl-1,3-Benzoselenazoles by Reaction of Bis(2-aminophenyl) diselenides with Aryl Aldehydes Using Sodium Metabisulfite', *Tetrahedron* **2013**, *69*, 1316-1321.
- [108] S. Redon, Y. Kabri, M. D. Crozet, P. Vanelle, 'One-Pot Preparation of 2-(Alkyl)arylbenzoselenazoles from the Corresponding N-(Acetyl)benzoyl-2-iodoanilines via a Microwave-assisted Methodology', *Tetrahedron Lett.* **2014**, *55*, 5052-5054.
- [109] T. Su, S. Xie, B. Li, J. Yan, L. Huang, X. Li, 'Copper-Catalyzed Three-Component One-Pot Synthesis of Substituted 2-Aryl-1,3-benzoselenazoles', *Synlett* **2015**, *26*, 215-220.

---

## **Chapter II**

# **Programming Recognition Arrays Through Double Chalcogen-Bonding Interactions**

---

In this chapter, we aim to design, synthesise and challenge a novel supramolecular synthon based on chalcogen-bonding interactions contemplating the  $\beta$ -fusion of a chalcogenazole ring to a pyridine moiety. Capitalising on recent achievements of our group on benzochalcogenazole derivatives, we present the chalcogenazolopyrine (CGP) recognition array as reliable, heat and moisture stable and of easy derivatisation, through the synthesis of 20 derivatives. The double chalcogen-bonding motif is probed at the solid state by single crystal X-ray diffraction analysis of those compounds. The system is challenged through different applications such as crystal engineering, soft material and organic semi-conductor. Part of this work has been published in a recent communication in *Chemistry – A European Journal*.<sup>[1]</sup>

The chapter is divided in seven sections. *Section II-1* covers a brief introduction of single and double chalcogen-bonded structure; *Section II-2* presents the design of the CGP array and the calculation results on substituent effect; *Section II-3* provides the synthesis of the targeted molecules; *Section II-4* shows the recognition at work through analysis of 18 crystal structures; *Section II-5* deals with the formation of ditopic CGP and benzochalcogenazole structures; *Section II-6* appraises the possibilities of soft materials based on chalcogen-bonding as non-covalent driving force; *Section II-7* is divided in five parts, from the design of an organic-semiconductor based on a pyrene structure relying on the inclusion of CGP recognition array to drive the supramolecular assembly; moving to the synthesis of those molecules, the characterisation of their optoelectronic properties in solution and their crystal structures to understand the results of the charge mobility experiments.

The work presented in this chapter has been realised thanks to the teaching of *Dr. B. Kariuki*, the crystals reported here served as training for single crystal X-ray diffraction technique. Advices from *Dr. O. Dumele* led to the synthesis of compound **II-14**. *Dr. S. Gambino* and *R. Mastria*, from CNR nanotech in Lecce (Italy) preformed the charge mobility experiments developed in *Section II-7*.

## II – 1 Introduction

As described in *Chapter I*, the principle of molecular recognition sits at the core of supramolecular chemistry.<sup>[2]</sup> The storage of bonding information in a recognition arrays is, thus, crucial to trigger the formation of specific array of intermolecular non-covalent interactions that have the ability to drive molecules into complex architectures through programmed association.<sup>[3]</sup> As a summary of the introductory chapter, some key supramolecular structures formed through single and double chalcogen-bonding interactions are reported below (Figure II – 1). The anion recognition described by *Taylor*,<sup>[4]</sup> the macrocyclic assemblies covered by *Vargas-Baca*,<sup>[5]</sup> and wire-like structure introduced by us formed through single Y...E contacts.<sup>[6]</sup> The most common structure featuring multiple chalcogen-bonding interactions is the ribbon formed by 1,2,5-telluradiazole implying a first nearest neighbour (FNN) type motif.<sup>[7, 8]</sup> Bifurcated chalcogen-bonds have also been described by *Reid* and co-workers,<sup>[9]</sup> with the E atom acting as double EB donor and by successive work of *Taylor*,<sup>[10]</sup> *Matile*,<sup>[11, 12]</sup> *Beer*,<sup>[13, 14]</sup> and *Huber*,<sup>[15, 16]</sup> capitalising on a confocal approach of the  $\sigma$ -holes with Y being double chalcogen bond acceptor. This work focuses on dimer formation through double chalcogen-bonding interaction featuring a second nearest neighbour (SNN) type motif.

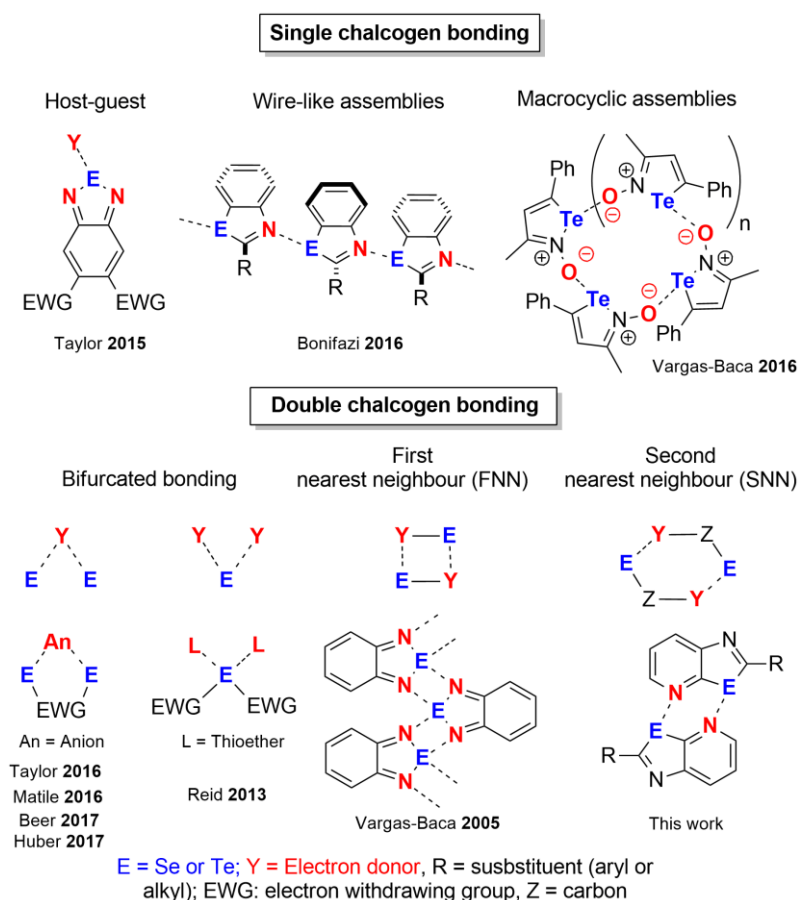


Figure II - 1: Brief summary of supramolecular structure formed by single and double chalcogen-bonding interactions. Reproduced with permission,<sup>[1]</sup> copyright 2018 Willey-VCH Verlag GmbH & Co. KGaA, Weinheim.

## II – 2 Design

Building on the results obtained with the benzo-1,3-chalcogenazole scaffolds,<sup>[6]</sup> in this part of the thesis, we report on a molecular motifs leading to double chalcogen-bonded EY-type arrays with high recognition fidelity, chemical and thermal stability and synthetic ease of derivatisation. Provided that a carbon atom is replaced by a basic heteroatom (Y) in the benzenic ring of a benzochalcogenazole,<sup>[6]</sup> one can expect to program a recognition motif giving a double chalcogen-bonded array (Figure II – 2). Thus, we conjectured that the  $\beta$ -fusion of a chalcogenazole to a pyridine ring to give a chalcogenazolo[5,4- $\beta$ ]pyridine unit (abbreviated as CGP, Figure II – 2) should lead to a self-complementary motif that, through the peripheral exposition of second nearest neighbouring (SNN) chalcogen-bonding donor (E) and acceptor (Y) atoms, can undergo dimerization. To validate this recognition ability, we used electrostatic surface potential (ESP)<sup>[4, 17-19]</sup> and estimated the value ( $V_{s,max}$ ) at the point of the highest potential for both donor and acceptor atoms.<sup>[4, 17-19]</sup> The ESPs of H-substituted models for the Se- and Te-doped CGPs are shown below (Figure II – 2). In addition, the relevant molecular orbital for each structure are reported, displaying the lone pair ( $n$ ) and  $\sigma^*$  containing MO.

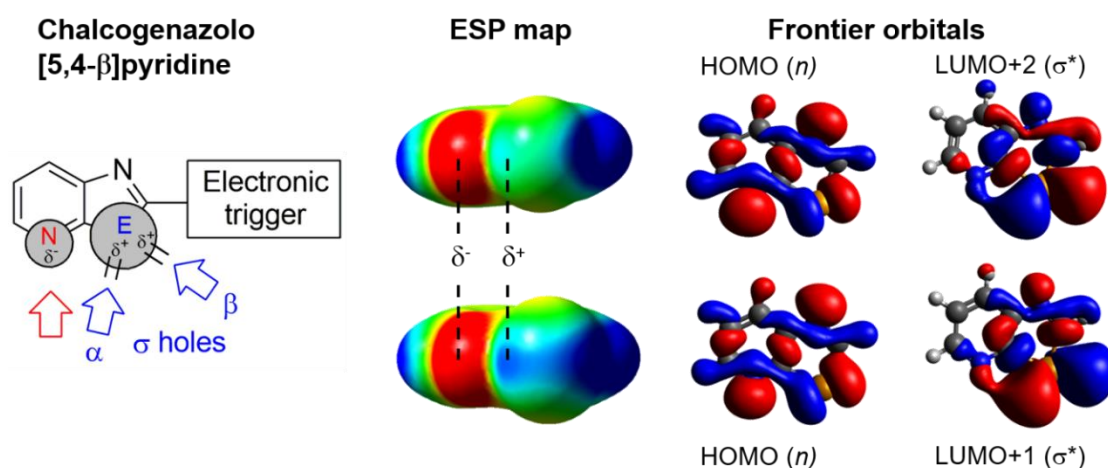
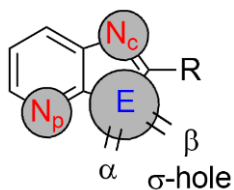
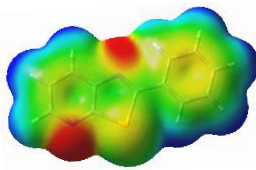
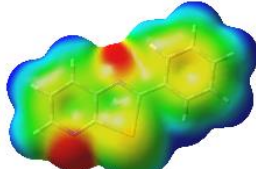
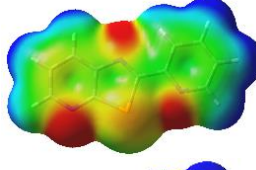
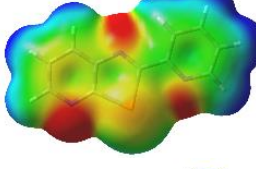
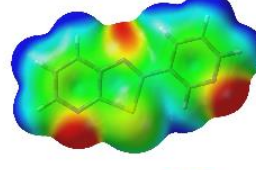
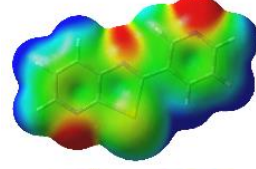
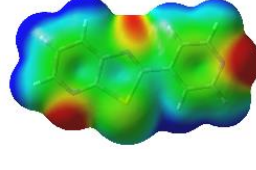


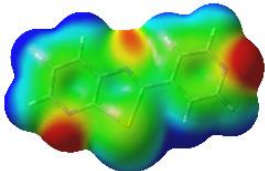
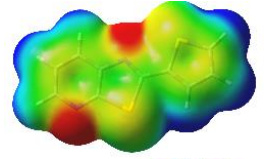
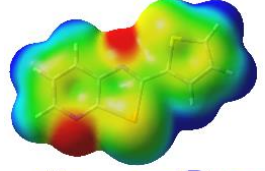
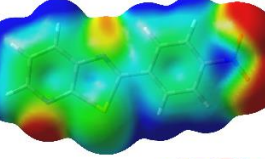
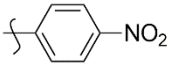
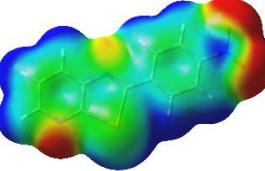
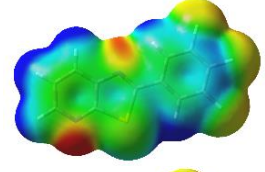
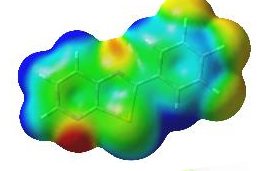
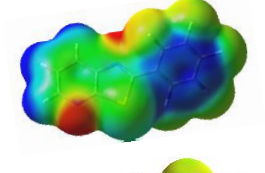
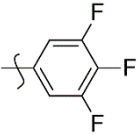
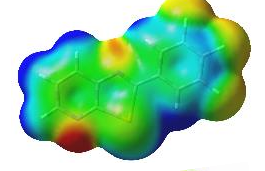
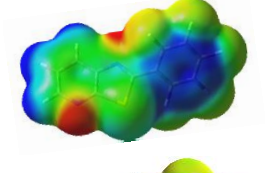
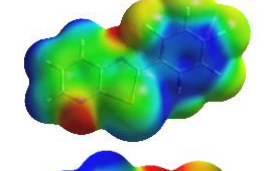
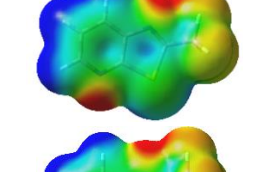
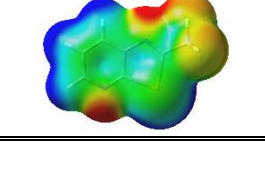
Figure II - 2: General structure of differently functionalised CGP motif (left). ESP (calculated using Gaussian 09 at B97-D3/def2-TZVP level of theory)<sup>[4]</sup> mapped on the van-der-Waals surface of the CGP motifs (centre, Se top and Te bottom) along with the relevant molecular orbitals involved in the interactions (right). Reproduced with permission;<sup>[1]</sup> copyright 2018 Willey-VCH Verlag GmbH & Co. KGaA, Weinheim.

As expected, electron deficient  $\sigma$ -holes ( $\alpha$ ) and  $\sigma$ -holes ( $\beta$ ) are present on the chalcogen atom,<sup>[6]</sup> with that in  $\alpha$  being the depleted region engaging into the non-covalent array through  $n^2 \rightarrow \sigma^*$  orbital delocalization.<sup>[6]</sup> The calculated  $V_{s,max}$  values are +5.4 and +10.5 kcal mol<sup>-1</sup> for the  $\sigma$ -holes ( $\alpha$ ) of the Se- and Te-congeners, respectively. Those potentials are lower in comparison to their benzo-1,3-chalcogenazoles analogues (+18.8 and +21.3 kcal mol<sup>-1</sup>,<sup>[6]</sup> respectively) inferring a weaker Lewis acidity at the chalcogen atom for the CGP derivatives.

Table II - 1: Calculated  $V_{s,max}$  values for CGP derivatives and their respective Electrostatic Surface Potential maps (using Gaussian 09 at B97-D3/def2-TZVP level of theory).<sup>[4]</sup> Geometries are relaxed coordinate of the corresponding crystal structures.



Entry	E	ESP maps	$V_{s,max}$ (kcal mol <sup>-1</sup> )		
			N <sub>c</sub>	N <sub>p</sub>	σ-hole (α)
1	Se		-19.4	-30.7	+2.29
	Te		-17.9	-30.0	+7.71
2	Se		-19.4	-32.0	-0.36
	Te		-18.5	-32.0	+5.67
3	Se		-15.7	-28.8	+5.02
	Te		-14.4	-27.0	+10.7
4	Se		-15.1	-26.8	+7.09

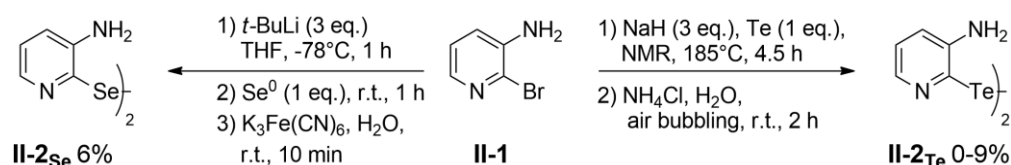
5		Te		-13.9	-26.1	+12.5
		Se		-24.1	-30.5	+3.70
		Te		-22.3	-29.6	+9.53
		Se		-11.6	-24.5	+9.84
6		Te		-10.2	-24.0	+15.5
		Se		-13.6	-25.9	+7.84
		Te		-12.1	-25.9	+13.4
		Se		-23.1	-26.6	+8.30
7		Te		-12.1	-25.9	+13.4
		Se		-23.1	-26.6	+8.30
		Te		-22.0	-26.0	+14.1
		Se		-24.1	-23.6	+12.7
9		Te		-23.6	-23.0	+19.1

This behaviour can be rationalized by the partial overlap of the lone pair of the N atom with the  $\sigma$ -hole ( $\alpha$ ) of the Chalcogen atoms (see LUMO +2 and LUMO +1 for Se and Te, respectively).  $V_{s,max}$  values of similar magnitude were obtained for the pyridyl N atom (abbreviated  $N_p$ ) of both Se and Te derivatives (-28.7 and -27.8 kcal mol<sup>-1</sup>, respectively, vs 35.5 kcal mol<sup>-1</sup> for naked pyridine<sup>[6]</sup>), whereas weaker potentials were found for the chalcogenazole N atom (abbreviated  $N_c$ , -26.5 and -25.1 kcal mol<sup>-1</sup>, respectively). Building on these computational results, one can envisage that the chalcogen interactions will be preferentially established through  $N_p$  atom. We thus engineered Se- and Te-containing CGPs bearing different substituents at the 2-position, calculating their  $V_{s,max}$  values at both  $N_p$  and  $N_c$  positions and at the  $\alpha$   $\sigma$ -hole of the Chalcogen (Table II – 1).

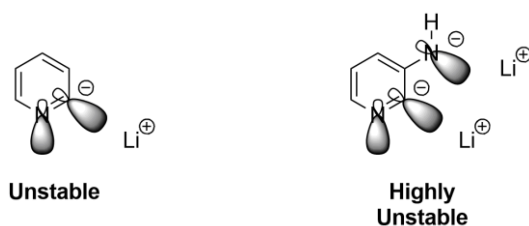
Derivatives bearing a phenyl moiety in 2-position (entry 1, Table II – 1) will be used as synthetic reference for this work. It has to be noted that the potential values at the  $\sigma$ -hole ( $\alpha$ ) (+2.29 and +7.71 kcal mol<sup>-1</sup>, for Se and Te, respectively) are smaller than in the case of the un-substituted ones (+5.4 and +10.5 kcal mol<sup>-1</sup> for Se and Te respectively). Introduction of pyrid-2-yl (entry 2) lowers further those numbers (-0.36 and +5.67 kcal mol<sup>-1</sup>, for Se and Te, respectively) due to the partial electron donation from the N atom of the 2-substituent and the  $\sigma$ -hole ( $\beta$ ) of the chalcogen. Other aromatics have similar  $V_{s,max}$  values (between +3.70 and +7.09 kcal mol<sup>-1</sup> for Se- and +9.53 and +12.5 kcal mol<sup>-1</sup> for Te-derivatives, entries 3, 4, 5). Electron withdrawing substituents (entries 6, 7 and 8) increases the values up to +9.84 for Se and +15.5 kcal mol<sup>-1</sup> for Te. Whereas the maximum is reached by the CF<sub>3</sub> moiety (entry 9) of +12.7 and +19.1 kcal mol<sup>-1</sup>, for Se and Te, respectively. Moreover, one can easily observe that the more positive are the  $\sigma$ -holes the less negative are the potentials around the  $N_p$  atoms (from -32.0 to -23.6 kcal mol<sup>-1</sup> for Se-derivatives and from -32.0 to -23.0 kcal mol<sup>-1</sup> for Te-analogues). Nonetheless, we anticipate at this stage of the work the formation of a dimeric structure with shorter distance of interaction with derivative presenting the deepest  $\sigma$ -holes. It is also expected of the Se-congener bearing smaller  $V_{s,max}$  to form weaker interactions or no chalcogen bond (particularly in the case of entry 2 whereas this value is negative).

## II – 3 Synthesis

At the synthetic planning level, we contemplated the dehydrative cyclization reaction as the key synthetic step for the preparation of CGP derivatives.<sup>[20]</sup> The synthesis commenced with the formation of the dichalcogenide **II-2** starting from 3-amino-2-bromopyridine. In a first approach, the reaction conditions developed for the preparation of 2,2'-diselanediyldianiline and 2,2'-ditellanediyldianiline in our previous work have been applied (Scheme II - 1).<sup>[20]</sup>

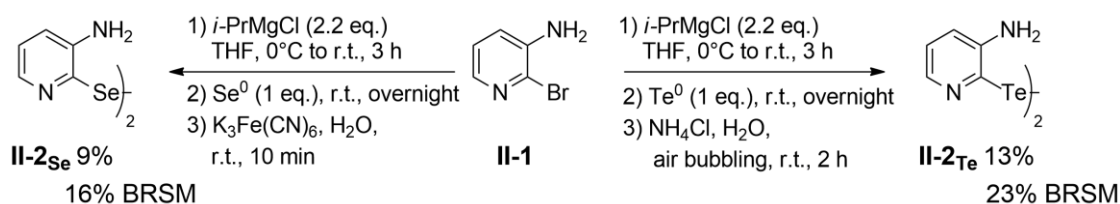
Scheme II - 1: Synthesis of **II-2<sub>Se</sub>** and **II-2<sub>Te</sub>**.

In the case of the Se-derivative, **II-1** was treated with 3 equivalents of *t*-BuLi in dry THF at  $-78^{\circ}\text{C}$ , the resulting mixture was reacted with elemental selenium powder and, after oxidation, **II-2<sub>Se</sub>** was obtained in 6% yield. For the second analogue, elemental Te powder was treated with an excess of NaH and the resulting mixture was reacted with **II-1** to afford ditelluride **II-2<sub>Te</sub>** in up to 9% yield after oxidation. Both protocols are low yielding, more particularly for **II-2<sub>Te</sub>**, the reaction revealed to be unreliable with tedious purification. For **II-2<sub>Se</sub>**, a problem in the metal-halogen exchange process has been noted. According to the work of *Parham et al.* on lithiation of 2-bromopyridine,<sup>[21]</sup> the organometallic intermediate resulting of the bromine-lithium exchange displays two pairs of unshared electrons which are co-planar in close proximity (Scheme II - 2), destabilising the resulting aryllithiums derivative. Moreover, in the case of 3-amino-2-bromopyridine, deprotonation of the amino group must occur prior to the exchange. The proximity of the negatives charges destabilises the metalated intermediate leading to decomposition.

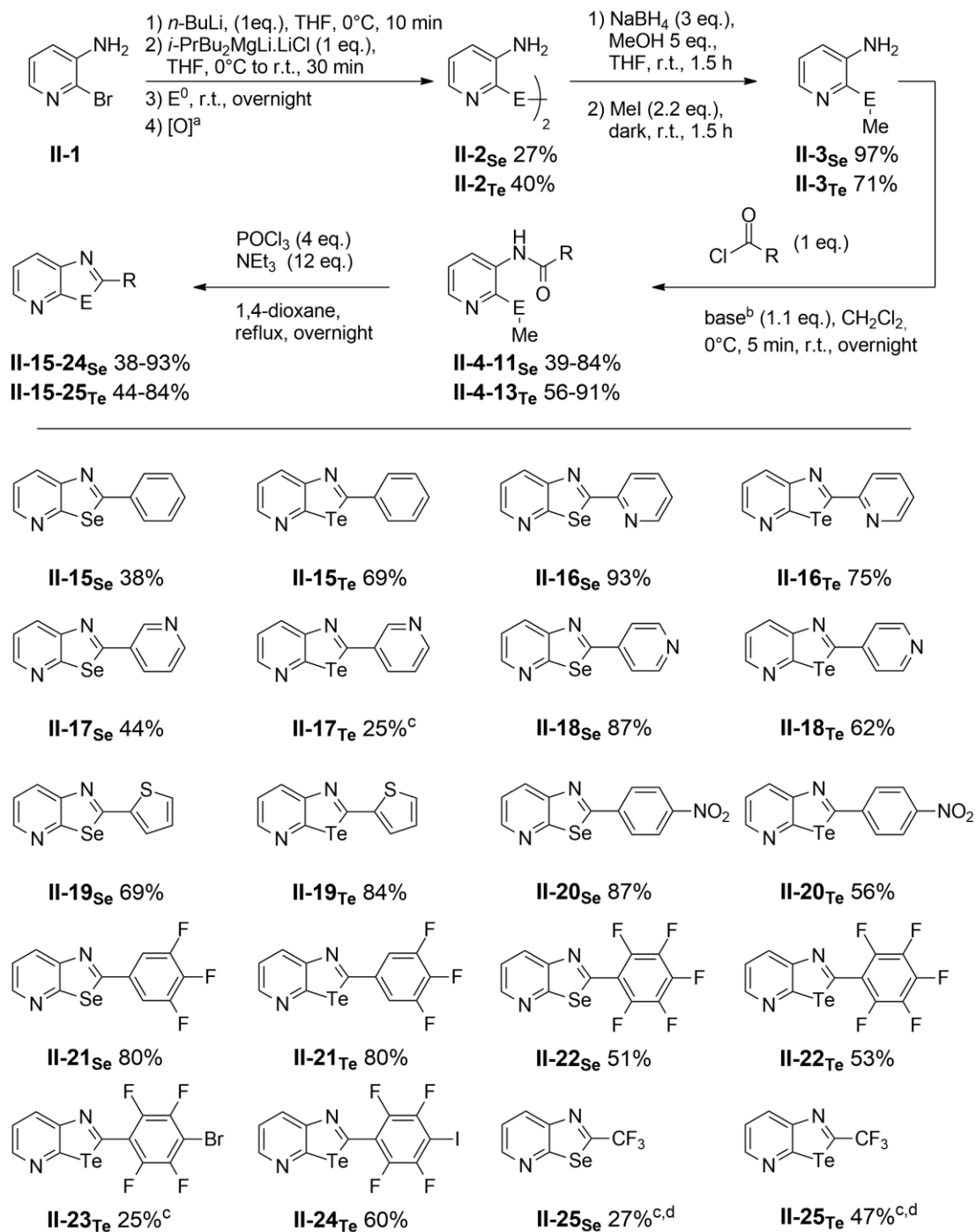


Scheme II - 2: Lithiated intermediates from 2-bromopyridine (left) and 2-bromo-3-aminopyridine (right).

In order to overcome the problem of the metalation of 2-bromopyridine, *Song* and co-workers proposed to use Grignard reagent *i*-PrMgCl with success.<sup>[22]</sup> The same strategy was applied to 3-amino-2-bromopyridine (Scheme II - 3), the metalated intermediate was treated with elemental chalcogen powder and after oxidation, **II-2<sub>Se</sub>** and **II-2<sub>Te</sub>** were obtained in 9% and 13% yield, respectively.

Scheme II - 3: Synthesis of **II-2<sub>Se</sub>** and **II-2<sub>Te</sub>** using *i*-PrMgCl.

In both cases, the isolated yield increased compared with the previous reaction conditions (Scheme II – 1). However, only 50% of **II-1** was converted during the metal-halogen exchange step. This allowed to perform the reaction multiple times recycling the starting material, giving yields of 16% and 23% BRSM (based on the recovery of the starting material), respectively.



Scheme II - 4: Synthetic route for preparing the CGP synthon through the dehydrative cyclization reaction. *E* = Se or Te; a) for **II-2**<sub>Se</sub>  $K_3\text{Fe(CN)}_6$  in  $\text{H}_2\text{O}$  for 10 min, while for **II-2**<sub>Te</sub> air bubbling in a buffered  $\text{NH}_4\text{Cl}$  aq. solution for 2h; b) dry pyridine was generally used as base at the exception of **II-4**<sub>Se</sub>, **II-5**<sub>E</sub>, and **II-10**<sub>Te</sub> for which dry  $\text{NEt}_3$  was used; c) the yield calculated over two steps; d)  $(\text{CF}_3\text{CO})_2\text{O}$  was used for the amidation step.

In this case, the magnesium cation has the effect of stabilising the corresponding metalated intermediate that does not undergo decomposition reactions. Nonetheless, the stabilisation effect is not sufficient to shift the metal-halogen exchange equilibrium completely towards the formation of the product. This idea led us to use a more reactive organometallic specie, namely trialkyl magnesate, first introduced by *Wittig* in 1951.<sup>[23]</sup> This ate complex, formed by treating *i*-PrMgCl with two equivalent of *n*-BuLi, is used to perform metalation reactions on electron-rich aromatic substituents.<sup>[24]</sup> In the case of 3-amino-2-bromopyridine **II-1**, a deprotonation with *n*-BuLi is required prior to the reaction with *i*-PrBu<sub>2</sub>MgLi•LiCl (Scheme II – 4). This reagent is able to shift the exchange equilibrium completely towards the formation of the metalated intermediate. Subsequent treatment of the reaction mixture with the corresponding freshly ground elemental chalcogen powder (E = Se and Te) followed by oxidation led to the formation of **II-2<sub>Se</sub>** and **II-2<sub>Te</sub>** in 27 and 40%, respectively. Reductive cleavage of the dichalcogenide using NaBH<sub>4</sub> in the presence of MeOH in THF gave the corresponding pyridylchalcogenolate that, reacting with MeI, could be transformed into the relevant pyridine derivative **II-3<sub>E</sub>**. From those amines, we could synthesise a series of Se- (**II-4<sub>Se</sub>** – **II-11<sub>Se</sub>**) and Te-bearing (**II-4<sub>Te</sub>** – **II-13<sub>Te</sub>**) amides with very good yields upon reaction with the appropriate acyl chloride. With these intermediates in our hands, we could prepare 2-substituted Se- (**II-15<sub>Se</sub>** – **II-22<sub>Se</sub>**, **II-25<sub>Se</sub>**) and Te-congeners (**II-15<sub>Te</sub>** – **II-25<sub>Te</sub>**) in good to excellent yields (38-93%), following the dehydrative cyclisation protocol developed in our group (POCl<sub>3</sub> in the presence of NEt<sub>3</sub> under reflux in 1,4-dioxane).<sup>[6, 20]</sup> CGP derivatives were successfully synthesised bearing different aromatic moieties in 2-position (**II-15<sub>E</sub>**, **II-20<sub>E</sub>**, **II-21<sub>E</sub>**, **II-22<sub>E</sub>**, **II-23<sub>Te</sub>** and **II-24<sub>Te</sub>**), as well as heterocyclic rings, like thiophenyl (**II-19<sub>E</sub>**) and pyridyl (**II-16<sub>E</sub>**, **II-17<sub>E</sub>** and **II-18<sub>E</sub>**) substituents (Scheme II – 4). All structures were fully characterized by <sup>1</sup>H- and <sup>13</sup>C-NMR spectroscopy, IR, and HR-Mass spectrometry (See *chapter VI*).

## II – 4 Solid-state analysis

The association properties of the CGP **II-15<sub>E</sub>** – **II-25<sub>E</sub>** derivatives were probed in the solid state by means of X-ray analysis of the single crystals obtained by slow evaporation of the solution of all the relevant compounds in CHCl<sub>3</sub> or EtOH. However, despite the best of our effort, no single crystal suitable for X-ray diffraction analysis could be grown for derivative **II-20<sub>E</sub>**.

### II – 4.1 Recognition at work – Tellurium containing derivatives

Compound **II-15<sub>Te</sub>** crystallises in a P2/c space group and the asymmetric unit is constituted by one molecule. As conjectured in our programming strategy, one can easily observe that this derivative associates into dimer (**II-15<sub>Te</sub>**)<sub>2</sub>, through double N···Te interactions ( $d_{N...Te} = 3.006 \text{ \AA}$ , C-Te···N angle = 171°), involving the chalcogen  $\sigma$ -hole ( $\alpha$ ) and the N<sub>p</sub> atom (Figure II – 3, a). In the array, both CGP

and phenyl moieties are co-planar and undergo  $\pi$ - $\pi$  stacking arrangements ( $d_{\pi-\pi} = 3.477 \text{ \AA}$ ) with an off-set of  $5.808 \text{ \AA}$  (Figure II – 3, b). It is interesting to note that the distance of interaction is shorter in the present case than with the benzo-1,3-tellurazole ( $3.428 \text{ \AA}$  for the wire-like structure)<sup>[6, 25]</sup> despite the  $V_{s,\max}$  of  $\sigma$ -hole having been calculated smaller ( $+7.71$  vs  $+19.0 \text{ kcal mol}^{-1}$ , respectively). This can be rationalized by the fact that here two anti-parallel interactions come into play, strengthening the dimer formation.

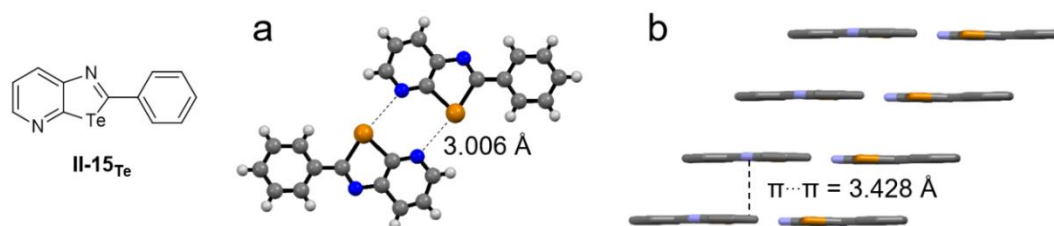


Figure II - 3: X-ray structure of **II-15<sub>Te</sub>**; a) top view, ball and stick representation; b) side view, stick representation, H atoms are omitted for sake of clarity. Space group:  $P2_1/c$ , solvent of crystallisation:  $\text{CHCl}_3$ .

Derivative **II-16<sub>Te</sub>** substituted with a 2-pyridyl crystallises in a  $P2_1/c$  space group with an asymmetric unit constituted by one molecule. X-ray analysis (Figure II – 4, a) reveals the formation of dimer (**II-16<sub>Te</sub>**)<sub>2</sub> through double Chalcogen-bonding interaction ( $d_{\text{N}\cdots\text{Te}} = 3.079 \text{ \AA}$ , C-Te $\cdots$ N angle =  $166^\circ$ ). Compared to **II-15<sub>Te</sub>**, the distance between N<sub>p</sub> and Te atoms is slightly longer, due to the intramolecular EB taking place between the N atom from the 2-pyridyl. In addition, the molecules interact through  $\pi$ - $\pi$  stacking ( $d_{\pi-\pi} = 3.413 \text{ \AA}$ ) with an off-set of  $5.908 \text{ \AA}$  (Figure II – 4, b).

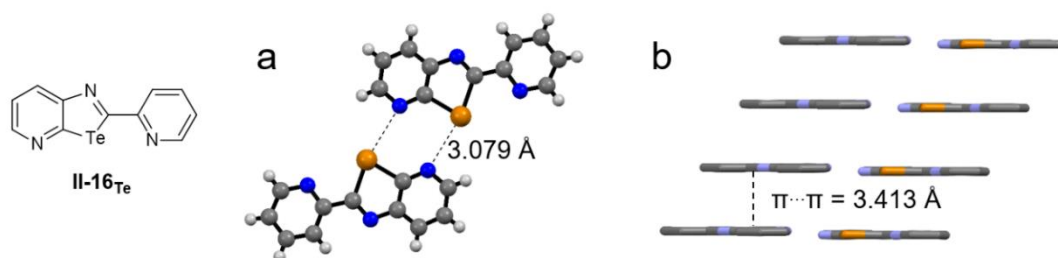


Figure II - 4: X-ray structure of **II-16<sub>Te</sub>**; a) top view, ball and stick representation; b) side view, stick representation, H atoms are omitted for sake of clarity. Space group:  $P2_1/c$ , solvent of crystallisation:  $\text{CHCl}_3$ .

Isomer **II-17<sub>Te</sub>** crystallises in a  $P2_1/c$  and one molecule composes the asymmetric unit. The compound forms dimer (**II-17<sub>Te</sub>**)<sub>2</sub> at the solid state (Figure II – 5, a) through double chalcogen-bonding interactions ( $d_{\text{N}\cdots\text{Te}} = 3.094 \text{ \AA}$ , C-Te $\cdots$ N angle =  $168^\circ$ ). An additional EB takes place involving the N atom of the pyrid-3-yl and the  $\sigma$ -hole ( $\beta$ ) of the Te atom ( $d_{\text{N}\cdots\text{Te}} = 3.480 \text{ \AA}$ , C-Te $\cdots$ N angle =  $169^\circ$ ). Molecules form columnar arrangement through  $\pi$ - $\pi$  stacking ( $d_{\pi-\pi} = 3.423 \text{ \AA}$ ) with an offset of  $5.295 \text{ \AA}$  (Figure II – 5, b).

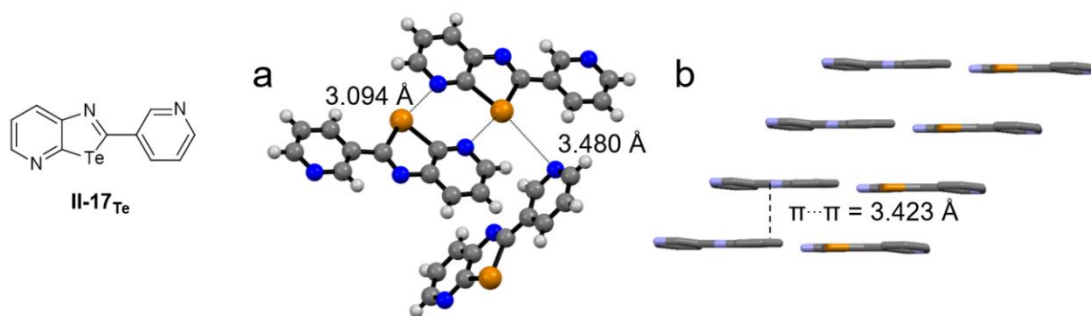


Figure II - 5: X-ray structure of **II-17<sub>Te</sub>**; a) top view, ball and stick representation; b) side view, stick representation, H atoms are omitted for sake of clarity. Space group:  $P2_1/c$ , solvent of crystallisation:  $CHCl_3$ .

Moving to the third isomer, compound **II-18<sub>Te</sub>** crystallises in a  $P\bar{1}$  space group and the asymmetric unit is composed of one molecule. The molecules form dimer (**II-18<sub>Te</sub>**)<sub>2</sub> at the solid state (Figure II – 6, a) through double chalcogen bonds ( $d_{N...Te} = 3.013 \text{ \AA}$ , C-Te...N angle =  $170^\circ$ ). The 4-pyridyl moiety is engaged in hydrogen-bonding interactions ( $d_{N...C} = 3.474 \text{ \AA}$ ). In the solid state, the combination of the two non-covalent bonds leads to the formation of ribbons, which interact through  $\pi-\pi$  stacking ( $d_{\pi-\pi} = 3.485 \text{ \AA}$ ) with an offset of  $5.580 \text{ \AA}$  (Figure II – 6, b).

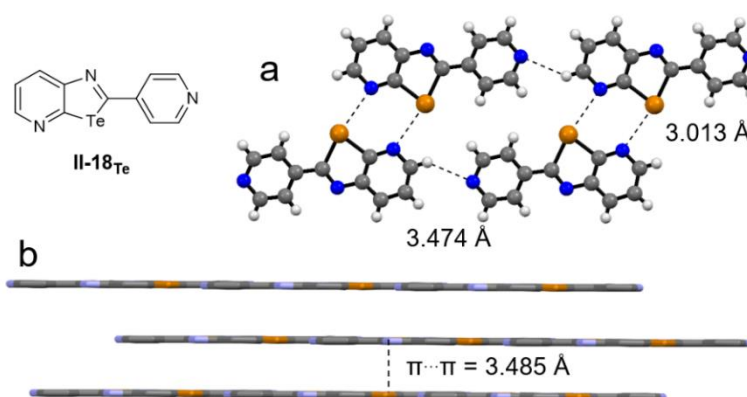


Figure II - 6: X-ray structure of **II-18<sub>Te</sub>**; a) top view, ball and stick representation; b) side view, stick representation, H atoms are omitted for sake of clarity. Space group:  $P\bar{1}$ , solvent of crystallization:  $CHCl_3$ .

Thiophenyl derivative **II-19<sub>Te</sub>** crystallises in a  $I2/a$  space group and the asymmetric unit is constituted by one molecule. The compound arranges in a dimeric structure (Figure II – 7, a) through double chalcogen-bonding interactions ( $d_{N...Te} = 2.998 \text{ \AA}$ , C-Te...N angle =  $172^\circ$ ). Interestingly, only one configuration of the molecule is observed being the one with  $N_c$  and S atoms in close proximity ( $d_{N...S} = 3.077 \text{ \AA}$ ). Indeed, an intramolecular EB takes place between those locking the conformation during the crystallisation process. Moreover, the molecules form a columnar arrangement through  $\pi-\pi$  stacking ( $d_{\pi-\pi} = 3.512 \text{ \AA}$ ) with an offset of  $5.379 \text{ \AA}$  (Figure II – 7, b).

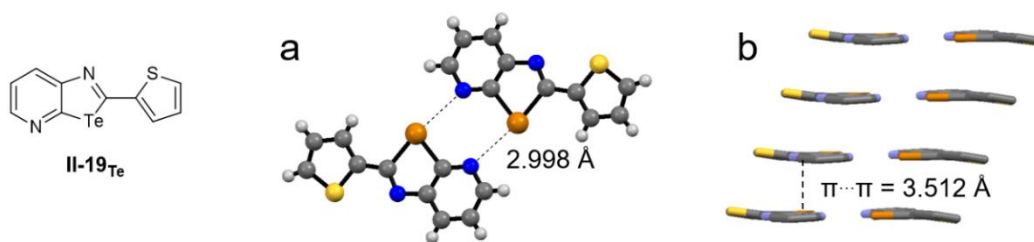


Figure II - 7: X-ray structure of **II-19<sub>Te</sub>**; a) top view, ball and stick representation; b) side view, stick representation, H atoms are omitted for sake of clarity. Space group  $I2/a$ , solvent of crystallisation:  $\text{CHCl}_3$ .

Substitution of the phenyl ring in compound **II-15<sub>Te</sub>** with other heterocycles such as pyridyl (**II-16<sub>Te</sub>**, **II-17<sub>Te</sub>** and **II-18<sub>Te</sub>**) or thiophenyl (**II-19<sub>Te</sub>**) does not alter either the planarity or the recognition fidelity of the CGP motif, which in all cases gave double  $\text{N}^{\cdots}\text{Te}$  arrays. As anticipated, distances of interaction are longer in the case **II-16<sub>Te</sub>** ( $d_{\text{N}\cdots\text{Te}} = 3.079 \text{ \AA}$  vs  $3.006 \text{ \AA}$  for **II-15<sub>Te</sub>**) which is due to the electron donation from the pyrid-2-yl to the  $\sigma$ -hole ( $\beta$ ) of the Te atom. This intramolecular EB has for effect to decrease the electronegativity of the chalcogen atom, reduce the size of the  $\sigma$ -hole ( $\alpha$ ) ( $V_{s,\text{max}} = +5.67 \text{ kcal mol}^{-1}$  vs  $+7.72 \text{ kcal mol}^{-1}$  for **II-15<sub>Te</sub>**) and thus the strength of the interaction. However, derivatives **II-17<sub>Te</sub>** and **II-18<sub>Te</sub>** do not follow the trend given by the gas phase calculation as their distance of interaction are larger ( $d_{\text{N}\cdots\text{Te}} = 3.094 \text{ \AA}$  and  $3.013 \text{ \AA}$ , respectively) than the reference compound with more positive  $V_{s,\text{max}}$  ( $+10.7$  and  $+12.5 \text{ kcal mol}^{-1}$ , respectively). This is due to additional hydrogen bonds present in the crystal packing.

#### II – 4.2 Strengthening of the interaction – Tellurium containing derivatives

Introduction of electrowithdrawing group (EWG) in 2-position of the CGP recognition array is expected to increase the strength of interaction between the two subunits of our dimer. Thus, derivatives bearing 3,4,5-trifluorophenyl, pentafluorophenyl and trifluoromethyl moieties have been envisaged, featuring a lower surface potential at the  $\sigma$ -hole ( $V_{s,\text{max}} = +13.4$ ,  $+14.1$  and  $+19.1 \text{ kcal mol}^{-1}$ , respectively) than reference **II-15<sub>Te</sub>** ( $V_{s,\text{max}} = +7.71 \text{ kcal mol}^{-1}$ ). Those compounds have been synthesised and crystallised by slow evaporation of  $\text{CHCl}_3$  solutions.

Crystals of **II-21<sub>Te</sub>** grow in a  $P\bar{1}$  space group and its asymmetric unit is composed of one molecule (Figure II – 8). The CGP dimer is formed through EB ( $d_{\text{N}\cdots\text{Te}} = 3.058 \text{ \AA}$ ,  $\text{C-Te}\cdots\text{N}$  angle =  $168^\circ$ ) and trifluorophenyl substituents engage in HB through the interaction of F and H atoms ( $d_{\text{F}\cdots\text{C}} = 3.350 \text{ \AA}$ ). In addition, the ribbons interact through  $\pi$ - $\pi$  stacking ( $d_{\pi-\pi} = 3.272 \text{ \AA}$ ) with an off-set of  $5.789 \text{ \AA}$  (Figure II – 8, b).

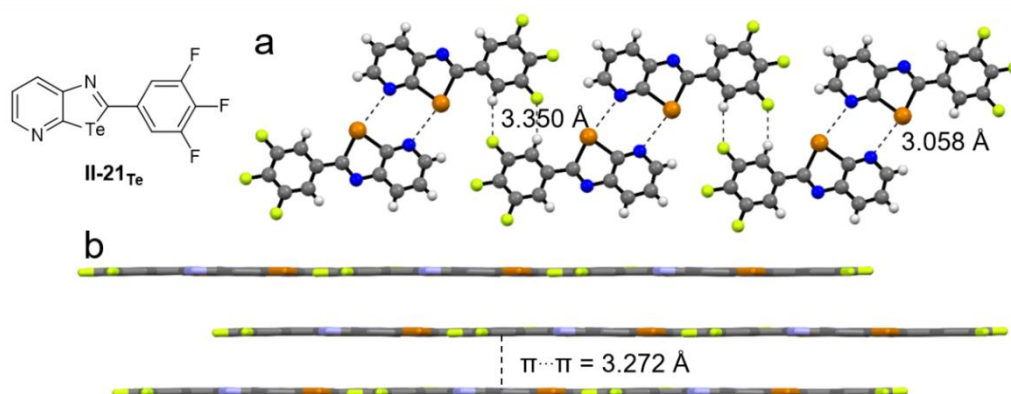


Figure II - 8: X-ray structure of **II-21<sub>Te</sub>**; a) top view, ball and stick representation; b) side view, stick representation, H atoms are omitted for sake of clarity. Space group:  $P\bar{1}$ , solvent of crystallisation:  $\text{CHCl}_3$ .

Moving to pentafluorophenyl derivative **II-22<sub>Te</sub>**, the material crystallises in a  $P2_1/c$  space group and the asymmetric unit contains one molecule. The CGP dimer (Figure II – 9, a) is formed through double N...Te contact ( $d_{\text{N...Te}} = 2.972 \text{ \AA}$ , C-Te...N angle =  $170^\circ$ ). Those dimers hierarchically form columnar arrangement through  $\pi$ - $\pi$  stacking ( $d_{\pi-\pi} = 3.503 \text{ \AA}$ ) with an off-set of  $2.855 \text{ \AA}$  (Figure II – 9, b).

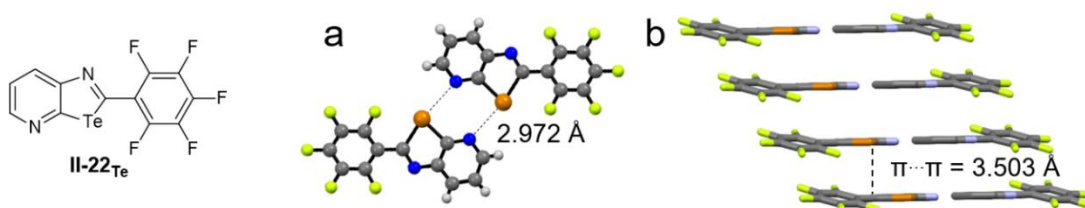


Figure II - 9: X-ray structure of **II-22<sub>Te</sub>**; a) top view, ball and stick representation; b) side view, stick representation, H atoms are omitted for sake of clarity. Space group:  $P2_1/c$ , solvent of crystallisation:  $\text{CHCl}_3$ .

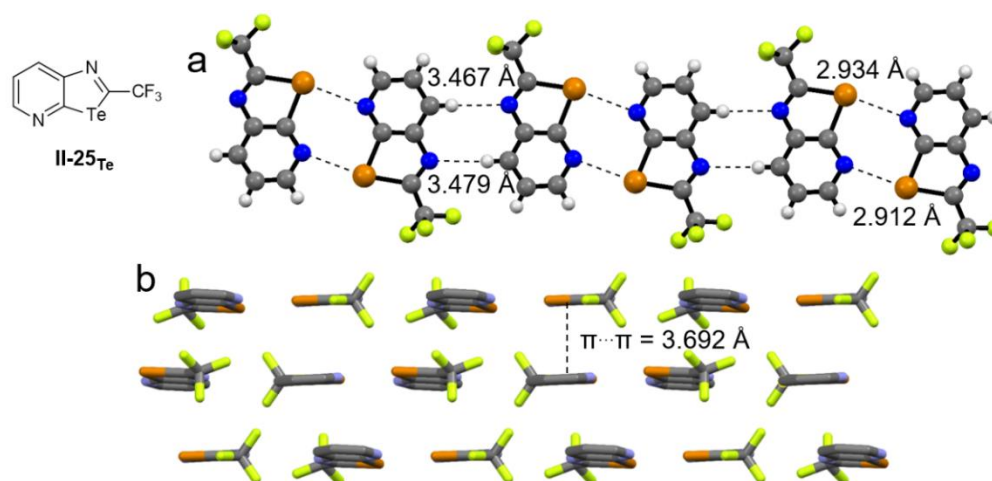


Figure II - 10: X-ray structure of **II-25<sub>Te</sub>**; a) top view, ball and stick representation; b) side view, stick representation, H atoms are omitted for sake of clarity. Space group:  $P\bar{1}$ , solvent of crystallisation:  $\text{CHCl}_3$ .

Trifluoromethyl substituted derivative **II-25<sub>Te</sub>** crystallises in a  $P\bar{1}$  space group and its asymmetric unit contains two molecules. X-ray diffraction analysis reveals the formation of ribbon at the solid state through double chalcogen- and double hydrogen-bonding interactions (Figure II – 10, a). The CGP dimer is formed through EB involving N<sub>p</sub> and Te atoms ( $d_{N...Te} = 2.912 - 2.934$  Å, N-Te...C angle = 168°). Those are further connected by HB taking place between the N<sub>c</sub> and the H atom in 7-position of the CGP moiety ( $d_{N...C} = 3.467 - 3.479$  Å, C-H...N angle = 174°). In addition, molecules interact in a head-to-tail arrangement (Figure II – 10, b) through  $\pi$ - $\pi$  stacking interaction ( $d_{\pi-\pi} = 3.692$  Å).

Notably, when passing to a more electron-withdrawing substituent such as pentafluorophenyl (**II-22<sub>Te</sub>**) derivative (Figure II - 9), a shortening of the N...Te distance to 2.971 Å for dimers (**II-22<sub>Te</sub>**)<sub>2</sub> is observed. This can be rationalized by an increase of the  $V_{s,max}$  value of the  $\sigma$ -hole ( $\alpha$ ) from +7.71 kcal mol<sup>-1</sup> for phenyl derivative **II-15<sub>Te</sub>** to +14.1 kcal mol<sup>-1</sup> for pentafluorophenyl-substituted **II-22<sub>Te</sub>** (Table II - 1). To further corroborate this effect, we also prepared 2-trifluoromethano derivative **II-25<sub>Te</sub>**. As expected, the presence of the CF<sub>3</sub> moiety further shifts the  $V_{s,max}$  value of the  $\sigma$ -hole ( $\alpha$ ) to +19.1 kcal mol<sup>-1</sup>, shortening the N...Te distance to 2.912 – 2.934 Å. However, 3,4,5-trifluorophenyl derivative **II-21<sub>Te</sub>**, which was expected to feature intermediate length of interaction between **II-15<sub>Te</sub>** and **II-22<sub>Te</sub>**, displays a distance N...Te longer than the one observed for reference **II-15<sub>Te</sub>** ( $d_{N...Te} = 3.058$  Å vs 3.006 Å). However, the crystal must accommodate both HB and EB interactions in the packing. This leads to a weakening of the chalcogen-bonding interaction.

Looking at molecule **II-22<sub>Te</sub>**, one can envisage replace the *para*-fluorine atom by other halogens. Bromo- and iodo- bearing molecules were synthesised and both crystallised. Crystals of **II-23<sub>Te</sub>** grow in a  $P2_1/c$  space group and the asymmetric unit is constituted by one molecule. Dimers (**II-23<sub>Te</sub>**)<sub>2</sub> (Figure II – 11, a) are formed through double chalcogen-bonding interactions ( $d_{N...Te} = 2.961$  Å, C-Te...N angle = 168°). Moreover,  $\pi$ - $\pi$  stacking takes place forming columnar arrangement ( $d_{\pi-\pi} = 3.514$  Å) with an off-set of 3.026 Å (Figure II – 11, b).

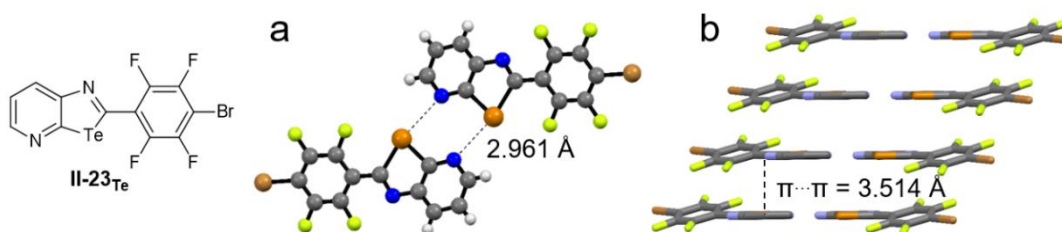


Figure II - 11: X-ray structure of **II-23<sub>Te</sub>**; a) top view, ball and stick representation; b) side view, stick representation, H atoms are omitted for sake of clarity. Space group:  $P2_1/c$ , solvent of crystallisation:  $CHCl_3$ .

Moving to iodo-derivative **II-24<sub>Te</sub>**, crystals grow in a  $P2_1/c$  space group and the asymmetric unit is composed of two molecules. The compound organises in a supramolecular polymer (Figure II – 12) formed through halogen-bonding interactions between  $N_p$  and I atoms ( $d_{N...I} = 2.854\text{--}2.890 \text{ \AA}$ ,  $C-I\cdots N$  angle =  $159\text{--}161^\circ$ ).

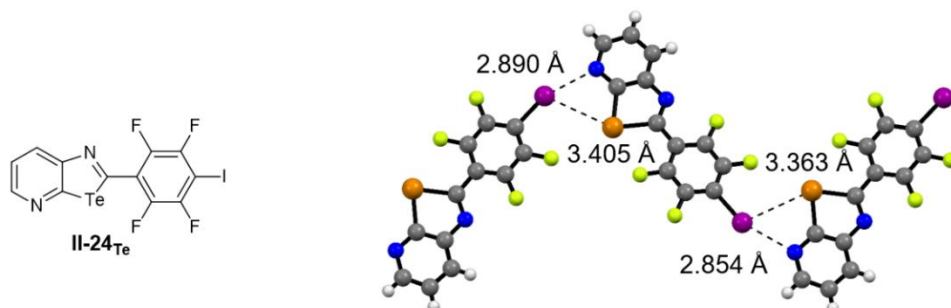


Figure II - 12: X-ray structure of **II-24<sub>Te</sub>**. Space group:  $P2_1/c$ , solvent of crystallisation:  $CHCl_3$  and pyridine.

While the three halo-derivatives are very similar in molecular structure, their solid-state arrangement is very different (Figure II – 9, 11, 12). Fluoro- and bromo-derivatives form the dimeric arrangement through frontal double chalcogen bonds with similar distance of interaction ( $d_{N...Te} = 2.972 \text{ \AA}$  and  $2.961 \text{ \AA}$ , respectively). The iodo-analogue shows a prevalence of halogen-bonding over the CGP recognition model. The heavily electron depleted region of the I atom interacts with the  $N_p$  forming a supramolecular polymeric chain of **II-24<sub>Te</sub>**. Interestingly, bromo-derivative **II-23<sub>Te</sub>** crystallised easily from  $CHCl_3$  solution in a similar fashion than the Te-bearing CGP derivatives synthesised so far, while the iodo-derivative **II-24<sub>Te</sub>** crystallised in large prism from a mixture of  $CHCl_3$  and pyridine, possibly displaying a templating effect. Nonetheless, the ability of **II-24<sub>Te</sub>** to form halogen-bonding interactions with itself led us to consider the synergy between XB and EB at the solid state and study their possible use in crystal engineering of multi-component systems (See chapter III).

#### II – 4.3 The case of selenium

To further study the CGP recognition array at the solid-state, Se-analogues have been synthesised and crystallised. Moving upward in the chalcogen group, weaker chalcogen-bonding interactions are expected due to lower polarizability of the Se atom (supported by calculation, see Table II – 1). Phenyl substituted analogue **II-15<sub>Se</sub>** crystallises in a  $Pna2_1$  space group and one molecule constitutes the asymmetric unit. In contrast to that observed for derivative **II-15<sub>Te</sub>**, the Se-compound does not dimerise through double chalcogen bonds (Figure II – 13, a) but instead forms a  $\pi-\sigma^*$  interaction ( $d_{C...Se} = 3.465 \text{ \AA}$ ). Moreover, the molecules interact through  $\pi-\pi$  stacking forming columnar arrangement ( $d_{\pi-\pi} = 3.597 \text{ \AA}$ ) with an off-set of  $4.191 \text{ \AA}$  (Figure II – 13, b).

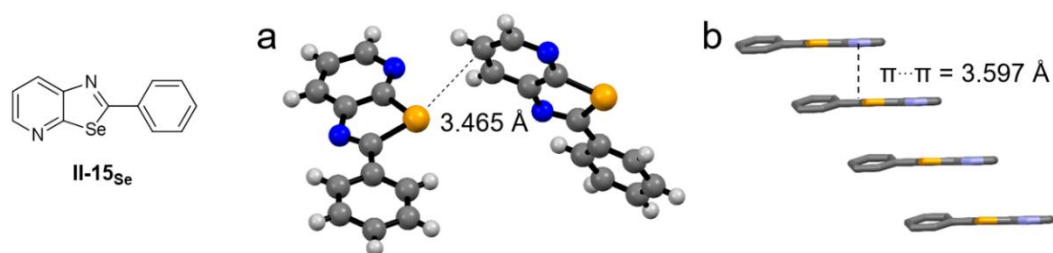


Figure II - 13: X-ray structure of **II-15<sub>Se</sub>**; a) ball and stick representation; b) side view, stick representation, H atoms are omitted for sake of clarity. Space group:  $Pna2_1$ , solvent of crystallisation:  $CHCl_3$ .

Derivative **II-16<sub>Se</sub>**, which is bearing a 2-pyridyl as substituent, crystallises in a  $P2_1/n$  space group and the asymmetric unit is constituted of one molecule. Those arrange in a dimer (Figure II – 14, a) through double H-bonds ( $d_{N...C} = 3.628$  Å) involving  $N_C$  and the H atoms in the 7-position of the CGP moiety. It is interesting to note that, in this case, the two subunits are not brought in the same plane by the non-covalent interaction and a misalignment of 0.799 Å can be observed. The molecules form columnar arrangement through  $\pi$ - $\pi$  stacking interaction ( $d_{\pi-\pi} = 3.413$  Å) with an off-set of 1.569 Å (Figure II – 14, b).

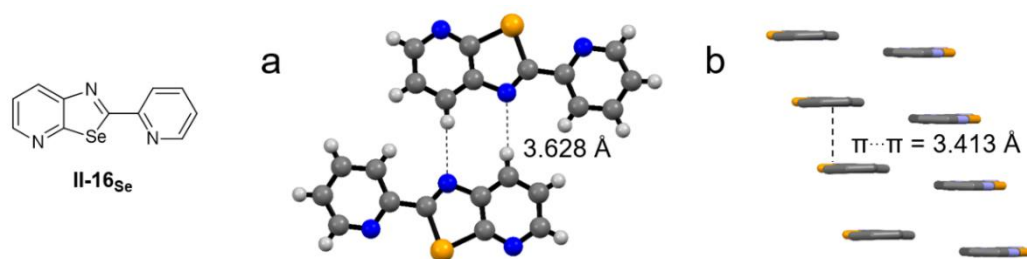


Figure II - 14: X-ray structure of **II-16<sub>Se</sub>**; a) top view, ball and stick representation; b) side view, stick representation, H atoms are omitted for sake of clarity. Space group:  $P2_1/n$ , solvent of crystallisation:  $CHCl_3$ .

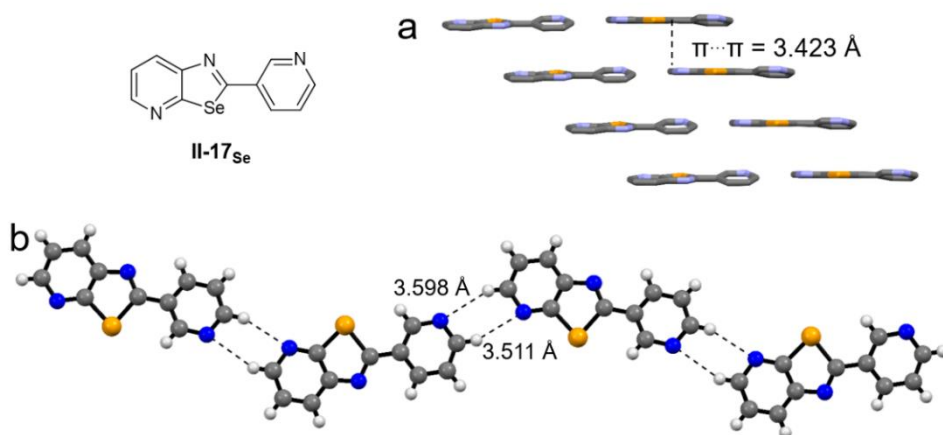


Figure II - 15: X-ray structure of **II-17<sub>Se</sub>**; a) side view, stick representation; H atoms are omitted for sake of clarity; b) top view, ball and stick representation. Space group:  $P2_1/c$ , solvent of crystallisation:  $CHCl_3$ .

Isomer **II-17<sub>se</sub>** crystallises in a  $P2_1/c$  space group and the asymmetric unit consists of one molecule. The compound organises in a supramolecular polymer by means of hydrogen-bonding interactions (Figure II – 15, a) established between the N atom of the pyridyl moiety and the H atom in 5-position of the CGP group ( $d_{N...C} = 3.518 \text{ \AA}$ ) and between  $N_p$  and H atom in 6-position of the pyridyl substituent ( $d_{N...C} = 3.511 \text{ \AA}$ ). In addition, the molecules interact through  $\pi$ - $\pi$  stacking interactions ( $d_{\pi-\pi} = 3.423 \text{ \AA}$ ) with an off-set of  $4.361 \text{ \AA}$  (Figure II – 15, b).

Moving to the last pyridyl isomer, crystals of **II-18<sub>se</sub>** grow in a  $P2_1/c$  space group and the asymmetric unit is composed by one molecule. The material organises as a supramolecular polymer (Figure II – 16, a and c). The CGP and the pyridyl moieties self-recognise and associate through double hydrogen-bonding interactions ( $d_{N...C} = 3.518$  and  $3.428 \text{ \AA}$ , respectively). In addition, the molecules form columnar arrangement through  $\pi$ - $\pi$  stacking interactions ( $d_{\pi-\pi} = 3.624 \text{ \AA}$ ) with an off-set of  $5.186 \text{ \AA}$  (Figure II – 16, b).

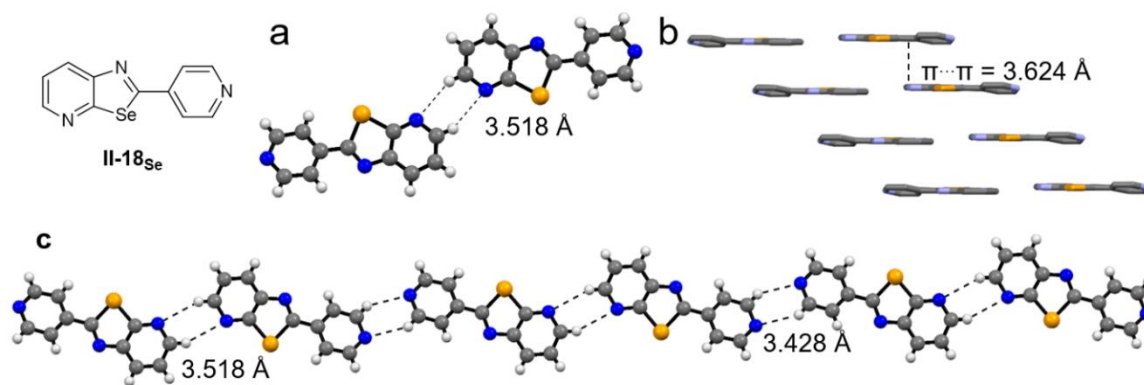


Figure II - 16: X-ray structure of **II-18<sub>se</sub>**; a) top view, ball and stick representation; b) side view, stick representation, H atoms are omitted for sake of clarity; c) top view of the ribbon structure in ball and stick representation. Space group:  $P2_1/c$ , solvent of crystallisation:  $CHCl_3$ .

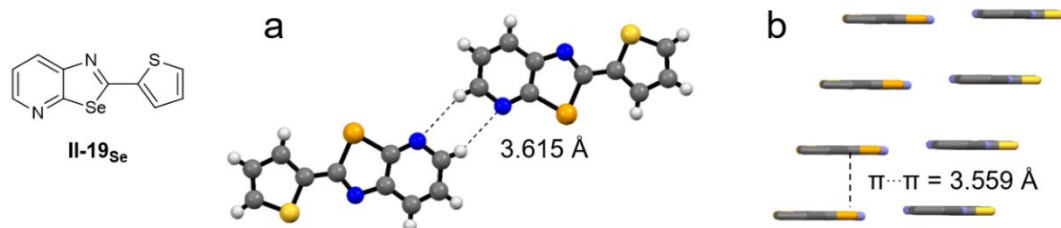


Figure II - 17: X-ray structure of **II-19<sub>se</sub>**; a) top view, ball and stick representation; b) side view, stick representation, H atoms are omitted for sake of clarity. Space group:  $P2_1/c$ , solvent of crystallisation:  $CHCl_3$ .

Thiophenyl derivative **II-19<sub>Se</sub>** crystallises in a  $P2_1/c$  space group and the asymmetric unit contains one molecule. The compound dimerises at the solid state through two H-bonds (Figure II – 17, a) involving  $N_p$  and the H atom in 5-position of the CGP moiety ( $d_{N...H} = 3.615 \text{ \AA}$ ). Similarly to the Te-congener, an intramolecular chalcogen-bond takes place between the  $N_c$  and S atoms ( $d_{N...S} = 3.010 \text{ \AA}$ ) leading to this configuration in the crystal. The molecules form columnar arrangements through  $\pi-\pi$  stacking interactions ( $d_{\pi-\pi} = 3.559 \text{ \AA}$ ) with an off-set of  $4.739 \text{ \AA}$  (Figure II – 18, b).

When programming the CGP moiety with Se atoms, a certain variability of the recognition behaviour was observed instead. For instance, no  $N...Se$  short contacts have been detected for the Se congeners **II-15<sub>Se</sub>** – **II-19<sub>Se</sub>**. Rather, molecules **II-16<sub>Se</sub>**, **II-17<sub>Se</sub>**, **II-18<sub>Se</sub>** and **II-19<sub>Se</sub>** arrange into dimeric species through double H-bonding interactions involving the  $N_c$  atom of either the chalcogenazole unit (**II-16<sub>Se</sub>**) or that of the CGP (**II-18<sub>Se</sub>** and **II-19<sub>Se</sub>**) moiety. Interestingly, **II-17<sub>Se</sub>** and **II-18<sub>Se</sub>** forms supramolecular polymer though HB between the two different pyridyl units through hetero- and homo-moiety assembly, respectively. Conversely, only  $Se... \pi$  contacts were present in the crystal architecture of **II-16<sub>Se</sub>**. The potential values of the  $\sigma$ -hole ( $\alpha$ ) for the selenium derivatives (Table II – 1) lies between  $-0.36$  and  $+7.09 \text{ kcal mol}^{-1}$  for the above-mentioned compounds. Remarkably, Te-bearing compounds form dimers with  $V_{s,max}$  values as low as  $+5.67 \text{ kcal mol}^{-1}$ . Compound **II-18<sub>Se</sub>** features a larger potential value ( $+7.09 \text{ kcal mol}^{-1}$ ) but HB still prevails over EB in the crystal structure. This shows that, despite being a handy and rapid tool to design EB synthons, ESP maps and  $V_{s,max}$  values have limitations.

#### II – 4.4 Strengthening of the interaction – Effect of EWG

Similarly to the Te-analogues, EWG were inserted in the 2-position of the Se-bearing CGP molecules. As seen from the calculation table (Table II - 1), *p*-Nitro-, 3,4,5-trifluoro-, pentafluoro-phenyl and trifluoromethyl deepens the  $\sigma$ -hole ( $\alpha$ ) significantly ( $+7.84$  to  $+12.7 \text{ kcal mol}^{-1}$ ). Derivatives **II-21<sub>Se</sub>**, **II-22<sub>Se</sub>** and **II-25<sub>Se</sub>** were successfully crystallised from  $CHCl_3$  solution while for molecule **II-20<sub>Se</sub>**, it was not possible to grow single crystals suitable for X-ray diffraction analysis.

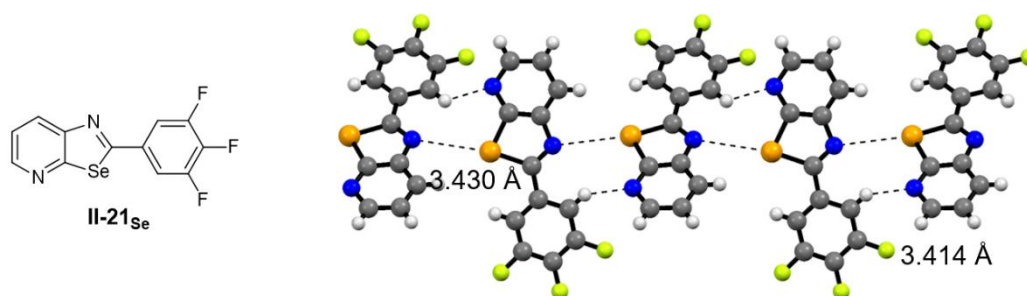


Figure II - 18: X-ray structure of **II-21<sub>Se</sub>**. Space group:  $P2_1/c$ , solvent of crystallisation:  $CHCl_3$ .

Particularly, trifluorophenyl compound **II-21<sub>se</sub>** adopt a  $P2_1/C$  space group and one molecule composes the asymmetric unit. Interestingly, chalcogen-bonding interactions are formed between  $N_c$  and Se atoms ( $d_{N...Se} = 3.430 \text{ \AA}$ ) leading to the formation of a rod-like structure (Figure II – 18). hydrogen-bonds involving  $N_p$  and one of the H atoms of the trifluorophenyl moiety ( $d_{N...C} = 3.414 \text{ \AA}$ ) contributes to stabilise the structure.

Pentafluorophenyl derivative **II-22<sub>se</sub>** crystallises in a  $P2_1/c$  space group and the asymmetric unit is composed by one molecule. The compound dimerises at the solid-state through double chalcogen-bonding interactions ( $d_{N...Se} = 2.964 \text{ \AA}$ , C-Se...N angle =  $175^\circ$ ; Figure II – 19, a). The molecules interact through  $\pi$ - $\pi$  stacking ( $d_{\pi-\pi} = 3.459 \text{ \AA}$ ) with an off-set of  $3.051 \text{ \AA}$  forming columnar arrangement (Figure II – 19, b).

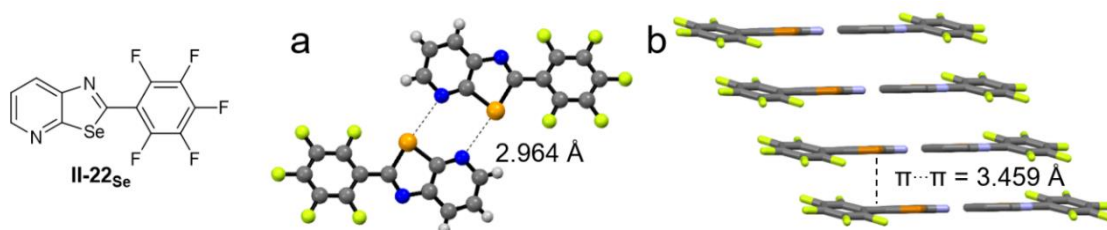


Figure II - 19: X-ray structure of **II-22<sub>se</sub>**; a) top view, ball and stick representation; b) side view, stick representation, H atoms are omitted for sake of clarity. Space group:  $P2_1/c$ , solvent of crystallisation:  $CHCl_3$ .

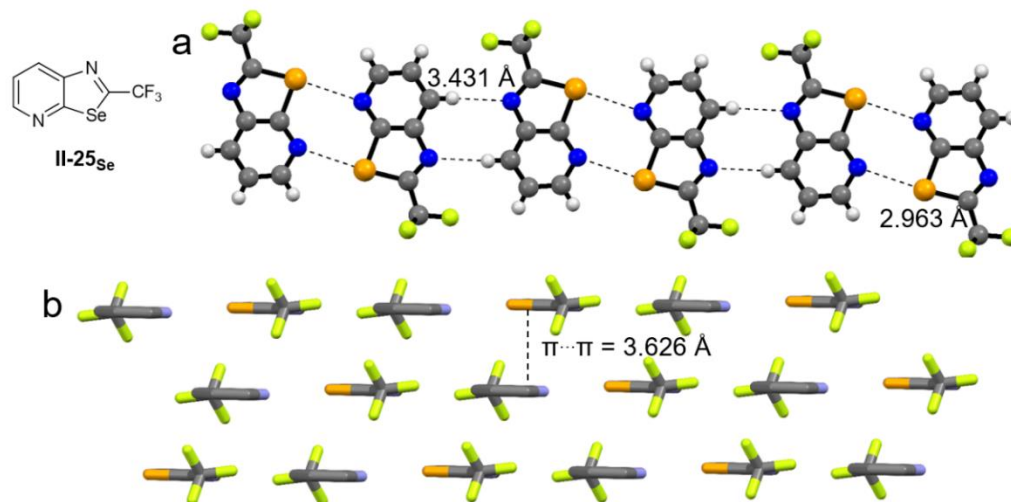


Figure II - 20: X-ray structure of **II-25<sub>se</sub>**; a) top view, ball and stick representation; b) side view, stick representation, H atoms are omitted for sake of clarity. Space group:  $P\bar{1}$ , solvent of crystallisation:  $CHCl_3$ .

Crystals of **II-25<sub>se</sub>** grow in a  $P\bar{1}$  space group and the asymmetric unit is composed by one molecule. Those arrange in a ribbon structure through simultaneous chalcogen and hydrogen-bonding interactions (Figure II – 20, a). A double EB takes place between  $N_p$  and Se atoms ( $d_{N...Se} = 2.963 \text{ \AA}$ ,

C–Se $\cdots$ N angle = 173°) and a double HB is formed by N<sub>c</sub> and the H atom in 7-position of the CGP moiety ( $d_{N\cdots C}$  = 3.431 Å). In addition, the ribbons interact through  $\pi$ – $\pi$  stacking interaction ( $d_{\pi-\pi}$  = 3.626 Å) in a head-to-tail fashion (Figure II – 20, b).

In the case of Se-derivatives, only CGP molecules bearing strong EWG in the 2-position form chalcogen-bonding interactions. Particularly, trifluorophenyl derivative **II-21<sub>se</sub>** crystallises as rod-like polymers featuring weak N $\cdots$ Se interactions ( $d_{N\cdots Se}$  = 3.414–3.430 Å) involving the N<sub>c</sub> atom.<sup>[6]</sup> It has to be noted that additional hydrogen bonds participate to the packing involving the H atom from the trifluorophenyl moiety and the N<sub>p</sub> atom. Pentafluorophenyl **II-22<sub>se</sub>** and trifluoromethano derivative **II-25<sub>se</sub>** gave dimeric complexes through double chalcogen-bonding interactions ( $d_{N\cdots Se}$  = 2.964 and 2.963 Å, respectively). This suggests that, for the less polarizable Se atom, only motifs bearing strong electron-withdrawing groups lead to double chalcogen-bonded arrays.

## II – 5 Synthesis of symmetric ditopic derivatives

Capitalising on those results, we aim to synthesise a ditopic molecule bearing two CGP bonding sites directly connected to each other anticipating a supramolecular polymer based on chalcogen-bonding interaction (Figure II – 21). Building on the co-planar dimeric arrangement discussed previously, we expect self-association of the molecule in the solid state into flat ribbons.

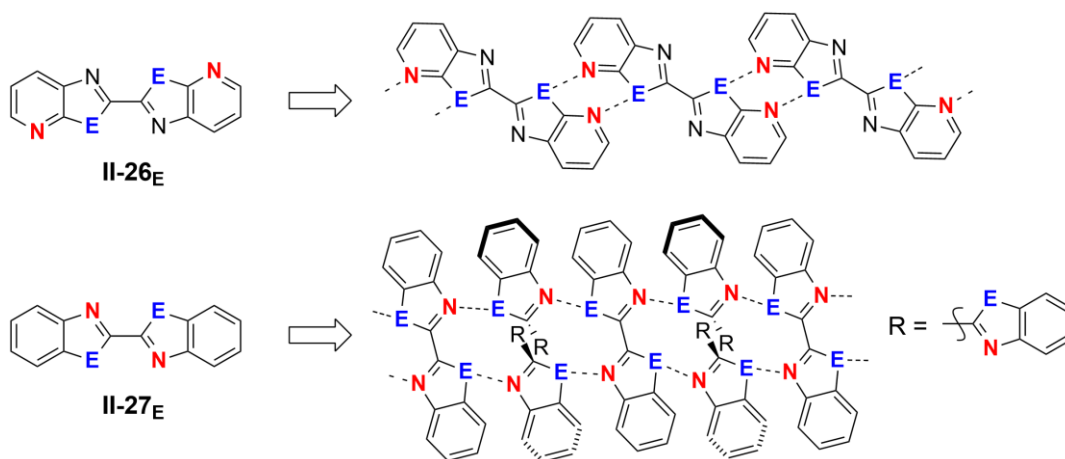
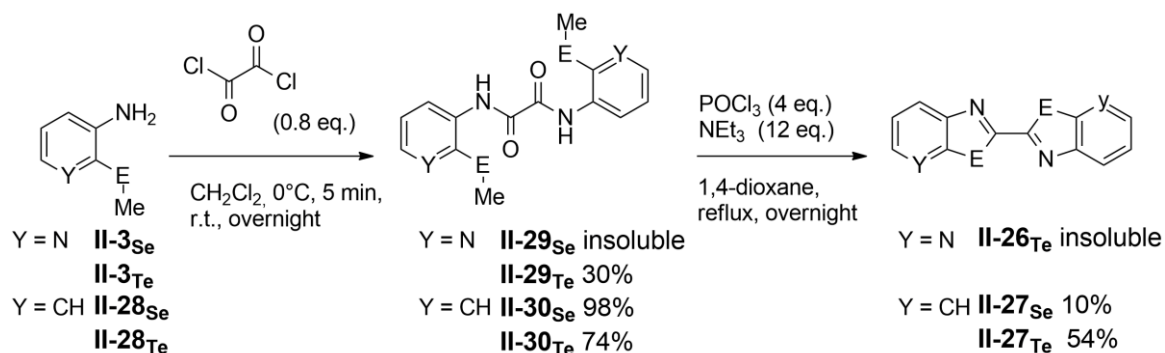


Figure II - 21: Design of supramolecular polymer base on a bis-CGP and bis-benzochalcogenazole moieties.

Both Se and Te containing derivatives **II-26<sub>E</sub>** will be synthesised and compared to their benzochalcogenazole analogues **II-27<sub>E</sub>**. Those compounds are expected to form wire-like structures.<sup>[6]</sup> However, the presence of two chalcogenazole rings could lead to the formation of entanglement at the molecular level (Figure II – 21).

The synthesis of all four compounds was attempted following the protocol previously described in Scheme II – 5. First, amine **II-3<sub>E</sub>** and **II-28<sub>E</sub>** were reacted with oxalyl chloride in CH<sub>2</sub>Cl<sub>2</sub> affording in bis-carboxamides **II-29<sub>Te</sub>** and **II-30<sub>E</sub>**. Both benzo derivatives were obtained in good yield (Se 98% and 60

Te 74%), however **II-29<sub>Se</sub>** could not be obtained *via* this method and difficulties in the purification of **II-29<sub>Te</sub>** were encountered leading to 30% isolated yield. Cyclised compound **II-27<sub>E</sub>** were achieved from bis-carboxamides through dehydrative cyclisation in the presence of POCl<sub>3</sub> and NEt<sub>3</sub> in refluxing dioxane. Derivative **II-27<sub>Te</sub>** was obtained in 54% yield without notable problem. However, **II-27<sub>Se</sub>** revealed to be rather insoluble and could be isolated in only 10% yield through consecutive re-crystallisations from hot CHCl<sub>3</sub>. The same reaction was performed on **II-29<sub>Te</sub>** and led to the formation of a yellow precipitate that could not be characterised due to very low solubility in common organic solvents (THF, CHCl<sub>3</sub>, toluene, ...).



Scheme II - 5: Attempt in the synthesis of **II-26<sub>E</sub>** and **II-27<sub>E</sub>**.

Having in hand compounds **II-27<sub>Te</sub>** and **II-27<sub>Se</sub>**, both materials were crystallised from slow evaporation of a CHCl<sub>3</sub> solution and slow cooling of a hot CHCl<sub>3</sub> solution, respectively. Crystals of the Te-derivative grow in a Pbc<sub>a</sub> space group and the asymmetric unit is composed of one molecule. The compound arranges in a wire-like structure (Figure II – 22) through chalcogen-bonding interactions involving N and Te atoms ( $d_{N...Te} = 3.338 \text{ \AA}$ , angle C-Te...N = 166°). Additional short contacts are present involving the p-orbital of one Te atom and the  $\sigma$ -hole ( $\alpha$ ) of a second Te atom ( $d_{Te...Te} = 3.866 \text{ \AA}$ , angle C-Te...Te = 156°). Moreover, molecules **II-27<sub>Te</sub>** form columnar arrangement through  $\pi$ - $\pi$  stacking interactions ( $d_{\pi-\pi} = 3.693 \text{ \AA}$ ) with an off- set of 4.773  $\text{\AA}$  (Figure II – 22, b).

Compound **II-27<sub>Se</sub>** crystallises in a P2<sub>1</sub>/c space group and the asymmetric unit is composed of one molecule. At the solid state, two different chalcogen-bonds can be observed (Figure II – 23, a). One takes place between N atom of the chalcogenazole ring and the facing Se atom ( $d_{N...Se} = 3.234 \text{ \AA}$ , angle C-Se...N = 177°), whereas the second bond involves two Se atoms from different chalcogenazole rings ( $d_{Se...Se} = 3.722 \text{ \AA}$ , angle C-Se...Se = 162°). Interestingly, each Se atom is involved in three interactions leading to a very tight packing in the form of an entangled wire-like structure (Figure II – 23, c).

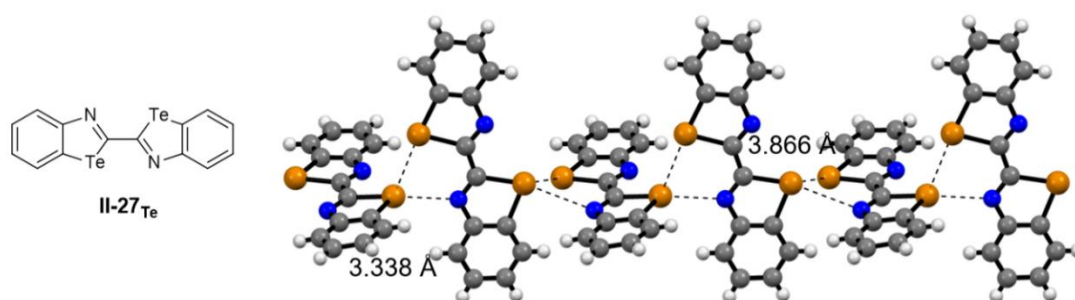


Figure II - 22: X-ray structure of *II-27<sub>Te</sub>*. Space group: *Pbca*, solvent of crystallisation: *CHCl<sub>3</sub>*.

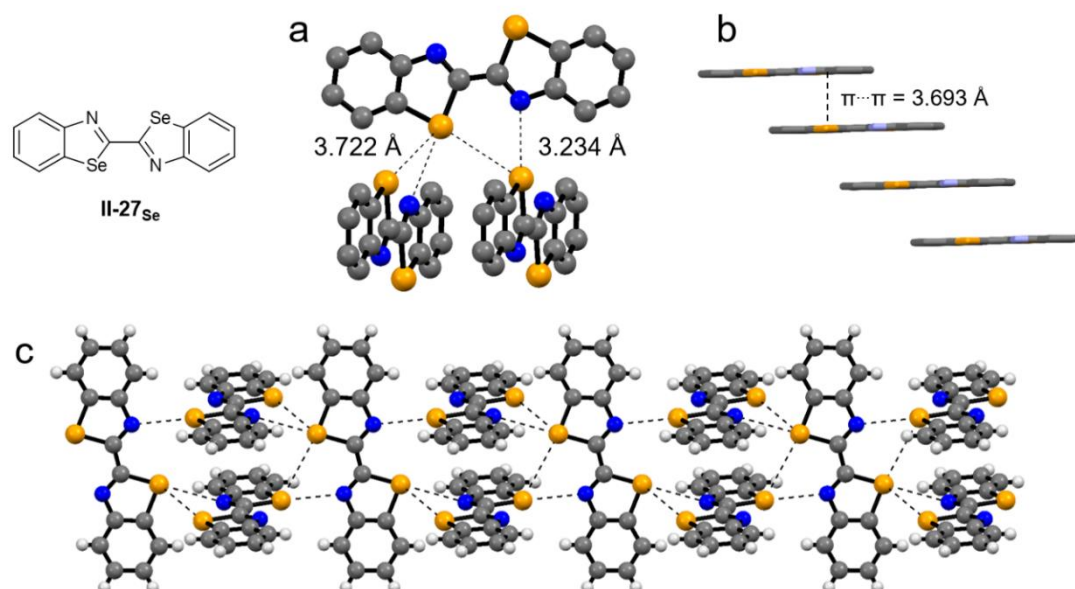


Figure II - 23: X-ray structure of *II-27<sub>Se</sub>*, a) ball and stick representation, H atoms are removed for sake of clarity, b) stick representation of the columnar arrangement, c) ball and stick representation of the entangled wire-like structure. Space group *P2<sub>1</sub>/c*, solvent of crystallisation: *CHCl<sub>3</sub>*.

## II – 6 Inclusion of the CGP motif in functional system: towards chalcogen-bonded soft materials

### II – 6.1 Gel design: programming “acrylamide” polymer with EB interactions

In a second avenue, we aimed to synthesise functional materials integrating the CGP array and exploit chalcogen-bonding interactions to form gels. The acrylamide polymer is known to form hydrogels with interesting swelling properties,<sup>[26]</sup> elasticity<sup>[27]</sup> and the polymer-solvent interaction has been widely studied.<sup>[28, 29]</sup> Such materials are generally obtained *via* free radical co-polymerization of *N*-isopropylacrylamide (NIPA) and *N,N'*-methylenebisacrylamide (MBAA) in the

presence of ammonium peroxydisulfate (APS) and *N,N,N',N'*-tetramethylethylenediamine (TMEDA) or azobisisobutyronitrile (AIBN) in water or polar organic solvent such as EtOH or DMF.<sup>[28]</sup> The resulting material is formed by linear poly(NIPA) chains crosslinked with MBAA and presenting some entanglement (Figure II - 24), the structure is thus able to trap solvent molecules forming a gel. The crosslinking of the polymer is essential to the formation of the gel. The idea, in this case, is to replace the covalent crosslinker (MBAA) by a non-covalent dimer based on a Te-bearing CGP derivative substituted with an acrylamide moiety as crosslinker (Figure II – 24).

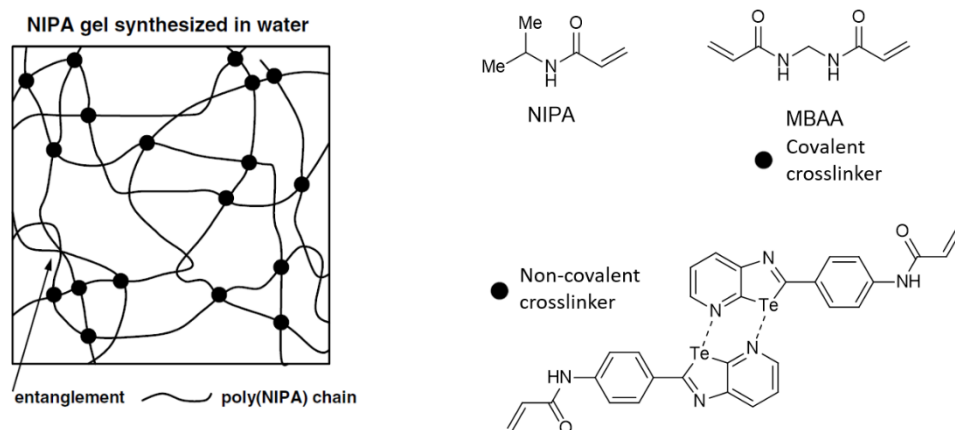
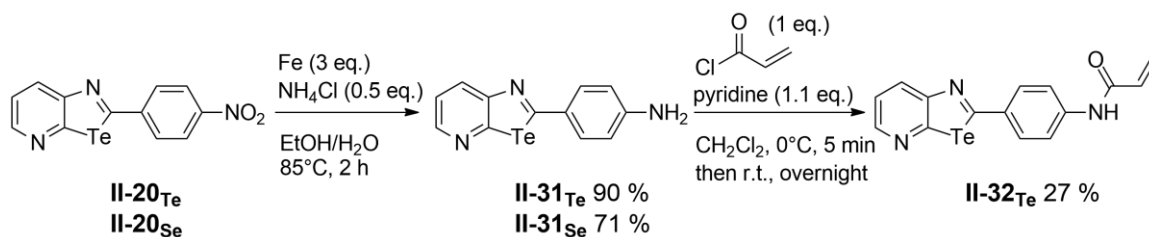


Figure II - 24: Nano-structure of co-polymer NIPA-MBAA gel synthesised in water (left) and the molecular structure of NIPA, MBAA and our concept of crosslinker replacement being *N*-(4-([1,3]tellurazolo[5,4-*b*]pyridin-2-yl)phenyl)acrylamide dimer. Adapted with permission;<sup>[28]</sup> copyright 2007 Elsevier Ltd.

The synthesis of our modified crosslinker started with the previously obtained nitro derivative **II-20<sub>Te</sub>** (Scheme II - 6). Compound **II-20<sub>Te</sub>** was treated with iron powder to afford amine **II-31<sub>Te</sub>** in 90% yield. Equally, the reaction was performed on Se analogues **II-20<sub>Se</sub>** to give **II-31<sub>Se</sub>** in 71% yield. Subsequently, **II-31<sub>Te</sub>** was submitted to amidation reaction with the corresponding acyl chloride in CH<sub>2</sub>Cl<sub>2</sub> in the presence of pyridine affording desired product **II-32<sub>Te</sub>** in modest yield (27%).



Scheme II - 6: Representation of the synthesis of **II-32<sub>Te</sub>**.

NIPA was co-polymerised with different percentages of **II-32<sub>Te</sub>** in EtOH or EtOH/H<sub>2</sub>O solutions using APS or AIBN as radical initiator. However, no formation of gel was observed possibly due to interaction of Te-atom with the radical polymerisation process.<sup>[30, 31]</sup> Single crystal of the acrylamide derivative **II-32<sub>Te</sub>** were obtained from slow cooling of a hot toluene solution. X-ray diffraction analysis revealed an unexpected packing (Figure II - 25). Indeed, the amide group interacts with the

pyridyl of the CGP group through HB ( $d_{N\dots N} = 2.996 \text{ \AA}$ ) and form a weak EB by donation of the p-orbital of the N atom into the  $\sigma^*$  orbital of the Te atom ( $d_{N\dots Te} = 3.503 \text{ \AA}$ ). Having those results in hand, the synthesis of reference **II-32<sub>Se</sub>** was not attempted.

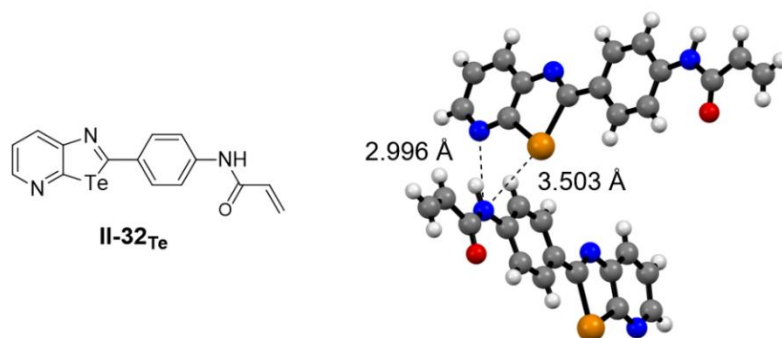


Figure II - 25: X-ray structure of **II-32<sub>Te</sub>**. Space group:  $P2_1/c$ , solvent of crystallization: hot toluene.

## II – 6.2 Ditopic derivatives with an alkyl spacer: Supramolecular polymers

Another approach to form gel relies on the formation of linear supramolecular polymers based on two molecular recognition sites connected through a flexible linker. Those supramolecules arrange in a three-dimensional entangled fibrillar network that feature the ability to block the flow of bulk solvent.<sup>[32]</sup> Building on this concept, we envisaged the synthesis of ditopic molecules bearing two CGP moieties connected by an alkyl spacer (Figure II – 26).

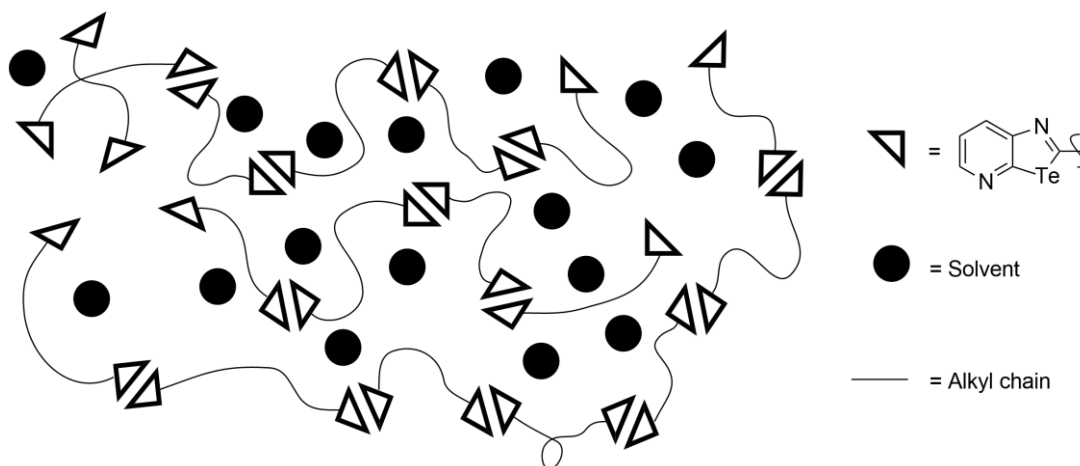
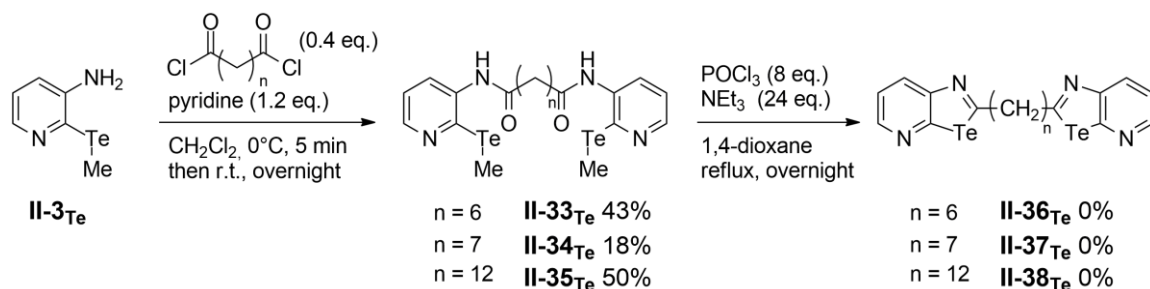


Figure II - 26: Anticipated nanostructure of a ditopic derivative featuring an alkyl spacer.

The spacer has been chosen to be an alkyl chain of 6, 7 or 12 carbons connecting two tellurazopyridine units through 2-positions. Molecules were anticipated to form flexible linear supramolecular polymer through double chalcogen-bonding interactions involving the CGP units. The resulting 3D material would arrange in bundle and trap solvent molecules leading to a gel.

The synthesis (Scheme II – 7) started from amine **II-3<sub>Te</sub>** that underwent amidation reaction with freshly prepared octanedioyl, nonanedioyl and tetradecanedioyl dichloride, respectively, from their

corresponding carboxylic acids. Compounds **II-33<sub>Te</sub>**, **II-34<sub>Te</sub>** and **II-35<sub>Te</sub>** were obtained in 43, 18 and 50% yield, respectively. Subsequently the dehydrative cyclisation step was performed and the three reactions afforded a black material that revealed to be insoluble in most organic solvents (THF, CHCl<sub>3</sub>, toluene, *o*-dichlorobenzene, diphenyl ether), even at their boiling point. Only **II-38<sub>Te</sub>** could be characterized by LR-MALDI MASS analysis (Figure II – 27) and partially solubilised in boiling diphenyl ether.



Scheme II - 7: Attempt in the synthesis of bis([1,3]-tellurazolo[5,4-β]pyrine)alkane **II-36<sub>Te</sub>**, **II-37<sub>Te</sub>** and **II-38<sub>Te</sub>**.

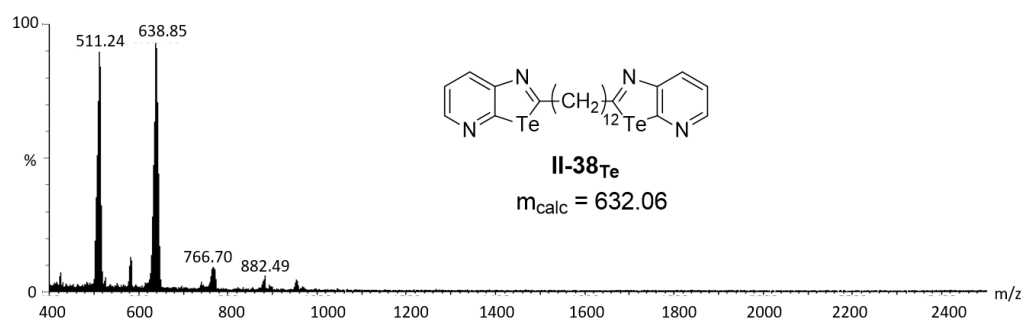


Figure II - 27: LR-MALDI MASS spectrum of the crude material issued from the synthesis of **II-38<sub>Te</sub>**.

## II – 7 Chalcogen-bonding vs $\pi$ - $\pi$ stacking interactions: from dimers to semi-conductor materials

### II – 7.1 Introduction

#### II – 7.1.1 Organic semiconductors

In this part of the work, we aim to synthesise an organic semiconductor material using chalcogen bonding interaction to rule the organisation at the solid state. Those materials usually rely on  $\pi$ -conjugated molecules for application in electronic devices with the advantages of affording high operating speeds, low device density, low cost and flexibility.<sup>[33, 34]</sup> The material of choice for organic electronic is graphene, a monoatomic thin 2D material composed of C atoms arranged in honeycomb lattice. This monolayer exhibits a high crystallographic quality and ultra-high electron

transport ability.<sup>[35]</sup> However, those advantages are hampered by the absence of a bandgap that prevent an “on/off” behaviour that is required for semi-conductors applications.<sup>[36]</sup> Thus, chemists have engineered graphitic structures such as graphene nanoribbons (charge mobility up to  $1500 \text{ cm}^2 \text{ V}^{-1} \text{ s}^{-1}$ )<sup>[36]</sup> and conductive polymers (such as rr-P3HT, charge mobility of  $1.3 \cdot 10^{-4} \text{ cm}^2 \text{ V}^{-1} \text{ s}^{-1}$ )<sup>[37]</sup> as 1D materials presenting a high charge carrier mobility ( $\mu$ ). However, those materials often come with the cost of low processability and reproducibility.<sup>[38]</sup> In order to overcome this problem, small  $\pi$ -conjugated molecules offering a highly planar molecular structure and good crystallinity have attracted continuous interest.<sup>[38]</sup>

As the charge transport mobility is the key aspect determining the performance of devices, it is crucial to understand the parameters of influence. The charges (electrons or holes) must travel within the molecules (molecular properties), between the molecules (supramolecular properties) and between crystals or grains (morphological properties) in a given device.<sup>[39]</sup> To control the molecular and supramolecular aspects, the scaffolds of choice usually are the polycyclic aromatic hydrocarbons (PAHs) that are known to be hole transporters.<sup>[40]</sup> PAHs molecules interact through  $\pi$ - $\pi$  stacking interactions that facilitate the hopping of the charge (hole or electron) from one aromatic core to the next one. The charge mobility between the molecules is maximised when the overlap of the aromatic faces is maximised.<sup>[41]</sup> Those materials have proven their use as organic semiconductor in organic field effect transistors (OFETs), organic light emitting diodes (OLEDs), and organic solar cells (OSCs). In addition, peripherally functionalised PAHs derivatives are easily processible from solution to prepare nanostructured materials.<sup>[38, 42, 43]</sup> Those material present a good charge carrier mobility ranging from  $10^{-6}$  to  $3.3 \text{ m}^2 \text{ V}^{-1} \text{ s}^{-1}$ .<sup>[38]</sup> To further control the property of PAHs derivatives, we anticipate the use of chalcogen-bonding interaction to drive the supramolecular association of those molecules. Two positive effects are expected due to the presence of chalcogen atoms. First heavy atoms having access to d orbitals are known to increase charge mobility.<sup>[44]</sup> *Seferos, Pisula* and co-workers recently published a study showing that the doping effect drastically improves the charge carrier mobility moving from poly-thiophene to poly-selenophene and poly-tellurophene ( $\mu = 6.2 \cdot 10^{-5}$ ,  $8.0 \cdot 10^{-4}$  and  $2.5 \cdot 10^{-2} \text{ cm}^2 \text{ V}^{-1} \text{ s}^{-1}$ , respectively).<sup>[45]</sup> On the other hand, chalcogen-bonding interactions will allow control over the structure of the materials and organise the molecules in flat dimers allowing face-to-face  $\pi$ - $\pi$  stacking that will maximise the overlap of the aromatic surfaces. Moreover, EB interactions will allow charges to travel through the non-covalent bonds. Unlike hydrogen-bonding interactions that rely exclusively on coulombic forces, EB are largely composed by orbital contribution. The charges could potentially travel from one molecule to the other by tunnelling effect. Thus, we expect an enhancement of the charge mobility thanks to the combination of those effects triggered by the presence of chalcogen-bonding interactions.

## II – 7.1.2 Charge mobility through Space-Charge Limited Current experiments

The charge mobility is typically measured from Space-Charge Limited Current (SCLC) experiments. This method is a versatile technique for material benchmarking applications. It consists in injecting a non-equilibrium density of charges in a hole-only or electron-only diode device and measuring the resulting current.<sup>[46]</sup> This method has the advantage of being steady state, reproducing the conditions relevant to the application in OLED and OPV devices. Electrons or holes travel perpendicular to the different layers of material, namely bottom electrode, charge-injector, organic semi-conductor layers and top electrode (Figure II – 28). Solid-state organisation of the organic layer is crucial as the charges must travel through the supramolecular structure as the best charge mobility values are obtained for compound arranging in a graphitic-like structures (molecules are co-planar in a 2D level and the layers are organised one on top of another in the third dimension, Figure II – 28).

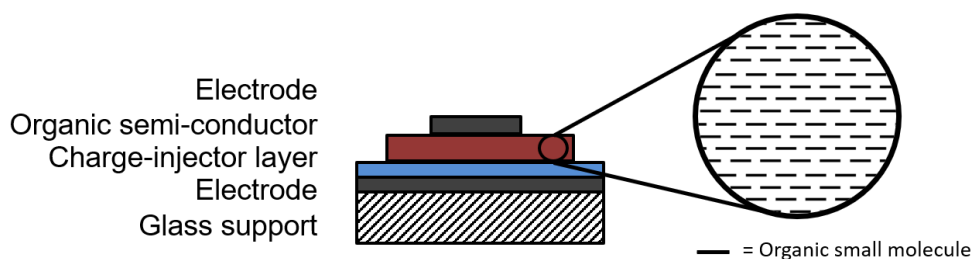
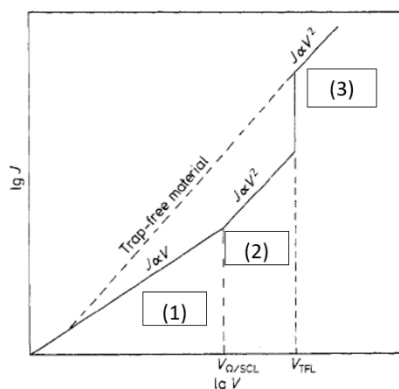


Figure II - 28: Layered structure of an electron/hole only device and zoom on the molecular arrangement.

In such devices, the measured current ( $J$ ), upon application of a potential ( $V$ ), travels perpendicularly to the plane of the different layers and follows a tendency described below (Figure II – 29). Three different regions are present, defining different regimes. The first describes the ohmic current (1), the second the current in a trap-limited regime (2) and the third the current in a trap-free situation (3). The ohmic region is governed by the number of mobile charge ( $n$ ) injected in the material and the charge mobility ( $\mu$ ),  $L$  being the thickness of the device. However, as a precise count of the holes present in the material is unnecessarily complicated on a practical point of view,  $\mu$  measurements are usually performed in region 2 or 3 (Figure II – 29). Those sections significantly differ from region 1 due to the quadratic relationship between  $J$  and  $V$  ( $J \propto V^2$ ). The current is no longer proportional to  $n$  but is affected by the quantity of trap present in the organic material ( $\theta_0$ ) and the dielectric constant of the material ( $\epsilon\epsilon_0$ ). While  $V$  increases, the trap gets filled up and the third regime is reached when a shift in the  $J$  values is observed (Figure II – 29). In order to evaluate the charge mobility, the experimental data in regime 2 or 3 are fitted using the respective equations by varying the  $\mu$  parameters along with  $V$ ,  $L$  and  $\epsilon$ .



$$J_{\Omega} = ne\mu \frac{V}{L} \quad (1)$$

$$J_{SCL} = \frac{9}{8} \epsilon \epsilon_0 \mu \frac{V^2}{L^3} \theta_0 \quad (2)$$

$$J_{TF-SCL} = \frac{9}{8} \epsilon \epsilon_0 \mu \frac{V^2}{L^3} \quad (3)$$

Figure II - 29: Theoretical graph of SCLC measurement, each regime is described by one equation.

## II – 7.2 Design of the pyrene-based molecular building blocks

Our goal is to engineer a novel organic semi-conductor material and establish a clear structure-property relationship. At the molecular level, the properties will be governed by the choice of PAHs. In this optic we have selected pyrene, as this aromatic has been widely studied over the years being an easily modified, large and highly planar electron-rich  $\pi$ -surface. This compound crystallises in a herringbone structure (Figure II – 30).<sup>[47]</sup> The aromatic molecules interact through face-to-face  $\pi$ - $\pi$  stacking ( $d_{\pi-\pi} = 3.475 \text{ \AA}$ , with an off-set of  $1.629 \text{ \AA}$ ) and C-H $\cdots\pi$  interaction ( $d_{C\cdots\pi} = 3.714 \text{ \AA}$ ). While the herringbone structure hampers optimal charge mobility between the molecules, we contemplate the conjugation of the CGP moiety to the pyrenyl ring in order to tune the supramolecular contacts. With that information in mind, we designed molecule **II-39<sub>Te</sub>** (Figure II – 31). In the presence of a double chalcogen-bond motif, we anticipate constraining the PAH cores into pairs in flat complexes.

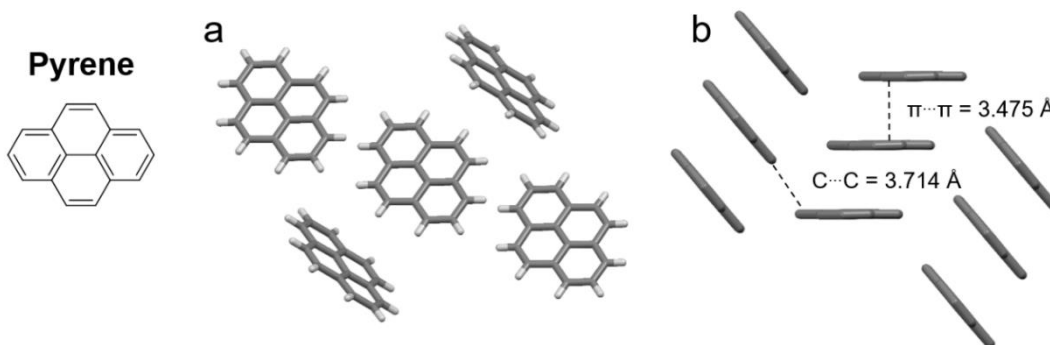


Figure II - 30: X-ray structure of pyrene a) top view, stick representation; b) side view, stick representation, H atoms are omitted for sake of clarity. Space group  $P2_1/a$ .<sup>[47]</sup>

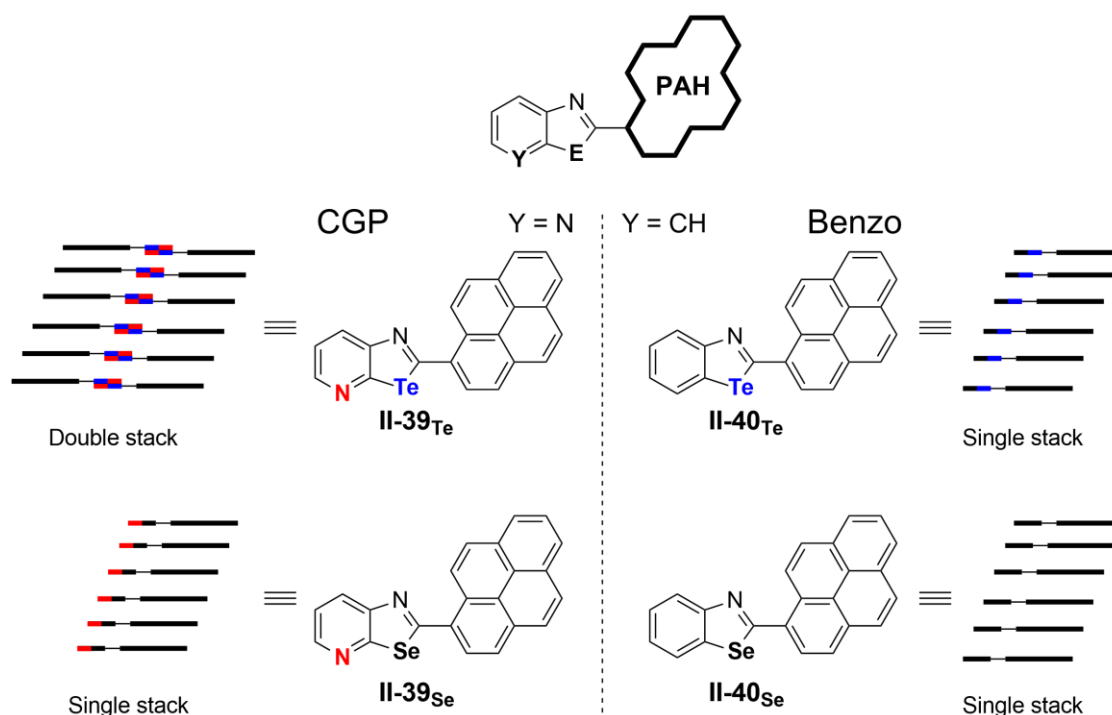
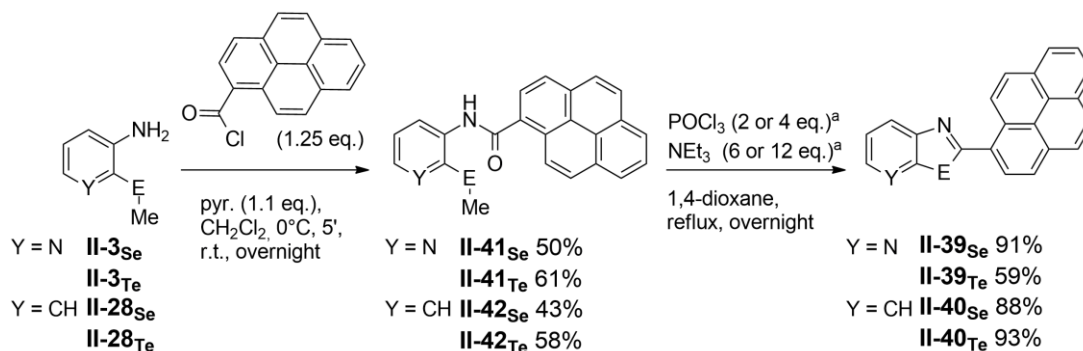


Figure II - 31: Selection of pyrene derivatives and their respective anticipated supramolecular arrangement.

We anticipate these dimers to arrange in columnar structures through  $\pi$ - $\pi$  stacking interactions (Figure II – 31). No  $N_p \cdots Se$  short contacts are expected for **II-39<sub>Se</sub>**, thus, no dimeric arrangements are anticipated leading to a single-stack columnar arrangement. The difference from double to single column structure will give a comparison point for the charge mobility values, highlighting the effect of chalcogen bonds in these systems. However, swapping Te for a Se atom in the structure could also influence the result of the experiment. In order to evaluate this change, compounds **II-40<sub>E</sub>** will be synthesised bearing a benzochalcogenazole functionality instead of the CGP moiety. Replacement of the pyridyl-ring by a benzo-ring prevent dimer association through double EB interactions. The differences in charge mobility between derivatives **II-40<sub>Te</sub>** and **II-40<sub>Se</sub>** should be solely attributed to the chalcogen atom present in the molecule (Figure II – 31). Despite benzo-derivatives **II-40<sub>E</sub>** being different molecular scaffolds compared to CGP **II-39<sub>E</sub>**, we consider that swapping Te for Se atoms will have the same impact on the electronic properties for both series. Thus, evaluation of the molecular and supramolecular properties of the four derivatives will give us a deep insight in the structure-property relationship of this system. The effect on the charge mobility of the chalcogen atom will be addressed by using **II-40<sub>E</sub>** materials. The same effect will be observed with compounds **II-39<sub>E</sub>** in addition of the influence of single/double stack structures.

## II – 7.3 Synthesis

The synthesis of CGP **II-39<sub>E</sub>** and benzochalcogenazole **II-40<sub>E</sub>** has been undertaken following the strategy previously developed (Scheme II – 8). Amines **II-3<sub>E</sub>** and **II-28<sub>E</sub>** are transformed to amides **II-41<sub>E</sub>** and **II-42<sub>E</sub>** by reaction with pyrene-1-carbonyl chloride in the presence of pyridine in CH<sub>2</sub>Cl<sub>2</sub> according to the protocol of *Cho et al.*<sup>[48]</sup> (**II-41<sub>Se</sub>** 50 %, **II-41<sub>Te</sub>** 61 %, **II-42<sub>Se</sub>** 43 % and **II-42<sub>Te</sub>** 58 % yield). A dehydrative cyclisation using POCl<sub>3</sub> and NEt<sub>3</sub> was performed to afford chalcogenazoles **II-39<sub>E</sub>** and **II-40<sub>E</sub>** (**II-39<sub>Se</sub>** 91 %, **II-39<sub>Te</sub>** 59 %, **II-40<sub>Se</sub>** 88 % and **II-40<sub>Te</sub>** 93 % yield).



Scheme II - 8: Synthesis of CGP **II-39<sub>E</sub>** and benzochalcogenazoles **II-40<sub>E</sub>**; a) POCl<sub>3</sub> 4 eq. and NEt<sub>3</sub> 12 eq. for Y = N, POCl<sub>3</sub> 2 eq. NEt<sub>3</sub> 6 eq. for Y = CH.

## II – 7.4 Frontier orbital characterisation

## II – 7.4.1 Photophysical properties

The absorption spectra of pyrene and compounds **II-39<sub>E</sub>** and **II-40<sub>E</sub>** have been recorded in air equilibrated CHCl<sub>3</sub> at room temperature (Figure II – 32). The key photophysical data are highlighted in Table II – 2. The absorption graphs for each chalcogenazole derivative depicts a broad absorption band corresponding to the  $\pi-\pi^*$  transition and presents similar profiles. A small increase in the absorption band around 380 nm is observed when moving from Te- to Se-analogues **II-39<sub>E</sub>** ( $\epsilon = 21\ 100$  and  $22\ 800\ \text{M}^{-1}\text{cm}^{-1}$ , respectively). A similar trend was observed for derivatives **II-40<sub>E</sub>** for the band at 370 nm ( $\epsilon = 23\ 100$  and  $25\ 300\ \text{M}^{-1}\text{cm}^{-1}$  for Te- and Se-analogues, respectively). Specifically, a slight blue shift is observed comparing **II-39<sub>Te</sub>** and **II-39<sub>Se</sub>** ( $\lambda_{max} = 384$  and  $375$  nm, respectively). Both Te-containing derivatives show a shoulder at higher wavelength around 400 nm (398 and 402 nm for **II-39<sub>Te</sub>** and **II-40<sub>Te</sub>**, respectively). A general decrease in absorption level is observed while moving from the benzo- to the CGP derivatives. The optical bandgap ( $\Delta E_{op}$ ) has been calculated using the absorption edge value and those present very little variation: 2.78 eV for **II-39<sub>Te</sub>**, 2.87 eV for **II-39<sub>Se</sub>**, 2.80 eV for **II-40<sub>Te</sub>** and 2.88 eV for **II-40<sub>Se</sub>** (Table II – 2). The  $\Delta E_{op}$  values are slightly larger moving from the Te-derivatives to their Se-congeners. Those experiments show little influence of the nature of the chalcogen atom on the absorption properties of those 1-substituted pyrene derivatives, moreover the CGP or benzo-derivatives present similar profiles.

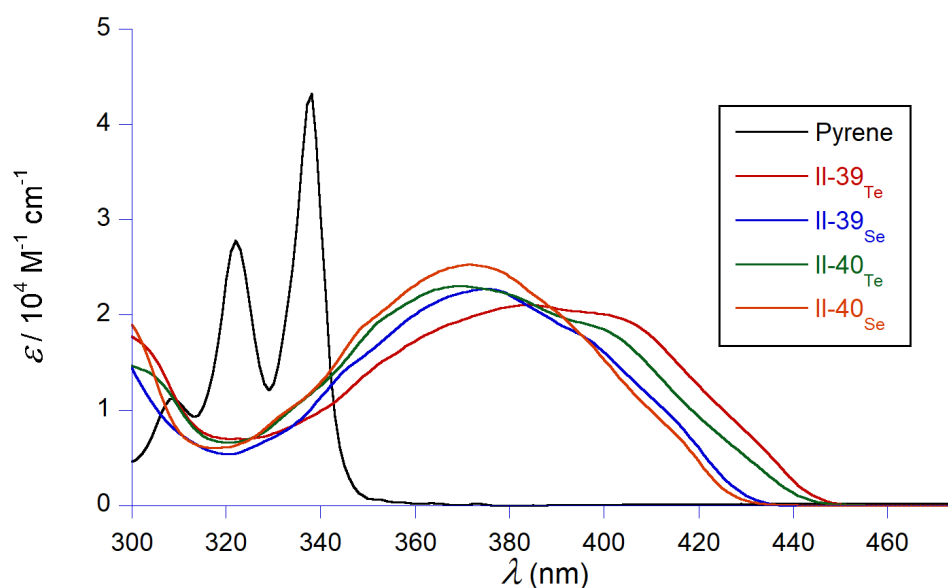


Figure II - 32: Absorption spectra of **II-39<sub>E</sub>** and **II-40<sub>E</sub>** in air equilibrated  $\text{CHCl}_3$  at room temperature.

Table II - 2: Photophysical data in aerated  $\text{CHCl}_3$  at room temperature for **II-39<sub>E</sub>** and **II-40<sub>E</sub>**.

Compound	$\lambda_{max}$ (nm)	$\epsilon$ ( $\text{M}^{-1} \text{cm}^{-1}$ )	$\Delta E_{op}$ (eV)
<b>Pyrene</b>	338	43200	3.61
<b>II-39<sub>Te</sub></b>	384	21100	2.78
<b>II-39<sub>Se</sub></b>	375	22800	2.87
<b>II-40<sub>Te</sub></b>	370	23100	2.80
<b>II-40<sub>Se</sub></b>	371	25300	2.88

As one can notice, the UV-vis envelopes of Se and Te derivatives are very different to the unsubstituted pyrene in an air-equilibrated  $\text{CHCl}_3$  solution (Figure II – 32). Pyrene presents three sharp peaks at 338 nm, 322 nm and 308 nm ( $\epsilon = 43\,200$ ,  $27\,800$  and  $11\,200 \text{ M}^{-1} \text{cm}^{-1}$ , respectively). The intense absorption band at 338 nm and its vibronic replicas at 322 nm and 308 nm corresponds to the  $S_0 \rightarrow S_2$  transition.<sup>[49]</sup> However, conjugation of the pyrenyl ring with CGP and benzochalcogenazole moieties either leads to a large red shift of this absorption band or the intensification of the symmetry forbidden  $S_0 \rightarrow S_1$  transition with a less defined vibronic structure. We tentatively explain that the effect of heavy atom is responsible for the difference observed in the UV-vis absorption spectra.

## 7.4.2 Electrochemical properties

Cyclic voltammetry (CV) experiments were carried out (Figure II – 33) in  $\text{CH}_2\text{Cl}_2$ . Each measurement was fully performed before adding ferrocene (the  $\text{Fc}^+/\text{Fc}$  redox couple was used as internal reference). CGP derivatives **II-39<sub>E</sub>** present an irreversible oxidation wave with an edge potential ( $E^e$ ) of 0.645 eV and 0.827 eV vs  $\text{Fc}^+/\text{Fc}$  for the Te- and the Se-bearing compounds, respectively. Edge potentials are calculated by performing a linear regression on the oxidation wave and the potential at which  $I = 0$  mA is defined as  $E^e$ . Such value is an approximation of the reduction/oxidation potential that can be used when the half-wave potential is not accessible.

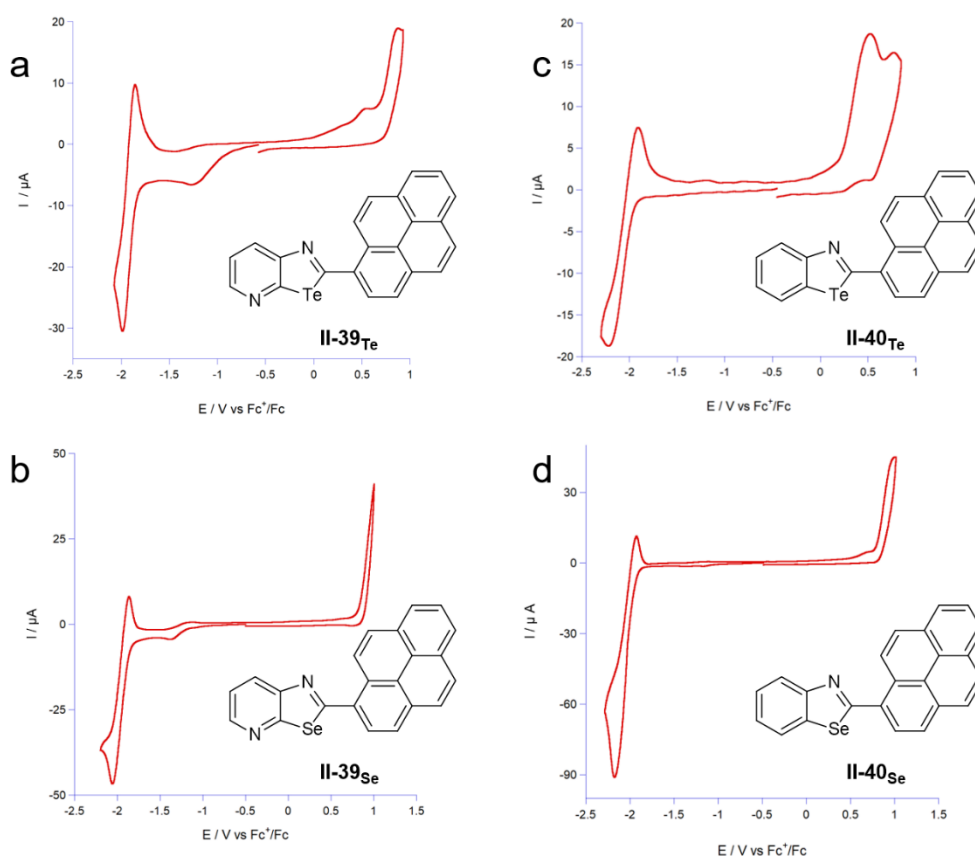


Figure II - 33: Cyclic voltammograms in  $\text{CH}_2\text{Cl}_2$  at r.t. under  $\text{N}_2$  at scan rate of  $120 \text{ mV}\cdot\text{s}^{-1}$  of a) **II-39<sub>Te</sub>**; b) **II-39<sub>Se</sub>**; c) **II-40<sub>Te</sub>** and d) **II-40<sub>Se</sub>**. Electrolyte:  $\text{Bu}_4\text{NPF}_6$  (0.1 M). Ferrocene is used as internal reference, 3mm glassy carbon as working electrode, platinum as counter electrode and silver wire as pseudo-reference electrode.

Benzochalcogenazoles **II-40<sub>E</sub>** show a similar irreversible oxidation wave at  $E^e = 0.356$  eV and 0.768 eV for Te- and Se-derivatives, respectively (Figure II – 33). It has to be noted that CV analysis of **II-40<sub>Te</sub>** did not allow a clear measurement of the oxidation potential value due to the presence of additional chemical species obtained from aggregation. The irreversible nature of the oxidation waves can be related to the electropolymerisation of pyrene which proceed at around 0.75 eV vs  $\text{Fc}^+/\text{Fc}$ .<sup>[40]</sup> Indeed, the radical cations obtained through oxidation react leading to the formation of films on the working electrode. Thus, the oxidation potential has been approximated using  $E^e$  (edge

potential) instead of the half-wave potential ( $E^{1/2}$ ), resulting in an under estimation of the actual value.

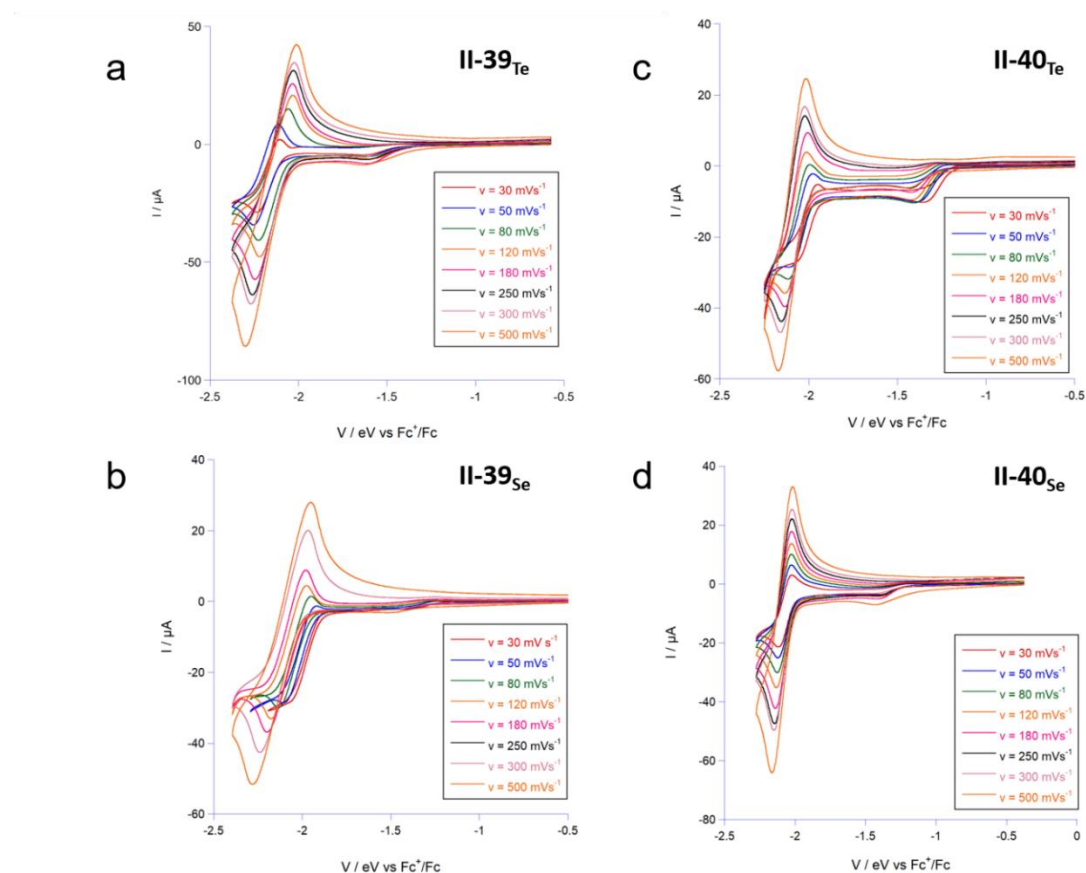


Figure II - 34: Graphs of the reduction wave at different scan rate ( $\nu$ ) for a) **II-39<sub>Te</sub>**; b) **II-39<sub>Se</sub>**; c) **II-40<sub>Te</sub>** and d) **II-40<sub>Se</sub>**. Electrolyte:  $\text{Bu}_4\text{NPF}_6$  (0.1 M). Ferrocene is used as internal reference, 3 mm glassy carbon as working electrode, platinum as counter electrode and silver wire as pseudo-reference electrode.

On the other hand, reduction waves were observed around -2 eV vs  $\text{Fc}^+/\text{Fc}$  for **II-39<sub>E</sub>** and **II-40<sub>E</sub>**. CV experiments at different scan rates ( $\nu$ ) have been performed (Figure II – 34). The resulting current values ( $I$ ) have been plotted against the square root of  $\nu$  (Figure II – 35) and fitted by linear regression for both cathodic and anodic currents (goodness of fit:  $R > 0.99$ ). Those results (Figure II – 35) suggest a reversible reduction reaction under diffusion control.<sup>[50]</sup>  $E^{1/2}$  were calculated to be -1.92 eV and -1.95 eV vs  $\text{Fc}^+/\text{Fc}$  for **II-39<sub>Te</sub>** and **II-39<sub>Se</sub>**, respectively. A similar half-wave potential was obtained for **II-40<sub>Te</sub>** and **II-40<sub>Se</sub>** at -2.06 and -2.04 eV vs  $\text{Fc}^+/\text{Fc}$ , respectively.

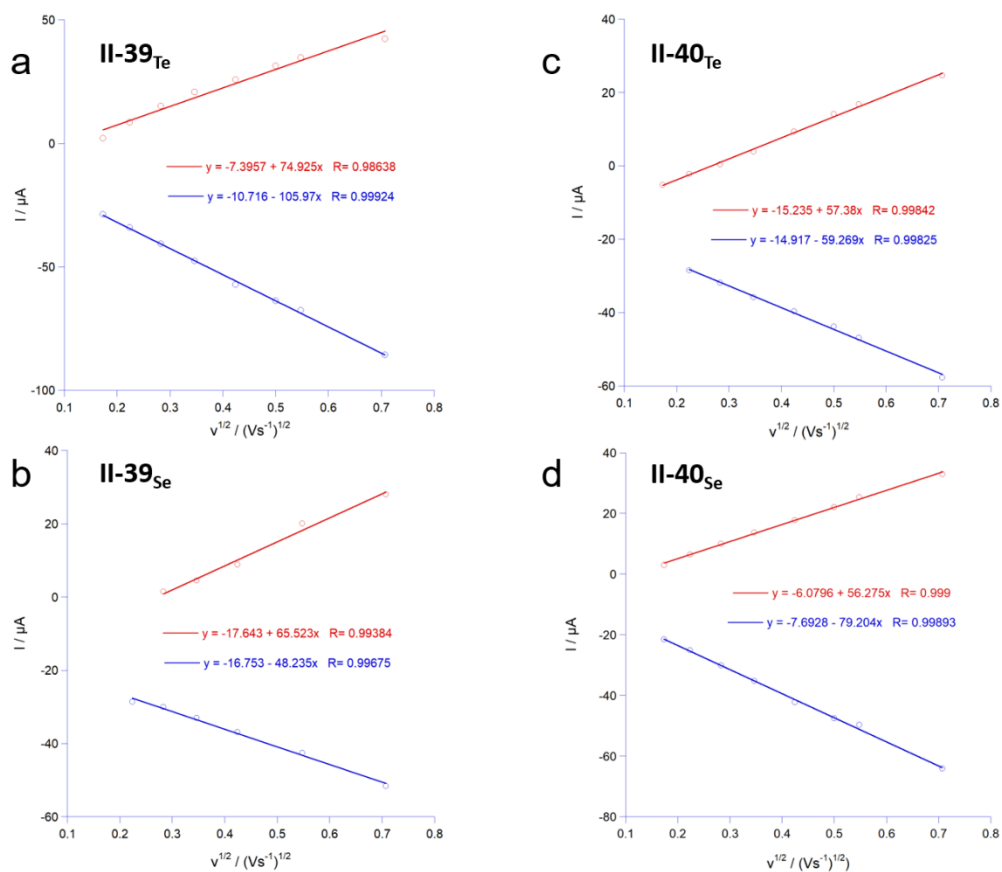


Figure II - 35: Graphs of the cathodic (red) and anodic (blue) current ( $I$ ) against the square root of the scan rate ( $v$ ) for a) II-39<sub>Te</sub>; b) II-39<sub>Se</sub>; c) II-40<sub>Te</sub> and d) II-40<sub>Se</sub>.

#### 7.4.3 Energy diagram of pyrene derivatives II-39<sub>E</sub> and II-40<sub>E</sub>

Building on the results of the absorption spectra and the CV experiments, frontier orbital energy levels were constructed (Figure II – 36). The LUMO energy levels were calculated, from the reduction waves, at -3.21 eV and -3.17 eV vs vacuum for II-39<sub>Te</sub> and II-39<sub>Se</sub>, respectively. Similar values of -3.07 eV and -3.08 eV were obtained for II-40<sub>Te</sub> and II-40<sub>Se</sub>. Interestingly, exchanging Te for Se atom does not affect the LUMO level, indicating that the molecular orbital is centred on the pyrenyl moiety. Moving from the CGP to the benzo analogues, a small decrease in the LUMO energy level is observed (0.14 eV for the Te- and 0.09 eV for the Se-analogues).

HOMO energy levels were estimated by the  $E^e$  values to be -5.78 eV, -5.94 eV and -5.90 eV vs vacuum for II-39<sub>Te</sub>, II-39<sub>Se</sub> and II-40<sub>Se</sub>, respectively (Figure II – 36). There is a difference in energy of 0.16 eV moving from Te- to Se- bearing CGP molecules and a marginal change (0.04 eV) between Se-containing CGP and benzo-analogues. Using those values, the bandgap energy ( $\Delta E_{el}$ ) is 2.46 eV, 2.67 eV and 2.74 eV for II-39<sub>Te</sub>, II-39<sub>Se</sub> and II-40<sub>Se</sub>, respectively (Figure II – 36). The  $\Delta E_{el}$  value for the Te-containing CGP differs from that of the others compound. These findings contrast the values found by UV-vis absorption experiments. However, measuring the redox potential by the edge method underestimate the actual value, which influences those  $\Delta E_{el}$ .

More accurate HOMO energy levels were calculated using the optical band gap ( $\Delta E_{op}$ ) obtained by absorption experiments (Table II – 2) following the equation:  $E_{HOMO} = E_{LUMO} - \Delta E_{op}$ .<sup>[51]</sup> HOMO energy levels are -5.99 eV and -5.84 eV vs vacuum for compounds **II-39<sub>Te</sub>** and **II-39<sub>Se</sub>**, respectively and -5.81 eV and -5.88 eV for **II-40<sub>Te</sub>** and **II-40<sub>Se</sub>**, respectively. Interestingly, the energy levels are very similar, and no particular trend is observed moving from Te to Se analogues or from CGP to benzo-derivatives. In summary, the CV measurements show that the frontier orbital energy levels for benzo **II-40<sub>E</sub>** and CGP **II-39<sub>E</sub>** are similar and there is little influence of the chalcogen atom (Se or Te) on those electronic properties.

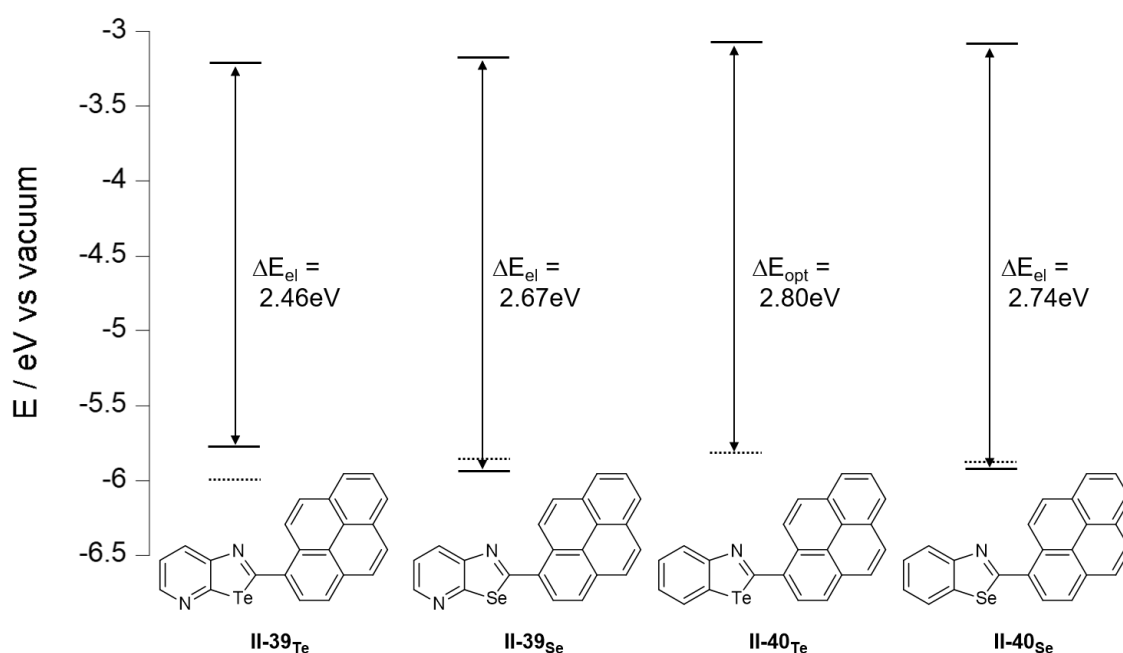


Figure II - 36: Frontier orbital energies for **II-39<sub>E</sub>** and **II-40<sub>E</sub>** in  $\text{CH}_2\text{Cl}_2$ . HOMO orbital for **II-40<sub>Te</sub>** could not be obtained by CV experiment. The dashed lines correspond to the HOMO energy calculated using the optical band gap following the formula:  $E_{HOMO} = E_{LUMO} - \Delta E$  (eV).<sup>[51]</sup> The potential of reference redox couple  $\text{Fc}^+/\text{Fc}$  is assumed to be at -5.13 eV vs vacuum.<sup>[52]</sup>

#### 7.4.4 Computed molecular orbitals and energy diagram of pyrene derivatives **II-39<sub>E</sub>** and **II-40<sub>E</sub>**

To further shed light on the electronic properties of pyrene derivatives **II-39<sub>E</sub>** and **II-40<sub>E</sub>**, DFT calculation were performed using Gaussian 09 including the D01 revision at B97-D3/LanL2DZ level of theory.<sup>[53, 54]</sup> Geometry optimisation for **II-39<sub>E</sub>** and **II-40<sub>E</sub>** were performed in vacuum and global minima were determined by the absence of imaginary frequencies. Frontier molecular orbitals have been calculated and reported in an energy diagram (Figure II – 37). The LUMO energy levels for **II-39<sub>Te</sub>** and **II-39<sub>Se</sub>** were evaluated at -2.98 eV and -2.99 eV vs vacuum, respectively. Similarly, the values for **II-40<sub>Te</sub>** and **II-40<sub>Se</sub>** are both -2.82 eV vs vacuum. The HOMO energy levels were calculated to be -4.98 eV and -5.02 eV vs vacuum for **II-39<sub>Te</sub>** and **II-40<sub>Se</sub>**, respectively. For benzochalcogenazole

**II-40<sub>Te</sub>** and **II-40<sub>Se</sub>**, the values are -4.86 eV and -4.89 eV, respectively. A theoretical band gap ( $\Delta E_{cal}$ ) was calculated at 2.01 eV for **II-39<sub>Te</sub>**, 2.04 eV for both **II-39<sub>Se</sub>** and **II-40<sub>Te</sub>** and 2.07 eV for **II-40<sub>Se</sub>**.

Both HOMO and LUMO energy levels rigidly shift to lower values when passing from Te- to Se-analogues (identical  $\Delta E_{cal}$ ). In addition, both HOMO and LUMO are higher in energy moving from the CGP to the benzo-analogues. These calculations further support the idea that CGP **II-39<sub>E</sub>** and benzo-derivatives **II-40<sub>E</sub>** have similar electronic properties and swapping Te for Se atoms has little influence on the molecular orbital energy levels.

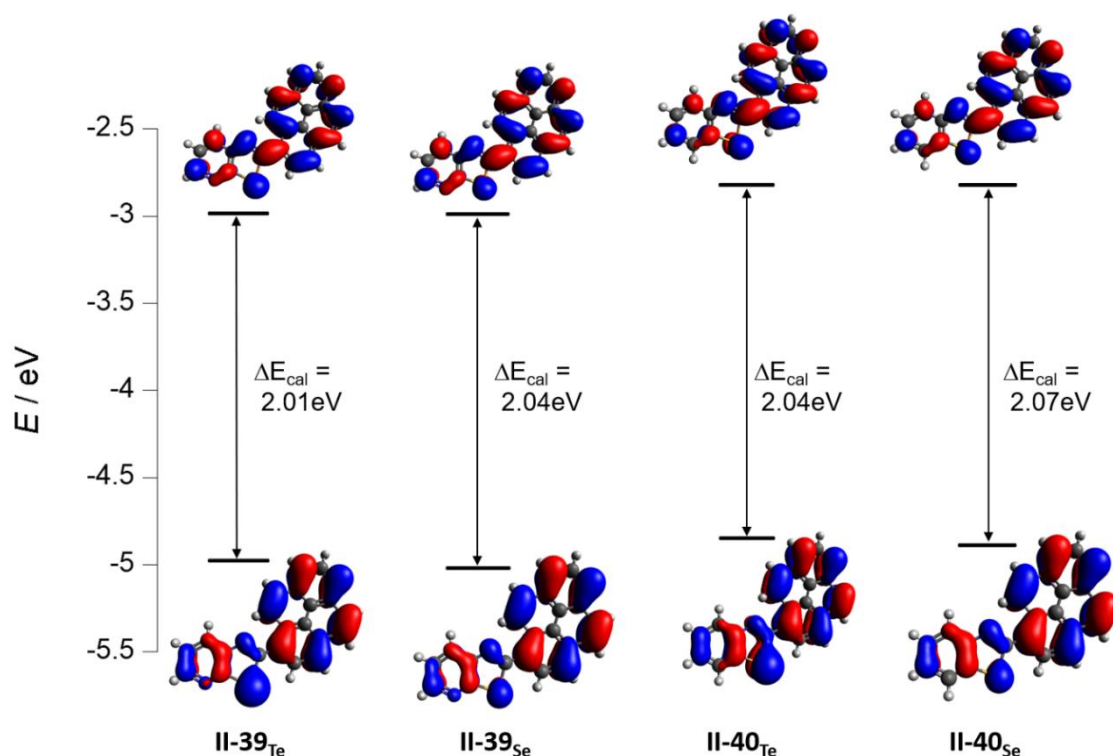


Figure II - 37: Energy diagram of the frontier orbital for **II-39<sub>Te</sub>**, **II-39<sub>Se</sub>**, **II-40<sub>Te</sub>** and **II-40<sub>Se</sub>**. Calculations have been carried out using Gaussian09 including the D01 revision at B97-D3/LanL2DZ level of theory. <sup>[53, 54]</sup>

LUMOs of **II-39<sub>E</sub>** and **II-40<sub>E</sub>** are mainly centred on the pyrenyl ring (Figure II – 37) while the HOMO is more spread over the molecule. As one can easily notice (Figure II – 38), the  $\sigma^*$  of Te-derivatives **II-39<sub>Te</sub>** and **II-40<sub>Te</sub>** lies in LUMO+1 (-1.933 eV and -1.891 eV, respectively) and **II-39<sub>Se</sub>** and **II-40<sub>Se</sub>** LUMO+4 (-1.171 eV) and LUMO+3 (-1.177 eV), respectively. On the other hand, and the lone pair ( $n$ ) lies in HOMO-1, which is centred on N<sub>p</sub> for CGP derivatives **II-39<sub>Te</sub>** and **II-39<sub>Se</sub>** (-5.461 eV and -5.637 eV, respectively) and **II-40<sub>Te</sub>** and **II-40<sub>Se</sub>** present the lone pair from N<sub>c</sub> in the HOMO-3 (-5.821 eV) and HOMO-4 (-6.023 eV), respectively.

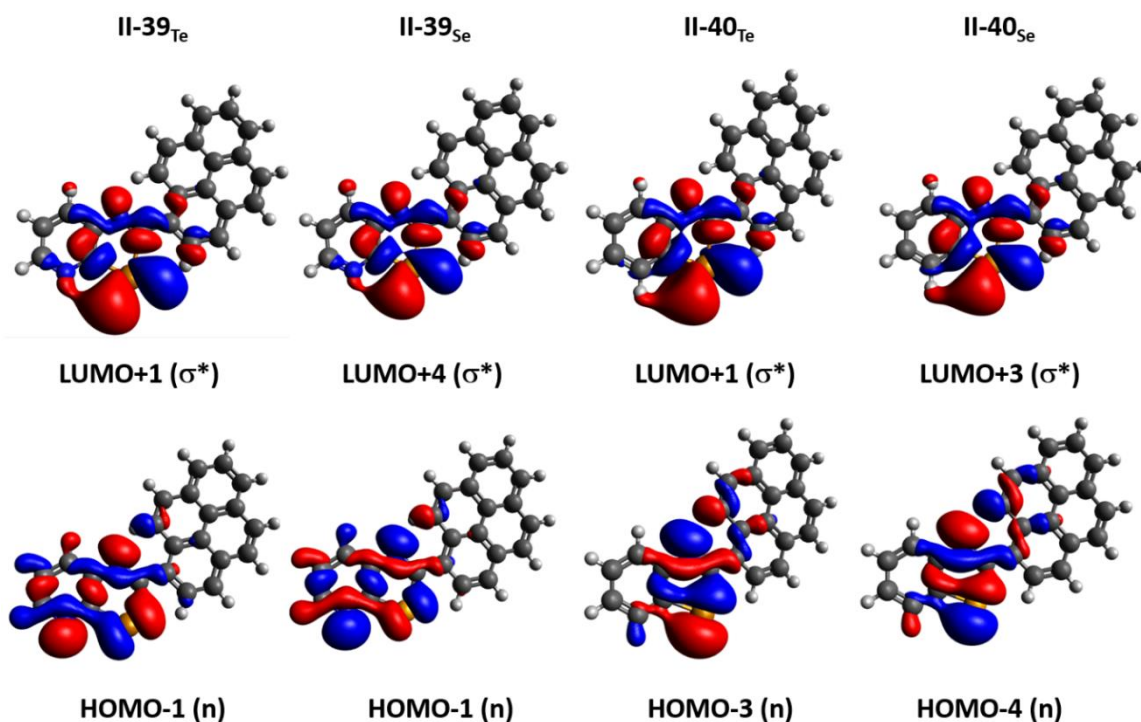


Figure II - 38: Molecular orbital containing  $\sigma^*$  and  $n$  for **II-39<sub>Te</sub>**, **II-39<sub>Se</sub>**, **II-40<sub>Te</sub>** and **II-40<sub>Se</sub>**.

## II – 7.5 Solid-state organisation

In order to probe the supramolecular organisation of the pyrene derivatives, crystals of **II-39<sub>E</sub>** and **II-40<sub>E</sub>** have been obtained from  $\text{CHCl}_3$  solutions by slow evaporation and analysed by X-ray diffraction experiments. Crystals of **II-39<sub>Te</sub>** grow in a  $P2_1/c$  space group and the asymmetric unit is composed by one molecule. The CGP moiety is almost coplanar to the aromatic substituent (angle between the two aromatic planes =  $10^\circ$ ). X-ray analysis (Figure II – 39, a) revealed the formation of dimeric structure (**II-39<sub>Te</sub>**)<sub>2</sub>, where the CGP motifs frontally couple through double chalcogen-bonding interactions ( $d_{\text{N} \cdots \text{Te}} = 3.046 \text{ \AA}$ ) bringing the pyrenyl cores of the two molecules essentially on the same plane. The dimers form a columnar arrangement through  $\pi$ - $\pi$  stacking interactions ( $d_{\pi-\pi} = 3.428 \text{ \AA}$ ), with an offset of  $3.155 \text{ \AA}$  (Figure II – 39, b).

Compound **II-39<sub>Se</sub>** crystallises in a  $Pca2_1$  space group and the asymmetric unit is composed of one molecule. In this case, an angle of  $45^\circ$  is observed between the planes of the CGP moiety and the pyrenyl ring. The X-ray structure shows no particular short contact involving the Se and N atoms (Figure II – 40, a). However, molecules interact through  $\pi$ - $\pi$  stacking interactions ( $d_{\pi-\pi} = 3.502 \text{ \AA}$ , with an offset of  $1.578 \text{ \AA}$ ) leading to the formation of a columnar arrangement (Figure II – 40, b). In contrast to Te-derivative **II-39<sub>Te</sub>**, no interactions are responsible for connecting the columns together.

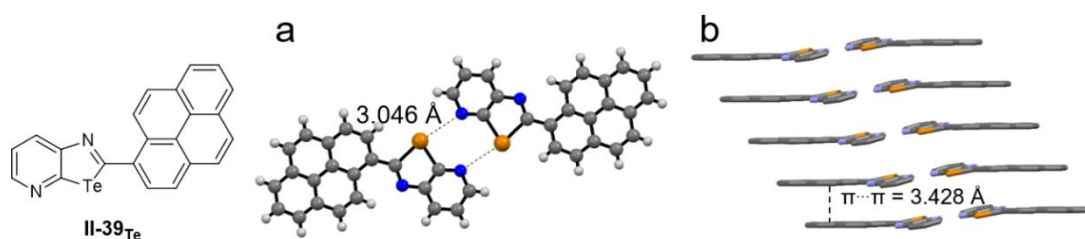


Figure II - 39: X-ray structure of **II-39<sub>Te</sub>**, a) top view, ball and stick representation of the dimer; b) side view, stick representation of the columnar arrangement, H atoms omitted for clarity. Space group:  $P2_1/C$ , solvent of crystallization:  $CHCl_3$ .

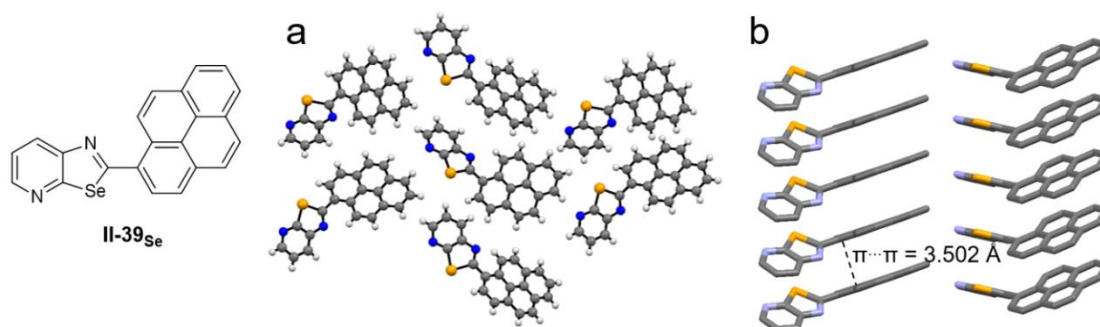


Figure II - 40: X-ray structure of **II-39<sub>Se</sub>**, a) top view, ball and stick representation of the dimer; b) side view, stick representation of the columnar arrangement, H atoms omitted for clarity. Space group:  $Pca2_1$ , solvent of crystallization:  $CHCl_3$ .

The crystals of **II-40<sub>Te</sub>** grow in a  $Pbca$  space group and the asymmetric unit is constituted by one molecule. At the molecular level, the planes of the benzotellurazole unit and the pyrenyl ring form an angle of  $45^\circ$ . Unlike **II-39<sub>Te</sub>**, X-ray analysis (Figure II – 41) reveals an arrangement driven by  $C-H \cdots \pi$  interactions between the benzo- and the pyrenyl-rings. Notably, columns are formed along the crystallographic  $b$ -axis by  $C-H \cdots \pi$  interaction ( $d_{C \cdots \pi} = 3.387 \text{ \AA}$  and  $3.469 \text{ \AA}$ ) with the pyrene moiety acting as HB donor (Figure II – 41, a). Along the  $c$ -axis (Figure II – 41, b), edge-to-face interaction involving the  $p$ -surface of the pyrenyl rings and the H atoms issued from the benzotellurazole moieties ( $d_{C \cdots \pi} = 3.423 \text{ \AA}$  and  $3.466 \text{ \AA}$ ). No particular arrangement has been noted along the  $a$ -axis. Surprisingly, no face-to-face  $\pi$ – $\pi$  stacking interactions are observed.

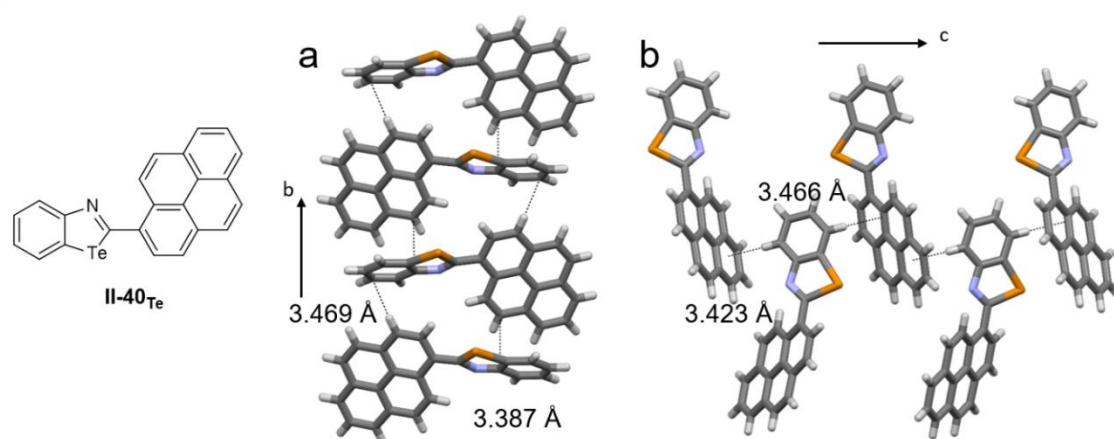


Figure II - 41: X-ray structure in stick representation of **II-40<sub>Te</sub>**; a) arrangement along *b*-axis; b) arrangement along the *c*-axis. Space group: *Pbca*, solvent of crystallization:  $\text{CHCl}_3$ .

Finally, compound **II-40<sub>Se</sub>** crystallises in a  $P2_1/c$  and the asymmetric unit is composed by one molecule. An angle of  $43^\circ$  is observed between the planes of the benzoselenazole moiety and the pyrenyl ring. Similarly to the structure of **II-39<sub>Se</sub>**, no particular  $\text{N}\cdots\text{Se}$  short contact are revealed by X-ray analysis (Figure II – 42, a). However, columnar arrangement (Figure II – 42, b) is observed through  $\pi$ - $\pi$  stacking interactions ( $d_{\pi-\pi} = 3.537 \text{ \AA}$ , with an offset of  $1.571 \text{ \AA}$ ). Interestingly, stacks come in pair with a misalignment of  $1.357 \text{ \AA}$ .

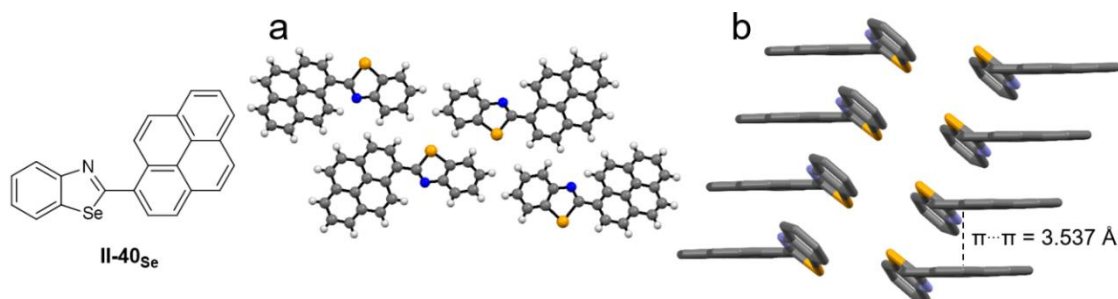


Figure II - 42: X-ray structure of **II-40<sub>Se</sub>**, a) top view, ball and stick representation of the dimer; b) side view, stick representation of the columnar arrangement, hydrogen atoms omitted for clarity. Space group:  $P2_1/c$ , solvent of crystallization:  $\text{CHCl}_3$ .

X-ray analysis of derivatives **II-39<sub>E</sub>** and **II-40<sub>E</sub>** show a strong tendency to form columnar arrangement by means of face-to-face  $\pi$ - $\pi$  stacking interactions at the solid state except for **II-40<sub>Te</sub>**, which organise through  $\text{C-H}\cdots\pi$  contact. As anticipated, dimer formation through double chalcogen bonding was only obtained for **II-39<sub>Te</sub>**. This interaction leads to a non-covalent levelling of the pyrene cores and brings the columnar stacks in pair. Compound **II-40<sub>Se</sub>** also organise in double columnar arrangement, however no notable driving force is observed.

## II – 7.6 Charge mobility measurements

In collaboration with the group of Dr. *Salvatore Gambino* in CNR nanotec in Lecce (Italy), charge transporter devices were built using **II-39<sub>E</sub>** and **II-40<sub>E</sub>** materials as semiconductors. Space-Charge Limited Current (SCLC) experiments were performed to evaluate the charge mobility of all four derivatives. The devices for the SCLC measurements are built in a hole-only architecture (Figure II – 43, a). In a sandwich-type structure, they were fabricated by spin coating of a solution of the organic material in  $\text{CHCl}_3$  onto a patterned transparent ITO (Indium Tin Oxide,  $\text{In}_2\text{O}_3/\text{SnO}_2$ ) coated glass substrate covered with PEDOT:PSS (Poly(3,4-ethylenedioxythiophene)-poly(styrenesulfonate)). The thickness of the organic films was evaluated to be around 150 nm (measured with a profilometer). Images of thin films of **II-39<sub>Se</sub>** and **II-39<sub>Te</sub>** were acquired using an optical microscope (Figure II – 44). The surfaces were covered with the top electrodes by sequential thermal evaporation of  $\text{MoO}_3$  and Au, defining active device areas of  $4 \text{ mm}^2$ . It has to be pointed out that the organic thin films reorganise over time leading to short circuit over 24 h making the device inoperative. For this reason, SCLC measurements had to be performed quickly after the realisation of the device to ensure reproducibility.

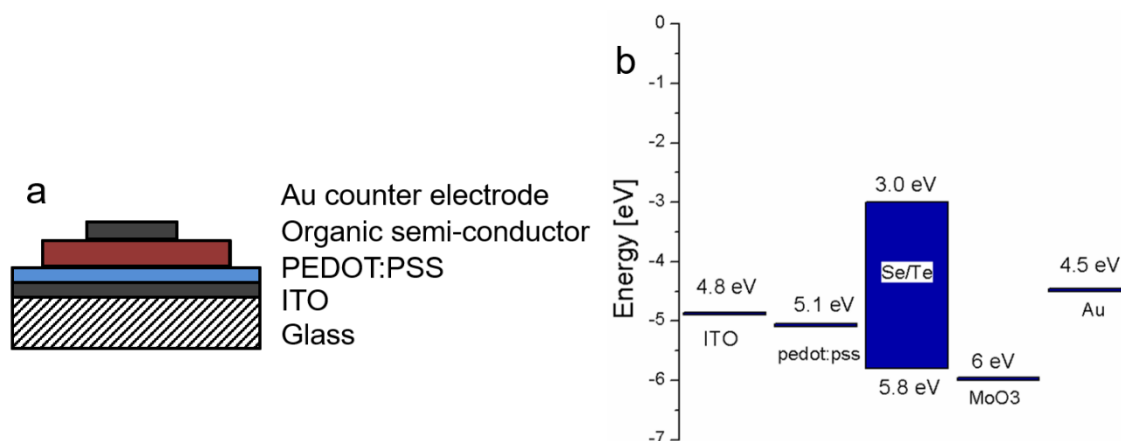


Figure II - 43: a) Sandwiched-type architecture of a hole only devices used in this study, b) Energy level and work function of the different materials used in the device, **II-39<sub>E</sub>** and **II-40<sub>E</sub>** gap energy is shown in blue.

PEDOT:PSS (work function of 5.1 eV)<sup>[55]</sup> acts as a transparent hole-injection layer (HIL) and electron-blocking layer. An energetic barrier is expected for hole injection from PEDOT:PSS (~0.5 – 0.7 eV barrier). Gold was used as a top electrode, its Fermi level (4.5 eV)<sup>[55]</sup> lying within the band gap of all materials and presenting an energetic barrier to injection of both electrons and holes.  $\text{MoO}_3$  acts as a HIL with a high work function (6 eV) that is enough to inject holes efficiently into all four materials (Figure II – 42, b).

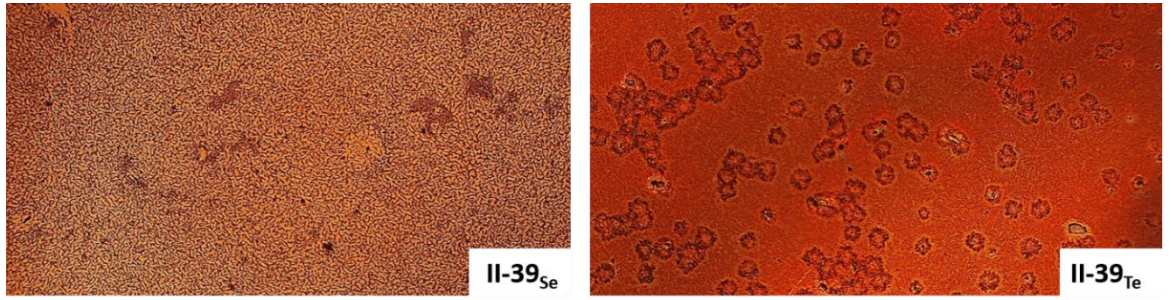


Figure II - 44: Optical microscopy image of a thin film containing II-39<sub>Se</sub> and II-39<sub>Te</sub>, respectively.

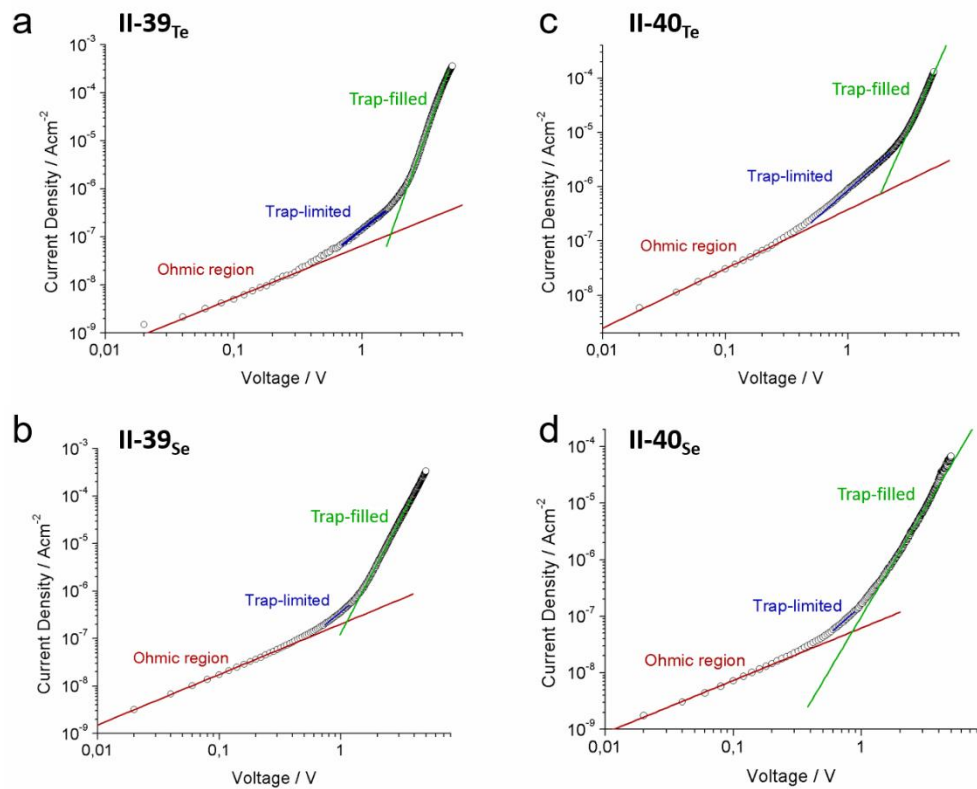


Figure II - 45: Graphs of the current density against the voltage in SCLC measurement for a) II-39<sub>Te</sub>; b) II-39<sub>Se</sub>; c) II-40<sub>Te</sub> and d) II-40<sub>Se</sub>.

Each material was tested according to the method explained above. The graphs of the current density ( $J$ ) against the voltage applied ( $V$ ) are reported in Figure II – 45. The  $J$ - $V$  curves are characteristic for such measurements (Figure II – 28). The graphs for the four materials are divided in three sections, namely the ohmic region (in red), the trap-limited region (in blue) and the trap-filled region (in green).

The charge mobility values could be extracted from the zero-field trap-limited regime (Table II – 3). One can easily notice that the highest value was obtained with II-39<sub>Te</sub> ( $4.8 \cdot 10^{-9} \text{ cm}^2 \text{ V}^{-1} \text{ s}^{-1}$ ), followed

by **II-40<sub>Se</sub>** ( $4.4 \cdot 10^{-9} \text{ cm}^2 \text{ V}^{-1} \text{ s}^{-1}$ ). Lower charge mobility has been obtained with **II-40<sub>Te</sub>** ( $2.2 \cdot 10^{-9} \text{ cm}^2 \text{ V}^{-1} \text{ s}^{-1}$ ) and **II-39<sub>Se</sub>** ( $9.6 \cdot 10^{-10} \text{ cm}^2 \text{ V}^{-1} \text{ s}^{-1}$ ). Those values are comparable with the hole mobility values found in the literature for polymers supporting our idea that **II-39<sub>E</sub>** and **II-40<sub>E</sub>** could be used as valuable materials. For example,  $\mu_0$  equals  $5 \cdot 10^{-7} \text{ cm}^2 \text{ V}^{-1} \text{ s}^{-1}$  for poly(2-methoxy,5-(2'-ethylhexoxy)-*p*-phenylene vinylene (MEH-PPV),  $1.2 \cdot 10^{-5} \text{ cm}^2 \text{ V}^{-1} \text{ s}^{-1}$  for poly(2,5-bis(2-ethylhexyloxy)-1,4-phenylene vinylene (DEH-PPV) and  $1.3 \cdot 10^{-4} \text{ cm}^2 \text{ V}^{-1} \text{ s}^{-1}$  for regioregular poly(3-hexylthiophene) (rr-P3HT).<sup>[37]</sup>

Table II - 3: Hole mobility values at zero-field at room temperature extracted from SCLC measurement.

Compound	$\mu_0$ ( $\text{cm}^2 \text{ V}^{-1} \text{ s}^{-1}$ )	Compound	$\mu_0$ ( $\text{cm}^2 \text{ V}^{-1} \text{ s}^{-1}$ )
<b>II-39<sub>Te</sub></b>	$4.8 \cdot 10^{-9}$	<b>II-40<sub>Te</sub></b>	$2.2 \cdot 10^{-9}$
<b>II-39<sub>Se</sub></b>	$9.6 \cdot 10^{-10}$	<b>II-40<sub>Se</sub></b>	$4.4 \cdot 10^{-9}$

The molecular properties of **II-39<sub>E</sub>** and **II-40<sub>E</sub>** being similar, the differences in the charge mobility originates from their supramolecular organisations. As anticipated, the highest charge carrier mobility was obtained from devices built with **II-39<sub>Te</sub>** as an organic semi-conductor material ( $4.8 \cdot 10^{-9} \text{ cm}^2 \text{ V}^{-1} \text{ s}^{-1}$ ). In the solid-state, **II-39<sub>Te</sub>** organise into dimeric structures *via* double chalcogen bonds. Those dimers interact through  $\pi$ - $\pi$  stacking interactions forming a double columnar arrangement, maximising the overlap of the  $\pi$ -surfaces. This shows that the supramolecular structure of the pyrene-based material can be controlled by chalcogen-bonding interactions resulting in an enhancement of its charge mobility property (hole mobility value increasing from  $9.6 \cdot 10^{-10}$  to  $4.8 \cdot 10^{-9} \text{ cm}^2 \text{ V}^{-1} \text{ s}^{-1}$  moving from **II-39<sub>Se</sub>** to **II-39<sub>Te</sub>**). However, at this stage of the research, the charge transport mechanism in such architecture has not been investigated. Charge hopping between the aromatic units present in the columnar arrangements could be envisaged. We are also considering possible tunnelling of the charges traveling through the chalcogen bonds.

However, it has to be noted that the second highest charge mobility was reached for compound **II-40<sub>Se</sub>** ( $4.4 \cdot 10^{-9} \text{ cm}^2 \text{ V}^{-1} \text{ s}^{-1}$ ) that also forms double-stack columnar arrangement in the solid state. This organisation reflects that found with **II-39<sub>Te</sub>** without EB interactions in the case of **II-40<sub>Se</sub>**. Both arrangements maximise the overlap of the  $\pi$ -surface, leading to a higher charge mobility compared to that of **II-39<sub>Se</sub>** and **II-40<sub>Te</sub>**. Compound **II-39<sub>Se</sub>** form single-molecule width columns and present the lowest charge mobility value ( $9.6 \cdot 10^{-10} \text{ cm}^2 \text{ V}^{-1} \text{ s}^{-1}$ ). Derivative **II-40<sub>Te</sub>** should be left outside the comparison as it does not follow a similar face-to-face  $\pi$ - $\pi$  stacking, but arrange in a herringbone structure. Those structural differences in relation with the  $\mu$  values show how one can control the solid-state arrangement of 1-substituted pyrene using chalcogen bonds to form organic semi-

conductor materials. In order to complete the study, electron mobility measurements will be performed in parallel to theoretical calculations.

## II – 8 Conclusion

In the first part of this work (Section II – 2), we have designed a double chalcogen-bonding array (namely CGP) that, through self-complementarity, forms dimer at the solid state. The key aspect of this motif is the  $\beta$ -junction of a pyridyl and a chalcogenazole moiety that places a N atom in close proximity to the chalcogen atom forming a donor-acceptor motif. The CGP synthons frontally couple through double chalcogen-bonding interactions. We synthesised twenty molecules bearing different substituents such as aromatic moieties (phenyl **II-15<sub>E</sub>**, p-nitrophenyl **II-20<sub>E</sub>**, 3,4,5-trifluorophenyl **II-21<sub>E</sub>** and pentafluorophenyl **II-22<sub>E</sub>**), heterocyclic rings (pyridyl **II-16<sub>E</sub>**, **II-17<sub>E</sub>** and **II-18<sub>E</sub>** and thiophenyl **II-19<sub>E</sub>**) and a CF<sub>3</sub> group (**II-25<sub>E</sub>**). Most of the compounds were crystallised and analysed by X-ray diffraction. The strongest recognition persistence was observed for the Te-congeners, which led to dimer formation in the solid state regardless of the substituent in the 2-position. Strengthening of the interactions was achieved upon addition of EWG in 2-position. However, a certain variability was noted for the Se-analogues that associate through hydrogen-bonding interactions to form dimers or supramolecular polymers. Phenyl substituted **II-15<sub>Se</sub>** interacts through  $\pi$ - $\sigma^*$  interactions. Nonetheless, association through double chalcogen bonds was obtained for pentafluorophenyl and CF<sub>3</sub> substituted derivatives (**II-22<sub>Se</sub>** and **II-25<sub>Se</sub>**). Those behaviours were correlated by calculation of the  $V_{s,max}$  values around the chalcogen atoms.

In some cases, variability has been observed in Te-containing systems while introducing other non-covalent interactions such as halogen- or hydrogen-bonding (**II-24<sub>Te</sub>** and **II-32<sub>Te</sub>**, respectively). XB and HB overcome the double EB array leading to the formation of structures featuring unplanned interactions. Multi-type interactions systems will be the focus point in the next chapters (*chapter III* for XB and *chapter IV* for HB).

We also have designed a ditopic synthon based on the CGP and benzochalcogenazole moieties and anticipated their supramolecular arrangement. Unfortunately, CGP containing **II-26<sub>E</sub>** could not be synthesised or isolated. More particularly for the Te-analogue, a problem of solubility has been encountered. However, both derivatives **II-27<sub>E</sub>** were isolated and crystallised. The solid-state structure of **II-27<sub>Te</sub>** shows a wire-like structure through chalcogen-bonding interactions, while that of **II-27<sub>Se</sub>** reveals a tightly packed arrangement. In the case of the Te-analogues, the two benzotellurazole units behave differently, one being involved in the supramolecular backbone of the wire-like structure and the second one present as support. On the contrary, the crystal structure

of **II-27<sub>Se</sub>** does not show any difference between the two benzoselenazole units optimising every interaction to form an entangled structure.

Finally, organic semi-conductor materials based on the conjugation of pyrenyl group and the CGP moiety (**II-39<sub>E</sub>**) was synthesised. As a comparison, Se- and Te-containing benzochalcogenazole derivatives (**II-40<sub>E</sub>**) were also prepared. The compounds were characterised in solution by UV-vis absorption and cyclic-voltammetry experiments to evaluate the electronic properties. The solid-state arrangement was probed by single crystal X-ray diffraction analysis. At the molecular level, little variation was detected while drastic differences were observed regarding to their crystal structures. Compound **II-39<sub>Te</sub>** organises in columnar arrangement formed by dimer connected through double chalcogen-bonding interactions. This appraises the possibility of using simultaneously EB and  $\pi$ - $\pi$  staking interactions to control the crystal packing. While compound **II-40<sub>Se</sub>** also forms double-stack arrangement through  $\pi$ - $\pi$  stacking interactions, **II-39<sub>Se</sub>** assembles into single columnar structure and **II-40<sub>Te</sub>** in a herringbone structure. The supramolecular properties are reflected on the hole mobility of those materials, the highest  $\mu$  value being achieved for **II-39<sub>Te</sub>** and **II-40<sub>Se</sub>** that maximise the overlap of the  $\pi$ -surface. In contrast, **II-39<sub>Se</sub>** and **II-40<sub>Te</sub>** feature smaller hole mobility values alongside crystal structures that do not favour the face-to-face  $\pi$ -contacts. We foresee that the recognition persistence of Te-containing CGP arrays and the easy derivatisation of the pyrene core conjugated will lead to the engineering of unprecedented materials in the near future.

## II – 9 Bibliography

- [1] N. Biot, D. Bonifazi, 'Programming Recognition Arrays through Double Chalcogen-Bonding Interactions', *Chem. Eur. J.* **2018**, *24*, 5439-5443.
- [2] J.-M. Lehn, *From Molecular to Supramolecular Chemistry*, Wiley-VCH Verlag GmbH & Co. KGaA, 2006.
- [3] J.-M. Lehn, 'Toward Self-Organization and Complex Matter', *Science* **2002**, *295*, 2400-2403.
- [4] G. E. Garrett, G. L. Gibson, R. N. Straus, D. S. Seferos, M. S. Taylor, 'Chalcogen Bonding in Solution: Interactions of Benzotelluradiazoles with Anionic and Uncharged Lewis Bases', *J. Am. Chem. Soc.* **2015**, *137*, 4126-4133.
- [5] P. C. Ho, P. Szydlowski, J. Sinclair, P. J. W. Elder, J. Kubel, C. Gendy, L. M. Lee, H. Jenkins, J. F. Britten, D. R. Morim, I. Vargas-Baca, 'Supramolecular Macrocycles Reversibly Assembled by Te ... O Chalcogen Bonding', *Nat. Commun.* **2016**, *7*, 11299.
- [6] A. Kremer, A. Fermi, N. Biot, J. Wouters, D. Bonifazi, 'Supramolecular Wiring of Benzo-1,3-chalcogenazoles through Programmed Chalcogen Bonding Interactions', *Chem. Eur. J.* **2016**, *22*, 5665-5675.
- [7] A. F. Cozzolino, I. Vargas-Baca, S. Mansour, A. H. Mahmoudkhani, 'The Nature of the Supramolecular Association of 1,2,5-Chalcogenadiazoles', *J. Am. Chem. Soc.* **2005**, *127*, 3184-3190.
- [8] A. F. Cozzolino, I. Vargas-Baca, 'The Supramolecular Chemistry of 1,2,5-Chalcogenadiazoles', *J. Organomet. Chem.* **2007**, *692*, 2654-2657.

- [9] A. Jolleys, W. Levason, G. Reid, 'Thioether Coordination to Divalent Selenium Halide Acceptors – Synthesis, Properties and Structures', *Dalton Trans.* **2013**, 42, 2963-2972.
- [10] G. E. Garrett, E. I. Carrera, D. S. Seferos, M. S. Taylor, 'Anion Recognition by a Bidentate Chalcogen Bond Donor', *Chem. Commun.* **2016**, 52, 9881-9884.
- [11] S. Benz, M. Macchione, Q. Verolet, J. Mareda, N. Sakai, S. Matile, 'Anion Transport with Chalcogen Bonds', *J. Am. Chem. Soc.* **2016**, 138, 9093-9096.
- [12] S. Benz, J. López-Andarias, J. Mareda, N. Sakai, S. Matile, 'Catalysis with Chalcogen Bonds', *Angew. Chem. Int. Ed.* **2017**, 56, 812-815.
- [13] J. Y. C. Lim, I. Marques, A. L. Thompson, K. E. Christensen, V. Félix, P. D. Beer, 'Chalcogen Bonding Macrocycles and [2]Rotaxanes for Anion Recognition', *J. Am. Chem. Soc.* **2017**, 139, 3122-3133.
- [14] J. Y. C. Lim, J. Y. Liew, P. D. Beer, 'Thermodynamics of Anion Binding by Chalcogen Bonding Receptors', *Chem. Eur. J.* **2018**, 24, 14560-14566.
- [15] P. Wonner, L. Vogel, M. Düser, L. Gomes, F. Kniep, B. Mallick, D. B. Werz, S. M. Huber, 'Carbon–Halogen Bond Activation by Selenium-Based Chalcogen Bonding', *Angew. Chem. Int. Ed.* **2017**, 56, 12009-12012.
- [16] P. Wonner, L. Vogel, F. Kniep, S. M. Huber, 'Catalytic Carbon–Chlorine Bond Activation by Selenium-Based Chalcogen Bond Donors', *Chem. Eur. J.* **2017**, 23, 16972-16975.
- [17] T. Clark, M. Hennemann, J. S. Murray, P. Politzer, 'Halogen bonding: the sigma-hole. Proceedings of "Modeling interactions in biomolecules II", Prague, September 5th-9th, 2005', *J. Mol. Model.* **2007**, 13, 291-296.
- [18] J. S. Murray, P. Lane, P. Politzer, 'A predicted new type of directional noncovalent interaction', *Int. J. Quantum Chem.* **2007**, 107, 2286-2292.
- [19] P. Politzer, J. S. Murray, T. Clark, 'Halogen bonding and other [sigma]-hole interactions: a perspective', *Phys. Chem. Chem. Phys.* **2013**, 15, 11178-11189.
- [20] A. Kremer, C. Aurisicchio, F. De Leo, B. Ventura, J. Wouters, N. Armaroli, A. Barbieri, D. Bonifazi, 'Walking Down the Chalcogenic Group of the Periodic Table: From Singlet to Triplet Organic Emitters', *Chem. Eur. J.* **2015**, 21, 15377-15387.
- [21] W. E. Parham, R. M. Piccirilli, 'Selective halogen-lithium exchange in 2,5-dibromobenzenes and 2,5-dibromopyridine', *J. Org. Chem.* **1977**, 42, 257-260.
- [22] J. J. Song, N. K. Yee, Z. Tan, J. Xu, S. R. Kapadia, C. H. Senanayake, 'Synthesis of 5-Bromopyridyl-2-magnesium Chloride and Its Application in the Synthesis of Functionalized Pyridines', *Org. Lett.* **2004**, 6, 4905-4907.
- [23] G. Wittig, F. J. Meyer, G. Lange, 'Über das Verhalten von Diphenylmetallen als Komplexbildner', *Justus Liebigs Ann. Chem.* **1951**, 571, 167-201.
- [24] A. Inoue, K. Kitagawa, H. Shinokubo, K. Oshima, 'Selective Halogen–Magnesium Exchange Reaction via Organomagnesium Ate Complex', *J. Org. Chem.* **2001**, 66, 4333-4339.
- [25] A. é. Mistryukov, I. D. Sadekov, V. S. Sergienko, G. M. Abakarov, M. A. Porai-Koshits, A. A. Shneider, A. D. Garnovskii, 'Nitrogen-tellurium-containing heterocycles. 4. X-ray structure of 2-phenylbenzotellurazole', *Chem. Heterocycl. Compd.* **1989**, 25, 1407-1409.
- [26] S. Hirotsu, Y. Hirokawa, T. Tanaka, 'Volume-phase transitions of ionized N-isopropylacrylamide gels', *J. Chem. Phys.* **1987**, 87, 1392-1395.
- [27] S. Hirotsu, 'Softening of bulk modulus and negative Poisson's ratio near the volume phase transition of polymer gels', *J. Chem. Phys.* **1991**, 94, 3949-3957.
- [28] H. Tokuyama, N. Ishihara, S. Sakohara, 'Effects of synthesis-solvent on swelling and elastic properties of poly(N-isopropylacrylamide) hydrogels', *Eur. Polym. J.* **2007**, 43, 4975-4982.
- [29] S. Hirotsu, 'Phase Transition of a Polymer Gel in Pure and Mixed Solvent Media', *J. Phys. Soc. Jpn.* **1987**, 56, 233-242.
- [30] S. Yamago, K. Iida, J.-i. Yoshida, 'Organotellurium Compounds as Novel Initiators for Controlled/Living Radical Polymerizations. Synthesis of Functionalized Polystyrenes and End-Group Modifications', *J. Am. Chem. Soc.* **2002**, 124, 2874-2875.

- [31] W. Fan, S. Yamago, 'Synthesis of Poly(N-vinylamide)s and Poly(vinylamine)s and Their Block Copolymers by Organotellurium-Mediated Radical Polymerization', *Angew. Chem. Int. Ed.* **2019**, *58*, 7113-7116.
- [32] S. Dong, Y. Luo, X. Yan, B. Zheng, X. Ding, Y. Yu, Z. Ma, Q. Zhao, F. Huang, 'A Dual-Responsive Supramolecular Polymer Gel Formed by Crown Ether Based Molecular Recognition', *Angew. Chem. Int. Ed.* **2011**, *50*, 1905-1909.
- [33] H. Yan, Z. Chen, Y. Zheng, C. Newman, J. R. Quinn, F. Dötz, M. Kastler, A. Facchetti, 'A high-mobility electron-transporting polymer for printed transistors', *Nature* **2009**, *457*, 679.
- [34] W. Wu, Y. Liu, D. Zhu, ' $\pi$ -Conjugated molecules with fused rings for organic field-effect transistors: design, synthesis and applications', *Chem. Soc. Rev.* **2010**, *39*, 1489-1502.
- [35] S. Pang, Y. Hernandez, X. Feng, K. Müllen, 'Graphene as Transparent Electrode Material for Organic Electronics', *Adv. Mater.* **2011**, *23*, 2779-2795.
- [36] X.-Y. Wang, X. Yao, K. Müllen, 'Polycyclic aromatic hydrocarbons in the graphene era', *Sci. China Chem.* **2019**, DOI: 10.1007/s11426-11019-19491-11422.
- [37] N. I. Craciun, J. Wildeman, P. W. M. Blom, 'Universal Arrhenius Temperature Activated Charge Transport in Diodes from Disordered Organic Semiconductors', *Phys. Rev. Lett.* **2008**, *100*, 056601.
- [38] Y. Gong, X. Zhan, Q. Li, Z. Li, 'Progress of pyrene-based organic semiconductor in organic field effect transistors', *Sci. China Chem.* **2016**, *59*, 1623-1631.
- [39] S. Tiwari, N. C. Greenham, 'Charge mobility measurement techniques in organic semiconductors', *Opt. Quantum Electron.* **2009**, *41*, 69-89.
- [40] J. C. Bachman, R. Kaviani, D. J. Graham, D. Y. Kim, S. Noda, D. G. Nocera, Y. Shao-Horn, S. W. Lee, 'Electrochemical polymerization of pyrene derivatives on functionalized carbon nanotubes for pseudocapacitive electrodes', *Nat. Commun.* **2015**, *6*, 7040.
- [41] J. E. Campbell, J. Yang, G. M. Day, 'Predicted energy-structure-function maps for the evaluation of small molecule organic semiconductors', *Journal of Materials Chemistry C* **2017**, *5*, 7574-7584.
- [42] C. Wang, H. Dong, W. Hu, Y. Liu, D. Zhu, 'Semiconducting  $\pi$ -Conjugated Systems in Field-Effect Transistors: A Material Odyssey of Organic Electronics', *Chem. Rev.* **2012**, *112*, 2208-2267.
- [43] T. M. Figueira-Duarte, K. Müllen, 'Pyrene-Based Materials for Organic Electronics', *Chem. Rev.* **2011**, *111*, 7260-7314.
- [44] S. Guo, Z. Zhu, X. Hu, W. Zhou, X. Song, S. Zhang, K. Zhang, H. Zeng, 'Ultrathin tellurium dioxide: emerging direct bandgap semiconductor with high-mobility transport anisotropy', *Nanoscale* **2018**, *10*, 8397-8403.
- [45] S. Ye, L. Janasz, W. Zajaczkowski, J. G. Manion, A. Mondal, T. Marszalek, D. Andrienko, K. Müllen, W. Pisula, D. S. Seferos, 'Self-Organization and Charge Transport Properties of Selenium and Tellurium Analogues of Polythiophene', *Macromol. Rapid Commun.* **2019**, *40*, 1800596.
- [46] P. W. M. Blom, M. J. M. d. Jong, J. J. M. Vlegaar, 'Electron and hole transport in poly(p-phenylene vinylene) devices', *Appl. Phys. Lett.* **1996**, *68*, 3308-3310.
- [47] G. R. Desiraju, A. Gavezzotti, 'From molecular to crystal structure; polynuclear aromatic hydrocarbons', *J. Chem. Soc., Chem. Commun.* **1989**, 621-623.
- [48] W. Cho, H. J. Lee, G. Choi, S. Choi, M. Oh, 'Dual Changes in Conformation and Optical Properties of Fluorophores within a Metal-Organic Framework during Framework Construction and Associated Sensing Event', *J. Am. Chem. Soc.* **2014**, *136*, 12201-12204.
- [49] A. T. Haedler, H. Misslitz, C. Buehlmeier, R. Q. Albuquerque, A. Köhler, H.-W. Schmidt, 'Controlling the  $\pi$ -Stacking Behavior of Pyrene Derivatives: Influence of H-Bonding and Steric Effects in Different States of Aggregation', *Chem. Phys. Chem.* **2013**, *14*, 1818-1829.
- [50] N. Elgrishi, K. J. Rountree, B. D. McCarthy, E. S. Rountree, T. T. Eisenhart, J. L. Dempsey, 'A Practical Beginner's Guide to Cyclic Voltammetry', *J. Chem. Educ.* **2018**, *95*, 197-206.

- [51] S. Yi, W. Deng, S. Sun, L. Lan, Z. He, W. Yang, B. Zhang, 'Trifluoromethyl-Substituted Large Band-Gap Polytriphenylamines for Polymer Solar Cells with High Open-Circuit Voltages', *Polymers* **2018**, *10*, 52.
- [52] E. Wang, Z. Ma, Z. Zhang, P. Henriksson, O. Inganäs, F. Zhang, M. R. Andersson, 'An isoindigo-based low band gap polymer for efficient polymer solar cells with high photo-voltage', *Chem. Commun.* **2011**, *47*, 4908-4910.
- [53] S. Grimme, S. Ehrlich, L. Goerigk, 'Effect of the Damping Function in Dispersion Corrected Density Functional Theory', *J. Comput. Chem.* **2011**, *32*, 1456-1465.
- [54] P. J. Hay, W. R. Wadt, 'Ab Initio Effective Core Potentials for Molecular Calculations. Potentials for the Transition Metal Atoms Sc to Hg', *J. Chem. Phys.* **1985**, *82*, 270-283.
- [55] H.-L. Yip, A. K. Y. Jen, 'Recent advances in solution-processed interfacial materials for efficient and stable polymer solar cells', *Energy Environ. Sci.* **2012**, *5*, 5994-6011.



---

## ***Chapter III***

# ***Synergy between Chalcogen and Halogen Bonding***

---

In this chapter, the design and the synthesis of supramolecular polymers based on orthogonal Secondary Bonding Interactions, namely chalcogen- and halogen-bonding, are described. Such compound have been analysed by means of single crystal X-ray diffraction analysis.

The chapter is divided in three main sections. *Section III-1* includes a brief introduction on orthogonal processes in supramolecular chemistry; *Section III-2* presents the design of the polymer and molecules chosen to interface both interactions and appraise their orthogonality; *Section III-3* provides an analysis of the crystal structures obtained in this context, this part is divided as follows: preparation of the materials, co-crystals with one component being molecules bearing a Te atom and halogen-bond acceptor moiety, co-crystals with one component being molecules bearing a Se atom and halogen-bond acceptor moiety and finally co-crystal involving CGP derivatives bearing a halogen-bond donor moiety.

The work presented in this chapter has been realised with the help of *Dr. Benson Kariuki* for the refinement of some crystal structures and with the assistance of *Samuel Bridgewater*, in the frame of his BSc. project, for the synthesis of 2-(pyridin-3-yl)-[1,3]tellurazolo[5,4- $\beta$ ]pyridine **III-2<sub>Te</sub>** and the co-crystallisation experiments with hexadecafluorodiiodooctane and diiodotetrafluorobenzene. The synthesis of 2-(pyridin-4-yl)benzo[d][1,3]tellurazole **III-3** was performed by *Dr. Adrian Kremer* (Belgium) during a past project of our group.

## III – 1 Introduction

### III – 1.1 The principle of orthogonality in supramolecular chemistry

The primary concern of supramolecular chemistry has always been to build the link between molecular chemistry and thermodynamically-stable architectures of higher complexity using non-covalent interactions.<sup>[1-3]</sup> In this respect, the possibility of simultaneously exploiting multiple interactions<sup>[4-6]</sup> allow chemists to engineer structures with multifunctional properties.<sup>[7]</sup> This has been achieved in recent decades through orthogonal processes<sup>[8]</sup> with most notable examples in material science<sup>[9, 10]</sup> by the use of Dynamic Covalent Chemistry (DCC),<sup>[11-13]</sup> hydrogen-bonding with precise recognition pattern<sup>[14]</sup> or interfacing non-covalent interactions different in nature.<sup>[10]</sup>

The concept of orthogonality was first introduced by *Merrifield* in 1977,<sup>[15]</sup> referring to protecting group removal strategy. Conceptually, in a series of protecting groups, one could be cleaved by chemical reaction without interfering with the others. Since then, the term has been widely employed in various domains of chemistry where it reached precise but different meanings depending on the field. For example, orthogonal glycosylation refers to different sets of glycosyl donor distinct in composition and activation conditions.<sup>[16]</sup> Chromatic orthogonality applies to the selective reactivity of one functional group in the presence of others towards a specific colour of light beam.<sup>[17]</sup> Click reactions, by definition, relies heavily on orthogonality as their components are highly reactive species tolerating a broad range of reagents, solvents and functional groups.<sup>[18]</sup> Furthermore, the *Staudinger-Bertozzi* reaction has been shown to be applicable in biological media such as bacterial cultures and mice leading to the concept of biorthogonality.<sup>[19-21]</sup>

In supramolecular chemistry, in a given system, two non-covalent interactions are said to be orthogonal if they occur with no cross-talk.<sup>[8]</sup> This means that, in a given supramolecular assembly, two or more recognition patterns can be used simultaneously without interference and each one can bring a set property to the resulting material. The non-covalent interactions can be responsible for the growth of a supramolecular polymer in one or more directions, the presence of functional molecules on a particular backbone, the solid-state organisation, etc. Unlike the case of molecular synthesis where orthogonality relies on irreversible chemoselective reactions, supramolecular media are in equilibrium and interactions are continuously exchanged. Although this allows proof-reading and self-correction, it remains challenging in the conception and design of such systems. From a synthetic aspect, it is important that the different types of interactions used are mutually compatible, *i.e.* orthogonal.<sup>[22]</sup> Thus a particular attention has to be brought to functional groups or non-covalent interactions choice.

## III – 1.2 Orthogonal functionalisation of macromolecular backbones

As an first example, *Weck* and co-workers engineered a stimuli-responsive terpolymer synthesized through ring-opening metathesis of norbornene (Figure III – 1).<sup>[9]</sup> This material bears three different receptor sites along its main chain, namely palladated sulfur-carbon-sulfur (SCS) pincer, cyanuric acid, and thymine moieties. The side chains can be non-covalently functionalised adding pyridine, diaminopyridine and the Hamilton wedge,<sup>[23]</sup> respectively. Each recognition motif is orthogonal to one another, the first one being based on metal coordination and the two others on different hydrogen-bonded patterns. The three interactions are taking place simultaneously in CH<sub>2</sub>Cl<sub>2</sub> without interfering with each other. However, if the polarity of solvent is changed (CHCl<sub>3</sub>:dioxane 85:15) the association constant is tuned for each interaction site resulting in one of the hydrogen-bonded groups being cleaved from the polymer.

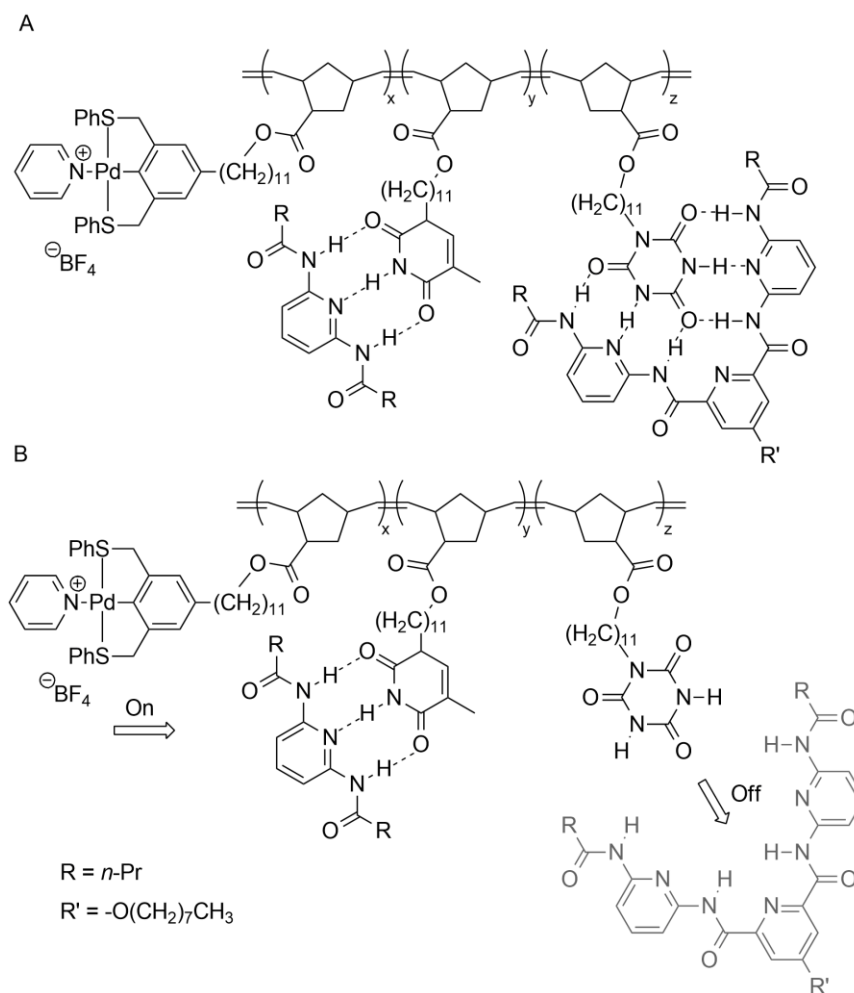


Figure III - 1: Stimuli-responsive terpolymer of norbornene bearing palladated sulfur-carbon-sulfur (SCS) pincer, cyanuric acid, and thymine moieties interacting orthogonally with pyridine, diaminopyridine and the Hamilton wedge fully associated in CH<sub>2</sub>Cl<sub>2</sub> (A) or selectively cleaved in CHCl<sub>3</sub>:dioxane 85:15 (B). Adapted with permission;<sup>[9]</sup> copyright 2008 Wiley Periodicals, Inc.

Thus, different strategies of orthogonality are employed in this system. First, the polymer is formed from simple building blocks in one reaction and displays three different recognition sites along the

chain. The non-covalent functionalisation can be achieved by adding three small molecular compounds forming metal coordination and hydrogen bonds. The two interactions are orthogonal by their binding nature and two different HB patterns are used for selective recognition. Moreover, one group can be cleaved without affecting the others by changing the polarity of the solvent. The resulting macromolecule is thus a complex system built from simple molecular building block through different orthogonal key strategies.

### III – 1.3 Supramolecular polymers through orthogonal non-covalent interactions

In the field of supramolecular polymers (polymolecular entities formed by the association of molecular monomers via non-covalent intermolecular interactions),<sup>[3]</sup> Gröhn and Schmuck designed a low molecular weight heteroditopic synthon with two recognition sites (Figure III – 2).<sup>[24]</sup> The two orthogonal interactions in play are metal-ligand binding and ion pair formation. Interestingly, the formation of the polymer backbone can be switched on and off (reversible formation) due to the nature of its supramolecular structure and, thus, is responsive to stimuli such as pH, concentration, temperature, solvent and the presence of ions. Indeed, the initial salt does not self-associate. However, upon addition of metal ions or base, the molecules form dimers through metal coordination (Figure III – 2, B) or ion pairing (Figure III – 2, C), respectively. Moreover, in the presence of both stimuli, a linear supramolecular polymer can be obtained (Figure III – 2, D). The self-assembly can be reversed upon addition of *N*-(2-hydroxyethyl) ethylenediaminetriacetic acid (HEEDTA), acid or base (optimal pH for the ion pairing = 5-7). This system efficiently uses different aspects of orthogonality. First, the two selected interactions are different in nature and can take place simultaneously without interference. Moreover, the activation/deactivation of the two recognition motifs are orthogonal, which means that one can be switched on and off independently of the presence or the absence of the second interaction. This combination results in a highly stimuli responsive material grown from a simple building block.

Furthermore, crystal engineering is the rational design of functional molecular solids. This field of chemistry aims to build crystal structures from organic and organometallic species using a deep understanding of intermolecular interactions, ideally aiming for a specific function. It requires a systematic strategy, a precise blueprint for the design of crystalline entities.<sup>[25]</sup> In this context, Aakeröy and co-workers built numerous multi-component crystals interfacing different non-covalent bonds. One example of this work is the realisation of co-crystals based on hydrogen- and halogen-bonding interactions.<sup>[26]</sup> A ladder type motif is achieved by the co-crystallisation of 1-(2-amino-4-methylpyrimidin-6-yl)-2-(3-methoxypyridin-5-yl)-ethyne and 4-iodobenzoic acid (Figure III – 3) where orthogonal HB and XB are observed. Hydrogen bonds take place involving OH $\cdots$ N ( $d_{\text{N}\cdots\text{O}}$  = 2.643 Å) and NH $\cdots$ O ( $d_{\text{O}\cdots\text{N}}$  = 2.987 Å) in addition to a halogen bond between O and I atoms ( $d_{\text{O}\cdots\text{I}}$  =

3.265 Å) resulting in an infinite chain at the solid state, *i.e.* supramolecular polymer. In this case, the nature of the interactions leads to the orthogonality. One mainly relying on electrostatic contribution (hydrogen bonding interaction) and the other based on orbital and electrostatic contribution (halogen bonding interaction) in addition of dispersion energy.

In particular, the halogen bonding interaction, since its resurgence in the 90's thanks to the work of Resnati and Metrangolo,<sup>[27-29]</sup> has been widely applied to crystal engineering,<sup>[30-34]</sup> liquid crystals,<sup>[35-40]</sup> functional materials,<sup>[41-48]</sup> etc. As just shown, it has been proven to be orthogonal to hydrogen-bonding interactions in precedent studies<sup>[49-51]</sup> and thus has been widely applied in biological systems.<sup>[52, 53]</sup>

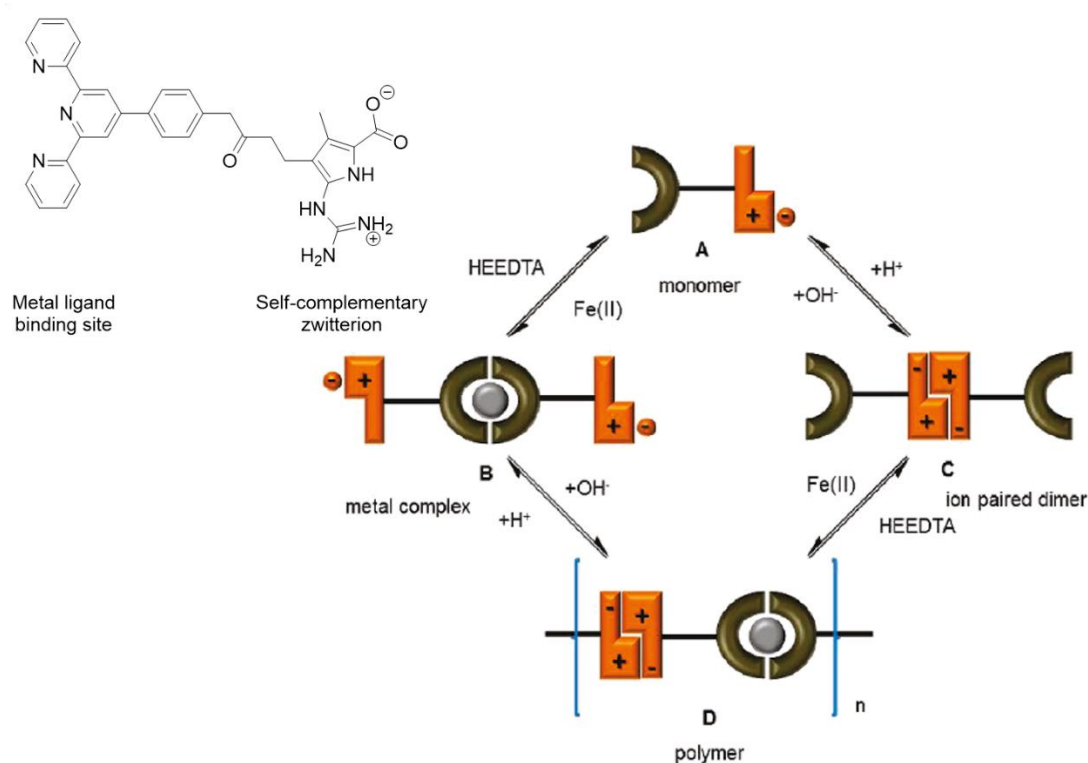


Figure III - 2: Molecule designed by Gröhn and Schmuck in its zwitterionic form. It aggregates as monomeric salt (A), dimer upon addition of metal ion (B) or base (C) and linear polymer in the presence of both (D).  
Reproduced with permission;<sup>[24]</sup> copyright 2011 American Chemical Society.

In this context, one can easily understand the importance of orthogonal processes applied to supramolecular chemistry. Assemblies of higher complexity take place using two or more non-covalent interactions of different nature or precise bonding pattern. Furthermore, stimuli responsive materials can even be achieved if one of the bonding motifs can be shut down independently of the others. This part of the work aims to synthesise supramolecular polymers *via* the association of small molecules through simultaneous halogen- and chalcogen-bonding interactions. The formation of those entities will be evaluated by single-crystal X-ray diffraction.

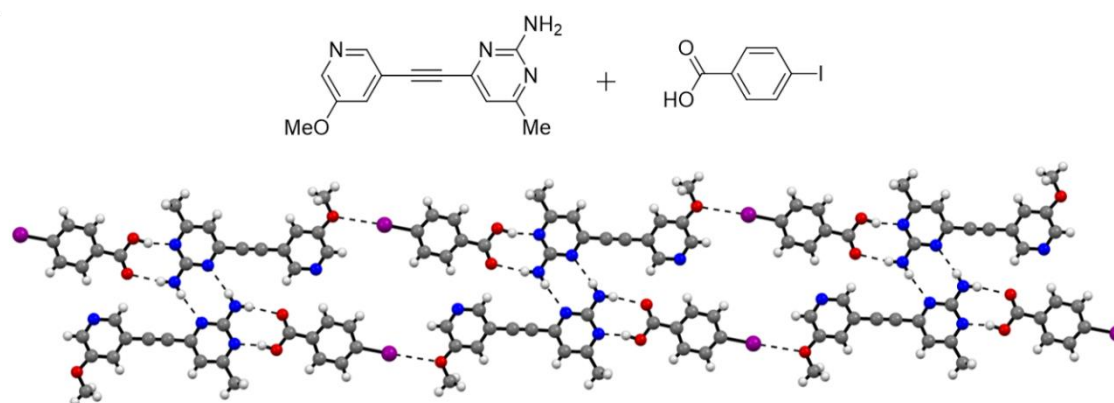


Figure III - 3: X-ray structure of 1:1 co-crystal of 1-(2-Amino-4-methylpyrimidin-6-yl)-2-(3-methoxy-5-pyridinyl)-ethyne.4-iodobenzoic acid.<sup>[26]</sup>

### III – 2 Design of multi-component orthogonal supramolecular polymers

In our crystal-engineering approach, the idea is to prepare supramolecular polymers in the solid state through the co-crystallisation of two ditopic molecular modules: the chalcogen (Ch) and halogen (Hal) modules, respectively (Figure III – 4). While the Ch modules are heterotopic, i.e. bearing two diverse recognition groups, the Hal synthons are homotopic. The Ch modules are supposed to undergo self-association through double EB interactions as established through the CGP-based recognition unit, whereas the Hal building blocks should interact with the Ch counterpart through XB interactions.

Depending on the role taken in the formation of the interaction and the nature of the functional group on the Ch synthon, the Hal module can act either as XB-donor or EB-acceptor.<sup>[27, 31]</sup> Supramolecular polymers in the solid state with a repetition unit of  $(\text{Ch}_2\text{Hal})_n$  are expected to form upon evaporation of a solution containing a mixture of both Ch and Hal components. The designed supramolecular Ch and Hal synthons are depicted in Scheme III – 1. While CGP-based molecules **III-1<sub>E</sub>** and **III-2<sub>E</sub>** feature a XB-acceptor pyridyl-type substituent, modules **III-4** and **III-5** expose at 2-position bromo- and iodo-tetrafluorophenyl moieties.

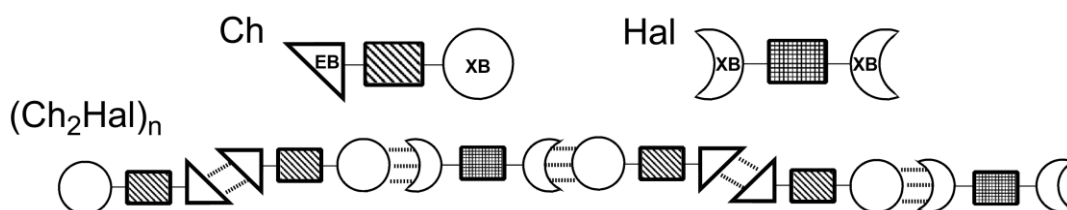
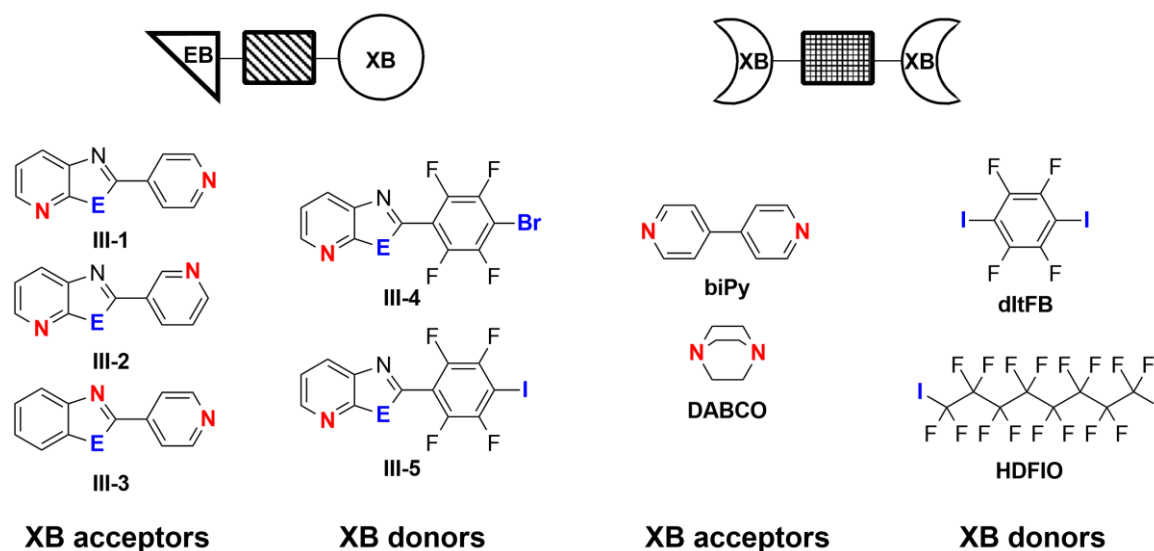


Figure III - 4: Architecture of supramolecular polymers  $(\text{Ch}_2\text{Hal})_n$  expressing orthogonal chalcogen- and halogen-bonding interactions through the association of Ch and Hal modules.

As far as the ditopic Hal synthons are concerned, hexadecafluoro-1,8-diiodooctane (**HDFIO**) and 1,4-diiodo-2,3,5,6-tetrafluorobenzene (**DITFB**) were chosen as XB donors, and 4,4'-bipyridyl (**biPy**) and 1,4-diazabicyclo[2.2.2]octane (**DABCO**) as XB acceptors. These modules are well-known building blocks used to trigger XB interactions forming heteromolecular polymers in the solid state.<sup>[54-57]</sup> **DABCO** is particularly known to form very strong XB with iodo-derivatives due to secondary hydrogen-bonding interactions taking place between the H atoms of the bicyclic molecule and the negative belt of the I atom.<sup>[57]</sup> At last, reference benzochalcogenazole **III-3**,<sup>[58]</sup> capable of making intermolecular chalcogen bonds, was also studied in combinations with the appropriate XB donor (Scheme III – 1). Thus, it is expected that molecule **III-3** forms wire-like structures through N $\cdots$ Te interactions,<sup>[58]</sup> and lateral XB contacts engaging the pyridyl moiety with the ditopic XB acceptor (Hal).



*Scheme III - 1: Representation of the different synthons of the XB/EB orthogonal supramolecular polymer.*

The anticipated repeating units of the designed supramolecular polymers are reported in Tables III – 1 and 2. Te-analogues **III-1<sub>Te</sub>** and **III-2<sub>Te</sub>** are expected to engage in frontal double chalcogen-bonding interactions leading to dimers, which could successively express XB contacts with either **HDFIO** or **DITFB** (Table III – 1). Likewise, molecules **III-4** and **III-5** (Table III – 2) are expected to dimerise though double chalcogen-bonding interactions and undergo polymerisation in the presence of **biPy** and **DABCO** through halogen-bonding interactions with Br/I atoms. To validate the recognition abilities of the designed self-assembling synthons, we used electrostatic surface potential (ESP) and estimated the value ( $V_{s,max}$ ) at the point of the highest charge for both donor and acceptor atoms at B97D3/Def2-TZVP level of theory using Gaussian09 including D01 revision (Table III – 3).<sup>[59, 60]</sup> The images highlight positive potential regions (blue) around Te, Se, Br and I atoms and electron donor as negative potential region (red) around N atoms. The surface around the halogens and chalcogen atoms are clearly distributed in two parts: the  $\sigma$ -hole (in blue) and the

negative belt (yellow-green). As expected, the  $\sigma$ -holes are deeper for Te and I than for Se and Br atoms.

Table III - 1: Representation of the repeating unit for the anticipated supramolecular polymer for molecules III-1, III-2 and III-3 with HDFIO and DITFB.

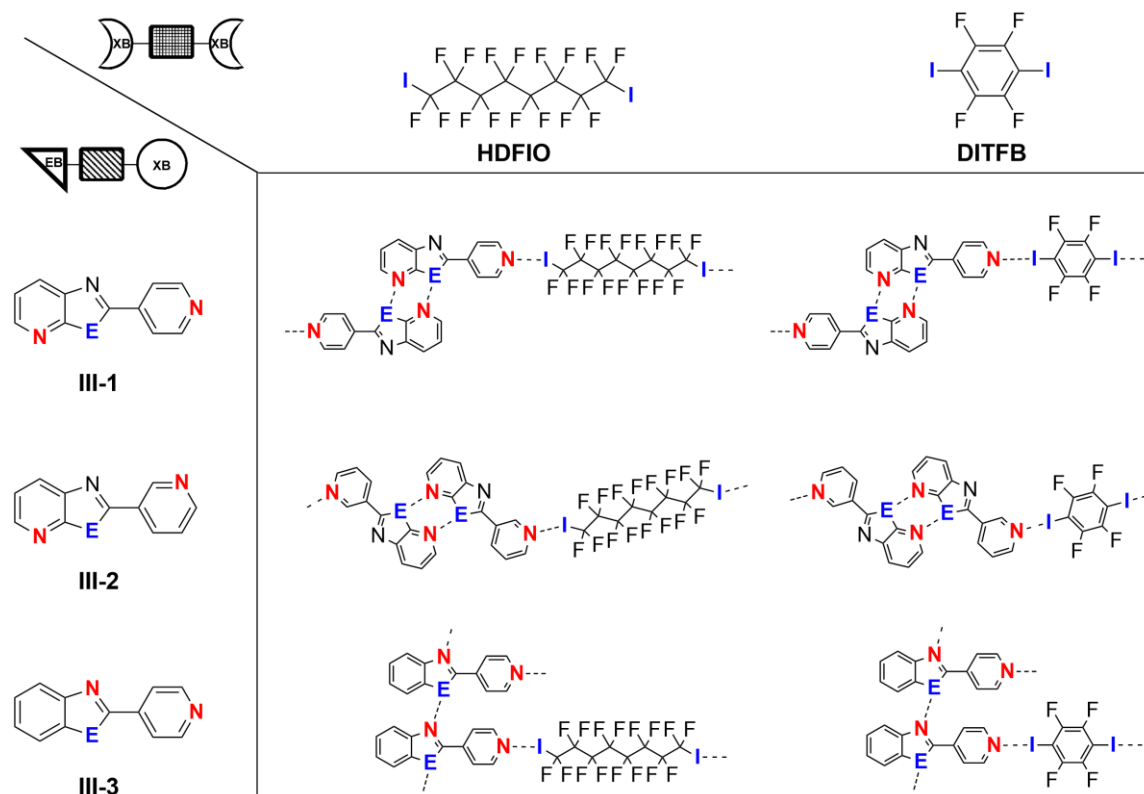


Table III - 2: Representation of the repeating unit for the anticipated supramolecular polymer for molecules III-4 and III-5 with biPy and DABCO.

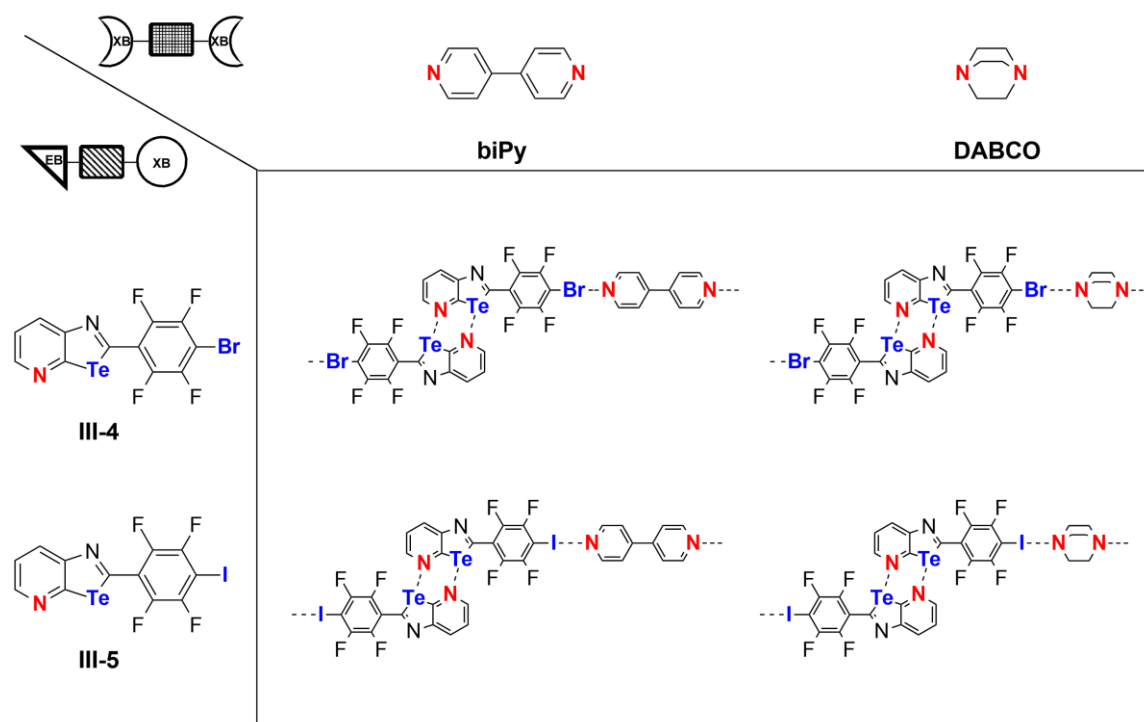


Table III - 3: Electrostatic surface potential for each supramolecular synthon. Level of theory: B97D3/Def2-TZVP using Gaussian09 including D01 revision.

	Synthons	Electrostatic Surface Potential maps	
		Top view	Side view
III-1 <sub>Te</sub>			
III-1 <sub>Se</sub>			
III-2 <sub>Te</sub>			
III-2 <sub>Se</sub>			
III-3 <sub>Te</sub>			
III-4			
III-5			
HDFIO			
DITFB			-
biPy			-
DABCO			

-0.025 a.u. +0.025 a.u.

### III – 3 Crystal structure analysis

#### III – 3.1 Co-crystal preparation

All co-crystallisation attempts and their outputs are summarized in Table III - 4. Solutions of the given components in a stoichiometry of choice were prepared in  $\text{CHCl}_3$  and left standing for slow evaporation. All crystals were analysed by X-ray diffraction analysis. The unit cells were first acquired for every type of crystalline material with pre-experiments to probe the successful formation of co-crystals or the segregation of the individual components.

Table III - 4: Co-crystallisation attempts, stoichiometries in solution (o:p)<sup>sol</sup> and in the resulting co-crystal (o:p)<sup>coc</sup> (with o and p standing for the Ch and Hal components, respectively). Solvent of crystallisation:  $\text{CHCl}_3$ .  
<sup>a</sup>Crystal segregation.

Entry	Ch	Hal	(o:p) <sup>sol</sup>	(o:p) <sup>coc</sup>	Co-crystal	Supramolecular entity
1	III-1 <sub>Te</sub>	HDFIO	2:1	2:1	(III-1 <sub>Te</sub> ) <sub>2</sub> •HDFIO	((III-1 <sub>Te</sub> ) <sub>2</sub> •HDFIO) <sub>n</sub>
2	III-1 <sub>Te</sub>	DITFB	2:1	2:1	(III-1 <sub>Te</sub> ) <sub>2</sub> •DITFB	((III-1 <sub>Te</sub> ) <sub>2</sub> •DITFB) <sub>2</sub>
3	III-1 <sub>Te</sub>	DITFB	1:1	1:1	III-1 <sub>Te</sub> •DITFB	(III-1 <sub>Te</sub> •DITFB) <sub>n</sub>
4	III-1 <sub>Te</sub>	DITFB	1:10	1:2	III-1 <sub>Te</sub> •(DITFB) <sub>2</sub>	(III-1 <sub>Te</sub> •(DITFB) <sub>2</sub> ) <sub>n</sub>
5	III-2 <sub>Te</sub>	HDFIO	2:1	- <sup>a</sup>	-	-
6	III-2 <sub>Te</sub>	DITFB	2:1	2:1	(III-2 <sub>Te</sub> ) <sub>2</sub> •DITFB	((III-2 <sub>Te</sub> ) <sub>2</sub> •DITFB) <sub>n</sub>
7	III-2 <sub>Te</sub>	DITFB	1:1	2:1	(III-2 <sub>Te</sub> ) <sub>2</sub> •DITFB	((III-2 <sub>Te</sub> ) <sub>2</sub> •DITFB) <sub>n</sub>
8	III-2 <sub>Te</sub>	DITFB	1:3	2:1	(III-2 <sub>Te</sub> ) <sub>2</sub> •DITFB	((III-2 <sub>Te</sub> ) <sub>2</sub> •DITFB) <sub>n</sub>
9	III-3	HDFIO	2:1	2:1	(III-3) <sub>2</sub> •HDFIO	(III-3) <sub>2</sub> •HDFIO
10	III-3	DITFB	2:1	2:1	(III-3) <sub>2</sub> •DITFB	(III-3) <sub>2</sub> •DITFB
11	III-1 <sub>Se</sub>	HDFIO	2:1	- <sup>a</sup>	-	-
12	III-1 <sub>Se</sub>	DITFB	2:1	2:1	(III-1 <sub>Se</sub> ) <sub>2</sub> •DITFB	((III-1 <sub>Se</sub> ) <sub>2</sub> •DITFB) <sub>2</sub>
13	III-1 <sub>Se</sub>	DITFB	1:1	2:1	(III-1 <sub>Se</sub> ) <sub>2</sub> •DITFB	((III-1 <sub>Se</sub> ) <sub>2</sub> •DITFB) <sub>2</sub>
14	III-1 <sub>Se</sub>	DITFB	1:10	1:2	III-1 <sub>Se</sub> •(DITFB) <sub>2</sub>	(III-1 <sub>Se</sub> •(DITFB) <sub>2</sub> ) <sub>n</sub>
15	III-2 <sub>Se</sub>	DITFB	2:1	2:1	(III-2 <sub>Se</sub> ) <sub>2</sub> •DITFB	((III-2 <sub>Se</sub> ) <sub>2</sub> •DITFB) <sub>n</sub>
16	III-4	biPy	1:2	- <sup>a</sup>	-	-
17	III-4	DABCO	1:2/1:10	- <sup>a</sup>	-	-
18	III-5	biPy	1:2/1:10	- <sup>a</sup>	-	-
19	III-5	DABCO	2:1	- <sup>a</sup>	-	-
20	III-5	DABCO	1:5	2:1	(III-5) <sub>2</sub> •DABCO	((III-5) <sub>2</sub> •DABCO) <sub>n</sub>
21	III-5	DABCO	1:10	1:1	III-5•DABCO	(III-5•DABCO) <sub>2</sub>
22	III-1 <sub>Te</sub>	III-5	1:1	1:1	III-1 <sub>Te</sub> •III-5	(III-1 <sub>Te</sub> •III-5) <sub>n</sub>

The nomenclature of each co-crystals is given by the minimal repetition unit of the supramolecular structure formed in the solid state, whereas the supramolecular species (oligomers and polymers) triggered by the chalcogen- and halogen-bonding interactions in the co-crystal are labelled as polymeric structures (Table III - 4). As one can clearly evidence, molecule **III-1<sub>Te</sub>** forms co-crystals 2:1 with both **HDFIO** and **DITFB**, mirroring the solution stoichiometry (entries 1 and 2). Co-crystals with 1:1 and 1:2 stoichiometries containing supramolecular polymers **(III-1<sub>Te</sub>•DITFB)<sub>n</sub>** and aggregate **(III-1<sub>Te</sub>•(DITFB)<sub>2</sub>)<sub>n</sub>** could be obtained with **DITFB** when starting from solutions of 1:1 and 1:10 ratios, respectively (entries 3 and 4). Crystal segregation was observed when isomer **III-2<sub>Te</sub>** was co-crystallised with **HDFIO** (entry 5), whereas polymer **((III-2<sub>Te</sub>)<sub>2</sub>•DITFB)<sub>n</sub>** crashed out from the solution with **DITFB**, independent on the stoichiometry in solution (entries 6–8). Notably, reference molecule **III-3<sub>Te</sub>** forms co-crystals with 2:1 stoichiometry with both XB donors (entries 9 and 10, respectively).

Evaporation of a solution of Se-analogue **III-1<sub>Se</sub>** with **HDFIO** did not give rise to any co-crystals (entry 11), whereas solutions containing 2:1 and 1:1 ratio of **DITFB** (entries 12 and 13, respectively) exclusively gave co-crystals with stoichiometry of 2:1, with the molecules aggregated as supramolecular hexamers **((III-1<sub>Se</sub>)<sub>2</sub>•DITFB)<sub>2</sub>**. Notably, when using an excess of **DITFB** (1:10), co-crystal of aggregate **(III-1<sub>Se</sub>•(DITFB)<sub>2</sub>)<sub>n</sub>** was formed (entry 14), as observed with the Te-analogue. Moving to the pyrid-3-yl isomer **III-2<sub>Se</sub>**, co-crystal of stoichiometry 2:1 were obtained as large yellow plates, also containing a polymer-like organisation (entry 15). When we reversed the XB demand, co-crystallisation experiments with compound **III-4** in the presence of **biPy** and **DABCO** were unsuccessful (entries 16 and 17, respectively) and segregation was observed. Similar results were obtained with iodo-derivative **III-5** with both **biPy** and **DABCO**. However, when using an excess of **DABCO**, co-crystals with 2:1 and 1:1 stoichiometries were obtained as large yellow prisms (entries 20 and 21, respectively). While the 2:1 solid contains supramolecular polymer **((III-5)<sub>2</sub>•DABCO)<sub>n</sub>**, in the 1:1 co-crystal the molecules are arranged as tetrameric species, **(III-5•DABCO)<sub>2</sub>**. Finally, when mixing XB acceptor **III-1<sub>Te</sub>** and XB donor **III-5** in a 1:1 ratio in  $\text{CHCl}_3$ , formation of co-crystal 1:1 containing polymer **(III-1<sub>Te</sub>•III-5)<sub>n</sub>** was obtained.

As previously observed by our group with benzochalcogenazoles,<sup>[58]</sup> all the C-Se, C-Te N-C, C-I and C-Br bonds do not significantly differ between the different molecules bearing the same chalcogen and halogen atoms. This suggests that the crystal organization does not alter the covalent molecular skeleton. The formation of the supramolecular polymers is discussed considering the ESP displayed in Table III - 3. As already suggested previously, the  $\sigma$ -hole displaying the highest positive  $V_{s,\text{max}}$  value will engage in the SBI with the functional group featuring the most electronegative heteroatom (*i. e.*, the most negative  $V_{s,\text{max}}$  value).

## III – 3.2 Co-crystals: Tellurium containing CGP bearing a halogen-bond acceptor

Co-crystal **(III-1<sub>Te</sub>)<sub>2</sub>•HDFIO** crystallised in a  $P\bar{1}$  space group and the asymmetric unit consists of four molecules of **III-1<sub>Te</sub>** and two of **HDFIO**. X-ray diffraction analysis reveals the formation of a supramolecular polymer (Figure III – 5, a) through the association of both components in a 2:1 ratio by the means of halogen- and chalcogen-bonding interactions. One can easily observe the formation of the double EB of the CGP motif ( $d_{N\dots Te} = 2.998 \text{ \AA}$ ) and **HDFIO** sandwiched by two pyrid-4-yl moieties through XBs ( $d_{N\dots I} = 2.732 \text{ \AA}$ ). In addition, 2-(pyrid-4-yl)tellurazolopyridine **III-1<sub>Te</sub>** forms columns by quasi-parallel  $\pi$ - $\pi$  stacking (estimated  $d_{\pi-\pi} = 3.465 \text{ \AA}$ ) in a head-to-tail arrangement (Figure III – 5, c) separated by layers of **HDFIO**. This arrangement results in a segregation between fluorinated (pink arrows) and non-fluorinated (grey arrows) domains (Figure III – 5, b).

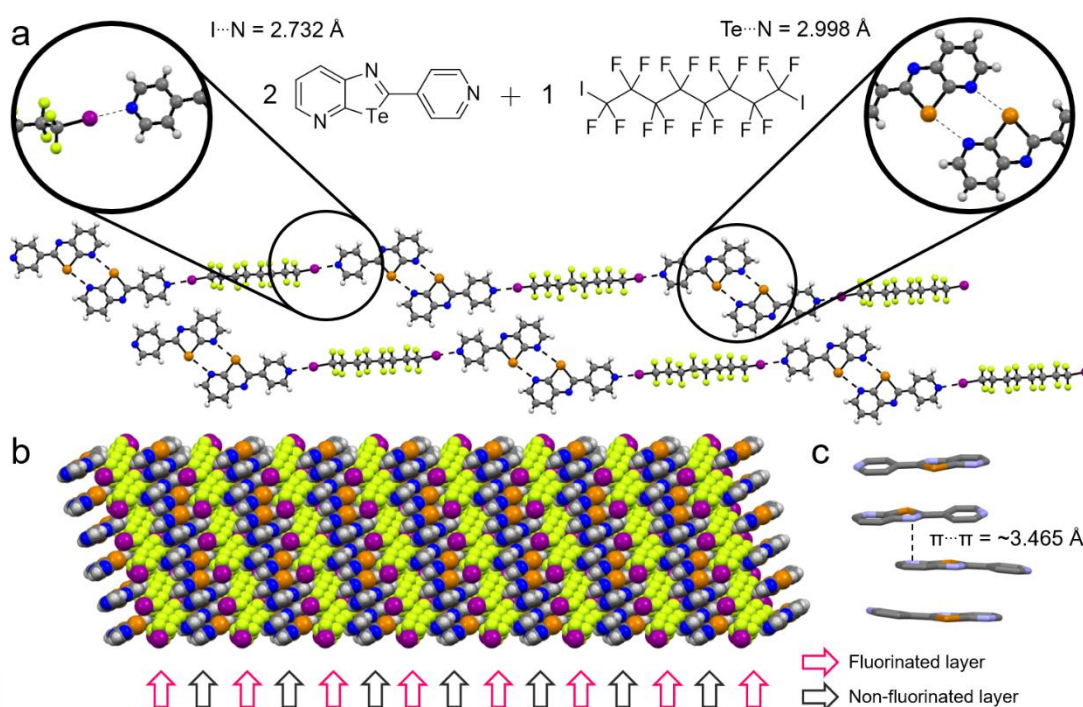


Figure III - 5: X-ray structure of co-crystal **(III-1<sub>Te</sub>)<sub>2</sub>•HDFIO**; a) Supramolecular polymer, key interactions are highlighted; b) vdW sphere representation of the layered organisation; c) Capped stick representation of the  $\pi$ - $\pi$  stacking, H atoms are omitted for clarity. Space group:  $P\bar{1}$ , solvent of crystallisation:  $CHCl_3$ .

The replacement of **HDFIO** with **DITFB** led to formation of co-crystal **(III-1<sub>Te</sub>)<sub>2</sub>•DITFB** (Figure III – 6, a) in a  $P\bar{1}$  space group with an asymmetric unit of two molecules of **III-1<sub>Te</sub>** and one of **DITFB**. Hexameric structure **((III-1<sub>Te</sub>)<sub>2</sub>•DITFB)<sub>2</sub>** is formed (highlighted in the red dashed line), where the two central CGP derivatives connect through a frontal double chalcogen bonds ( $d_{N\dots Te} = 3.164 \text{ \AA}$ ) and **DITFB** is sandwiched by the pyrid-4-yl moieties through XB interactions ( $d_{N\dots I} = 2.793 \text{ \AA}$ ). Each hexamer is brought together by hydrogen-bonding interactions between the H atoms in 6-position of the terminal CGP groups and two F atoms from **DITFB** ( $d_{F\dots C} = 3.078 \text{ \AA}$ ). Those interactions

organise the molecules in a quasi-planar arrangement presenting a slight misalignment of 0.912 Å (Figure III – 6, c).

In addition, perpendicular to the EB/XB hexamer, **DITFB** interacts with two CGP units through quasi-parallel  $\pi$ - $\pi$  stacking interaction (Figures III – 6, b and 7). Molecules of **III-1<sub>Te</sub>** arrange in a head-to-tail fashion (estimated  $d_{\pi-\pi}$  = 3.490 Å) and the fluorinated aromatic is sandwiched by two tellurazolopyridine derivatives (estimated  $d_{\pi-\pi}$  = 3.580 Å). Looking at the ESP map, one can observe that the  $\pi$ -surface of **DITFB** is charge depleted (blue or positive region) opposite the CGP group (green or neutral region). This complementary quadrupolar charge is likely to govern the face-to-face arrangement of the molecules at the solid state.

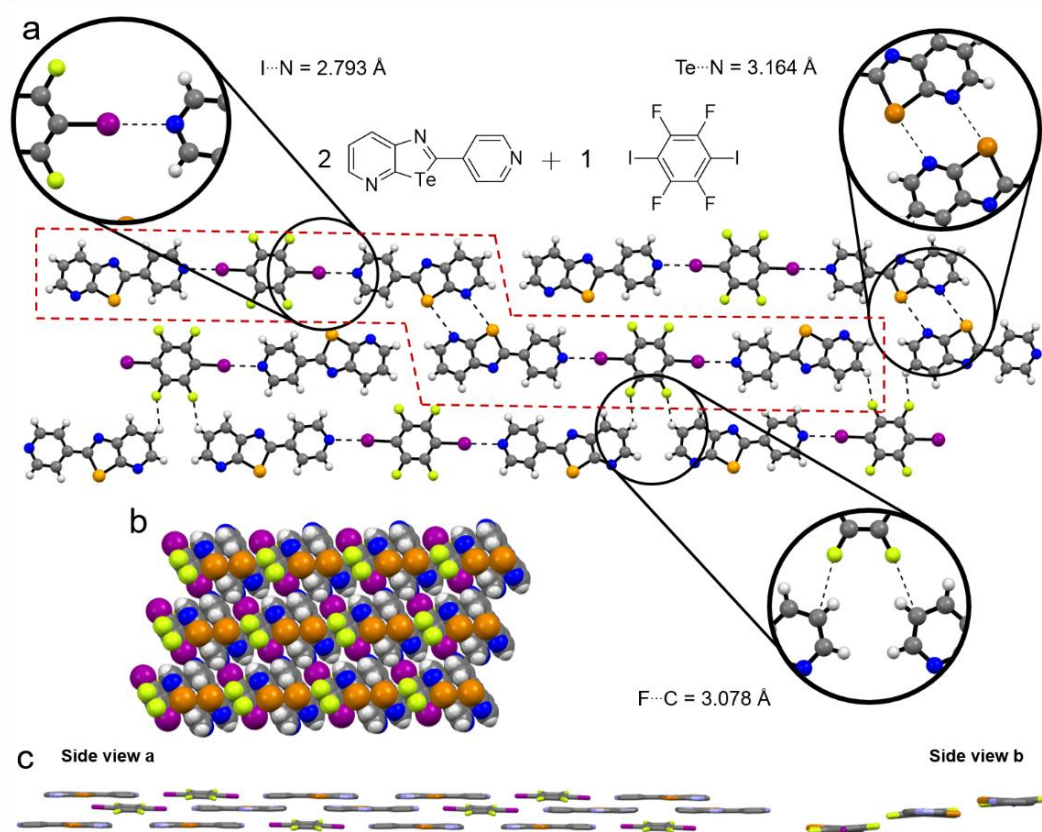


Figure III - 6: X-ray structure of co-crystal  $(\text{III-1}_{\text{Te}})_2 \cdot \text{DITFB}$ ; a) Hexamer is shown by the red dashed lines, key interactions are highlighted; b) vdW sphere representation of the layered organisation; c) Capped stick representation of miss-alignment, H atoms are omitted for clarity. Space group:  $P\bar{1}$ , solvent of crystallisation:  $\text{CHCl}_3$ .

Moving to  $\text{III-1}_{\text{Te}} \cdot \text{DITFB}$ , the supramolecular polymer crystallised in a  $P2_1/n$  space group, the asymmetric unit is composed of one molecule of **III-1<sub>Te</sub>** and one of **DITFB**. X-ray diffraction analysis shows an alternance of the two components linked to each other by two different halogen bonds (Figure III - 8). The pyrid-4-yl moiety interacts with one of the I atom ( $d_{\text{N} \cdots \text{I}} = 2.854 \text{ \AA}$ ) and the CGP group with another I atom from **DITFB** ( $d_{\text{N} \cdots \text{I}} = 2.925 \text{ \AA}$ ). Difference of 0.071 Å might be due to a misalignment between the three atoms involved in the interaction ( $\text{C-I} \cdots \text{N}$  angle =  $173^\circ$  vs  $166^\circ$ ) as

the strength of XB is reduced dramatically with the decrease of the angle. Moreover, it has to be noted that a weak chalcogen-bonding interaction is taking place between Te and I atoms ( $d_{I...Te} = 4.018 \text{ \AA}$ ,  $\Sigma_{vdW} = 4.04 \text{ \AA}$ ). The interaction involves the negative belt of the halogen atom as electron donor and the  $\sigma$ -hole of the chalcogen as electron acceptor (Figure III – 8; see also ESP map Figure III – 7, b).

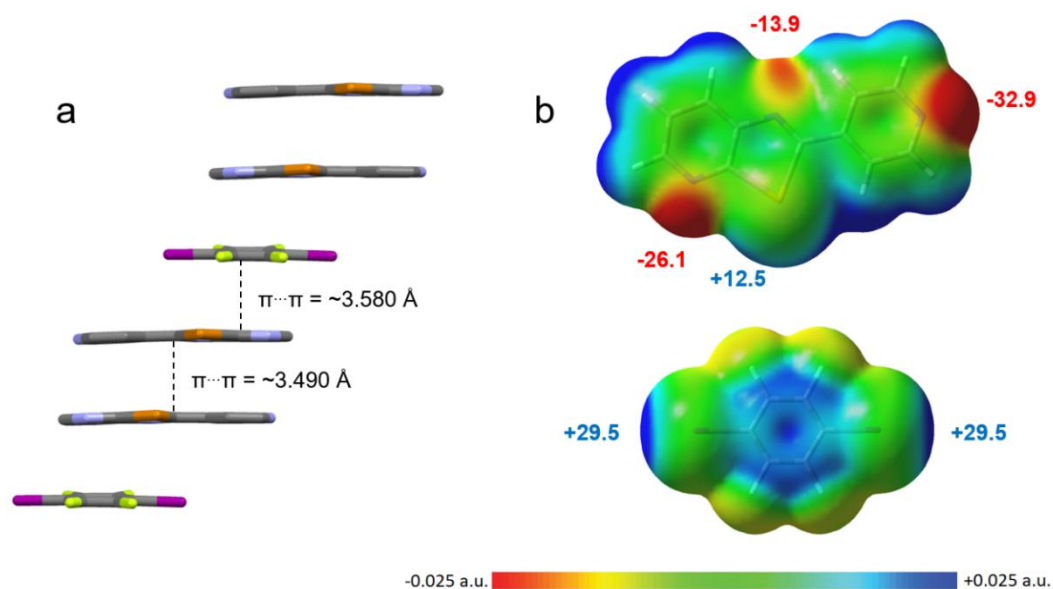


Figure III - 7: a) X-ray structure of co-crystal  $(III-1Te)_2 \cdot DITFB$ ,  $\pi$ - $\pi$  stacking is highlighted, H atoms are omitted for clarity. Space group:  $P\bar{1}$ , solvent of crystallisation:  $CHCl_3$ ; b) ESP map of  $III-1Te$  and  $DITFB$ , level of theory: B97D3/Def2-TZVP using Gaussian09 including D01 revision.

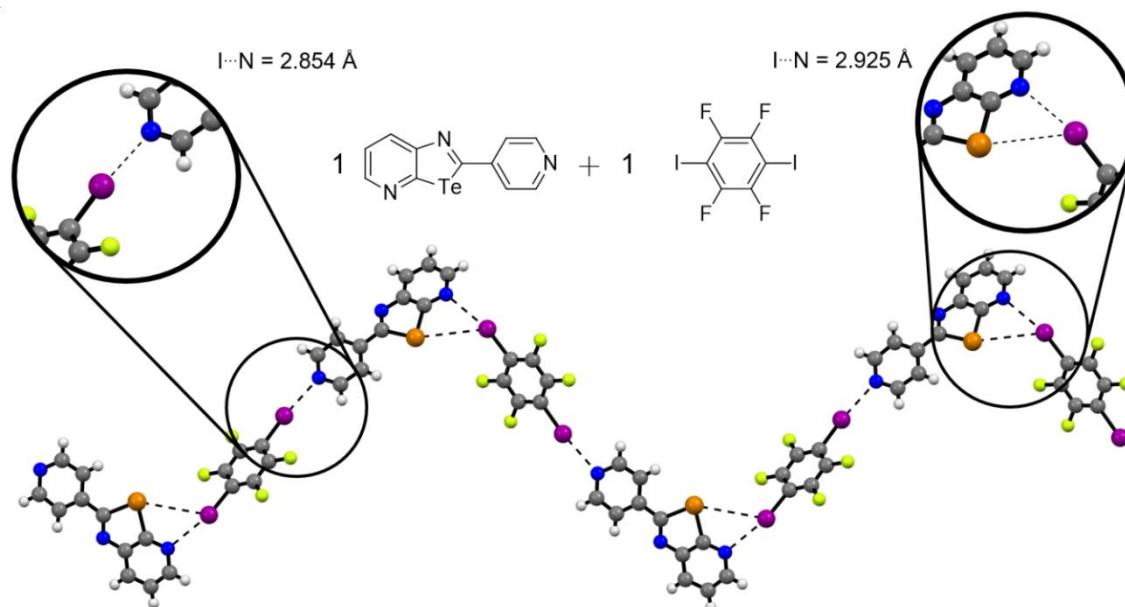


Figure III - 8: X-ray structure of co-crystal  $III-1Te \cdot DITFB$ . Space group:  $P2_1/n$ , solvent of crystallisation:  $CHCl_3$ .

Co-crystal **III-1<sub>Te</sub>•(DITFB)<sub>2</sub>** has a  $P\bar{1}$  space group and the asymmetric unit is composed by one molecule of **III-1<sub>Te</sub>** and one full and two halves of **DITFB**. In this structure, only halogen- and hydrogen-bonding interactions are present (Figure III – 9). **DITFB** interacts through XB with the pyrid-4-yl ( $d_{N\dots I}$  2.804 Å) and the CGP group ( $d_{N\dots I} = 2.754$  Å). Compared to the structure of **III-1<sub>Te</sub>•DITFB** (Figure III – 8), the halogen bond involving  $N_p$  is shorter and the angles are closer to 180° ( $C-I\dots N$  angle = 176° for pyrid-4-yl vs 177° for  $N_p$ ). As observed for **III-1<sub>Te</sub>•DITFB**, I and Te atoms interact through a weak chalcogen bond ( $d_{I\dots Te} = 4.005$  Å,  $\Sigma_{vdW} = 4.04$  Å), an electrostatic interaction taking place between the negative belt of the former and the  $\sigma$ -hole of the latter.

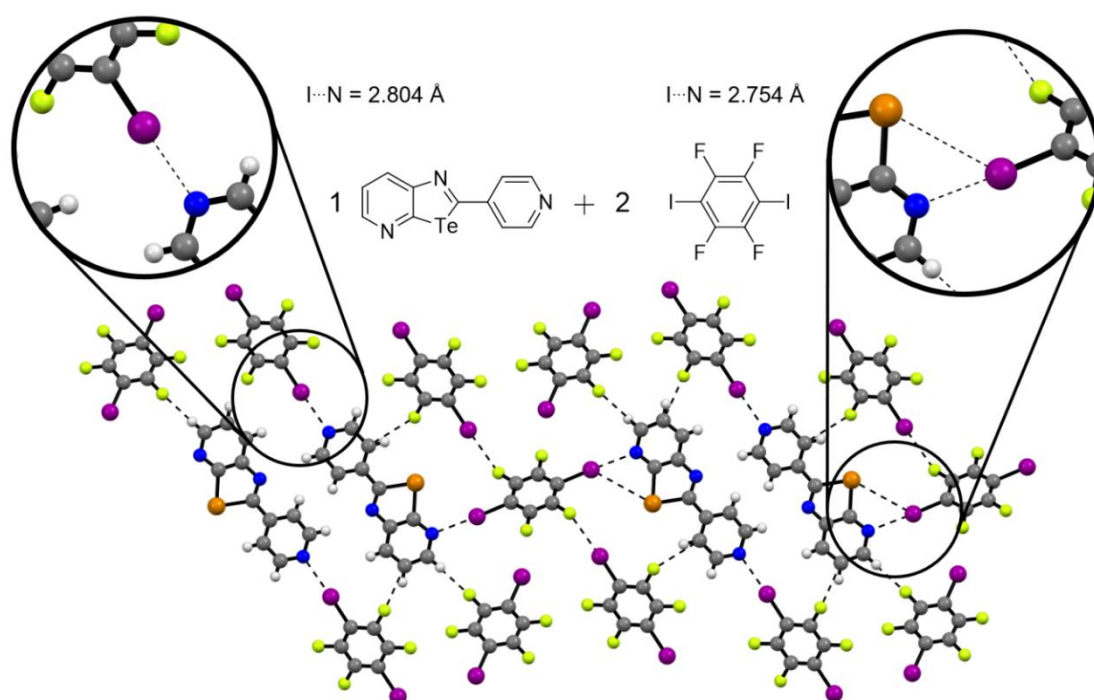


Figure III - 9: X-ray structure of co-crystal **III-1<sub>Te</sub>•(DITFB)<sub>2</sub>**. Space group:  $P\bar{1}$ , solvent of crystallisation:  $CHCl_3$ .

Moving to **(III-2<sub>Te</sub>)<sub>2</sub>•DITFB**, the material crystallised in a  $P\bar{1}$  space group and the asymmetric unit consist in one molecule of **III-2<sub>Te</sub>** and half of **DITFB**. The structure (Figure III – 10) displays a supramolecular polymer where dimers are formed through double-chalcogen bonds ( $d_{N\dots Te} = 3.068$  Å), exposing two pyrid-3-yl moieties that form halogen bonds ( $d_{N\dots I} = 2.738$  Å) with **DITFB**. **III-2<sub>Te</sub>** also  $\pi$ - $\pi$  stacks ( $d_{\pi-\pi} = 3.544$  Å) with an off-set of 2.945 Å. Similarly, **DITFB** self associate through  $\pi$ - $\pi$  stacking interactions ( $d_{\pi-\pi} = 3.459$  Å) with an off set of 3.339 Å (Figure III – 11). Those molecules assemble in a columnar arrangement achieving segregation of fluorinated and non-fluorinated parts.

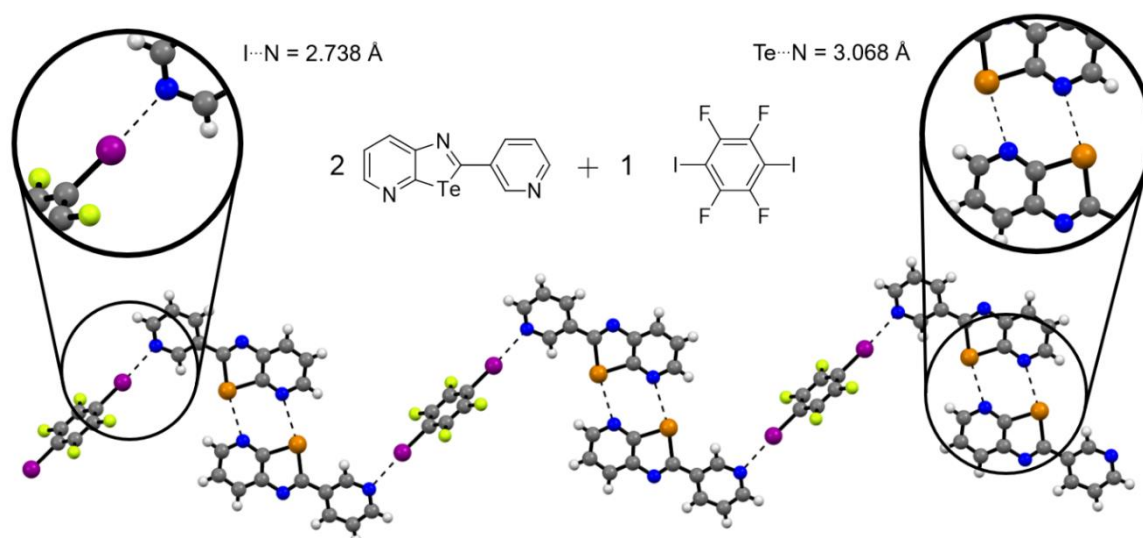


Figure III - 10: X-ray structure of co-crystal  $(\text{III-2Te})_2 \cdot \text{DITFB}$ . Space group:  $P\bar{1}$ , solvent of crystallisation:  $\text{CHCl}_3$ .

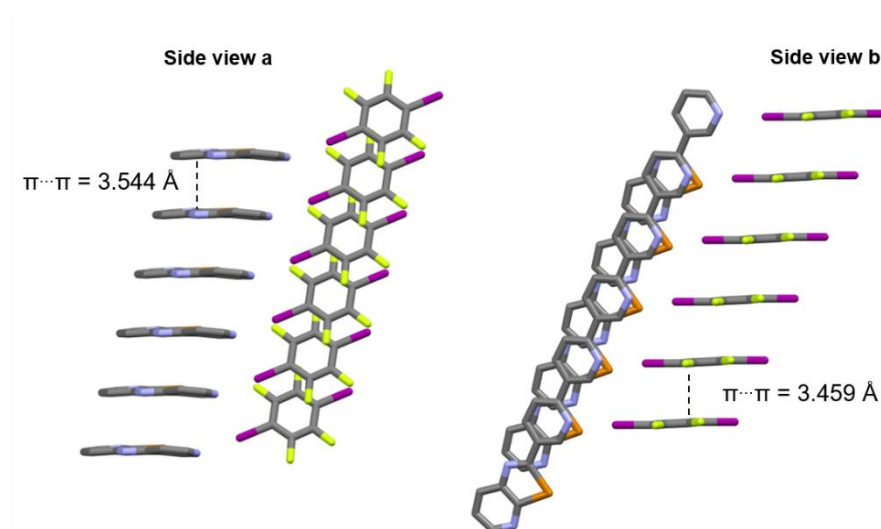


Figure III - 11: X-ray structure of co-crystal  $(\text{III-2Te})_2 \cdot \text{DITFB}$ ,  $\pi$ - $\pi$  stacking is highlighted, H atoms are omitted for clarity. Space group:  $P\bar{1}$ , solvent of crystallisation:  $\text{CHCl}_3$ .

In addition, a mispacking can be observed (Figure III – 12, a). In the co-crystal  $(\text{III-2Te})_2 \cdot \text{DITFB}$ , some of molecules  $\text{III-2Te}$  have an inverted orientation along the supramolecular chain ( $\sim 15\%$  in the crystal used for diffraction analysis). This results in a pyrid-4-yl interacting with a CGP moiety through chalcogen-bonding ( $d_{\text{N}\dots\text{Te}} = 3.000 \text{ \AA}$ ) and hydrogen-bonding interactions ( $d_{\text{N}\dots\text{C}} = 3.568 \text{ \AA}$ ), replacing the double EBs recognition motif. The  $\text{N}_p$  atom of the inverted molecule interacts through halogen-bonding interaction with  $\text{DITFB}$  ( $d_{\text{N}\dots\text{I}} = 2.984 \text{ \AA}$ ). This disorder could be due to either a very close configurational energy or a kinetic effect during the crystallisation process. At the molecular level, one can easily observe the rather symmetric potential pattern on the ESP map (Figure III – 12, b). Such a charge distribution supports the fact that both orientation of molecule  $\text{III-2Te}$  are possible without significantly disrupting the crystal organisation.

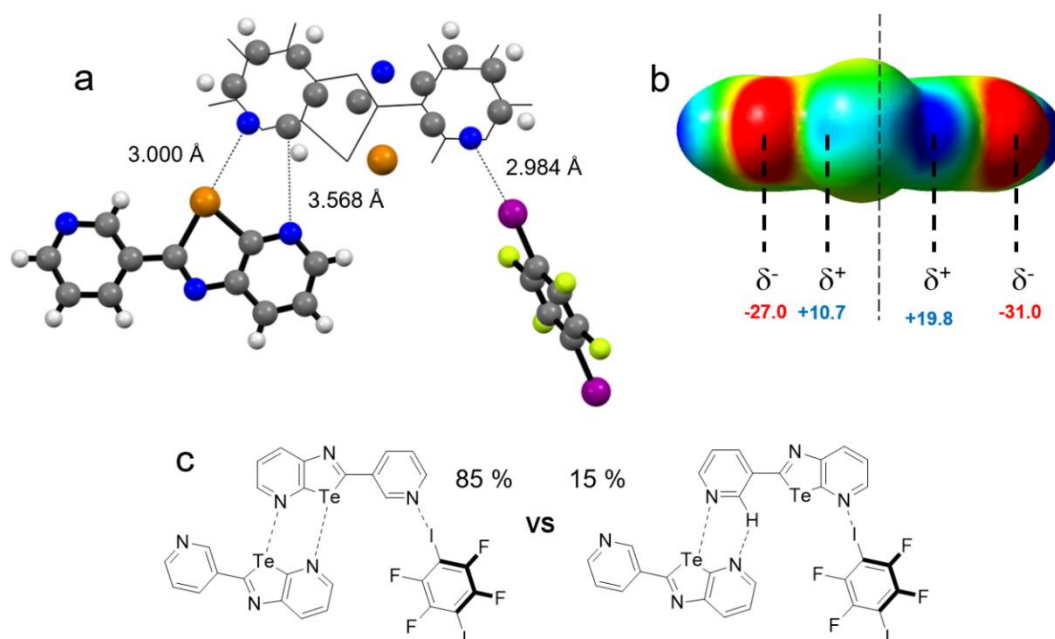


Figure III - 12: a) Error in the packing of co-crystal  $(\text{III-2Te})_2 \cdot \text{DITFB}$ . The original position is displayed in wireframe and the second conformation overlaps in atoms only view. Space group:  $P\bar{1}$ , solvent of crystallisation:  $\text{CHCl}_3$ . b) ESP map on  $\text{III-2Te}$ , level of theory: B97D3/Def2-TZVP using Gaussian09 including D01 revision. c) Schematic representation of the mispacking.

Moving to reference **III-3**, co-crystals of  $(\text{III-3})_2 \cdot \text{HDFIO}$  were obtained in  $P\bar{1}$  space group, the asymmetric unit is constituted by two molecules of benzotellurazole derivative and one of **HDFIO**. As anticipated, the pyrid-4-yl moieties engage through halogen-bonding interactions with both end of the XB donor molecule ( $d_{\text{N}\dots\text{I}} = 2.772 \text{ \AA}$  and  $2.819 \text{ \AA}$ ) forming a trimeric structure (Figure III – 13). Surprisingly, no chalcogen-bonding interactions have been observed in this case. This absence can be rationalised by the fact that single EBs formed by the  $\text{N}_c$  atom of tellurazoles as anticipated previously (Table III – 1) is possibly too weak to be selected in the crystal packing. Molecules of **III-3** arrange in column (Figure III – 13) through  $\pi$ - $\pi$  stacking interaction in a quasi-parallel fashion (estimated  $d_{\pi-\pi} = 3.592 \text{ \AA}$ ). Similarly to  $(\text{III-1Te})_2 \cdot \text{HDFIO}$ , segregation of fluorinated (indicated by pink arrows) and non-fluorinated (indicated by grey arrows) moieties is observed.

Replacing **HDFIO** by **DITFB** in  $(\text{III-3})_2 \cdot \text{HDFIO}$  led to the formation of co-crystal  $(\text{III-3Te})_2 \cdot \text{DITFB}$ . This material crystallises in a  $P\bar{1}$  space group and the asymmetric unit consists in one molecule of **III-3Te** and half of **DITFB**. The X-ray diffraction analysis (Figure III – 14) shows a trimeric structure, in which the XB donor is sandwiched between two pyrid-4-yl moieties through halogen-bonding interactions ( $d_{\text{N}\dots\text{I}} = 2.823 \text{ \AA}$ ). Moreover, the tellurazole unit is engaged in a chalcogen bond with one of the F atoms of **DITFB** ( $d_{\text{F}\dots\text{Te}} = 3.294 \text{ \AA}$ ). Similarly to co-crystal  $(\text{III-1Te})_2 \cdot \text{DITFB}$ , quasi-parallel  $\pi$ - $\pi$  stacks are formed by alternating one **DITFB** and two **III-3** (between **DITFB** and **III-3** estimated  $d_{\pi-\pi} = 3.370$

Å, between two **III-3**  $d_{\pi-\pi} = 3.690$  Å), the latter being arranged in a head-to-tail fashion (Figure III – 14, b and c).

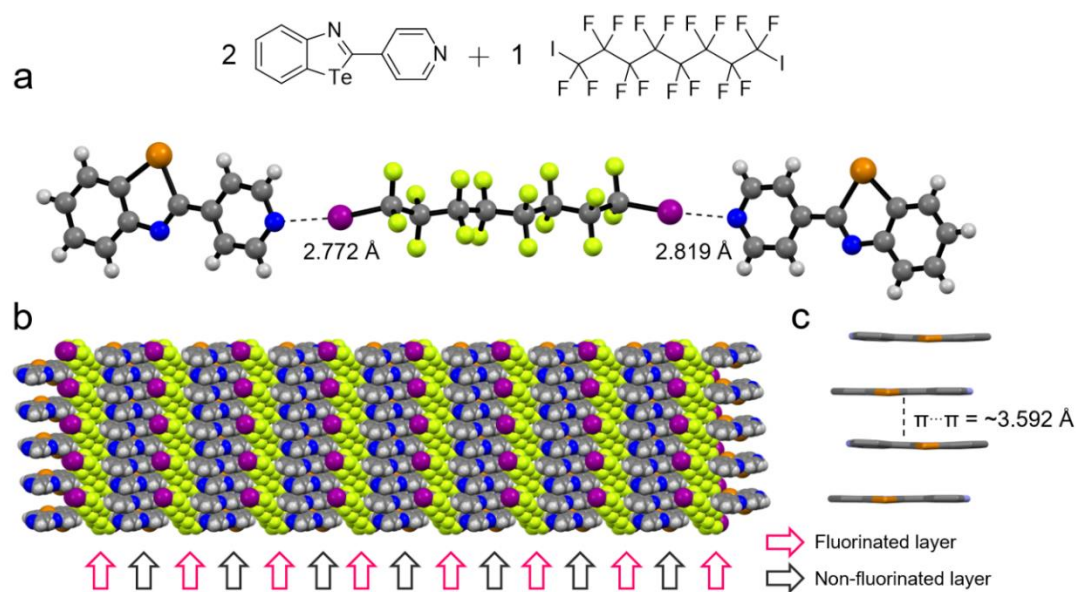


Figure III - 13: X-ray structure of co-crystal  $(\text{III-3})_2 \cdot \text{HDFIO}$ . a) Trimer, key interactions are highlighted; b) vdW sphere representation of the layered organisation; c) Capped stick representation of the  $\pi$ - $\pi$  stacking, H atoms are omitted for clarity. Space group:  $P\bar{1}$ , solvent of crystallisation:  $\text{CHCl}_3$ .

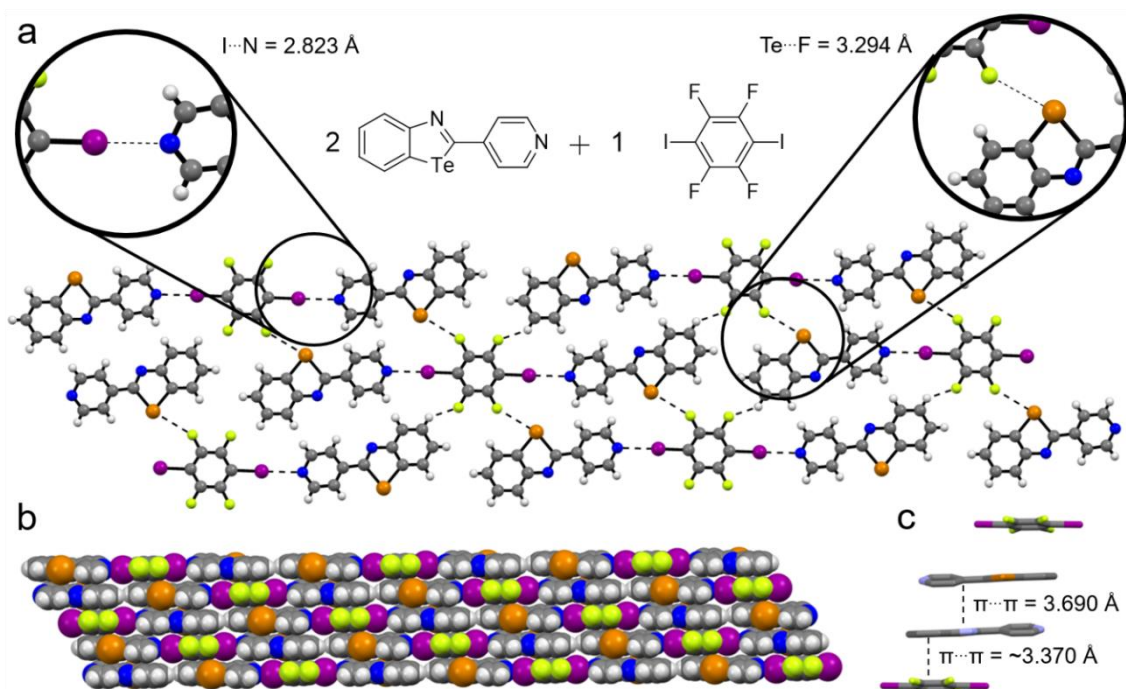


Figure III - 14: X-ray structure of co-crystal  $(\text{III-3})_2 \cdot \text{DITFB}$ . a) Tetramer, key interactions are highlighted; b) vdW sphere representation; c) Capped stick representation of the  $\pi$ - $\pi$  stacking, H atoms are omitted for clarity. Space group:  $P\bar{1}$ , solvent of crystallisation:  $\text{CHCl}_3$ .

The structures of **(III-3)<sub>2</sub>•HDFIO** and **(III-3<sub>Te</sub>)<sub>2</sub>•DITFB** displayed halogen bonds but no chalcogen bond through N<sup>⋯</sup>Te contact, contrasting with co-crystals containing **III-1<sub>Te</sub>** and **III-2<sub>Te</sub>**. The major difference between those molecular entities is the absence of N<sub>p</sub> atom in close vicinity of the Te atom forming the CGP recognition array. Thus, it seems that the benzotellurazole motif is not well-suited to engineer supramolecular crystals based on orthogonal halogen- and chalcogen-bonding interactions, on the opposite of the CGP array.

### III – 3.3 Co-crystals: Selenium containing CGP bearing halogen bond acceptor

As described in *chapter II*, The Te atom can be exchanged with the Se in the CGP motif while preserving the recognition through double chalcogen-bonding interactions in the solid state when substituted by an EWG in 2-position. This part of the study aims to evaluate the compatibility of this weaker double EB array with regards to our designed orthogonal halogen- and chalcogen-bonded supramolecular polymer.

Co-crystal **(III-1<sub>Se</sub>)<sub>2</sub>•DITFB** is iso-structural to its tellurium analogue **(III-1<sub>Te</sub>)<sub>2</sub>•DITFB**, the material crystallises in a  $P\bar{1}$  space group and the asymmetric unit consist in two molecules **III-1<sub>Se</sub>** and one of **DITFB**. X-ray diffraction analysis (Figure III – 15, a) reveals that the molecules associate in a hexamer structures (highlighted in red dashed line). The two central CGP groups interact through two frontal chalcogen-bonds ( $d_{N\dots Se} = 3.294 \text{ \AA}$ ), while each one connects **DITFB** through halogen bonds ( $d_{N\dots I} = 2.779 \text{ \AA}$ ) that both interact with two other molecules **III-1<sub>Se</sub>**. In the crystal packing, those hexamers are connected through HBs between the H in 6-position of the terminal CGP groups and two F atoms from **DITFB** ( $d_{F\dots C} = 3.088 \text{ \AA}$ ). This results in an organisation of the molecules in a quasi-planar arrangement presenting a slight misalignment of  $0.976 \text{ \AA}$  (Figure III – 15, c).

In contrast to single component crystal of **III-1<sub>Se</sub>**, in which the compound dimerises though hydrogen bonds, the molecules of **III-1<sub>Se</sub>** engage in a double EB interactions in the centre of the hexamer of **(III-1<sub>Se</sub>)<sub>2</sub>•DITFB**. This can be rationalised by the fact that once the pyrid-4-yl connect with **DITFB**, it gives partially its electron density to the C-I  $\sigma$ -hole. This increases the electron-withdrawing effect of this aromatic group, which deepens the electron depletion on the selenium atom. This explanation is supported by calculation of the  $V_{s,max}$  on the ESP map of molecules **III-1<sub>Se</sub>** alone and **III-1<sub>Se</sub>** interacting with **DITFB** (Figure III – 16). The potential of the  $\sigma$ -hole ( $\alpha$ ) of the Se atom is  $+7.09 \text{ kcal}\cdot\text{mol}^{-1}$  for molecule **III-1<sub>Se</sub>**, however, this value increases to  $+11.3 \text{ kcal}\cdot\text{mol}^{-1}$  upon interaction with **DITFB**. Thus, this rises the ability of this molecule to form chalcogen-bonding interaction.

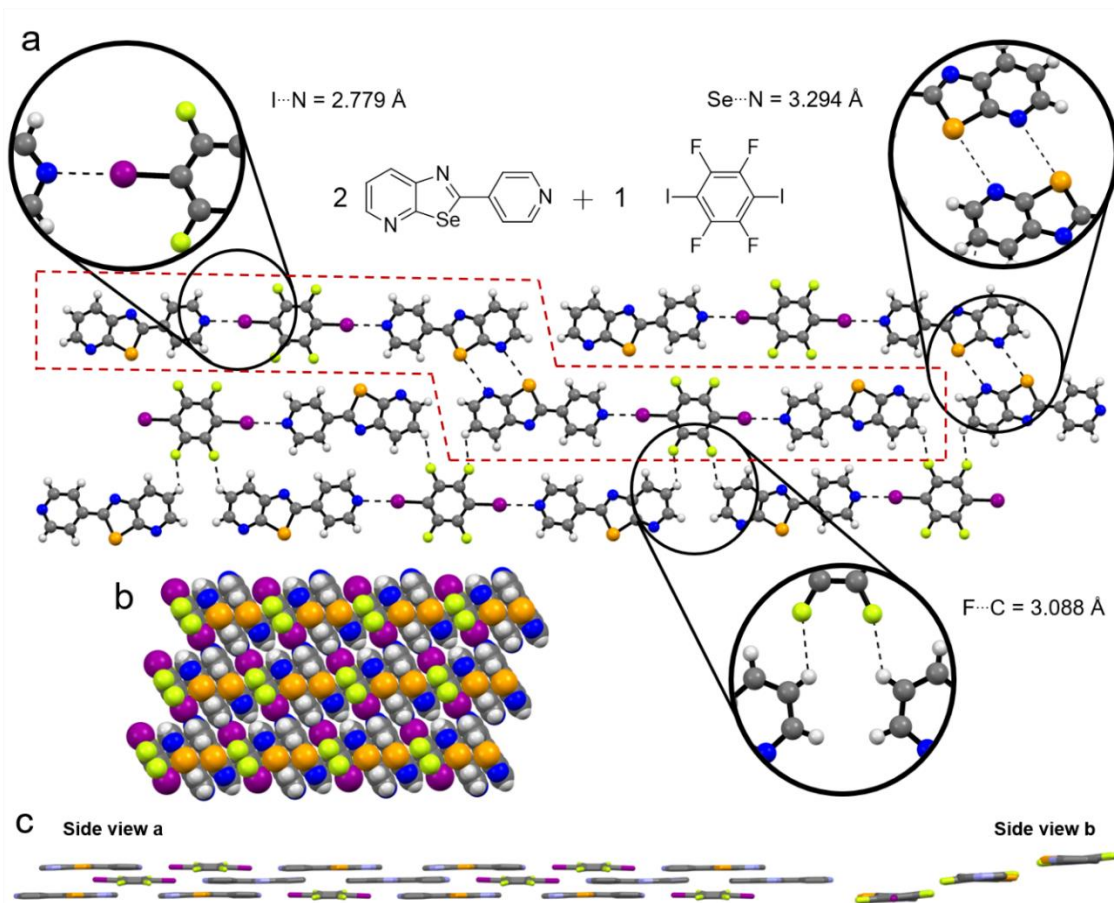


Figure III - 15: X-ray structure of co-crystal  $(\text{III-1}_{\text{se}})_2 \cdot \text{DITFB}$ . a) Tetramer is shown by the red dashed line, key interactions are highlighted; b) vdW sphere representation; c) Capped stick representation of miss-alignment, H atoms are omitted for clarity. Space group:  $P\bar{1}$ , solvent of crystallisation:  $\text{CHCl}_3$ .

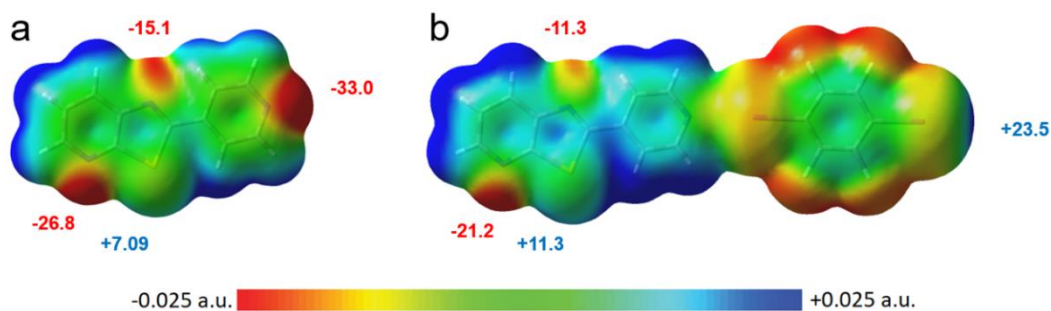


Figure III - 16: ESP map of a)  $\text{III-1}_{\text{se}}$  and b)  $\text{III-1}_{\text{se}}$  interacting with  $\text{DITFB}$  through Halogen Bonding.  $V_{s,\text{max}}$  are highlighted and expressed in  $\text{kcal mol}^{-1}$ . Level of theory: B97D3/Def2-TZVP using Gaussian09 including D01 revision.

Co-crystal  $\text{III-1}_{\text{se}} \cdot (\text{DITFB})_2$  is iso-structural to  $\text{III-1}_{\text{Te}} \cdot (\text{DITFB})_2$ . It crystallises in a  $P\bar{1}$  space group and the asymmetric unit is composed by one molecule of  $\text{III-1}_{\text{se}}$  and one full and two halves of  $\text{DITFB}$ . In the structure (Figure III - 16) pyrid-4-yl groups and the CGP moiety interact with two crystallographically independent molecules of diiodotetrafluorobenzene through XB ( $d_{\text{N}\cdots\text{I}}$  2.804 Å

and  $d_{N...I} = 2.798 \text{ \AA}$ , respectively). In contrast to the co-crystal **III-1<sub>Te</sub>**•(**DITFB**)<sub>2</sub>, no chalcogen-bonding interaction is observed involving the Se atom and the negative belt of the I atom.

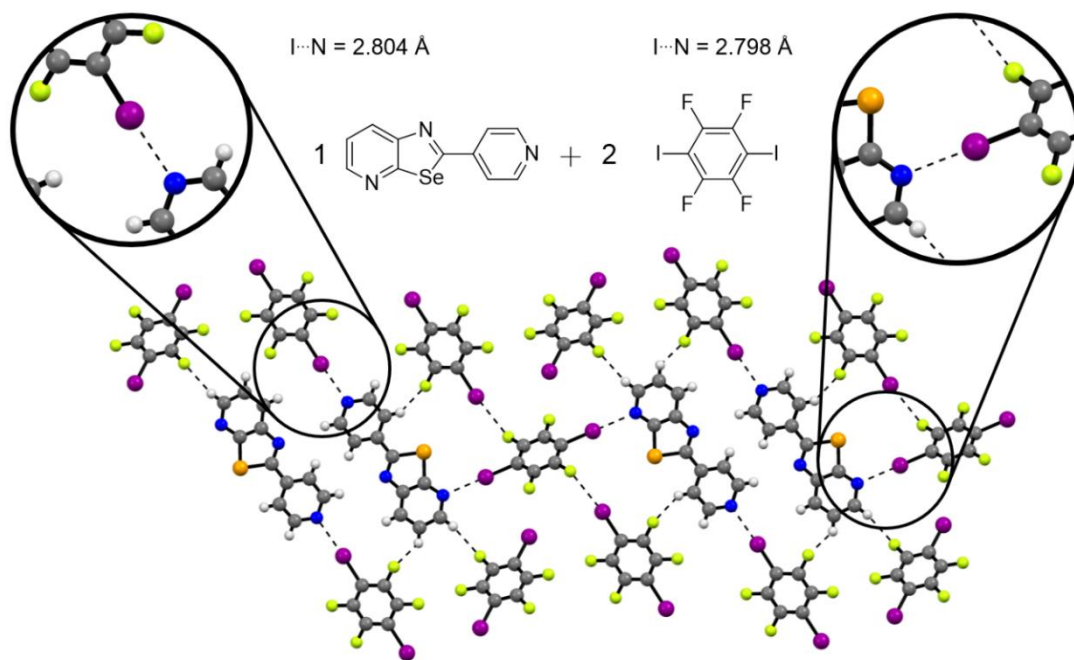


Figure III - 17: X-ray structure of co-crystal **III-1<sub>se</sub>**•(**DITFB**)<sub>2</sub>. Space group:  $P\bar{1}$ , solvent of crystallisation:  $CHCl_3$ .

Crystallisation using isomer **III-2<sub>se</sub>** led to co-crystal **(III-2<sub>se</sub>)<sub>2</sub>**•**DITFB** (Figure III – 18, a), the space group is  $P\bar{1}$  and the asymmetric unit is composed by one molecule of the CGP derivative and half of **DITFB**. In the structure, the Se derivative associate as a dimer through hydrogen-bonding interactions ( $d_{N...c} = 3.560 \text{ \AA}$ ) and develop into the supramolecular polymer through XB contacts with the I atoms ( $d_{N...I} = 2.858 \text{ \AA}$ ). This results in a quasi-co-planar organisation of the molecules. In addition, **III-2<sub>se</sub>** and **DITFB** interact with their own congeners through  $\pi$ - $\pi$  stacking interactions ( $d_{\pi-\pi} = 3.548 \text{ \AA}$  and  $3.409 \text{ \AA}$ , respectively with an off-set of  $1.843 \text{ \AA}$  and  $2.089 \text{ \AA}$ , respectively) forming columns leading to segregation of fluorinated (indicated by pink arrows) and non-fluorinated (indicated by grey arrows) parts (Figure III – 18, b and c).

Interestingly, **(III-2<sub>se</sub>)<sub>2</sub>**•**DITFB** does not form chalcogen-bonding interactions at the crystalline state in contrast to **(III-1<sub>se</sub>)<sub>2</sub>**•**DITFB**. ESP map analysis of **III-2<sub>se</sub>** and **III-1<sub>se</sub>** (Figure III – 19 and 16, respectively) showed a smaller potential value of the  $\sigma$ -hole ( $\alpha$ ) for the pyrid-3-yl isomer than for the pyrid-4-yl isomer ( $V_{s,max} = +5.02 \text{ kcal mol}^{-1}$  and  $+7.09 \text{ kcal mol}^{-1}$ , respectively). Upon interaction with **DITFB**, an increase of  $4 \text{ kcal mol}^{-1}$  in both cases can be observed ( $V_{s,max} = +9.41 \text{ kcal mol}^{-1}$  and  $+11.3 \text{ kcal mol}^{-1}$ , respectively). The potential value in **(III-2<sub>se</sub>)<sub>2</sub>**•**DITFB**, is too weak to trigger the formation of the double chalcogen-bonded array. The two regioisomers only differ by the connectivity of the pyridyl moiety to the CGP group, **III-2<sub>se</sub>** being *meta* and **III-1<sub>se</sub>** being *para*. This

distinction rationalises the difference in  $V_{s,\max}$  between the two molecules as the effect of EWG is stronger in *para*- than in *meta*-position.

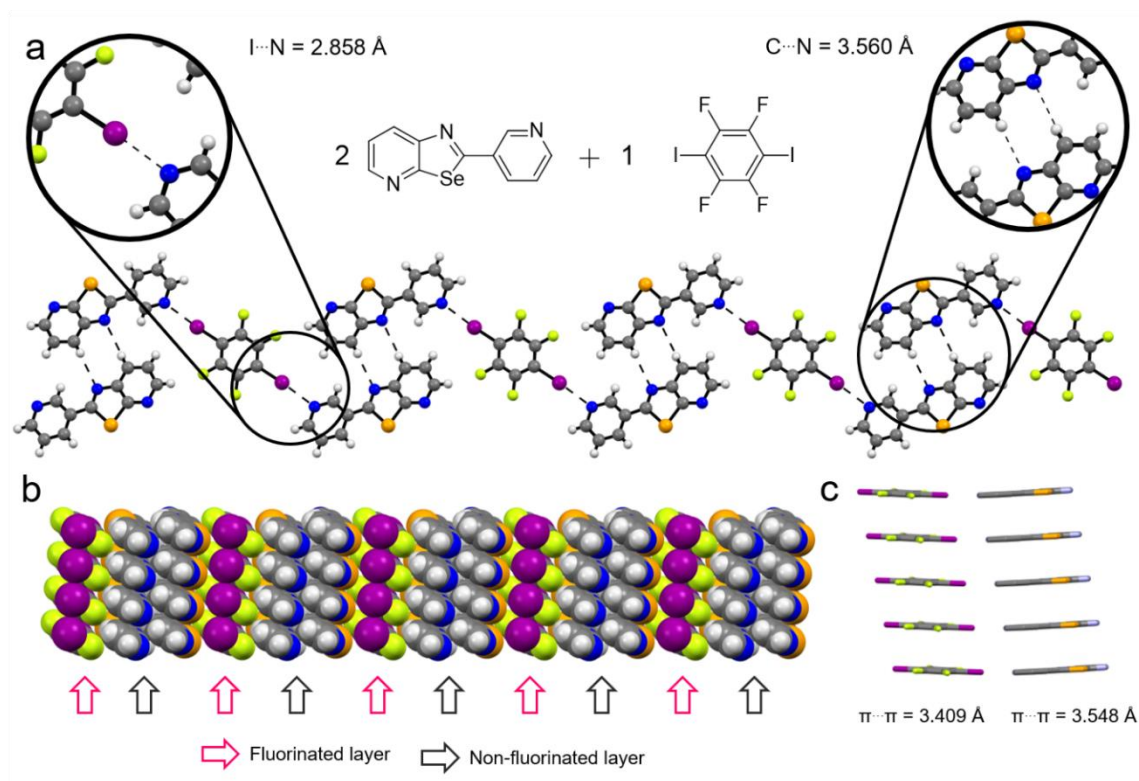


Figure III - 18: X-ray structure of co-crystal  $(\text{III-2}_{\text{se}})_2 \cdot \text{DITFB}$ . a) Supramolecular polymer, key interactions are highlighted; b) vdW sphere representation of the layered organisation; c) Capped stick representation of the  $\pi$ - $\pi$  stacking, H atoms are omitted for clarity. Space group:  $P\bar{1}$ , solvent of crystallisation:  $\text{CHCl}_3$ .

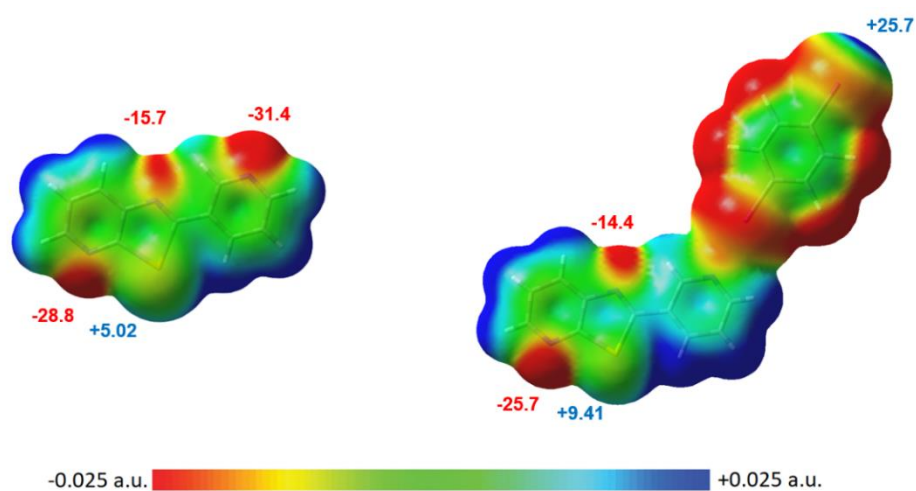


Figure III - 19: ESP map of  $\text{III-2}_{\text{se}}$  (left) and  $\text{III-2}_{\text{se}}$  interacting with  $\text{DITFB}$  through a halogen-bonding interaction (right). Extreme values of interest are highlighted and expressed in  $\text{kcal mol}^{-1}$ . Level of theory: B97D3/Def2-TZVP using Gaussian09 including D01 revision. Geometry taken for crystal structure.

## III – 3.4 Co-crystals: CGP bearing halogen bond donor

Moving to the CGP substituted with 4-iodo-tetrafluorophenyl, co-crystal **(III-5)<sub>2</sub>•DABCO** was obtained. This material crystallises in the  $P\bar{1}$  space group and the asymmetric unit consist of two molecules of **III-5** and one of **DABCO** (Figure III – 20, a). The CGP molecules dimerise through double chalcogen-bonding interactions ( $d_{N\dots Te} = 2.923 \text{ \AA}$ ), and **(III-5)<sub>2</sub>** units are bridged together by **DABCO** through halogen bonds ( $d_{N\dots I} = 2.722 \text{ \AA}$ ) forming a supramolecular polymer. In addition, **III-5** forms  $\pi$ – $\pi$  stacking arrangement with its congener in a quasi-parallel head-to-tail fashion (estimated  $d_{\pi-\pi} = 3.710 \text{ \AA}$ , Figure III – 20, b and c). **DABCO** is sandwiched between two CGP molecules through CH– $\pi$  interactions ( $d_{C\dots C} = 3.229\text{--}3.684 \text{ \AA}$ , Figure III – 20, d).

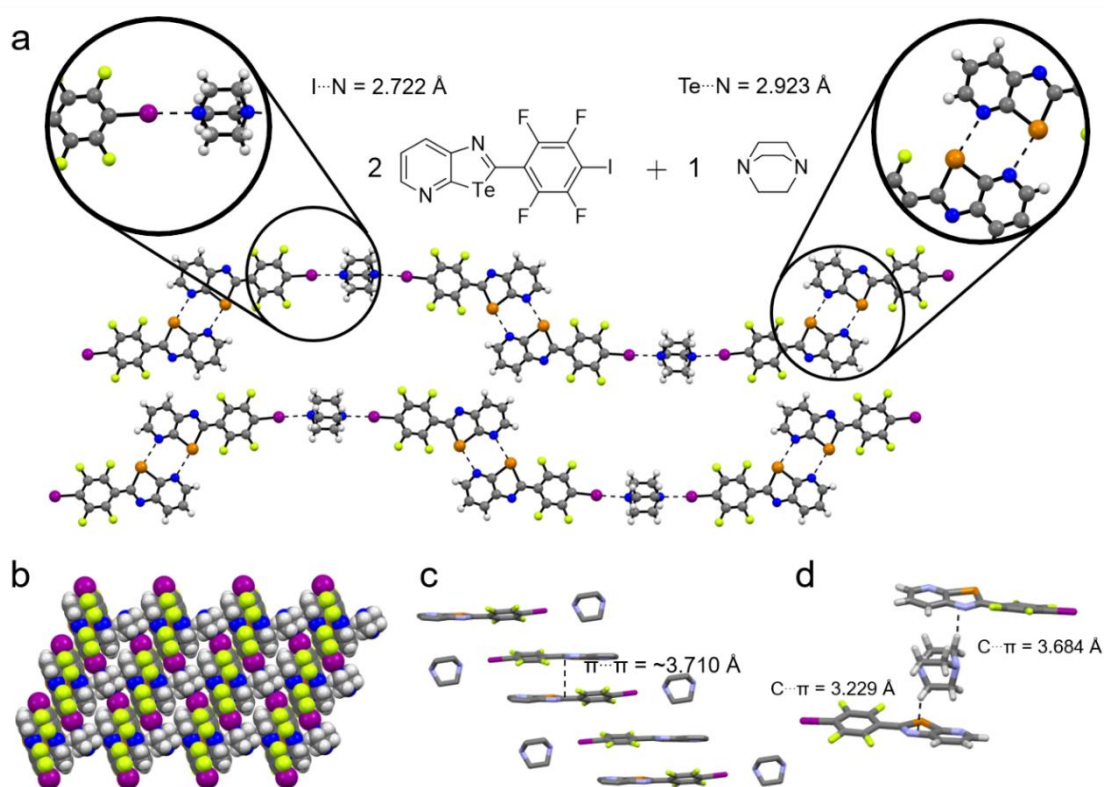


Figure III - 20: X-ray structure of co-crystal **(III-5)<sub>2</sub>•DABCO**. a) Supramolecular polymer, key interactions are highlighted; b) vdW sphere representation of the layered organisation; c) Capped stick representation of the  $\pi$ – $\pi$  stacking, H atoms are omitted for clarity; d) Capped stick representation of the CH– $\pi$  interaction. Space group:  $P\bar{1}$ , solvent of crystallisation:  $CHCl_3$ .

Another co-crystal of **(III-5)<sub>2</sub>•DABCO** was obtained from a different batch. This polymorph grows in a  $P2_1/n$  space group and the asymmetric unit contains two molecules of **III-5** and one of **DABCO**. The CGP molecules interact through double chalcogen-bonding interactions ( $d_{N\dots Te} = 2.974 \text{ \AA}$ ). **DABCO** is sandwiched by dimers **(III-5)<sub>2</sub>** through halogen bonds ( $d_{N\dots I} = 2.694 \text{ \AA}$ ) leading to the formation of a supramolecular polymer. **III-5** interact with its congener through  $\pi$ – $\pi$  stacking interactions (Figure III – 21, b), however one CGP molecule in the asymmetric unit is distorted. The two aromatic rings of that particular molecule do not lie in the same plane, an angle of  $23^\circ$  is

observed (Figure III – 21, c). This crystal packing was obtained more consistently than the one described above (Figure III – 20), which has been obtained only once. This second structure was obtained while attempting to reproduce the crystallisation condition of the first one. A precise control of the ambient humidity and temperature is possibly required in order to favour one crystal structure rather than the other.

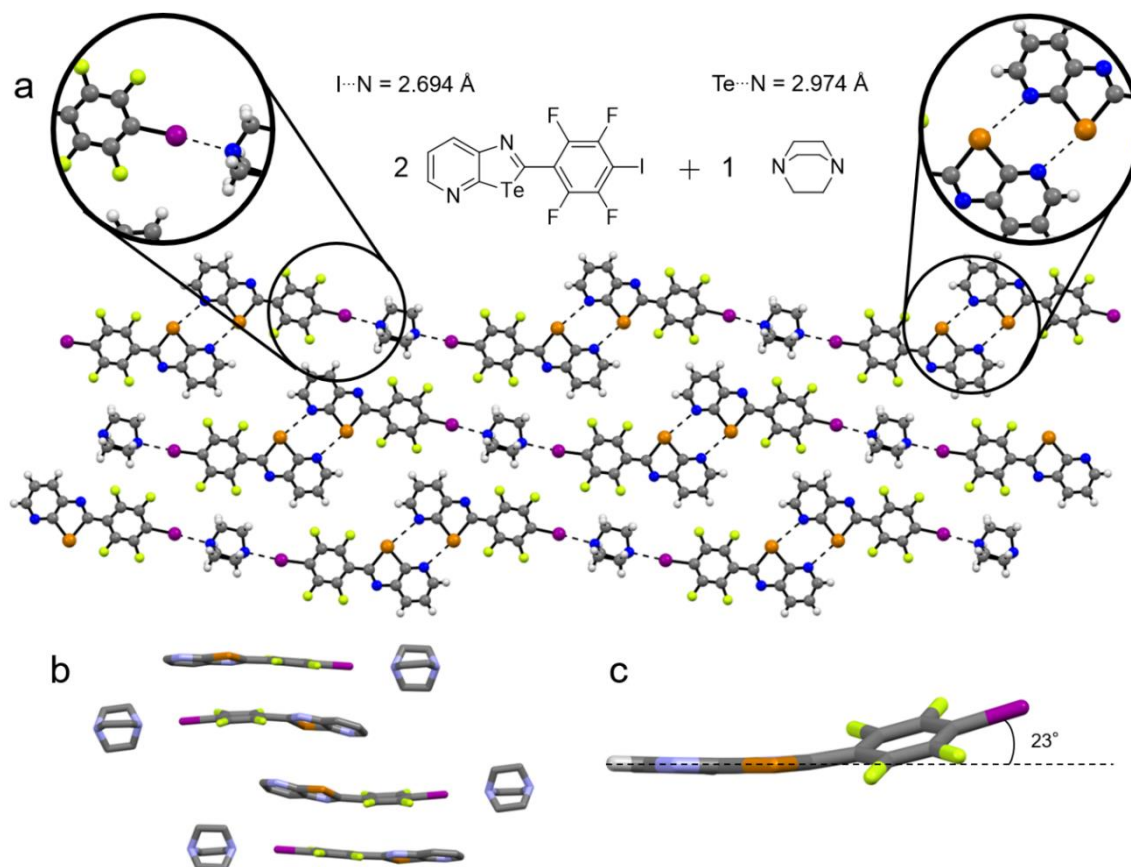
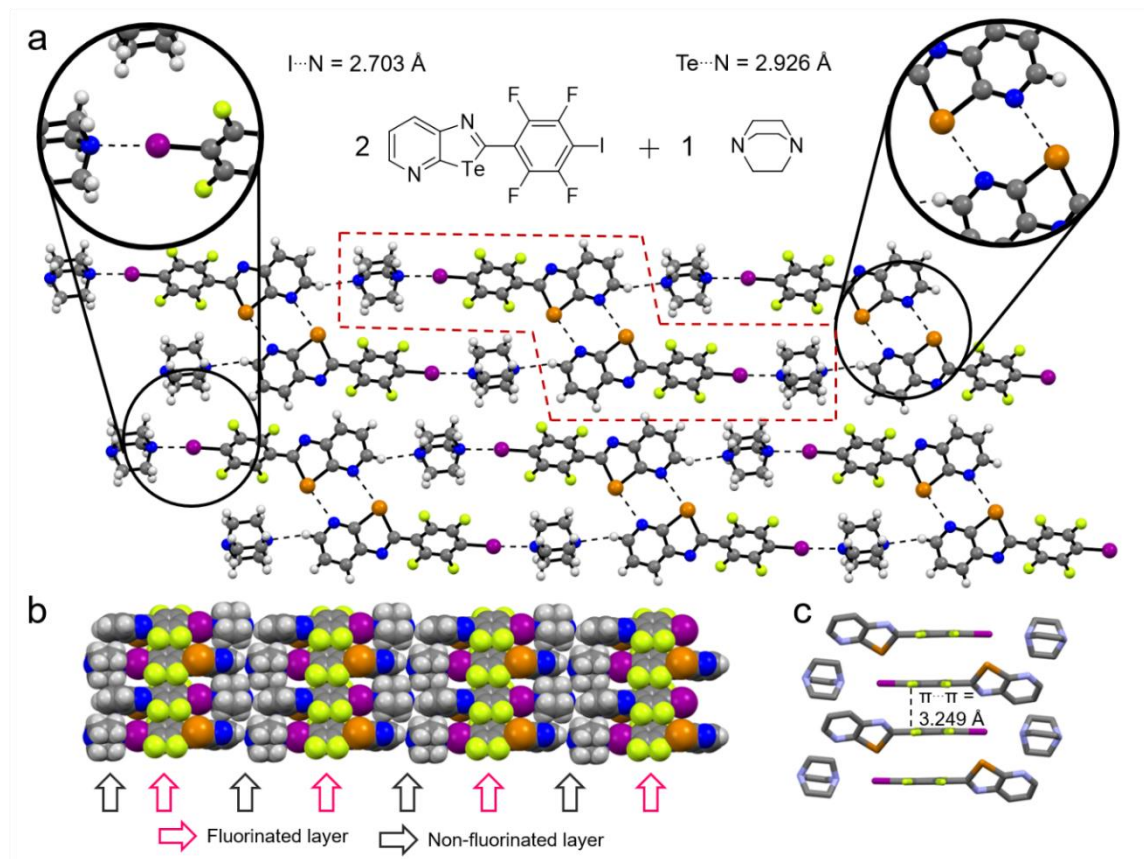


Figure III - 21: X-ray structure of co-crystal **(III-5)<sub>2</sub>.DABCO**. a) Supramolecular polymer, key interactions are highlighted; b) Capped stick representation of the  $CH-\pi$  interaction, H atoms are omitted for clarity; c) Capped stick representation the distortion of **III-5**. Space group:  $P2_1/n$ , solvent of crystallisation:  $CHCl_3$ .

Co-crystal **III-5.DABCO** has a  $P\bar{1}$  space group and an asymmetric unit constituted by one molecule of **III-5** and one of **DABCO**. The two components arrange in tetramers (Figure III – 22, a highlighted in red dashed line) where the two central CGP derivatives interact together through double chalcogen bonds ( $d_{N \cdots Te} = 2.926 \text{ \AA}$ ) and with two **DABCO** molecules through halogen bonds ( $d_{N \cdots I} = 2.703 \text{ \AA}$ ). **III-5** presents a dihedral angle of  $45^\circ$  between the tellurazopyridine unit and the fluorinated ring. The molecules interact through  $\pi-\pi$  stacking interactions between 4-iodotetrafluorophenyl moieties ( $d_{\pi-\pi} = 3.289 \text{ \AA}$ , Figure III – 22, c), which leads to segregation of the fluorinated (indicated by pink arrows) and non-fluorinated (indicated by grey arrows) parts (Figure III – 22, b).



Finally, **III-1<sub>Te</sub>**•**III-5** crystallises in a  $P2_1/n$  space group and the asymmetric unit is composed by one molecule of **III-1<sub>Te</sub>** and one of **III-5**. The two constituents form a supramolecular polymer by alternating halogen- and chalcogen-bonding interactions (Figure III – 23). One can easily notice that **III-1<sub>Te</sub>** interacts with **III-5** forming a heteromolecular dimer through EBs ( $d_{\text{N}\dots\text{Te}} = 3.033 \text{ \AA}$ ), an angle of  $33^\circ$  between the planes of the two CGP rings can be observed. The two molecules interact through XB in a linear fashion ( $d_{\text{N}\dots\text{I}} = 2.802 \text{ \AA}$ ,  $\text{C-I}\dots\text{N}$  angle =  $172^\circ$ ). Interestingly, strains of **III-1<sub>Te</sub>**•**III-5** arrange in a triple helix structure (Figure III – 23, b, each strand is highlighted in Red, Blue and Green, respectively). In addition, molecules of **III-1<sub>Te</sub>** and **III-5** interact through quasi-parallel  $\pi$ - $\pi$  stacking in a head-to-tail arrangement (Figure III – 24). ESP analysis shows that the 4-iodotetrafluorophenyl moiety is electron poor and the CGP, electron rich. This complementary quadrupolar charge distribution is likely to govern the face-to-face arrangement of the molecules at the solid state.

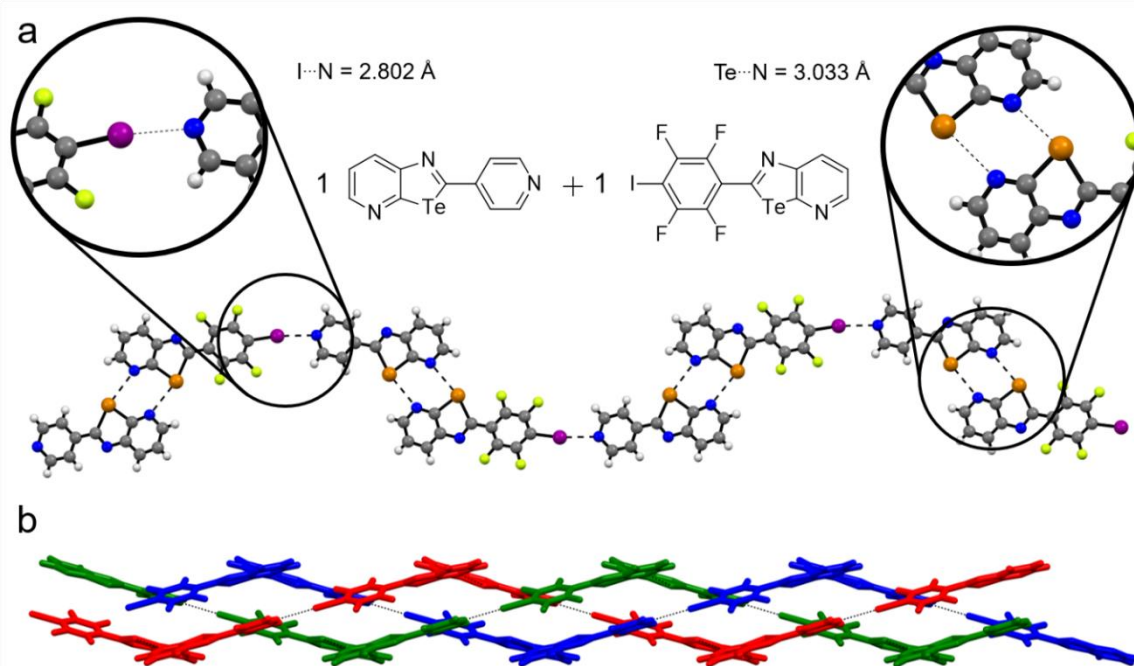


Figure III - 23: X-ray structure of co-crystal **III-1<sub>Te</sub>•III-5**. a) Supramolecular polymer, key interactions are highlighted; b) Capped stick representation of the triple helix, each strand is highlighted in Red, Blue and Green, respectively. Space group:  $P2_1/n$ , solvent of crystallisation:  $CHCl_3$ .

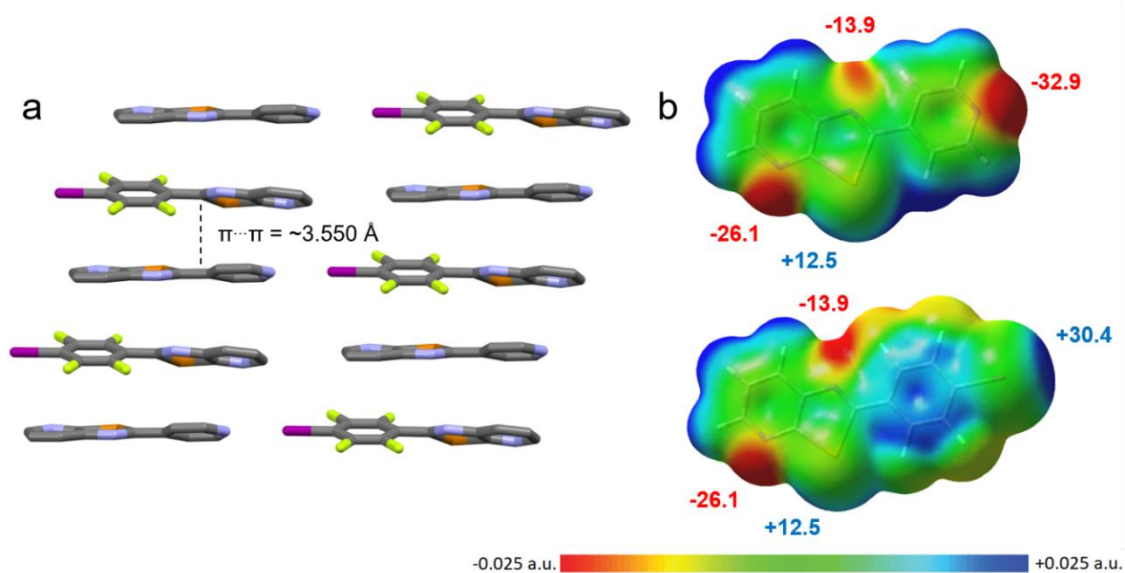


Figure III - 24: a) X-ray structure of co-crystal **III-1<sub>Te</sub>•III-5**,  $\pi$ - $\pi$  stacking is highlighted. Space group:  $P2_1/n$ , solvent of crystallisation:  $CHCl_3$ ; b) ESP map of **III-1<sub>Te</sub>** and **III-5**.

## III – 4 Conclusion

In summary, we have demonstrated the possibility of forming supramolecular polymers in the solid-state based on the orthogonal use of halogen and chalcogen bonding through 14 different co-crystals. Supramolecular polymer  $[(\text{III-1}_{\text{Te}})_2 \cdot \text{HDFIO}]_n$  confirms the design discussed previously by connecting molecules of **III-1<sub>Te</sub>** and hexadecafluorodiiodoctane by alternating two EBs and two XBs. The CGP dimer forms a ditopic halogen bond acceptor that, interacting with **HDFIO**, establish the repeating unit leading to infinite chains. The results in this chapter have been discussed in term of orthogonality, however, the more correct approach would be to refer to EB and XB as concurring interactions in the solid state.

Mixing **III-1<sub>Te</sub>** and **DITFB**, different materials could be obtained depending on the ratio of the two components in the initial solution.  $(\text{III-1}_{\text{Te}})_2 \cdot \text{DITFB}$  formed a hexameric structure through EBs and XBs, **III-1<sub>Te</sub>•DITFB** formed supramolecular polymer by means of XBs and **III-1<sub>Te</sub>•(DITFB)<sub>2</sub>** formed aggregates in which **III-1<sub>Te</sub>** interacts with **DITFB** through XBs. Those three cases show that our design is able to answer to condition of crystallisation such as stoichiometry. On the opposite, isomer **III-2<sub>Te</sub>** led to the formation of  $(\text{III-2}_{\text{Te}})_2 \cdot \text{DITFB}$ , which formed a supramolecular polymer, independently of the initial ratio of the two components.

Benzotellurazole **III-3** formed trimers in the solid-state with **HDFIO** and **DITFB** through halogen-bonding interactions, which highlight the importance of a strong recognition motif based on chalcogen-bonds to achieve an orthogonal supramolecular polymer. Se- containing **III-1<sub>Se</sub>** formed with **DITFB** co-crystal  $(\text{III-1}_{\text{Te}})_2 \cdot \text{DITFB}$ , which is isostructural to its Te- analogue  $(\text{III-1}_{\text{Te}})_2 \cdot \text{DITFB}$ . Hexamers containing chalcogen- and halogen-bonding interactions were observed. This reveals that **III-1<sub>Se</sub>** is able to dimerise through double EBs upon formation of a XB. In contrast, isomer **III-2<sub>Se</sub>** led to the formation of  $(\text{III-2}_{\text{Se}})_2 \cdot \text{DITFB}$  as a supramolecular polymer in which the components are held together by means of hydrogen- and halogen-bonding interactions.

Reversing the halogen bond demand, *i. e.* placing the XB donor moiety on the CGP derivative, led to the formation of **III-5•DABCO** and  $(\text{III-5})_2 \cdot \text{DABCO}$  co-crystals. In the first case, a tetrameric arrangement was obtained and in the second, a supramolecular polymer. Both were formed through the association of halogen- and chalcogen-bonding interactions. Furthermore, mixing molecules **III-1<sub>Te</sub>** and **III-5** led to the formation of co-crystal **III-1<sub>Te</sub>•III-5**. The two components associate through the formation of a hetero-recognition system through orthogonal XB and EB achieving a supramolecular polymer. In conclusion, this new orthogonal system sets the first stepping stone towards more complex functional material achievable with defined building blocks based on halogen- and chalcogen-bonding interactions.

## III – 5 Bibliography

- [1] J.-M. Lehn, 'Perspectives in Chemistry—Steps towards Complex Matter', *Angew. Chem. Int. Ed.* **2013**, *52*, 2836-2850.
- [2] P. A. Korevaar, S. J. George, A. J. Markvoort, M. M. J. Smulders, P. A. J. Hilbers, A. P. H. J. Schenning, T. F. A. De Greef, E. W. Meijer, 'Pathway Complexity in Supramolecular Polymerization', *Nature* **2012**, *481*, 492.
- [3] J.-M. Lehn, *From Molecular to Supramolecular Chemistry*, Wiley-VCH Verlag GmbH & Co. KGaA, 2006.
- [4] M. W. Hosseini, 'Molecular Tectonics: from Molecular Recognition of Anions to Molecular Networks', *Coord. Chem. Rev.* **2003**, *240*, 157-166.
- [5] M. W. Hosseini, 'Self-Assembly and Generation of Complexity', *Chem. Commun.* **2005**, 5825-5829.
- [6] M. W. Hosseini, 'Molecular Tectonics: From Simple Tectons to Complex Molecular Networks', *Acc. Chem. Res.* **2005**, *38*, 313-323.
- [7] E. Mattia, S. Otto, 'Supramolecular Systems Chemistry', *Nat. Nanotechnol.* **2015**, *10*, 111.
- [8] C.-H. Wong, S. C. Zimmerman, 'Orthogonality in organic, polymer, and supramolecular chemistry: from Merrifield to click chemistry', *Chem. Commun.* **2013**, *49*, 1679-1695.
- [9] C. Burd, M. Weck, 'Solvent Influence on the Orthogonality of Noncovalently Functionalized Terpolymers', *J. Polym. Sci., Part A: Polym. Chem.* **2008**, *46*, 1936-1944.
- [10] E. Elacqua, D. S. Lye, M. Weck, 'Engineering Orthogonality in Supramolecular Polymers: From Simple Scaffolds to Complex Materials', *Acc. Chem. Res.* **2014**, *47*, 2405-2416.
- [11] S. J. Rowan, S. J. Cantrill, G. R. L. Cousins, J. K. M. Sanders, J. F. Stoddart, 'Dynamic Covalent Chemistry', *Angew. Chem. Int. Ed.* **2002**, *41*, 898-952.
- [12] A. Wilson, G. Gasparini, S. Matile, 'Functional Systems with Orthogonal Dynamic Covalent Bonds', *Chem. Soc. Rev.* **2014**, *43*, 1948-1962.
- [13] K.-D. Zhang, S. Matile, 'Complex Functional Systems with Three Different Types of Dynamic Covalent Bonds', *Angew. Chem. Int. Ed.* **2015**, *54*, 8980-8983.
- [14] S. K. Yang, S. C. Zimmerman, 'Hydrogen Bonding Modules for Use in Supramolecular Polymers', *Isr. J. Chem.* **2013**, *53*, 511-520.
- [15] G. Barany, R. B. Merrifield, 'A New Amino Protecting Group Removable by Reduction. Chemistry of the Dithiasuccinoyl (Dts) Function', *J. Am. Chem. Soc.* **1977**, *99*, 7363-7365.
- [16] O. Kanie, Y. Ito, T. Ogawa, 'Orthogonal Glycosylation Strategy in Oligosaccharide Synthesis', *J. Am. Chem. Soc.* **1994**, *116*, 12073-12074.
- [17] C. G. Bochet, 'Chromatic Orthogonality in Organic Synthesis', *Synlett* **2004**, 2268-2274.
- [18] H. C. Kolb, M. G. Finn, K. B. Sharpless, 'Click Chemistry: Diverse Chemical Function from a Few Good Reactions', *Angew. Chem. Int. Ed.* **2001**, *40*, 2004-2021.
- [19] E. Saxon, C. R. Bertozzi, 'Cell Surface Engineering by a Modified Staudinger Reaction', *Science* **2000**, *287*, 2007.
- [20] K. L. Kiick, E. Saxon, D. A. Tirrell, C. R. Bertozzi, 'Incorporation of Azides into Recombinant Proteins for Chemoselective Modification by the Staudinger Ligation', *PNAS* **2002**, *99*, 19.
- [21] J. A. Prescher, D. H. Dube, C. R. Bertozzi, 'Chemical Remodelling of Cell Surfaces in Living Animals', *Nature* **2004**, *430*, 873-877.
- [22] W. T. S. Huck, R. Hulst, P. Timmerman, F. C. J. M. van Veggel, D. N. Reinhoudt, 'Noncovalent Synthesis of Nanostructures: Combining Coordination Chemistry and Hydrogen Bonding', *Angew. Chem. Int. Ed.* **1997**, *36*, 1006-1008.
- [23] S. K. Chang, A. D. Hamilton, 'Molecular Recognition of Biologically Interesting Substrates: Synthesis of an Artificial Receptor for Barbiturates Employing Six Hydrogen Bonds', *J. Am. Chem. Soc.* **1988**, *110*, 1318-1319.
- [24] G. Gröger, W. Meyer-Zaika, C. Böttcher, F. Gröhn, C. Ruthard, C. Schmuck, 'Switchable Supramolecular Polymers from the Self-Assembly of a Small Monomer with Two Orthogonal Binding Interactions', *J. Am. Chem. Soc.* **2011**, *133*, 8961-8971.

- [25] G. R. Desiraju, 'Crystal Engineering: A Brief Overview', *J. Chem. Sci.* **2010**, *122*, 667-675.
- [26] C. B. Aakeröy, N. C. Schultheiss, A. Rajbanshi, J. Desper, C. Moore, 'Supramolecular Synthesis Based on a Combination of Hydrogen and Halogen Bonds', *Cryst. Growth Des.* **2009**, *9*, 432-441.
- [27] V. Amico, S. V. Meille, E. Corradi, M. T. Messina, G. Resnati, 'Perfluorocarbon-Hydrocarbon Self-Assembling. 1D Infinite Chain Formation Driven by Nitrogen...Iodine Interactions', *J. Am. Chem. Soc.* **1998**, *120*, 8261-8262.
- [28] A. Lunghi, P. Cardillo, T. Messina, P. Metrangolo, W. Panzeri, G. Resnati, 'Perfluorocarbon-hydrocarbon Self assembling. Thermal and Vibrational Analyses of One-dimensional Networks Formed by  $\alpha,\omega$ -Diiodoperfluoroalkanes with K.2.2. and K.2.2.2', *J. Fluorine Chem.* **1998**, *91*, 191-194.
- [29] P. Metrangolo, G. Resnati, 'Chemistry. Halogen Versus Hydrogen', *Science* **2008**, *321*, 918-919.
- [30] K. Raatikainen, J. Huuskonen, M. Lahtinen, P. Metrangolo, K. Rissanen, 'Halogen Bonding Drives the Self-Assembly of Piperazinecyclophanes into Tubular Structures', *Chem. Commun.* **2009**, 2160-2162.
- [31] P. Metrangolo, F. Meyer, T. Pilati, D. M. Proserpio, G. Resnati, 'Highly Interpenetrated Supramolecular Networks Supported by N...I Halogen Bonding', *Chem. Eur. J.* **2007**, *13*, 5765-5772.
- [32] C. B. Aakeröy, D. Welideniya, J. Desper, C. Moore, 'Halogen-Bond Driven Co-crystallization of Potential Anti-Cancer Compounds: a Structural Study', *Cryst. Eng. Comm.* **2014**, *16*, 10203-10209.
- [33] L. Catalano, S. Pérez-Estrada, G. Terraneo, T. Pilati, G. Resnati, P. Metrangolo, M. A. Garcia-Garibay, 'Dynamic Characterization of Crystalline Supramolecular Rotors Assembled through Halogen Bonding', *J. Am. Chem. Soc.* **2015**, *137*, 15386-15389.
- [34] W. Navarrini, P. Metrangolo, T. Pilati, G. Resnati, 'Crown Ethers as Pre-organised Exo-receptors in the Divergent Recognition of  $\alpha,\omega$ -Diiodoperfluoroalkanes', *New J. Chem.* **2000**, *24*, 777-780.
- [35] M. Saccone, M. Spengler, M. Pfletscher, K. Kuntze, M. Virkki, C. Wölper, R. Gehrke, G. Jansen, P. Metrangolo, A. Priimagi, M. Giese, 'Photoresponsive Halogen-Bonded Liquid Crystals: The Role of Aromatic Fluorine Substitution', *Chem. Mater.* **2019**, *31*, 462-470.
- [36] H. L. Nguyen, P. N. Horton, M. B. Hursthouse, A. C. Legon, D. W. Bruce, 'Halogen Bonding: A New Interaction for Liquid Crystal Formation', *J. Am. Chem. Soc.* **2004**, *126*, 16-17.
- [37] J. Xu, X. Liu, J. K.-P. Ng, T. Lin, C. He, 'Trimeric Supramolecular Liquid Crystals Induced by Halogen Bonds', *J. Mater. Chem.* **2006**, *16*, 3540-3545.
- [38] J. Xu, X. Liu, T. Lin, J. Huang, C. He, 'Synthesis and Self-Assembly of Difunctional Halogen-Bonding Molecules: A New Family of Supramolecular Liquid-Crystalline Polymers', *Macromolecules* **2005**, *38*, 3554-3557.
- [39] N. Houbenov, R. Milani, M. Poutanen, J. Haataja, V. Dichiarante, J. Sainio, J. Ruokolainen, G. Resnati, P. Metrangolo, O. Ikkala, 'Halogen-Bonded Mesogens Direct Polymer Self-Assemblies up to Millimetre Length Scale', *Nat. Commun.* **2014**, *5*, 4043.
- [40] J. Vapaavuori, A. Siiskonen, V. Dichiarante, A. Forni, M. Saccone, T. Pilati, C. Pellerin, A. Shishido, P. Metrangolo, A. Priimagi, 'Supramolecular Control of Liquid Crystals by Doping with Halogen-Bonding Dyes', *RSC Adv.* **2017**, *7*, 40237-40242.
- [41] A. Priimagi, G. Cavallo, P. Metrangolo, G. Resnati, 'The Halogen Bond in the Design of Functional Supramolecular Materials: Recent Advances', *Acc. Chem. Res.* **2013**, *46*, 2686-2695.
- [42] C. B. Aakeröy, T. K. Wijethunga, J. Benton, J. Desper, 'Stabilizing Volatile Liquid Chemicals Using Co-crystallization', *Chem. Commun.* **2015**, *51*, 2425-2428.
- [43] W. Zhu, R. Zheng, Y. Zhen, Z. Yu, H. Dong, H. Fu, Q. Shi, W. Hu, 'Rational Design of Charge-Transfer Interactions in Halogen-Bonded Co-crystals toward Versatile Solid-State Optoelectronics', *J. Am. Chem. Soc.* **2015**, *137*, 11038-11046.

- [44] M. Virkki, O. Tuominen, A. Forni, M. Saccone, P. Metrangolo, G. Resnati, M. Kauranen, A. Priimagi, 'Halogen Bonding Enhances Nonlinear Optical Response in Poled Supramolecular Polymers', *J. Mater. Chem. C* **2015**, *3*, 3003-3006.
- [45] M. Saccone, V. Dichiarante, A. Forni, A. Goulet-Hanssens, G. Cavallo, J. Vapaavuori, G. Terraneo, C. J. Barrett, G. Resnati, P. Metrangolo, A. Priimagi, 'Supramolecular Hierarchy among Halogen and Hydrogen Bond Donors in Light-Induced Surface Patterning', *J. Mater. Chem. C* **2015**, *3*, 759-768.
- [46] J. Vapaavuori, I. T. S. Heikkinen, V. Dichiarante, G. Resnati, P. Metrangolo, R. G. Sabat, C. G. Bazuin, A. Priimagi, C. Pellerin, 'Photomechanical Energy Transfer to Photopassive Polymers through Hydrogen and Halogen Bonds', *Macromolecules* **2015**, *48*, 7535-7542.
- [47] A. Priimagi, G. Cavallo, A. Forni, M. Gorynsztein-Leben, M. Kaivola, P. Metrangolo, R. Milani, A. Shishido, T. Pilati, G. Resnati, G. Terraneo, 'Halogen Bonding versus Hydrogen Bonding in Driving Self-Assembly and Performance of Light-Responsive Supramolecular Polymers', *Adv. Funct. Mater.* **2012**, *22*, 2572-2579.
- [48] F. Meyer, P. Dubois, 'Halogen Bonding at Work: Recent Applications in Synthetic Chemistry and Materials Science', *Cryst. Eng. Comm.* **2013**, *15*, 3058-3071.
- [49] S. Zhu, C. Xing, W. Xu, G. Jin, Z. Li, 'Halogen Bonding and Hydrogen Bonding Coexist in Driving Self-Assembly Process', *Cryst. Growth Des.* **2004**, *4*, 53-56.
- [50] V. Vasylyeva, S. K. Nayak, G. Terraneo, G. Cavallo, P. Metrangolo, G. Resnati, 'Orthogonal Halogen and Hydrogen Bonds Involving a Peptide Bond Model', *Cryst. Eng. Comm.* **2014**, *16*, 8102-8105.
- [51] A. R. Voth, P. Khuu, K. Oishi, P. S. Ho, 'Halogen Bonds as Orthogonal Molecular Interactions to Hydrogen Bonds', *Nat. Chem.* **2009**, *1*, 74.
- [52] E. Persch, O. Dumele, F. Diederich, 'Molecular Recognition in Chemical and Biological Systems', *Angew. Chem. Int. Ed.* **2015**, *54*, 3290-3327.
- [53] P. Auffinger, F. A. Hays, E. Westhof, P. S. Ho, 'Halogen Bonds in Biological Molecules', *PNAS* **2004**, *101*, 16789.
- [54] P. Metrangolo, F. Meyer, T. Pilati, G. Resnati, G. Terraneo, 'Halogen Bonding in Supramolecular Chemistry', *Angew. Chem. Int. Ed.* **2008**, *47*, 6114-6127.
- [55] M. Fourmigué, 'Halogen Bonding: Recent Advances', *Curr. Opin. Solid State Mater. Sci.* **2009**, *13*, 36-45.
- [56] P. Metrangolo, G. Resnati, 'Halogen Bonding: A Paradigm in Supramolecular Chemistry', *Chem. Eur. J.* **2001**, *7*, 2511-2519.
- [57] R. Cabot, C. A. Hunter, 'Non-Covalent Interactions Between Iodo-perfluorocarbons and Hydrogen Bond Acceptors', *Chem. Commun.* **2009**, 2005-2007.
- [58] A. Kremer, A. Fermi, N. Biot, J. Wouters, D. Bonifazi, 'Supramolecular Wiring of Benzo-1,3-chalcogenazoles through Programmed Chalcogen Bonding Interactions', *Chem. Eur. J.* **2016**, *22*, 5665-5675.
- [59] G. E. Garrett, G. L. Gibson, R. N. Straus, D. S. Seferos, M. S. Taylor, 'Chalcogen Bonding in Solution: Interactions of Benzotelluradiazoles with Anionic and Uncharged Lewis Bases', *J. Am. Chem. Soc.* **2015**, *137*, 4126-4133.
- [60] T. Clark, M. Hennemann, J. S. Murray, P. Politzer, 'Halogen Bonding: the  $\sigma$ -Hole', *J. Mol. Model.* **2007**, *13*, 291-296.

---

## **Chapter IV**

### **Blending Chalcogen and Hydrogen**

#### **Bonding: Multipoint Recognition Motifs**

---

In this chapter, we design and synthesise new supramolecular synthons based on 2,5-substituted CGP derivatives aiming for a multiply-bonded system based on hydrogen- and chalcogen-bonding interactions. Different crystal structures can be obtained based on the steric repulsion between the different substituents of the molecules. The rational design and synthesis of a potential tetra-chalcogen bonding recognition motif are presented. Finally, a hetero-molecular recognition system could be engineered and led to the formation of co-crystals based on simultaneous HB and EB.

This chapter is divided in six main sections. *Section IV-1* presents a brief introduction on multiply bonded system through simultaneous HB interactions and on the rational of multipoint hydrogen bonding; *Section IV-2* provides the design and the synthetic plan of 2,5-disubstituted CGP derivatives; *Section IV-3* contains the synthesis of the targeted molecules; *Section IV-4* is divided in two parts, the first one focuses on the DFT calculation results of the obtained molecule and the second describes the single component crystal structures of those compound; *Section IV-5* deals with the design of a potential tetra-chalcogen bonded recognition array through DFT calculation, its synthesis and the X-ray diffraction analysis; *Section IV-6* grants a discussion about the engineering of a heteromolecular recognition motif based on HB and EB and the achievement of such hybrid system through the analysis of co-crystals.

The work presented in this chapter has been realised with the help of *Dr. Benson Kariuki* (Cardiff University, UK) for the refinement of the crystal structure of **IV-13** and *Deborah Romito* (Cardiff University, UK), who synthesised 2-(2-(trifluoromethyl)-[1,3]selenazolo[5,4- $\beta$ ]pyridin-5-yl)oxazole **IV-29** following the procedure developed within this chapter. She also showed the compatibility of Pd cross-coupling reaction with the CGP moiety during her Master thesis on a related project.

## IV – 1 Introduction

In preceding chapters, we have attained a recognition motif built on frontal double chalcogen bonds, showed its compatibility with  $\pi$ - $\pi$  interactions and appraised the orthogonality with regard to halogen bonding interactions through different crystal structures. However, we have encountered few examples for which hydrogen-bonds, without precise recognition pattern, came into play leading to different associations at the solid-state. This chapter pursues the evaluation of the compatibility of chalcogen bonding among other non-covalent interactions, more particularly hydrogen bonding.

### IV – 1.1 Chalcogen- and hydrogen-bonding interactions

In the literature, halogen- and chalcogen-bonding are regularly compared to hydrogen-bonding and often seen as competitive interactions with the latter.<sup>[1-6]</sup> This relationship is due to the close nature of the functional groups involved in those non-covalent bonds. SBI acceptor (such as pyridine) can equally act as HB and EB acceptor. Thus, precise controlled patterns are required in order to interface XB/EB and HB interactions in a supramolecular systems.<sup>[6]</sup> In the case of chalcogen bonding, no clear example of cooperativity with HB have been described. Here we highlight two examples previously discussed showing the interference of hydrogen bonds with our CGP recognition array.

The structure of Se bearing CGP substituted with trifluorophenyl **II-21<sub>Se</sub>** (Figure IV – 1, a) forms a wire-like structure in the solid state. A single chalcogen-bonding interaction is taking place between the N atom of the selenazole ring and the facing Se atom ( $d_{N...Se} = 3.415 \text{ \AA}$ ) and a hydrogen bond between the N atom of the pyridyl moiety and one of the H atoms of the trifluorophenyl group ( $d_{N...C} = 3.419 \text{ \AA}$ ). The molecules **II-32<sub>Te</sub>**, Te containing CGP substituted with a phenyl acrylamide moiety (Figure IV – 1, b), connect through HB involving the H atom of the amide group and the N atom of the pyridyl ring ( $d_{N...N} = 2.996 \text{ \AA}$ ) and through a single EB taking place between the N atom of the same amide group and the facing Te atom.

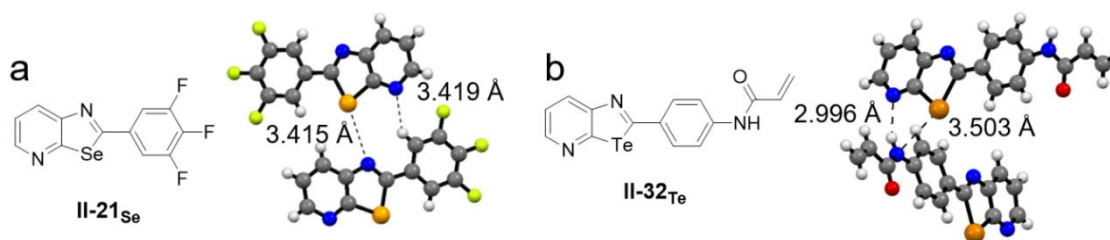
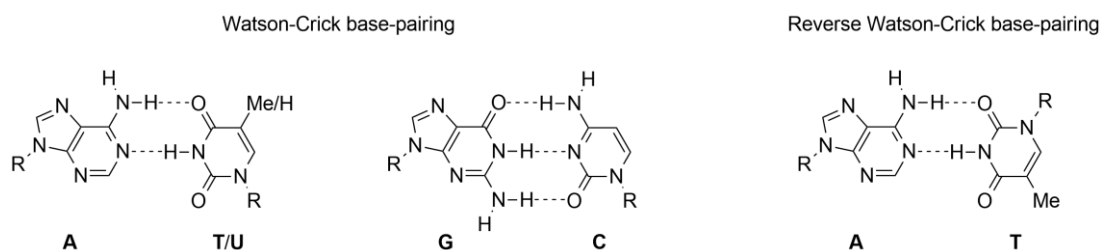


Figure IV - 1: X-ray structure of a) 2-(3,4,5-trifluorophenyl)-[1,3]selenazolo[5,4- $\beta$ ]pyridine **II-21<sub>Se</sub>** and b) N-(4-((1,3)tellurazolo[5,4- $\beta$ ]pyridin-2-yl)phenyl)acrylamide **II-32<sub>Te</sub>**. Space group:  $P2_1/c$  and  $I4/a$ , solvent of crystallisation:  $CHCl_3$  and hot toluene, respectively.

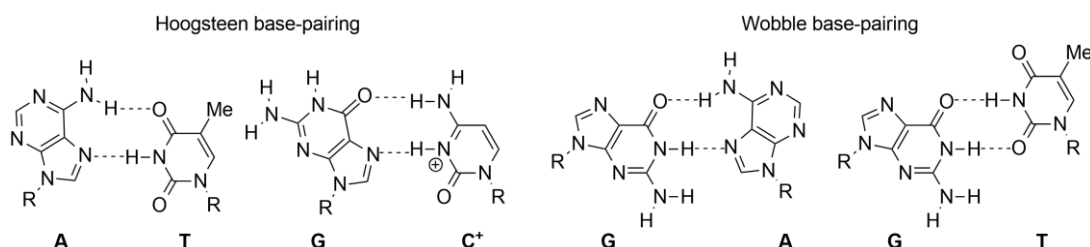
As discussed in *chapter II*, both structures present unanticipated hydrogen-bonding patterns. In the case of **II-21<sub>se</sub>**, EB takes place and is supported by HB. In the second case, the HB formation prevents dimer association through double chalcogen-bonding interactions. Those results led us to reinvestigate the bonding motifs that can be formed by hydrogen-bonds and design new molecules displaying a precise recognition motif blending the two interactions cooperatively.

#### IV – 1.2 Multivalent hydrogen-bonded system

One of the most famous examples of defined multiply hydrogen-bonded system in nature is the DNA double helix. This molecule is constituted by a phosphate deoxyribose backbone bearing nucleobases that primarily mediate the self-assembly. The four nucleobases, adenine (A), thymine (T), guanine (G) and cytosine (C), form selective hetero-dimers in the DNA as A-T and G-C through defined hydrogen-bonding patterns. In addition, the overall structure is stabilized by means of  $\pi$ - $\pi$  stacking interactions and hydrophobic effects. Moving away from the double helix structure, utilisation of single base-pairing can be tedious due to the absence of those other non-covalent interactions. Moreover, all nucleobases - plus uracil (U), which replaces thymine in RNA - offer various potential hydrogen-bonded motifs. No less than 28 possible base associations can be formed by mixing the four nucleobases.<sup>[7]</sup> The most important ones being those present in DNA and discovered by *Watson and Crick* (Scheme IV – 1).<sup>[8, 9]</sup>



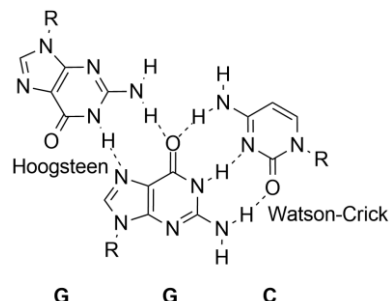
Scheme IV - 1: Watson-Crick base pairing A-T/U and G-C and an example of reverse Watson-Crick base pairing A-T.<sup>[8, 9]</sup>



Scheme IV - 2: Hoogsteen base pairing A-T and G-C<sup>+</sup> and Wobble (mismatched) base-pairing.<sup>[8, 9]</sup>

Nucleobases binding motif different from the canonical Watson-Crick geometry can be achieved when the recognition is not constrained by the double helix. For example, the reverse Watson-Crick

base-pairing is formed when one of the partner changes orientation (Scheme IV – 1). The Hoogsteen base-pairing can be achieved if different bonding sites are involved or the Wobble base-pair can be obtained in case of a mismatch (Scheme IV – 2). Even more complex organisations can be achieved by using the different recognition sites simultaneously (Scheme IV – 3).<sup>[8, 9]</sup>



Scheme IV - 3: Representation of trimer G-G-C associated through Hoogsteen and Watson-crick base-pairing motif.<sup>[8, 9]</sup>

Thus, in order to design and synthesise well defined architectures relying on multipoint hydrogen-bonded motifs, precise bonding arrays are required in addition of a deeper understanding of the nature of those associations. During the 90's *Jorgensen* established the role of secondary interactions in multiply hydrogen-bonded systems.<sup>[10, 11]</sup> Consequently a large library of high-fidelity multipoint recognition motifs has been developed. This rule states the influence of the spatial organisation of the interactions in the recognition motif in multivalent arrays due to the large electrostatic contribution of HB. In the case of a triple hydrogen-bonded systems (Figure IV – 2), three patterns are possible, namely DAD•ADA, DDA•AAD and DDD•AAA. The first one alternate between donors and acceptors, which leads to homo-repulsion between the donor and acceptor (indicated by red arrows). The second one forms two positive (indicated in blue) and two negative secondary interactions. In the last case, the three hydrogen bonds have the same orientation, which results in four positive secondary interactions, maximizing the strength of the association.

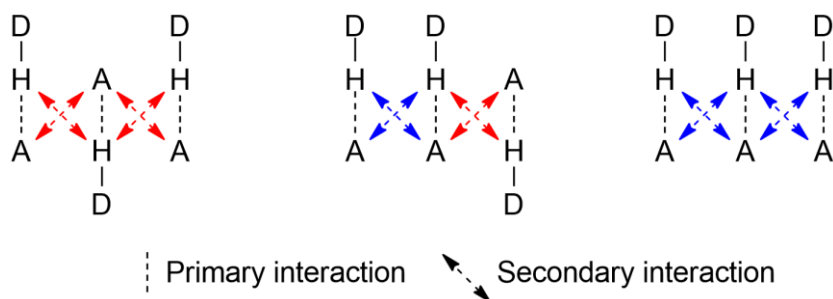
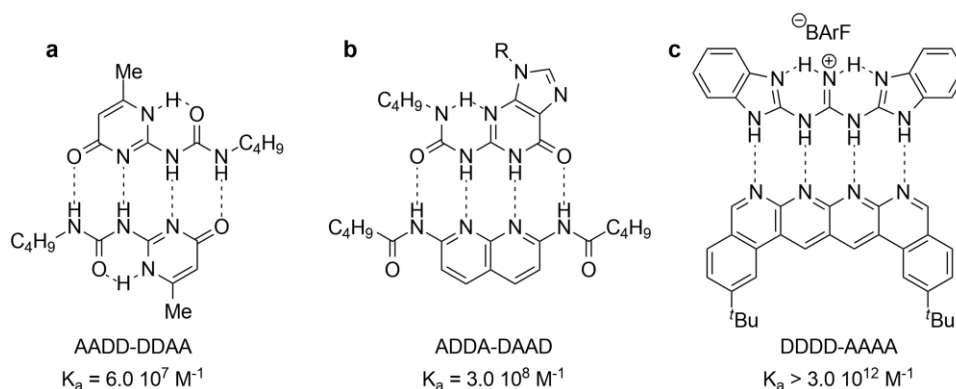


Figure IV - 2: Schematic representation of the principle of secondary interaction introduced by Jorgensen.<sup>[10, 11]</sup> D-H stands for hydrogen-bond donor and A for hydrogen-bond acceptor. Blue colour represents positive interactions while red the negative ones.

This concept has been widely used in the design of several recognition system throughout the years to tune the association constant of molecular assembly.<sup>[12-17]</sup> Here we show some examples of tetra hydrogen-bonded systems developed by *Meijer*,<sup>[18]</sup> *Zimmerman*,<sup>[19]</sup> *Leigh*,<sup>[20]</sup> and their respective co-workers. Ureidopyrimidone dimerises in an AADD•DDAA motif ( $K_a = 6 \cdot 10^7 \text{ M}^{-1}$  in  $\text{CH}_2\text{Cl}_2$ , Scheme IV – 4, a). In this case, four positive and two negative secondary interactions are observed. The hetero-complex involving 2,7-diamido-1,8-naphthyridine and an ureidoguanine derivative are formed through ADDA•DAAD ( $K_a = 3 \cdot 10^8 \text{ M}^{-1}$  in  $\text{CHCl}_3$ , Scheme IV – 4, b). An intramolecular HB prevents the change of conformation of the ureido compound and thus allow the formation of dimer which includes four negative and two positive secondary interactions. Another example of tetra hydrogen-bonded system is the DDDD•AAAA hetero-dimer formed between an iminium derivative and bis-isoquinolinonaphthyridine (Scheme IV – 4, c). The presence of the positive charge and the fact of having all the HB donor on one side and all the acceptors on the other one maximizes the strength of interaction ( $K_a > 3 \cdot 10^{12} \text{ M}^{-1}$  in  $\text{CH}_2\text{Cl}_2$ ). While the two first examples exhibit similar association constants, the third one shows an increase of four order of magnitude. This shows the importance of the geometrical design of such multiply non-covalently bonded systems.



Scheme IV - 4: Tetra hydrogen-bonded systems in a) AADD•DDAA; b) ADDA•DAAD and c) DDDD•AAAA systems with their respective association constant.<sup>[17-20]</sup> BARF =  $[(3,5-(\text{CF}_3)_2\text{C}_6\text{H}_3)_4\text{B}]^-$

Thus, if one wants to introduce hydrogen bonds in a hybrid multi-type interactions motif, there is a need of a controlled bonding array in order to avoid undesired interactions or associations. This can be achieved by pre-organisation of the supramolecular synthons leading to a high-fidelity recognition system.

## IV – 2 Strategy: Introduction of a substituent in the 5-position of the CGP scaffold

Therefore, we pursue the idea of enlarging the possibility of functionalisation of the CGP core and expanding the knowledge and understanding of multiple non-covalently bonded systems blending chalcogen-bonding with other interactions. We propose the insertion of various substituents in close proximity to the pyridyl group (Figure IV – 3). Depending on the nature of the functionality in 2- and 5-position (represented in green and orange, respectively), we foresaw different supramolecular structures at the solid state.

Face-to-face dimer association through double chalcogen bonds could be achieved by minimizing hetero-repulsions between the two substituents (Figure IV – 3, A). As developed in *Chapter II*, this discrete structure is easily obtained if a H atom sits in 5-position. If the green and orange groups do not tolerate proximity, the repulsion can be minimized through the formation of a head-to-tail ribbon involving simultaneous EB and HB (Figure IV – 3, B). A single chalcogen bond would be established by the N atom of the chalcogenazole ring ( $N_c$ ) and a hydrogen bond would take place between the N atom of the pyridyl ring ( $N_p$ ) and the facing H atom.

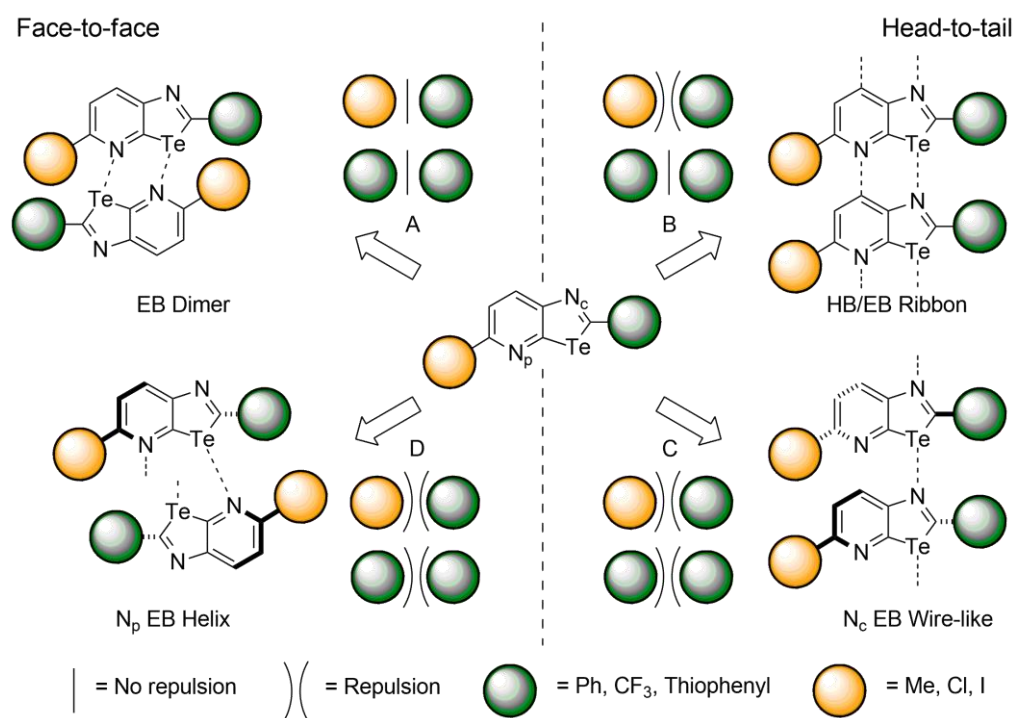


Figure IV - 3: Representation of the design of 2- and 5-substituted CGP core and the possible outcome for solid state organisation depending on the repulsion between orange and green moieties.

However, if the green moieties are self-repulsing, the CGP derivatives would not remain co-planar and either a wire-like (head-to-tail) or a helical (face-to-face) structure could be formed. A single chalcogen-bonding interaction would take place involving  $N_c$  or  $N_p$  atoms, respectively (Figure IV –

3, C or D, respectively). The key design element in those systems is the hetero- (green – orange) and homo- (green – green) repulsion between substituents (Figure IV – 3). The repulsive forces taking place here can be either of steric or electrostatic nature.

The steric demand of the substituents is a key element in this study. However, there is no physical measurement that directly relate to this concept. In this work, we will refer to the A-values as evaluation of the steric bulk of the selected groups (Table IV – 1). This factor is defined as the energy of the axial conformation over the equatorial conformation of a mono-substituted cyclohexyl derivative.<sup>[21]</sup> If a substituents has a large A-value, it is considered more sterically demanding. For the 2-position, Ph (A-value = 3.0 kcal mol<sup>-1</sup>), thiophenyl and CF<sub>3</sub> (A-value = 2.1 kcal mol<sup>-1</sup>) moieties have been chosen (value for thiophenyl was not reported in the literature but assumed intermediate between Ph and CF<sub>3</sub> groups). For the 5-position, small substituents such as Cl and I atoms (A-value = 0.43 kcal mol<sup>-1</sup> for both) and the Me group (A-value = 1.70 kcal mol<sup>-1</sup>) have been selected.

Table IV - 1: A-values for the selected 2- and 5-substituent.<sup>[21]</sup>

2-substituent	A-Value (kcal mol <sup>-1</sup> )	5-substituent	A-Value (kcal mol <sup>-1</sup> )
Ph	3.0	Me	1.70
Thiophenyl	-	Cl	0.43
CF <sub>3</sub>	2.1	I	0.43

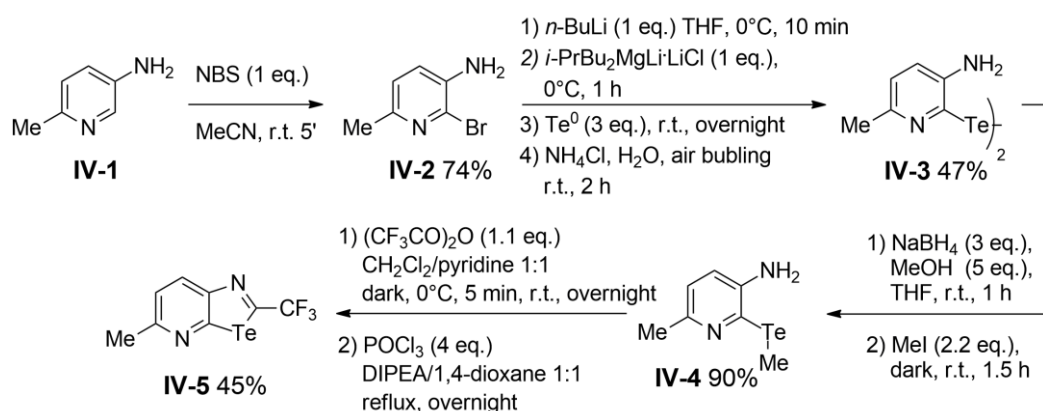
With regard to the A-values, we anticipate a face-to-face EB dimerization (Figure IV – 3, a) when Green and Orange substituents less sterically demanding are paired together (Green = CF<sub>3</sub> and Orange = Cl or I). Increasing the steric bulk of the 5-substituent (Orange = Me), and thus the hetero-repulsion, would lead to the formation of head-to-tail HB/EB ribbon. On the other hand, a more sterically demanding 2-substituent (Green = Ph or thiophenyl) would be either wire-like or helical structures due to steric hetero- and homo-repulsion. The molecules are expected to organise depending on their ability to form chalcogen bond with N<sub>c</sub> or N<sub>p</sub> atoms in the crystal packing.

## IV – 3 Synthesis

### IV – 3.1 Synthesis of Methyl 5-substituted CGP

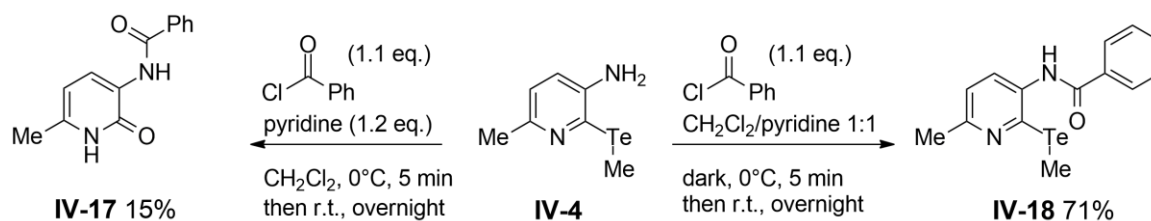
The synthesis started with the selective bromination reaction of amine **IV-1** in the presence of *N*-bromo succinimide (NBS) in MeCN (Scheme IV – 5).<sup>[22]</sup> The reaction was first tested in an NMR tube in CD<sub>3</sub>CN and the <sup>1</sup>H-NMR spectrum revealed complete conversion of the starting material into **IV-2** leaving succinimide as sole side product. The batch reaction produced similar results and the purification afforded the desired product in 74% yield. Compound **IV-2** was sequentially treated

with *n*-BuLi and trialkyl magnesate in THF and the resulting organometallic intermediate reacted with elemental Te powder. After oxidation the corresponding ditelluride **IV-3** was obtained in 47% yield. It has to be noted that compound **IV-2** is more electron rich than 3-amino-2-bromopyridine due to the presence of the Me group, resulting in a slower metal-halogen exchange (1 h and 0.5 h, respectively). Reductive cleavage was then performed on derivative **IV-3** in the presence of NaBH<sub>4</sub> and MeOH in THF and the tellurolate intermediate quenched with MeI leading to amine **IV-4** in excellent yield. Finally, the one-pot amidation/cyclisation reaction was performed using (CF<sub>3</sub>CO)<sub>2</sub>O in a 1:1 mixture of pyridine and CH<sub>2</sub>Cl<sub>2</sub> followed by the addition of POCl<sub>3</sub> in 1:1 DIPEA:dioxane solution at reflux affording compound **IV-5** in 45% yield.



Scheme IV - 5: Representation of the synthesis of **IV-5**.

During an attempt to synthesise benzamide **IV-18** (Scheme IV – 6) using the reaction conditions reported in *Chapter II*, decomposition of amine **IV-4** was observed and only compound **IV-17** could be isolated (confirmed by single crystal X-ray diffraction, Figure II – 4). The difference in the  $pK_a$  values of pyridine ( $pK_a = 5.25$ ) and picoline ( $pK_a = 6$ ) have been previously reported, showing that the introduction of the methyl moiety leads to a higher basicity.<sup>[23]</sup> A similar difference could be expected between **IV-4** and its non-substituted analogue, which contain the same functionalities. The product of the reaction could then react with water, leading to **IV-17**, through nucleophilic aromatic substitution due to protonation in solution. The structure of this compound was unambiguously identified by X-ray diffraction analysis. Thus, an excess of pyridine was used (Scheme IV – 6) in the reaction media to afford desired compound **IV-18** in good yield.



Scheme IV - 6: Representation of the synthesis of product **IV-17** and **IV-18**.

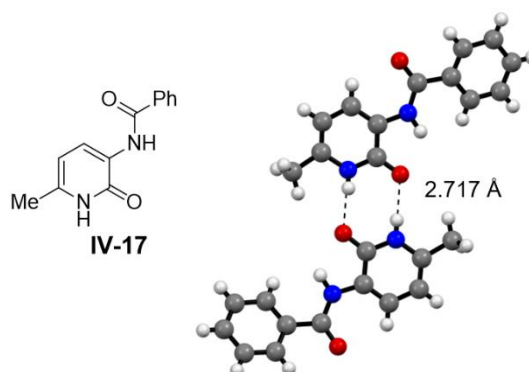
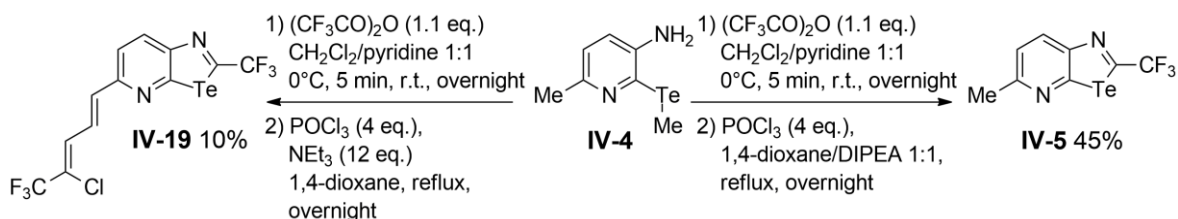


Figure IV - 4: X-ray structure of product **IV-17**. Space group:  $P2_1/n$ . Solvent of crystallisation: MeOH.

The modified amidation protocol developed for compound **IV-18** (Scheme IV – 6) was applied in an attempt to form **IV-5** from **IV-4** following one pot reaction procedure (Scheme IV – 7). However, unexpected compound **IV-19** was obtained as major product. Even if the mechanism leading to such a product remains uncertain, replacing  $\text{NEt}_3$  by an excess of DIPEA afforded desired **IV-5** product in 45% yield (Scheme IV – 7).

The structure of **IV-19** was confirmed by X-ray diffraction analysis (Figure IV – 5). The crystals grow in a  $P\bar{1}$  space group by slow evaporation of a  $\text{CHCl}_3$  solution. The molecules arranged in a flat polymeric arrangement held together by means of double chalcogen-bonding interactions between Cl and Te atoms ( $d_{\text{Cl}\dots\text{Te}} = 3.974 \text{ \AA}$ ) and double hydrogen-bonding interactions between H and N atoms ( $d_{\text{N}\dots\text{C}} = 3.560 \text{ \AA}$ ). Derivative **IV-19** features a small substituent in 2-position ( $\text{CF}_3$ ) and a larger group in 5-position (4-chloro-5,5,5-trifluoropenta-1,3-diene). According to the general scheme (Figure IV – 3), hetero-repulsion should drive the crystal packing towards a ribbon, a wire-like or a helical structure. However, the chlorine atom at the 4-position of the pentadiene form a chalcogen bond, which leads to a face-to-face EB dimer. On the contrary to our original CGP design, the lone pair donor and the chalcogen atom are distant from each other in the molecular structure. This could be interesting to engineer new recognition array relying on molecular synthons featuring the EB donor and acceptors sites on two different part of the molecule.



Scheme IV - 7: Synthesis of **IV-19**.

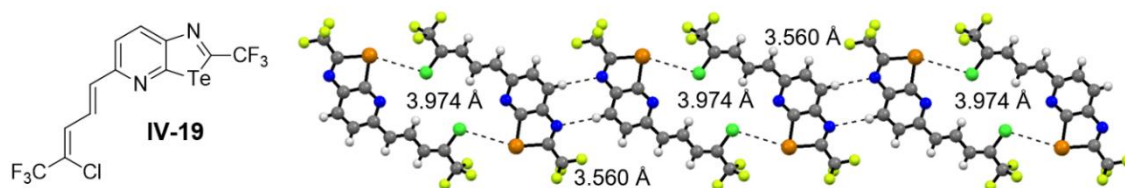
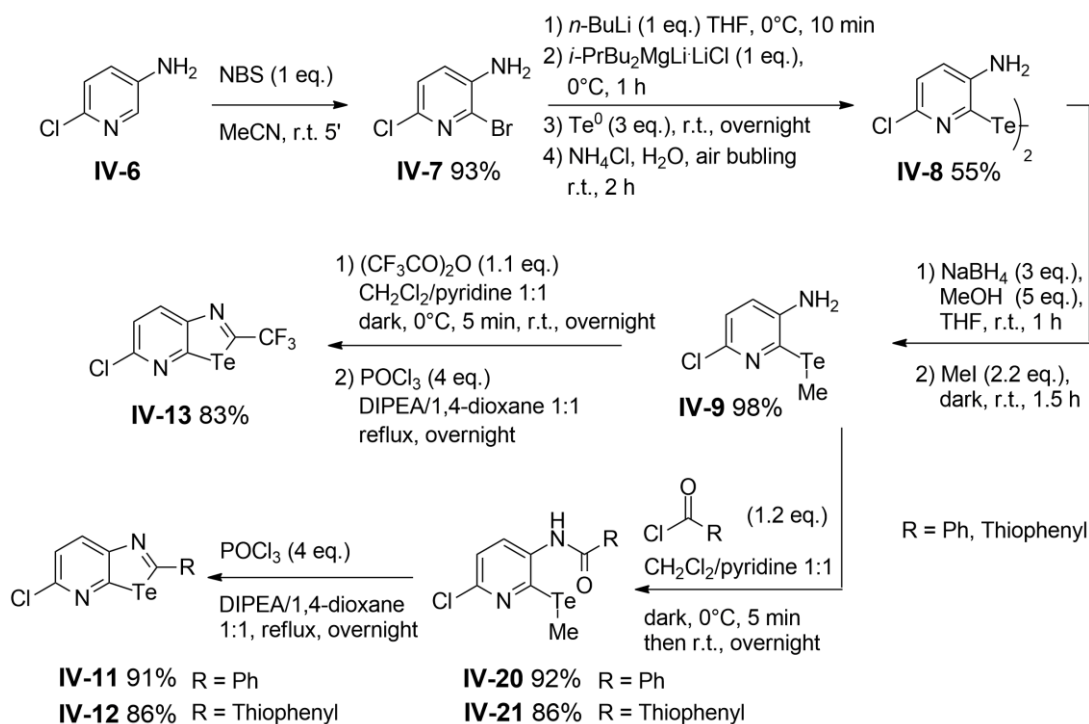


Figure IV - 5: X-ray structure of **IV-19**. Space group  $P\bar{1}$ , solvent of crystallisation:  $\text{CHCl}_3$ .

### IV – 3.2 Synthesis of Halogen 5-substituted CGP

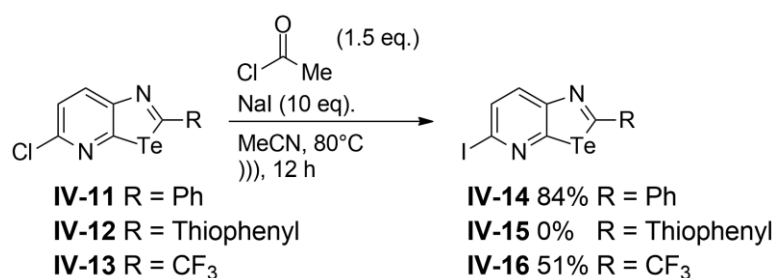
Moving to the Cl and I 5-substituted CGP molecules, the synthesis commenced with the bromination of 6-chloropyridin-3-amine using NBS in MeCN affording selectively compound **IV-7** in excellent yield (Scheme IV – 8). Resulting 2-bromo-6-chloropyridin-3-amine was then sequentially treated with one equivalent of *n*-BuLi and one equivalent of trialkyl magnesate in THF at 0°C. The organometallic intermediate was reacted with elemental Te powder and, after oxidation, afforded bitelluride **IV-8** in 55% yield. The latter compound underwent reductive cleavage in the presence of  $\text{NaBH}_4$  and MeOH in THF at room temperature and the resulting telluroate was treated with MeI affording compound **IV-9** in excellent yield (98 %). The resulting amine was reacted with  $(\text{CF}_3\text{CO})_2\text{O}$  in  $\text{CH}_2\text{Cl}_2$  and pyridine to afford the corresponding amide, which was cyclised in the presence of  $\text{POCl}_3$  in DIPEA and 1,4-dioxane leading to derivative **IV-13** in 83 % yield.



Scheme IV - 8: Synthesis of **IV-11**, **IV-12** and **IV-13**.

In parallel, amine **IV-9** could be transformed into benzamide **IV-20** and thiophenyl carboxamide **IV-21** in excellent yield upon reaction with the corresponding acyl chloride in the dark in  $\text{CH}_2\text{Cl}_2$  and pyridine (Scheme IV – 8). Both amides could then be transformed into targeted derivatives **IV-11** and **IV-12**, respectively, by dehydrative cyclisation using  $\text{POCl}_3$ .

Finally, an iodine-chlorine exchange was performed (Scheme IV – 9) using the protocol developed in the work of *Bissember* and *Banwell*.<sup>[24]</sup> Under microwave irradiation, chloro-derivatives **IV-11** and **IV-13** were reacted with NaI in the presence of acetyl chloride in MeCN at  $80^\circ\text{C}$  leading to the formation of iodine containing molecules **IV-14** and **IV-16**, respectively. Complete conversion could not be reached for **IV-12**, affording an inseparable mixture of chloro- and iodo- derivatives.



Scheme IV - 9: Synthesis of iodo-derivatives **IV-14** and **IV-16**.

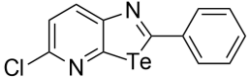
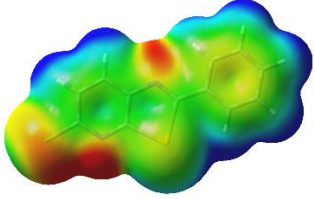
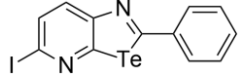
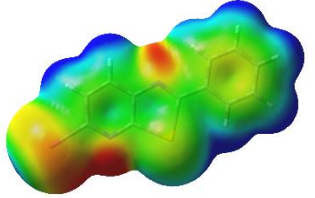
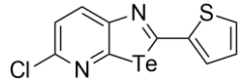
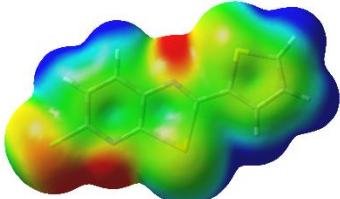
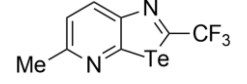
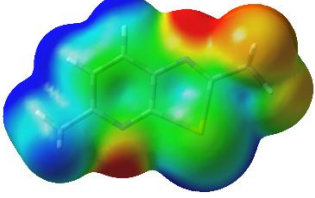
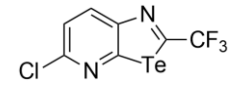
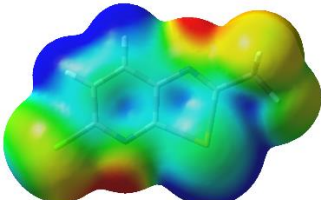
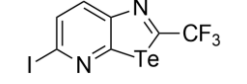
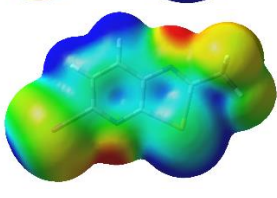
## IV – 4 Solid-state analysis

### IV – 4.1 Electrostatic surface potential

ESP maps of the synthesised compound (Table IV – 2) were computed to support the different crystal packing discussed in this section. The table organises the molecules from most to less sterically demanding 2-substituent. As one can notice, the potential values around  $N_p$  atoms are influenced by the substituent in 2-position. In particular, the  $V_{s,\text{max}}$  for  $N_p$  in the case of phenyl- and thiophenyl-bearing molecules **IV-11**, **IV-12** and **IV-14** are larger ( $V_{s,\text{max}} = -28.8$ ,  $-26.3$ ,  $-28.5$   $\text{kcal mol}^{-1}$ , respectively) than for  $\text{CF}_3$  bearing derivatives **IV-5**, **IV-13**, **IV-16** ( $V_{s,\text{max}} = -21.6$ ,  $-21.9$  and  $-20.1$   $\text{kcal mol}^{-1}$ , respectively). On the contrary, potential values around  $N_c$  are less negative phenyl ( $V_{s,\text{max}} = -14.1$  and  $-13.8$   $\text{kcal.mole}^{-1}$  for **IV-11** and **IV-14**, respectively), than for thiophenyl ( $V_{s,\text{max}} = -18.8$   $\text{kcal mol}^{-1}$  for **IV-12**) and particularly  $\text{CF}_3$  moieties ( $V_{s,\text{max}} = -23.2$ ,  $-19.6$  and  $-20.1$  for **IV-5**, **IV-13** and **IV-16**, respectively). The  $\sigma$ -hole ( $\alpha$ ) of the Te atom follows a similar trend, being more positive moving from phenyl ( $V_{s,\text{max}} = +10.5$  and  $+11.0$   $\text{kcal.mol}^{-1}$  for **IV-11** and **IV-14**, respectively), thiophenyl ( $V_{s,\text{max}} = +12.5$   $\text{kcal.mol}^{-1}$  for **IV-12**) to  $\text{CF}_3$  groups ( $V_{s,\text{max}} = +17.6$ ,  $+21.9$ ,  $+22.3$   $\text{kcal.mol}^{-1}$  for **IV-5**, **IV-13** and **IV-16**, respectively). Interestingly, the  $\sigma$  hole of the halogen atoms is also influenced by the substituent in 2-position, being more positive in the presence of EWG. The  $V_{s,\text{max}}$  values are, for the Cl atoms,  $+3.8$   $\text{kcal.mol}^{-1}$  for phenyl and thiophenyl derivatives (**IV-11** and **IV-12**,

respectively), and +9.5 kcal.mol<sup>-1</sup> for CF<sub>3</sub> moiety (IV-13). For the I atom, the potential value of the  $\sigma$ -hole is +13.9 kcal.mol<sup>-1</sup> for phenyl IV-14 and +19.1 kcal.mol<sup>-1</sup> for CF<sub>3</sub> derivatives IV-16.

Table IV - 2: Representation of selected molecules IV-5 and IV-11-16 and their respective ESP map with their associated  $V_{s,max}$  values (expressed in kcal mol<sup>-1</sup>) for  $N_p$ ,  $N_c$ ,  $\sigma$  hole [ $\alpha$ ] of the Te atom and  $\sigma$  hole of the halogen if applicable.

Compound	ESP map	$V_{s,max}$			
		$N_p$	$N_c$	$\sigma$ hole ( $\alpha$ )	$\sigma$ hole halogen
IV-11 		-28.8	-14.1	+10.5	+3.8
IV-14 		-26.3	-13.8	+11.0	+13.9
IV-12 		-28.5	-18.8	+12.5	+3.8
IV-5 		-21.6	-23.2	+17.6	-
IV-13 		-21.9	-19.6	+21.9	+9.5
IV-16 		-20.1	-19.4	+22.3	+19.1

-0.025 a.u.  +0.025 a.u.

## IV – 4.2 Single component crystals

IV – 4.2.1 CF<sub>3</sub> substituted derivatives: face-to-face dimer vs head-to-tail ribbon

In order to appraise the multiply bonded design introduced in section IV – 2 (Figure IV - 3), single crystals suitable for X-ray diffraction analysis have been grown. Molecules **IV-5** and **IV-13** exhibit a CF<sub>3</sub> moiety in 2-position and either a Me or Cl in 5-position, respectively (Figure IV – 6). The crystals are isostructural and grow in a P2<sub>1</sub>/m space group despite having seemingly different electrostatic surface potential maps. Their asymmetric unit contains only one molecule that forms ribbons at the solid state through single chalcogen-bonding ( $d_{\text{Nc}\cdots\text{Te}} = 3.423 \text{ \AA}$  and  $3.406 \text{ \AA}$  with C-Te $\cdots$ N angles =  $179^\circ$  and  $177^\circ$  for **IV-5** and **IV-13**, respectively) and a directional single hydrogen-bonding interaction ( $d_{\text{Np}\cdots\text{C}} = 3.420 \text{ \AA}$  and  $3.385 \text{ \AA}$  with C-Te $\cdots$ N angles =  $178^\circ$  and  $180^\circ$ , respectively). In addition, molecules  $\pi$ - $\pi$  stack in a head-to-tail fashion ( $d_{\pi-\pi} = 3.529 \text{ \AA}$  and  $3.484 \text{ \AA}$ , respectively).

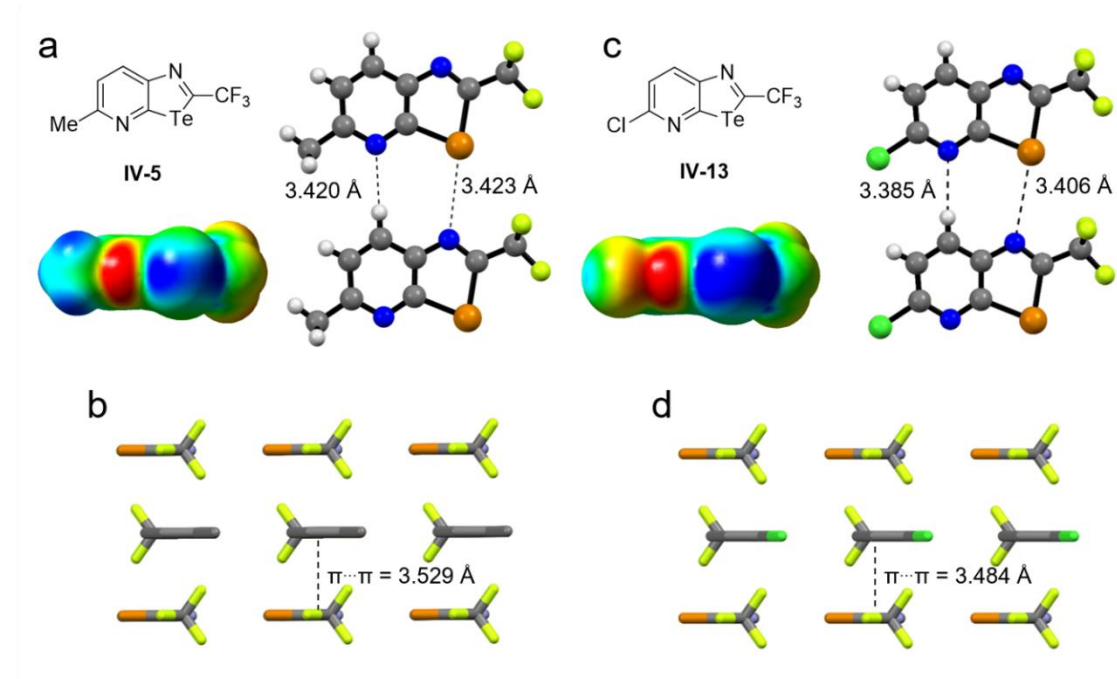


Figure IV - 6: X-ray structure and their respective ESP map of a) **IV-5**; c) **IV-13**; b)  $\pi$ - $\pi$  stacking arrangements of **IV-5**; d)  $\pi$ - $\pi$  stacking arrangements of **IV-13**. Space group: P2<sub>1</sub>/m, Solvent of crystallisation: CHCl<sub>3</sub>.

The two molecules organise in the same crystal packing while the two substituents in 5-position have different steric bulk (A-value =  $1.30 \text{ kcal.mol}^{-1}$  for Me group and  $0.43 \text{ kcal.mol}^{-1}$  for Cl atom) and different electrostatic map (Me group being mostly positive and Cl atom mostly negative, Figure IV – 6). The two hetero-repulsions (CF<sub>3</sub> $\cdots$ Me and CF<sub>3</sub> $\cdots$ Cl) are different in nature. The one involving Me group is mainly steric, while the one involving Cl atom is steric and electrostatic. These structures indicates that we can rely on both kinds of repulsive forces to direct the organisation of the 2,5-disubstituted CGP derivatives into an HB/EB ribbon (Figure IV – 7) and prevent the formation of discrete EB dimer.

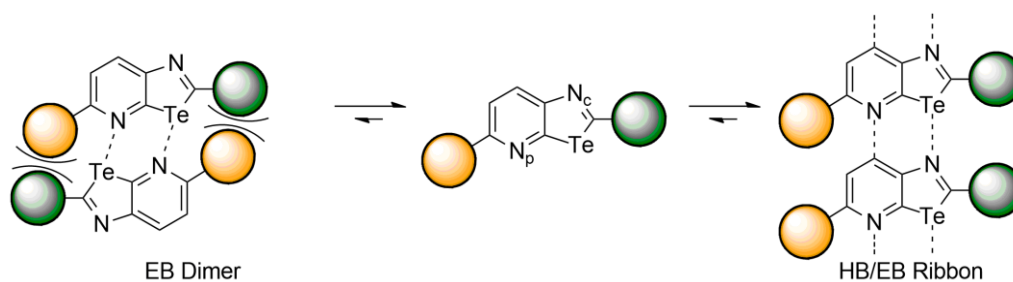


Figure IV - 7: Equilibrium leading to the formation of HB/EB ribbon over EB dimer.

Moving to iodo-derivative **IV-16**, the compound crystallises in a  $C2/c$  space group and the asymmetric unit contains one molecule. The x-ray analysis of this material (Figure IV – 8, a) revealed the formation of EB dimer between the CGP moieties ( $d_{N...Te} = 3.217 \text{ \AA}$ ,  $C-Te...N$  angle =  $176^\circ$ ). In this case, the distance of interaction is longer than that obtained with **II-25<sub>Te</sub>** ( $d_{N...Te} = 2.912 \text{ \AA}$ ) discussed in *chapter II*. This difference suggests that the dimer association is weaker in the case of **IV-16** than **II-25<sub>Te</sub>**. For the iodo-derivative the hetero-repulsion between I atom and the  $CF_3$  moiety forces an angle between the plane of the two, CGPs (dihedral angle =  $64^\circ$ ) which weakens the interactions. Moreover, (**IV-16**)<sub>2</sub> associates through double hydrogen-bonding interactions ( $d_{N...H} = 3.486 \text{ \AA}$ ) which bring the dimers in a polymeric arrangement. The combination of interactions leads to the formation of a kinked ribbon in the solid state (Figure IV – 8, c). In addition,  $\pi-\pi$  stacking can be observed ( $d_{\pi-\pi} = 3.824 \text{ \AA}$  with an off-set of  $2.585 \text{ \AA}$ ) and each stack is connected to each other through halogen bonding where the I atom acts as a donor and an acceptor of electron at the same time (Figure IV – 8, b). This behaviour is easily explained by the ESP map where the  $\sigma$ -hole and the electron belt of the I atom are clearly visible.

Interestingly, different crystal packing was obtained moving from chloro-derivative **IV-13** to iodo-derivative **IV-16**, suggesting that the  $CF_3...I$  repulsion is weaker than that of  $CF_3...Cl$ . However, the two halogens have the same steric requirement as indicated by the A-value ( $0.43 \text{ kcal.mol}^{-1}$ ). The difference in organisation can be rationalised by a weaker electrostatic contribution of the hetero-repulsion in the case of **IV-16** compared to that of **IV-13**. This is supported by ESP being less negative around the I atom than around the Cl atom (Figure IV – 6 and 8). Thus, the overall repulsive forces are weaker for  $CF_3...I$  compared that of  $CF_3...Cl$ , leading to the formation of an EB dimer for compound **IV-16** and a HB/EB ribbon for derivative **IV-13**. This result shows that the hetero-repulsion is a key element in the formation of discrete dimers through double chalcogen-bonding interactions.

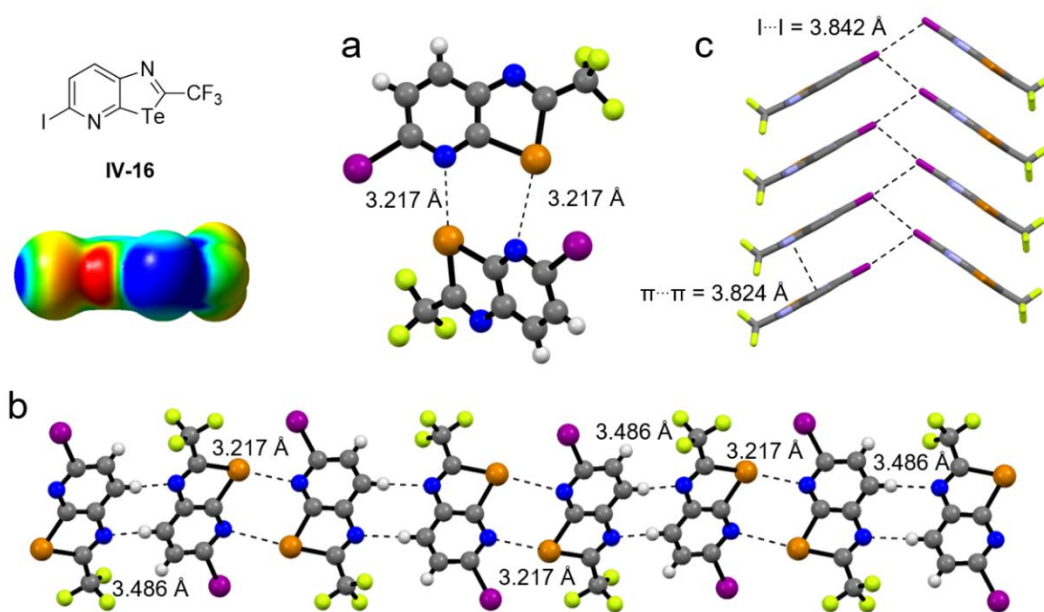


Figure IV - 8: X-ray structure of **IV-16** and its ESP map, highlighted are a) dimer; b) kinked ribbon; c)  $\pi$ - $\pi$  stacking and halogen-bonding interactions, H atoms are omitted for clarity. Space group C2/c, Solvent of crystallisation:  $\text{CHCl}_3$ .

#### IV – 4.2.2 Phenyl and thiophenyl substituted derivatives: wire-like structures

Compound **IV-11** crystallises in a Pbc space group and the asymmetric unit consists in one molecule. X-ray diffraction analysis reveals a wire-like arrangement<sup>[25]</sup> (Figure IV – 9, a). The CGP derivatives connect through single EB interactions between the  $\text{N}_c$  atom and the facing Te atom ( $d_{\text{N}\cdots\text{Te}} = 3.464 \text{ \AA}$ ,  $\text{C-Te}\cdots\text{N}$  angle =  $177^\circ$ ).

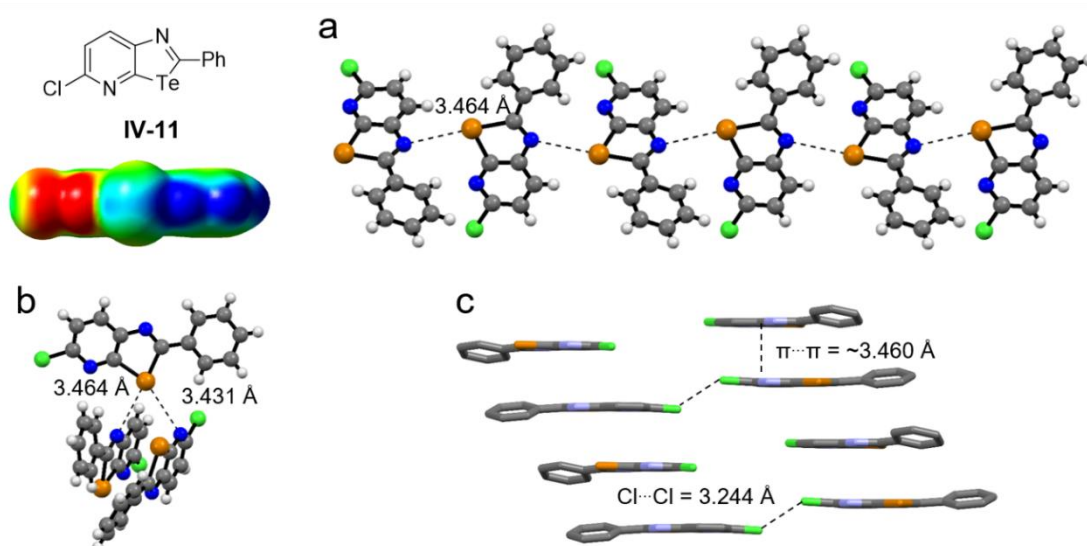


Figure IV - 9: X-ray structure of **IV-11** and its ESP map, are highlighted a) the wire-like structure; b) EBs linking wire-like structure together; c)  $\pi$ - $\pi$  stacking and halogen-bonding interactions, H atoms are omitted for clarity. Space group Pbc, solvent of crystallisation:  $\text{CHCl}_3$ .

Wire-like structures are connected together through another EB taking place between the  $N_p$  and  $\sigma$ -hole ( $\beta$ ) of the Te atom ( $d_{N\dots Te} = 3.431 \text{ \AA}$ , C-Te $\cdots$ N angle =  $153^\circ$ , Figure IV – 9, b). In addition, the molecules form  $\pi$ - $\pi$  stacking interactions in a quasi-parallel fashion (estimated  $d_{\pi-\pi} = 3.460 \text{ \AA}$ ) and the columnar arrangements are connected together through halogen bonds ( $d_{Cl\dots Cl} = 3.244 \text{ \AA}$ ) involving the negative belt and the sigma hole of the Cl atom (Figure IV – 9, c; see also ESP).

Moving to the iodo-derivative **IV-14**, the material crystallises in a  $P2_1/c$  space group and its asymmetric unit contains two crystallographically independent molecules. These arrange in a wire-like structure (Figure IV – 10, b) through single chalcogen bonding interactions involving the  $N_c$  atom ( $d_{N\dots Te} = 3.460 \text{ \AA}$  and  $3.582 \text{ \AA}$ , C-Te $\cdots$ N angles =  $176^\circ$ ). Hydrogen bonds are present between the  $N_p$  atom and one of the H atoms of the Ph moiety ( $d_{N\dots C} = 3.237 \text{ \AA}$  and  $3.321 \text{ \AA}$ ). In addition, the molecules  $\pi$ - $\pi$  stack in a quasi-parallel head-to-tail fashion (estimated  $d_{\pi-\pi} = 3.542 \text{ \AA}$ ). Those columns connect together through  $\pi$ - $\sigma^*$  interaction involving the I atom ( $d_{C\dots I} = 3.505 \text{ \AA}$ ) to form herringbone arrangement.

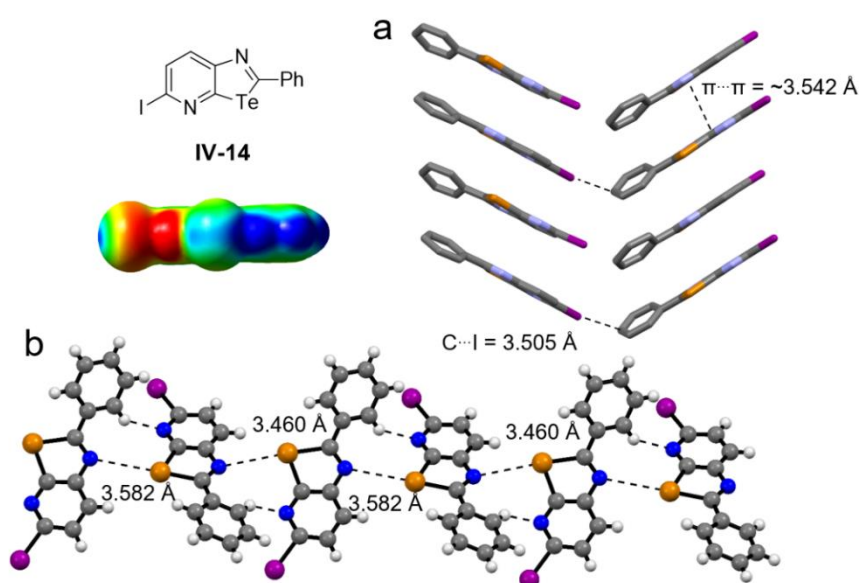


Figure IV - 10: X-ray structure of **IV-14** and its ESP map, are highlighted a) the herringbone columnar arrangement formed by  $\pi$ - $\pi$  stacking and halogen-bonding interaction, H atoms are omitted for clarity; b) wire-like structure. Space group  $P2_1/c$ , solvent of crystallisation:  $CHCl_3$ .

Finally, compound **IV-12** crystallises in a  $P2_1/c$  space group and its asymmetric unit contains 2 crystallographically independent molecules. Those arrange in a wire-like structures (Figure IV – 11) through single chalcogen-bonding interactions involving  $N_c$  atom and the facing Te atom ( $d_{N\dots Te} = 3.385 \text{ \AA}$ , C-Te $\cdots$ N angle =  $176^\circ$ ). In this case, the thiophenyl moiety behaves similarly to the phenyl group of molecule **IV-11**.

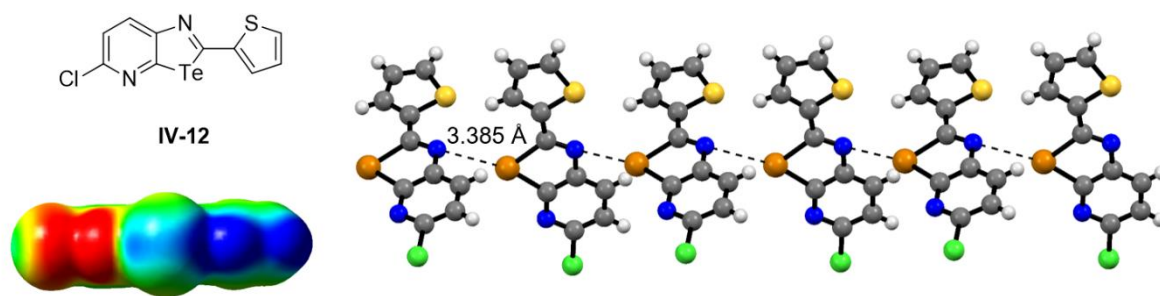


Figure IV - 11: X-ray structure of **IV-12** and its ESP map. Space group  $P2_1/c$ . Solvent of crystallisation:  $CHCl_3$ .

Combination of hetero- and homo-repulsion leads to the formation of the wire-like structure over the EB dimer and HB/EB ribbon. The crystal structure of **IV-11**, **IV-14** and **IV-12** show the arrangement at the solid state of 2,5-disubstituted CGP derivative bearing sterically demanding substituents in the 2-position (phenyl,  $A$ -value =  $3.0 \text{ kcal mol}^{-1}$ , and thiophenyl). Those molecules form wire-like structures through  $N_c \cdots Te$  chalcogen-bonding interactions. This arrangement is favoured due to the intermolecular hetero- and homo-repulsion of substituents in 2- and 5-position as anticipated (Figure IV – 3). Surprisingly, the more electron rich  $N_p$  atom (compare to  $N_c$  atom) did not drive the crystal packing to form a helical structure. The pyridyl moiety only engages in a chalcogen-bonding interaction with the  $\sigma$ -hole ( $\beta$ ) in the structure of **IV-11** (Figure IV – 9) and hydrogen-bonding in the packing of **IV-14** (Figure IV – 10).

Thus, from the four anticipated supramolecular arrangements, EB dimer, HB/EB ribbon and EB wire-like have been achieved. At the molecular level, one can easily store the recognition information in 2,5-disubstituted CGP building block aiming for a specific structure by choosing the relevant substituent to increase or decrease the hetero- and homo-repulsion. The wire-like structure is easily obtained by using a group of the size of a phenyl moiety in 2-position and a substituent in 5-position. The ribbon arrangement is achieved if the substituent in 2-position is not self-repulsing and allows hetero-repulsion with the group in 5-position. However, the dimerisation in the presence of a substituent in 5-position is still difficult to control in a reliable fashion.

## IV – 5 En route to a homo-molecular self-recognition system through tetra-chalcogen-bonding interactions

### IV – 5.1 Head-to-tail vs face-to-face: from ribbon to dimer

During the course of this work, we aim to synthesize a 5-substituted CGP molecule, which would reliably lead to the formation of a face-to-face dimer through multiple chalcogen bonds. Such a structure could be achieved exploiting both  $\sigma$ -holes of the chalcogen atom (Figure IV – 12). Conceptually, the molecular synthon should bear a second electron donor moiety ( $N_p$ ) in close

proximity to the pyridyl group. Hetero-repulsion between the groups in 2- and 5-positions must be limited to form discrete dimer, substituents will be chosen especially. Particularly, the presence of a  $N_Y$  substituent could also lead to the formation of an additional hydrogen bond which could favour the head-to-tail ribbon formation (Figure IV – 12).

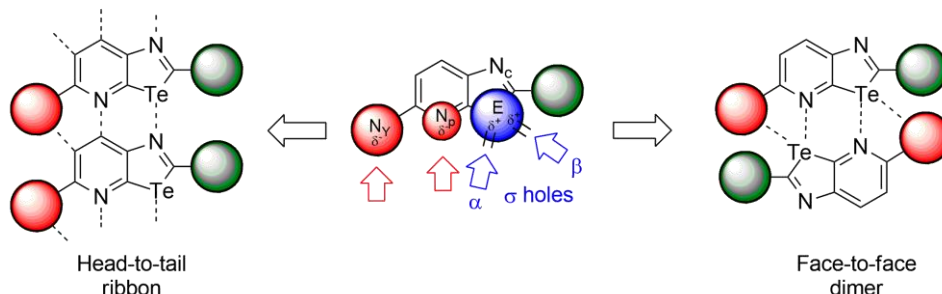


Figure IV - 12: Design of CGP building block bearing a lone pair donor substituent in 5-position and two possible supramolecular arrangement, left head-to-tail ribbon; right, face-to-face dimer.

The iterative design of the supramolecular synthons is reported in Figure IV – 13, geometry optimisations of the expected dimers were performed in vacuum at B3LYP/LanL2DZ<sup>[26, 27]</sup> level of theory and ESP maps were realized at B97D3/def2-TZVP<sup>[28-30]</sup> using Gaussian09 including the D01 revision.<sup>[31, 32]</sup>

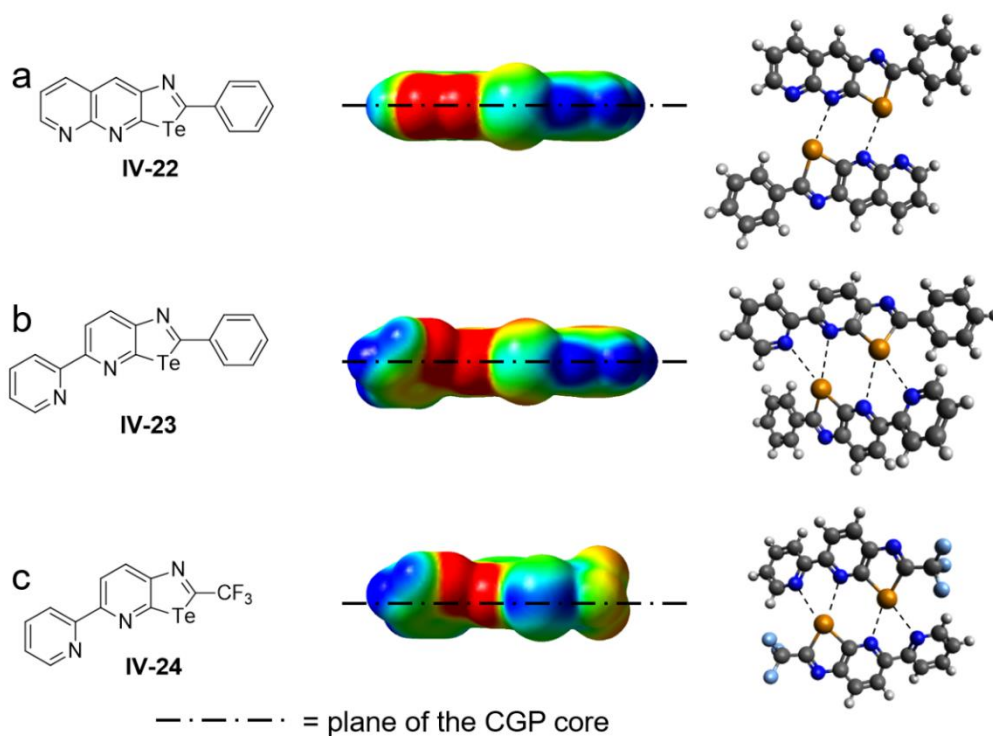


Figure IV - 13: Optimised geometries and ESP map of a) 2-phenyl-[1,3]tellurazolo[5,4-β][1,8]naphthyridine **IV-22**; b) 2-phenyl-5-(pyridin-2-yl)-[1,3]tellurazolo[5,4-β]pyridine **IV-23** and c) 5-(pyridin-2-yl)-2-(trifluoromethyl)-[1,3]tellurazolo[5,4-β]pyridine **IV-24**. Level of theory: B97D3/def2-TZVP for the ESP maps and B3LYP/LanL2DZ for geometries using Gaussian09 including the D01 revision.

In an initial approach, molecule **IV-22** was been envisaged (Figure IV – 13, a), the 1,8-naphthyridyl moiety minimizing hetero-repulsion, a flat dimer can be formed. However, one of the N atoms is out of alignment to interact through chalcogen bond. A 2,2'-bipyridyl moiety was proposed with molecule **IV-23** (Figure IV – 13, b) and its cove structure is expected to embrace both  $\sigma$ -holes of the Te atom. Geometry optimisation showed a dimer formation in gas phase with the two N atoms interacting with the Te atom (C-Te $\cdots$ N angles = 163° and 160°). In this case, the pyridyl substituent is not co-planar to the CGP moiety (dihedral angle = 35°). Moreover, the two sub-units of the dimer are not co-planar due to hetero-repulsion (steric hindrance) between the substituents in 2- and 5-position of the CGP core (dihedral angle = 16°). In molecule **IV-24**, replacing the phenyl group by a CF<sub>3</sub> moiety reduces the steric clash (Figure IV – 13, c) and increase the size of the  $\sigma$ -holes on the Te atom (ESP maps). Nevertheless, the dimers formed does not adopt a flat arrangement (dihedral angle = 13°).

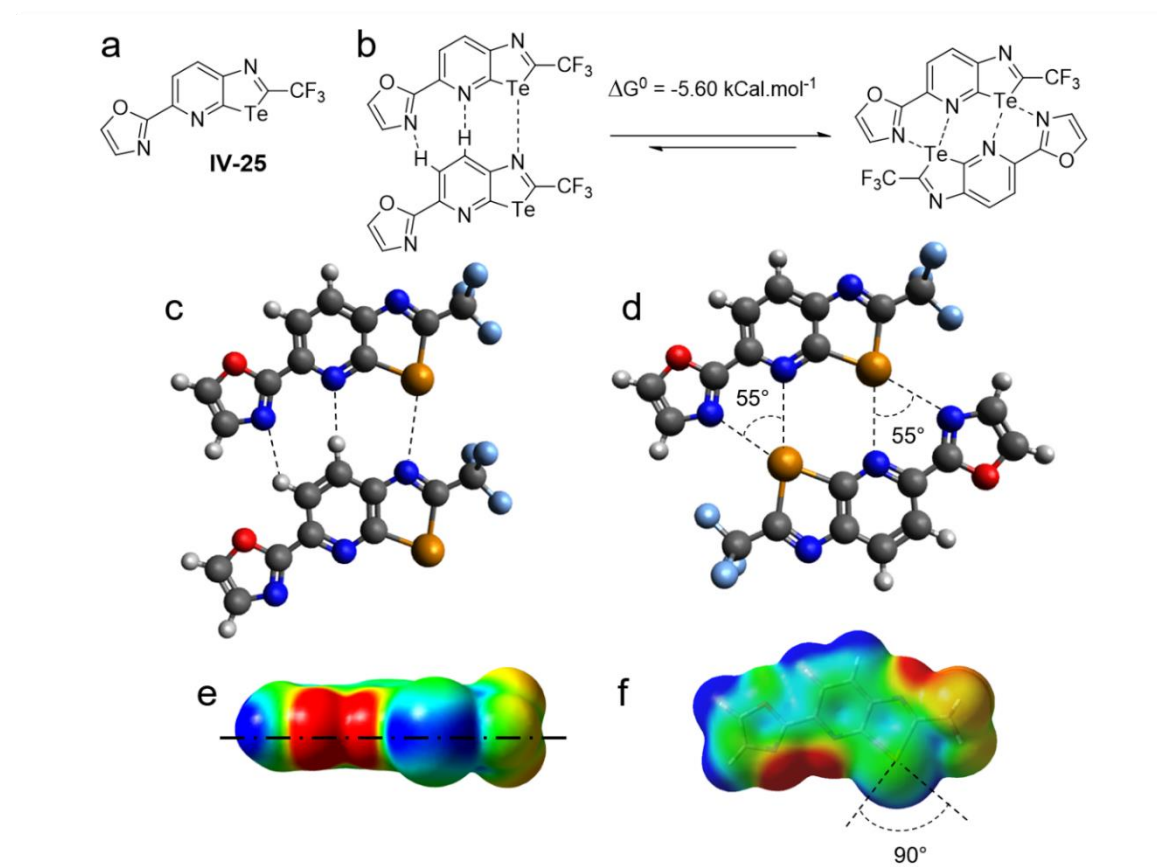


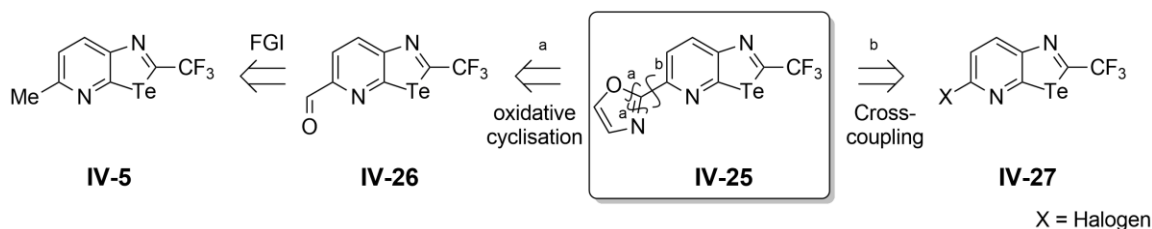
Figure IV - 14: a) Molecular structure of 5-(oxazol-2-yl)-2-(trifluoromethyl)-[1,3]tellurazolo[5,4- $\beta$ ]pyridine **IV-25**; b) difference of free enthalpy between HB/EB dimer and EB dimer structures c) optimised geometry of the head-to-tail dimer; d) optimised geometry of the face-to-face dimer; e) ESP map, side view; f) ESP map, top view. Level of theory: B97D3/def2-TZVP for the ESP maps and B3LYP/LanL2DZ for geometries using Gaussian09 including the D01 revision.

Building on those results, molecule **IV-25** bearing an oxazole as substituent was proposed (Figure IV – 14, a). Calculation predicted a flat dimer arrangement where both N atoms are aligned with

the C-Te sigma bonds (C-Te...N angles = 167° and 172°; Figure IV – 14, d). Structure of 2-(2-(trifluoromethyl)-[1,3]tellurazolo[5,4-β]pyridin-5-yl)oxazole **IV-25** was thus selected as model design. The association of two molecules of **IV-25** in a head-to-tail fashion through EB and HB interactions as found in the ribbon structure has also been considered. Geometry optimisation of this structure was performed (Figure IV – 14, c). The Gibbs free energy between the two possible conformations was evaluated in gas phase including the counterpoise correction ( $\Delta G^0 = -5.60$  kcal.mol<sup>-1</sup>) and favours the face-to-face dimer formation (Figure IV – 14, b). Further analysis of the optimised geometry of face-to-face dimer (**IV-25**)<sub>2</sub> reveals a N...Te...N angle of 55°, which does not match with the 90° angle observed between the two sigma holes (Figure IV – 14, d and f). In the literature, bifurcated chalcogen bonds are usually established with an angle included between 88 and 134°. [33-36] This mismatch could possibly destabilise the resulting dimer and lead to a head-to-tail ribbon.

#### IV – 5.2 Retrosynthetic analysis

Introduction of the oxazole moiety on the CGP scaffold can be performed in two ways (Scheme IV – 10). The first pathway (a) consists in performing an oxidative cyclisation on aldehyde **IV-26** which can be obtained by functional group interconversion (FGI) of the Me group in 5-position of tellurazolopyridine **IV-5**. Selective oxidation of Me moiety can be achieved by reaction with SeO<sub>2</sub>. [37]



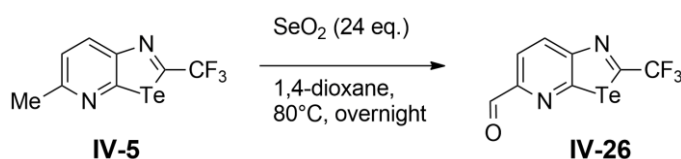
Scheme IV - 10: Retrosynthetic analysis of 2-(2-(trifluoromethyl)-[1,3]tellurazolo[5,4-β]pyridin-5-yl)oxazole **IV-25**.

The second pathway (b) relies on a Negishi cross-coupling reaction from CGP **IV-27** bearing a halogen atom in the 5-position. This strategy has been inspired by the work of *Piersanti, Minetti* and co-workers, who have reported the synthesis of 3-nitro-6-oxazol-2-ylpyridine-2-carbonitrile through the insertion of an oxazole moiety on a pyridyl derivative starting from the corresponding chlorinated analogue. [38]

#### IV – 5.3 Synthesis: Oxidative cyclisation pathway

The first step of this synthesis requires the selective oxidation of the Me in 5-position of the CGP derivative. Compound **IV-5** was reacted with an excess of SeO<sub>2</sub> in 1,4-dioxane overnight to afford corresponding aldehyde **IV-26** (Scheme IV – 11). <sup>1</sup>H-NMR experiment in CDCl<sub>3</sub> (Figure IV – 15) of the crude reaction mixture was performed (blue line) and compared to the one of starting material **IV-5**

(red line). One can easily notice the disappearance of the peak at 2.67 ppm (Me) and the appearance of a peak at 9.54 ppm corresponding to an aldehyde proton. However, the main side product of the reaction is red selenium, an allotrope of elemental Se, which is known to be soluble in common organic solvents and cannot be separated from organic compounds by silica gel chromatography.<sup>[39]</sup> The resulting mixture was then unpurifiable despite the best of our effort: columns chromatography, preparative TLC, and sublimation. Attempts to convert red selenium into its grey allotrope, which is insoluble in most organic solvents, by boiling in DMF solution led to decomposition of **IV-26**. Thus, we decided to undertake the cross-coupling pathway.



Scheme IV - 11: Synthesis of **IV-26**.

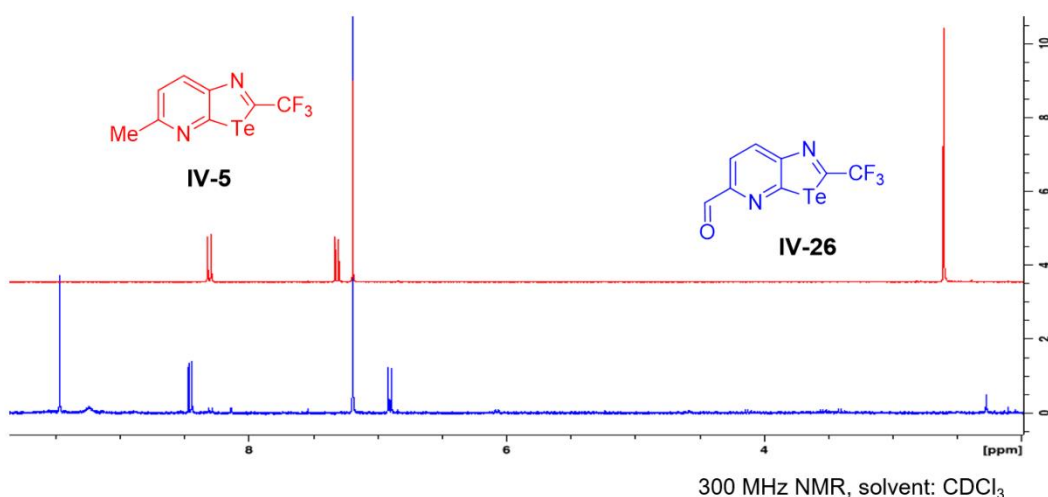
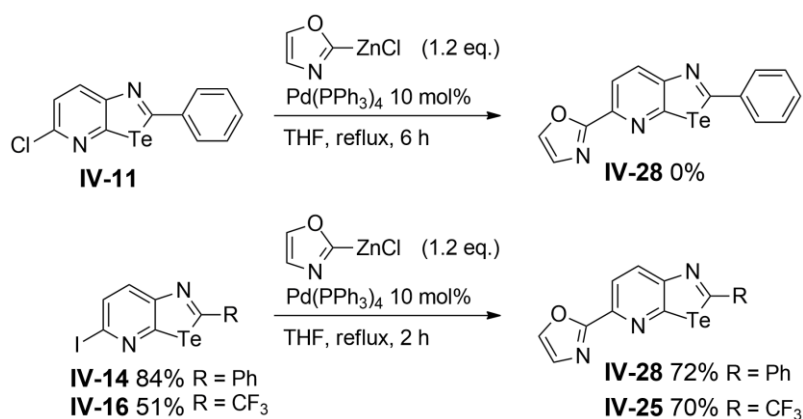


Figure IV - 15: <sup>1</sup>H-NMR spectra of **IV-5** (red) and the crude reaction mixture (blue) containing **IV-26**.

#### IV – 5.4 Synthesis: Cross-coupling pathway

A Negishi cross-coupling reaction was attempted on chloro-derivative **IV-11** aiming for oxazole **IV-28** (Scheme IV – 12) following the reaction conditions developed by *Piersanti, Minetti* and co-workers.<sup>[38]</sup> However, no conversion of substrate **IV-11** was observed. However, iodo-derivatives **IV-14** and **IV-16** were reacted with oxazolylzinc chloride in the presence of palladium tetrakis at the reflux of THF for 2h affording oxazoles **IV-28** and **IV-25** in 72% and 70% yield, respectively (Scheme IV – 12). Those compounds are stable to air, moisture and heat. However, complete decomposition over few days has been observed when dissolved in chlorinated solvent such as CH<sub>2</sub>Cl<sub>2</sub> or CHCl<sub>3</sub> leading to insoluble materials.

Scheme IV - 12: Synthesis of **IV-25** and **IV-28**.

## IV – 5.5 X-Ray analysis

Crystallisation attempts for oxazoles **IV-25** and **IV-28** were performed. Only the CF<sub>3</sub> derivative afforded single crystals suitable for X-ray diffraction analysis. The material crystallises from an EtOH solution in a Pnma space group and its asymmetric unit contains one molecule. These molecules arrange in a HB/EB ribbon (Figure IV – 16, a and b). A single chalcogen bond takes place between the N<sub>c</sub> and the Te atom from the adjacent molecule ( $d_{\text{N}\cdots\text{Te}} = 3.355 \text{ \AA}$ , C-Te $\cdots$ N angles = 172°). This chalcogen bond is supported by two hydrogen-bonding interactions involving the N atoms from the oxazole and the pyridine moieties clamping the H atoms in position 6 and 7 of the facing CGP molecule ( $d_{\text{N}\cdots\text{C}} = 3.207 \text{ \AA}$  and 3.427  $\text{\AA}$ , respectively). The first H-bond is less directional than the second (C-H $\cdots$ N angles = 139° and 170°, respectively). In addition, the ribbons interact through anti-parallel  $\pi$ - $\pi$  stacking interactions ( $d_{\pi-\pi} = 3.327 \text{ \AA}$ ; Figure IV – 16, c).

As reference, the Se analogue **IV-26** was synthesised in our group. The compound crystallises in a  $P\bar{1}$  space group and the asymmetric unit is composed by two molecules. Those arrange in a ribbon structure (Figure IV – 17) through double hydrogen-bonding interactions involving the N atom of the oxazole, the N<sub>p</sub> and H atoms in 6- and 7-position of the CGP moiety ( $d_{\text{N}\cdots\text{C}} = 3.332 \text{ \AA}$  and 3.460  $\text{\AA}$ , respectively). The first H-bond is less directional than the second (C-H $\cdots$ N angles = 140° and 171°, respectively). However, no chalcogen bond could be observed between N<sub>c</sub> and the facing Se atom, which distance being longer than the sum of their vdW radii ( $d_{\text{N}\cdots\text{Se}} = 3.547 \text{ \AA} > \sum_{\text{vdW}} = 3.45 \text{ \AA}$ , Figure IV – 17, b). In addition, ribbons interact through  $\pi$ - $\pi$  stacking interactions in a parallel (estimated  $d_{\pi-\pi} = 3.403 \text{ \AA}$ ) and anti-parallel ( $d_{\pi-\pi} = 3.420 \text{ \AA}$ ) fashion (Figure IV – 17, c).

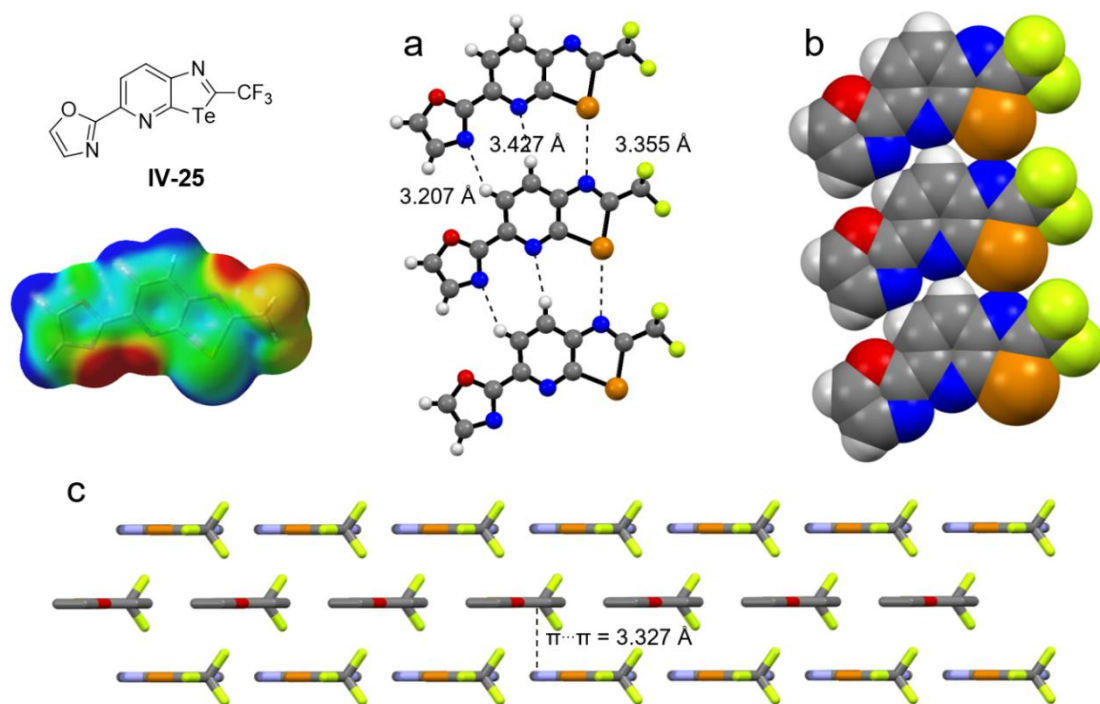


Figure IV - 16: X-ray structure of **IV-25** and its ESP, are highlighted a) ball and stick representation of the ribbon structure; b) vdW sphere representation; c) stick representation of the  $\pi$ - $\pi$  stacking, H atoms are omitted for clarity. Space group:  $Pnma$ , Solvent of crystallisation: EtOH.

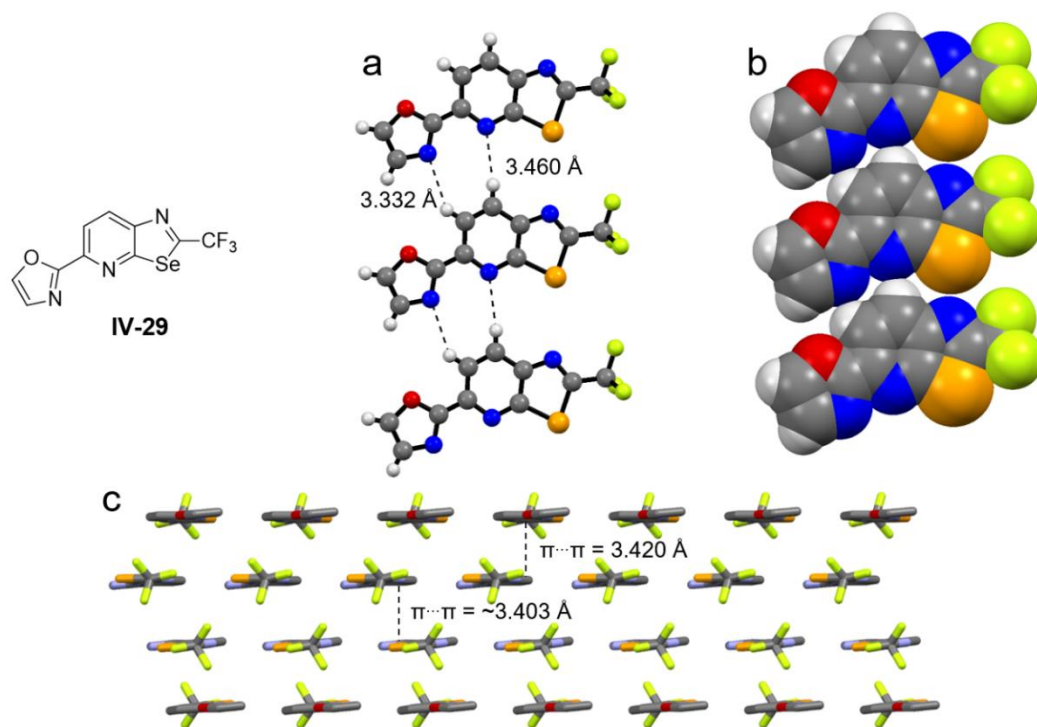


Figure IV - 17: X-ray structure of **IV-29** a) ball and stick representation of the ribbon structure; b) vdW sphere representation; c) stick representation of the  $\pi$ - $\pi$  stacking, H atoms are omitted for clarity. Space group:  $P\bar{1}$ , Solvent of crystallisation: C<sub>6</sub>H<sub>6</sub>.

These two crystal structures highlight the difficulty of 5-substituted CGP derivatives to form discrete dimers through EB interactions. Despite the calculation predicting a face-to-face organisation of **IV-25**, a head-to-tail ribbon arrangement is preferred in the solid-state. The introduction of an EB/HB acceptor in proximity of the pyridyl-moiety provides an additional hydrogen bond that stabilise ribbon formation. Moreover, substitution of the Te-atom by a Se-atom in molecule **IV-29** leads to a similar arrangement in the solid-state excluding the chalcogen-bonding interactions.

## IV – 6 Heteromolecular recognition through multi-type interactions

### IV – 6.1 Design

Capitalising on the result obtained with a 2,5-substituted CGP derivative, we aimed for the synthesis of heteromolecular recognition systems exploiting the simultaneous use of chalcogen- and hydrogen-bonding interactions (Figure IV – 18). If one wants to program such motif using one HB and one EB, two configurations are possible: HB donor (DH) and EB acceptor (Y) on the same side and HB acceptor (A) and EB donor (E) on the other or DH and E on one side and A and Y on the other. The former case leads to two negative secondary interactions and the latter to two positive ones. However, due to the close nature of A and Y, they could be inverted in the second situation (Figure IV – 18, right) leading to a non-selective recognition (if  $A \neq Y$ ). As a first step, we intend to form a persistent and specific complementary system, thus the AE•DHY motif has been chosen.

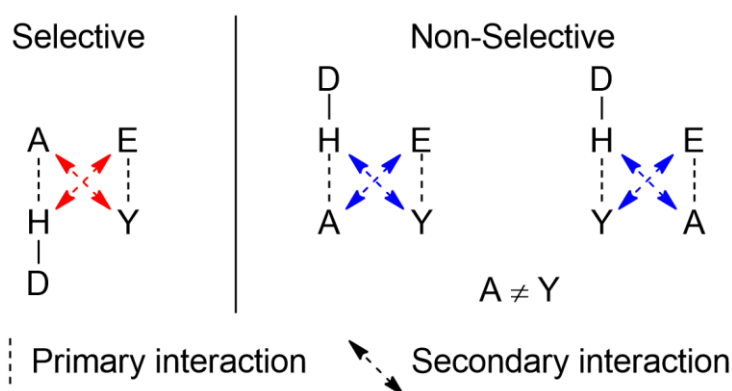


Figure IV - 18: Schematic representation of hybrid system based on hydrogen- and chalcogen-bonding. Secondary interactions are highlighted. D-H stands for hydrogen-bond donor, A for hydrogen-bond acceptor, E for chalcogen-bond donor and Y for chalcogen-bond acceptor. Blue colour represents positive secondary interactions while red the negative ones.

The design of such motif relies on the insertion of a steric blocker (in orange, Figure IV – 19, b) in 5-position of the CGP molecule to prevent the formation of homo-dimer through double chalcogen bonding interactions (Figure IV – 19, a) and a small 2-substituent to prevent hetero-repulsion between the two molecules. For those reasons, derivative **IV-5** has been selected (orange = Me and

green = CF<sub>3</sub>). The DHY partner (Figure IV – 19, c) features the complementary electrostatic organisation.

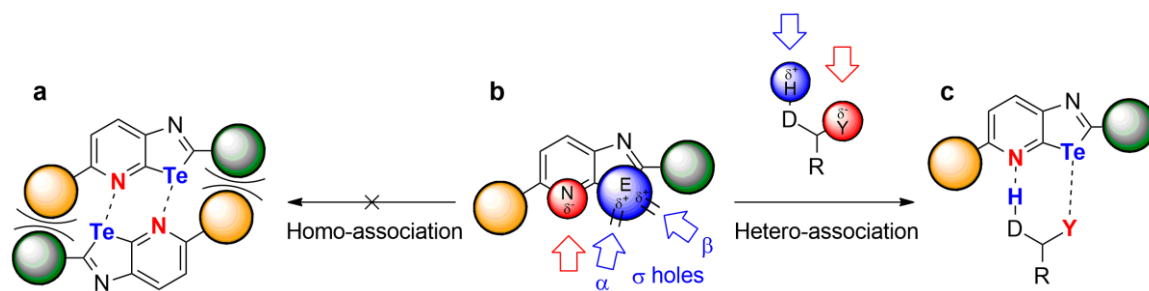
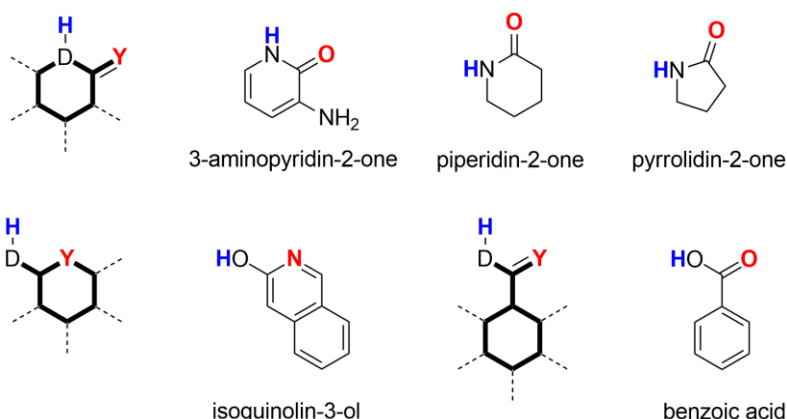


Figure IV - 19: Representation of the design of a recognition motif capitalizing on the simultaneous chalcogen- and hydrogen-bonding interactions based on a functionalized CGP molecule. a) EB dimer; b) designed array and c) hetero-molecular association.

The selected DHY molecular partners are 3-aminopyridin-2-one, piperidin-2-one and pyrrolidin-2-one, isoquinolin-3-ol and benzoic acid (Scheme IV – 13). The first three compounds present a lactam moiety and the two others a 2-hydroxypyridine and a carboxylic acid, respectively. Those compounds have been selected to probe the functional group recognition of the 2,5-disubstituted CGP synthon.



Scheme IV - 13: Representation of the selected candidate molecules to form heterodimer with derivative IV-5.

#### IV – 6.2 Co-crystals X-ray analysis

Solutions of **IV-5** in CHCl<sub>3</sub> containing each of the above-mentioned molecules in a 1:1 ratio were realised and left standing for slow evaporation. The resulting solids were analysed by single crystal X-ray diffraction. Amorphous material was obtained in the case of 3-aminopyridin-2-one. Large crystals of **IV-5** grew from the solution with piperidin-2-one and pyrrolidin-2-one. Co-crystals **IV-5•PhCOOH** and **IV-5•isoquinolin-3-ol** were achieved from the corresponding solutions. As reference for this study, similar co-crystallisation attempts have been realized with 2-(trifluoromethyl)-[1,3]tellurazolo[5,4-β]pyridine **II-25<sub>Te</sub>**, which does not bear a Me group in 5-

position. Crystal segregation was observed after slow evaporation of those solution, suggesting the importance of the Me moiety as steric blocker in CGP **IV-5** the formation of these multimolecular crystals.

A 1:1 Mixture of compound **IV-5** and benzoic acid led to the formation of **IV-5•PhCOOH**. This material crystallises in a  $P2_1/n$  space group and the asymmetric unit contains one molecule of each constituent. The molecules arrange in a hetero-dimer and are held together by means of hybrid chalcogen- and hydrogen-bonding interactions (Figure IV – 20, a). EB takes place between the O atom of the carbonyl and the Te atom ( $d_{O\dots Te} = 2.956 \text{ \AA}$ ,  $C\text{-Te}\cdots O$  angle =  $166^\circ$ ). HB involves the OH of the carboxylic acid and the N atom of the CGP ( $d_{N\dots O} = 2.588 \text{ \AA}$ ,  $O\text{-H}\cdots N$  angle =  $171^\circ$ ). In addition, the dimers  $\pi\text{-}\pi$  stack in a head-to-tail fashion ( $d_{\pi\text{-}\pi} = 3.371 \text{ \AA}$ ) forming columnar arrangements displaying a reduced off-set organisation (Figure IV – 20, b).

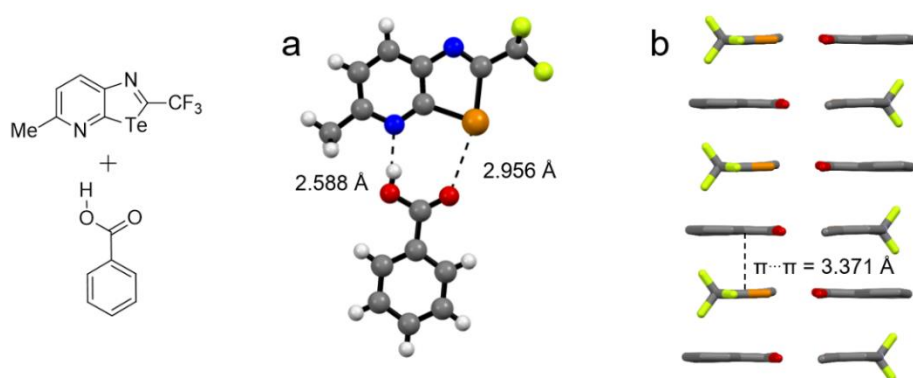


Figure IV - 20: X-ray structure of **PhCOOH•IV-5**, a) ball and stick representation of the hetero-dimer association; b) stick representation of  $\pi\text{-}\pi$  stack of the dimers, H atoms are omitted for clarity. Space group:  $P2_1/n$ , solvent of crystallisation:  $CHCl_3$ .

Moving to isoquinolin-3-ol, co-crystal **isoquinolin-3-ol•IV-5** was obtained. The material crystallises in a  $P2_1/c$  space group and the asymmetric unit contains one molecule of each component. A tetrameric structure is formed through the combination of chalcogen- and hydrogen-bonding interactions (Figure IV – 21, a). The CGP derivative connect to isoquinolin-3-ol by EB between the N atom of the isoquinoline and the facing Te atom ( $d_{N\dots Te} = 2.886 \text{ \AA}$ ,  $C\text{-Te}\cdots N$  angle =  $167^\circ$ ) and by HB involving the OH group and the pyridyl moiety ( $d_{N\dots O} = 2.706 \text{ \AA}$ ,  $O\text{-H}\cdots N$  angle =  $169^\circ$ ). Dimers of **isoquinolin-3-ol•IV-5** associate with each other through H-bonding contacts ( $d_{N\dots C} = 3.472 \text{ \AA}$ ,  $C\text{-H}\cdots N$  angle =  $169^\circ$ ). In addition, the tetramers  $\pi\text{-}\pi$  stack ( $d_{\pi\text{-}\pi} = 3.281 \text{ \AA}$ ) with an off-set of  $4.573 \text{ \AA}$  (Figure IV – 21, b).

Those two co-crystals have appraised the possibility to use 2,5-disubstituted **IV-5** in the formation of hetero-dimer through simultaneous chalcogen- and hydrogen-bonding interactions with carboxylic acid and a 2-hydroxypyridyl functional groups. Those results are the proof of concept

that will lead to more elaborated supramolecular architectures capitalising on this new designed hetero-recognition array.

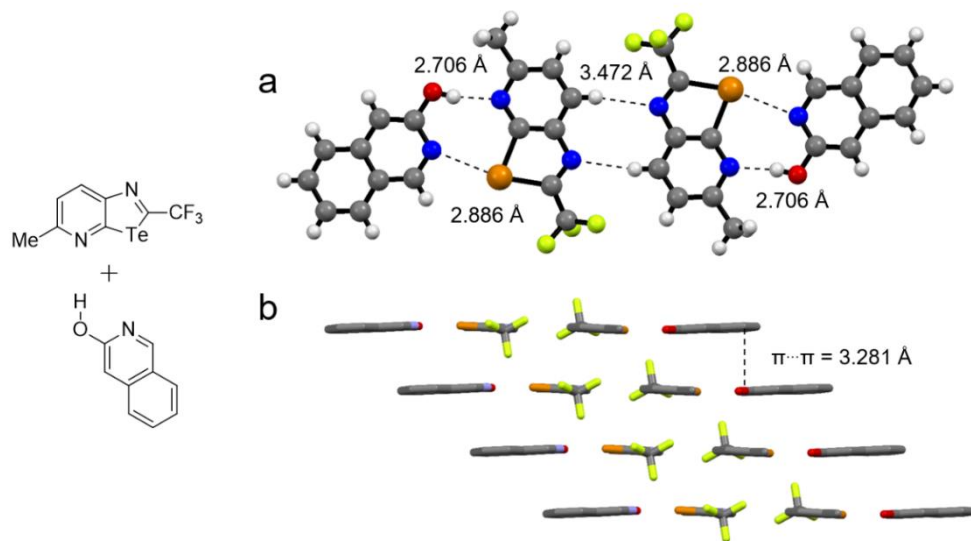


Figure IV - 21: X-ray structure of **IV-5•isoquinolin-3-ol**, a) ball and stick representation of the tetramer association; b) stick representation of the  $\pi$ - $\pi$  stack of the tetramers, H atoms are omitted for clarity. Space group:  $P2_1/c$ , solvent of crystallisation:  $CHCl_3$ .

## IV – 7 Conclusion

In summary of this part of the work, we have extended the possible recognition motifs involving the CGP moiety. By introduction of substituents in 2- and 5-position, we have been able to tune the assembly pattern of the molecules by increasing or decreasing hetero- and homo-repulsion. This has been achieved through the synthesis of a series of derivatives bearing Ph, thiophenyl and  $CF_3$  moieties in 2-position and Me group, Cl and I atoms in the 5-position. Reactions forming the CGP core were successfully performed in the presence of the Me- and Cl-substituents. The iodo-derivatives were synthesised from the corresponding chlorinated ones through iodine-chlorine exchange reaction.

Having those compounds in hand, our rational design was probed in the solid state by single crystal X-ray diffraction analysis. Molecules bearing the less sterically demanding  $CF_3$  group in 2-position led to the formation of head-to-tail HB/EB ribbon in the case of Me- and Cl-substituent in 5-position and a kinked ribbon relying on EB dimers in the case of I-substituent. More sterically demanding phenyl and thiophenyl groups lead to the formation of head-to-tail  $N_c$  wire-like structures due to homo-repulsion of the 2-substituents.

Expanding further the functionalisation in 5-position, we synthesised oxazolyl-bearing CGP derivatives **IV-25** and **IV-28** through Negishi cross-coupling reaction from iodo-derivatives **IV-14** and **IV-16** aiming for the formation of a discrete dimer through a tetra chalcogen-bonded motif.

Single crystals suitable for X-ray diffraction analysis could be obtained only for the CF<sub>3</sub> 2-substituted molecule. A HB/EB ribbon was obtained achieving a single EB involving N<sub>c</sub> atom and a double hydrogen-bonded pattern between the N<sub>p</sub> atom and the N atom from the oxazolyl group and the H atoms in 6- and 7-position of the CGP group. A similar structure has been obtained from the Se analogue **IV-29**, which excludes the formation of a chalcogen-bonding interaction.

Those results show that discrete face-to-face dimers are difficult to obtain in the presence of substituents in 5-position of the CGP moiety. Those tend to form polymeric assembly such as ribbon or wire-like structures in a head-to-tail fashion. Depending on the steric bulk of the 2-substituent, one can selectively grow one arrangement or the other.

Capitalising on those structures, we aimed to form hetero molecular dimers. Anticipating the formation of a HB/EB hybrid recognition system we achieved the association of **IV-5** with carboxylic acid and 2-hydroxypyridine containing molecules. Through those co-crystals we opened this system to the possibilities of selective recognition of molecules of higher complexity.

This part of the work has successfully widened the possibilities of use of chalcogen-bonding interactions in supramolecular structures. This will lead to the design and synthesis of novel architectures blending hydrogen- and chalcogen-bonding interactions and thus more complexity in rational systems. Furthermore, we will revisit our designed tetra EBs recognition array and aim for the synthesis of such a system, which could show application at the solid state and in solution.

## IV – 8 Bibliography

- [1] P. Politzer, J. S. Murray, P. Lane, 'σ-Hole Bonding and Hydrogen Bonding: Competitive Interactions', *Int. J. Quantum Chem.* **2007**, *107*, 3046-3052.
- [2] S. Zhu, C. Xing, W. Xu, G. Jin, Z. Li, 'Halogen Bonding and Hydrogen Bonding Coexist in Driving Self-Assembly Process', *Cryst. Growth Des.* **2004**, *4*, 53-56.
- [3] A. Priimagi, G. Cavallo, A. Forni, M. Gorynsztein-Leben, M. Kaivola, P. Metrangolo, R. Milani, A. Shishido, T. Pilati, G. Resnati, G. Terraneo, 'Halogen Bonding versus Hydrogen Bonding in Driving Self-Assembly and Performance of Light-Responsive Supramolecular Polymers', *Adv. Funct. Mater.* **2012**, *22*, 2572-2579.
- [4] A. Mukherjee, S. Tothadi, G. R. Desiraju, 'Halogen Bonds in Crystal Engineering: Like Hydrogen Bonds yet Different', *Acc. Chem. Res.* **2014**, *47*, 2514-2524.
- [5] S. Scheiner, 'Forty Years of Progress in the Study of the Hydrogen Bond', *Struct. Chem.* **2019**, *30*, 1119-1128.
- [6] E. Corradi, S. V. Meille, M. T. Messina, P. Metrangolo, G. Resnati, 'Halogen Bonding versus Hydrogen Bonding in Driving Self-Assembly Processes', *Angew. Chem. Int. Ed.* **2000**, *39*, 1782-1786.
- [7] W. Saenger, in *Principles of Nucleic Acid Structure* (Ed.: W. Saenger), Springer New York, New York, NY, 1984, pp. 116-158.
- [8] S. Sivakova, S. J. Rowan, 'Nucleobases as Supramolecular Motifs', *Chem. Soc. Rev.* **2005**, *34*, 9-21.
- [9] J. L. Sessler, C. M. Lawrence, J. Jayawickramarajah, 'Molecular Recognition via Base-Pairing', *Chem. Soc. Rev.* **2007**, *36*, 314-325.

- [10] J. Pranata, S. G. Wierschke, W. L. Jorgensen, 'OPLS Potential Functions for Nucleotide Bases. Relative Association Constants of Hydrogen-Bonded Base Pairs in Chloroform', *J. Am. Chem. Soc.* **1991**, *113*, 2810-2819.
- [11] W. L. Jorgensen, J. Pranata, 'Importance of Secondary Interactions in Triply Hydrogen Bonded Complexes: Guanine-Cytosine vs Uracil-2,6-Diaminopyridine', *J. Am. Chem. Soc.* **1990**, *112*, 2008-2010.
- [12] F. H. Beijer, H. Kooijman, A. L. Spek, R. P. Sijbesma, E. W. Meijer, 'Self-Complementarity Achieved through Quadruple Hydrogen Bonding', *Angew. Chem. Int. Ed.* **1998**, *37*, 75-78.
- [13] P. S. Corbin, S. C. Zimmerman, 'Self-Association without Regard to Prototropy. A Heterocycle That Forms Extremely Stable Quadruply Hydrogen-Bonded Dimers', *J. Am. Chem. Soc.* **1998**, *120*, 9710-9711.
- [14] G. Gröger, W. Meyer-Zaika, C. Böttcher, F. Gröhn, C. Ruthard, C. Schmuck, 'Switchable Supramolecular Polymers from the Self-Assembly of a Small Monomer with Two Orthogonal Binding Interactions', *J. Am. Chem. Soc.* **2011**, *133*, 8961-8971.
- [15] S. Djurdjevic, D. A. Leigh, H. McNab, S. Parsons, G. Teobaldi, F. Zerbetto, 'Extremely Strong and Readily Accessible AAA-DDD Triple Hydrogen Bond Complexes', *J. Am. Chem. Soc.* **2007**, *129*, 476-477.
- [16] B. A. Blight, A. Camara-Campos, S. Djurdjevic, M. Kaller, D. A. Leigh, F. M. McMillan, H. McNab, A. M. Z. Slawin, 'AAA-DDD Triple Hydrogen Bond Complexes', *J. Am. Chem. Soc.* **2009**, *131*, 14116-14122.
- [17] D. A. Leigh, C. C. Robertson, A. M. Z. Slawin, P. I. T. Thomson, 'AAAA-DDDD Quadruple Hydrogen-Bond Arrays Featuring NH...N and CH...N Hydrogen Bonds', *J. Am. Chem. Soc.* **2013**, *135*, 9939-9943.
- [18] F. H. Beijer, R. P. Sijbesma, H. Kooijman, A. L. Spek, E. W. Meijer, 'Strong Dimerization of Ureidopyrimidones via Quadruple Hydrogen Bonding', *J. Am. Chem. Soc.* **1998**, *120*, 6761-6769.
- [19] T. Park, S. C. Zimmerman, S. Nakashima, 'A Highly Stable Quadruply Hydrogen-Bonded Heterocomplex Useful for Supramolecular Polymer Blends', *J. Am. Chem. Soc.* **2005**, *127*, 6520-6521.
- [20] B. A. Blight, C. A. Hunter, D. A. Leigh, H. McNab, P. I. T. Thomson, 'An AAAA-DDDD Quadruple Hydrogen-Bond Array', *Nature Chem.* **2011**, *3*, 244.
- [21] J. A. Hirsch, in *Topics in Stereochemistry* (Eds.: N. L. Allinger, E. E. L.), 2007, pp. 199-222.
- [22] A. D. Dunn, A. Currie, L. E. Hayes, 'Bromination of Pyridines. II. Bromination of Aminopicolines', *J. Prakt. Chem.* **1989**, *331*, 369-374.
- [23] R. Linnell, 'Notes- Dissociation Constants of 2-Substituted Pyridines', *J. Org. Chem.* **1960**, *25*, 290-290.
- [24] A. C. Bissember, M. G. Banwell, 'Microwave-Assisted Trans-Halogenation Reactions of Various Chloro-, Bromo-, Trifluoromethanesulfonyloxy- and Nonfluorobutanesulfonyloxy-Substituted Quinolines, Isoquinolines, and Pyridines Leading to the Corresponding Iodinated Heterocycles', *J. Org. Chem.* **2009**, *74*, 4893-4895.
- [25] A. Kremer, A. Fermi, N. Biot, J. Wouters, D. Bonifazi, 'Supramolecular Wiring of Benzo-1,3-chalcogenazoles through Programmed Chalcogen Bonding Interactions', *Chem. Eur. J.* **2016**, *22*, 5665-5675.
- [26] P. J. Hay, W. R. Wadt, 'Ab Initio Effective Core Potentials for Molecular Calculations. Potentials for the Transition Metal Atoms Sc to Hg', *J. Chem. Phys.* **1985**, *82*, 270-283.
- [27] A. D. Becke, 'A New Mixing of Hartree-Fock and Local Density - Functional Theories', *J. Chem. Phys.* **1993**, *98*, 1372-1377.
- [28] F. Weigend, R. Ahlrichs, 'Balanced Basis Sets of Split Valence, Triple Zeta Valence and Quadruple Zeta Valence Quality for H to Rn: Design and Assessment of Accuracy', *Phys. Chem. Chem. Phys.* **2005**, *7*, 3297-3305.

- [29] A. F. Cozzolino, I. Vargas-Baca, S. Mansour, A. H. Mahmoudkhani, 'The Nature of the Supramolecular Association of 1,2,5-Chalcogenadiazoles', *J. Am. Chem. Soc.* **2005**, *127*, 3184-3190.
- [30] S. Grimme, S. Ehrlich, L. Goerigk, 'Effect of the Damping Function in Dispersion Corrected Density Functional Theory', *J. Comput. Chem.* **2011**, *32*, 1456-1465.
- [31] G. W. T. M. J. Frisch, H. B. Schlegel, G. E. Scuseria, M. A. Robb, J. R. Cheeseman, G. Scalmani, V. Barone, B. Mennucci, G. A. Petersson, H. Nakatsuji, M. Caricato, X. Li, H. P. Hratchian, A. F. Izmaylov, J. Bloino, G. Zheng, J. L. Sonnenberg, M. Hada, M. Ehara, K. Toyota, R. Fukuda, J. Hasegawa, M. Ishida, T. Nakajima, Y. Honda, O. Kitao, H. Nakai, T. Vreven, J. A. Montgomery Jr., J. E. Peralta, F. Ogliaro, M. J. Bearpark, J. Heyd, E. N. Brothers, K. N. Kudin, V. N. Staroverov, R. Kobayashi, J. Normand, K. Raghavachari, A. P. Rendell, J. C. Burant, S. S. Iyengar, J. Tomasi, M. Cossi, N. Rega, N. J. Millam, M. Klene, J. E. Knox, J. B. Cross, V. Bakken, C. Adamo, J. Jaramillo, R. Gomperts, R. E. Stratmann, O. Yazyev, A. J. Austin, R. Cammi, C. Pomelli, J. W. Ochterski, R. L. Martin, K. Morokuma, V. G. Zakrzewski, G. A. Voth, P. Salvador, J. J. Dannenberg, S. Dapprich, A. D. Daniels, Ö. Farkas, J. B. Foresman, J. V. Ortiz, J. Cioslowski, D. J. Fox, *Gaussian, Inc., Wallingford, CT* **2013**.
- [32] G. E. Garrett, G. L. Gibson, R. N. Straus, D. S. Seferos, M. S. Taylor, 'Chalcogen Bonding in Solution: Interactions of Benzotelluradiazoles with Anionic and Uncharged Lewis Bases', *J. Am. Chem. Soc.* **2015**, *137*, 4126-4133.
- [33] A. F. Cozzolino, I. Vargas-Baca, 'The Supramolecular Chemistry of 1,2,5-Chalcogenadiazoles', *J. Organomet. Chem.* **2007**, *692*, 2654-2657.
- [34] D. B. Werz, R. Gleiter, F. Rominger, 'Nanotube Formation Favored by Chalcogen-Chalcogen Interactions', *J. Am. Chem. Soc.* **2002**, *124*, 10638-10639.
- [35] A. Jolleys, W. Levason, G. Reid, 'Thioether Coordination to Divalent Selenium Halide Acceptors – Synthesis, Properties and Structures', *Dalton Trans.* **2013**, *42*, 2963-2972.
- [36] S. Bhandary, A. Sirohiwal, R. Kadu, S. Kumar, D. Chopra, 'Dispersion Stabilized Se/Te... $\pi$  Double Chalcogen Bonding Synthons in in Situ Cryocrystallized Divalent Organochalcogen Liquids', *Cryst. Growth Des.* **2018**, *18*, 3734-3739.
- [37] S. Picard, E. Genin, G. Clermont, V. Hugues, O. Mongin, M. Blanchard-Desce, 'Octupolar Chimeric Compounds Built from Quinoline Caged Acetate Moieties: a Novel Approach for 2-Photon Uncaging of Biomolecules', *New J. Chem.* **2013**, *37*, 3899-3913.
- [38] G. Piersanti, L. Giorgi, F. Bartocchini, G. Tarzia, P. Minetti, G. Gallo, F. Giorgi, M. Castorina, O. Ghirardi, P. Carminati, 'Synthesis of Benzo[1,2-d;3,4-d]diimidazole and 1H-pyrazolo[4,3-b]pyridine as Putative A2A Receptor Antagonists', *Org. Biomol. Chem.* **2007**, *5*, 2567-2571.
- [39] T. G. Back, in *Organoselenium Chemistry, A Practical Approach* (Ed.: T. G. Back), Oxford University Press, 1999, p. 93.

---

## ***Chapter V***

### ***Conclusion and Outlooks***

---

During the course of this work, we have developed a new recognition array relying on double chalcogen-bonding interactions, the CGP motif (Figure V – 1). The key design element is the  $\beta$ -junction of a pyridyl and a chalcogenazole moieties, placing a chalcogen-bond acceptor atom in close proximity of the chalcogen-bond donor atom. Se- and Te-containing CGP derivatives bearing different substituent in 2-position were synthesised. A strong recognition persistence has been observed throughout the X-ray analysis of different Te-containing derivatives. In the solid state, those self-complementary molecules associate in dimers through double EB interactions and strengthening was achieved upon addition of EWG in 2-position. On the other hand, a certain variability was noted for the Se-analogues that associate through hydrogen-bonding interaction or, in the case of phenyl substituted derivative, through  $\pi$ - $\sigma^*$  interactions. Dimerization through double chalcogen bonds was only obtained for the derivatives bearing strong EWG such as pentafluorophenyl or  $\text{CF}_3$ .

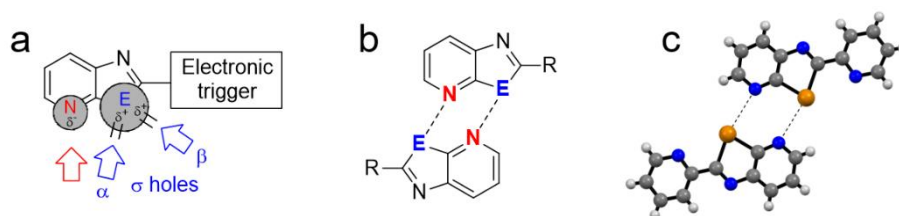


Figure V - 1: a) CGP supramolecular synthon; b) dimerization through double chalcogen-bonding interactions; c) X-ray structure of 2-phenyl-tellurazopyridine.

Blending chalcogen-bonding with  $\pi$ - $\pi$  stacking interactions led to the formation of organic semiconductor materials. Particularly, compound **II-39<sub>Te</sub>** features the conjugation of CGP to a pyrenyl ring and its X-ray structure show the non-covalent levelling of the aromatic cores in one plane upon dimerization through double EBs. Those dimers interact via  $\pi$ - $\pi$  stacking interaction forming columnar arrangement maximising the overlap of the  $\pi$ -surface. This organisation is suitable for the transport of charges, SCLC (space charge limited current) measurements show a hole mobility similar to that of benchmark polymers reported in the literature. The Se-containing analogue **II-39<sub>Se</sub>** and Se- and Te-containing benzochalcogenazole **II-40<sub>E</sub>** have also been considered for comparison. Compounds **II-39<sub>E</sub>** and **II-40<sub>E</sub>** showed similar electronic properties from UV-vis absorption and CV experiments. However, different organisations in the solid state were observed by X-ray diffraction analysis. Compound **II-40<sub>Se</sub>** also forms a double-stack arrangement through  $\pi$ - $\pi$  stacking but the columns are not connected through other non-covalent interactions. This is reflected on the charge mobility being only slightly smaller than that of **II-39<sub>Te</sub>**. On the other hand, **II-39<sub>Se</sub>** organises in a single-molecule wide columnar arrangement, while **II-40<sub>Te</sub>** in a herringbone structure. Both compounds showed a lower hole mobility values of the series.

Nonetheless, a certain variability has been observed in Te-containing systems while introducing other non-covalent interactions such as halogen- or hydrogen-bonding (**II-24<sub>Te</sub>** and **II-32<sub>Te</sub>**, respectively). XB and HB overcome the double EB array in those situations, leading to the formation of structures featuring uncontrolled associations. Capitalising on those results we engineered multi-molecular crystals featuring simultaneous halogen- and chalcogen-bonding interactions in a controlled fashion. Supramolecular polymer **((III-1<sub>Te</sub>)<sub>2</sub>•HDFIO)<sub>n</sub>** was synthesised by mixing CGP **III-1<sub>Te</sub>** bearing pyrid-4-yl and hexadecafluorodiiodooctane (Figure V – 2, a).

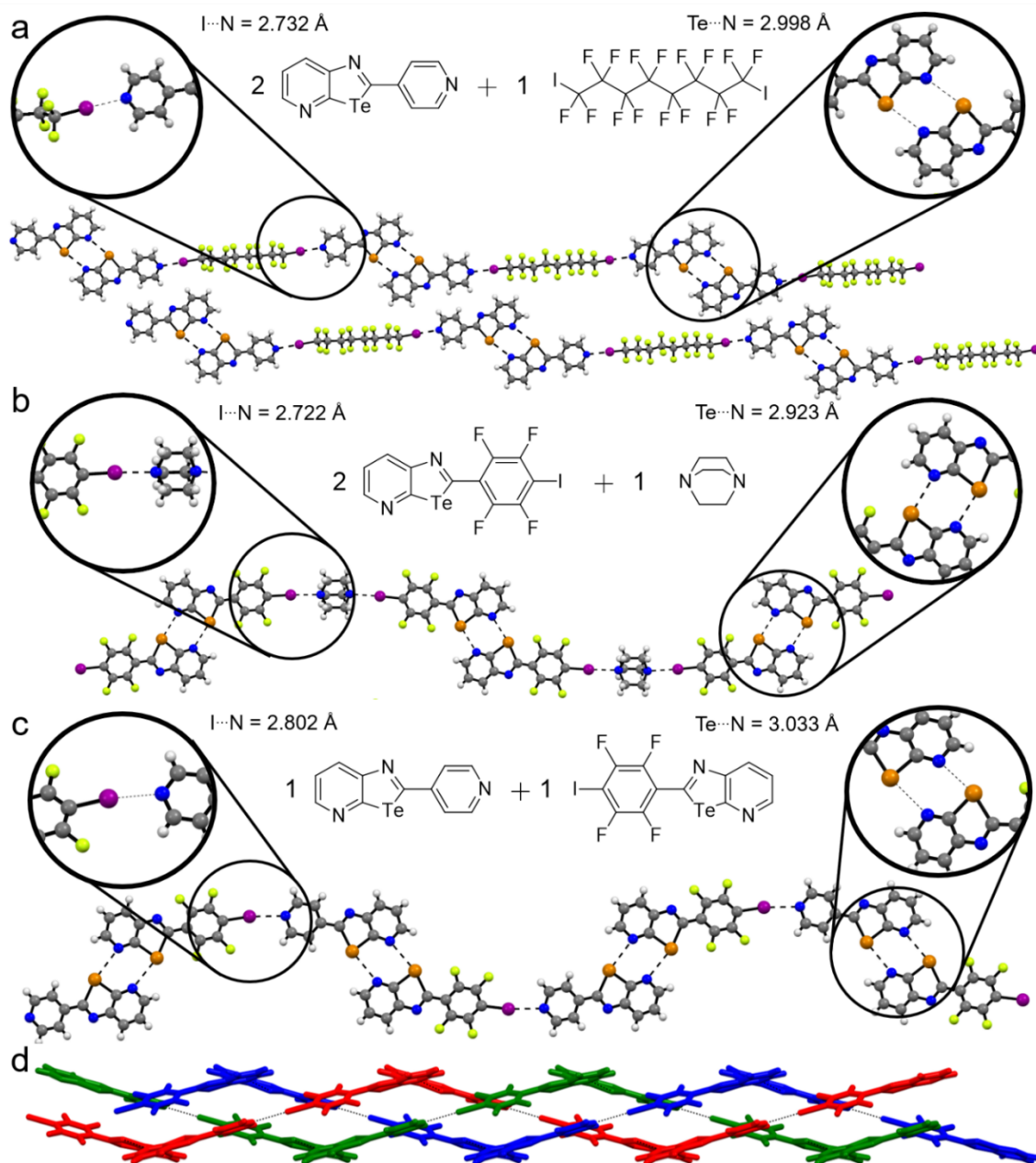


Figure V - 2: Crystal structures of a) co-crystal  $(\text{III-1}_{\text{Te}})_2 \cdot \text{HDFIO}$ ; b) co-crystal  $(\text{III-5})_2 \cdot \text{DABCO}$  and c) co-crystal  $\text{III-1}_{\text{Te}} \cdot \text{III-5}$ ; d) Capped stick representation of the triple helix, each strain is highlighted in Red, Blue and Green. Space group:  $P\bar{1}$ ,  $P\bar{1}$  and  $P2_1/n$ , respectively.

The X-ray structure analysis reveals an alternation of EBs and XBs. The CGP dimer forms a ditopic halogen-bond acceptor that, interacting with **HDFIO**, establish the repeating unit leading to infinite chains. Compound **III-1<sub>Te</sub>** was also mixed with **DITFB** leading to the formation of three different materials reflecting the ratio of the two components in the initial solution. In contrast, CGP **III-2<sub>Te</sub>** bearing a pyrid-3-yl moiety led to the formation of **(III-2<sub>Te</sub>)<sub>2</sub>•DITFB**, which formed a supramolecular polymer, independently at the initial ratio of the two components.

Benzotellurazole **III-3** formed trimeric structures through XBs with **HDFIO** and **DITFB**, showing that weaker EBs recognition motifs do not form supramolecular polymers through simultaneous use of both interactions. Se-containing **III-1<sub>Se</sub>** in the presence of **DITFB** also formed materials reflecting the initial solution stoichiometry. Interestingly, co-crystal **(III-1<sub>Te</sub>)<sub>2</sub>•DITFB** is isostructural to Te-analogue **(III-1<sub>Te</sub>)<sub>2</sub>•DITFB** featuring simultaneous chalcogen- and halogen-bonding interactions. This reveals that, upon formation of XB, **III-1<sub>Se</sub>** can dimerise through double EBs. In contrast, isomer **III-2<sub>Se</sub>** led to the formation of **(III-2<sub>Se</sub>)<sub>2</sub>•DITFB** as a supramolecular polymer through HB and XB interactions.

Co-crystals were also obtained while reversing the halogen-bond demand, iodo-derivative **III-5** mixed with **DABCO**, led to the formation of **III-5•DABCO** and **(III-5)<sub>2</sub>•DABCO**, organising in a tetramer and supramolecular polymer (Figure V – 2, b), respectively. Co-crystal **III-1<sub>Te</sub>•III-5** was obtained mixing molecules **III-1<sub>Te</sub>** and **III-5**. The two components associate to form a hetero recognition system through orthogonal XB and EB achieving a supramolecular polymer (Figure V – 2, c and d).

By introduction of substituents in 2- and 5-position of the CGP scaffold, we have been able to tune the assembly pattern of the molecules by increasing or decreasing steric hetero- and homo-repulsion. This strategy led to the formation of face-to-face EB dimers, head-to-tail HB/EB ribbon and wire-like structures depending on the substituents. In particular, the ribbon arrangement relied on the presence of simultaneous hydrogen- and chalcogen-bonding interactions (Figure V – 3, a and b). We also synthesised oxazolyl-bearing CGP derivatives **IV-25** and **IV-28** through Negishi cross-coupling reaction from the corresponding iodo-derivatives aiming for the formation of a discrete dimer through a tetra chalcogen-bonded motif. X-ray structure of **IV-25** showed a HB/EB ribbon through chalcogen bond involving N<sub>c</sub> atom and a double hydrogen-bonded pattern between the N<sub>p</sub> atom and the N atom from the oxazolyl group and the H atoms in 6- and 7-position of the CGP group. A similar structure has been obtained from the Se analogue **IV-29**, which excludes the formation of a chalcogen-bonding interaction. Capitalizing on those structures, we designed heteromolecular HB/EB hybrid recognition system (Figure V – 3, c and d). Specifically, compound **IV-5** was co-crystallised with benzoic acid and isoquinolin-3-ol.

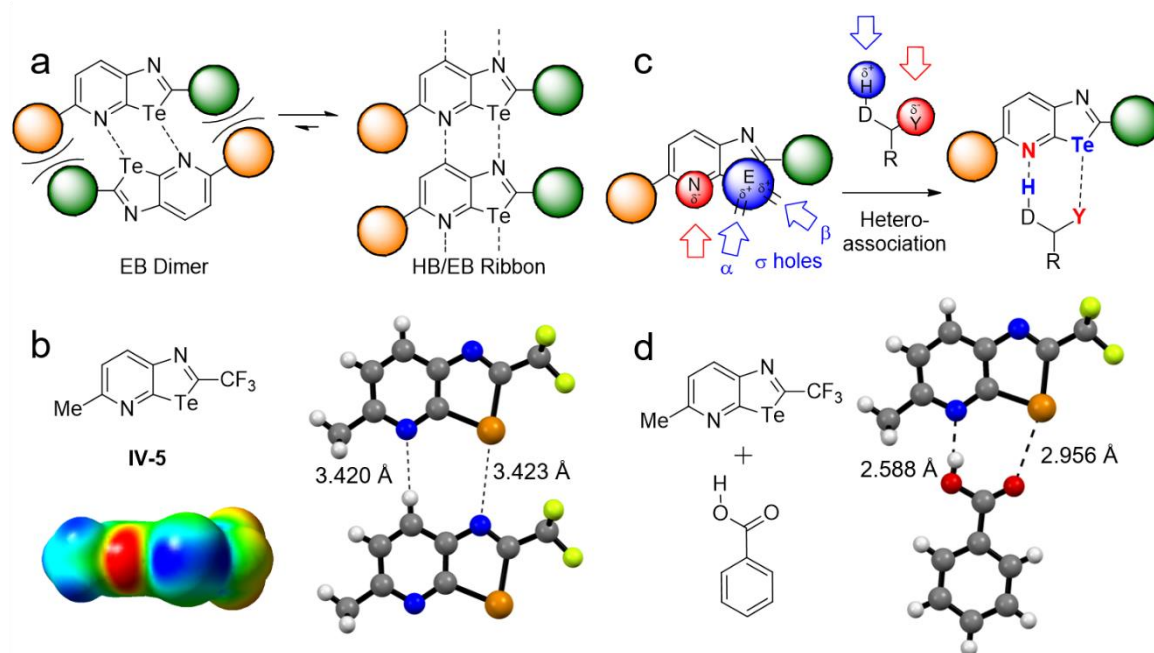


Figure V - 3: a) Equilibrium leading to the formation of HB/EB ribbon over EB dimer; b) X-ray structure and ESP map of **IV-5**; c) Hetero-molecular association based on simultaneous EB and HB interactions ; d) X-ray structure of **IV-5•PhCOOH**. Space group:  $P21/m$  and  $P2_1/n$ , respectively.

In summary of this work, we provide a novel recognition motif that showed strong recognition persistence and self-organise into dimer through double chalcogen-bonding interactions at the solid-state. The CGP core can be easily functionalised in the 2-position, which allows versatility of the building block. For instance, we have achieved the synthesis of organic semi-conductor material with pyrene substituted **II-39<sub>Te</sub>**. This compound also showed the possible parallel use of chalcogen-bonding and  $\pi$ - $\pi$  stacking interactions. The preliminary results obtained by SCLC measurement encourage us to continue the study on the pyrenyl derivatives and perform electron mobility measurement. Moreover, theoretical calculation will be performed to inform us on the mechanism followed by the charges to travel through the material. Considering this idea, 1D or 2D supramolecular polymers/dendrimers composed of PAHs organised by multiple chalcogen-bonded motifs could enhance further the charge mobility property of the material.

Functionalisation of CGP in 2-position with pyrid-4-yl, pyrid-3-yl or iodotetrafluorophenyl allowed the growth, with the relevant molecular partner, of co-crystals featuring simultaneous chalcogen- and halogen-bonding interactions. Thus, this orthogonality could be used in the future to organise complex multi-component systems from simple building blocks. Functionalisation in 5-position allowed the formation of different recognition arrays relying on the synergetic use of chalcogen- and hydrogen-bonding interactions. These systems can be used to assemble molecules bearing carboxylic acid or 2-hydroxypyridine moieties.

However, the systems developed so far do not present detectable recognition in solution. Strengthening of the chalcogen-bonds in the CGP array is thus necessary to expand its application beyond the solid-state. A possible route to tackle this issue is the synthesis of a tetra-chalcogen-bonded system. Building on the results obtained with oxazol derivative **II-25**, one could design such motif by choosing the appropriate functional group to place in 5-position of the CGP scaffold.

---

## ***Chapter VI***

### ***Experimental Section***

---

In this chapter, we report on the experimental procedure and the full characterisation of the compound synthesised during the course of this work.

## VI – 1 General remarks

### VI – 1.1 Instrumentation

**Thin layer chromatography** (TLC) was conducted on pre-coated aluminum sheets with 0.20 mm *Merck Millipore* Silica gel 60 with fluorescent indicator F254. *Column chromatography* was carried out using *Merck Gerduran* silica gel 60 (particle size 40-63  $\mu\text{m}$ ). **Microwave reactions** were performed on a *Biotage AB Initiator microwave instrument* producing controlled irradiation at 2.450 GHz. **Melting points** (mp) were measured on a *Gallenkamp* apparatus in open capillary tubes and have not been corrected. **Nuclear magnetic resonance:** (NMR) spectra were recorded on a Bruker Fourier 300 MHz spectrometer equipped with a dual ( $^{13}\text{C}$ ,  $^1\text{H}$ ) probe, a Bruker AVANCE III HD 400MHz NMR spectrometer equipped with a Broadband multinuclear (BBFO) SmartProbe™ or a Bruker AVANCE III HD 500MHz Spectrometer equipped with Broadband multinuclear (BBO) Prodigy CryoProbe.  $^1\text{H}$  spectra were obtained at 300, 400 or 500 MHz,  $^{13}\text{C}$  spectra were obtained at 75, 100 or 125 MHz NMR and  $^{19}\text{F}$  spectra were obtained at 376 or 470 MHz. All spectra were obtained at r.t. otherwise stated. Chemical shifts were reported in ppm according to tetramethylsilane using the solvent residual signal as an internal reference ( $\text{CDCl}_3$ :  $\delta_{\text{H}} = 7.26$  ppm,  $\delta_{\text{C}} = 77.16$  ppm;  $\text{DMSO}-d_6$ :  $\delta_{\text{H}} = 2.50$  ppm,  $\delta_{\text{C}} = 39.52$  ppm;  $\text{CD}_2\text{Cl}_2$ :  $\delta_{\text{H}} = 5.32$  ppm,  $\delta_{\text{C}} = 53.84$  ppm). Coupling constants ( $J$ ) were given in Hz and rounded up or down. Resonance multiplicity was described as *s* (singlet), *d* (doublet), *t* (triplet), *dd* (doublet of doublets), *dt* (doublet of triplets), *dm* (doublet of multiplet), *td* (triplet of doublets), *q* (quartet), *m* (multiplet) and *bs* (broad signal). Carbon spectra were acquired with a complete decoupling for the proton. **Infrared spectra** (IR) were recorded on a Shimadzu IR Affinity 1S FTIR spectrometer in ATR mode with a diamond mono-crystal. **Mass spectrometry:** (i) High-resolution ESI mass spectra (HRMS) were performed on a Waters LCT HR TOF mass spectrometer in the positive or negative ion mode. MALDI TOF mass spectrometer at Analytical service at School of Chemistry, Cardiff University. The samples were prepared by mixing 10  $\mu\text{L}$  of the compound dissolved in  $\text{CH}_2\text{Cl}_2$  (approx. 1mg/mL) with 10  $\mu\text{L}$  of DCTB matrix dissolved in  $\text{CH}_2\text{Cl}_2$  (15 mg/mL). 1 $\mu\text{L}$  was spotted on the plate. The data was acquired in positive reflectron mode. All analysis were carried out at Cardiff university. **Photophysical analysis:** Absorption spectra of compounds were recorded on air equilibrated solutions at room temperature with an Agilent Cary 5000 UV-Vis spectrophotometer, using quartz cells with path length of 1.0 cm. **X-ray measurements:** Crystallographic studies were undertaken on single

crystal mounted in paratone and studied on an Agilent SuperNova Dual three-circle diffractometer using Cu-K $\alpha$  ( $\lambda = 1.540598 \text{ \AA}$ ) or Mo-K $\alpha$  ( $\lambda = 0.7093187 \text{ \AA}$ ) radiation and a CCD detector. Measurements were typically made at 150(2) K with temperatures maintained using an Oxford Cryostream unless otherwise stated. Data were collected, integrated and corrected for absorption using a numerical absorption correction based on gaussian integration over a multifaceted crystal model within CrysAlisPro.<sup>[1]</sup> The structures were solved by direct methods and refined against  $F^2$  within SHELXL-2013.<sup>[2]</sup> A summary of crystallographic data are available as ESI and the structures deposited with the Cambridge Structural Database (CCDC deposition numbers 1584203-1584205, 1584366-1584378, 1954220-1954233, 1954235, 1954271-1954280, 1954286-1954291 and 1955118). These data can be obtained free of charge from The Cambridge Crystallographic Data Centre via [www.ccdc.cam.ac.uk/data\\_request/cif](http://www.ccdc.cam.ac.uk/data_request/cif).

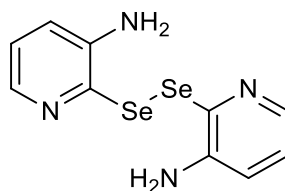
Single crystal **III-1<sub>Te</sub>•III-5** was grown by slow evaporation of CHCl<sub>3</sub>. Crystallographic studies were undertaken on single crystal mounted in paratone and studied at Diamond Light Source Beamline I19-1 using Synchrotron radiation ( $\lambda = 0.6889 \text{ \AA}$ ) and a CCD detector. Measurements were typically made at 100(2) K with temperatures maintained using an Oxford Cryostream unless otherwise stated. Data were collected, integrated and corrected for absorption using a numerical absorption correction based on gaussian integration over a multifaceted crystal model within CrysAlisPro.<sup>[1]</sup> The structures were solved by direct methods and refined against  $F^2$  within SHELXL-2018.<sup>[3]</sup> A summary of crystallographic data are available as ESI and the structures deposited with the Cambridge Structural Database (CCDC deposition number 1954234). These data can be obtained free of charge from The Cambridge Crystallographic Data Centre via [www.ccdc.cam.ac.uk/data\\_request/cif](http://www.ccdc.cam.ac.uk/data_request/cif).

## VI – 1.2 Materials and methods

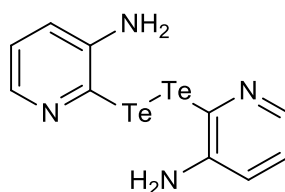
Chemicals were purchased from *Sigma Aldrich*, *Acros Organics*, *TCI*, *Apollo Scientific*, *ABCR*, *Alfa Aesar*, *Carbosynth* and *Fluorochem* and were used as received. Solvents were purchased from *Fluorochem*, *Fisher Chemical* and *Sigma Aldrich*, while deuterated solvents from *Eurisotop* and *Sigma Aldrich*. THF, Et<sub>2</sub>O and CH<sub>2</sub>Cl<sub>2</sub> were dried on a Braun MB SPS-800 solvent purification system. MeOH, CHCl<sub>3</sub> and acetone were purchased as reagent-grade and used without further purification. Et<sub>3</sub>N was distilled from CaH<sub>2</sub> and then stored over KOH. Anhydrous dioxane and pyridine were purchased from *Sigma Aldrich*. Sulfuric acid (H<sub>2</sub>SO<sub>4</sub> >95%) was purchased from *Fluorochem*. Solution of iso-propyl magnesium chloride

in THF were freshly prepared according to a procedure of Lin et al.<sup>[4]</sup> and titrated with the Paquette method,<sup>[5]</sup> or directly purchased from *Sigma Aldrich*. Low temperature baths were prepared using different solvent mixtures depending on the desired temperature: -84 °C with ethyl acetate/liq. N<sub>2</sub>, and 0 °C with ice/H<sub>2</sub>O. Anhydrous conditions were achieved by flaming two necked flasks with a heat gun under vacuum and purging with N<sub>2</sub>. The inert atmosphere was maintained using Nitrogen-filled balloons equipped with a syringe and needle that was used to penetrate the silicon stoppers closing the flask's necks. Additions of liquid reagents were performed using dried plastic or glass syringes. All reactions were performed in dry conditions and under inert atmosphere unless otherwise stated.

## VI – 2 Synthetic procedure and spectral data

**2,2'-diselanediybis(pyridin-3-amine) II-2<sub>Se</sub>****II-2<sub>Se</sub>**

2,2'-diselanediybis(pyridin-3-amine) **II-2<sub>Se</sub>** was synthesised following a procedure inspired by the work of *Bashin et al.*<sup>[6]</sup> and *Innoue et al.*<sup>[7]</sup> To a diluted solution of *i*-PrMgCl (0.5 mL, 1 mmol) in dry THF (2 mL) under anhydrous condition was added dropwise *n*-BuLi (1.6 M, 1.25 mL, 2 mmol) at 0°C. The resulting mixture was stirred at the same temperature for 10 minutes. In parallel, to a solution of 2-bromo-3-aminopyridine (178 mg, 1 mmol) in dry THF (8 mL) under anhydrous condition was added dropwise *n*-BuLi (1.6 M, 0.63 mL, 1 mmol) at 0°C. The reaction was stirred 10 minutes at the same temperature then the tri-alkyl magnesate solution freshly prepared was added dropwise. The reaction was stirred for 30 minutes at 0°C, elemental selenium powder was added in once while a brisk flux of Nitrogen was passed through the flask. The mixture was stirred overnight and poured in a solution of K<sub>3</sub>Fe(CN)<sub>6</sub> (237 mg, 3 mmol) in water (40 mL). The resulting mixture was stirred at room temperature for 10 minutes and the aqueous phase was extracted with Et<sub>2</sub>O (6 x 20 mL). The combined organic extracts were washed with water (15 mL), brine (15 mL), and dried over Na<sub>2</sub>SO<sub>4</sub>. The solvents were removed under reduced pressure. The crude was purified by silica gel chromatography (CHCl<sub>3</sub>/MeOH 2%) to give pure **II-2<sub>Se</sub>** as a dark solid (46 mg, 27%); mp = 187-188 °C. IR:  $\nu$  (cm<sup>-1</sup>): 3435, 3265, 3090, 1610, 1571, 1454, 1417, 1317, 1259, 1222, 1134, 1082, 1056, 729, 661; <sup>1</sup>H NMR (400 MHz, DMSO)  $\delta_{\text{H}}$ : 7.74 (dd, *J* = 4.3, 1.2 Hz, 2H), 7.07 (dd, *J* = 7.9, 4.3 Hz, 2H), 6.99 (dd, *J* = 7.9, 1.2 Hz, 2H), 5.82 (s, NH<sub>2</sub>, 4H); <sup>13</sup>C NMR (75 MHz, DMSO)  $\delta_{\text{C}}$ : 145.7 x2, 137.4 x2, 135.7 x2, 124.4 x2, 120.7 x2; ESI-HRMS: [M + H]<sup>+</sup> calcd for [C<sub>10</sub>H<sub>11</sub>N<sub>4</sub><sup>76</sup>Se<sub>2</sub>]<sup>+</sup>: 338.9368; found: 338.9370.

**2,2'-ditellanediybis(pyridin-3-amine) II-2<sub>Te</sub>****II-2<sub>Te</sub>**

2,2'-ditellanediybis(pyridin-3-amine) **II-2<sub>Te</sub>** was synthesised following a procedure inspired by the work of *Bashin et al.*<sup>[6]</sup> and *Innoue et al.*<sup>[7]</sup> To a diluted solution of *i*-PrMgCl (0.5 mL, 1 mmol) in dry THF (2 mL) under dry condition was added dropwise *n*-BuLi (1.6 M, 1.25 mL, 2 mmol) at 0°C. The resulting mixture was stirred at the same temperature for 10 minutes. In parallel, to a solution of 2-bromo-3-aminopyridine (178 mg, 1 mmol) in dry THF (8 mL) under anhydrous condition was added dropwise *n*-BuLi (1.6 M, 0.63 mL, 1 mmol) at 0°C. The reaction was stirred 10 minutes at the same temperature then the tri-alkyl magnesiate solution freshly prepared was added dropwise. The reaction was stirred for 30 minutes at 0°C, freshly grounded elemental tellurium powder was added in once while a brisk flux of Nitrogen was passed through the flask. The resulting mixture was stirred overnight, poured in a solution of NH<sub>4</sub>Cl (165 mg) in water (40 mL) and air bubbled through for 2h. The aqueous phase was extracted with Et<sub>2</sub>O (10 x 20 mL). The combined organic extracts were washed with brine (2 x 15 mL), and dried over Na<sub>2</sub>SO<sub>4</sub>. The solvents were removed under reduced pressure. The crude was purified by silica gel chromatography (CHCl<sub>3</sub>/MeOH 2%) to give pure **II-2<sub>Te</sub>** as a dark red solid (86 mg, 39%); mp = 154-155 °C. IR:  $\nu$  (cm<sup>-1</sup>): 3042, 2349, 1942, 1689, 1577, 1508, 1431, 1219, 1080, 961, 797, 739, 600; <sup>1</sup>H NMR (400 MHz, DMSO)  $\delta_{\text{H}}$ : 7.73 (dd, *J* = 4.5, 1.6 Hz, 2H), 7.01 (dd, *J* = 8.1, 4.5 Hz, 2H), 6.90 (dd, *J* = 8.1, 1.6 Hz, 2H), 5.71 (s, NH<sub>2</sub>, 4H); <sup>13</sup>C NMR (100 MHz, DMSO)  $\delta_{\text{C}}$ : 148.1 x2, 138.6 x2, 124.1 x2, 120.0 x2, 119.0 x2 ; API-HRMS: [M + H]<sup>+</sup> cacl'd for [C<sub>10</sub>H<sub>11</sub>N<sub>4</sub><sup>124</sup>Te<sub>2</sub>]<sup>+</sup>: 434.9040; found: 434.9048.

### 2-(methylselanyl)pyridin-3-amine **II-3<sub>Se</sub>**

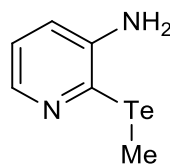


**II-3<sub>Se</sub>**

To a solution of 2,2'-diselanediybis(pyridin-3-amine) **II-2<sub>Se</sub>** (1.204 g, 3.5 mmol) in dry and degassed THF (75 mL) under N<sub>2</sub>, were added NaBH<sub>4</sub> (0.397 g, 10.5 mmol) and MeOH (0.71 mL, 0.561 g, 17.5 mmol) and the reaction was stirred at room temperature for 2 h (the dark red colour turned orange). MeI (0.48 mL, 1.093 g, 7.7 mmol) was added and the mixture stirred further at room temperature for 1.5h. Water (20 mL) was slowly added to the solution which was extracted with Et<sub>2</sub>O (3 x 70 mL). The combined organic extracts were washed with water (30 mL), brine (30 mL) and dried over Na<sub>2</sub>SO<sub>4</sub>. The solvents were removed under reduce pressure. The crude was purified by Silica Gel Chromatography (CHCl<sub>3</sub>/MeOH 1%) to give pure amine **II-3<sub>Se</sub>** as brownish oil (6.756 g, 97%). IR:  $\nu$  (cm<sup>-1</sup>): 3410, 3314, 3046, 2930, 1611, 1566, 1420, 1304, 1269, 1221, 1134, 1090, 1047, 908, 789, 727, 659; <sup>1</sup>H NMR (400 MHz, CDCl<sub>3</sub>)  $\delta_{\text{H}}$ : 7.99 (dd, *J* = 4.6, 1.6 Hz, 1H), 6.93 (dd, *J* = 7.9, 4.6

Hz, 1H), 6.87 (dd,  $J = 7.9, 1.6$  Hz, 1H), 3.80 (s, NH<sub>2</sub>, 2H), 2.48 (s, 3H); <sup>13</sup>C NMR (100 MHz, CDCl<sub>3</sub>) δ<sub>C</sub>: 142.4, 141.0, 140.4, 121.5, 120.4, 6.13; API-HRMS: [M + H]<sup>+</sup> calcd for [C<sub>6</sub>H<sub>9</sub>N<sub>2</sub><sup>76</sup>Se]<sup>+</sup>: 184.9958; found: 184.9952.

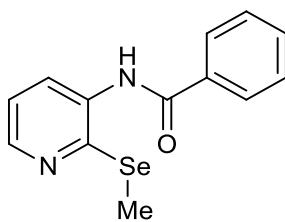
### 2-(methyltellanyl)pyridin-3-amine II-3<sub>Te</sub>



**II-3<sub>Te</sub>**

To a solution of 2,2'-diselanediybis(pyridin-3-amine) **II-2<sub>Te</sub>** (1.700 g, 3.85 mmol) in dry and degassed THF (85 mL) under N<sub>2</sub>, were added NaBH<sub>4</sub> (0.437 g, 11.55 mmol) and MeOH (0.78 mL, 0.617 g, 19.26 mmol) and the reaction was stirred at room temperature for 1 h (the dark red colour turned orange). MeI (0.53 mL, 1.200 g, 8.47 mmol) was added and the mixture was stirred at room temperature for 1.5h more. Water (20 mL) was slowly added to the solution and extracted with Et<sub>2</sub>O (3 x 50 mL). The combined organic extracts were washed with water (30 mL), brine (30 mL), and dried over Na<sub>2</sub>SO<sub>4</sub>. The solvents were removed under reduce pressure. The crude was purified by Silica Gel Chromatography (CHCl<sub>3</sub>/MeOH 1%) to give pure amine **II-3<sub>Te</sub>** as brownish oil (0.670g, 71%). IR: ν (cm<sup>-1</sup>): 3309, 3180, 3041, 2924, 1606, 1560, 1442, 1298, 1217, 1132, 1076, 1039, 789, 650; <sup>1</sup>H NMR (400 MHz, DMSO) δ<sub>H</sub>: 8.02 (dd,  $J = 4.5, 1.6$  Hz, 1H), 6.92 (dd,  $J = 8.0, 4.5$  Hz, 1H), 6.85 (dd,  $J = 8.0, 1.6$  Hz, 1H), 3.85 (s, NH<sub>2</sub>, 2H), 2.28 (s, 3H); <sup>13</sup>C NMR (100 MHz, CDCl<sub>3</sub>) δ<sub>C</sub>: 145.7, 141.8, 128.6, 122.2, 119.6, -15.46; API-HRMS: [M + H]<sup>+</sup> calcd for [C<sub>6</sub>H<sub>9</sub>N<sub>2</sub><sup>122</sup>Te]<sup>+</sup>: 230.9796; found: 230.9785.

### *N*-(2-(methylselanyl)pyridin-3-yl)benzamide II-4<sub>Se</sub>

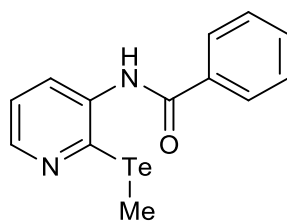


**II-4<sub>Se</sub>**

To a mixture of benzoyl chloride (0.12 mL, 140 mg, 1 mmol) in dry THF (2 mL) at 0 °C under anhydrous condition, a solution of 2-(methylselanyl)pyridin-3-amine **II-3<sub>Se</sub>** (187 mg, 1 mmol) and dry NEt<sub>3</sub> (0.17 mL, 120 mg, 1.2 mmol) in dry THF (2 mL) was added dropwise. The reaction was stirred 5 minutes at 0 °C then overnight at room temperature. The resulting mixture was filtrated and washed with Et<sub>2</sub>O (2 mL). The filtrate was recovered, and solvent removed under reduced pressure.

The crude material was purified by silica gel chromatography (CHCl<sub>3</sub>/MeOH 0.5%) to afford amide **II-4<sub>Se</sub>** as a beige solid (113 mg, 39 %); mp = 118-123 °C. IR:  $\nu$  (cm<sup>-1</sup>): 3224, 2930, 1651, 1601, 1576, 1514, 1487, 1487, 1386, 1296, 1201, 905, 791, 656; <sup>1</sup>H NMR (300 MHz, DMSO)  $\delta$ <sub>H</sub>: 10.17 (s, 1H), 8.44 (d, *J* = 2.8 Hz, 1H), 7.99 (d, *J* = 6.6 Hz, 2H), 7.66-7.51 (m, 4H), 7.26 (dd, *J* = 6.7, 4.7 Hz, 1H), 2.35 (s, 3H); <sup>13</sup>C NMR (75 MHz, CDCl<sub>3</sub>)  $\delta$ <sub>C</sub>: 165.8, 154.1, 147.7, 135.0, 133.7 (two peaks overlap, 2C), 131.9, 128.5 (two peaks overlap, 2C), 127.7 (two peaks overlap, 2C), 120.3, 5.06; ESI-HRMS: [M + H]<sup>+</sup> calcd for [C<sub>13</sub>H<sub>13</sub>N<sub>2</sub>O<sup>76</sup>Se]<sup>+</sup>: 289.0220; found: 289.0230.

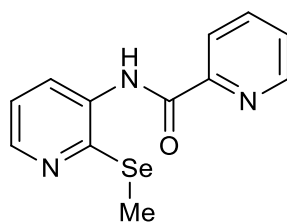
#### ***N*-(2-(methyltellanyl)pyridin-3-yl)benzamide II-4<sub>Te</sub>**



**II-4<sub>Te</sub>**

To a mixture of 2-(methyltellanyl)pyridin-3-amine **II-3<sub>Te</sub>** (210 mg, 1 mmol) and dry pyridine (0.09 mL, 88 mg, 1.1 mmol) in dry CH<sub>2</sub>Cl<sub>2</sub> (5 mL) at 0 °C under anhydrous condition, a solution of benzoyl chloride (0.12 mL, 140 mg, 1 mmol) in dry CH<sub>2</sub>Cl<sub>2</sub> (2 mL) was added dropwise. The reaction was stirred 5 minutes at 0 °C then overnight at room temperature. The resulting mixture was diluted with EtOAc (50 mL) and washed with water (15 mL), brine (15 mL), and dried over Na<sub>2</sub>SO<sub>4</sub>. The solvents were removed under reduced pressure. The crude was purified by silica gel chromatography (CHCl<sub>3</sub>/MeOH 1%) to give pure amide **II-4<sub>Te</sub>** as a beige solid (269 mg, 89%); mp = 145-146 °C. IR:  $\nu$  (cm<sup>-1</sup>): 3253, 1647, 1601, 1566, 1508, 1481, 1389, 1259, 1566, 1063, 1026, 837, 791, 712, 689, 648; <sup>1</sup>H NMR (400 MHz, DMSO)  $\delta$ <sub>H</sub>: 10.31 (s, 1H), 8.45 (dd, *J* = 4.7, 1.7 Hz, 1H), 7.99 (dd, *J* = 6.8, 1.6 Hz, 2H), 7.66-7.52 (m, 4H), 7.25 (dd, *J* = 7.9, 4.7, 1 Hz), 2.15 (s, 3H); <sup>13</sup>C NMR (100 MHz, DMSO)  $\delta$ <sub>C</sub>: 165.9, 148.4, 143.3, 137.9, 133.7, 133.6, 132.0, 128.5 (two peaks overlap, 2C), 127.8 (two peaks overlap, 2C), 120.9, -14.76; ESI-HRMS: [M + H]<sup>+</sup> calcd for [C<sub>13</sub>H<sub>13</sub>N<sub>2</sub>O<sup>122</sup>Te]<sup>+</sup>: 335.0058; found: 335.0058.

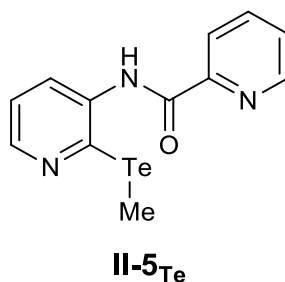
#### ***N*-(2-(methylselanyl)phenyl)picolinamide II-5<sub>Se</sub>**



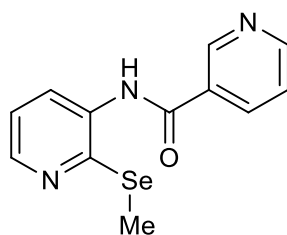
**II-5<sub>Se</sub>**

To a suspension of picolinoyl chloride hydrochloride (128 mg, 0.72 mmol) in dry  $\text{CH}_2\text{Cl}_2$  (3 mL) at 0 °C under anhydrous condition, a solution of 2-(methylselanyl)pyridin-3-amine **II-3<sub>Se</sub>** (112 mg, 0.6 mmol) and dry  $\text{NEt}_3$  (0.21 mL, 152 mg, 1.5 mmol) in dry  $\text{CH}_2\text{Cl}_2$  (3 mL) was added dropwise. The reaction was stirred 5 minutes at 0 °C then overnight at room temperature. The resulting mixture was diluted with EtOAc (50 mL), washed with water (5 mL), brine (5 mL), and dried over  $\text{Na}_2\text{SO}_4$ . The solvents were removed under reduced pressure. The crude was purified by silica gel chromatography ( $\text{CHCl}_3/\text{MeOH}$  1%) to give pure amide **II-5<sub>Se</sub>** as a white solid (127 mg, 72%); mp = 96-98 °C IR:  $\nu$  ( $\text{cm}^{-1}$ ): 3280, 2922, 2850, 1689, 1562, 1502, 1435, 1382, 1064, 1055, 1080, 734, 601, 590;  $^1\text{H}$  NMR (400 MHz,  $\text{CDCl}_3$ )  $\delta_{\text{H}}$ : 10.35 (s, 1H), 8.77 (ddd,  $J$  = 4.8, 1.6, 1.0 Hz, 1H), 8.38 (dd,  $J$  = 4.7, 1.6 Hz, 1H), 8.17 (ddd appearing dt,  $J$  = 7.7, 0.8 Hz, 1H), 8.12 – 8.04 (m, 2H), 7.72 (ddd,  $J$  = 7.5, 4.8, 1.3 Hz, 1H), 7.28 (dd,  $J$  = 7.9, 4.7 Hz, 1H), 2.43 (s, 3H);  $^{13}\text{C}$  NMR (100 MHz,  $\text{CDCl}_3$ )  $\delta_{\text{C}}$ : 162.6, 149.7, 148.8, 148.7, 146.5, 138.4, 133.5, 130.6, 127.4, 122.4, 120.7, 5.79; EI-HRMS:  $[\text{M} + \text{H}]^+$  calcd for  $[\text{C}_{12}\text{H}_{12}\text{N}_3\text{O}^{76}\text{Se}]^+$ : 289.0220; found: 289.0219.

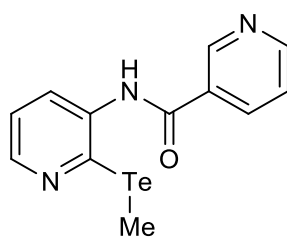
***N*-(2-(methyltellanyl)phenyl)picolinamide II-5<sub>Te</sub>**



To a suspension of picolinoyl chloride hydrochloride (214 mg, 1.2 mmol) in dry  $\text{CH}_2\text{Cl}_2$  (4 mL) at 0 °C under anhydrous condition, a solution of 2-(methyltellanyl)pyridin-3-amine **II-3<sub>Te</sub>** (236 mg, 1 mmol) and  $\text{NEt}_3$  (0.35 mL, 253 mg, 2.5 mmol) in dry  $\text{CH}_2\text{Cl}_2$  (4 mL) was added dropwise. The reaction was stirred 5 minutes at 0 °C then overnight at room temperature. The resulting mixture was diluted with EtOAc (90 mL) and washed with water (10 mL), brine (10 mL), and dried over  $\text{Na}_2\text{SO}_4$ . The solvents were removed under reduced pressure. The crude was purified by silica gel chromatography ( $\text{CHCl}_3/\text{MeOH}$  1%) to give pure amide **II-5<sub>Te</sub>** as a red-purple solid (310 mg, 91%); mp = 113-115 °C. IR:  $\nu$  ( $\text{cm}^{-1}$ ): 3244, 3057, 3037, 2924, 1689, 1566, 1512, 1377, 1290, 1001, 801, 727, 656, 619;  $^1\text{H}$  NMR (400 MHz, DMSO)  $\delta_{\text{H}}$ : 10.51 (s, 1H), 8.77 (ddd,  $J$  = 4.7, 1.6, 0.8 Hz, 1H), 8.41 (ddd,  $J$  = 4.7, 1.6, 0.8 Hz, 1H), 8.16 (d,  $J$  = 7.6 Hz, 1H), 8.11 – 8.05 (m, 1H), 7.81 (ddd,  $J$  = 8.0, 1.6, 1.0 Hz, 1H), 7.74-7.69 (m, 1H), 7.26 (dd,  $J$  = 8.0, 4.6 Hz, 1H), 2.18 (s, 3H);  $^{13}\text{C}$  NMR (100 MHz,  $\text{CDCl}_3$ )  $\delta_{\text{C}}$ : 163.0, 149.0, 148.7, 147.8, 140.4, 138.3, 137.5, 131.3, 127.4, 122.5, 121.1, -14.28; EI-HRMS:  $[\text{M}]^+$  calcd for  $[\text{C}_{12}\text{H}_{11}\text{N}_3\text{O}^{122}\text{Te}]^+$ : 335.0058; found: 335.0055.

***N*-(2-(methylselanyl)pyridin-3-yl)nicotinamide II-6<sub>Se</sub>****II-6<sub>Se</sub>**

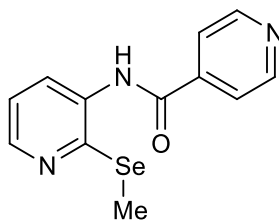
To a suspension of nicotinoyl chloride hydrochloride (214 mg, 1.2 mmol) in dry CH<sub>2</sub>Cl<sub>2</sub> (2 mL) at 0 °C under anhydrous condition, a solution of 2-(methylselanyl)pyridin-3-amine **II-3<sub>Se</sub>** (187 mg, 1 mmol) and dry pyridine (0.19 mL, 182 mg, 2.3 mmol) in dry CH<sub>2</sub>Cl<sub>2</sub> (5 mL) was added dropwise. The reaction was stirred 5 minutes at 0 °C then overnight at room temperature. The resulting mixture was diluted with EtOAc (70 mL) and washed with water (20 mL), brine (20 mL), and dried over Na<sub>2</sub>SO<sub>4</sub>. The solvents were removed under reduced pressure. The crude was purified by silica gel chromatography (CHCl<sub>3</sub>/MeOH 2%) to give pure amide **II-6<sub>Se</sub>** as a light orange solid (236 mg, 81%); mp = 128-130°C IR:  $\nu$  (cm<sup>-1</sup>): 3232, 1647, 1587, 1522, 1450, 1415, 1391, 1300, 120, 1067, 907, 826, 804, 734, 663; <sup>1</sup>H NMR (300 MHz, DMSO)  $\delta$ <sub>H</sub>: 10.42 (s, 1H), 9.15 (d, *J* = 1.8 Hz, 1H), 8.80 (dd, *J* = 4.8, 1.6 Hz, 1H), 8.46 (dd, *J* = 4.8, 1.8 Hz, 1H), 8.32 (dd appearing as dt, *J* = 8.0, 1.8 Hz, 1H), 7.67 (dd, *J* = 7.8, 1.6 Hz, 1H), 7.60 (dd, *J* = 8.0, 4.8 Hz, 1H), 7.27 (dd, *J* = 7.8, 4.8 Hz, 1H), 2.36 (s, 3H); <sup>13</sup>C NMR (75 MHz, CDCl<sub>3</sub>)  $\delta$ <sub>C</sub>: 164.5, 154.0, 152.6, 148.8, 148.0, 135.5, 135.1, 133.2, 129.4, 123.7, 120.4, 5.13; ESI-HRMS: [M + H]<sup>+</sup> calcd for [C<sub>12</sub>H<sub>12</sub>N<sub>3</sub>O<sup>80</sup>Se]<sup>+</sup>: 294.0146; found: 294.0152.

***N*-(2-(methyltellanyl)pyridin-3-yl)nicotinamide II-6<sub>Te</sub>****II-6<sub>Te</sub>**

To a suspension of nicotinoyl chloride hydrochloride (214 mg, 0.86 mmol) in dry CH<sub>2</sub>Cl<sub>2</sub> (2 mL) at 0 °C under anhydrous condition, a solution of 2-(methyltellanyl)pyridin-3-amine **II-3<sub>Te</sub>** (236 mg, 1 mmol) and dry pyridine (0.19 mL, 182 mg, 2.3 mmol) in dry CH<sub>2</sub>Cl<sub>2</sub> (5 mL) was added dropwise. The reaction was stirred 5 minutes at 0 °C then overnight at room temperature. The resulting mixture was diluted with EtOAc (70 mL) and washed with water (25 mL), brine (15 mL), and dried over Na<sub>2</sub>SO<sub>4</sub>, filtered and the solvent removed under reduced pressure. The crude was passed through

silica gel chromatography (CHCl<sub>3</sub>/MeOH 2%) to give amide **II-6<sub>Te</sub>** as a white solid (238 mg) that was used in the next step without further purification.

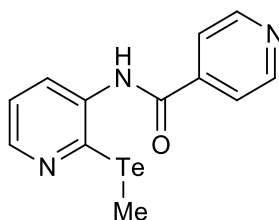
***N*-(2-(methylselanyl)phenyl)isonicotinamide II-7<sub>Se</sub>**



**II-7<sub>Se</sub>**

To a suspension of isonicotinoyl chloride hydrochloride (192 mg, 1.08 mmol) in dry CH<sub>2</sub>Cl<sub>2</sub> (2 mL) at 0 °C under anhydrous condition, a solution of 2-(methylselanyl)pyridin-3-amine **II-3<sub>Se</sub>** (186 mg, 0.90 mmol) and dry pyridine (0.17 mL, 164 mg, 2.07 mmol) in dry CH<sub>2</sub>Cl<sub>2</sub> (5 mL) was added dropwise. The reaction was stirred 5 minutes at 0 °C then overnight at room temperature. The resulting mixture was diluted with EtOAc (70 mL) and washed with water (20 mL), brine (20 mL), and dried over Na<sub>2</sub>SO<sub>4</sub>. The solvents were removed under reduced pressure. The crude was purified by silica gel chromatography (CHCl<sub>3</sub>/MeOH 2%) to give pure amide **II-7<sub>Se</sub>** as a light orange solid (243 mg, 92%); mp = 144-146 °C IR:  $\nu$  (cm<sup>-1</sup>): 3190, 1643, 1597, 1555, 1512, 1393, 1296, 1215, 1200, 1061, 991, 914, 829, 783, 687, 648, 590; <sup>1</sup>H NMR (400 MHz, DMSO)  $\delta$ <sub>H</sub>: 10.50 (s, 1H), 8.82 (dd, *J* = 4.6, 1.4 Hz, 2H), 8.46 (dd, *J* = 4.8, 1.6 Hz, 1H), 7.88 (dd, *J* = 4.6, 1.4 Hz, 2H), 7.66 (dd, *J* = 7.8, 1.6 Hz, 1H), 7.27 (dd, *J* = 7.8, 4.8 Hz, 1H), 2.36 (s, 3H); <sup>13</sup>C NMR (100 MHz, CDCl<sub>3</sub>)  $\delta$ <sub>C</sub>: 164.4, 154.0, 150.5 (two peaks overlap, 2C), 148.2, 140.8, 135.1, 133.1, 121.6 (two peaks overlap, 2C), 120.4, 5.14; ESI-HRMS: [M + H]<sup>+</sup> caclcd for [C<sub>12</sub>H<sub>12</sub>N<sub>3</sub>O<sup>76</sup>Se]<sup>+</sup>: 290.0172; found: 290.0169.

***N*-(2-(methyltellanyl)phenyl)isonicotinamide II-6<sub>Te</sub>**

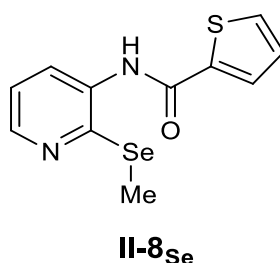


**II-6<sub>Te</sub>**

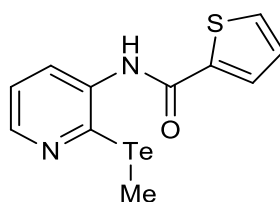
To a suspension of isonicotinoyl chloride hydrochloride (154 mg, 0.86 mmol) in dry CH<sub>2</sub>Cl<sub>2</sub> (2 mL) at 0 °C under anhydrous condition, a solution of 2-(methyltellanyl)pyridin-3-amine **II-3<sub>Te</sub>** (170 mg, 0.72 mmol) and dry pyridine (0.14 mL, 131 mg, 1.66 mmol) in dry CH<sub>2</sub>Cl<sub>2</sub> (4 mL) was added dropwise. The reaction was stirred 5 minutes at 0 °C then overnight at room temperature. The resulting

mixture was diluted with EtOAc (70 mL) and washed with water (25 mL), brine (15 mL), and dried over Na<sub>2</sub>SO<sub>4</sub>. The solvent were removed under reduced pressure. The crude was purified by silica gel chromatography (CHCl<sub>3</sub>/MeOH 2%) to give pure amide **II-7<sub>Te</sub>** as a white solid (166 mg, 68%); mp = 142-144°C. IR:  $\nu$  (cm<sup>-1</sup>): 3229, 1651, 1528, 1450, 1303, 1200, 1119, 1065, 910, 802, 733, 802, 733, 698, 656, 590, 498; <sup>1</sup>H NMR (400 MHz, DMSO)  $\delta_{\text{H}}$ : 10.62 (s, 1H), 8.83 (d, *J* = 4.8 Hz, 2H), 8.48 (d, *J* = 4.8 Hz, 1H), 7.88 (d, *J* = 4.8 Hz, 2H), 7.58 (d, *J* = 7.6 Hz, 1H), 7.27 (dd, *J* = 7.6, 4.8 Hz, 1H), 2.16 (s, 3H); <sup>13</sup>C NMR (100 MHz, CDCl<sub>3</sub>)  $\delta_{\text{C}}$ : 164.6, 150.6 (two peaks overlap, 2C, 148.9, 143.2, 140.7, 137.3, 133.9, 121.6 (two peaks overlap, 2C, 121.1, -14.54; ESI-HRMS: [M + H]<sup>+</sup> caclcd for [C<sub>12</sub>H<sub>12</sub>N<sub>3</sub>O<sup>122</sup>Te]<sup>+</sup>: 336.0011; found: 336.0020.

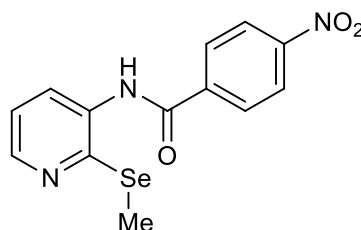
### ***N*-(2-(methylselanyl)pyridin-3-yl)thiophene-2-carboxamide **II-8<sub>Se</sub>****



To a solution of 2-(methylselanyl)pyridin-3-amine **II-3<sub>Se</sub>** (187 mg, 1 mmol) in dry CH<sub>2</sub>Cl<sub>2</sub> (5 mL) with dry pyridine (0.09 mL, 88 mg, 1.1 mmol) at 0°C under anhydrous condition, a mixture of thiophene carbonyl chloride (0.11 mL, 147 mg, 1 mmol) in dry CH<sub>2</sub>Cl<sub>2</sub> (2 mL) was added dropwise. The reaction was stirred 5 minutes at 0 °C then overnight at room temperature. The resulting mixture was diluted with EtOAc (50 mL) and washed with water (30 mL), brine (30 mL), and dried over Na<sub>2</sub>SO<sub>4</sub>. The solvents were removed under reduced pressure. The crude was purified by silica gel chromatography (CHCl<sub>3</sub>/MeOH 1%) to afford pure amide **II-8<sub>Se</sub>** as a yellow solid (249 mg, 84%); mp = 157-159 °C. IR:  $\nu$  (cm<sup>-1</sup>): 3239, 1638, 1572, 1524, 1393, 1292, 1271, 1244, 1202, 1098, 1065, 909, 860, 808, 900, 727, 656, 627; <sup>1</sup>H NMR (400 MHz, DMSO)  $\delta_{\text{H}}$ : 10.19 (s, 1H), 8.44 (dd, *J* = 4.8, 1.7 Hz, 1H), 8.00 (dd, *J* = 3.7, 1.0 Hz, 1H), 7.88 (dd, *J* = 5.0, 1.1 Hz, 1H), 7.62 (dd, *J* = 7.8, 1.7 Hz, 1H), 7.27 – 7.22 (m, 2H), 2.35 (s, 3H); <sup>13</sup>C NMR (100 MHz, CDCl<sub>3</sub>)  $\delta_{\text{C}}$ : 160.4, 1541, 147.8, 138.8, 135.1, 133.2, 132.1, 129.6, 128.2, 120.3, 5.05; ESI-HRMS: [M + H]<sup>+</sup> caclcd for [C<sub>11</sub>H<sub>11</sub>N<sub>2</sub>OS<sup>76</sup>Se]<sup>+</sup>: 294.9784; found: 294.9784.

**N-(2-(methyltellanyl)pyridin-3-yl)thiophene-2-carboxamide II-8<sub>Te</sub>****II-8<sub>Te</sub>**

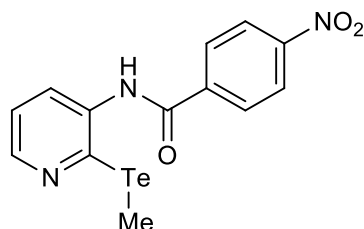
To a solution of 2-(methyltellanyl)pyridin-3-amine **II-3<sub>Te</sub>** (0.236 g, 1 mmol) in dry CH<sub>2</sub>Cl<sub>2</sub> (5 mL) with dry pyridine (0.09 mL, 88 mg, 1.1 mmol) at 0 °C under dry condition, a mixture of thiophene carbonyl chloride (0.11 mL, 147 mg, 1 mmol) in dry CH<sub>2</sub>Cl<sub>2</sub> (2 mL) was added dropwise. The reaction was stirred 5 minutes at 0 °C then overnight at room temperature. A yellow precipitate appeared and the mixture was filtrated, the solid recovered and purified by filtration over a silica pad (CHCl<sub>3</sub>/MeOH 1%) to afford pure amide **II-8<sub>Te</sub>** as yellow solid (263 mg, 76%); mp = 137-138 °C. IR:  $\nu$  (cm<sup>-1</sup>): 3232, 2924, 1635, 1568, 1526, 1391, 1290, 1242, 1213, 1061, 1051, 860, 806, 787, 725, 653, 584; <sup>1</sup>H NMR (400 MHz, DMSO)  $\delta_{\text{H}}$ : 10.32 (s, 1H), 8.45 (dd,  $J$  = 4.7, 1.7 Hz, 1H), 7.99 (d,  $J$  = 3.5, 1H), 7.89 (dd,  $J$  = 6.6 Hz, 1H), 7.55 (dd,  $J$  = 7.8, 1.7 Hz, 1H), 7.26 – 7.22 (m, 2H), 2.15 (s, 3H); <sup>13</sup>C NMR (100 MHz, CDCl<sub>3</sub>)  $\delta_{\text{C}}$ : 160.5, 148.6, 143.4, 138.7, 137.4, 133.8, 132.2, 129.7, 128.2, 120.9, -14.74; ESI-HRMS: [M + H]<sup>+</sup> caclcd for [C<sub>11</sub>H<sub>11</sub>N<sub>2</sub>OS<sup>122</sup>Te]<sup>+</sup>: 340.9623; found: 340.9629.

**N-(2-(methylselanyl)pyridin-3-yl)-4-nitrobenzamide II-9<sub>Se</sub>****II-9<sub>Se</sub>**

To a mixture of 2-(methylselanyl)pyridin-3-amine **II-3<sub>Se</sub>** (187 mg, 1 mmol) and pyridine (0.1 mL, 88 mg, 1.1 mmol) in dry CH<sub>2</sub>Cl<sub>2</sub> (5 mL) at 0 °C under anhydrous condition, a solution of *p*-nitrobenzoyl chloride (186 mg, 1 mmol) in dry CH<sub>2</sub>Cl<sub>2</sub> (2 mL) was added dropwise. The reaction was stirred 5 minutes at the same temperature then overnight at room temperature. The mixture was diluted with EtOAc (50 mL) and washed with water (15 mL), brine (15 mL), and dried over Na<sub>2</sub>SO<sub>4</sub>. The solvents were removed under reduced pressure. The crude was purified by silica gel chromatography (CHCl<sub>3</sub>/MeOH 1%) to give pure N-(2-(methylselanyl)pyridin-3-yl)-4-nitrobenzamide **II-9<sub>Se</sub>** as a yellow solid (283 mg, 84%); mp = 154-156 °C. IR:  $\nu$  (cm<sup>-1</sup>): 2922, 1578, 1575, 1476, 1418, 1371, 1285, 1233, 1211, 1111, 1080, 1049, 897, 851, 801, 737, 695, 664; <sup>1</sup>H NMR

(300 MHz, DMSO)  $\delta_{\text{H}}$ : 10.55 (s, 1H), 8.46 (dd  $J = 4.7, 1.3$  Hz, 1H), 8.40 (d,  $J = 8.7$  Hz, 2H), 8.21 (d,  $J = 8.7$  Hz, 2H), 7.67 (dd,  $J = 7.7, 1.3$  Hz, 1H), 7.28 (dd,  $J = 7.7, 4.7$  Hz, 1H), 2.37 (s, 3H);  $^{13}\text{C}$  NMR (125 MHz,  $\text{CDCl}_3$ )  $\delta_{\text{C}}$ : 164.3, 154.0, 149.4, 148.1, 139.3, 135.1, 133.2, 129.2 x2, 123.8 x2, 120.4, 5.11; ESI-HRMS:  $[\text{M} + \text{H}]^+$  calcd for  $[\text{C}_{13}\text{H}_{12}\text{N}_3\text{O}_3^{76}\text{Se}]^+$ : 334.0071; found: 334.0063.

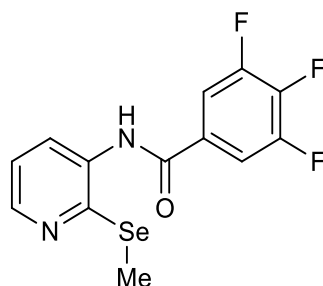
### ***N*-(2-(methyltellanyl)pyridin-3-yl)-4-nitrobenzamide II-9<sub>Te</sub>**



**II-9<sub>Te</sub>**

To a mixture of 2-(methyltellanyl)pyridin-3-amine **II-3<sub>Te</sub>** (471 mg, 2 mmol) and pyridine (0.18 mL, 174 mg, 2.2 mmol) in dry  $\text{CH}_2\text{Cl}_2$  (10 mL) at 0 °C under anhydrous conditions, a solution of *p*-nitrobenzoyl chloride (371 mg, 2 mmol) in dry  $\text{CH}_2\text{Cl}_2$  (4 mL) was added dropwise. The reaction was stirred 5 minutes at the same temperature then overnight at room temperature. The mixture was diluted with EtOAc (50 mL) and washed with water (20 mL), brine (20 mL) and dried over  $\text{Na}_2\text{SO}_4$ . The solvents were removed under reduced pressure. The crude was purified by silica gel chromatography ( $\text{CHCl}_3/\text{MeOH}1\%$ ) to give pure *N*-(2-(methyltellanyl)pyridin-3-yl)-4-nitrobenzamide **II-9<sub>Te</sub>** as an orange solid (593 mg, 77%); mp = 154-156 °C. IR:  $\nu$  ( $\text{cm}^{-1}$ ): 3227, 2361, 1645, 1584, 1520, 1391, 1296, 1261, 1053, 1005, 829, 802, 656;  $^1\text{H}$  NMR (300 MHz, DMSO)  $\delta_{\text{H}}$ : 10.66 (s, 1H), 8.48 (dd,  $J = 4.5, 1.0$  Hz, 1H), 8.41 (d,  $J = 8.5$  Hz, 2H), 8.21 (d,  $J = 8.5$  Hz, 2H), 7.59 (dd,  $J = 7.6, 1.0$  Hz, 1H), 7.27 (dd,  $J = 7.6, 4.5$  Hz, 1H), 2.17 (s, 3H);  $^{13}\text{C}$  NMR (100 MHz,  $\text{CDCl}_3$ )  $\delta_{\text{C}}$ : 164.4, 149.5, 148.8, 143.1, 139.2, 137.4, 133.8, 129.2 x2, 123.8 x2, 121.0, -14.62; ESI-HRMS:  $[\text{M} + \text{H}]^+$  calcd for  $[\text{C}_{13}\text{H}_{12}\text{N}_3\text{O}_3^{122}\text{Te}]^+$ : 379.9909; found: 379.9904.

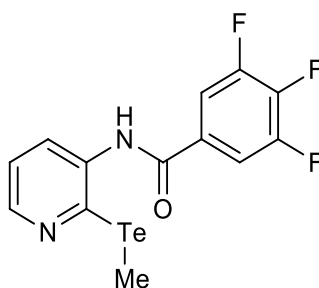
### **3,4,5-trifluoro-*N*-(2-(methylselanyl)pyridin-3-yl)benzamide II-10<sub>Se</sub>**



**II-10<sub>Se</sub>**

To a mixture of 2-(methylselenanyl)pyridin-3-amine **II-3<sub>se</sub>** (143 mg, 0.7 mmol) and dry pyridine (0.06 mL, 61 mg, 0.77 mmol) in dry CH<sub>2</sub>Cl<sub>2</sub> (3 mL) at 0 °C under anhydrous condition, a solution of trifluorobenzoyl chloride (0.09 mL, 137 mg, 0.7 mmol) in dry CH<sub>2</sub>Cl<sub>2</sub> (2 mL) was added dropwise. The reaction was stirred 5 minutes at 0 °C then overnight at room temperature. The resulting mixture was diluted with EtOAc (50 mL) and washed with water (2 x 15 mL), brine (20 mL), and dried over Na<sub>2</sub>SO<sub>4</sub>. The solvents were removed under reduced pressure. The crude was purified by silica gel chromatography (CHCl<sub>3</sub>/MeOH 1%) to give pure amide **II-10<sub>se</sub>** as a white solid (157 mg, 45%); mp = 143-145 °C. IR:  $\nu$  (cm<sup>-1</sup>): 3219, 2980, 1649, 1618, 1562, 1514, 1449, 1391, 1348, 1219, 1069, 1040, 889, 785, 748, 727, 673; <sup>1</sup>H NMR (400 MHz, DMSO)  $\delta_{\text{H}}$ : 10.38 (s, 1H), 8.46 (dd,  $J$  = 4.7, 1.5 Hz, 1H), 7.93 (dd,  $J$  = 8.2, 7.0 Hz, 2H), 7.63 (dd,  $J$  = 7.7, 1.5 Hz, 1H), 7.27 (dd,  $J$  = 7.7, 4.7 Hz, 1H), 2.36 (s, 3H); <sup>19</sup>F NMR (376 MHz, DMSO)  $\delta_{\text{F}}$ : -133.5 (d,  $J$  = 21.6 Hz, 2F), -155.7 (t,  $J$  = 21.6 Hz, 1F); <sup>13</sup>C NMR (100 MHz, CDCl<sub>3</sub>)  $\delta_{\text{C}}$ : 162.6, 154.0, 150.2 (ddd,  $J_{\text{CF}}$  = 249.8, 10.2, 3.6 Hz) (two peaks overlap, 2C), 148.1, 141.3 (dt,  $J_{\text{CF}}$  = 255.0, 15.6 Hz), 135.1, 133.0, 129.9 (m), 120.4, 112.9 (dd,  $J_{\text{CF}}$  = 16.0, 5.9 Hz) (two peaks overlap, 2C, 5.11; ESI-HRMS: [M + H]<sup>+</sup> caclcd for [C<sub>13</sub>H<sub>10</sub>N<sub>2</sub>OF<sub>3</sub><sup>76</sup>Se]<sup>+</sup>: 342.9937; found: 342.9931.

### 3,4,5-trifluoro-*N*-(2-(methyltellanyl)pyridin-3-yl)benzamide **II-10<sub>Te</sub>**

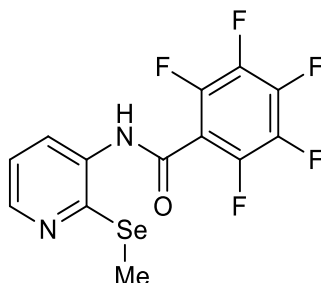


**II-10<sub>Te</sub>**

To a mixture of trifluorobenzoyl chloride (0.13 mL, 195 mg, 1 mmol) in dry CH<sub>2</sub>Cl<sub>2</sub> (5 mL) at 0 °C under anhydrous condition, a solution of 2-(methyltellanyl)pyridin-3-amine **II-3<sub>Te</sub>** (236 mg, 1 mmol) and dry NEt<sub>3</sub> (0.17 mL, 120 mg, 1.2 mmol) in dry CH<sub>2</sub>Cl<sub>2</sub> (2 mL) was added dropwise. The reaction was stirred 5 minutes at 0 °C then overnight at room temperature. The mixture was diluted with EtOAc (50 mL) and washed with water (10 mL), brine (10 mL), and dried over Na<sub>2</sub>SO<sub>4</sub>. The solvents were removed under reduced pressure. The crude was purified by silica gel chromatography (CHCl<sub>3</sub>/MeOH 1%) to give pure amide **II-10<sub>Te</sub>** as a white solid (274 mg, 70%); mp = 146-148 °C. IR:  $\nu$  (cm<sup>-1</sup>): 3674, 3211, 2980, 2361, 1643, 1618, 1508, 1435, 1045, 901, 864, 790, 748, 679, 665, 633; <sup>1</sup>H NMR (300 MHz, DMSO)  $\delta_{\text{H}}$ : 10.48 (s, 1H), 8.47 (dd,  $J$  = 4.7, 1.6 Hz, 1H), 7.93 (dd,  $J$  = 8.3, 7.0 Hz, 2H), 7.56 (dd,  $J$  = 7.8, 1.6 Hz, 1H), 7.26 (dd,  $J$  = 7.8, 4.7 Hz, 1H), 2.16 (s, 3H); <sup>19</sup>F NMR (376 MHz, DMSO)  $\delta_{\text{F}}$ : -133.4 (d,  $J$  = 21.5 Hz, 2F), -155.6 (t,  $J$  = 21.5 Hz, 1F); <sup>13</sup>C NMR (75 MHz, CDCl<sub>3</sub>)  $\delta_{\text{C}}$ : 162.7, 150.2

(ddd,  $J_{CF} = 249.0, 10.1, 3.5$  Hz) (two peaks overlap, 2C), 148.8, 143.1, 141.3 (dm,  $J_{CF} = 254.5$  Hz), 137.3, 133.8, 129.9 (m), 121.0, 112.9 (dd,  $J_{CF} = 16.6, 6.0$  Hz) (two peaks overlap, 2C), -14.60; ESI-HRMS:  $[M + H]^+$  calcd for  $[C_{13}H_{10}N_2OF_3^{122}Te]^+$ : 388.9776; found: 388.9790.

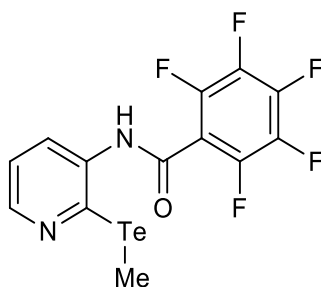
### 2,3,4,5,6-pentafluoro-*N*-(2-(methylselanyl)pyridin-3-yl)benzamide II-11<sub>Se</sub>



**II-11<sub>Se</sub>**

To a mixture of 2-(methylselanyl)pyridin-3-amine **II-3<sub>Se</sub>** (187 mg, 1 mmol) and dry pyridine (0.1 mL, 88 mg, 1.1 mmol) in dry  $CH_2Cl_2$  (5 mL) at 0 °C under anhydrous condition, a solution of pentafluorobenzoyl chloride (0.15 mL, 231 mg, 1 mmol) in dry  $CH_2Cl_2$  (2 mL) was added dropwise. The reaction was stirred 5 minutes at the same temperature then overnight at room temperature. The mixture was diluted with EtOAc (50 mL) and washed with water (15 mL), brine (15 mL), and dried over  $Na_2SO_4$ . The solvents were removed under reduced pressure. The crude was purified by silica gel chromatography ( $CHCl_3/MeOH$  1%) to give pure amide **II-11<sub>Se</sub>** as white solid (293 mg, 77%); mp = 156-158 °C. IR:  $\nu$  ( $cm^{-1}$ ): 3246, 2980, 2361, 1655, 1518, 1489, 1393, 1329, 1225, 1103, 1071, 999, 774, 652, 608;  $^1H$  NMR (300 MHz, DMSO)  $\delta_H$ : 10.78 (s, 1H), 8.47 (dd,  $J = 4.6, 1.1$  Hz, 1H), 7.68 (dd,  $J = 7.7, 1.1$  Hz, 1H), 7.27 (dd,  $J = 7.7, 4.56$ , 1 = H), 2.9 (s, 3H);  $^{19}F$  NMR (376 MHz, DMSO)  $\delta_F$ : -141.1 (dd,  $J = 23.8, 6.3$ , 2F), -151.9 (t, 22.0 Hz, 1F), -161.1 (m, 2F);  $^{13}C$  NMR (75 MHz,  $CDCl_3$ )  $\delta_C$ : 156.3, 152.7, 148.3, 143.3 (dm,  $J_{CF} = 248.9$  Hz) (two peaks overlap, 2C), 141.6 (dm,  $J_{CF} = 253.8$  Hz), 137.0 (dm,  $J_{CF} = 250.9$  Hz) (two peaks overlap, 2C), 134.3, 131.8, 120.4, 111.8 (m), 5.15; ESI-HRMS:  $[M + H]^+$  calcd for  $[C_{13}H_8N_2O^{76}Se]^+$ : 378.9749; found: 378.9739.

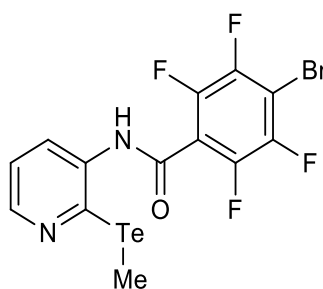
### 2,3,4,5,6-pentafluoro-*N*-(2-(methyltellanyl)pyridin-3-yl)benzamide II-11<sub>Te</sub>



**II-11<sub>Te</sub>**

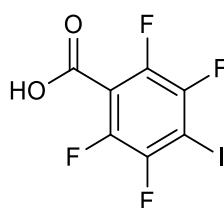
To a mixture of 2-(methyltellanyl)pyridin-3-amine **II-3<sub>Te</sub>** (211 mg, 0.90 mmol) and pyridine (0.08 mL, 78 mg, 0.99 mmol) in dry CH<sub>2</sub>Cl<sub>2</sub> (5 mL) at 0 °C under anhydrous condition, a solution of pentafluorobenzoyl chloride (0.13 mL, 207 mg, 0.90 mmol) in dry CH<sub>2</sub>Cl<sub>2</sub> (2 mL) was added dropwise. The reaction was stirred 5 minutes at the same temperature then overnight at room temperature. The mixture was diluted with EtOAc (50 mL) and washed with water (15 mL), brine (15 mL), and dried over Na<sub>2</sub>SO<sub>4</sub>. The solvents were removed under reduced pressure. The crude was purified by silica gel chromatography (CHCl<sub>3</sub>/MeOH 1%) to give pure amide **II-11<sub>Te</sub>** as white solid (218 mg, 56%); mp = 210-211 °C. IR:  $\nu$  (cm<sup>-1</sup>): 1653, 1635, 1585, 1518, 1489, 1418, 1392, 1342, 1093, 947, 988, 947, 777, 683, 667; <sup>1</sup>H NMR (400 MHz, DMSO)  $\delta$ <sub>H</sub>: 10, 85 (s, 1H), 8.49 (m, 1H), 7.57 (m, 1H), 7.26 (dd, *J* = 6.6, 5.4 Hz, 1H), 2.20 (s, 3H); <sup>19</sup>F NMR (376 MHz, DMSO)  $\delta$ <sub>F</sub>: -140.8 (m, 2F), 151.7 (t, *J* = 220.0 Hz, 1F), -161.0 (m, 2F); <sup>13</sup>C NMR (100 MHz, CDCl<sub>3</sub>)  $\delta$ <sub>C</sub>: 156.4, 149.2, 143.3 (dm, *J*<sub>CF</sub> = 250.0 Hz) (two peaks overlap, 2C), 141.6 (dm, *J*<sub>CF</sub> = 250.6 Hz), 141.8, 137.1 (dm, *J*<sub>CF</sub> = 251.6 Hz) (two peaks overlap, 2C), 136.1, 133.4, 121.0, 111.7 (m), -14.5; ESI-HRMS: [M - H]<sup>-</sup> calcd for [C<sub>13</sub>H<sub>6</sub>N<sub>2</sub>O<sup>122</sup>Te]: 422.9431; found: 422.9439.

### 2,3,5,6-tetrafluoro-4-bromo-N-(2-(methyltellanyl)pyridin-3-yl)benzamide **II-12<sub>Te</sub>**

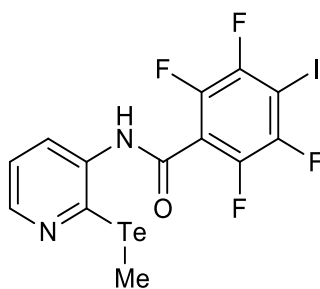


**II-12<sub>Te</sub>**

To a suspension of 2,3,5,6-tetrafluoro-4-bromobenzoic acid (242 mg, 0.87 mmol) in dry CH<sub>2</sub>Cl<sub>2</sub> (5 mL) under anhydrous condition, was added oxalyl chloride (0.75 mL, 1.11 g, 8.7 mmol) and three drops of DMF (gas formation). The reaction was stirred at room temperature for 2h (until complete dissolution). The liquids were removed under reduced pressure. The beige solid residue was dissolved in dry CH<sub>2</sub>Cl<sub>2</sub> (5 mL) and a solution of 2-(methyltellanyl)pyridin-3-amine **II-3<sub>Te</sub>** (188 mg, 0.8 mmol) and dry pyridine (0.08 mL, 79 mg, 1.1 mmol) in dry CH<sub>2</sub>Cl<sub>2</sub> (2 mL) was added dropwise at 0°C. The reaction was stirred 5 minutes at the same temperature then overnight at room temperature. The resulting mixture was diluted with EtOAc (50 mL) and washed with water (15 mL), brine (15 mL), and dried over Na<sub>2</sub>SO<sub>4</sub>. The solvents were removed under reduced pressure. The crude was purified by silica gel chromatography (CHCl<sub>3</sub>/MeOH 1%) to give 2,3,5,6-tetrafluoro-4-bromo-N-(2-(methyltellanyl)pyridin-3-yl)benzamide **II-12<sub>Te</sub>** as a white solid (178 mg) that was used in the next reaction without further purification.

**2,3,5,6-tetrafluoro-4-iodo-benzoic acid II-14****II-14**

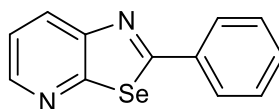
2,3,5,6-tetrafluoro-4-iodo-benzoic acid **II-14** was synthesised according to the procedure of *O. Dumele et al.*<sup>[8]</sup> To a mixture of 2,3,5,6-tetrafluoro-benzoic acid (970 mg, 5 mmol) in dry THF (80 mL) at  $-78^{\circ}\text{C}$  was added dropwise over a period of 25 minutes *n*-BuLi (2.5 M, 5.0 mL, 12.5 mmol). A solution of  $\text{I}_2$  (1.586 g, 6.25 mmol) in dry THF was added dropwise and the reaction was allowed to warm up to room temperature and stirred further at room temperature for 30 minutes. The resulting yellow mixture was diluted with a mixture of water and  $\text{H}_2\text{SO}_4$  (3:1, 100 mL), extracted with  $\text{Et}_2\text{O}$  (3 x 60 mL), washed with water (3 x 50 mL), a sat solution of  $\text{Na}_2\text{S}_2\text{O}_3$  (2 x 25 mL), water (50 mL), brine (50 mL), and dried over  $\text{MgSO}_4$ . Solvents were evaporated under reduced pressure and further dried overnight under high vacuum affording pure 2,3,5,6-tetrafluoro-4-iodobenzoic acid **II-14** as a white solid (1.390 g, 87%) that was used in the next reaction without further purification.

**2,3,5,6-tetrafluoro-4-iodo-*N*-(2-(methyltellanyl)pyridin-3-yl)benzamide II-13<sub>Te</sub>****II-13<sub>Te</sub>**

To a suspension of 2,3,5,6-tetrafluoro-4-iodobenzoic acid **II-14** (320 mg, 1 mmol) in dry  $\text{CH}_2\text{Cl}_2$  (5 mL) under anhydrous condition, was added oxalyl chloride (0.86 mL, 1.269 g, 1.2 mmol) and three drops of DMF (gas formation). The reaction was stirred at room temperature for 2h (until complete dissolution). The liquids were removed under reduced pressure. The beige solid residue was dissolved in dry  $\text{CH}_2\text{Cl}_2$  (5 mL) and a solution of 2-(methyltellanyl)pyridin-3-amine **II-3<sub>Te</sub>** (212 mg, 0.9 mmol) and dry pyridine (0.09 mL, 87 mg, 1.1 mmol) in dry  $\text{CH}_2\text{Cl}_2$  (2 mL) was added dropwise at  $0^{\circ}\text{C}$ . The reaction was stirred 5 minutes at the same temperature then overnight at room temperature. The resulting mixture was diluted with EtOAc (50 mL) and washed with water (15 mL), brine (15

mL), and dried over Na<sub>2</sub>SO<sub>4</sub>. The solvents were removed under reduced pressure. The crude was purified by silica gel chromatography (CHCl<sub>3</sub>/MeOH 1%) to give pure 2,3,5,6-tetrafluoro-4-iodo-N-(2-(methyltellanyl)pyridin-3-yl)benzamide **II-13<sub>Te</sub>** as a white solid (248 mg, 46%); mp = 198-200°C. IR:  $\nu$  (cm<sup>-1</sup>): 3219, 1739, 1653, 1634, 1574, 1522, 1464, 1385, 1296, 1206, 1063, 976.0, 760.0, 648.1; <sup>1</sup>H NMR (400 MHz, DMSO)  $\delta_{\text{H}}$ : 10.79 (s, 1H), 8.48 (dd,  $J$  = 4.6, 1.3 Hz, 1H), 7.57 (dd,  $J$  = 7.9, 1.3 Hz, 1H), 7.26 (dd,  $J$  = 7.9, 4.6 Hz, 1H), 2.20 (s, 3H); <sup>19</sup>F NMR (376 MHz, DMSO)  $\delta_{\text{F}}$ : -120.7 (dd,  $J$  = 26.2, 12.1 Hz, 2F), -139.6 (dd,  $J$  = 26.2, 12.1 Hz, 2F); <sup>13</sup>C NMR (125 MHz, CDCl<sub>3</sub>)  $\delta_{\text{C}}$ : 157.1, 149.2, 146.5 (dm,  $J_{\text{CF}}$  = 242 Hz) (two peaks overlap, 2C), 142.2 (dm,  $J_{\text{CF}}$  = 252 Hz) (two peaks overlap, 2C), 141.7, 136.1, 133.3, 120.9, 120.9, 116.6 (dd appearing t,  $J_{\text{CF}}$  = 21 Hz), -14.5; ESI-HRMS: [M + H]<sup>+</sup> calcd for [C<sub>13</sub>H<sub>8</sub>N<sub>2</sub><sup>130</sup>Te<sup>127</sup>]<sup>+</sup>: 540.8680; found: 540.8657.

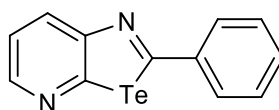
### 2-phenyl-[1,3]selenazolo[5,4- $\beta$ ]pyridine **II-15<sub>Se</sub>**



**II-15<sub>Se</sub>**

To a solution of N-(2-(methylselenanyl)pyridin-3-yl)benzamide **II-4<sub>Se</sub>** (99 mg, 0.34 mmol) and NEt<sub>3</sub> (0.57 mL, 413 mg, 4.08 mmol) in dry dioxane (3 mL) under anhydrous condition, POCl<sub>3</sub> (0.13 mL, 209 mg, 1.36 mmol) in dry dioxane (3 mL) was added dropwise. The reaction was heated to reflux and stirred overnight. The resulting mixture was diluted with CHCl<sub>3</sub> (40 mL), washed with a saturated solution of NaHCO<sub>3</sub> (2x20 mL), water (2x20 mL), brine (20 mL), and dried over Na<sub>2</sub>SO<sub>4</sub>. The solvents were removed under reduced pressure. The crude was purified by silica gel chromatography (pet. ether: EtOAc 9: 1) to give pure CGP **II-15<sub>Se</sub>** as a beige solid (32 mg, 38%); mp = 119-120°C. IR:  $\nu$  (cm<sup>-1</sup>): 1570, 1543, 1504, 1476, 1371, 1283, 1206, 1074, 941, 810, 762, 684, 665; <sup>1</sup>H NMR (400 MHz, CDCl<sub>3</sub>)  $\delta_{\text{H}}$ : 8.50 (dd,  $J$  = 4.7, 1.6 Hz, 1H), 8.30 (dd,  $J$  = 8.1, 1.6 Hz, 1H), 8.04 – 7.99 (m, 2H), 7.55 – 7.46 (m, 3H), 7.45 (dd,  $J$  = 8.1, 4.7 Hz, 1H); <sup>13</sup>C NMR (100 MHz, CDCl<sub>3</sub>)  $\delta_{\text{C}}$ : 174.7, 163.0, 150.3, 146.3, 136.1, 131.8, 131.6, 129.3 (two peaks overlap, 2C), 128.2 (two peaks overlap, 2C), 121.7; ESI-HRMS: [M + H]<sup>+</sup> calcd for [C<sub>12</sub>H<sub>9</sub>N<sub>2</sub><sup>76</sup>Se]<sup>+</sup>: 256.9958; found: 256.9968. Single crystals suitable for X-ray diffraction analysis were grown from slow evaporation of CHCl<sub>3</sub> solution.

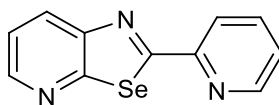
### 2-phenyl-[1,3]tellurazolo[5,4- $\beta$ ]pyridine **II-15<sub>Te</sub>**



**II-15<sub>Te</sub>**

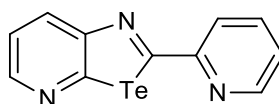
To a solution of N-(2-(methyltellanyl)pyridin-3-yl)benzamide **II-4<sub>Te</sub>** (0.221 g, 0.65 mmol) and NEt<sub>3</sub> (1.09 mL, 789 mg, 7.8 mmol) in dry dioxane (6.5 mL) under anhydrous condition, POCl<sub>3</sub> (0.24 mL, 399 mg, 2.6 mmol) in dry dioxane (6.5 mL) was added dropwise. The reaction was heated to reflux and stirred overnight. The resulting mixture was diluted with CHCl<sub>3</sub> (50 mL), washed with a saturated solution of NaHCO<sub>3</sub> (2 x 35 mL), water (15 mL), brine (15 mL), and dried over Na<sub>2</sub>SO<sub>4</sub>. The solvents were removed under reduced pressure. The crude was purified by silica gel chromatography (pet. ether : EtOAc 8 : 2) to give pure 2-(pyridin-2-yl)-[1,3]tellurazolo[5,4-β]pyridine **II-15<sub>Te</sub>** as a yellow solid (138 mg, 69%); mp = 148-149 °C. IR:  $\nu$  (cm<sup>-1</sup>): 2920, 1566, 1539, 1494, 1472, 1368, 1281, 1207, 1061, 932, 845, 797, 756, 675, 654, 579; <sup>1</sup>H NMR (400 MHz, CDCl<sub>3</sub>)  $\delta$ <sub>H</sub>: 8.47 (dd, *J* = 4.7, 1.5 Hz, 1H), 8.31 (dd, *J* = 7.8, 1.3 Hz, 1H), 7.89 (d, *J* = 7.0 Hz, 2H), 7.56-7.40 (m, 4H); <sup>13</sup>C NMR (100 MHz, CDCl<sub>3</sub>)  $\delta$ <sub>C</sub>: 177.4, 163.4, 158.2, 146.3, 141.2, 132.3, 131.6, 129.4 (two peaks overlap, 2C), 128.8 (two peaks overlap, 2C), 121.9; ESI-HRMS: [M]<sup>+</sup> calcd for [C<sub>12</sub>H<sub>8</sub>N<sub>2</sub><sup>122</sup>Te]<sup>+</sup>: 302.9796; found: 302.9794. Single crystals suitable for X-ray diffraction analysis were grown from slow evaporation of CHCl<sub>3</sub> solution.

### 2-(pyridin-2-yl)-[1,3]selenazolo[5,4-β]pyridine **II-16<sub>Se</sub>**

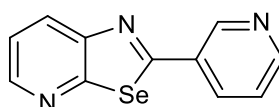


**II-16<sub>Se</sub>**

To a solution of N-(2-(methylselanyl)phenyl)picolinamide **II-5<sub>Se</sub>** (87 mg, 0.3 mmol) and NEt<sub>3</sub> (0.48 mL, 364 mg, 3.6 mmol) in dry dioxane (6 mL) under anhydrous condition, POCl<sub>3</sub> (0.11 mL, 184 mg, 1.2 mmol) was added dropwise. The reaction was heated to reflux and stirred overnight. The resulting mixture was diluted with a saturated solution of NaHCO<sub>3</sub> (10 mL). The aqueous fraction was extracted with CHCl<sub>3</sub> (3 x 20 mL). The solvent was removed under reduced pressure and the crude purified by silica gel chromatography (CHCl<sub>3</sub>/MeOH 1%) to give pure CGP **II-16<sub>Se</sub>** as a light orange solid (72 mg, 93%); mp = 173-175 °C. IR:  $\nu$  (cm<sup>-1</sup>): 3039, 1691, 1577, 1564, 1508, 1463, 1431, 1375, 1292, 1080, 1043, 994, 960, 797, 779, 739, 613, 600; <sup>1</sup>H NMR (300 MHz, CDCl<sub>3</sub>)  $\delta$ <sub>H</sub>: 8.69 (ddd, *J* = 4.8, 1.6, 0.9 Hz, 1H), 8.55 (dd, *J* = 4.7, 1.6 Hz, 1H), 8.35-8.27 (m, 2H), 7.87 (ddd appearing dt, *J* = 7.7, 1.6 Hz, 1H), 7.49-7.45 (m, 2H); <sup>13</sup>C NMR (100 MHz, CDCl<sub>3</sub>)  $\delta$ <sub>C</sub>: 176.9, 164.1, 153.1, 150.5, 150.1, 147.2, 137.2, 131.7, 125.9, 121.4, 119.9; EI-HRMS: [M - H]<sup>+</sup> calcd for [C<sub>11</sub>H<sub>6</sub>N<sub>3</sub><sup>76</sup>Se]<sup>+</sup>: 255.9754; found: 255.9762. Single crystals suitable for X-ray diffraction analysis were grown from slow evaporation of CHCl<sub>3</sub> solution.

**2-(pyridin-2-yl)-[1,3]tellurazolo[5,4- $\beta$ ] pyridine II-16<sub>Te</sub>****II-16<sub>Te</sub>**

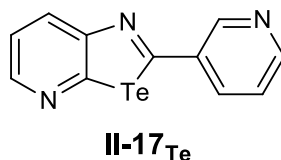
To a solution of N-(2-(methyltellanyl)phenyl)picolinamide **II-5<sub>Te</sub>** (200 mg, 0.59 mmol) and NEt<sub>3</sub> (0.99 mL, 716 mg, 12 mmol) in dry dioxane (12 mL) under anhydrous condition, POCl<sub>3</sub> (0.22 mL, 362 mg, 2.36 mmol) was added dropwise. The reaction was heated to reflux and stirred overnight. The resulting mixture was diluted with a saturated solution of NaHCO<sub>3</sub> (15 mL). The aqueous fraction was extracted with CHCl<sub>3</sub> (3 x 40 mL). The solvent removed under reduced pressure and the crude was purified by silica gel chromatography (CHCl<sub>3</sub>/MeOH 1%) to give pure CGP **II-16<sub>Te</sub>** as a yellow solid (137 mg, 75%); mp = 213-214 °C. IR:  $\nu$  (cm<sup>-1</sup>): 3026, 2999, 1573, 1534, 1541, 1494, 1458, 1433, 1369, 1290, 1151, 1118, 1091, 995, 949, 802, 735, 606, 581; <sup>1</sup>H NMR (300 MHz, CDCl<sub>3</sub>)  $\delta$ <sub>H</sub>: 8.59 (d, *J* = 8.59 Hz, 1H), 8.49 (dd, *J* = 4.7, 1.5 Hz, 1H), 8.31 (dd, *J* = 8.1 Hz, 1H), 8.19 (d, *J* = 7.8 Hz, 1H), 7.82 (ddd appearing dt, *J* = 7.7, 1.6 Hz, 1H), 7.45-7.37 (m, 2H); <sup>13</sup>C NMR (75 MHz, CDCl<sub>3</sub>)  $\delta$ <sub>C</sub>: 183.2, 163.6, 159.2, 156.6, 150.2, 146.3, 137.2, 132.9, 126.0, 121.6, 118.4; EI-HRMS: [M]<sup>+</sup> cacl'd for [C<sub>11</sub>H<sub>7</sub>N<sub>3</sub><sup>122</sup>Te]<sup>+</sup>: 302.9671; found: 302.9670. Single crystals suitable for X-ray diffraction analysis were grown from slow evaporation of CHCl<sub>3</sub> solution.

**2-(pyridin-3-yl)-[1,3]selenazolo[5,4- $\beta$ ]pyridine II-17<sub>Se</sub>****II-17<sub>Se</sub>**

To a solution of N-(2-(methylselanyl)phenyl)nicotinamide **II-6<sub>Se</sub>** (205 mg, 0.7 mmol) and NEt<sub>3</sub> (1.17 mL, 850 mg, 8.4 mmol) in dry dioxane (14 mL) under anhydrous condition, POCl<sub>3</sub> (0.26 mL, 429 mg, 2.8 mmol) was added dropwise. The reaction was heated to reflux and stirred overnight. The resulting solution was diluted with CHCl<sub>3</sub> (70 mL), washed with a saturated solution of NaHCO<sub>3</sub> (25 mL), water (20 mL), brine (20 mL), and dried over Na<sub>2</sub>SO<sub>4</sub>. The solvents were removed under reduced pressure. The crude was filtered on a pad of silica gel chromatography (CHCl<sub>3</sub>/MeOH 2%) to give pure CGP **II-17<sub>Se</sub>** as a yellow solid (80 mg, 44%); mp = 160-162°C. IR:  $\nu$  (cm<sup>-1</sup>): 1586, 1547, 1491, 1472, 1371, 1288, 1215, 1190, 1020, 947, 812, 694; <sup>1</sup>H NMR (300 MHz, CDCl<sub>3</sub>)  $\delta$ <sub>H</sub>: 9.19 (dd, *J* = 2.3, 0.8 Hz, 1H), 8.72 (dd, *J* = 4.8, 1.6 Hz, 1H), 8.50 (dd, *J* = 4.8, 1.6 Hz, 1H), 8.30-8.24 (m, 2H), 7.46-7.39 (m, 2H); <sup>13</sup>C NMR (75 MHz, CDCl<sub>3</sub>)  $\delta$ <sub>C</sub>: 170.7, 163.3, 152.2, 149.7, 149.1, 147.1, 135.0, 132.1,

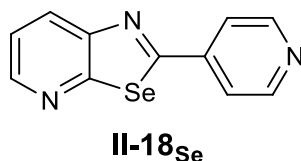
131.7, 124.0, 121.8; ESI-HRMS:  $[M + H]^+$  calcd for  $[C_{11}H_8N_3^{80}Se]^+$ : 261.9893; found: 261.9883. Single crystals suitable for X-ray diffraction analysis were grown from slow evaporation of  $CHCl_3$  solution.

### 2-(pyridin-3-yl)-[1,3]tellurazolo[5,4- $\beta$ ] pyridine II-17<sub>Te</sub>



To a solution of N-(2-(methyltellanyl)phenyl)nicotinamide **II-6<sub>Te</sub>** (136 mg, 0.4 mmol) and  $NEt_3$  (0.67 mL, 486 mg, 4.8 mmol) in dry dioxane (8 mL) under anhydrous condition,  $POCl_3$  (0.15 mL, 245 mg, 1.6 mmol) was added dropwise. The reaction was heated to reflux and stirred overnight. The resulting mixture was diluted with  $CHCl_3$  (50 mL), washed with a saturated solution of  $NaHCO_3$  (20 mL), water (20 mL), brine (20 mL), and dried over  $Na_2SO_4$ . The solvents were removed under reduced pressure. The crude was purified by silica gel chromatography ( $CHCl_3/MeOH$  1%) to give pure CGP **II-17<sub>Te</sub>** as a yellow solid (61 mg, 25%, over two steps); mp = 180-182°C. IR:  $\nu$  ( $cm^{-1}$ ): 1740, 1574, 1541, 1487, 1458, 1414, 1371, 1213, 1123, 1067, 1023, 932, 847, 808, 731, 698;  $^1H$  NMR (300 MHz,  $CDCl_3$ )  $\delta_H$ : 9.06 (dd,  $J = 2.3, 0.8$  Hz, 1H), 8.73 (dd,  $J = 4.8, 1.7$  Hz, 1H), 8.50 (dd,  $J = 4.6, 1.7$  Hz, 1H), 8.35 (dd,  $J = 8.1, 1.7$  Hz, 1H), 8.18 (ddd,  $J = 8.0, 2.3, 1.7$  Hz, 1H), 7.46 (dd,  $J = 8.1, 4.6$  Hz, 1H), 7.41 (ddd,  $J = 8.0, 4.8, 0.8$  Hz, 1H);  $^{13}C$  NMR (75 MHz,  $CDCl_3$ )  $\delta_C$ : 173.3, 163.6, 157.8, 152.2, 150.0, 146.7, 136.9, 135.3, 132.7, 124.1, 122.1; ESI-HRMS:  $[M + H]^+$  calcd for  $[C_{11}H_8N_3^{130}Te]^+$ : 311.9779; found: 311.9779. Single crystals suitable for X-ray diffraction analysis were grown from slow evaporation of  $CHCl_3$  solution.

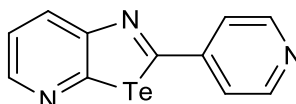
### 2-(pyridin-4-yl)-[1,3]selenazolo[5,4- $\beta$ ]pyridine II-18<sub>Se</sub>



To a solution of N-(2-(methylselanyl)phenyl)isonicotinamide **II-7<sub>Se</sub>** (205 mg, 0.7 mmol) and  $NEt_3$  (1.17 mL, 850 mg, 8.4 mmol) in dry dioxane (14 mL) under anhydrous condition,  $POCl_3$  (0.26 mL, 429 mg, 2.8 mmol) was added dropwise. The reaction was heated to reflux and stirred overnight. The resulting solution was diluted with  $CHCl_3$  (70 mL), washed with a saturated solution of  $NaHCO_3$  (25 mL), water (20 mL), brine (20 mL), and dried over  $Na_2SO_4$ . The solvents were removed under reduced pressure. The crude was filtered on a pad of silica gel chromatography ( $CHCl_3/MeOH$  2%) and purified further by a recrystallization in hot EtOH to give pure CGP **II-18<sub>Se</sub>** as a yellow solid (158 mg, 87%); mp = 162-164°C. IR:  $\nu$  ( $cm^{-1}$ ): 1589, 1539, 1466, 1404, 1362, 1280, 1226, 1200, 1061, 176

945, 802, 729, 651, 579, 556;  $^1\text{H}$  NMR (400 MHz,  $\text{CDCl}_3$ )  $\delta_{\text{H}}$ : 8.79 (dd,  $J = 4.5, 1.7$  Hz, 2H), 8.57 (dd,  $J = 4.6, 1.6$  Hz, 1H), 8.36 (dd,  $J = 8.2, 1.6$  Hz, 1H), 7.86 (dd,  $J = 4.5, 1.7$  Hz, 2H), 7.49 (dd,  $J = 8.2, 4.6$  Hz, 1H);  $^{13}\text{C}$  NMR (100 MHz,  $\text{CDCl}_3$ )  $\delta_{\text{C}}$ : 171.6, 163.5, 151.1 (two peaks overlap, 2C), 149.8, 147.7, 142.9, 132.3, 122.0, 121.7 (two peaks overlap, 2C); ESI-HRMS:  $[\text{M} + \text{H}]^+$  calcd for  $[\text{C}_{11}\text{H}_8\text{N}_3^{76}\text{Se}]^+$ : 257.9910; found: 257.9921. Single crystals suitable for X-ray diffraction analysis were grown from slow evaporation of  $\text{CHCl}_3$  solution.

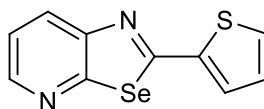
### 2-(pyridin-4-yl)-[1,3]tellurazolo[5,4- $\beta$ ]pyridine II-18<sub>Te</sub>



II-18<sub>Te</sub>

To a solution of N-(2-(methyltellanyl)phenyl)isonicotinamide II-7<sub>Te</sub> (136 mg, 0.4 mmol) and  $\text{NEt}_3$  (0.67 mL, 486 mg, 4.8 mmol) in dry dioxane (8 mL) under anhydrous condition,  $\text{POCl}_3$  (0.15 mL, 245 mg, 1.6 mmol) was added dropwise. The reaction was heated to reflux and stirred overnight. The resulting mixture was diluted with  $\text{CHCl}_3$  (50 mL), washed with a saturated solution of  $\text{NaHCO}_3$  (20 mL), water (20 mL), brine (20 mL), and dried over  $\text{Na}_2\text{SO}_4$ . The solvents were removed under reduced pressure. The crude was purified by silica gel chromatography ( $\text{CHCl}_3/\text{MeOH}$  1%) to give pure CGP II-18<sub>Te</sub> as a yellow solid (77 mg, 62%); mp = 168-170°C. IR:  $\nu$  ( $\text{cm}^{-1}$ ): 3032, 2978, 1593, 1573, 1543, 1504, 1477, 1404, 1292, 1207, 1080, 957, 806, 737, 682, 663, 602, 556;  $^1\text{H}$  NMR (400 MHz,  $\text{CDCl}_3$ )  $\delta_{\text{H}}$ : 8.75 (dd,  $J = 4.5, 1.6$  Hz, 2H), 8.52 (dd,  $J = 4.6, 1.6$  Hz, 1H), 8.38 (dd,  $J = 8.2, 1.6$  Hz, 1H), 7.72 (dd,  $J = 4.5, 1.6$  Hz, 2H), 7.47 (dd,  $J = 8.2, 4.6$  Hz, 1H);  $^{13}\text{C}$  NMR (100 MHz,  $\text{CDCl}_3$ )  $\delta_{\text{C}}$ : 174.7, 163.8, 157.8, 151.0 (two peaks overlap, 2C), 147.7, 147.1, 133.3, 122.3, 122.2 (two peaks overlap, 2C); ESI-HRMS:  $[\text{M} + \text{H}]^+$  calcd for  $[\text{C}_{11}\text{H}_8\text{N}_3^{122}\text{Te}]^+$ : 303.9749; found: 303.9736. Single crystals suitable for X-ray diffraction analysis were grown from slow evaporation of  $\text{CHCl}_3$  solution.

### 2-(thiophen-2-yl)-[1,3]selenazolo[5,4- $\beta$ ]pyridine II-19<sub>Se</sub>

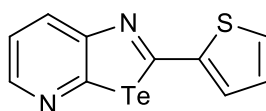


II-19<sub>Se</sub>

To a solution of N-(2-(methylselanyl)pyridin-3-yl)thiophene-2-carboxamide II-9<sub>Se</sub> (134 mg, 0.5 mmol) and  $\text{NEt}_3$  (0.84 mL, 607 mg, 6 mmol) in dry dioxane (5 mL) under anhydrous condition,  $\text{POCl}_3$  (0.19 mL, 307 mg, 2 mmol) in dry dioxane (4 mL) was added dropwise. The reaction was heated to reflux and stirred overnight. Then the reaction was diluted with  $\text{CHCl}_3$  (40 mL), washed with a

saturated solution of NaHCO<sub>3</sub> (2 x 20 mL), water (20 mL), brine (20 mL), and dried over Na<sub>2</sub>SO<sub>4</sub>. The solvents were removed under reduced pressure. The crude was purified by silica gel chromatography (CHCl<sub>3</sub>/MeOH 1%) to give pure CGP **II-19<sub>Se</sub>** as a yellow solid (92 mg, 69 %); mp = 135-137°C. IR:  $\nu$  (cm<sup>-1</sup>): 2922, 1578, 1575, 1476, 1418, 1371, 1285, 1233, 1211, 1111, 1080, 1049, 897, 851, 801, 737, 694, 664; <sup>1</sup>H NMR (300 MHz, CDCl<sub>3</sub>)  $\delta$ <sub>H</sub>: 8.46 (dd, *J* = 4.6, 1.5 Hz, 1H), 8.23 (ddd, *J* = 8.2, 1.5, 0.8 Hz, 1H), 7.64 (ddd appearing dt, *J* = 3.8, 1.1, 0.7 Hz, 1H), 7.56 (ddd appearing dt, *J* = 5.0, 1.1, 0.7 Hz, 1H), 7.42 (ddd, *J* = 8.2, 4.7, 0.8 Hz, 1H), 7.15 (ddd, *J* = 5.0, 3.8, 0.7 Hz, 1H); <sup>13</sup>C NMR (100 MHz, CDCl<sub>3</sub>)  $\delta$ <sub>C</sub>: 166.5, 162.8, 149.8, 146.0, 140.2, 131.1, 130.6 (two peaks overlap, 2C), 128.3, 121.7; ESI-HRMS: [M + H]<sup>+</sup> calcd for [C<sub>10</sub>H<sub>7</sub>N<sub>2</sub>S<sup>76</sup>Se]<sup>+</sup>: 262.9522; found: 262.9532. Single crystals suitable for X-ray diffraction analysis were grown from slow evaporation of CHCl<sub>3</sub> solution.

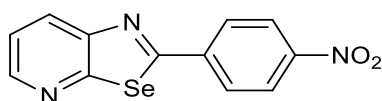
### 2-(thiophen-2-yl)-[1,3]tellurazolo[5,4- $\beta$ ]pyridine **II-19<sub>Te</sub>**



**II-19<sub>Te</sub>**

To a solution of N-(2-(methyltellanyl)pyridin-3-yl)thiophene-2-carboxamide **II-8<sub>Te</sub>** (0.225 g, 0.65 mmol) and NEt<sub>3</sub> (1.09 mL, 789 mg, 7.8 mmol) in dry dioxane (6.5 mL) under anhydrous condition, POCl<sub>3</sub> (0.24 mL, 399 mg, 2.6 mmol) in dry dioxane (6.5 mL) was added dropwise. The reaction was heated to reflux and stirred overnight. The resulting mixture was diluted with CHCl<sub>3</sub> (50 mL), washed with a saturated solution of NaHCO<sub>3</sub> (2 x 20 mL), water (20 mL), brine (20 mL), and dried over Na<sub>2</sub>SO<sub>4</sub>. The solvents were removed under reduced pressure. The crude was purified by silica gel chromatography (CHCl<sub>3</sub>/MeOH 1%) to give pure CGP **II-19<sub>Te</sub>** as a yellow solid (171 mg, 84%); mp = 137-138 °C. IR:  $\nu$  (cm<sup>-1</sup>): 3098, 2920, 2851, 1568, 1537, 1472, 1417, 1358, 1204, 1107, 1082, 888, 885, 791, 704, 656; <sup>1</sup>H NMR (400 MHz, CDCl<sub>3</sub>)  $\delta$ <sub>H</sub>: 8.42 (dd, *J* = 4.7, 1.7 Hz, 1H), 8.22 (dd, *J* = 8.1, 1.7 Hz, 1H), 7.53 (dd, *J* = 5.0, 1.1 Hz, 1H), 7.51 (dd, *J* = 3.8, 1.1 Hz, 1H), 7.38 (dd, *J* = 8.1, 4.7 Hz, 1H), 7.12 (dd, *J* = 5.0, 3.8 Hz, 1H); <sup>13</sup>C NMR (100 MHz, CDCl<sub>3</sub>)  $\delta$ <sub>C</sub>: 166.8, 162.9, 157.3, 146.2, 146.1, 131.7, 131.4, 130.4, 128.0, 122.0; ESI-HRMS: [M]<sup>+</sup> calcd for [C<sub>10</sub>H<sub>6</sub>N<sub>2</sub>S<sup>122</sup>Te]<sup>+</sup>: 308.9360; found: 308.9360. Single crystals suitable for X-ray diffraction analysis were grown from slow evaporation of CHCl<sub>3</sub> solution.

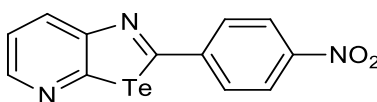
### 2-(4-nitrophenyl)-[1,3]selenazolo[5,4- $\beta$ ]pyridine **II-20<sub>Se</sub>**



**II-20<sub>Se</sub>**

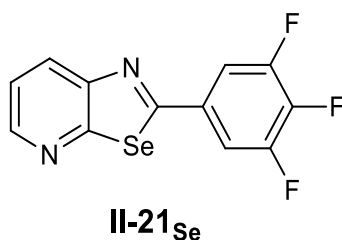
To a suspension of N-(2-(methylselanyl)pyridin-3-yl)-4-nitrobenzamide **II-9<sub>se</sub>** (202 mg, 0.6 mmol) and NEt<sub>3</sub> (1.00 mL, 729 mg, 17.15 mmol) in dry dioxane (6 mL) under anhydrous condition, a solution of POCl<sub>3</sub> (0.22 mL, 368 mg, 2.4 mmol) in dry dioxane (14 mL) was added dropwise. The mixture was heated to reflux and was stirred overnight. Then the reaction was diluted with CHCl<sub>3</sub> (70 mL), washed with a saturated solution of NaHCO<sub>3</sub> (3 x 15 mL), water (15 mL), brine (15 mL), and dried over Na<sub>2</sub>SO<sub>4</sub>. The solvents were removed under reduced pressure. The crude was purified by silica gel chromatography (CHCl<sub>3</sub>/MeOH1%) to give pure CGP **II-20<sub>se</sub>** as a yellow solid (96 mg, 53%); mp = 280-282 °C. IR:  $\nu$  (cm<sup>-1</sup>): 2980, 1593, 1572, 1543, 1468, 1466, 1373, 1321, 1283, 1111, 1080, 949, 851, 839, 804, 739, 687; <sup>1</sup>H NMR (300 MHz, CDCl<sub>3</sub>)  $\delta$ <sub>H</sub>: 8.58 (dd, *J* = 4.6, 1.4 Hz, 1H), 8.39-8.34 (m, 3H), 8.20 (d, *J* = 8.8 Hz, 2H), 7.51 (dd, *J* = 8.1, 4.6 Hz, 1H); <sup>13</sup>C NMR (100 MHz, CDCl<sub>3</sub>)  $\delta$ <sub>C</sub>: not recorded due to low solubility; ESI-HRMS: [M + H]<sup>+</sup> cacl'd for [C<sub>12</sub>H<sub>8</sub>N<sub>3</sub>O<sub>2</sub><sup>76</sup>Se]<sup>+</sup>: 301.9809; found: 301.9800.

### 2-(4-nitrophenyl)-[1,3]tellurazolo[5,4- $\beta$ ]pyridine **II-20<sub>Te</sub>**

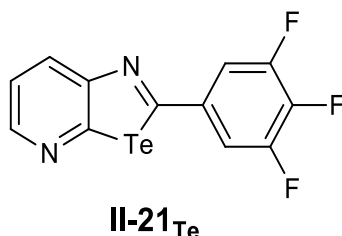


**II-20<sub>Te</sub>**

To a suspension of N-(2-(methyltellanyl)pyridin-3-yl)-4-nitrobenzamide **II-9<sub>Te</sub>** (550 mg, 1.43 mmol) and NEt<sub>3</sub> (2.40 mL, 1.735 g, 17.15 mmol) in dry dioxane (14 mL) under anhydrous condition, a solution of POCl<sub>3</sub> (0.53 mL, 877 mg, 5.72 mmol) in dry dioxane (14 mL) was added dropwise. The mixture was heated to reflux and was stirred overnight. The reaction was diluted with CHCl<sub>3</sub> (70 mL), washed with a saturated solution of NaHCO<sub>3</sub> (2 x 30 mL), water (30 mL), brine (30 mL), and dried over Na<sub>2</sub>SO<sub>4</sub>. The solvents were removed under reduced pressure. The crude was purified by silica gel chromatography (CHCl<sub>3</sub>/MeOH 1%) to give pure CGP **II-20<sub>Te</sub>** as a yellow solid (283 mg, 56%); mp = 276-278 °C. IR:  $\nu$  (cm<sup>-1</sup>): 3215, 1649, 1514, 1383, 1294, 1059, 828, 793, 718, 656; <sup>1</sup>H NMR (300 MHz, CDCl<sub>3</sub>)  $\delta$ <sub>H</sub>: 8.68 (d, *J* = 8.1 Hz, 1H), 8.57 (d, *J* = 5.2 Hz, 1H), 8.37 (d, *J* = 8.7 Hz, 2H), 8.11 (d, *J* = 8.7 Hz, 2H), 7.76 (dd, *J* = 8.1, 5.2 Hz, 1H); <sup>13</sup>C NMR (100 MHz, CDCl<sub>3</sub>)  $\delta$ <sub>C</sub>: not recorded due to low solubility; ESI-HRMS: [M + H]<sup>+</sup> cacl'd for [C<sub>12</sub>H<sub>8</sub>N<sub>3</sub>O<sub>2</sub><sup>122</sup>Se]<sup>+</sup>: 347.9647; found: 347.9655.

**2-(3,4,5-trifluorophenyl)-[1,3]selenazolo[5,4- $\beta$ ]pyridine II-21<sub>Se</sub>**

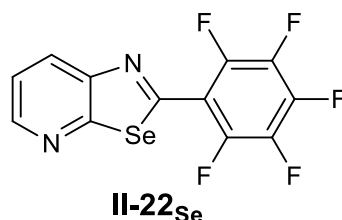
To a solution of 3,4,5-trifluoro-N-(2-(methylselenanyl)pyridin-3-yl)benzamide **II-10<sub>Se</sub>** (104 mg, 0.3 mmol) and  $\text{NEt}_3$  (0.50 mL, 364 mg, 3.6 mmol) in dry dioxane (3 mL) under anhydrous condition,  $\text{POCl}_3$  (0.11 mL, 184 mg, 1.2 mmol) in dry dioxane (3 mL) was added dropwise. The reaction was heated to reflux and stirred overnight. Then the reaction was diluted with  $\text{CHCl}_3$  (40 mL), washed with a saturated solution of  $\text{NaHCO}_3$  (2 x 15 mL), water (15 mL), brine (15 mL), and dried over  $\text{Na}_2\text{SO}_4$ . The solvents were removed under reduced pressure. The crude was purified by silica gel chromatography ( $\text{CHCl}_3/\text{MeOH}$  1%) to give pure CGP **II-21<sub>Se</sub>** as a white solid (75 mg, 80%); mp = 175–177 °C. IR:  $\nu$  ( $\text{cm}^{-1}$ ): 3078, 2980, 1944, 1736, 1620, 1597, 1528, 1497, 1375, 1348, 1244, 1020, 1165, 1151, 1033, 1220, 801, 733, 723;  $^1\text{H}$  NMR (400 MHz,  $\text{CDCl}_3$ )  $\delta_{\text{H}}$ : 8.53 (dd,  $J = 4.7, 1.5$  Hz, 1H), 8.29 (dd,  $J = 8.2, 1.5$  Hz, 1H), 7.67 (ddd,  $J = 8.0, 6.4, 1.1$  Hz, 2H), 7.47 (dd,  $J = 8.2, 4.7$  Hz, 1H);  $^{19}\text{F}$  NMR (376 MHz,  $\text{CDCl}_3$ )  $\delta_{\text{F}}$ : -132.1 (d,  $J = 20.4$  Hz, 2F), -154.8 (t,  $J = 20.4$  Hz, 1F);  $^{13}\text{C}$  NMR (100 MHz,  $\text{CDCl}_3$ )  $\delta_{\text{C}}$ : 170.3, 163.4, 151.8 (ddd,  $J_{\text{CF}} = 252, 10.4, 3.9$  Hz) (two peaks overlap, 2C), 149.8, 147.2, 141.9 (ddd appearing dt,  $J_{\text{CF}} = 256, 15.5$  Hz), 132.2 (d,  $J_{\text{CF}} = 4.6$  Hz), 132.0, 122.0, 112.3 (dd,  $J = 16.6, 6.5$  Hz) (two peaks overlap, 2C); ESI-HRMS:  $[\text{M} + \text{H}]^+$  calcd for  $[\text{C}_{12}\text{H}_6\text{N}_2\text{F}_3^{122}\text{Te}]^+$ : 310.9675; found: 310.9689. Single crystals suitable for X-ray diffraction analysis were grown from slow evaporation of  $\text{CHCl}_3$  solution.

**2-(3,4,5-trifluorophenyl)-[1,3]tellurazolo[5,4- $\beta$ ]pyridine II-21<sub>Te</sub>**

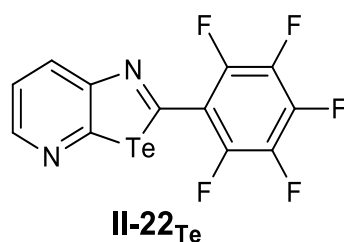
To a solution of 3,4,5-trifluoro-N-(2-(methyltellanyl)pyridin-3-yl)benzamide **II-10<sub>Te</sub>** (236 mg, 0.6 mmol) and  $\text{NEt}_3$  (1.00 mL, 729 mg, 7.2 mmol) in dry dioxane (6 mL) under anhydrous condition,  $\text{POCl}_3$  (0.22 mL, 368 mg, 2.4 mmol) in dry dioxane (6 mL) was added dropwise. The reaction was heated to reflux and stirred overnight. The resulting mixture was diluted with  $\text{CHCl}_3$  (50 mL), washed with a saturated solution of  $\text{NaHCO}_3$  (2 x 25 mL), water (15 mL), brine (15 mL), and dried over

Na<sub>2</sub>SO<sub>4</sub>. The solvents were removed under reduced pressure. The crude was purified by silica gel chromatography (CHCl<sub>3</sub>/MeOH 1%) to give pure CGP **II-21<sub>Te</sub>** as a yellow solid (173 mg, 80%); mp = 194-196 °C. IR:  $\nu$  (cm<sup>-1</sup>): 3649, 2980, 2359, 1603, 1526, 1477, 1354, 1256, 1042, 1042, 843, 801, 727, 716; <sup>1</sup>H NMR (400 MHz, CDCl<sub>3</sub>)  $\delta$ <sub>H</sub>: 8.50 (dd, *J* = 4.8, 1.6 Hz, 1H), 8.36 (dd, *J* = 8.1, 1.5 Hz, 1 H), 7.55 (dd appearing t, *J* = 6.8 Hz, 2 H), 7.49 (dd, *J* = 8.1, 4.8 Hz, 1H); <sup>19</sup>F NMR (376 MHz, CDCl<sub>3</sub>)  $\delta$ <sub>F</sub>: -132.4 (d, *J* = 20.4 Hz, 2F), -154.99 (t, *J* = 20.4 Hz, 1F); <sup>13</sup>C NMR (100 MHz, CDCl<sub>3</sub>)  $\delta$ <sub>C</sub>: 173.6, 163.3, 158.0, 151.7 (ddd, *J*<sub>CF</sub> = 250, 10.4, 4.0 Hz) (two peaks overlap, 2C), 146.1, 141.8 (dm, *J*<sub>CF</sub> = 258 Hz), 137.2, 133.3, 122.4, 112.5 (dd, *J*<sub>CF</sub> = 16.5, 6.5 Hz) (two peaks overlap, 2C); ESI-HRMS: [M]<sup>+</sup> calcd for [C<sub>12</sub>H<sub>6</sub>N<sub>2</sub>F<sub>3</sub><sup>122</sup>Te]<sup>+</sup>: 356.9514; found: 356.9496. Single crystals suitable for X-ray diffraction analysis were grown from slow evaporation of CHCl<sub>3</sub> solution.

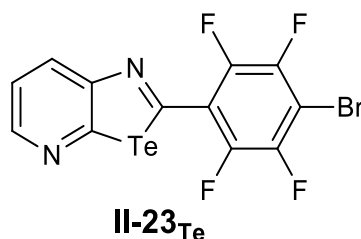
### 2-(perfluorophenyl)-[1,3]selenazolo[5,4- $\beta$ ]pyridine **II-22<sub>Se</sub>**



To a solution of 2,3,4,5,6-pentafluoro-N-(2-(methylselanyl)pyridin-3-yl)benzamide **II-11<sub>Se</sub>** (248 mg, 0.65 mmol) and NEt<sub>3</sub> (1.09 mL, 789 mg, 7.8 mmol) in dry dioxane (6.5 mL) under anhydrous condition, POCl<sub>3</sub> (0.24 mL, 389 mg, 2.6 mmol) in dry dioxane (6.5 mL) was added dropwise. The reaction was heated to reflux and stirred overnight. The resulting mixture was diluted with CHCl<sub>3</sub> (50 mL), washed with a saturated solution of NaHCO<sub>3</sub> (2 x 15 mL), water (15 mL), brine (15 mL), and dried over Na<sub>2</sub>SO<sub>4</sub>. The solvents were removed under reduced pressure. The crude was purified by silica gel chromatography (CHCl<sub>3</sub>/MeOH 1%) to give pure CGP **II-22<sub>Se</sub>** as a yellow solid (127 mg, 51%); mp = 108-110 °C. IR:  $\nu$  (cm<sup>-1</sup>): 3246, 2980, 2361, 1655, 1518, 1489, 1393, 1329, 1225, 1103, 1071, 999, 774, 652, 608; <sup>1</sup>H NMR (400 MHz, CDCl<sub>3</sub>)  $\delta$ <sub>H</sub>: 8.63 (dd, *J* = 4.6, 1.5 Hz, 1H), 8.44 (dd, *J* = 8.2, 1.5 Hz, 1H), 7.53 (dd, *J* = 8.2, 4.6 Hz, 1H); <sup>19</sup>F NMR (376 MHz, CDCl<sub>3</sub>)  $\delta$ <sub>F</sub>: -138.7 (m, 2F), -149.2 (t, *J* = 21 Hz, 1F), -160.3 (m, 2F); <sup>13</sup>C NMR (100 MHz, CDCl<sub>3</sub>)  $\delta$ <sub>C</sub>: 164.0 (t, *J*<sub>CF</sub> = 4.0 Hz), 157.9, 148.2, 147.8, 144.7 (dm, *J*<sub>CF</sub> = 260 Hz) (two peaks overlap, 2C), 142.5 (dm, *J*<sub>CF</sub> = 260 Hz), 138.3 (dm, *J*<sub>CF</sub> = 251 Hz) (two peaks overlap, 2C), 132.8, 121.9, 112.1 (m); ESI-HRMS: [M + H]<sup>+</sup> calcd for [C<sub>12</sub>H<sub>4</sub>N<sub>2</sub>F<sub>5</sub><sup>76</sup>Se]<sup>+</sup>: 346.9487; found: 346.9482. Single crystals suitable for X-ray diffraction analysis were grown from slow evaporation of CHCl<sub>3</sub> solution.

**2-(perfluorophenyl)-[1,3]tellurazolo[5,4- $\beta$ ]pyridine II-22<sub>Te</sub>**

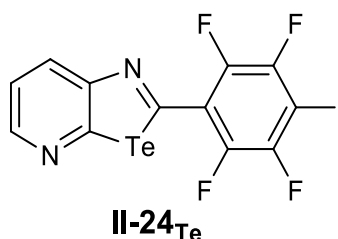
To a solution of 2,3,4,5,6-pentafluoro-N-(2-(methyltellanyl)pyridin-3-yl)benzamide **II-11<sub>Te</sub>** (193 mg, 0.45 mmol) and NEt<sub>3</sub> (0.75 mL, 546 mg, 5.4 mmol) in dry dioxane (4.5 mL) under anhydrous condition, POCl<sub>3</sub> (0.17 mL, 276 mg, 1.8 mmol) in dry dioxane (4.5 mL) was added dropwise. The reaction was heated to reflux and stirred overnight. The resulting mixture was diluted with CHCl<sub>3</sub> (50 mL), washed with a saturated solution of NaHCO<sub>3</sub> (2 x 15 mL), water (15 mL), brine (15 mL), and dried over Na<sub>2</sub>SO<sub>4</sub>. The solvents were removed under reduced pressure. The crude was purified by silica gel chromatography (CHCl<sub>3</sub>/MeOH 1%), the resulting orange material was purified further by preparative TLC (CHCl<sub>3</sub>/MeOH 1%) to give pure CGP **II-22<sub>Te</sub>** as a yellow solid (95 mg, 53%); mp = 197–198 °C. IR:  $\nu$  (cm<sup>-1</sup>): 2922, 1649, 1572, 1518, 1491, 1404, 1365, 1217, 1138, 986, 810, 731, 665, 573; <sup>1</sup>H NMR (400 MHz, CDCl<sub>3</sub>)  $\delta$ <sub>H</sub>: 8.59 (dd, *J* = 4.7, 1.5 Hz, 1H), 8.51 (dd, *J* = 8.2, 1.5 Hz, 1H), 7.53 (dd, *J* = 8.2, 4.7 Hz, 1H); <sup>19</sup>F NMR (376 MHz, CDCl<sub>3</sub>)  $\delta$ <sub>F</sub>: -139.8 (d, *J* = 18.0 Hz, 2F), -150.0 (dd appearing t, *J* = 20.9 Hz, 1F), -160.7 (m, 2F); <sup>13</sup>C NMR (100 MHz, CDCl<sub>3</sub>)  $\delta$ <sub>C</sub>: 165.3, 158.2, 155.9, 146.9, 144.0 (dm, *J*<sub>CF</sub> = 256 Hz) (two peaks overlap, 2C), 142.2 (dm, *J*<sub>CF</sub> = 252 Hz), 138.2 (dm, *J*<sub>CF</sub> = 253 Hz) (two peaks overlap, 2C), 134.2, 122.2, 116.9; ESI-HRMS: [M]<sup>+</sup> caclcd for [C<sub>12</sub>H<sub>3</sub>N<sub>2</sub>F<sub>5</sub><sup>122</sup>Te]<sup>+</sup>: 392.9325; found: 392.9331. Single crystals suitable for X-ray diffraction analysis were grown from slow evaporation of CHCl<sub>3</sub> solution.

**2-(2,3,5,6-tetrafluoro-4-bromophenyl)-[1,3]tellurazolo[5,4- $\beta$ ]pyridine II-23<sub>Te</sub>**

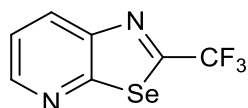
To a solution of 2,3,5,6-tetrafluoro-4-bromo-N-(2-(methyltellanyl)pyridin-3-yl)benzamide **II-12<sub>Te</sub>** (147 mg, 0.3 mmol) and NEt<sub>3</sub> (0.50 mL, 364 mg, 3.6 mmol) in dry dioxane (6 mL) under anhydrous condition, POCl<sub>3</sub> (0.11 mL, 180 mg, 1.2 mmol) was added dropwise. The reaction was heated to reflux and stirred overnight. The resulting mixture was diluted with CHCl<sub>3</sub> (70 mL), washed with a saturated solution of NaHCO<sub>3</sub> (10 mL), water (10 mL), brine (10 mL), and dried over Na<sub>2</sub>SO<sub>4</sub> and

solvents removed under reduced pressure. The crude was purified by silica gel chromatography ( $\text{CHCl}_3/\text{MeOH}$  0.5%), to give pure CGP **II-23<sub>Te</sub>** as a yellow solid (97 mg, 25%, over two steps); mp = 192-194 °C. IR:  $\nu$  ( $\text{cm}^{-1}$ ): 1570, 1539, 1485, 1396, 1364, 1292, 1215, 1028, 978, 837, 846, 760, 719;  $^1\text{H}$  NMR (400 MHz,  $\text{CDCl}_3$ )  $\delta_{\text{H}}$ : 8.50 (d,  $J = 4.0$  Hz, 1H), 8.40 (d,  $J = 8.0$  Hz, 1H), 7.41 (dd,  $J = 8.0, 4.0$  Hz, 1H);  $^{19}\text{F}$  NMR (376 MHz,  $\text{CDCl}_3$ )  $\delta_{\text{F}}$ : -132.1 (m, 2F), -139.4 (m, 2F);  $^{13}\text{C}$  NMR (125 MHz,  $\text{CDCl}_3$ )  $\delta_{\text{C}}$ : 166.0, 157.6, 155.7, 147.6, 145.7 (dm,  $J_{\text{CF}} = 240$  Hz, two peaks overlap, 2C), 143.7 (dm,  $J_{\text{CF}} = 240$  Hz, two peaks overlap, 2C), 133.9, 122.1, 120.7, 102.1; ESI-HRMS:  $[\text{M} + \text{H}]^+$  calcd for  $[\text{C}_{12}\text{H}_4\text{N}_2\text{F}_4\text{Br}^{130}\text{Te}]^+$ : 460.8556; found: 460.8552. Single crystals suitable for X-ray diffraction analysis were grown from slow evaporation of  $\text{CHCl}_3$  solution.

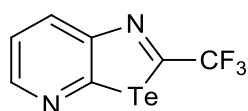
### 2-(2,3,5,6-tetrafluoro-4-iodophenyl)-[1,3]tellurazolo[5,4- $\beta$ ]pyridine **II-24<sub>Te</sub>**



To a solution of 2,3,5,6-tetrafluoro-4-iodo-N-(2-(methyltellanyl)pyridin-3-yl)benzamide **II-13<sub>Te</sub>** (53 mg, 0.45 mmol) and  $\text{NEt}_3$  (0.17 mL, 121 mg, 1.2 mmol) in dry dioxane (2 mL) under anhydrous condition,  $\text{POCl}_3$  (0.04 mL, 60 mg, 0.4 mmol) was added dropwise. The reaction was heated to reflux and stirred overnight. The resulting mixture was diluted with  $\text{CHCl}_3$  (30 mL), washed with a saturated solution of  $\text{NaHCO}_3$  (5 mL), water (5 mL), brine (5 mL), and dried over  $\text{Na}_2\text{SO}_4$  and solvents removed under reduced pressure. The crude was purified by silica gel chromatography ( $\text{CHCl}_3/\text{MeOH}$  0.5%) to give pure CGP **II-24<sub>Te</sub>** as a yellow solid (30 mg, 50%); mp = 230-232 °C. IR:  $\nu$  ( $\text{cm}^{-1}$ ): 2922, 1539, 1474, 1454, 1369, 1258, 1084, 1022, 966, 804, 716;  $^1\text{H}$  NMR (400 MHz,  $\text{CDCl}_3$ )  $\delta_{\text{H}}$ : 8.59 (d,  $J = 4.6$  Hz, 1H), 8.50 (d,  $J = 8.2$  Hz, 1H), 7.51 (dd,  $J = 8.0, 4.6$  Hz, 1H);  $^{19}\text{F}$  NMR (376 MHz,  $\text{CDCl}_3$ )  $\delta_{\text{F}}$ : -132.1 (m, 2F), -139.3 (m, 2F);  $^{13}\text{C}$  NMR (125 MHz,  $\text{CDCl}_3$ )  $\delta_{\text{C}}$ : 166.0, 157.9, 155.8, 147.9 (dm,  $J_{\text{CF}} = 248$  Hz, two peaks overlap, 2C), 147.5, 142.9 (dm,  $J_{\text{CF}} = 258$  Hz, two peaks overlap, 2C), 133.9, 129.9, 122.1, 101.8; ESI-HRMS:  $[\text{M} + \text{H}]^+$  calcd for  $[\text{C}_{12}\text{H}_4\text{N}_2\text{F}_4^{130}\text{Te}^{127}\text{I}]^+$ : 508.8418; found: 508.8408. Single crystals suitable for X-ray diffraction analysis were grown from slow evaporation of pyridine- $\text{CHCl}_3$  solution.

**2-(trifluoromethyl)-[1,3]selenazolo[5,4- $\beta$ ]pyridine II-25<sub>Se</sub>****II-25<sub>Se</sub>**

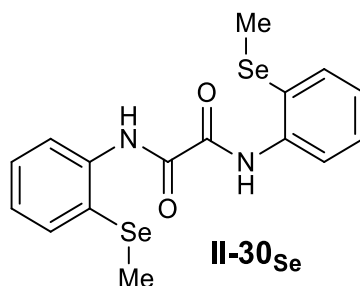
2-(trifluoromethyl)-[1,3]selenazolo[5,4- $\beta$ ]pyridine **II-25<sub>Se</sub>** was synthesised by a procedure inspired by the work of Monzón et al.<sup>[9]</sup> To a mixture of 2-(methyltellanyl)pyridin-3-amine **II-3<sub>Se</sub>** (131 mg, 0.7 mmol) and dry pyridine (0.06 mL, 61 mg, 0.77 mmol) in dry CH<sub>2</sub>Cl<sub>2</sub> (4 mL) under anhydrous condition at 0°C, a solution of trifluoroacetic acid anhydride (0.1 mL, 0.147 mg, 0.7 mmol) in dry CH<sub>2</sub>Cl<sub>2</sub> (2 mL) was added dropwise. The reaction (yellow solution) was stirred 5 minutes at 0°C then overnight at room temperature. Liquids were removed under reduced pressure, the yellow solid residue was dissolved in dry 1,4-dioxane (6 mL) and a solution of POCl<sub>3</sub> (0.26 mL, 429 mg, 2.8 mmol) and dry NEt<sub>3</sub> (1.08 mL, 855 mg, 8.4 mmol) in dry 1,4-dioxane (6 mL) was added dropwise. The reaction was heated to reflux and stirred for 8h. The resulting mixture was allowed to cool down to room temperature, diluted with CHCl<sub>3</sub> (70 mL), washed with a saturated solution of NaHCO<sub>3</sub> (20 mL), water (15 mL), brine (15 mL), and dried over Na<sub>2</sub>SO<sub>4</sub>. The solvents were removed under reduced pressure. The crude was purified by silica gel chromatography (CHCl<sub>3</sub>/MeOH 0 to 1%) to give pure CGP **II-25<sub>Se</sub>** as a yellow crystalline solid (48 mg, 27%). Remark: the compound sublime easily upon drying; mp = 98-100°C. IR:  $\nu$  (cm<sup>-1</sup>): 3366, 3046, 1612, 1578, 1552, 1506, 1381, 1312, 1248, 1220, 986, 854, 810, 727, 683, 665, 573, 524; <sup>1</sup>H NMR (500 MHz, CDCl<sub>3</sub>)  $\delta$ <sub>H</sub>: 8.67 (dd, *J* = 4.6, 1.5 Hz, 1H), 8.46 (dd, *J* = 8.2, 1.5 Hz, 1H), 7.56 (dd, *J* = 8.2, 4.6 Hz, 1H); <sup>19</sup>F NMR (470 MHz, CDCl<sub>3</sub>)  $\delta$ <sub>F</sub>: -62.4 (s, 3F); <sup>13</sup>C NMR (125 MHz, CDCl<sub>3</sub>)  $\delta$ <sub>C</sub>: 163.6, 162.1 (q, *J*<sub>CF</sub> = 42 Hz), 149.1, 147.6, 133.8, 122.4, 120.7 (q, *J*<sub>CF</sub> = 275 Hz); ESI-HRMS: [M]<sup>+</sup> cacl'd for [C<sub>7</sub>H<sub>3</sub>N<sub>2</sub><sup>80</sup>Se]<sup>+</sup>: 251.9414; found: 251.9417. Single crystals suitable for X-ray diffraction analysis were grown from slow evaporation of CHCl<sub>3</sub> solution.

**2-(trifluoromethyl)-[1,3]tellurazolo[5,4- $\beta$ ]pyridine II-25<sub>Te</sub>****II-25<sub>Te</sub>**

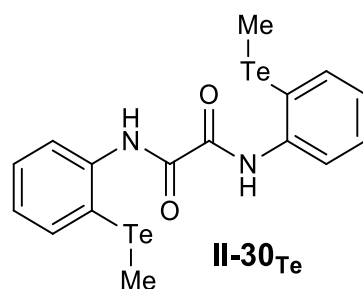
2-(trifluoromethyl)-[1,3]tellurazolo[5,4- $\beta$ ]pyridine **II-25<sub>Te</sub>** was synthesised by a procedure inspired by the work of Monzón et al.<sup>[9]</sup> To a mixture of 2-(methyltellanyl)pyridin-3-amine **II-3<sub>Te</sub>** (118 mg, 0.5 mmol) and dry pyridine (0.05 mL, 44 mg, 0.55 mmol) in dry CH<sub>2</sub>Cl<sub>2</sub> (3 mL) under anhydrous

condition at 0°C, a solution of trifluoroacetic acid anhydride (0.07 mL, 0.105 mg, 0.5 mmol) in dry CH<sub>2</sub>Cl<sub>2</sub> (1 mL) was added dropwise. The reaction (yellow solution) was stirred 5 minutes at 0°C then overnight at room temperature. Liquids were removed under reduced pressure, the yellow solid residue was dissolved in dry 1,4-dioxane (4 mL) and a solution of POCl<sub>3</sub> (0.19 mL, 307 mg, 2 mmol) and dry NEt<sub>3</sub> (0.83 mL, 607 mg, 6 mmol) in dry 1,4-dioxane (4 mL) was added dropwise. The reaction was heated to reflux and stirred for 8h. The resulting mixture was allowed to cool down to room temperature, diluted with CHCl<sub>3</sub> (70 mL), washed with a saturated solution of NaHCO<sub>3</sub> (20 mL), water (20 mL), brine (20 mL), and dried over Na<sub>2</sub>SO<sub>4</sub>. The solvents were removed under reduced pressure. The crude was purified by silica gel chromatography (CHCl<sub>3</sub>/MeOH 0 to 1%) to give pure CGP **II-25<sub>Te</sub>** as a brownish solid (71 mg, 47%); mp = 132-134°C. IR:  $\nu$  (cm<sup>-1</sup>): 3040, 1578, 1547, 1499, 1300, 1236, 1221, 1161, 1109, 968, 808, 719, 592, 569; <sup>1</sup>H NMR (500 MHz, CDCl<sub>3</sub>)  $\delta$ <sub>H</sub>: 8.62 (dd, *J* = 4.6, 1.6 Hz, 1H), 8.51 (dd, *J* = 8.2, 1.6 Hz, 1H), 7.55 (dd, *J* = 8.2, 4.6 Hz, 1H); <sup>19</sup>F NMR (470 MHz, CDCl<sub>3</sub>)  $\delta$ <sub>F</sub>: -62.6 (s, 3F); <sup>13</sup>C NMR (125 MHz, CDCl<sub>3</sub>)  $\delta$ <sub>C</sub>: 164.8, 164.4 (q, *J*<sub>CF</sub> = 41 Hz, 1C), 155.3, 148.2, 135.1, 123.6 (q, *J*<sub>CF</sub> = 275 Hz, 1C), 122.5; ESI-HRMS: [M]<sup>+</sup> cacl'd for [C<sub>7</sub>H<sub>3</sub>N<sub>2</sub><sup>130</sup>Te]<sup>+</sup>: 301.9311; found: 301.9313. Single crystals suitable for X-ray diffraction analysis were grown from slow evaporation of CHCl<sub>3</sub> solution.

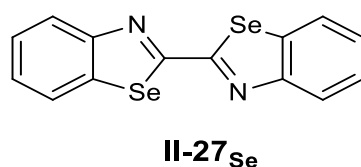
### **N<sup>1</sup>,N<sup>2</sup>-bis(2-(methylselanyl)phenyl)oxalamide II-30<sub>Se</sub>**



To a solution of 2-(methylselanyl)aniline **II-3<sub>Se</sub>** (465 mg, 2.5 mmol) in dry CH<sub>2</sub>Cl<sub>2</sub> (10 mL) under dry condition, was added dropwise oxalyl chloride (0.09 mL, 133 mg, 1.05 mmol). The reaction was stirred 30 minutes until complete discoloration. The resulting suspension was filtered and washed with MeOH (3 mL) to afford pure N<sup>1</sup>,N<sup>2</sup>-bis(2-(methylselanyl)phenyl)oxalamide **II-30<sub>Se</sub>** as a white powder (437 mg, 98 %); mp = 196-198°C. IR:  $\nu$  (cm<sup>-1</sup>): 3253, 1685, 1573, 1568, 1500, 1419, 1298, 1276, 1220, 1155, 1026, 920, 856, 785, 738, 542; <sup>1</sup>H NMR (300 MHz, DMSO)  $\delta$ <sub>H</sub>: 10.52 (s, 2H), 7.86 (dd, *J* = 7.8, 1.2 Hz, 2H), 7.64 (dd, *J* = 7.8, 1.2 Hz, 2H), 7.37 (ddd appearing as dt, *J* = 7.7, 1.2 Hz, 2H), 7.23 (ddd, appearing as dt, *J* = 7.7, 1.2 Hz, 2H), 2.29 (s, 6H); <sup>13</sup>C NMR (100 MHz, CDCl<sub>3</sub>)  $\delta$ <sub>C</sub>: not recorded due to low solubility; EI-HRMS: [M + Na]<sup>+</sup> cacl'd for [C<sub>16</sub>H<sub>16</sub>N<sub>2</sub>O<sub>2</sub>Na<sup>78</sup>Se]<sup>+</sup>: 446.9456; found: 446.9464.

***N*<sup>1</sup>,*N*<sup>2</sup>-bis(2-(methyltellanyl)phenyl)oxalamide II-30<sub>Te</sub>**

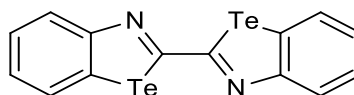
To a solution of 2-(methyltellanyl)aniline **II-3<sub>Te</sub>** (587 mg, 2.5 mmol) in dry CH<sub>2</sub>Cl<sub>2</sub> (10 mL) under dry condition, was added dropwise oxalyl chloride (0.09 mL, 133 mg, 1.05 mmol). The reaction was stirred 30 minutes until complete discoloration. The resulting suspension was filtered and washed with MeOH (3 mL) to afford pure *N*<sup>1</sup>,*N*<sup>2</sup>-bis(2-(methyltellanyl)phenyl)oxalamide **II-30<sub>Te</sub>** as grey needles (386 mg, 74 %); mp = 206-208°C. IR:  $\nu$  (cm<sup>-1</sup>): 3251, 1687, 1570, 1413, 1296, 1226, 1217, 1155, 1107, 1016, 844.8, 754.2, 709.8; <sup>1</sup>H NMR (400 MHz, DMSO)  $\delta$ <sub>H</sub>: 10.67 (s, 2H), 7.77 (d, *J* = 7.3 Hz, 2H), 7.65 (d, *J* = 7.3 Hz, 2H), 7.35 (dd appearing as t, *J* = 7.1, 6.4 Hz, 2H), 7.13 (dd appearing as t, *J* = 7.1, 6.4 Hz, 2H), 2.05 (s, 6H); <sup>13</sup>C NMR (100 MHz, CDCl<sub>3</sub>)  $\delta$ <sub>C</sub>: 158.2 (two peaks overlap, 2C), 139.3 (two peaks overlap, 2C), 137.8 (two peaks overlap, 2C), 128.3 (two peaks overlap, 2C), 126.9 (two peaks overlap, 2C), 123.6 (two peaks overlap, 2C), 112.5 (two peaks overlap, 2C), -14.75 (two peaks overlap, 2C); EI-HRMS: [M - H]<sup>+</sup> calcd for [C<sub>16</sub>H<sub>15</sub>N<sub>2</sub>O<sub>2</sub><sup>124</sup>Te]<sup>+</sup>: 514.9190; found: 514.9202.

**2,2'-bibenzo[ $\delta$ ][1,3]selenazole II-27<sub>Se</sub>**

To a solution of *N*<sup>1</sup>,*N*<sup>2</sup>-bis(2-(methylselenanyl)phenyl)oxalamide **II-30<sub>Se</sub>** (213 mg, 0.5 mmol) and dry NEt<sub>3</sub> (0.84 mL, 607 mg, 6 mmol) in dry dioxane (20 mL) under dry condition, POCl<sub>3</sub> (0.19 mL, 307 mg, 2 mmol) was added dropwise. The reaction was stirred at reflux for 2.5h. The resulting mixture was diluted with a saturated solution of NaHCO<sub>3</sub> in water (25 mL), extracted with CHCl<sub>3</sub> (3 x 50 mL). Organic extracts were combined and dried over Na<sub>2</sub>SO<sub>4</sub>. The solvents were removed under reduced pressure. The crude material was purified by recrystallization from CHCl<sub>3</sub> and the crystals obtained were washed with cold CHCl<sub>3</sub> (150 mL) to afford 2,2'-bibenzo[ $\delta$ ][1,3]selenazole **II-27<sub>Se</sub>** as yellowish crystals (20 mg, 10 %); mp = 334 °C. IR:  $\nu$  (cm<sup>-1</sup>): 3388, 3311, 3292, 3167, 3045, 1472, 1444, 1425, 1301, 1049, 1012, 850.6, 889.2, 758.0, 717.5, 468.7; <sup>1</sup>H NMR (300 MHz, DMSO)  $\delta$ <sub>H</sub>: 8.28 (d, *J* = 7.8 Hz, 2H), 8.21 (d, *J* = 7.8 Hz, 2H), 7.61 (dd appearing t, *J* = 7.3 Hz, 2H), 7.50 (dd appearing t, *J* = 7.3 Hz, 4H); <sup>13</sup>C NMR  $\delta$ <sub>C</sub>: Not recorded due to solubility issue; EI-HRMS: [M + H]<sup>+</sup> calcd for

$[\text{C}_{14}\text{H}_9\text{N}_2^{76}\text{Se}_2]^+$ : 356.9150; found: 356.9164. Single crystals suitable for X-ray diffraction analysis were grown from cool down of a hot  $\text{CHCl}_3$  solution.

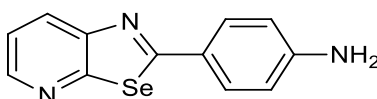
### 2,2'-bibenzo[ $\delta$ ][1,3]tellurazole **II-27<sub>Te</sub>**



**II-27<sub>Te</sub>**

To a solution of  $\text{N}^1, \text{N}^2$ -bis(2-(methyltellanyl)phenyl)oxalamide **II-30<sub>Te</sub>** (100 mg, 0.19 mmol) and dry  $\text{NEt}_3$  (0.32 mL, 233 mg, 2.30 mmol) in dry dioxane (10 mL) under dry condition,  $\text{POCl}_3$  (0.071 mL, 116 mg, 0.76 mmol) was added dropwise. The reaction was stirred at reflux for 2.5h. The resulting mixture was diluted with a saturated solution of  $\text{NaHCO}_3$  in water (25 mL), extracted with  $\text{CHCl}_3$  (3 x 50 mL). Organic extracts were combined and dried over  $\text{Na}_2\text{SO}_4$ . The solvents were evaporated under reduced pressure. The crude material was purified by recrystallization from EtOH to afford 2,2'-bibenzo[ $\delta$ ][1,3]tellurazole **II-27<sub>Te</sub>** as yellowish crystals (47 mg, 54 %); mp = 270 °C. IR:  $\nu$  ( $\text{cm}^{-1}$ ): 2960, 2920, 252, 1689, 1572, 1498, 1483, 1421, 1259, 1087, 1016, 866.0, 800.5, 756;  $^1\text{H}$  NMR (400 MHz, DMSO)  $\delta_{\text{H}}$ : 8.22 (d,  $J = 8.1$  Hz, 2H), 7.98 (d,  $J = 7.6$  Hz, 2H), 7.51 (dd appearing as t,  $J = 7.6$  Hz, 2H), 7.23 (dd appearing t,  $J = 7.4$  Hz, 2H);  $^{13}\text{C}$  NMR (100 MHz,  $\text{CDCl}_3$ )  $\delta_{\text{C}}$ : 160.9 (2C), 134.0 (2C), 132.2 (2C), 128.3 (2C), 127.7 (2C), 127.3 (2C), 126.2 (2C); EI-HRMS:  $[\text{M}]^+$  calcd for  $[\text{C}_{14}\text{H}_8\text{N}_2^{124}\text{Te}_2]^+$ : 451.8744; found: 451.8761. Single crystals suitable for X-ray diffraction analysis were grown from slow evaporation of  $\text{CHCl}_3$  solution.

### 4-([1,3]selenazolo[5,4- $\beta$ ]pyridin-2-yl)aniline **II-31<sub>Se</sub>**

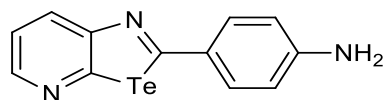


**II-31<sub>Se</sub>**

A suspension of 2-(4-nitrophenyl)-[1,3]selenazolo[5,4- $\beta$ ]pyridine **II-20<sub>Se</sub>** (152 mg, 0.50 mmol),  $\text{NH}_4\text{Cl}$  (14 mg, 0.25 mmol) and elemental Fe powder (84 mg, 1.50 mmol) in EtOH (4.5 mL) and water (2.3 mL) was stirred at 85°C for 2h. After cooling down, the reaction was filtered over celite and washed with toluene. Solvents were evaporated under reduce pressure. The crude material was purified by silica gel chromatography ( $\text{CHCl}_3/\text{MeOH}$  2%) to give pure CGP **II-31<sub>Se</sub>** as an orange solid (98 mg, 71%); mp = 204-206°C. IR:  $\nu$  ( $\text{cm}^{-1}$ ): 3302, 1736, 1597, 1548, 1479, 1375, 1292, 1211, 1175, 1078, 943, 826, 791;  $^1\text{H}$  NMR (300 MHz, DMSO)  $\delta_{\text{H}}$ : 8.40 (dd,  $J = 4.6, 1.6$  Hz, 1H), 8.19 (dd,  $J = 8.1, 1.6$  Hz, 1H), 7.75-7.69 (m, 2H), 7.48 (dd,  $J = 8.1, 4.6$  Hz, 1H), 6.68-6.62 (m, 2H), 6.06 (s,  $\text{NH}_2$ , 2H);  $^{13}\text{C}$  NMR

(75 MHz, CDCl<sub>3</sub>) δ<sub>C</sub>: 173.4, 161.7, 153.0, 149.8, 145.5, 129.8 (two peaks overlap, 2C), 129.6, 122.5, 121.8, 113.6 (two peaks overlap, 2C); ESI-HRMS: [M + H]<sup>+</sup> calcd for [C<sub>12</sub>H<sub>10</sub>N<sub>3</sub>O<sub>2</sub><sup>80</sup>Se]<sup>+</sup>: 276.0040; found: 276.0044.

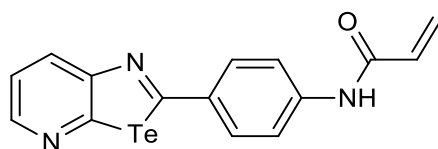
#### 4-([1,3]tellurazolo[5,4-β]pyridin-2-yl)aniline II-31<sub>Te</sub>



II-31<sub>Te</sub>

A suspension of 2-(4-nitrophenyl)-[1,3]tellurazolo[5,4-β]pyridine II-20<sub>Se</sub> (200 mg, 0.57 mmol), NH<sub>4</sub>Cl (15 mg, 0.29 mmol) and elemental Fe powder (96 mg, 1.71 mmol) in EtOH (4.5 mL) and water (2.3 mL) was stirred at 85°C for 2h. After cooling down, the reaction was filtered over celite and washed with toluene. Solvents were evaporated under reduce pressure. The crude material was purified by silica gel chromatography (CHCl<sub>3</sub>/MeOH 2%) to give pure CGP II-31<sub>Se</sub> as an orange solid (165 mg, 90%); mp = 180°C (decomposition). IR: ν (cm<sup>-1</sup>): 2920, 1686, 1593, 1530, 1477, 1391, 1369, 1325, 1244, 1206, 1180, 1167, 984, 968, 932, 920, 845, 796, 727; <sup>1</sup>H NMR (300 MHz, CDCl<sub>3</sub>) δ<sub>H</sub>: 8.37 (dd, *J* = 4.6, 1.2 Hz, 1H), 8.15 (dd, *J* = 8.1, 1.2 Hz, 1H), 7.64 (d, *J* = 8.4 Hz, 2H), 7.46 (dd, *J* = 8.1, 4.6 Hz, 1H), 6.60 (d, *J* = 8.4 Hz, 2H), 6.02 (s, NH<sub>2</sub>, 2H); <sup>13</sup>C NMR (75 MHz, CDCl<sub>3</sub>) δ<sub>C</sub>: not recorded due to low solubility; API-HRMS: [M + H]<sup>+</sup> calcd for [C<sub>12</sub>H<sub>10</sub>N<sub>3</sub><sup>122</sup>Te]<sup>+</sup>: 317.9905; found: 317.9905.

#### *N*-(4-([1,3]tellurazolo[5,4-β]pyridin-2-yl)phenyl)acrylamide II-32<sub>Te</sub>

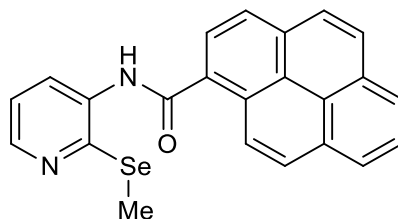


II-32<sub>Te</sub>

To a suspension of 4-([1,3]tellurazolo[5,4-β]pyridin-2-yl)aniline II-31<sub>Te</sub> (145 mg, 0.45 mmol) and pyridine (0.04 mL, 40 mg, 0.50 mmol) in dry CH<sub>2</sub>Cl<sub>2</sub> (11 mL) at 0 °C under dry condition, a solution of acryloyl chloride (37 μL, 41 mg, 0.45 mmol) in dry CH<sub>2</sub>Cl<sub>2</sub> (1 mL) was added dropwise. The reaction was stirred 5 minutes at the same temperature then overnight at room temperature. The mixture was diluted with water (40 mL), extracted with CHCl<sub>3</sub> (10 x 70 mL), washed with brine (20 mL) and dried over Na<sub>2</sub>SO<sub>4</sub>, filtered and the solvent removed under reduced pressure. The crude material was purified by silica gel chromatography (CHCl<sub>3</sub>/MeOH 2%) to give pure *N*-(4-([1,3]tellurazolo[5,4-β]pyridin-2-yl)phenyl)acrylamide II-32<sub>Te</sub> as a yellow solid (45 mg, 27%); mp = > 300°C. IR: ν (cm<sup>-1</sup>): 3240, 2922, 1688, 1591, 1530, 1476, 1323, 1244, 1206, 1180, 1167, 966, 920, 845, 795, 756; <sup>1</sup>H

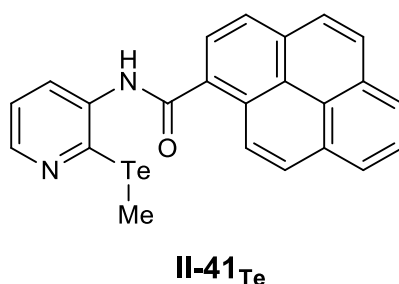
NMR (300 MHz, DMSO)  $\delta_{\text{H}}$ : 10.50 (s, 1H), 8.49 (d,  $J = 4.0$  Hz, 1H), 8.34 (dd,  $J = 8.2, 1.4$  Hz, 1H), 8.34 (dd,  $J = 8.2, 1.4$  Hz, 1H), 7.55 (dd,  $J = 8.2, 4.6$  Hz, 1H), 7.28-7.13 (m, 1H), 6.46 (dd,  $J = 16.9, 9.9$  Hz, 1H), 6.32 (dd,  $J = 16.9, 2.0$  Hz, 1H), 5.82 (dd,  $J = 9.9, 2.0$  Hz, 1H);  $^{13}\text{C}$  NMR (75 MHz,  $\text{CDCl}_3$ )  $\delta_{\text{C}}$ : not recorded due to low solubility; API-HRMS:  $[\text{M} + \text{H}]^+$  calcd for  $[\text{C}_{15}\text{H}_{12}\text{N}_3 \text{O}^{122}\text{Te}]^+$ : 372.0014; found: 372.0014. Single crystals suitable for X-ray diffraction analysis were grown from cool down of a hot toluene solution.

***N*-(2-(methylselanyl)pyridin-3-yl)pyrene-1-carboxamide II-41<sub>Se</sub>**

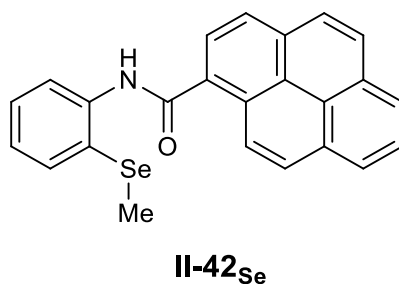


**II-41<sub>Se</sub>**

*N*-(2-(methylselanyl)pyridin-3-yl)pyrene-1-carboxamide **II-41<sub>Se</sub>** was synthesised following a procedure inspired by the work of Cho et al.<sup>[10]</sup> To a suspension of 1-pyrene carboxylic acid (222 mg, 1 mmol) in dry  $\text{CH}_2\text{Cl}_2$  (12 mL) was added oxalyl chloride (0.09 mL, 137 mg, 1.08 mmol) and three drops of DMF (gas formation). The reaction was stirred at room temperature for 2h (until complete dissolution, bright yellow solution). The liquids were removed under reduced pressure. The yellow solid residue was dissolved in dry  $\text{CH}_2\text{Cl}_2$  (12mL) and a solution of 2-(methylselanyl)pyridin-3-amine **II-3<sub>Te</sub>** (131 mg, 0.7 mmol) and dry pyridine (0.06 mL, 63 mg, 0.8 mmol) in dry  $\text{CH}_2\text{Cl}_2$  (2 mL) was added dropwise at  $0^\circ\text{C}$ . The reaction was stirred 5 minutes at the same temperature then overnight at room temperature. The resulting mixture was diluted with  $\text{CH}_2\text{Cl}_2$  (150 mL) and washed with water (25 mL), brine (25 mL), and dried over  $\text{Na}_2\text{SO}_4$ . The solvents were removed under reduced pressure. The crude was purified by silica gel chromatography ( $\text{CHCl}_3/\text{MeOH}$  1%) to give pure *N*-(2-(methylselanyl)pyridin-3-yl)pyrene-1-carboxamide **II-41<sub>Se</sub>** as a light yellow solid (151 mg, 50%); mp =  $216\text{-}220^\circ\text{C}$ . IR:  $\nu$  ( $\text{cm}^{-1}$ ): 3213, 3007, 1925, 1461, 1518, 1574, 1395, 1282, 1072, 856, 833, 785;  $^1\text{H}$  NMR (300 MHz, DMSO)  $\delta_{\text{H}}$ : 10.55 (s, 1H), 8.70 (d,  $J = 9.2$  Hz, 1H), 8.51-8.28 (m, 9H), 8.15 (dd, appearing t,  $J = 7.6$  Hz, 1H), 7.86 (d,  $J = 7.6$  Hz, 1H), 7.34 (dd,  $J = 7.4, 4.8$  Hz, 1H), 2.44 (s, 3H);  $^{13}\text{C}$  NMR (75 MHz,  $\text{CDCl}_3$ )  $\delta_{\text{C}}$ : 168.3, 153.9, 147.9, 135.0, 133.6, 132.1, 130.8, 130.7, 130.2, 128.7, 128.5, 128.2, 127.2, 126.8, 126.1, 125.9, 125.6, 124.6, 124.4, 123.8, 123.6, 120.4, 5.29; ESI-HRMS:  $[\text{M} + \text{H}]^+$  calcd for  $[\text{C}_{23}\text{H}_{17}\text{N}_2\text{O}^{80}\text{Se}]^+$ : 417.0501; found: 417.0506.

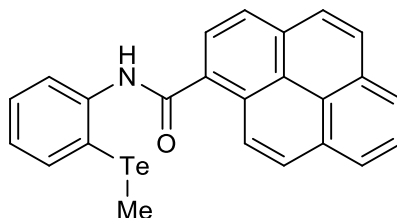
***N*-(2-(methyltellanyl)pyridin-3-yl)pyrene-1-carboxamide II-41<sub>Te</sub>**

*N*-(2-(methyltellanyl)pyridin-3-yl)pyrene-1-carboxamide **II-41<sub>Te</sub>** was synthesised following a procedure inspired by the work of Cho et al.<sup>[10]</sup> To a suspension of 1-pyrene carboxylic acid (246 mg, 1 mmol) in dry CH<sub>2</sub>Cl<sub>2</sub> (12 mL) was added oxalyl chloride (0.10 mL, 152 mg, 1.2 mmol) and three drops of DMF (gas formation). The reaction was stirred at room temperature for 2h (until complete dissolution, bright yellow solution). The liquids were removed under reduced pressure. The yellow solid residue was dissolved in dry CH<sub>2</sub>Cl<sub>2</sub> (12mL) and a solution of 2-(methyltellanyl)pyridin-3-amine **II-3<sub>Te</sub>** (189 mg, 0.8 mmol) and dry pyridine (0.07 mL, 71 mg, 0.9 mmol) in dry CH<sub>2</sub>Cl<sub>2</sub> (2 mL) was added dropwise at 0°C. The reaction was stirred 5 minutes at the same temperature then overnight at room temperature. The resulting mixture was diluted with CH<sub>2</sub>Cl<sub>2</sub> (150 mL) and washed with water (25 mL), brine (25 mL), and dried over Na<sub>2</sub>SO<sub>4</sub>. The solvents were removed under reduced pressure. The crude was purified by silica gel chromatography (CHCl<sub>3</sub>/MeOH 1%) to give pure *N*-(2-(methyltellanyl)pyridin-3-yl)pyrene-1-carboxamide **II-41<sub>Te</sub>** as a light yellow solid (229 mg, 61%); mp = 222-226°C. IR:  $\nu$  (cm<sup>-1</sup>): 3190, 2982, 3048, 1639, 1570, 1508, 1442, 1385, 1261, 1234, 1049, 849, 748, 706, 613, 559; <sup>1</sup>H NMR (400 MHz, DMSO)  $\delta$ <sub>H</sub>: 10.70 (s, 1H), 8.71 (d, *J* = 9.2 Hz, 1H), 8.51 (dd, *J* = 4.6, 1.1 Hz, 1H), 8.47-8.26 (m, 7H), 8.16 (d, *J* = 7.6 Hz, 1H), 8.16 (d, *J* = 7.6 Hz, 1H), 7.76 (dd, *J* = 7.8, 1.1 Hz, 1H), 7.33 (dd, *J* = 7.8, 4.7 Hz, 1H), 2.22 (s, 3H); <sup>13</sup>C NMR (100 MHz, CDCl<sub>3</sub>)  $\delta$ <sub>C</sub>: 168.4, 148.6, 143.0, 137.9, 133.7, 132.2, 130.8, 130.7, 130.2, 128.8, 128.6, 128.2, 127.3, 126.8, 126.1, 125.9, 125.7, 124.7, 124.5, 123.9, 123.6, 121.1, -14.31; ESI-HRMS: [M + H]<sup>+</sup> cacl'd for [C<sub>23</sub>H<sub>17</sub>N<sub>2</sub>O<sup>122</sup>Te]<sup>+</sup>: 459.0371; found: 459.0391.

***N*-(2-(methylselanyl)phenyl)pyrene-1-carboxamide II-42<sub>Se</sub>**

*N*-(2-(methylselanyl)phenyl)pyrene-1-carboxamide **II-42<sub>Se</sub>** was synthesised following a procedure inspired by the work of Cho et al.<sup>[10]</sup> To a suspension of 1-pyrene carboxylic acid (462 mg, 1.875 mmol) in dry CH<sub>2</sub>Cl<sub>2</sub> (20 mL) was added oxalyl chloride (0.19 mL, 276 mg, 2.176 mmol) and three drops of DMF (gas formation). The reaction was stirred at room temperature for 2h (until complete dissolution, bright yellow solution). The liquids were removed under reduced pressure. The yellow solid residue was dissolved in dry CH<sub>2</sub>Cl<sub>2</sub> (20 mL) and a solution of 2-(methylselanyl)aniline **II-28<sub>Se</sub>** (279 mg, 1.5 mmol) and dry pyridine (0.14 mL, 134 mg, 1.69 mmol) in dry CH<sub>2</sub>Cl<sub>2</sub> (3 mL) was added dropwise at 0°C. The reaction was stirred 5 minutes at the same temperature then overnight at room temperature. The resulting mixture was diluted with CH<sub>2</sub>Cl<sub>2</sub> (150 mL) and washed with water (25 mL), brine (25 mL), and dried over Na<sub>2</sub>SO<sub>4</sub>. The solvents were removed under reduced pressure. The crude was purified by silica gel chromatography (CHCl<sub>3</sub>/MeOH 1%) to give pure *N*-(2-(methylselanyl)phenyl)pyrene-1-carboxamide **II-42<sub>Se</sub>** as a light yellow solid (267 mg, 43%); mp = 160-162°C. IR:  $\nu$  (cm<sup>-1</sup>): 3215, 1643, 1578, 1512, 1422, 1296, 1136, 1030, 941, 914, 847, 820, 731; <sup>1</sup>H NMR (400 MHz, DMSO)  $\delta_{\text{H}}$ : 10.48 (s, 1H), 8.77 (d, *J* = 9.2 Hz, 1H), 8.48-8.40 (m, 4H), 8.39-8.30 (m, 3H), 8.19 (dd appearing t, *J* = 7.6 Hz, 1H), 7.63-7.56 (m, 2H), 7.43-7.33 (m, 2H), 2.40 (s, 3H); <sup>13</sup>C NMR (100 MHz, CDCl<sub>3</sub>)  $\delta_{\text{C}}$ : 168.0, 136.9, 132.0, 131.3, 131.1, 130.7, 130.2, 129.9, 128.6, 128.4, 128.1, 127.3 (two peaks overlap, 2C), 127.3, 126.7, 126.3, 126.0, 125.8, 125.5, 124.8, 124.5, 123.9, 123.6, 6.74; ESI-HRMS: [M + H]<sup>+</sup> calcd for [C<sub>24</sub>H<sub>18</sub>NO<sup>76</sup>Se]<sup>+</sup>: 412.0581; found: 412.0575.

***N*-(2-(methyltellanyl)pyridin-3-yl)pyrene-1-carboxamide II-42<sub>Te</sub>**

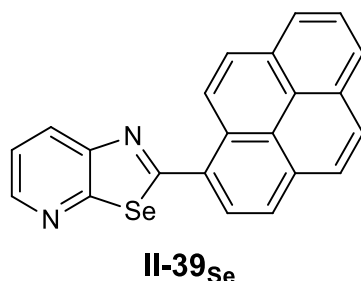


**II-42<sub>Te</sub>**

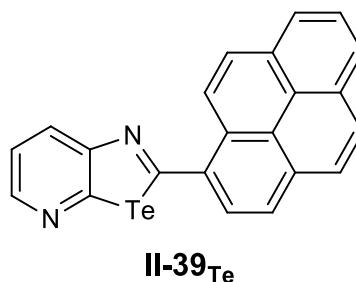
*N*-(2-(methyltellanyl)phenyl)pyrene-1-carboxamide **II-42<sub>Te</sub>** was synthesised following a procedure inspired by the work of Cho et al.<sup>[10]</sup> To a suspension of 1-pyrene carboxylic acid (446 mg, 1.813 mmol) in dry CH<sub>2</sub>Cl<sub>2</sub> (20 mL) was added oxalyl chloride (0.19 mL, 276 mg, 2.176 mmol) and three drops of DMF (gas formation). The reaction was stirred at room temperature for 2h (until complete dissolution, bright yellow solution). The liquids were removed under reduced pressure. The yellow solid residue was dissolved in dry CH<sub>2</sub>Cl<sub>2</sub> (20 mL) and a solution of 2-(methyltellanyl)aniline **II-28<sub>Te</sub>** (340 mg, 1.45 mmol) and dry pyridine (0.32 mL, 312 mg, 1.63 mmol) in dry CH<sub>2</sub>Cl<sub>2</sub> (3 mL) was added dropwise at 0°C. The reaction was stirred 5 minutes at the same temperature then overnight at room temperature. The resulting mixture was diluted with CH<sub>2</sub>Cl<sub>2</sub> (150 mL) and washed with water

(25 mL), brine (25 mL), and dried over Na<sub>2</sub>SO<sub>4</sub>. The solvents were removed under reduced pressure. The crude was purified by silica gel chromatography (CHCl<sub>3</sub>/MeOH 1%) to give pure *N*-(2-(methyltellanyl)phenyl)pyrene-1-carboxamide **II-42<sub>Te</sub>** as a light yellow solid (388 mg, 58%); mp = 158-160°C. IR:  $\nu$  (cm<sup>-1</sup>): 3242, 1736, 1634, 1601, 1576, 1514, 1464, 1300, 1150, 1024, 920, 856, 833, 800, 748; <sup>1</sup>H NMR (400 MHz, DMSO)  $\delta_{\text{H}}$ : 10.68 (s, 1H), 8.74 (d, *J* = 9.2 Hz, 1H), 8.46-8.36 (m, 4H), 8.35-8.25 (m, 3H), 8.15 (dd appearing t, *J* = 7.6 Hz, 1H), 7.73 (d, *J* = 7.6 Hz, 1H), 7.45 (d, *J* = 7.4 Hz, 1H), 7.37 (dd appearing t, *J* = 7.4 Hz, 1H), 7.21 (dd appearing t, *J* = 7.0 Hz, 1H), 2.10 (s, 3H); <sup>13</sup>C NMR (100 MHz, CDCl<sub>3</sub>)  $\delta_{\text{C}}$ : 168.1, 140.4, 135.6, 132.0, 131.1, 130.7, 130.2, 128.6, 128.4, 128.2, 127.5, 127.3, 127.1, 126.7, 126.4, 126.2, 126.0, 125.8, 125.7, 124.8, 124.5, 123.9, 123.6, -15.24; ESI-HRMS: [M + H]<sup>+</sup> calcd for [C<sub>24</sub>H<sub>18</sub>NO<sup>122</sup>Te]<sup>+</sup>: 458.0419; found: 458.0414.

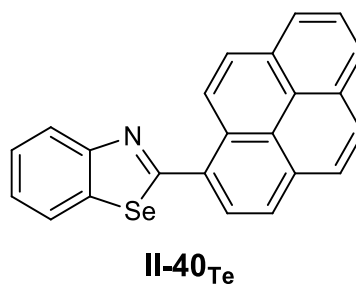
### 2-(pyren-1-yl)-[1,3]selnazolo[5,4- $\beta$ ]pyridine **II-39<sub>Se</sub>**



To a solution of *N*-(2-(methylselanyl)pyridin-3-yl)pyrene-1-carboxamide **II-41<sub>Se</sub>** (117 mg, 0.28 mmol) and NEt<sub>3</sub> (0.47 mL, 366 mg, 3.6 mmol) in dry dioxane (6 mL) under anhydrous condition, POCl<sub>3</sub> (0.11 mL, 184 mg, 1.2 mmol) was added dropwise. The reaction was heated to reflux and stirred overnight. The resulting mixture was diluted with CHCl<sub>3</sub> (50 mL), washed with a saturated solution of NaHCO<sub>3</sub> (20 mL), water (20 mL), brine (20 mL), and dried over Na<sub>2</sub>SO<sub>4</sub>. The solvents were removed under reduced pressure. The crude was purified by silica gel chromatography (CHCl<sub>3</sub>/MeOH 1%) to give pure CGP **II-39<sub>Se</sub>** as a bright yellow solid (98 mg, 91%); mp = 156-158°C. IR:  $\nu$  (cm<sup>-1</sup>): 3038, 1576, 1512, 1373, 1207, 1186, 945, 820, 839, 795, 735, 630; <sup>1</sup>H NMR (300 MHz, CD<sub>2</sub>Cl<sub>2</sub>)  $\delta_{\text{H}}$ : 9.38 (d, *J* = 9.5 Hz, 1H), 8.57 (dd, *J* = 4.7, 1.6 Hz, 1H), 8.46 (dd, *J* = 8.2, 1.6 Hz, 1H), 8.40 (d, *J* = 8.0 Hz, 1H), 8.31 – 8.19 (m, 5H), 8.15 – 8.06 (m, 2H), 7.53 (dd, *J* = 8.2, 4.7 Hz, 1H); <sup>13</sup>C NMR (75 MHz, CD<sub>2</sub>Cl<sub>2</sub>)  $\delta_{\text{C}}$ : 174.8, 164.7, 150.5, 147.1, 133.3, 131.8, 131.7, 131.2, 130.1, 129.9, 129.8, 129.6, 128.6, 127.6, 126.9, 126.6, 126.2, 125.4, 125.3 (two peaks overlap, 2C), 124.7, 121.9; ESI-HRMS: [M + H]<sup>+</sup> calcd for [C<sub>22</sub>H<sub>13</sub>N<sub>2</sub><sup>80</sup>Se]<sup>+</sup>: 385.0244; found: 385.0241. Single crystals suitable for X-ray diffraction analysis were grown from slow evaporation of CHCl<sub>3</sub> solution.

**2-(pyren-1-yl)-[1,3]tellurazolo[5,4- $\beta$ ]pyridine II-39<sub>Te</sub>**

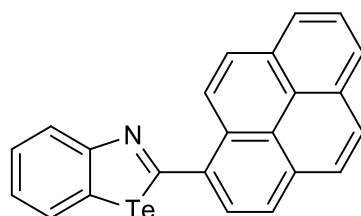
To a solution of *N*-(2-(methyltellanyl)pyridin-3-yl)pyrene-1-carboxamide **II-41<sub>Te</sub>** (93 mg, 0.2 mmol) and NEt<sub>3</sub> (0.34 mL, 243 mg, 2.4 mmol) in dry dioxane (4 mL) under anhydrous condition, POCl<sub>3</sub> (0.08 mL, 123 mg, 0.8 mmol) was added dropwise. The reaction was heated to reflux and stirred overnight. The resulting mixture was diluted with CHCl<sub>3</sub> (50 mL), washed with a saturated solution of NaHCO<sub>3</sub> (20 mL), water (20 mL), brine (20 mL), and dried over Na<sub>2</sub>SO<sub>4</sub>. The solvents were removed under reduced pressure. The crude was purified by silica gel chromatography (CHCl<sub>3</sub>/MeOH 1%) to give pure CGP **II-39<sub>Te</sub>** as a bright yellow solid (51 mg, 59%); mp = 188-190°C. IR:  $\nu$  (cm<sup>-1</sup>): 1573, 1535, 1473, 1365, 1207, 1180, 934, 837, 791, 578, 478; <sup>1</sup>H NMR (500 MHz, CD<sub>2</sub>Cl<sub>2</sub>)  $\delta$ <sub>H</sub>: 9.35 (d, *J* = 9.4 Hz, 1H), 8.54 (dd, *J* = 4.6, 1.6 Hz, 1H), 8.49 (dd, *J* = 8.0, 1.6 Hz, 1H), 8.31 – 8.06 (m, 5H), 8.21 (d, *J* = 8.9 Hz, 1H), 8.14 – 8.06 (m, 2H), 7.53 (dd, *J* = 8.0, 4.6 Hz, 1H); <sup>13</sup>C NMR (125 MHz, CD<sub>2</sub>Cl<sub>2</sub>)  $\delta$ <sub>C</sub>: 178.0, 165.8, 158.7, 146.7, 135.3, 133.0, 132.8, 131.9, 131.3, 130.8, 129.6, 129.5, 127.7, 127.4, 127.0, 126.5, 126.1, 125.5, 125.4 (two peaks overlap, 2C), 124.8, 122.3; ESI-HRMS: [M + H]<sup>+</sup> calcd for [C<sub>22</sub>H<sub>13</sub>N<sub>2</sub><sup>122</sup>Te]<sup>+</sup>: 427.0109; found: 427.0124. Single crystals suitable for X-ray diffraction analysis were grown from slow evaporation of CHCl<sub>3</sub> solution.

**2-(pyren-1-yl)benzo[ $\delta$ ][1,3]selenazole II-40<sub>Se</sub>**

To a solution of *N*-(2-(methylselanyl)phenyl)pyrene-1-carboxamide **II-42<sub>Se</sub>** (228 mg, 0.55 mmol) and NEt<sub>3</sub> (0.46 mL, 366 mg, 3.3 mmol) in dry dioxane (11 mL) under anhydrous condition, POCl<sub>3</sub> (0.10 mL, 184 mg, 1.1 mmol) was added dropwise. The reaction was heated to reflux and stirred for 5h. The resulting mixture was diluted with CHCl<sub>3</sub> (100 mL), washed with a saturated solution of NaHCO<sub>3</sub> (30 mL), with water (30 mL), brine (30 mL), and dried over MgSO<sub>4</sub>. The solvent removed under

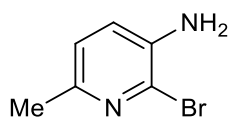
reduced pressure. The crude was purified by silica gel chromatography ( $\text{CHCl}_3$ ) to give pure CGP **II-40<sub>Se</sub>** as a bright yellow solid (184 mg, 88%); mp = 130-132°C. IR:  $\nu$  ( $\text{cm}^{-1}$ ): 3215, 1643, 1584, 1522, 1501, 1431, 1387, 1304, 1213, 1186, 1067, 941, 817, 746, 708;  $^1\text{H}$  NMR (300 MHz,  $\text{CD}_2\text{Cl}_2$ )  $\delta_{\text{H}}$ : 9.41 (d,  $J = 9.6$  Hz, 1H), 8.40 (d,  $J = 8.0$  Hz, 1H), 8.30-8.23 (m, 5H), 8.20 (d,  $J = 9.0$  Hz, 1H), 8.14 – 8.05 (m, 3H), 7.59 (ddd,  $J = 8.5, 7.3, 1.3$  Hz, 1H), 7.41 (ddd,  $J = 8.5, 7.3, 1.3$  Hz, 1H);  $^{13}\text{C}$  NMR (100 MHz,  $\text{CD}_2\text{Cl}_2$ )  $\delta_{\text{C}}$ : 172.8, 156.6, 140.0, 133.1, 131.7, 131.2, 130.2, 129.7, 129.5, 129.4, 128.6, 127.6, 126.9, 126.8, 126.5, 126.1, 125.7, 125.6, 125.5 (two peaks overlap, 2C), 125.2, 125.1, 124.7; ESI-HRMS:  $[\text{M} + \text{H}]^+$  calcd for  $[\text{C}_{23}\text{H}_{14}\text{N}^{76}\text{Se}]^+$ : 380.0318; found: 380.0312. Single crystals suitable for X-ray diffraction analysis were grown from slow evaporation of  $\text{CHCl}_3$  solution.

### 2-(pyren-1-yl)benzo[ $\delta$ ][1,3]tellurazole **II-40<sub>Te</sub>**

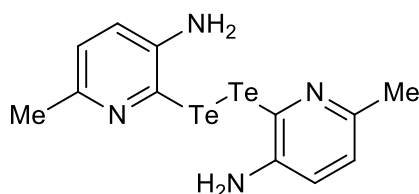


**II-40<sub>Te</sub>**

To a solution of *N*-(2-(methyltellanyl)phenyl)pyrene-1-carboxamide **II-42<sub>Te</sub>** (349 mg, 0.75 mmol) and  $\text{NEt}_3$  (0.63 mL, 455 mg, 4.5 mmol) in dry dioxane (15 mL) under anhydrous condition,  $\text{POCl}_3$  (0.14 mL, 225 mg, 1.5 mmol) was added dropwise. The reaction was heated to reflux and stirred for 2h. The resulting mixture was diluted with  $\text{CHCl}_3$  (150 mL), washed with a saturated solution of  $\text{NaHCO}_3$  (30 mL), water (30 mL), brine (30 mL), and dried over  $\text{Na}_2\text{SO}_4$ . The solvents were removed under reduced pressure. The crude was purified by silica gel chromatography ( $\text{CHCl}_3$ ) to give pure CGP **II-40<sub>Te</sub>** as a bright yellow solid (300 mg, 93%); mp = 134-136°C. IR:  $\nu$  ( $\text{cm}^{-1}$ ): 3021, 1580, 1503, 1429, 1290, 1173, 1063, 1018, 924, 839, 756;  $^1\text{H}$  NMR (400 MHz,  $\text{CD}_2\text{Cl}_2$ )  $\delta_{\text{H}}$ : 9.37 (d,  $J = 9.4$  Hz, 1H), 8.38 (ddd,  $J = 8.1, 1.2, 0.5$  Hz, 1H), 8.29-8.15 (m, 6H), 8.10-8.03 (m, 3H), 7.59 (ddd,  $J = 8.1, 7.2, 1.3$  Hz, 1H), 7.28 (ddd,  $J = 7.8, 7.2, 1.2$  Hz, 1H);  $^{13}\text{C}$  NMR (125 MHz,  $\text{CD}_2\text{Cl}_2$ )  $\delta_{\text{C}}$ : 173.7, 162.8, 136.9, 135.3, 132.7, 132.0, 131.8, 131.3, 130.6, 129.4, 129.2, 127.6, 127.5, 127.2, 127.2, 126.9, 126.3, 126.0, 125.6, 125.4, 125.4, 125.3, 124.8; ESI-HRMS:  $[\text{M} + \text{H}]^+$  calcd for  $[\text{C}_{23}\text{H}_{14}\text{N}^{122}\text{Te}]^+$ : 426.0157; found: 426.0154. Single crystals suitable for X-ray diffraction analysis were grown from slow evaporation of  $\text{CHCl}_3$  solution.

**2-bromo-6-methylpyridin-3-amine VI-2****IV-2**

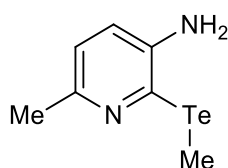
2-Bromo-6-methylpyridin-3-amine **VI-2** was synthesised following a procedure developed by Dunn et al.<sup>[11]</sup> To a solution of 6-methylpyridin-3-amine **IV-1** (5.407 g, 50 mmol) in MeCN (250 mL) was added portion wise NBS (8.894 g, 50 mmol). The reaction was stirred at room temperature for 5 minutes (orange colour turned dark red). The solvent is evaporated under reduced pressure and the crude material mixture was purified by silica gel chromatography (CHCl<sub>3</sub>/MeOH 1%) to afford the desired product **IV-2** as a beige solid (6.950 g, 37 mmol, 74%). mp = 80-82 °C. IR:  $\nu$  (cm<sup>-1</sup>): 3443, 3294, 3175, 1616, 1553, 1472, 1377, 1310, 1260, 1142, 1109, 1053, 988, 867, 822, 671; <sup>1</sup>H NMR (300 MHz, CDCl<sub>3</sub>)  $\delta_{\text{H}}$ : 6.89 (d,  $J$  = 7.9 Hz, 1H), 6.86 (d,  $J$  = 7.9 Hz, 1H), 3.98 (s, NH<sub>2</sub>, 2H), 2.36 (s, 3H); <sup>13</sup>C NMR (75 MHz, CDCl<sub>3</sub>)  $\delta_{\text{C}}$ : 148.2, 138.8, 128.5, 123.2, 123.1, 22.89; ESI-HRMS: [M + H]<sup>+</sup> calcd for [C<sub>6</sub>H<sub>8</sub>N<sub>2</sub>Br]<sup>+</sup>: 186.9871; found: 186.9863.

**2,2'-ditellanediybis(6-methylpyridin-3-amine) IV-3****IV-3**

To a diluted solution of *i*-PrMgCl (3 mL, 6 mmol) in dry THF (13.2 mL) under dry condition, *n*-BuLi (1.6 M, 7.5 mL, 12 mmol) was added dropwise at 0°C. The resulting mixture was stirred at the same temperature for 10 minutes. In parallel, to a solution of 2-bromo-6-methylpyridin-3-amine **IV-2** (1.128 g, 6 mmol) in dry THF (47 mL) under anhydrous condition, *n*-BuLi (1.6 M, 3.8 mL, 6 mmol) was added dropwise at 0°C. The reaction was stirred 10 minutes at the same temperature then the tri-alkyl magnesate solution freshly prepared was added dropwise. The reaction was stirred for 1h at 0°C, freshly grounded elemental tellurium powder (2.287 g, 18 mmol) was added in once while a brisk flux of Nitrogen was passed through the flask. The resulting mixture was stirred overnight, poured in a solution of NH<sub>4</sub>Cl (1.000 g) in water (70 mL) and air bubbled through for 2h. The aqueous phase was extracted with Et<sub>2</sub>O (6 x 30 mL). The combined organic extracts were washed with water

(25 mL), brine (25 mL), and dried over Na<sub>2</sub>SO<sub>4</sub>. The solvents were removed under reduced pressure. The crude was purified by silica gel chromatography (CHCl<sub>3</sub>/MeOH 2%) to give pure **IV-3** as a dark red solid (667 mg, 47%); mp = 132-136 °C. IR:  $\nu$  (cm<sup>-1</sup>): 3400, 3362, 3312, 3169, 2916, 1624, 1591, 1574, 1541, 1447, 1285, 1250, 1132, 1036, 984, 822; <sup>1</sup>H NMR (300 MHz, DMSO)  $\delta_{\text{H}}$ : 6.87 (d, *J* = 8.2 Hz, 2H), 6.84 (d, *J* = 8.2 Hz, 2H), 5.55 (s, NH<sub>2</sub>, 4H); <sup>13</sup>C NMR (75 MHz, DMSO)  $\delta_{\text{C}}$ : 146.4 (two peaks overlap, 2C), 145.8 (two peaks overlap, 2C), 123.5 (two peaks overlap, 2C), 120.0 (two peaks overlap, 2C), 119.3 (two peaks overlap, 2C), 22.26 (two peaks overlap, 2C); ESI-HRMS: [M + H]<sup>+</sup> calcd for [C<sub>12</sub>H<sub>15</sub>N<sub>4</sub><sup>128</sup>Te<sub>2</sub>]<sup>+</sup>: 470.9386; found: 470.9398.

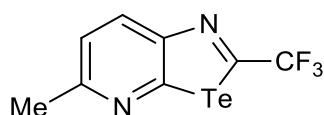
#### 6-methyl-2-(methyltellanyl)pyridin-3-amine **IV-4**



**IV-4**

To a solution of 2,2'-ditellanediybis(6-methylpyridin-3-amine) **IV-3** (469 mg, 1 mmol) in dry and degassed THF (25 mL) under N<sub>2</sub>, were added NaBH<sub>4</sub> (114 mg, 3 mmol) and MeOH (0.20 mL, 160 mg, 5 mmol) and the reaction was stirred at room temperature for 1 h (the dark orange colour turned lighter). MeI (0.14 mL, 312 mg, 2.2 mmol) was added and the mixture was stirred at room temperature for 1.5h more. Water (10 mL) was slowly added to the solution and extracted with Et<sub>2</sub>O (3 x 30 mL). The combined organic extracts were washed with water (15 mL), brine (15 mL), and dried over Na<sub>2</sub>SO<sub>4</sub>. The solvents were removed under reduce pressure. The crude was purified by Silica Gel Chromatography (CHCl<sub>3</sub>/MeOH 1%) to give pure amine **IV-4** as yellow oil (0.450g, 90%). IR:  $\nu$  (cm<sup>-1</sup>): 3318, 3204, 2920, 2363, 2313, 1609, 1558, 1508, 1445, 1373, 1281, 1213, 1138, 1099, 1049, 820, 662; <sup>1</sup>H NMR (300 MHz, DMSO)  $\delta_{\text{H}}$ : 6.79 (s, 2H), 3.71 (s, NH<sub>2</sub>, 2H), 2.43 (s, 3H), 2.28 (s, 3H); <sup>13</sup>C NMR (75 MHz, CDCl<sub>3</sub>)  $\delta_{\text{C}}$ : 150.3, 143.2, 127.6, 121.7, 120.7, 23.50, -15.37; API-HRMS: [M + H]<sup>+</sup> calcd for [C<sub>7</sub>H<sub>11</sub>N<sub>2</sub><sup>122</sup>Te]<sup>+</sup>: 244.9953; found: 244.9954.

#### 5-methyl-2-(trifluoromethyl)-[1,3]tellurazolo[5,4- $\beta$ ]pyridine **IV-5**

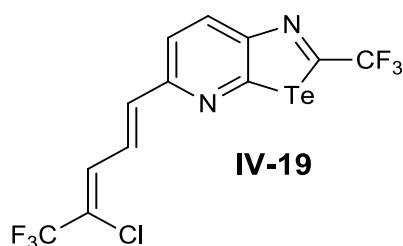


**IV-5**

To a solution of 6-methyl-2-(methyltellanyl)pyridin-3-amine **IV-4** (333 mg, 1.3 mmol) in dry pyridine (4 mL) and dry CH<sub>2</sub>Cl<sub>2</sub> (4 mL) under anhydrous condition at 0°C, trifluoroacetic acid anhydride (0.22

mL, 335 mg, 1.6 mmol) was added dropwise. The reaction was stirred 5 minutes at the same temperature then overnight at room temperature. Liquids were removed under reduced pressure, the yellow solid residue was dissolved in in dry 1,4-dioxane (10 mL) and dry DIPEA (10 mL) and a POCl<sub>3</sub> (0.48 mL, 799 mg, 5.32 mmol) was added dropwise. The reaction was heated to reflux and stirred overnight. The resulting mixture was allowed to cool down to room temperature, diluted with CHCl<sub>3</sub> (70 mL), washed with a saturated solution of NaHCO<sub>3</sub> (25 mL), with water (20 mL), brine (20 mL), and dried over Na<sub>2</sub>SO<sub>4</sub>. The solvents were removed under reduced pressure. The crude was purified twice by silica gel chromatography (CHCl<sub>3</sub>/MeOH 0 to 1%) to give pure **IV-5** as an off-white solid (189 mg, 45%); mp = 110-112 °C. IR:  $\nu$  (cm<sup>-1</sup>): 3017, 2970, 1738, 1549, 1495, 1300, 1157, 1126, 1065, 968, 833, 716, 640; <sup>1</sup>H NMR (500 MHz, CDCl<sub>3</sub>)  $\delta$ <sub>H</sub>: 8.36 (d, *J* = 8.3 Hz, 1H), 7.37 (d, *J* = 8.3 Hz, 1H), 2.67 (s, 3H); <sup>19</sup>F NMR (470 MHz, CDCl<sub>3</sub>)  $\delta$ <sub>F</sub>: -62.5 (s, 3F); <sup>13</sup>C NMR (125 MHz, CDCl<sub>3</sub>)  $\delta$ <sub>C</sub>: 164.4, 162.6 (q, *J*<sub>CF</sub> = 41 Hz, 1C), 158.2, 153.3, 134.9, 123.6 (q, *J*<sub>CF</sub> = 274 Hz, 1C), 122.5, 24.66; ESI-HRMS: [M + H]<sup>+</sup> calcd for [C<sub>8</sub>H<sub>6</sub>N<sub>2</sub>F<sub>3</sub><sup>130</sup>Te]<sup>+</sup>: 316.9545; found: 316.9547. Single crystals suitable for X-ray diffraction analysis were grown from slow evaporation of CHCl<sub>3</sub> solution.

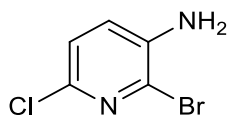
**5-((1E,3Z)-4-chloro-5,5,5-trifluoropenta-1,3-dien-1-yl)-2-(trifluoromethyl)-[1,3]tellurazolo[5,4-β]pyridine IV-19**



To a solution of 6-methyl-2-(methyltellanyl)pyridin-3-amine **IV-4** (405 mg, 1.6 mmol) in dry pyridine (5 mL) and dry CH<sub>2</sub>Cl<sub>2</sub> (5 mL) under anhydrous condition at 0°C, trifluoroacetic acid anhydride (0.27 mL, 403 mg, 1.92 mmol) was added dropwise. The reaction was stirred 5 minutes at the same temperature then overnight at room temperature. Solvents were removed under reduced pressure, the yellow solid residue dissolved in in dry 1,4-dioxane (10 mL) and dry NEt<sub>3</sub> (10 mL) and a POCl<sub>3</sub> (0.58 mL, 962 mg, 6.4 mmol) was added dropwise. The reaction was heated to reflux and stirred overnight. The resulting mixture was allowed to cool down to room temperature, diluted with CHCl<sub>3</sub> (70 mL), washed with a saturated solution of NaHCO<sub>3</sub> (25 mL), with water (20 mL), brine (20 mL), and dried over Na<sub>2</sub>SO<sub>4</sub>. The solvents were removed under reduced pressure. The crude was purified by silica gel chromatography (CHCl<sub>3</sub>) to give **IV-19** as a dark solid (74 mg, 10%); mp = 112-114°C. IR:  $\nu$  (cm<sup>-1</sup>): 3044, 2926, 1634, 1570, 1499, 1342, 1300, 1254, 1169, 1121, 1061, 966, 939, 897, 829, 737, 719; <sup>1</sup>H NMR (400 MHz, CDCl<sub>3</sub>)  $\delta$ <sub>H</sub>: 8.46 (d, *J* = 8.4 Hz, 1H), 7.67 (ddd, *J* = 15.3, 10.9, 1.0 Hz, 1H), 7.58 (d, *J* = 8.4 Hz, 1H), 7.13-7.00 (m, 2H); <sup>19</sup>F NMR (376 MHz, CDCl<sub>3</sub>)  $\delta$ <sub>F</sub>: -62.6 (s,

3F), -68.6 (s, 3F);  $^{13}\text{C}$  NMR  $\delta_{\text{C}}$ : Not recorded due to solubility issue; ESI-HRMS:  $[\text{M} + \text{H}]^+$  calcd for  $[\text{C}_{12}\text{H}_6\text{N}_2\text{F}_6^{130}\text{Te}]^+$ : 456.9186; found: 456.9185. Single crystals suitable for X-ray diffraction analysis were grown from slow evaporation of  $\text{CHCl}_3$  solution.

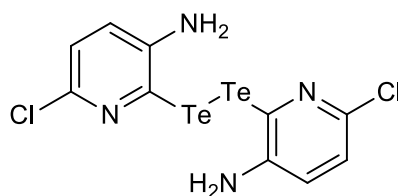
### 2-bromo-6-chloropyridin-3-amine IV-7



**IV-7**

2-bromo-6-chloropyridin-3-amine **VI-7** was synthesised following a procedure developed by Dunn et al.<sup>[11]</sup> To a solution of 6-chloropyridin-3-amine (3.214 g, 25 mmol) in MeCN (125 mL) was added portion wise NBS (4.447 g, 25 mmol). The reaction was stirred at room temperature for 5 minutes. The solvent is evaporated under reduced pressure and the crude material mixture was purified by SGC ( $\text{CHCl}_3$ ) to afford the desired product **IV-7** as a white solid (5.021 g, 24.2 mmol, 97%). mp = 140-142 °C. IR:  $\nu$  ( $\text{cm}^{-1}$ ): 3441, 3325, 1609, 1543, 1441, 1373, 1304, 1267, 1142, 1105, 1047, 851, 827, 696, 644;  $^1\text{H}$  NMR (300 MHz,  $\text{CDCl}_3$ )  $\delta_{\text{H}}$ : 7.07 (d,  $J = 8.2$  Hz, 1H), 6.99 (d,  $J = 8.1$  Hz, 1H), 4.17 (s,  $\text{NH}_2$ , 2H);  $^{13}\text{C}$  NMR (75 MHz, DMSO)  $\delta_{\text{C}}$ : 140.7, 137.8, 126.9, 124.6, 124.0; ESI-HRMS:  $[\text{M} + \text{H}]^+$  calcd for  $[\text{C}_5\text{H}_5\text{N}_2\text{ClBr}]^+$ : 206.9325; found: 206.9328.

### 2,2'-ditellanediybis(6-chloropyridin-3-amine) IV-8

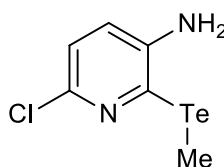


**IV-8**

To a diluted solution of *i*-PrMgCl (0.5 mL, 1 mmol) in dry THF (2 mL) under dry condition, *n*-BuLi (2.5 M, 0.8 mL, 2 mmol) was added dropwise at 0°C. The resulting mixture was stirred at the same temperature for 10 minutes. In parallel, to a solution of 2-bromo-6-chloropyridin-3-amine **IV-7** (207 mg, 1 mmol) in dry THF (8 mL) under anhydrous condition, *n*-BuLi (2.5 M, 0.4 mL, 1 mmol) was added dropwise at 0°C. The reaction was stirred 10 minutes at the same temperature then the tri-alkyl magnesate solution freshly prepared was added dropwise. The reaction was stirred for 1h at 0°C, freshly grounded elemental tellurium powder (381 mg, 3 mmol) was added in once while a brisk flux of Nitrogen was passed through the flask. The resulting mixture was stirred overnight, poured in a solution of  $\text{NH}_4\text{Cl}$  (495 mg) in water (40 mL) and air bubbled through for 2h. The aqueous

phase was extracted with Et<sub>2</sub>O (5 x 20 mL). The combined organic extracts were washed with water (15 mL), brine (15 mL), and dried over Na<sub>2</sub>SO<sub>4</sub>. The solvents were removed under reduced pressure. The crude was purified by silica gel chromatography (CHCl<sub>3</sub>/MeOH 2%) to give pure **IV-8** as a dark red solid (141 mg, 55%); mp = 162-164 °C. IR:  $\nu$  (cm<sup>-1</sup>): 3460, 3362, 1599, 1558, 1539, 1296, 1244, 1142, 1117, 1030, 841, 824, 673, 635; <sup>1</sup>H NMR (300 MHz, DMSO)  $\delta_{\text{H}}$ : 7.09 (d, *J* = 8.4 Hz, 2H), 6.98 (d, *J* = 8.4 Hz, 2H), 5.83 (s, NH<sub>2</sub>, 4H); <sup>13</sup>C NMR (100 MHz, DMSO)  $\delta_{\text{C}}$ : 147.8 (two peaks overlap, 2C), 135.8 (two peaks overlap, 2C), 124.1 (two peaks overlap, 2C), 122.2 (two peaks overlap, 2C), 117.8 (two peaks overlap, 2C); ESI-HRMS: [M + H]<sup>+</sup> calcd for [C<sub>10</sub>H<sub>9</sub>N<sub>4</sub><sup>128</sup>Te<sup>130</sup>Te]<sup>+</sup>: 512.8311; found: 512.8297.

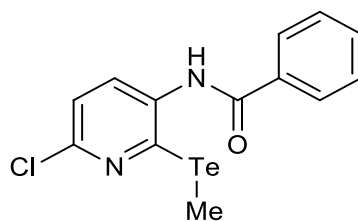
### 6-chloro-2-(methyltellanyl)pyridin-3-amine **IV-9**



**IV-9**

To a solution of 2,2'-ditellanediybis(6-chloropyridin-3-amine) **IV-8** (714 mg, 1.4 mmol) in dry and degassed THF (35 mL) under N<sub>2</sub>, were added NaBH<sub>4</sub> (159 mg, 4.2 mmol) and MeOH (0.28 mL, 224 mg, 5 mmol) and the reaction was stirred at room temperature for 1 h (the dark orange colour turned lighter). MeI (0.19 mL, 437 mg, 3.08 mmol) was added and the mixture was stirred at room temperature for 1.5h more. Water (15 mL) was slowly added to the solution and extracted with Et<sub>2</sub>O (3 x 30 mL). The combined organic extracts were washed with water (15 mL), brine (15 mL), and dried over Na<sub>2</sub>SO<sub>4</sub>. The solvents were removed under reduce pressure. The crude was purified by silica gel chromatography (CHCl<sub>3</sub>) to give pure amine **IV-9** as yellow oil (0.745g, 98%). IR:  $\nu$  (cm<sup>-1</sup>): 3422, 3316, 6026, 2926, 1607, 1557, 1418, 1366, 1281, 1250, 1215, 1121, 1090, 1042, 843, 816, 679, 637; <sup>1</sup>H NMR (300 MHz, DMSO)  $\delta_{\text{H}}$ : 6.92 (d, *J* = 8.3 Hz, 1H), 6.81 (dd, *J* = 8.3 Hz, 1H), 3.80 (s, NH<sub>2</sub>, 2H), 2.32 (s, 3H); <sup>13</sup>C NMR (100 MHz, CDCl<sub>3</sub>)  $\delta_{\text{C}}$ : 144.8, 141.1, 127.7, 122.4, 122.0, -14.37; ESI-HRMS: [M + H]<sup>+</sup> calcd for [C<sub>6</sub>H<sub>8</sub>N<sub>2</sub>Cl<sup>122</sup>Te]<sup>+</sup>: 264.9407; found: 264.9418.

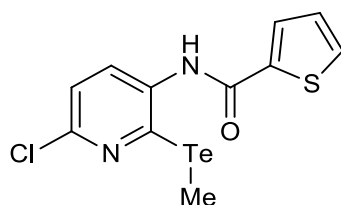
### *N*-(6-chloro-2-(methyltellanyl)pyridin-3-yl)benzamide **IV-20**



**IV-20**

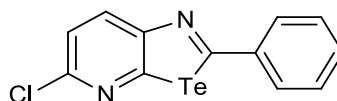
To a solution of 6-chloro-2-(methyltellanyl)pyridin-3-amine **IV-9** (95 mg, 0.35 mmol) in dry pyridine (1 mL) and dry CH<sub>2</sub>Cl<sub>2</sub> (1 mL) at 0 °C under anhydrous condition, benzoyl chloride (0.05 mL, 59 mg, 0.42 mmol) was added dropwise. The reaction was stirred 5 minutes at 0 °C then overnight at room temperature. The resulting mixture was diluted with EtOAc (30 mL) and washed with water (10 mL), extracted with EtOAc (2 x 10 mL), organic phases were combined and washed with brine (10 mL), and dried over Na<sub>2</sub>SO<sub>4</sub>. The solvents were removed under reduced pressure. The crude was purified by silica gel chromatography (CHCl<sub>3</sub>/MeOH 1%) to give pure amide **IV-20** as a white solid (120 mg, 92%); mp = 138-140 °C. IR:  $\nu$  (cm<sup>-1</sup>): 3229, 1647, 1558, 1501, 1485, 1339, 1215, 1126, 1107, 1051, 907, 827, 710; <sup>1</sup>H NMR (300 MHz, DMSO)  $\delta_{\text{H}}$ : 10.38 (s, 1H), 8.00-7.96 (m, 2H), 7.65-7.53 (m, 4H), 7.35 (d,  $J$  = 8.2 Hz, 1H), 2.14 (s, 3H); <sup>13</sup>C NMR (75 MHz, DMSO)  $\delta_{\text{C}}$ : 165.9, 147.8, 144.4, 137.6, 136.4, 133.4, 132.2, 128.6 (two peaks overlap, 2C), 127.8 (two peaks overlap, 2C), 120.9, -13.57; ESI-HRMS:  $[M + H]^+$  calcd for [C<sub>13</sub>H<sub>12</sub>N<sub>2</sub>OCl<sup>130</sup>Te]<sup>+</sup>: 376.9700; found: 376.9708.

#### ***N*-(6-chloro-2-(methyltellanyl)pyridin-3-yl)thiophene-2-carboxamide IV-21**

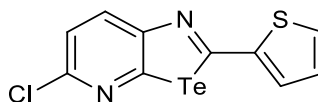


**IV-21**

To a solution of 6-chloro-2-(methyltellanyl)pyridin-3-amine **IV-9** (656 mg, 2.43 mmol) in dry pyridine (6 mL) and dry CH<sub>2</sub>Cl<sub>2</sub> (6 mL) at 0 °C under anhydrous condition, thiophene-2-carbonyl chloride (0.31 mL, 427 mg, 2.91 mmol) was added dropwise. The reaction was stirred 5 minutes at 0 °C then overnight at room temperature. The resulting mixture was diluted with EtOAc (75 mL) and washed with water (25 mL), extracted with EtOAc (2 x 15 mL), organic phases were combined and washed with brine (25 mL), and dried over Na<sub>2</sub>SO<sub>4</sub>. The solvents were removed under reduced pressure. The crude was purified by silica gel chromatography (CHCl<sub>3</sub>/MeOH 1%) to give pure amide **IV-21** as a bright yellow solid (794 mg, 86%); mp = 154-156 °C. IR:  $\nu$  (cm<sup>-1</sup>): 3237, 2970, 1739, 1632, 1557, 1520, 1489, 1404, 1352, 1331, 1287, 1217, 1125, 1094, 1057, 901, 808, 738, 714; <sup>1</sup>H NMR (300 MHz, DMSO)  $\delta_{\text{H}}$ : 10.39 (s, 1H), 7.99 (dd,  $J$  = 3.8, 1.0 Hz, 1H), 7.91 (dd,  $J$  = 5.0, 1.0 Hz, 1H), 7.58 (d,  $J$  = 8.2 Hz, 1H), 7.34 (d,  $J$  = 8.2 Hz, 1H), 7.25 (dd,  $J$  = 5.0, 3.8 Hz), 2.14 (s, 3H); <sup>13</sup>C NMR (75 MHz, DMSO)  $\delta_{\text{C}}$ : 160.5, 148.0, 144.5, 138.4, 137.1, 136.6, 132.5, 129.9, 128.3, 120.9, -13.53; ESI-HRMS:  $[M + H]^+$  calcd for [C<sub>11</sub>H<sub>10</sub>N<sub>2</sub>OSCl<sup>130</sup>Te]<sup>+</sup>: 382.9265; found: 382.9254.

**5-chloro-2-phenyl-[1,3]tellurazolo[5,4- $\beta$ ]pyridine IV-11****IV-11**

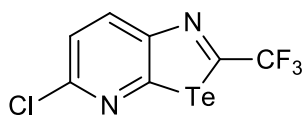
To a solution of *N*-(6-chloro-2-(methyltellanyl)pyridin-3-yl)benzamide **IV-20** (105 mg, 0.28 mmol) in dry DIPEA (3 mL) in dry dioxane (3 mL) under anhydrous condition, POCl<sub>3</sub> (0.10 mL, 172 mg, 1.12 mmol) was added dropwise. The reaction was heated to reflux and stirred overnight. The resulting mixture was diluted with CHCl<sub>3</sub> (30 mL), washed with a saturated solution of NaHCO<sub>3</sub> (10 mL), water (10 mL), brine (10 mL), and dried over Na<sub>2</sub>SO<sub>4</sub>. The solvents were removed under reduced pressure. The crude was purified by silica gel chromatography (CHCl<sub>3</sub>) to give pure 5-chloro-2-phenyl-[1,3]tellurazolo[5,4- $\beta$ ]pyridine **IV-11** as a yellowish solid (87 mg, 91%); mp = 166-168 °C. IR:  $\nu$  (cm<sup>-1</sup>): 1557, 1476, 1385, 1329, 1115, 1084, 1057, 916, 829, 758, 729, 685, 559; <sup>1</sup>H NMR (300 MHz, CDCl<sub>3</sub>)  $\delta$ <sub>H</sub>: 8.20 (d, *J* = 8.5 Hz, 1H), 7.87-7.82 (m, 2H), 7.55-7.42 (m, 3H), 7.40 (d, *J* = 8.5 Hz, 1H); <sup>13</sup>C NMR (100 MHz, CDCl<sub>3</sub>)  $\delta$ <sub>C</sub>: 178.2, 162.3, 157.3, 146.7, 140.8, 134.0, 131.8, 129.4, 128.7, 122.4; ESI-HRMS: [M]<sup>+</sup> calcd for [C<sub>12</sub>H<sub>8</sub>N<sub>2</sub>Cl<sup>130</sup>Te]<sup>+</sup>: 344.9438; found: 344.9436. Single crystals suitable for X-ray diffraction analysis were grown from slow evaporation of CHCl<sub>3</sub> solution.

**5-chloro-2-(thiophen-2-yl)-[1,3]tellurazolo[5,4- $\beta$ ]pyridine IV-12****IV-12**

To a solution of *N*-(6-chloro-2-(methyltellanyl)pyridin-3-yl)thiophene-2-carboxamide **IV-21** (761 mg, 2 mmol) in dry DIPEA (20 mL) in dry dioxane (20 mL) under anhydrous condition, POCl<sub>3</sub> (0.73 mL, 1.202 g, 8 mmol) was added dropwise. The reaction was heated to reflux and stirred overnight. The resulting mixture was diluted with CHCl<sub>3</sub> (100 mL), washed with a saturated solution of NaHCO<sub>3</sub> (40 mL), water (40 mL), brine (40 mL), and dried over Na<sub>2</sub>SO<sub>4</sub>. The solvents were removed under reduced pressure. The crude was purified by silica gel chromatography (CHCl<sub>3</sub>) to give pure 5-chloro-2-(thiophen-2-yl)-[1,3]tellurazolo[5,4- $\beta$ ]pyridine **IV-12** as a yellow solid (598 mg, 86%); mp = 168-170 °C. IR:  $\nu$  (cm<sup>-1</sup>): 1740, 1566, 1526, 1466, 1416, 1385, 1337, 1274, 1059, 1047, 887, 856, 839, 827, 716, 696; <sup>1</sup>H NMR (300 MHz, CDCl<sub>3</sub>)  $\delta$ <sub>H</sub>: 8.12 (d, *J* = 8.5 Hz, 1H), 7.54 (dd, *J* = 5.1, 1.1 Hz, 1H), 7.49 (dd, *J* = 3.8, 1.1 Hz, 1H), 7.37 (d, *J* = 8.5 Hz, 1H), 7.11 (dd, *J* = 5.1, 3.8 Hz, 1H); <sup>13</sup>C NMR (75 MHz, CDCl<sub>3</sub>)  $\delta$ <sub>C</sub>: 167.5, 161.8, 156.5, 146.6, 145.8, 133.4, 131.5, 130.7, 128.1, 122.5; ESI-HRMS: [M + H]<sup>+</sup>

calcd for  $[\text{C}_{10}\text{H}_6\text{N}_2\text{SCl}^{130}\text{Te}]^+$ : 350.9003; found: 350.8991. Single crystals suitable for X-ray diffraction analysis were grown from slow evaporation of  $\text{CHCl}_3$  solution.

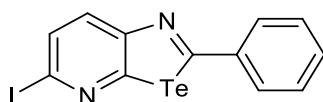
### 5-chloro-2-(trifluoromethyl)-[1,3]tellurazolo[5,4- $\beta$ ]pyridine **IV-13**



**IV-13**

To a solution of 6-chloro-2-(methyltellanyl)pyridin-3-amine **IV-9** (736 mg, 2.7 mmol) in dry pyridine (6 mL) and dry  $\text{CH}_2\text{Cl}_2$  (6 mL) under anhydrous condition at  $0^\circ\text{C}$ , trifluoroacetic acid anhydride (0.46 mL, 693 mg, 3.3 mmol) was added dropwise. The reaction was stirred 5 minutes at the same temperature then overnight at room temperature. Liquids were removed under reduced pressure, the yellow solid residue was dissolved in dry 1,4-dioxane (25 mL) and dry DIPEA (25 mL) and a  $\text{POCl}_3$  (0.98 mL, 1.623 mg, 10.8 mmol) was added dropwise. The reaction was heated to reflux and stirred overnight. The resulting mixture was allowed to cool down to room temperature, diluted with  $\text{CHCl}_3$  (150 mL), washed with a saturated solution of  $\text{NaHCO}_3$  (35 mL), water (25 mL), brine (25 mL), and dried over  $\text{Na}_2\text{SO}_4$ . The solvents were removed under reduced pressure. The crude was purified by silica gel chromatography ( $\text{CHCl}_3$ ) to give pure **IV-13** as a white solid (746 mg, 83%); mp =  $140\text{--}142^\circ\text{C}$ . IR:  $\nu$  ( $\text{cm}^{-1}$ ): 3021, 1562, 1524, 1485, 1396, 1354, 1296, 1250, 1233, 1128, 1119, 1061, 968, 854, 835, 737, 704, 640;  $^1\text{H}$  NMR (500 MHz,  $\text{CDCl}_3$ )  $\delta_{\text{H}}$ : 8.42 (d,  $J = 8.5$  Hz, 1H), 7.54 (d,  $J = 8.5$  Hz, 1H);  $^{19}\text{F}$  NMR (376 MHz,  $\text{CDCl}_3$ )  $\delta_{\text{F}}$ : -62.6 (s, 3F);  $^{13}\text{C}$  NMR (125 MHz,  $\text{CDCl}_3$ )  $\delta_{\text{C}}$ : 164.8 (q,  $J_{\text{CF}} = 42$  Hz, 1C), 164.0, 154.5, 149.1, 136.7, 123.4, 123.2 (q,  $J_{\text{CF}} = 275$  Hz, 1C); EI-HRMS:  $[\text{M}]^+$  calcd for  $[\text{C}_7\text{H}_2\text{N}_2\text{ClF}_3^{130}\text{Te}]^+$ : 335.8921; found: 335.8916. Single crystals suitable for X-ray diffraction analysis were grown from slow evaporation of  $\text{CHCl}_3$  solution.

### 5-iodo-2-phenyl-[1,3]tellurazolo[5,4- $\beta$ ]pyridine **IV-14**

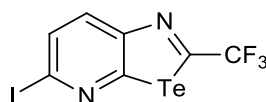


**IV-14**

5-iodo-2-phenyl-[1,3]tellurazolo[5,4- $\beta$ ]pyridine **IV-14** was synthesised following a procedure inspired by the work of *Bissember* and *Banwell*.<sup>[12]</sup> A micro-wave vial was loaded with, in that order,  $\text{NaI}$  (360 mg, 2.4 mmol), 5-chloro-2-phenyl-[1,3]tellurazolo[5,4- $\beta$ ]pyridine **IV-11** (84 mg, 0.24 mmol), dry MeCN (1.2 mL) and acetyl chloride (0.03 mL, 28 mg, 0.36 mmol) under nitrogen atmosphere. The reaction was stirred under micro-wave irradiation at  $80^\circ\text{C}$  for 12h. The resulting

mixture was diluted with MeCN (10 mL), washed with a saturated solution of  $K_2CO_3$  (10 mL), a saturated solution of  $Na_2S_2O_6$  (10 mL), brine (10 mL), and dried over  $Na_2SO_4$ . The solvents were removed under reduced pressure. The crude material was purified by silica gel chromatography ( $CHCl_3$ ) to give pure **IV-14** as a yellowish solid (87 mg, 84 %); mp = 164-168°C. IR:  $\nu$  ( $cm^{-1}$ ): 2922, 1557, 1495, 1474, 1443, 1329, 1211, 1082, 1055, 829, 758, 727, 685, 559;  $^1H$  NMR (300 MHz,  $CDCl_3$ )  $\delta_H$ : 7.92 (d,  $J = 8.4$  Hz, 1H), 7.88-7.84 (m, 2H), 7.79 (d,  $J = 8.4$  Hz, 1H), 7.56-7.43 (m, 3H);  $^{13}C$  NMR (100 MHz,  $CDCl_3$ )  $\delta_C$ : 178.5, 164.0, 157.8, 140.9, 133.4, 132.8, 131.9, 129.4 (two peaks overlap, 2C), 128.8 (two peaks overlap, 2C), 112.5; ESI-HRMS:  $[M + H]^+$  calcd for  $[C_{12}H_8N_2F_3^{130}Te^{127}I]^+$ : 436.8795; found: 436.8802. Single crystals suitable for X-ray diffraction analysis were grown from slow evaporation of  $CHCl_3$  solution.

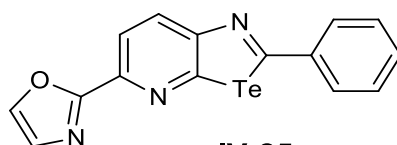
### 5-iodo-2-(trifluoromethyl)-[1,3]tellurazolo[5,4- $\beta$ ]pyridine **IV-16**



**IV-16**

5-iodo-2-(trifluoromethyl)-[1,3]tellurazolo[5,4- $\beta$ ]pyridine **IV-16** was synthesised following a procedure inspired by the work of *Bissember and Banwell*.<sup>[12]</sup> A micro-wave vial was loaded with, in that order, NaI (0.750 g, 5 mmol), 5-chloro-2-(trifluoromethyl)-[1,3]tellurazolo[5,4- $\beta$ ]pyridine **IV-13** (167 mg, 0.5 mmol), dry MeCN (2.5 mL) and acetyl chloride (0.05 mL, 59 mg, 0.75 mmol) under nitrogen atmosphere. The reaction was stirred under micro-wave irradiation at 80°C for 12h. The resulting mixture was diluted with MeCN (5 mL), washed with a saturated solution of  $K_2CO_3$  (5 mL), brine (5 mL), and dried over  $Na_2SO_4$ . The solvents were removed under reduced pressure. The crude material was purified by silica gel chromatography ( $CHCl_3$ ) to give pure **IV-16** as a white solid (109 mg, 51 %); mp = 170-172°C. IR:  $\nu$  ( $cm^{-1}$ ): 3032, 2970, 1738, 1557, 1489, 1383, 1292, 1237, 1182, 1132, 1088, 1059, 964, 849, 829, 725;  $^1H$  NMR (300 MHz,  $CDCl_3$ )  $\delta_H$ : 8.12 (d,  $J = 8.4$  Hz, 1H), 7.91 (d,  $J = 8.4$  Hz, 1H);  $^{19}F$  NMR (376 MHz,  $CDCl_3$ )  $\delta_F$ : -62.6 (s, 3F);  $^{13}C$  NMR (125 MHz,  $CDCl_3$ )  $\delta_C$ : 165.3, 165.1 (q,  $J_{CF} = 42$  Hz, 1C), 154.9, 135.9, 133.6, 123.4 (q,  $J_{CF} = 276$  Hz, 1C), 115.5; ESI-HRMS:  $[M + H]^+$  calcd for  $[C_7H_3N_2F_3^{130}Te^{127}I]^+$ : 428.8355; found: 428.8355. Single crystals suitable for X-ray diffraction analysis were grown from slow evaporation of  $CHCl_3$  solution.

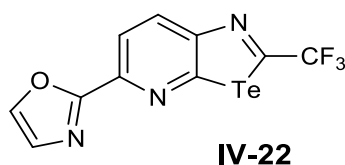
### 2-(2-(phenyl)-[1,3]tellurazolo[5,4- $\beta$ ]pyridin-5-yl)oxazole **IV-25**



**IV-25**

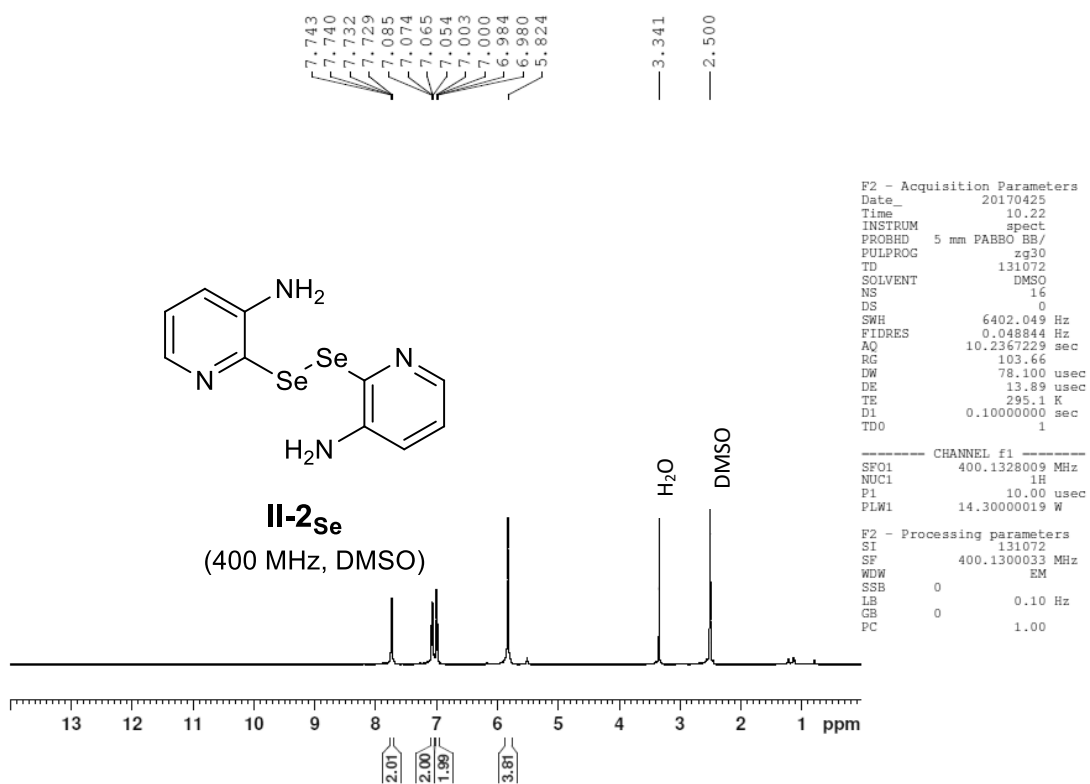
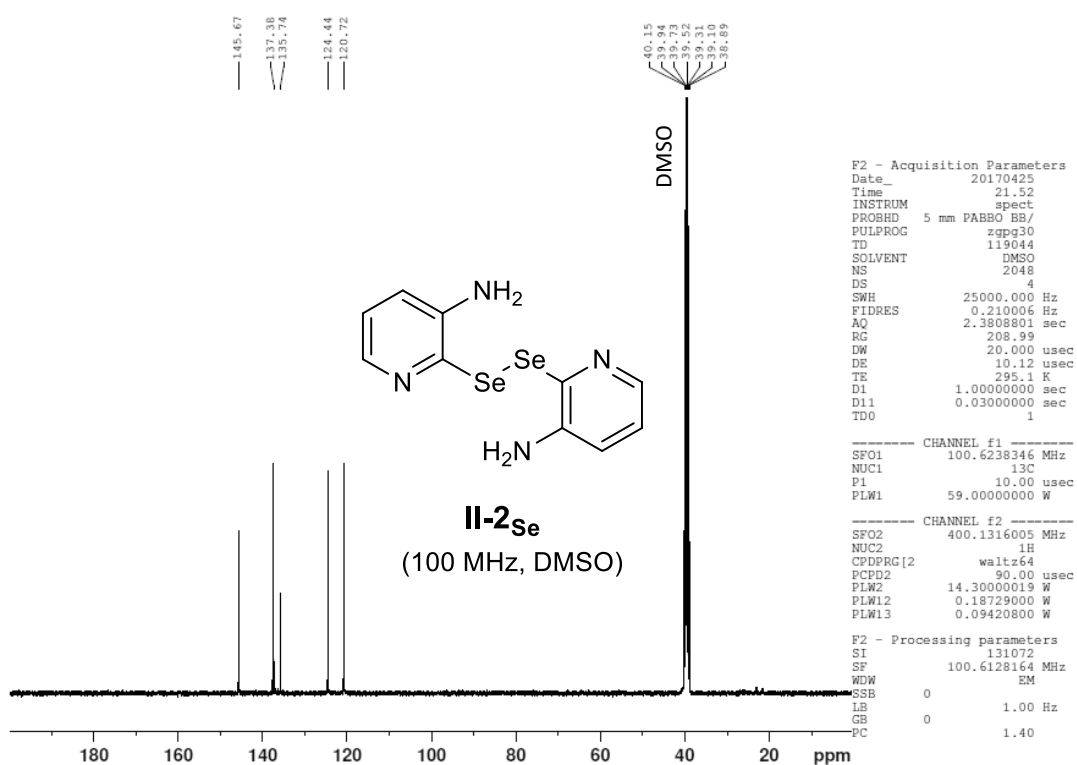
2-(2-(phenyl)-[1,3]tellurazolo[5,4- $\beta$ ]pyridin-5-yl)oxazole **IV-25** was synthesised following a procedure inspired by the work of Piersanti *et al.*<sup>[13]</sup> To a solution of oxazole (0.03 mL, 35 mg, 0.5 mmol) in dry and degassed THF (0.5 mL) at -84°C under anhydrous conditions was added n-BuLi (2.5 M, 0.2 mL, 0.5 mmol). The reaction is stirred at the same temperature for 30 minutes and a solution of ZnCl<sub>2</sub> in Et<sub>2</sub>O (1M, 1.5 mL, 1.5 mmol) was added dropwise. The mixture was stirred further at 0°C for 1h (white suspension). A separated flask was loaded with 5-iodo-2-(trifluoromethyl)-[1,3]tellurazolo[5,4- $\beta$ ]pyridine **IV-14** (85 mg, 0.20 mmol) and [Pd(Ph<sub>3</sub>)<sub>4</sub>] (0.023 mg, 0.02 mmol) in dry and degassed THF under anhydrous condition and oxazolylzinc chloride suspension (1.2mL) was added. The reaction was stirred at reflux for 2h. The resulting mixture was diluted with EtOAc (20 mL), washed with water (10 mL), brine (10 mL), and dried over Na<sub>2</sub>SO<sub>4</sub>. The solvents were evaporated under reduced pressure. The crude material was purified by silica gel chromatography (petroleum ether/EtOAc 6:4) to afford 2-(2-(phenyl)-[1,3]tellurazolo[5,4- $\beta$ ]pyridin-5-yl)oxazole **IV-25** as a yellow solid (54 mg, 72%); mp = 180-182°C. IR:  $\nu$  (cm<sup>-1</sup>): 1555, 1470, 1396, 1340, 1271, 1252, 1211, 1111, 1082, 1055, 912, 847, 752, 719, 683, 663, 596; <sup>1</sup>H NMR (300 MHz, C<sub>6</sub>D<sub>6</sub>)  $\delta$ <sub>H</sub>: 8.18 (d, J = 8.5 Hz, 1H), 7.97 (d, J = 8.5 Hz, 1H), 7.74-7.70 (m, 2H), 7.10-6.95 (m, 5H); <sup>13</sup>C NMR (75 MHz, C<sub>6</sub>D<sub>6</sub>)  $\delta$ <sub>C</sub>: 178.7, 163.2, 160.9, 158.6, 142.4, 141.3, 139.6, 132.1, 131.2, 129.0, 128.9 (two peaks overlap, 2C), 128.7 (two peaks overlap, 2C), 120.6; ESI-HRMS: [M]<sup>+</sup> calcd for [C<sub>15</sub>H<sub>10</sub>N<sub>3</sub>O<sup>130</sup>Te]<sup>+</sup>: 377.9886; found: 377.9882. Single crystals suitable for X-ray diffraction analysis were grown from slow evaporation of CHCl<sub>3</sub> solution.

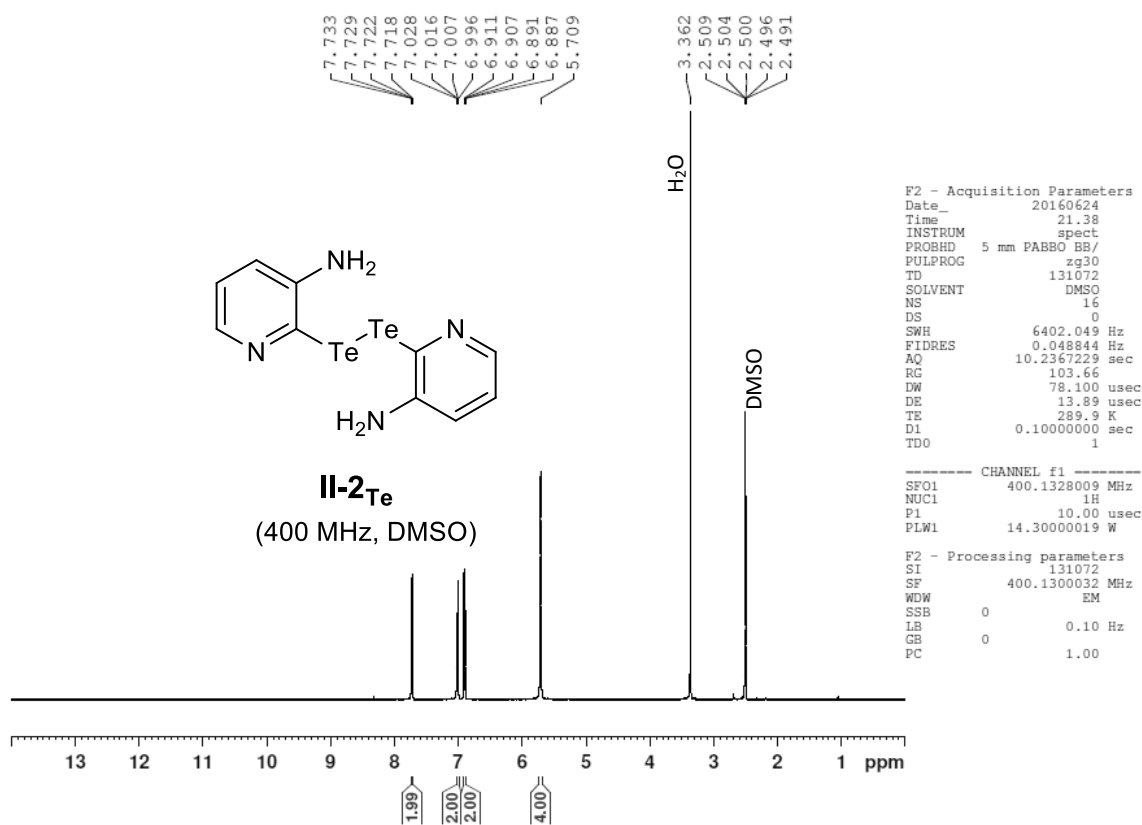
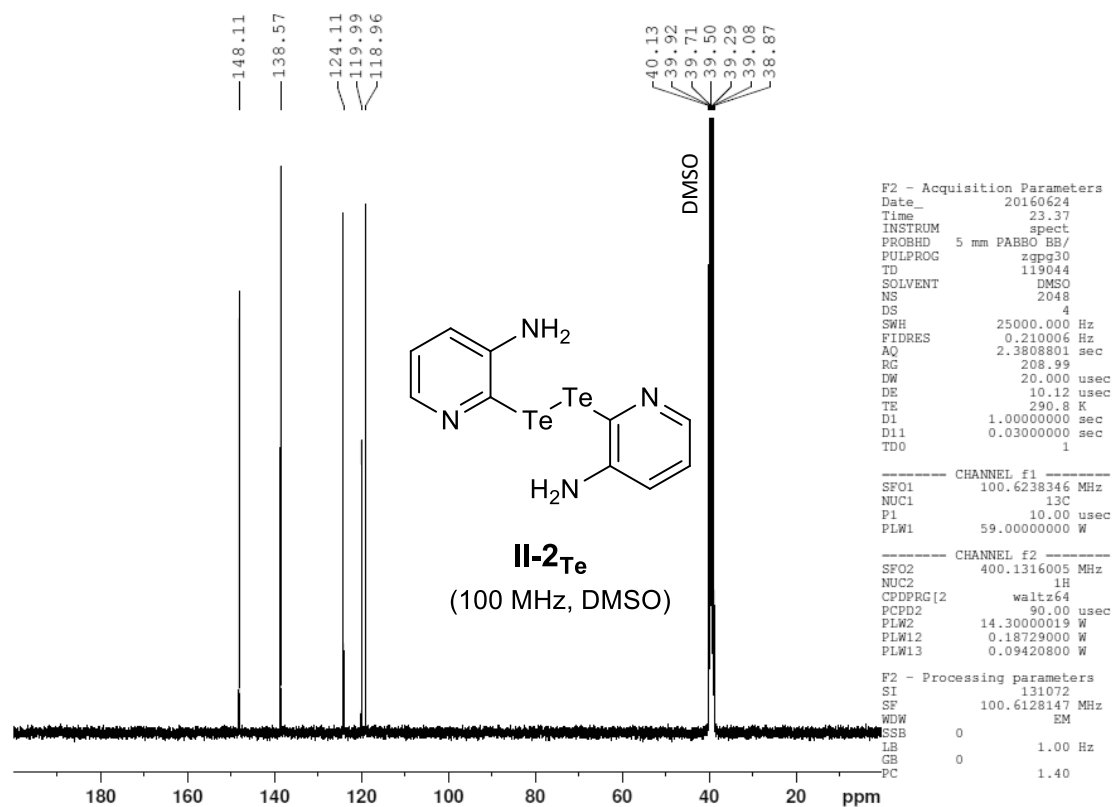
### 2-(2-(trifluoromethyl)-[1,3]tellurazolo[5,4- $\beta$ ]pyridin-5-yl)oxazole **IV-22**

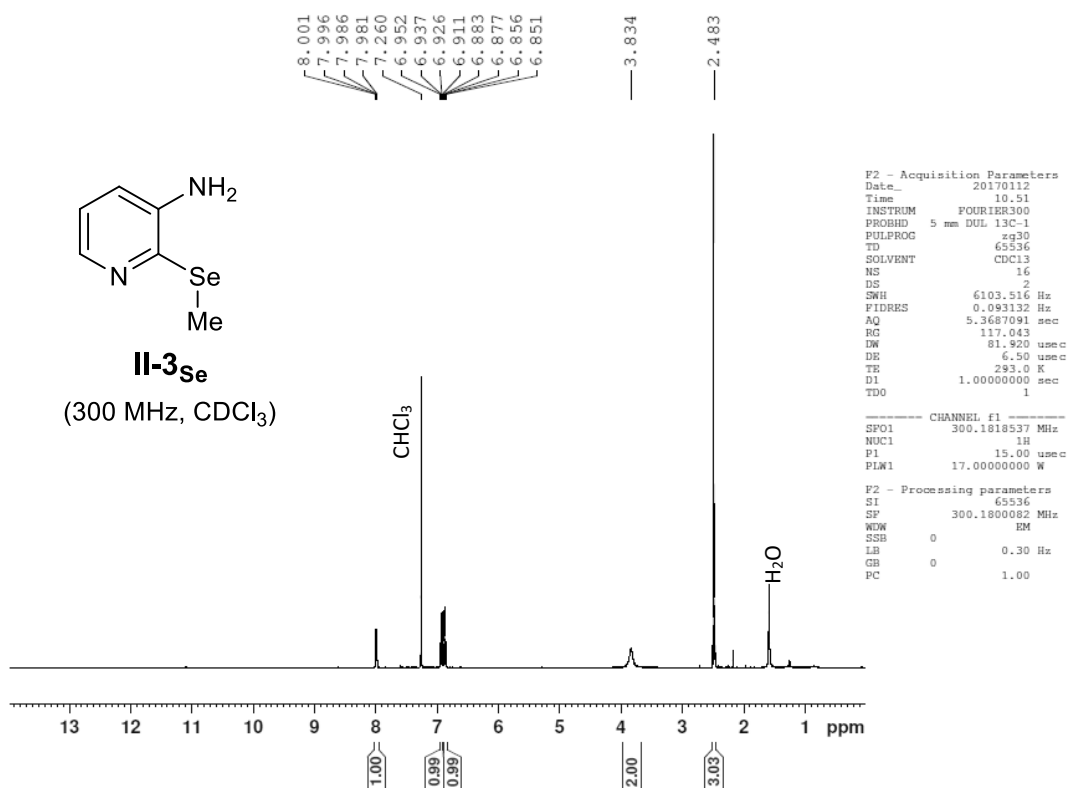
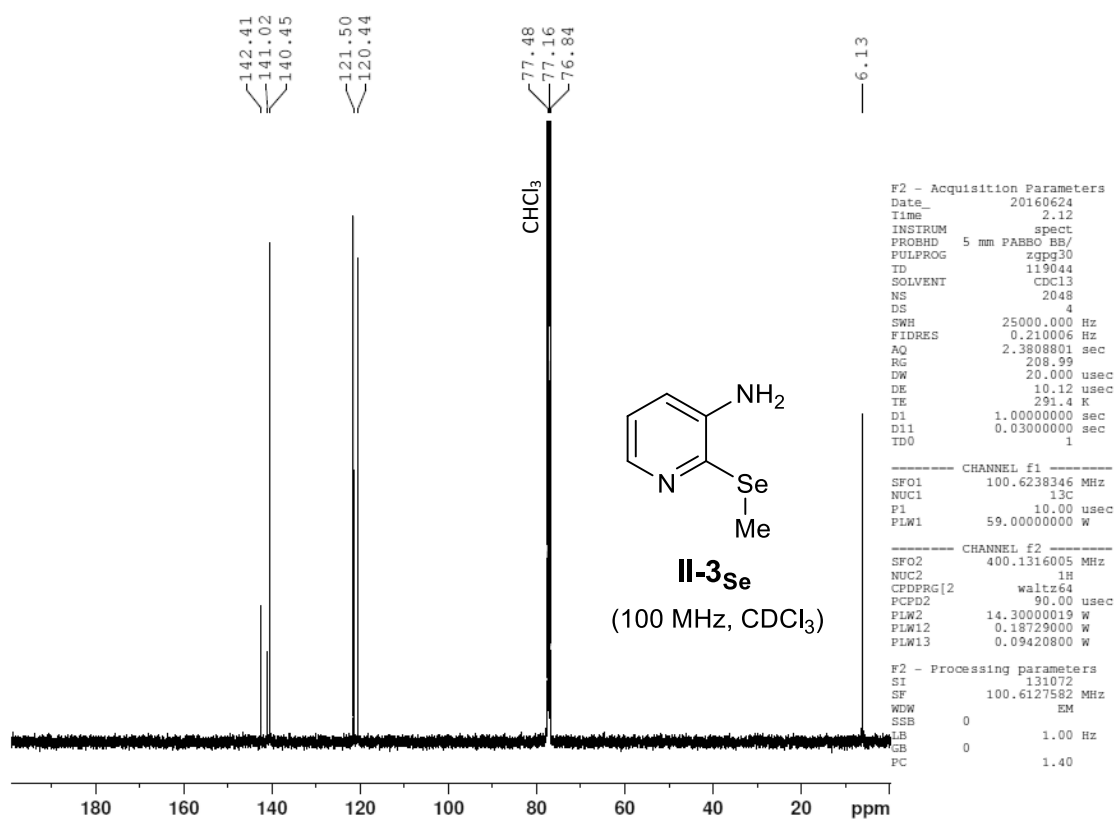


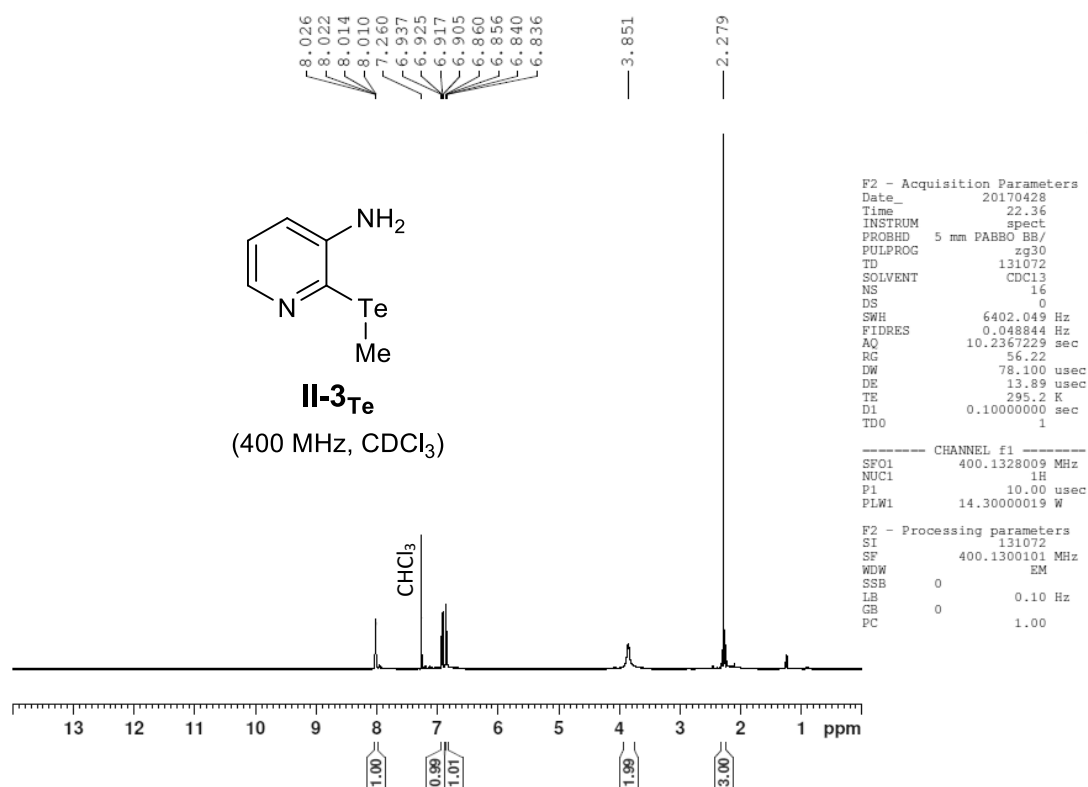
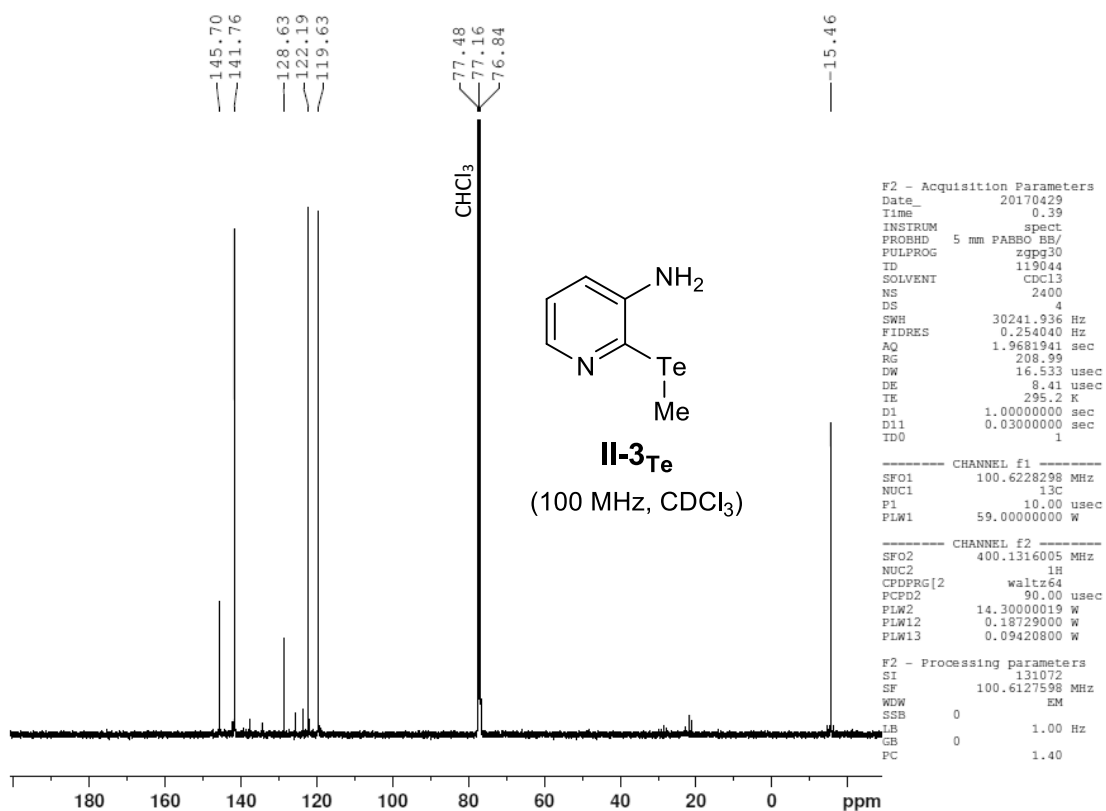
2-(2-(trifluoromethyl)-[1,3]tellurazolo[5,4- $\beta$ ]pyridin-5-yl)oxazole **IV-22** was synthesised following a procedure inspired by the work of Piersanti *et al.*<sup>[13]</sup> To a solution of oxazole (0.03 mL, 35 mg, 0.5 mmol) in dry and degassed THF (0.5 mL) at -84°C under anhydrous conditions was added n-BuLi (2.5 M, 0.2 mL, 0.5 mmol). The reaction is stirred at the same temperature for 30 minutes and a solution of ZnCl<sub>2</sub> in Et<sub>2</sub>O (1M, 1.5 mL, 1.5 mmol) added dropwise. The mixture was stirred further at 0°C for 1h (white suspension). A separated flask was loaded with 5-iodo-2-(trifluoromethyl)-[1,3]tellurazolo[5,4- $\beta$ ]pyridine **IV-16** (85 mg, 0.20 mmol) and [Pd(Ph<sub>3</sub>)<sub>4</sub>] (0.023 mg, 0.02 mmol) in dry and degassed THF under anhydrous condition and oxazolylzinc chloride suspension (1.2 mL) was added. The reaction was stirred at reflux for 2h. The resulting mixture was diluted with EtOAc (20 mL), washed with water (10 mL), brine (10 mL), and dried over Na<sub>2</sub>SO<sub>4</sub>. The solvents were

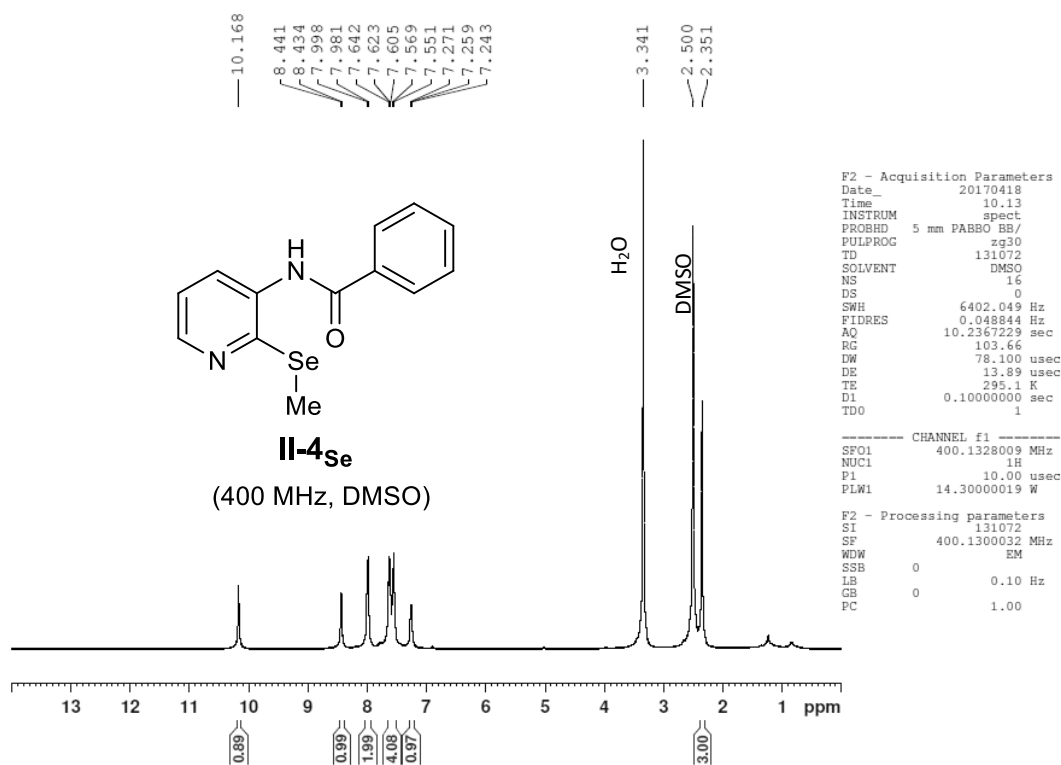
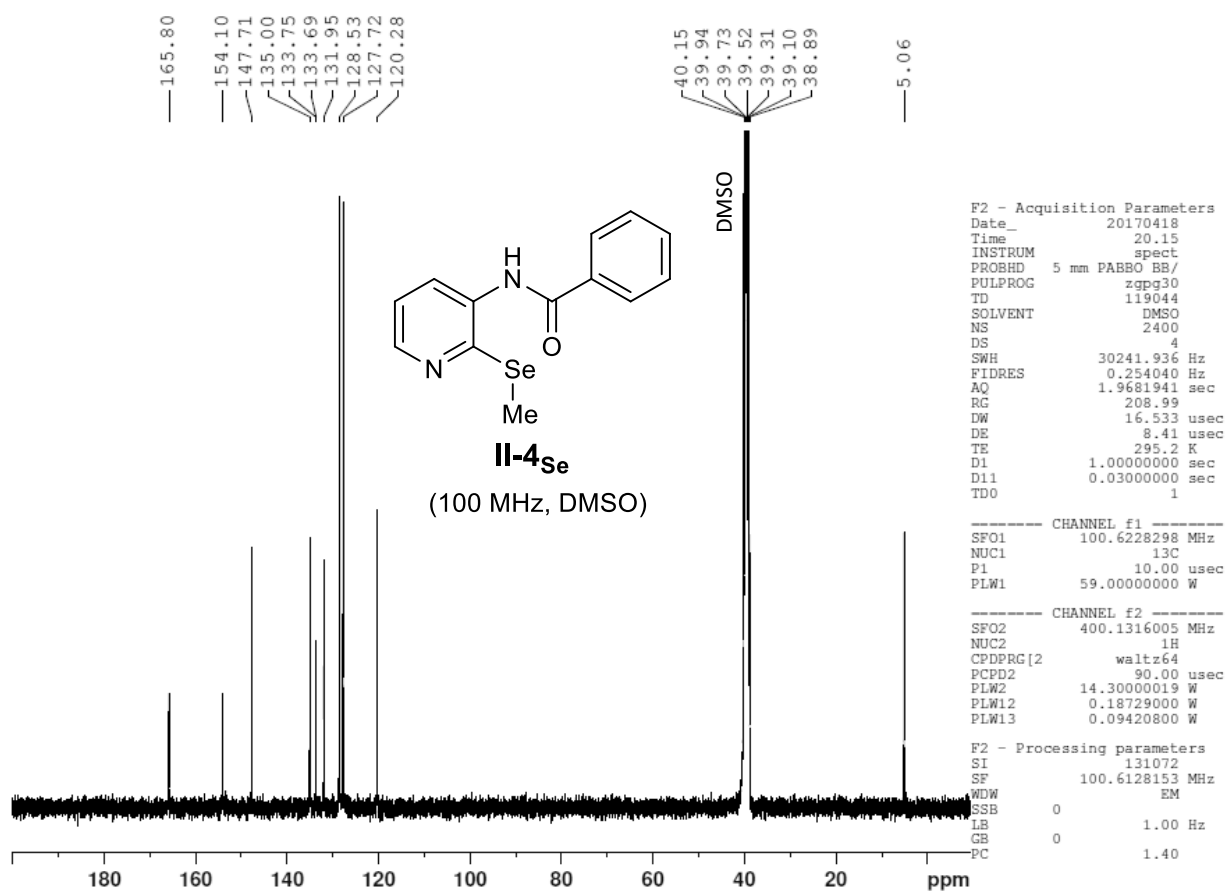
evaporated under reduced pressure. The crude material was purified by silica gel chromatography (petroleum ether/EtOAc 6:4) to afford 2-(2-(trifluoromethyl)-[1,3]tellurazolo[5,4- $\beta$ ]pyridin-5-yl)oxazole **IV-22** as a yellow solid (51 mg, 70%); mp = 200-204°C. IR:  $\nu$  (cm<sup>-1</sup>): 3022, 1574, 1553, 1543, 1487, 1398, 1346, 1302, 1252, 1163, 1126, 1114, 1053, 970, 910, 849, 762, 735; <sup>1</sup>H NMR (500 MHz, CDCl<sub>3</sub>)  $\delta_{\text{H}}$ : 8.61 (d,  $J$  = 8.5 Hz, 1H), 8.36 (d,  $J$  = 8.5 Hz, 1H), 7.88 (dd,  $J$  = 0.8 Hz, 1H), 7.39 (dd,  $J$  = 0.8 Hz, 1H); <sup>19</sup>F NMR (470 MHz, CDCl<sub>3</sub>)  $\delta_{\text{F}}$ : -62.7 (s, 3F); <sup>13</sup>C NMR (125 MHz, CDCl<sub>3</sub>)  $\delta_{\text{C}}$ : 166.3 (q,  $J_{\text{CF}}$  = 40 Hz, 1C), 165.1, 160.0, 155.7, 143.9, 140.6, 135.6, 129.7, 123.5 (q,  $J_{\text{CF}}$  = 274 Hz, 1C), 121.0; ESI-MS: [M + H]<sup>+</sup> calcd for [C<sub>10</sub>H<sub>5</sub>N<sub>3</sub>O<sup>130</sup>Te]<sup>+</sup>: 369.9447; found: 369.9442.

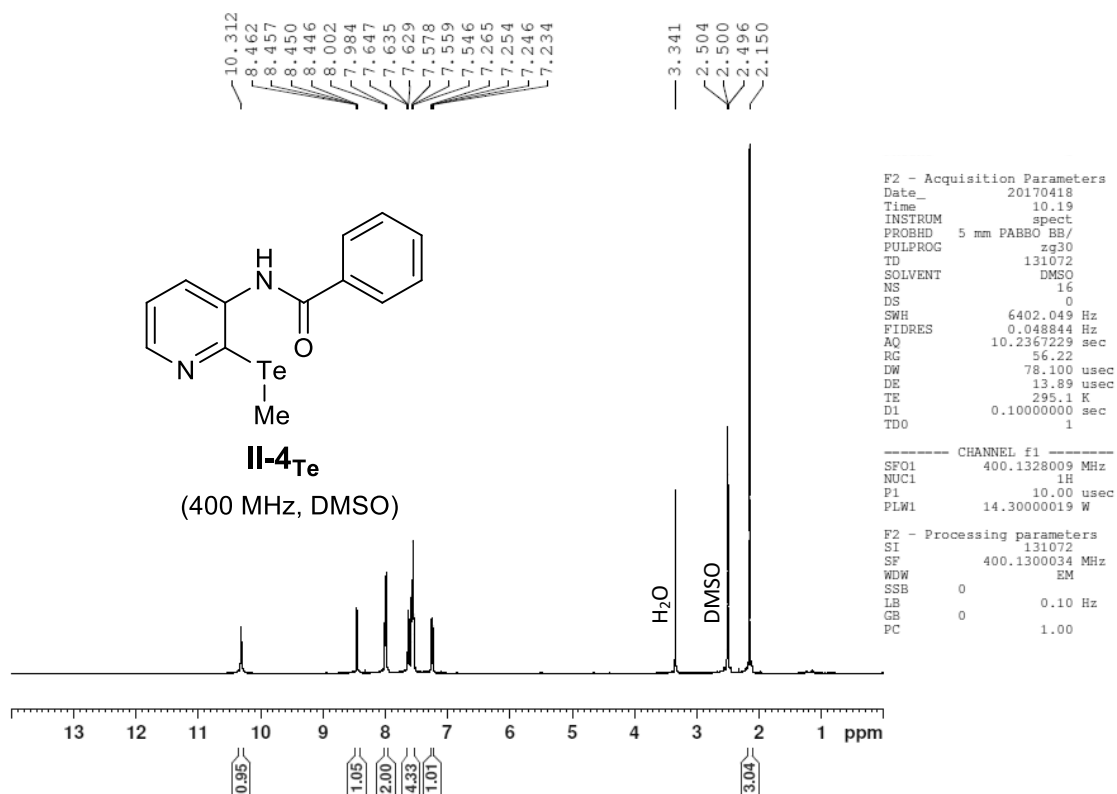
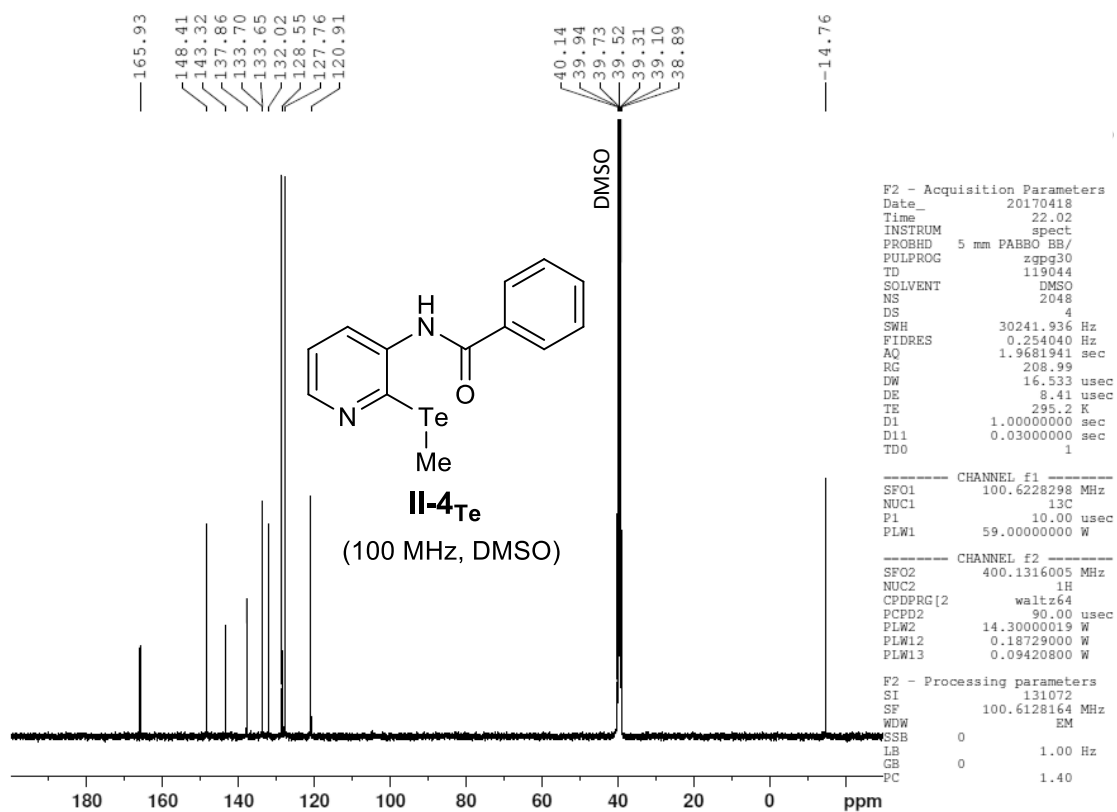
VI – 3  $^1\text{H}$ ,  $^{13}\text{C}$  and  $^{19}\text{F}$  spectraFigure VI - 1: 400 MHz  $^1\text{H}$ -NMR in DMSO of molecule **II-2<sub>Se</sub>**.Figure VI - 2: 100 MHz  $^{13}\text{C}$ -NMR in DMSO of molecule **II-2<sub>Se</sub>**.

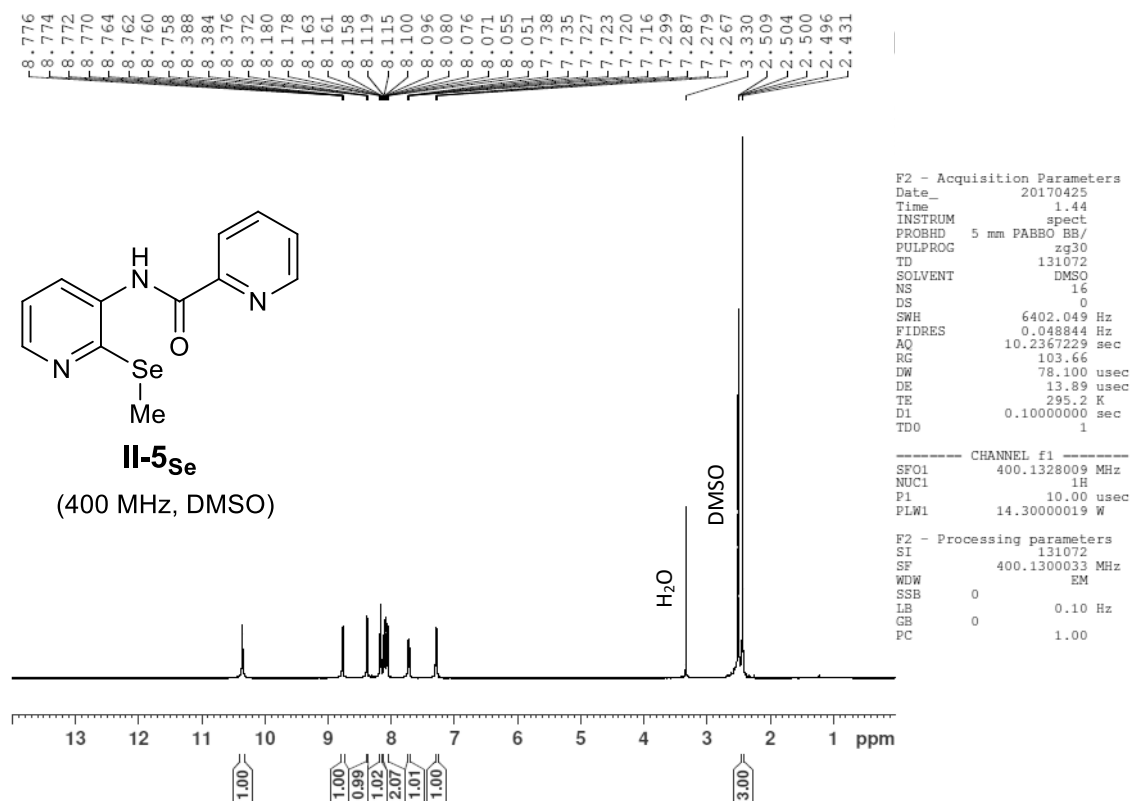
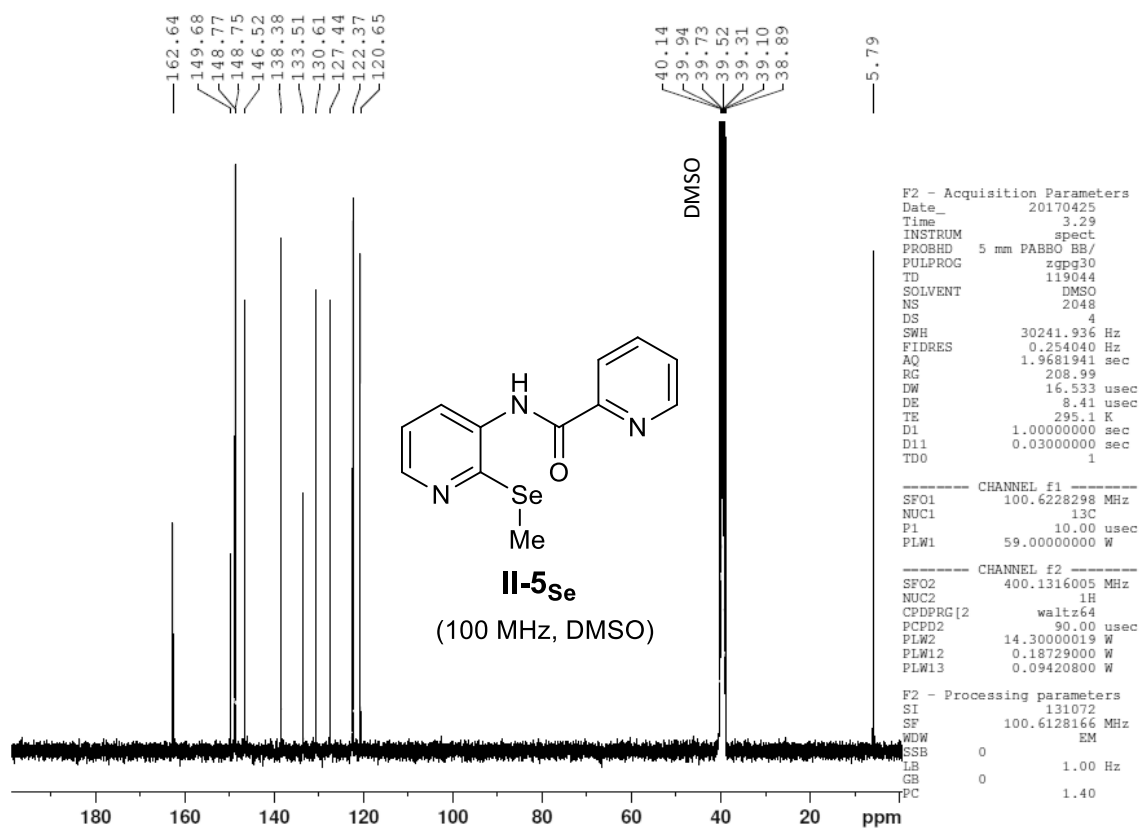
Figure VI - 3: 400 MHz <sup>1</sup>H-NMR in DMSO of molecule II-2<sub>Te</sub>.Figure VI - 4: 100 MHz <sup>13</sup>C-NMR spectrum in DMSO of molecule II-2<sub>Te</sub>.

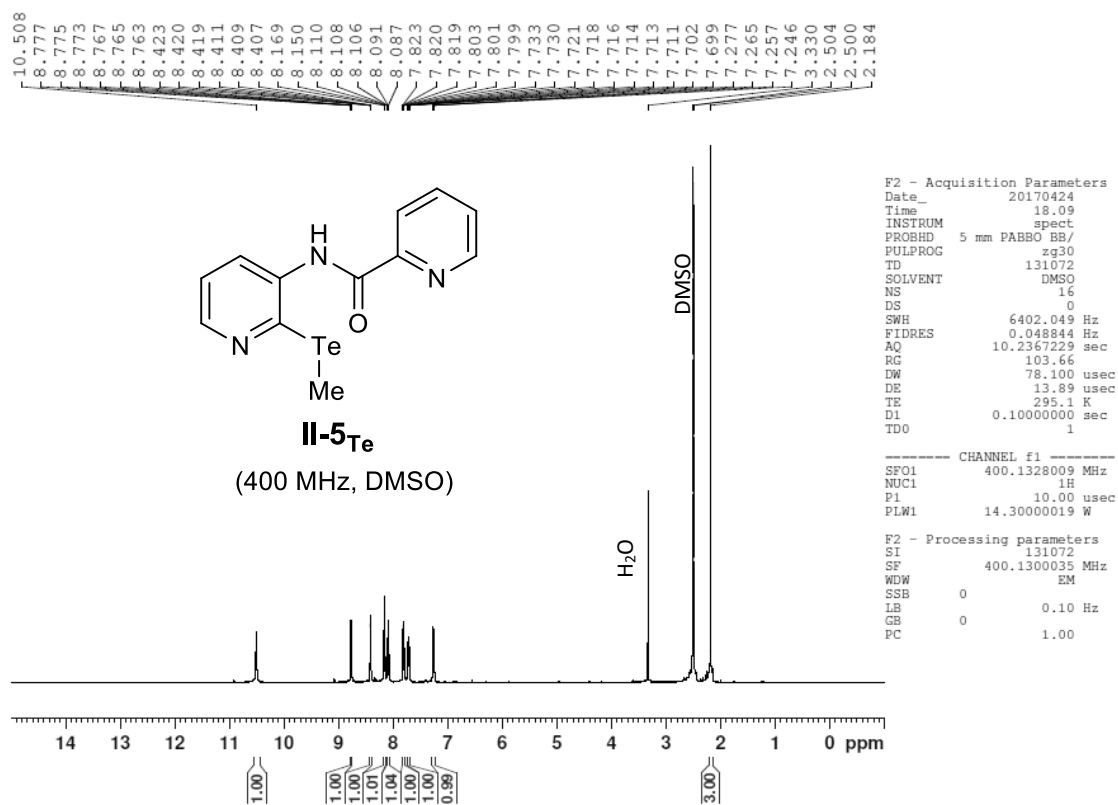
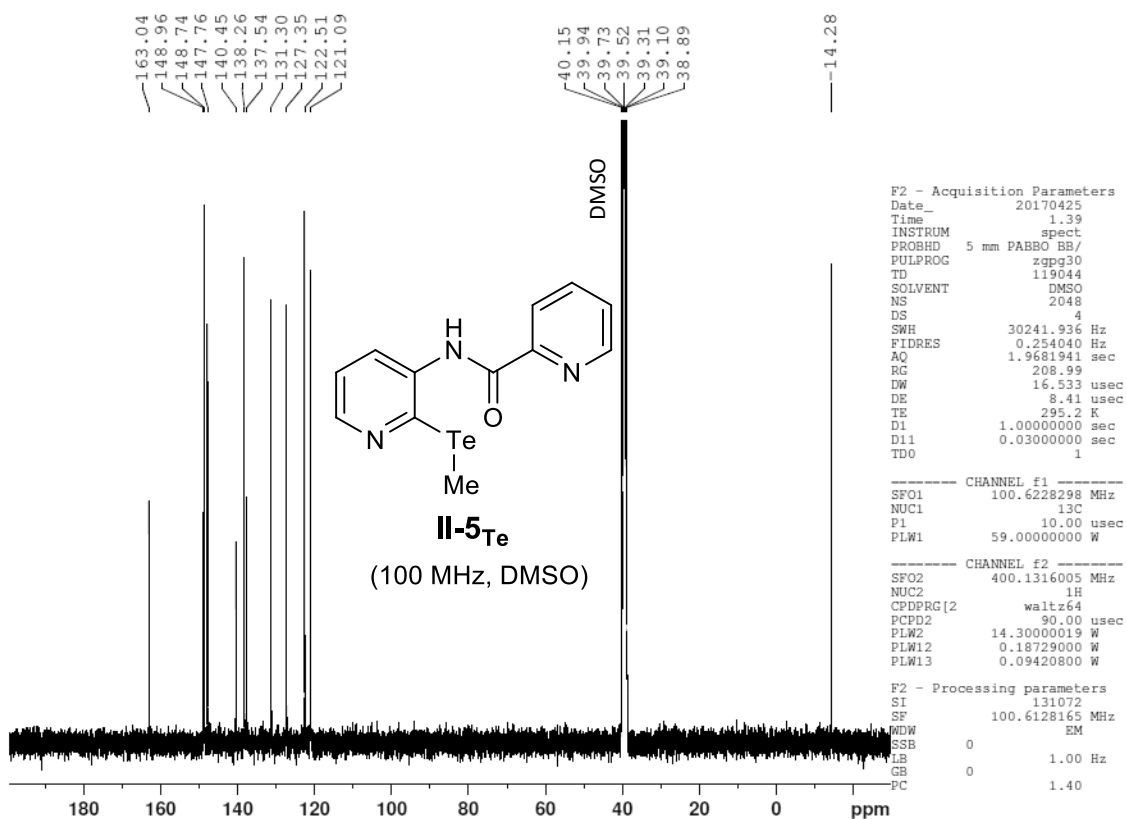
Figure VI - 5: 400 MHz <sup>1</sup>H-NMR in CDCl<sub>3</sub> of molecule II-3<sub>Se</sub>.Figure VI - 6: 100 MHz <sup>13</sup>C-NMR in DMSO of molecule II-3<sub>Se</sub>.

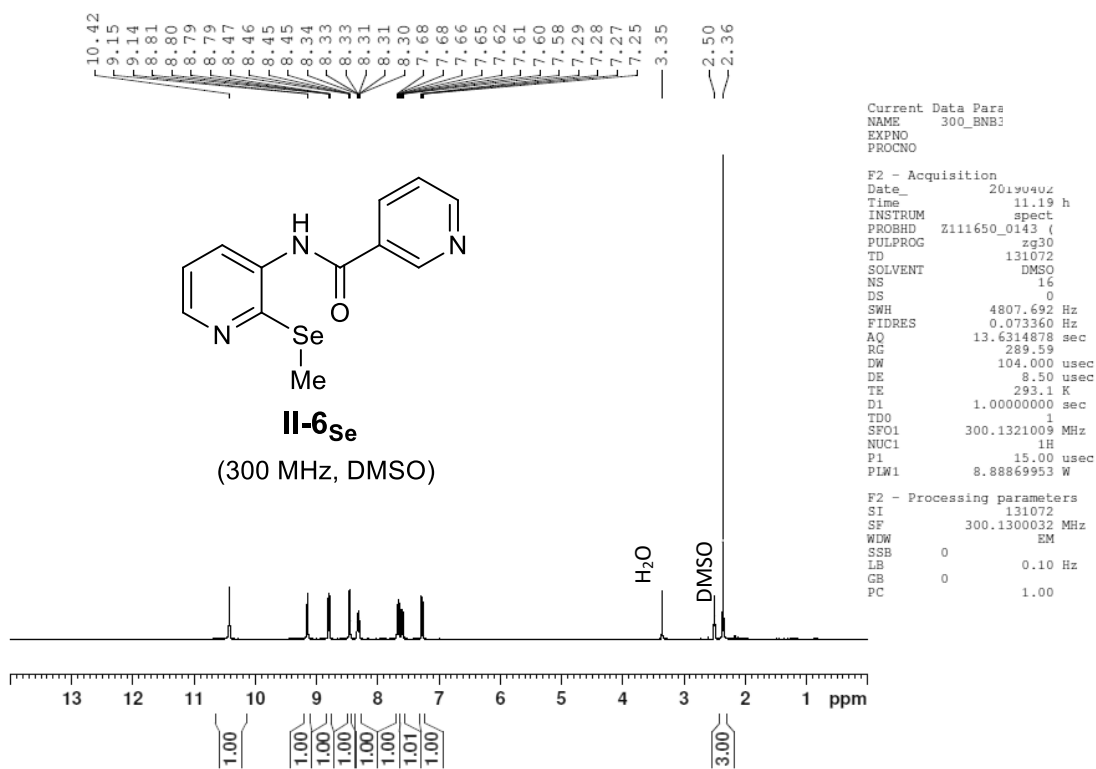
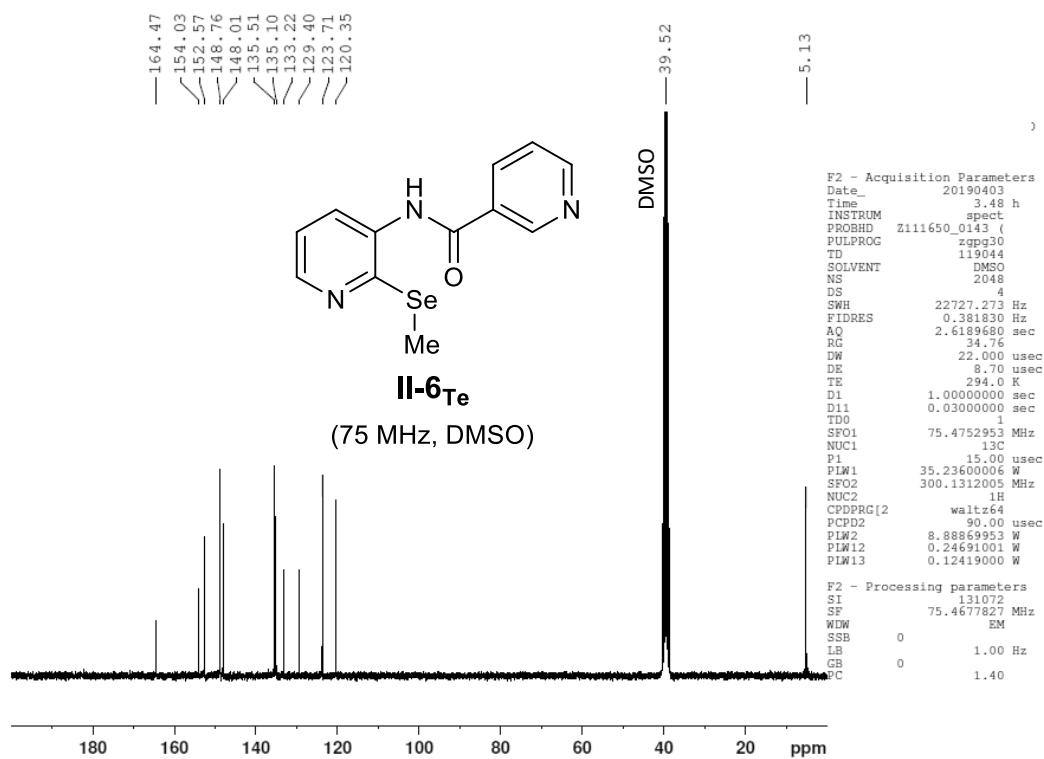
Figure VI - 7: 400 MHz <sup>1</sup>H-NMR in CDCl<sub>3</sub> of molecule II-3<sub>Te</sub>.Figure VI - 8: 100 MHz <sup>13</sup>C-NMR in CDCl<sub>3</sub> of molecule II-3<sub>Te</sub>.

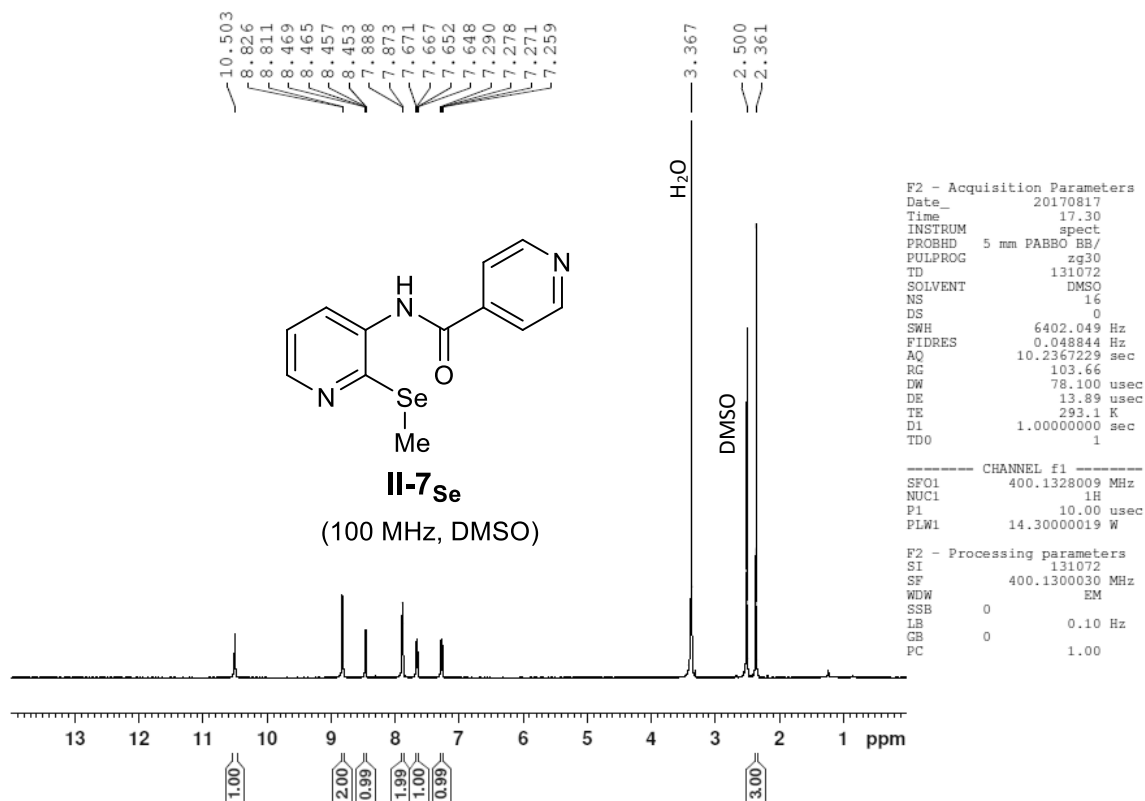
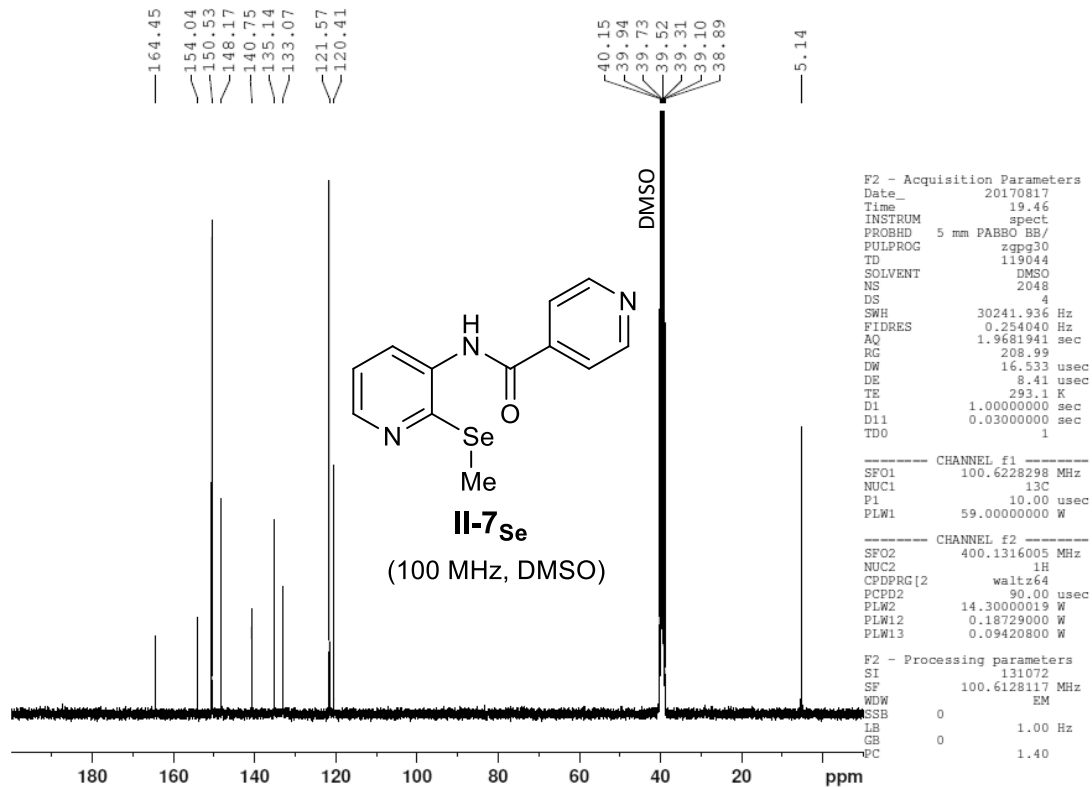
Figure VI - 9: 400 MHz <sup>1</sup>H-NMR in DMSO of molecule **II-4<sub>Se</sub>**.Figure VI - 10: 100 MHz <sup>13</sup>C-NMR in DMSO of molecule **II-4<sub>Se</sub>**.

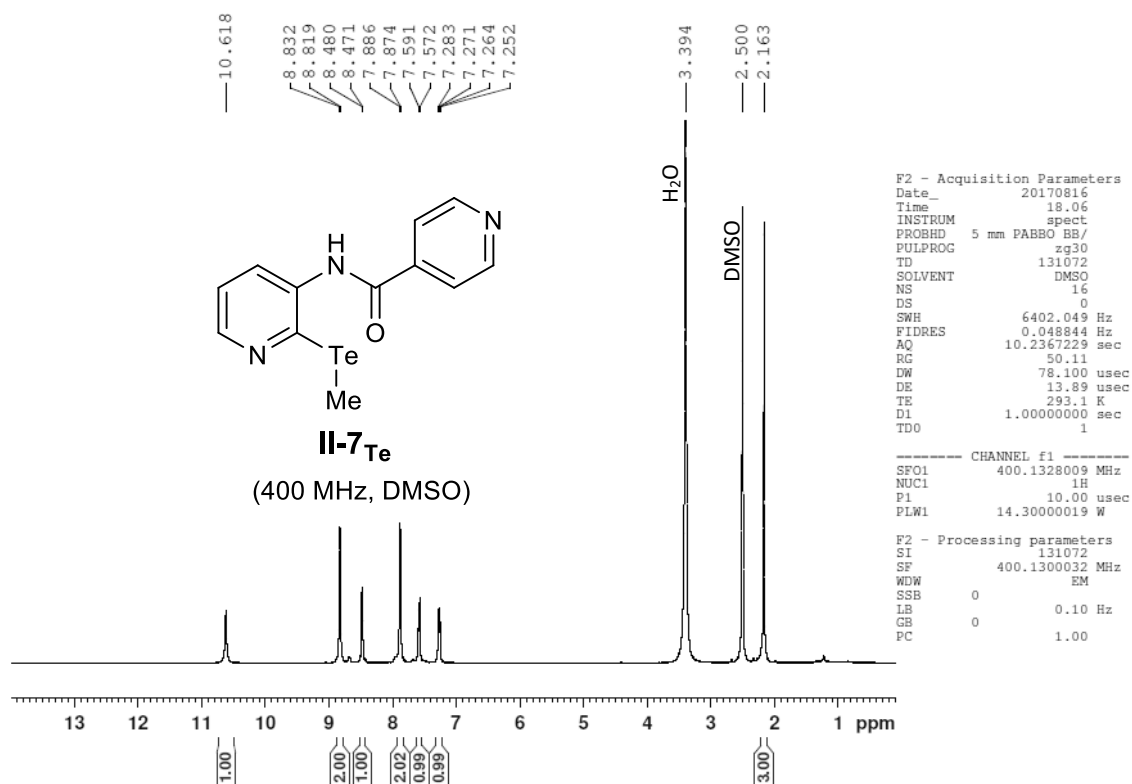
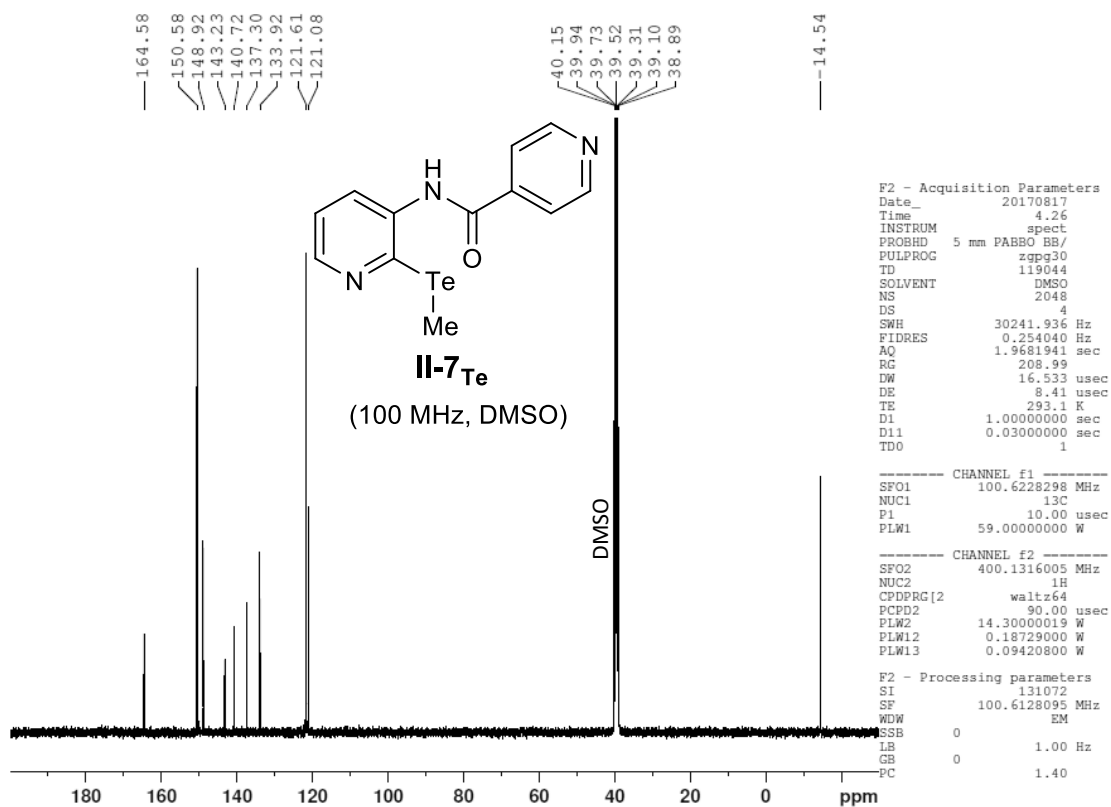
Figure VI - 11: 400 MHz  $^1\text{H}$ -NMR in DMSO of molecule **II-4<sub>Te</sub>**.Figure VI - 12: 100 MHz  $^{13}\text{C}$ -NMR in DMSO of molecule **II-5<sub>Te</sub>**.

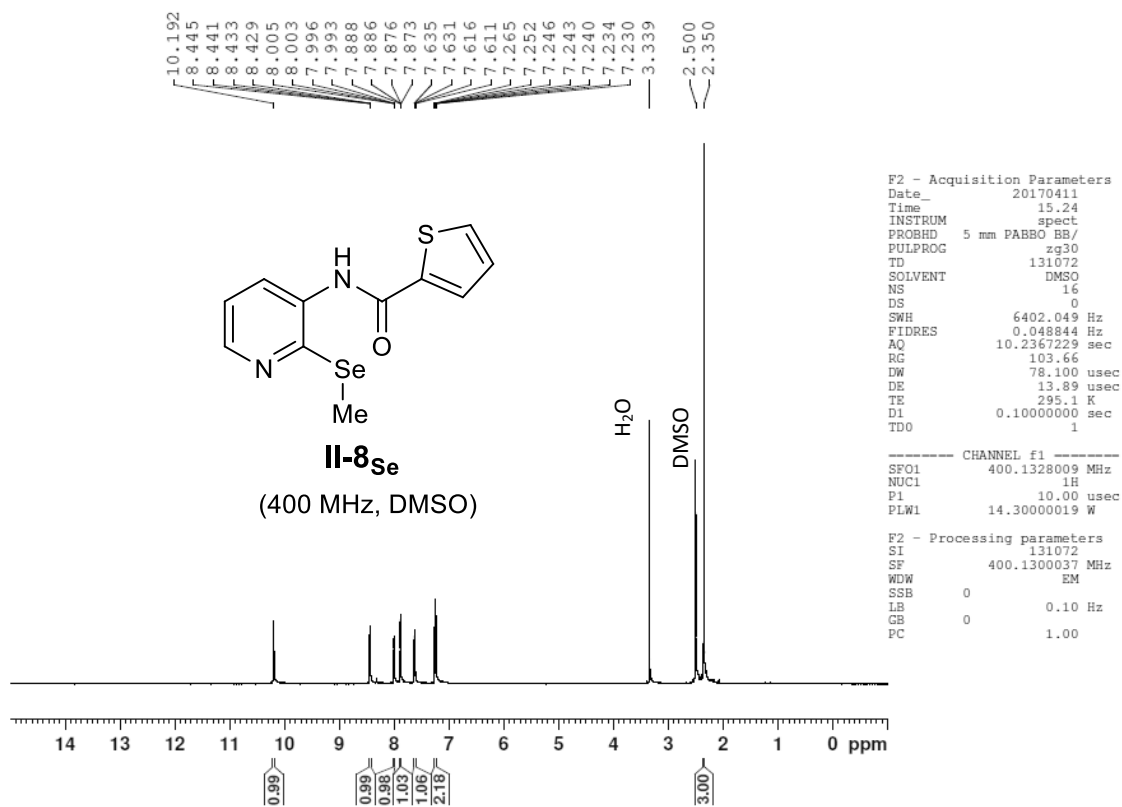
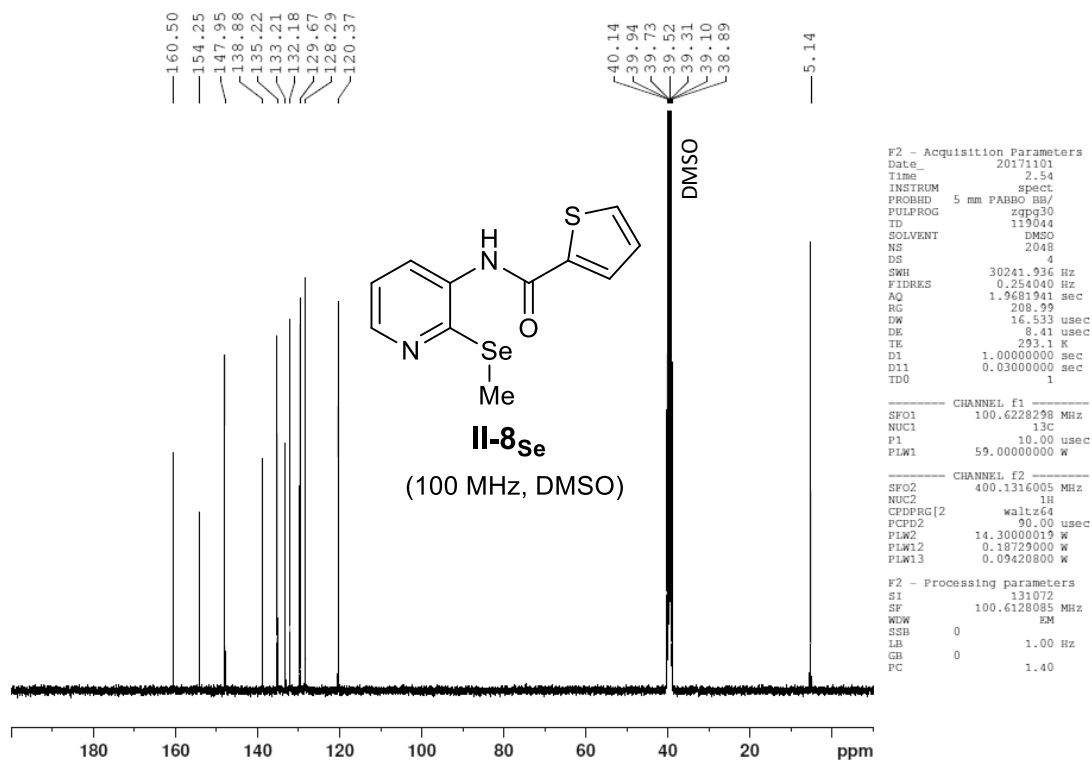
Figure VI - 13: 400 MHz  $^1\text{H}$ -NMR in DMSO of molecule II-5<sub>Se</sub>.Figure VI - 14: 100 MHz  $^{13}\text{C}$ -NMR in DMSO of molecule II-5<sub>Se</sub>.

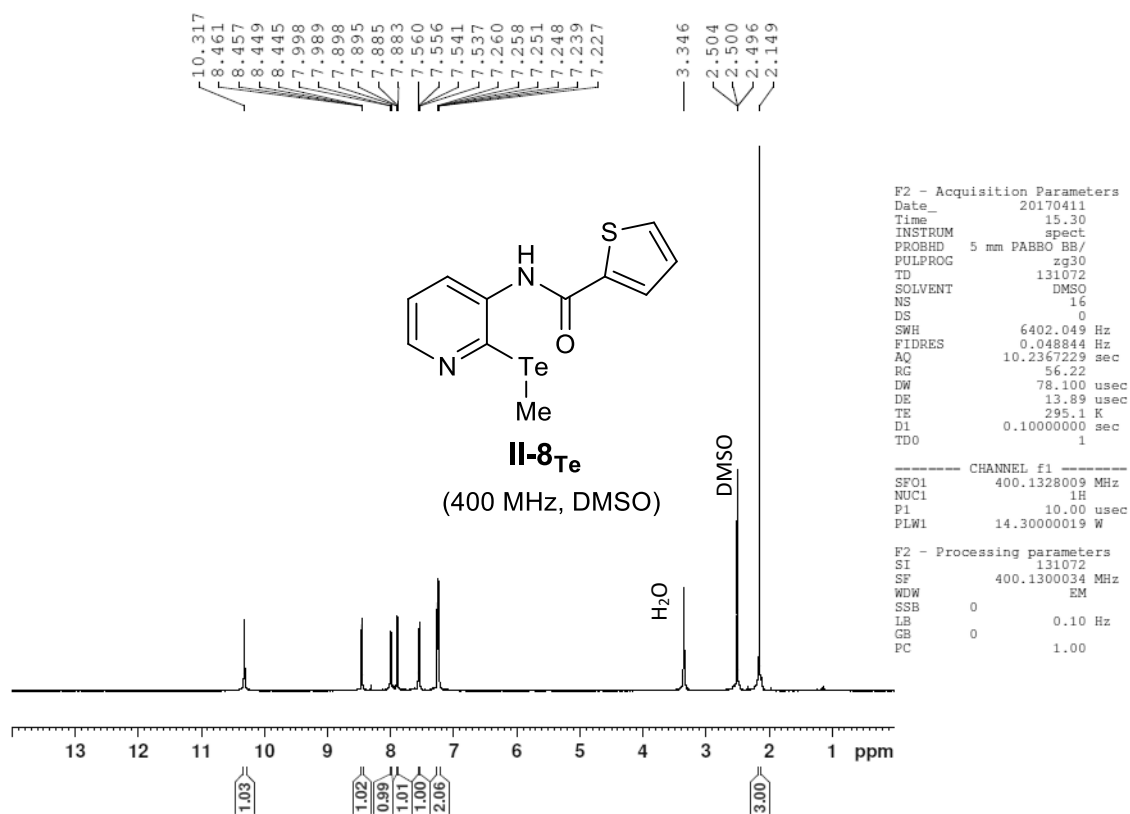
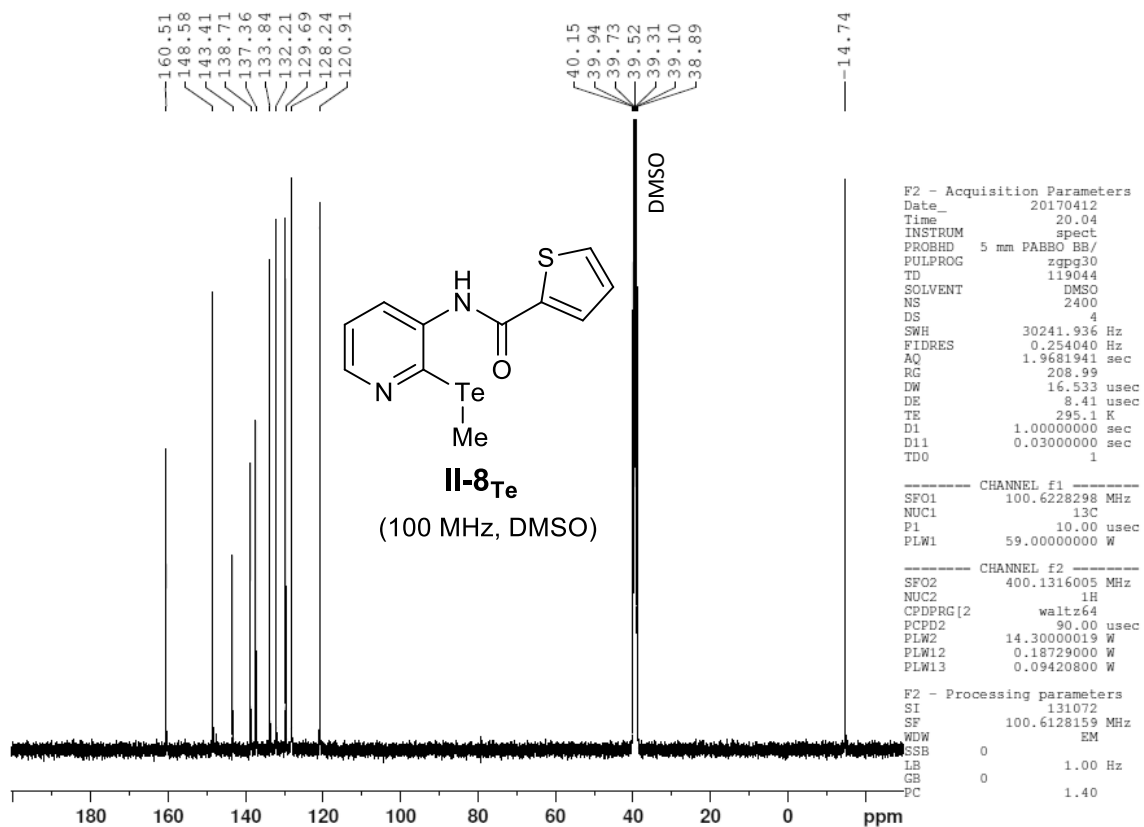
Figure VI - 15: 400 MHz <sup>1</sup>H-NMR in DMSO of molecule II-5<sub>Te</sub>.Figure VI - 16: 100 MHz <sup>13</sup>C-NMR in DMSO of molecule II-5<sub>Te</sub>.

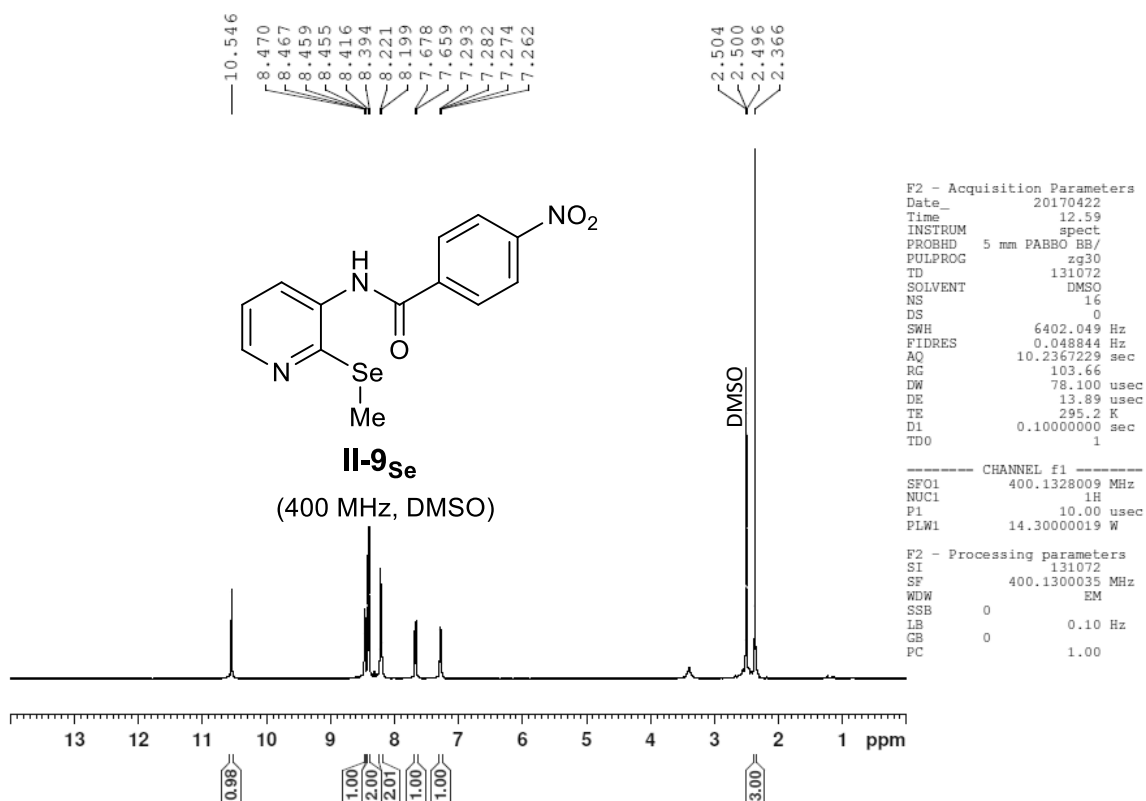
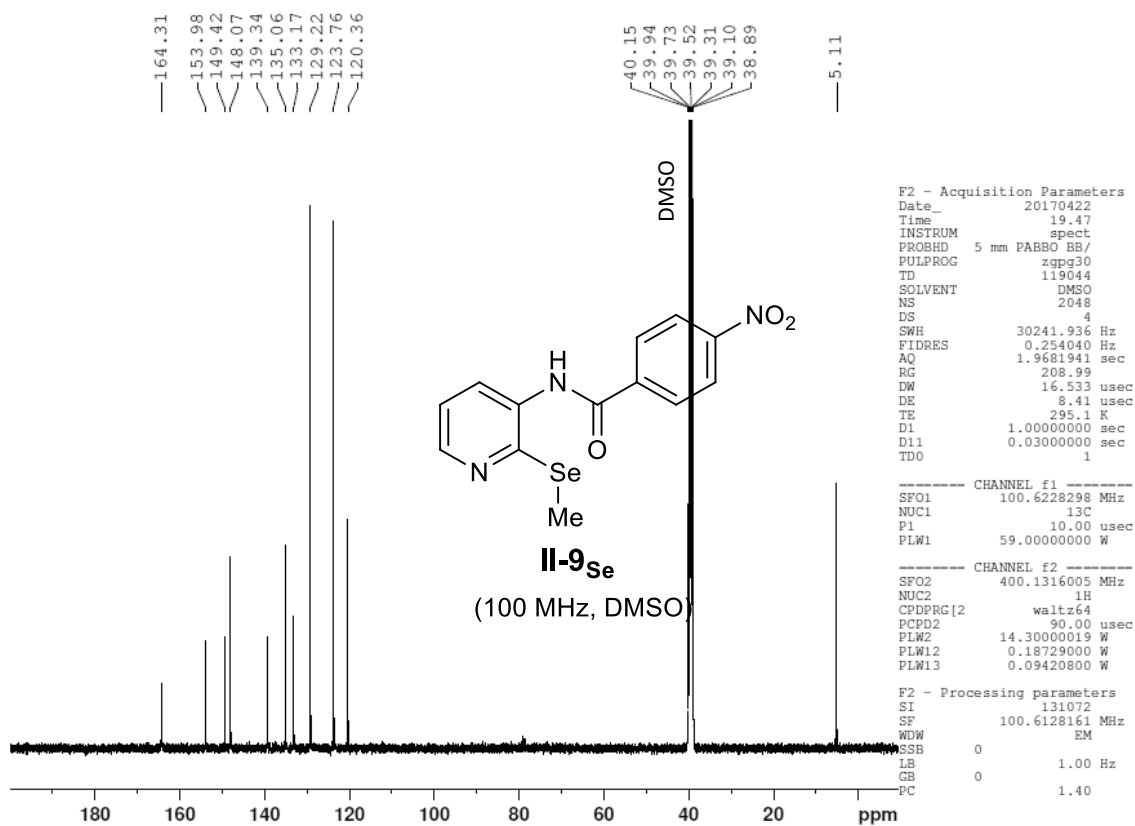
Figure VI - 17: 300 MHz  $^1\text{H}$ -NMR in DMSO of molecule **II-6<sub>Se</sub>**.Figure VI - 18: 100 MHz  $^{13}\text{C}$ -NMR in DMSO of molecule **II-6<sub>Te</sub>**.

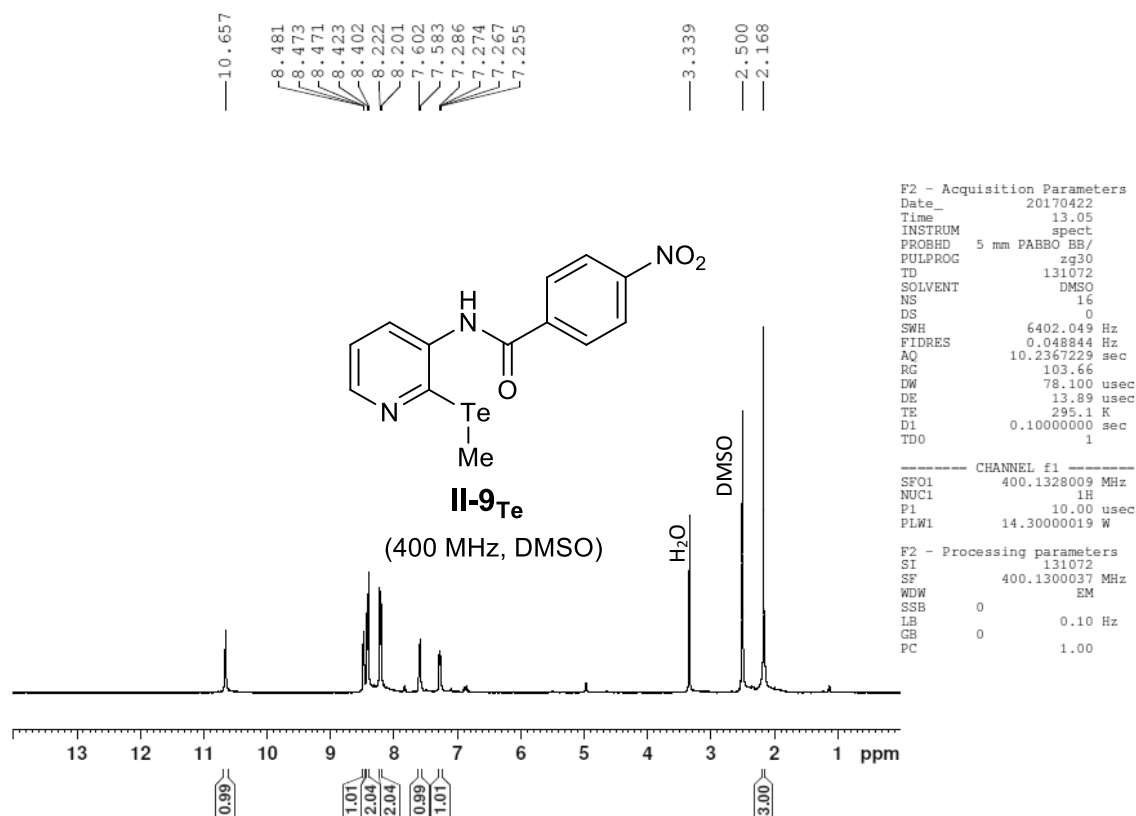
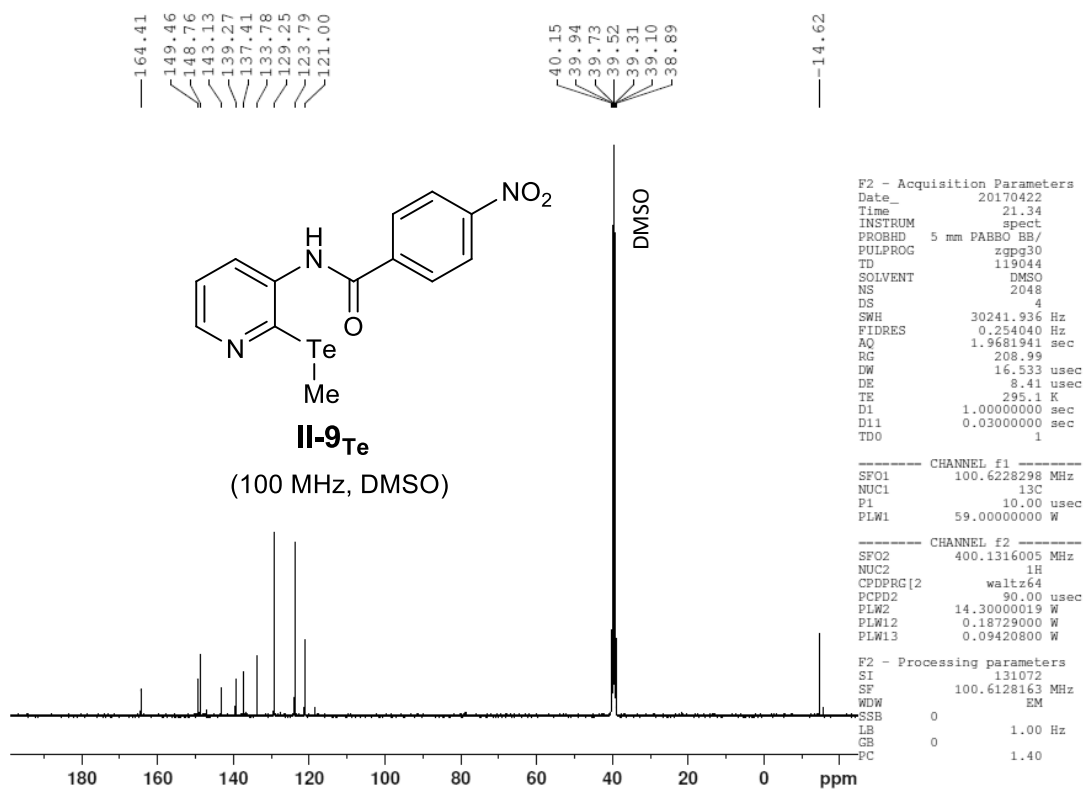
Figure VI - 19: 400 MHz <sup>1</sup>H-NMR in DMSO of molecule II-7<sub>se</sub>.Figure VI - 20: 100 MHz <sup>13</sup>C-NMR in DMSO of molecule II-7<sub>se</sub>.

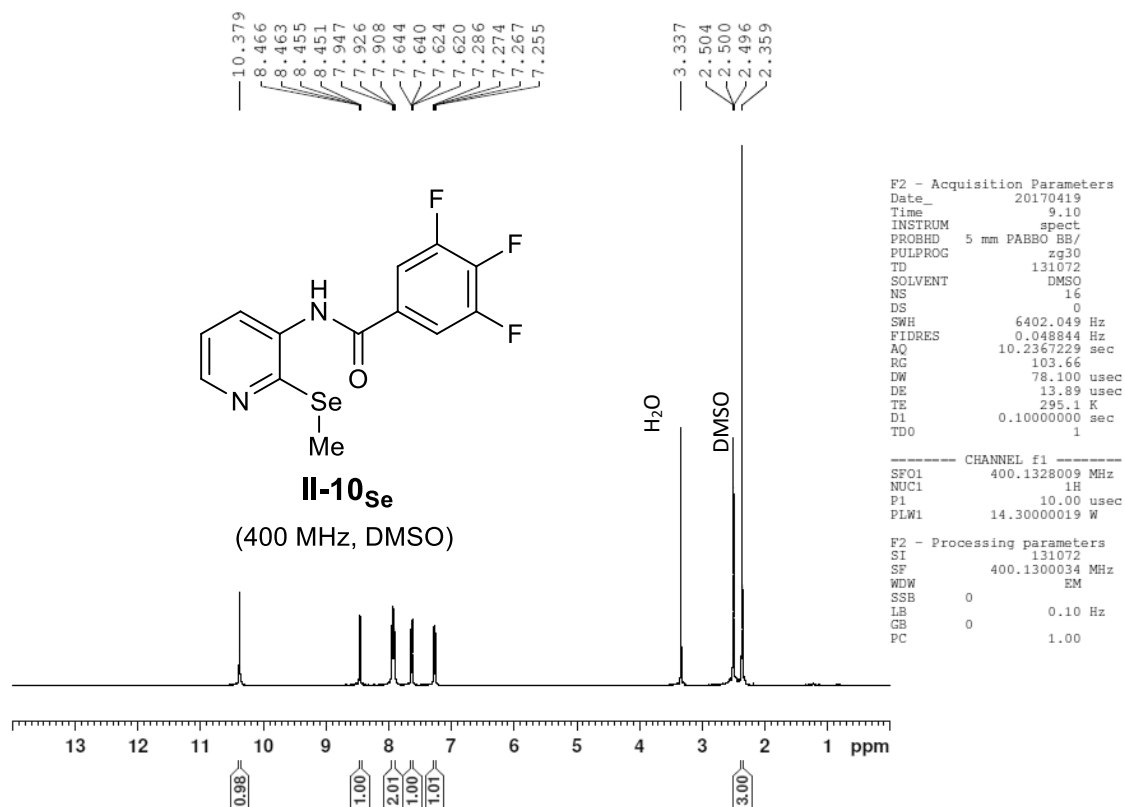
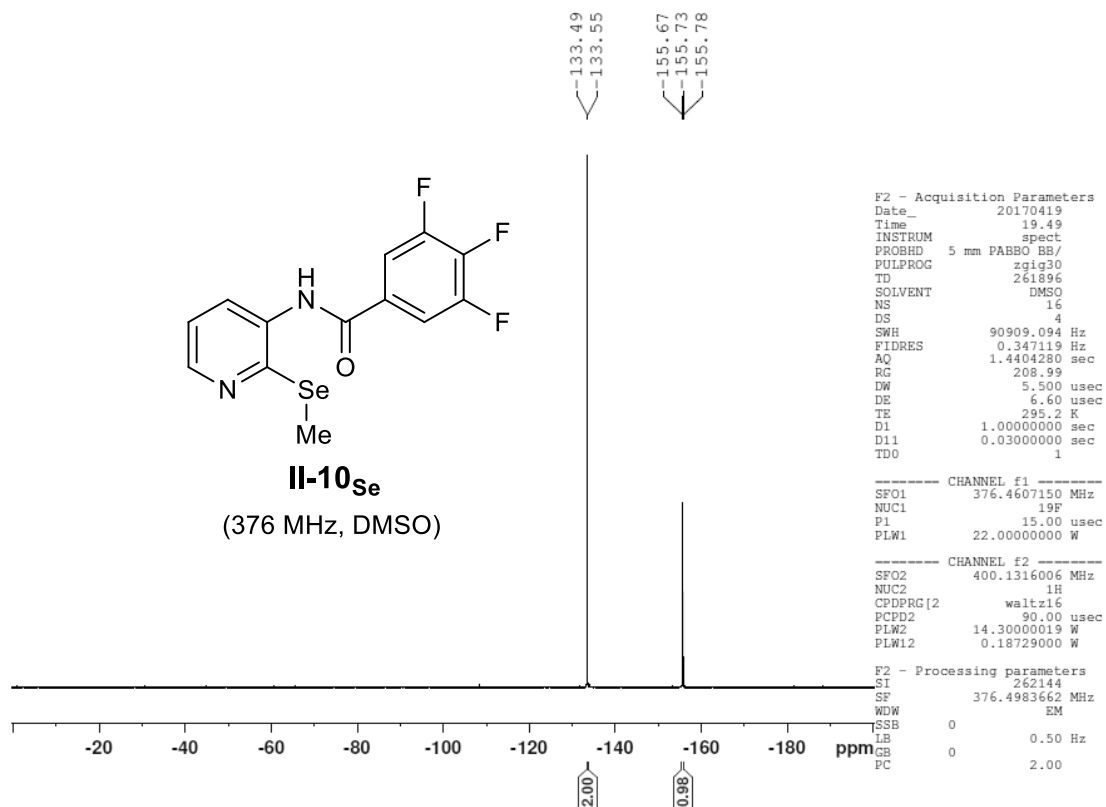
Figure VI - 21: 400 MHz <sup>1</sup>H-NMR in DMSO of molecule II-7<sub>Te</sub>.Figure VI - 22: 100 MHz <sup>13</sup>C-NMR in DMSO of molecule II-7<sub>Te</sub>.

Figure VI - 23: 400 MHz <sup>1</sup>H-NMR in DMSO of molecule **II-8<sub>Se</sub>**.Figure VI - 24: 100 MHz <sup>13</sup>C-NMR in DMSO of molecule **II-8<sub>Se</sub>**.

Figure VI - 25: 400 MHz <sup>1</sup>H-NMR in DMSO of molecule II-8<sub>Te</sub>.Figure VI - 26: 100 MHz <sup>13</sup>C-NMR in DMSO of molecule II-8<sub>Te</sub>.

Figure VI - 27: 400 MHz <sup>1</sup>H-NMR in DMSO of molecule II-9<sub>Se</sub>.Figure VI - 28: 100 MHz <sup>13</sup>C-NMR in DMSO of molecule II-9<sub>Se</sub>.

Figure VI - 29: 400 MHz <sup>1</sup>H-NMR in DMSO of molecule **II-9<sub>Te</sub>**.Figure VI - 30: 100 MHz <sup>13</sup>C-NMR in DMSO of molecule **II-9<sub>Te</sub>**.

Figure VI - 31: 400 MHz  $^1\text{H}$ -NMR in DMSO of molecule II-10<sub>se</sub>.Figure VI - 32: 376 MHz  $^{19}\text{F}$ -NMR in DMSO of molecule II-10<sub>se</sub>.

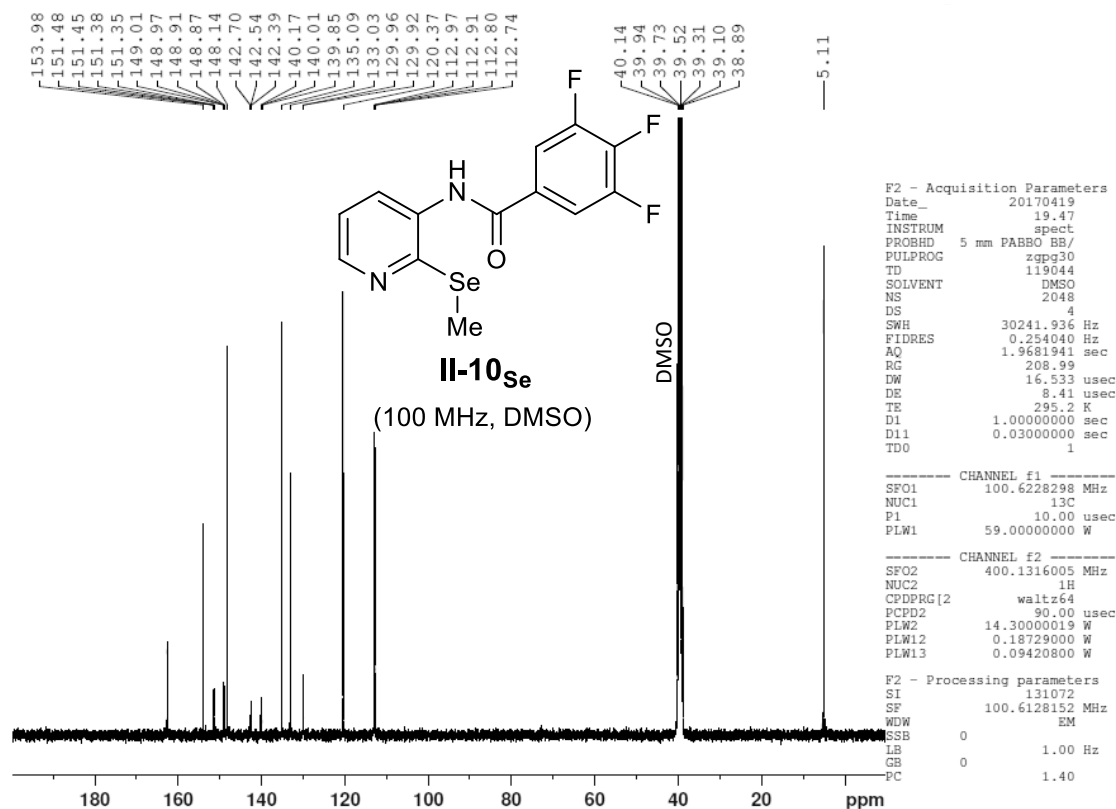


Figure VI - 33: 400 MHz  $^1\text{H}$ -NMR in DMSO of molecule **II-10<sub>Se</sub>**. Due to  $^{13}\text{C}$ - $^{19}\text{F}$  coupling: Peak 150.2 splits into 151.48, 151.45, 151.38, 149.00, 148.97, 148.91, 148.87; Peak 141.3 splits into 142.70, 142.54, 142.39, 140.17, 140.01, 139.85; Peak 112.9 splits into 112.96, 112.91, 112.80, 112.74.

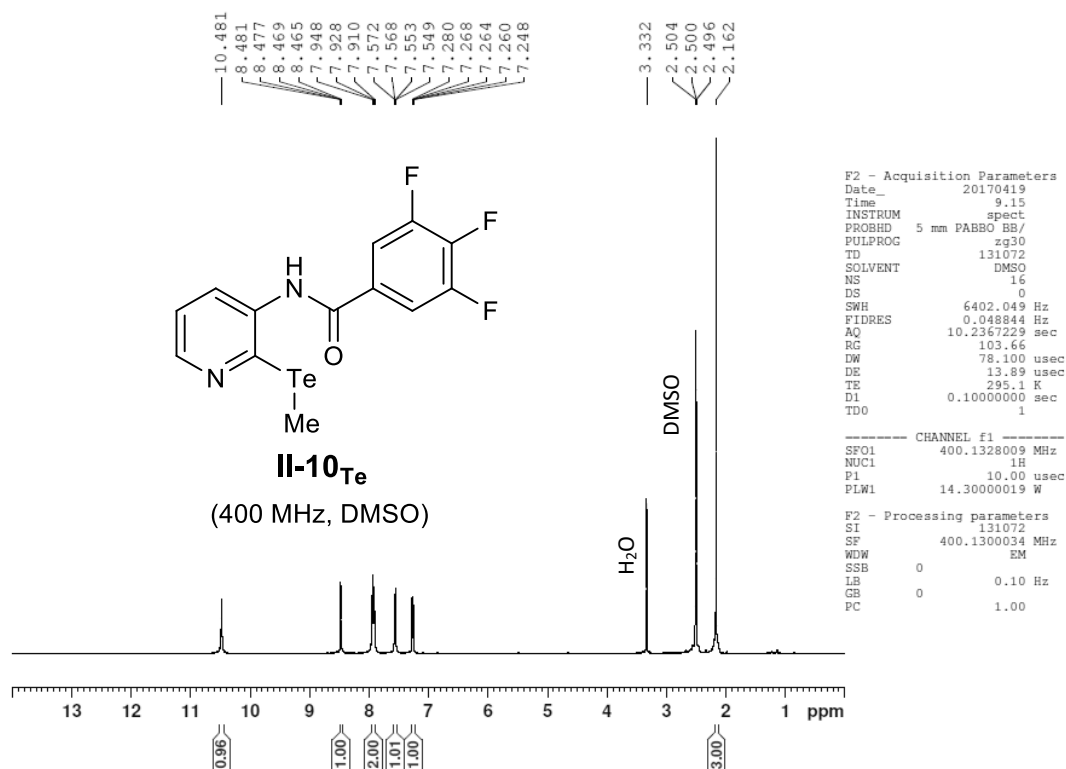


Figure VI - 34: 400 MHz  $^1\text{H}$ -NMR in DMSO of molecule **II-10<sub>Te</sub>**.

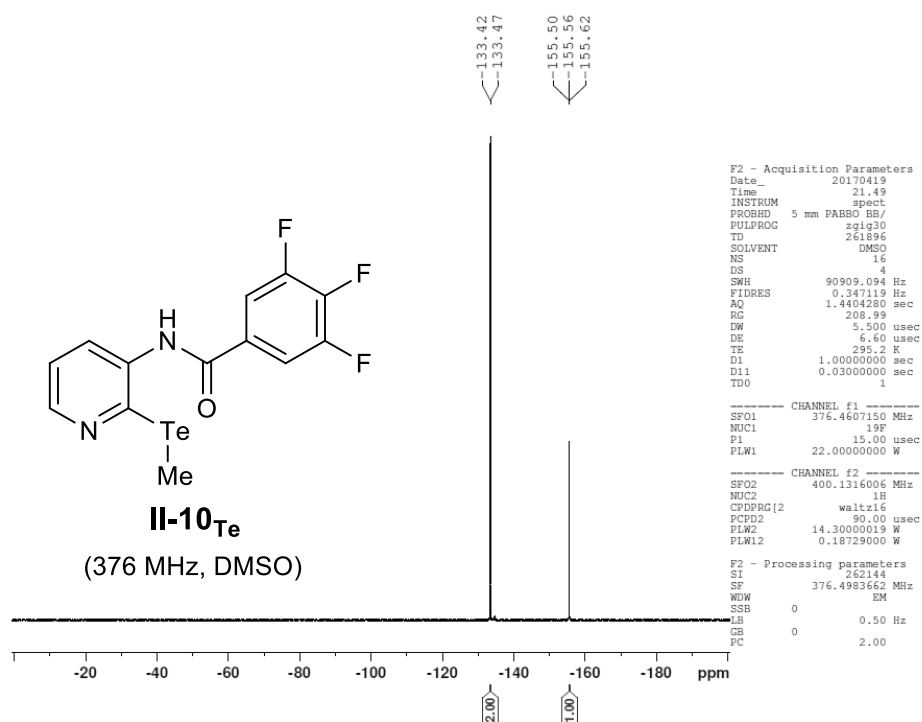
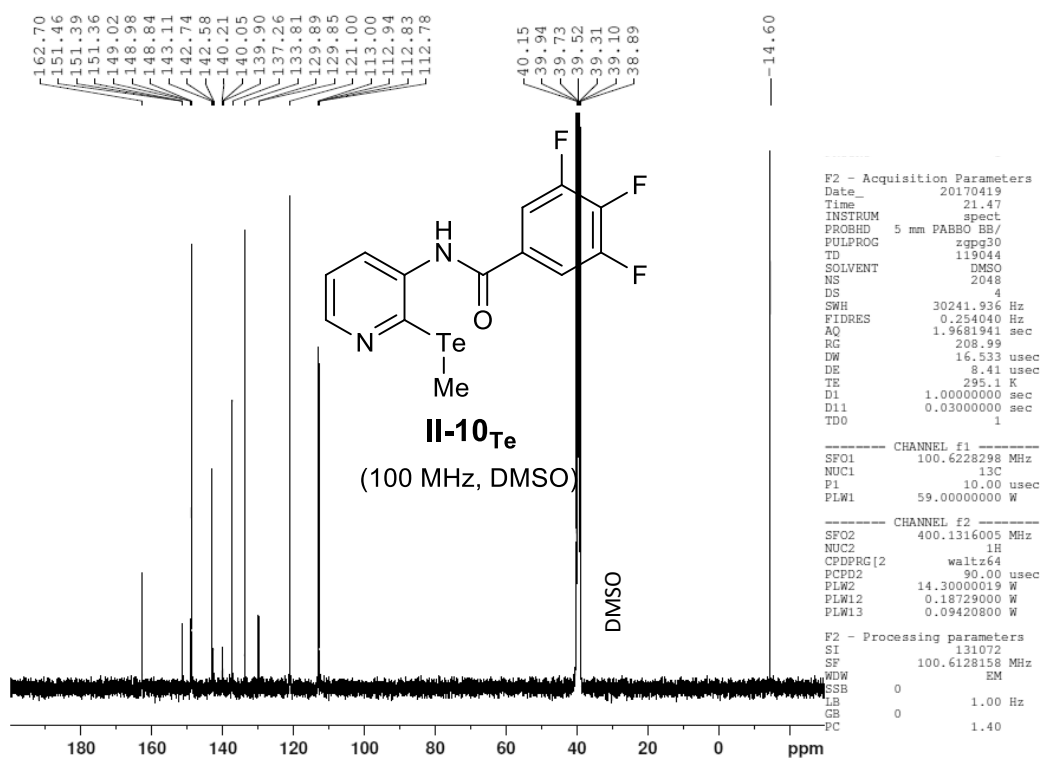
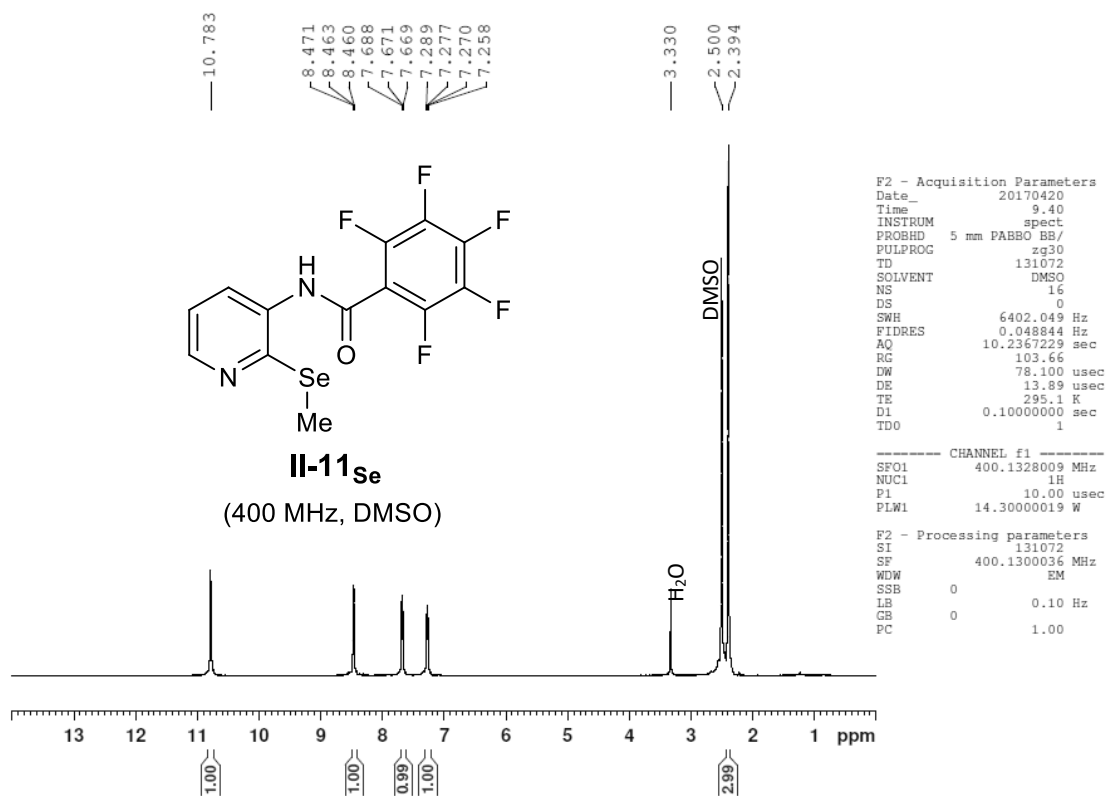
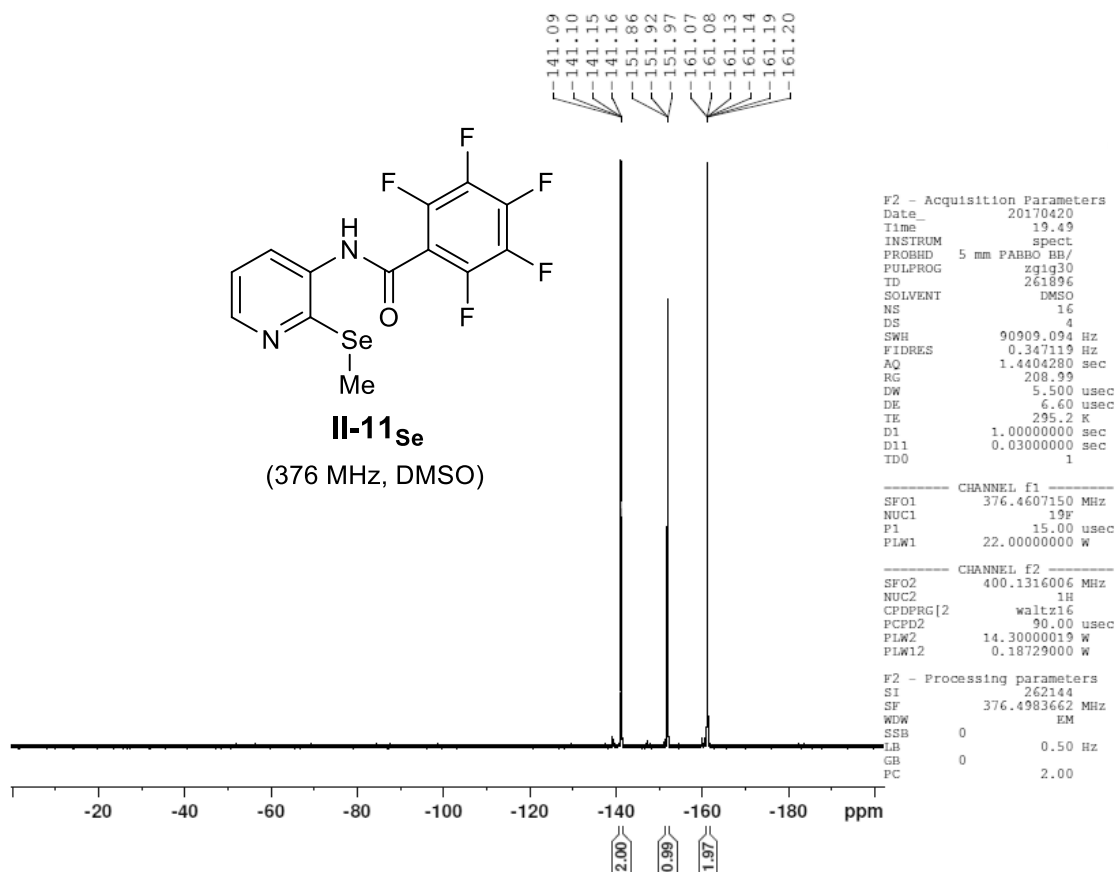
Figure VI - 35: 376MHz <sup>19</sup>F-NMR in DMSO of molecule II-10<sub>Te</sub>.

Figure VI - 36: 100 MHz <sup>13</sup>C-NMR in DMSO of molecule II-10<sub>Te</sub>. Due to <sup>13</sup>C-<sup>19</sup>F coupling: Peak 150.2 splits into 151.46, 151.39, 151.36, 149.02, 148.98, 148.84; Peak 141.3 splits into 142.74, 142.58, 140.21, 140.05, 139.90; Peak 112.9 splits into 113.00, 112.94, 112.83, 112.78.

Figure VI - 37: 400 MHz  $^1\text{H}$ -NMR in DMSO of molecule **II-11<sub>se</sub>**.Figure VI - 38: 376 MHz  $^{19}\text{F}$ -NMR in DMSO of molecule **II-11<sub>se</sub>**.

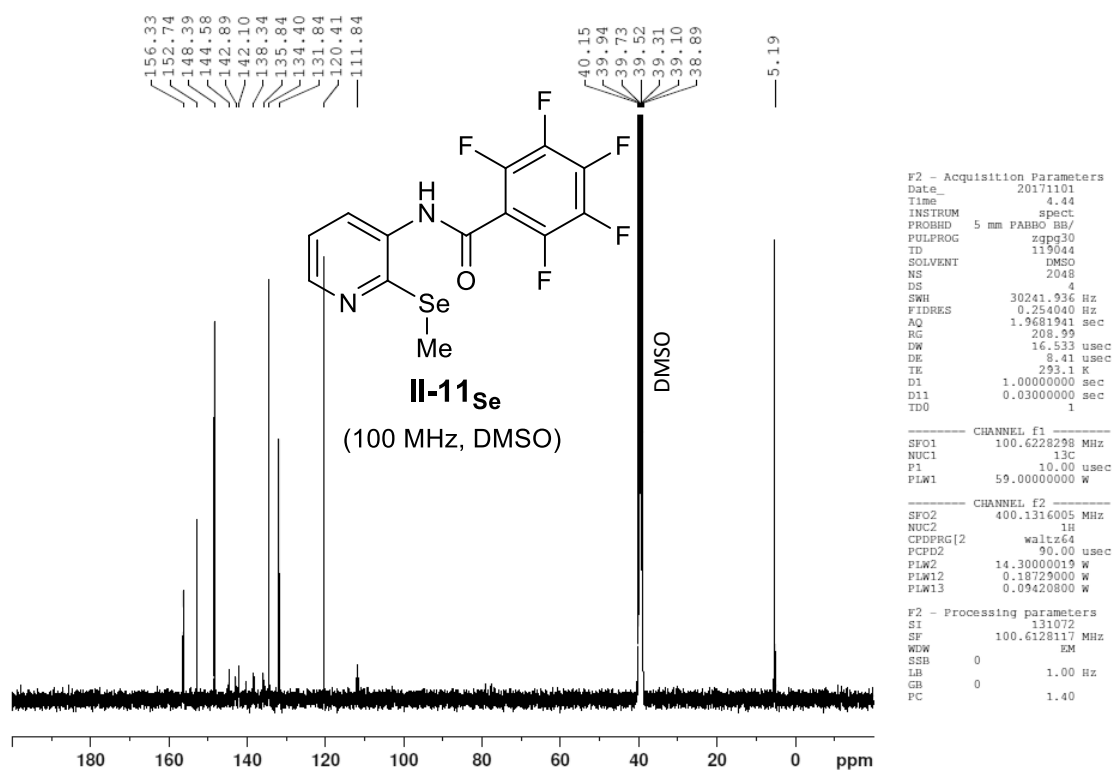


Figure VI - 39: 100 MHz  $^{13}\text{C}$ -NMR in DMSO of molecule **II-11<sub>Se</sub>**. Due to  $^{13}\text{C}$ - $^{19}\text{F}$  coupling: Peak 143.3 splits into 144.58 and 142.10; Peak 141.6 splits into 142.89 and 140.39; Peak 137.0 splits into 138.34 and 135.84.

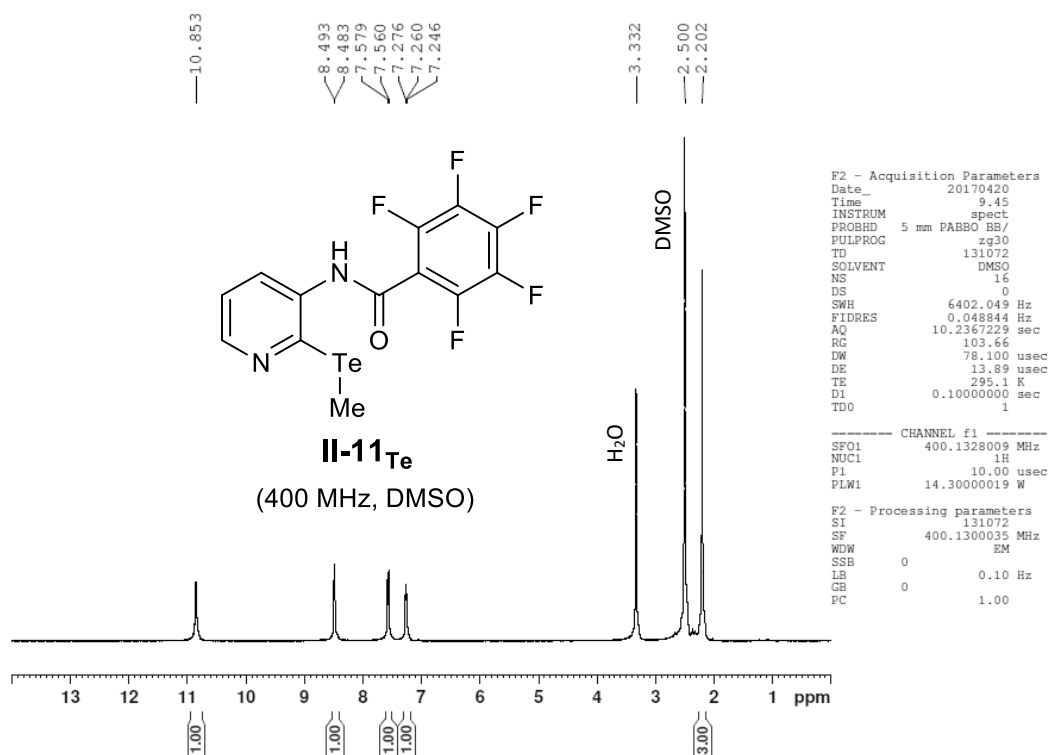
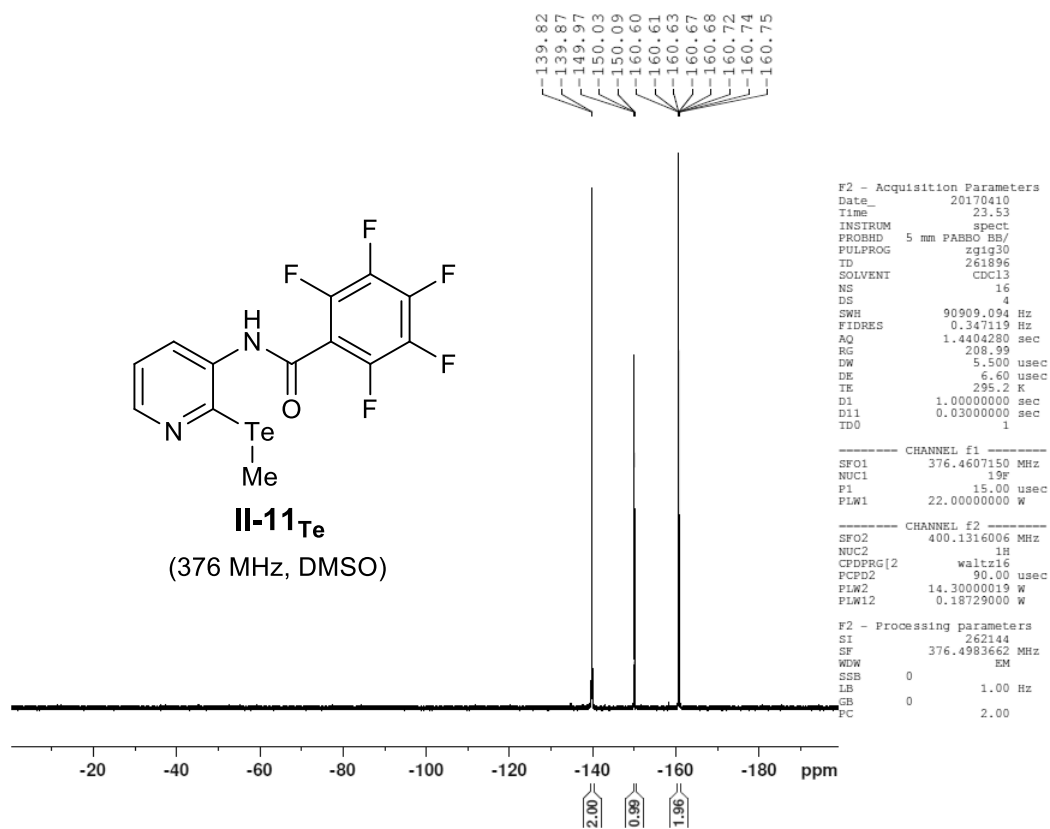
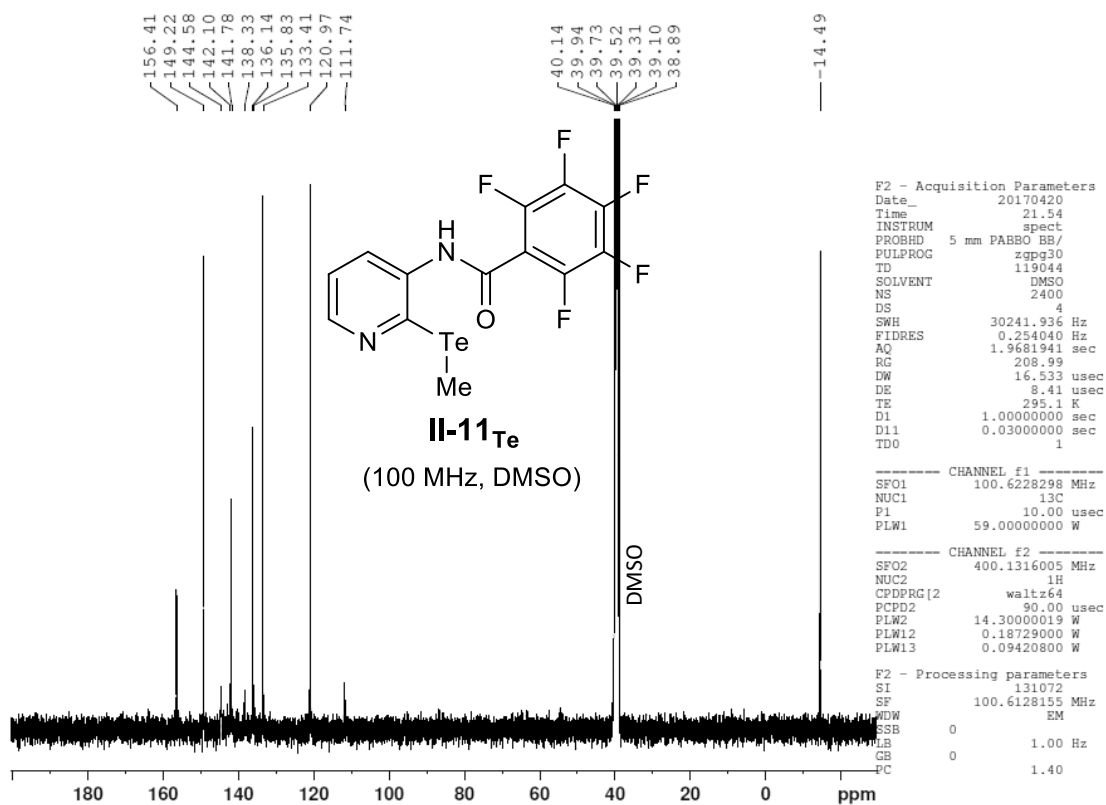
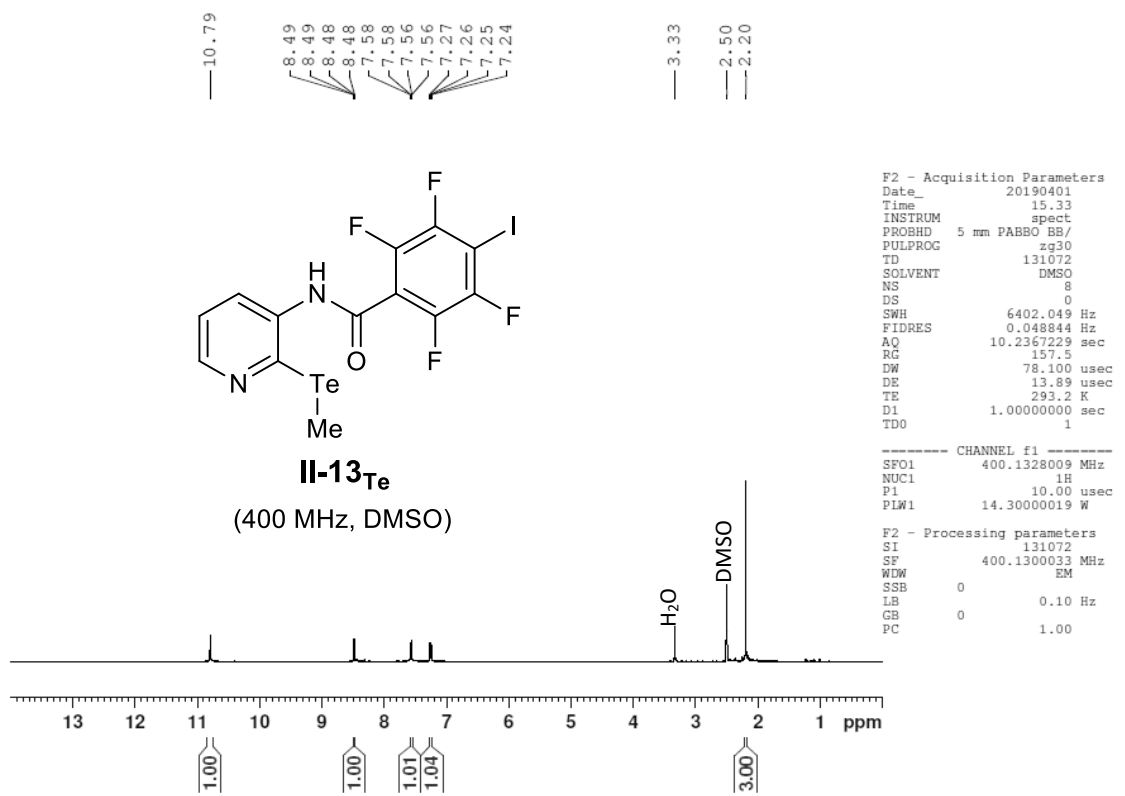
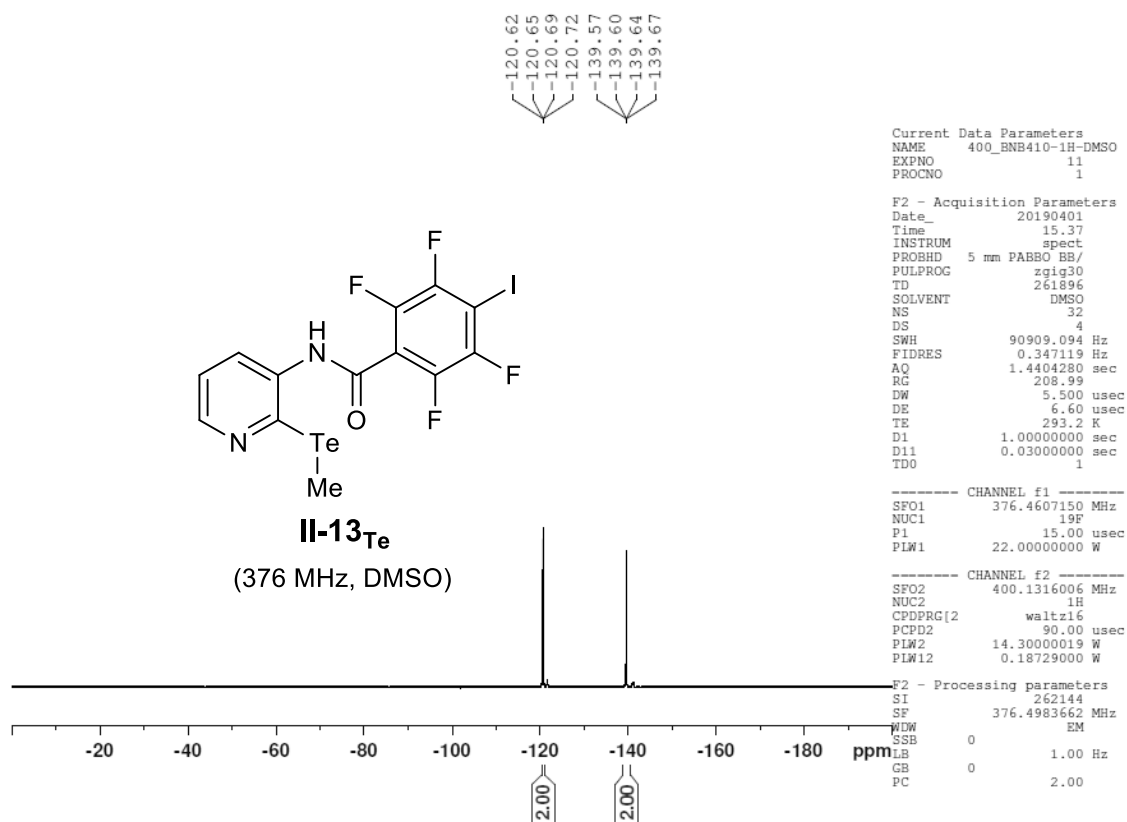


Figure VI - 40: 400 MHz  $^1\text{H}$ -NMR in DMSO of molecule **II-11<sub>Te</sub>**.

Figure VI - 41: 376 MHz  $^{13}\text{C}$ -NMR in DMSO of molecule **II-11<sub>Te</sub>**.Figure VI - 42: 100 MHz  $^{13}\text{C}$ -NMR in DMSO of molecule **II-11<sub>Te</sub>**. Due to  $^{13}\text{C}$ - $^{19}\text{F}$  coupling: Peak 143.3 splits into 144.58 and 142.09; Peak 141.6 splits into 142.87 and 140.41; Peak 137.1 splits into 138.33 and 135.83

Figure VI - 43: 400 MHz <sup>1</sup>H-NMR in DMSO of molecule II-13<sub>Te</sub>.Figure VI - 44: 376 MHz <sup>19</sup>F-NMR in DMSO of molecule II-13<sub>Te</sub>.

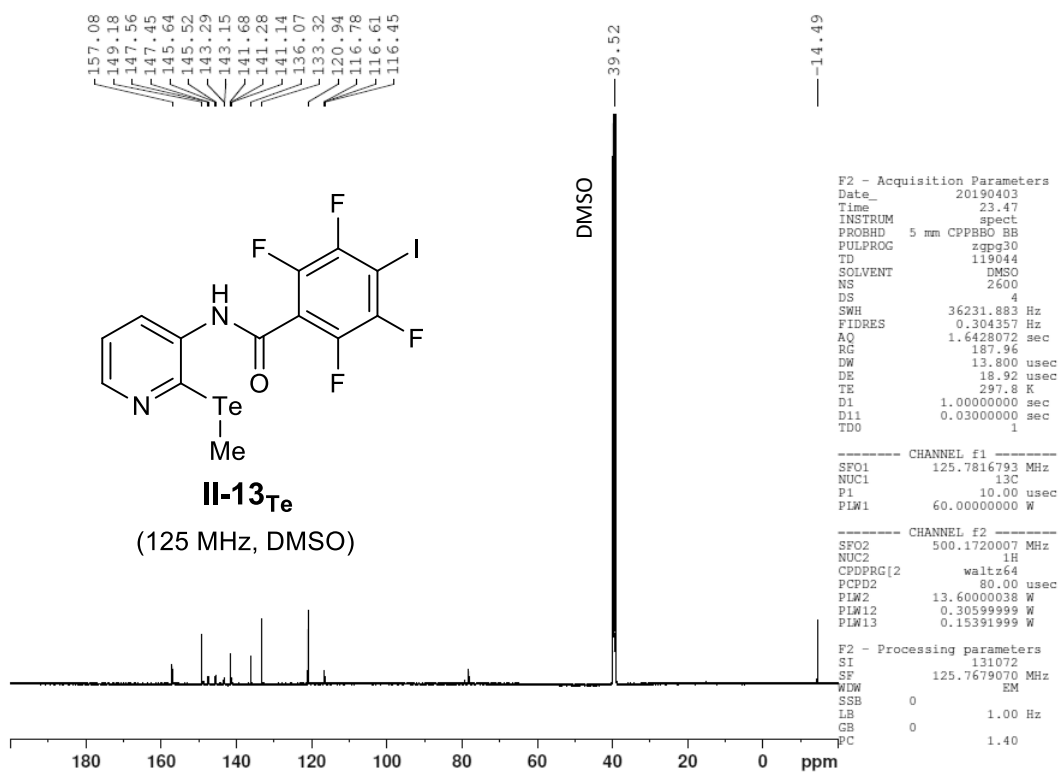


Figure VI - 45: 125 MHz  $^{13}\text{C}$ -NMR in DMSO of molecule **II-13<sub>Te</sub>**. Due to  $^{13}\text{C}$ - $^{19}\text{F}$  coupling: Peak 146.5 splits into 147.56, 147.45, 145.64 and 145.52; Peak 142.2 splits into 143.29, 143.15, 141.28 and 141.27.

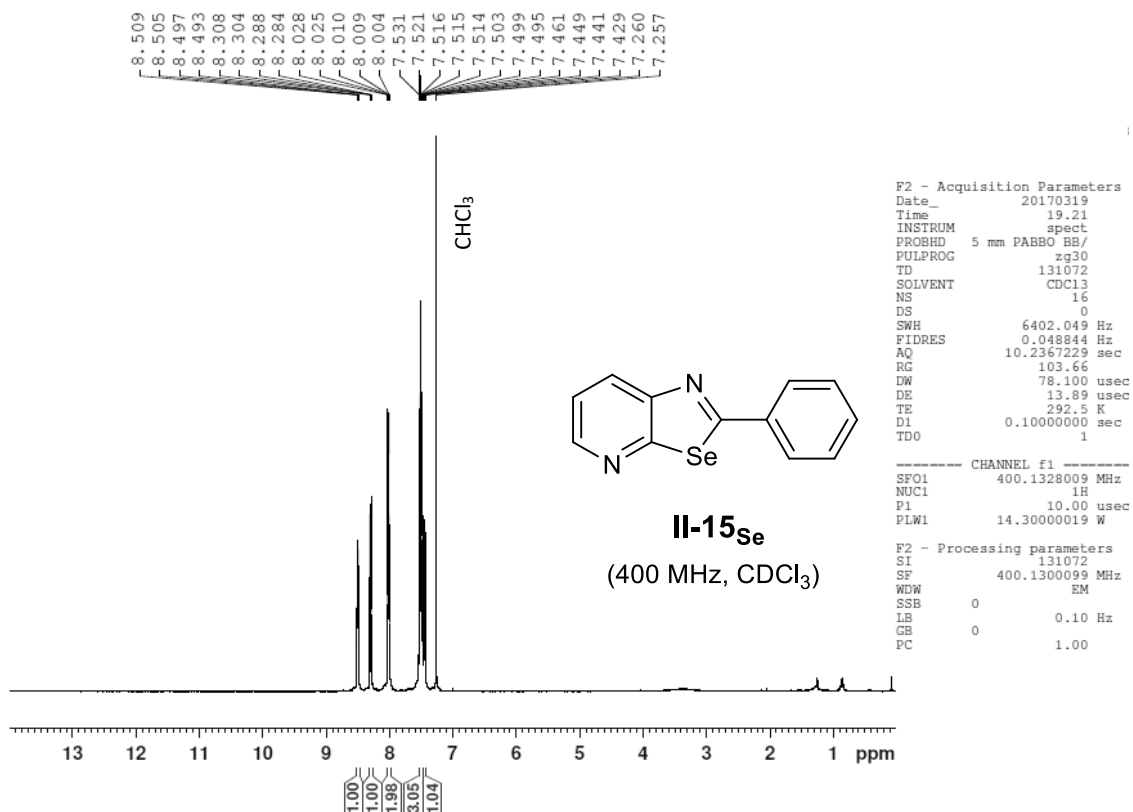
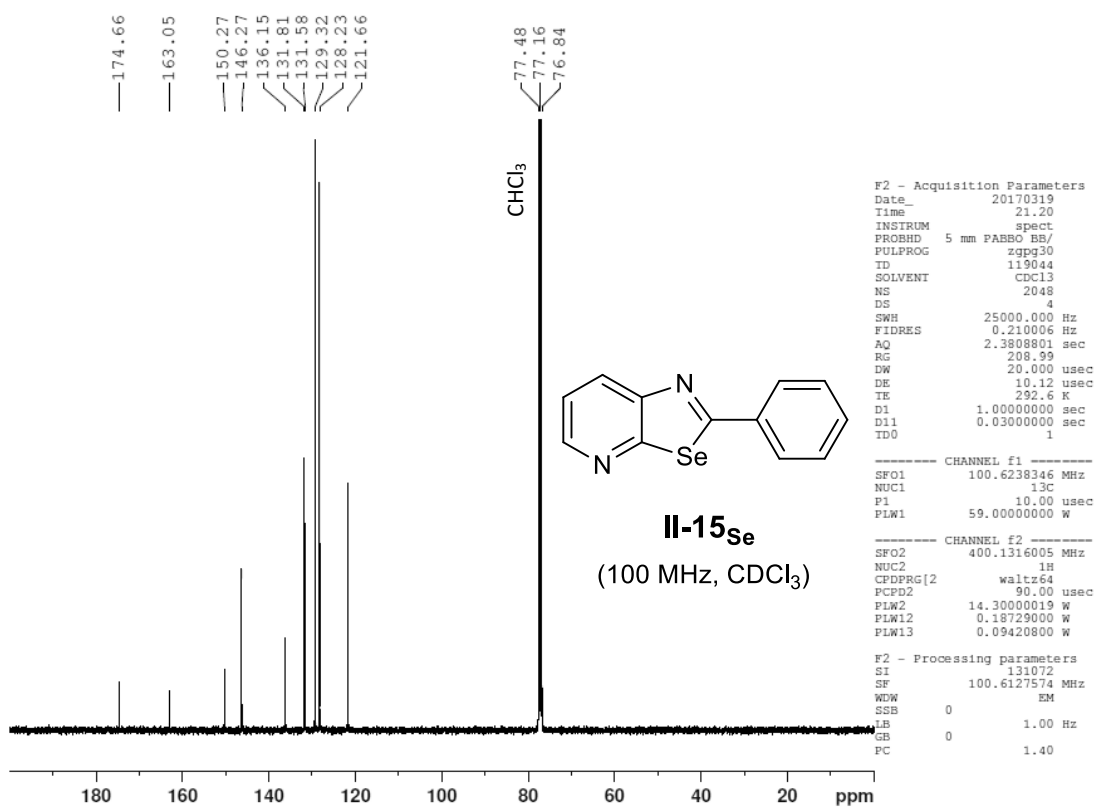
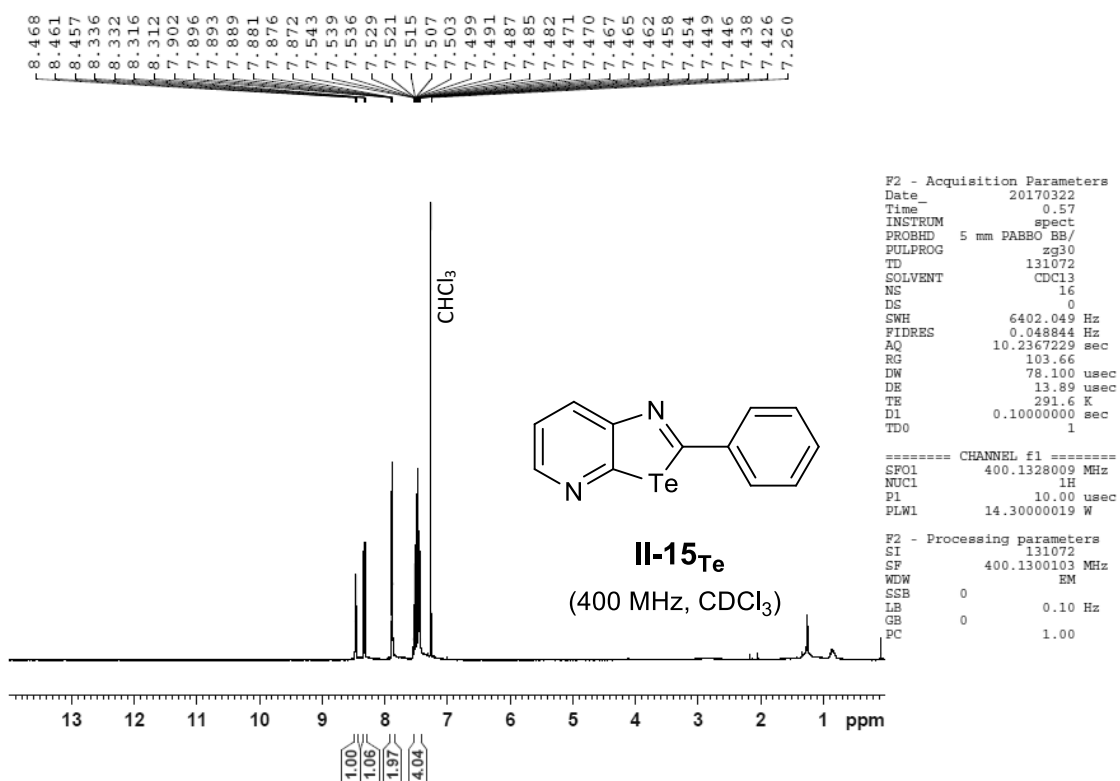
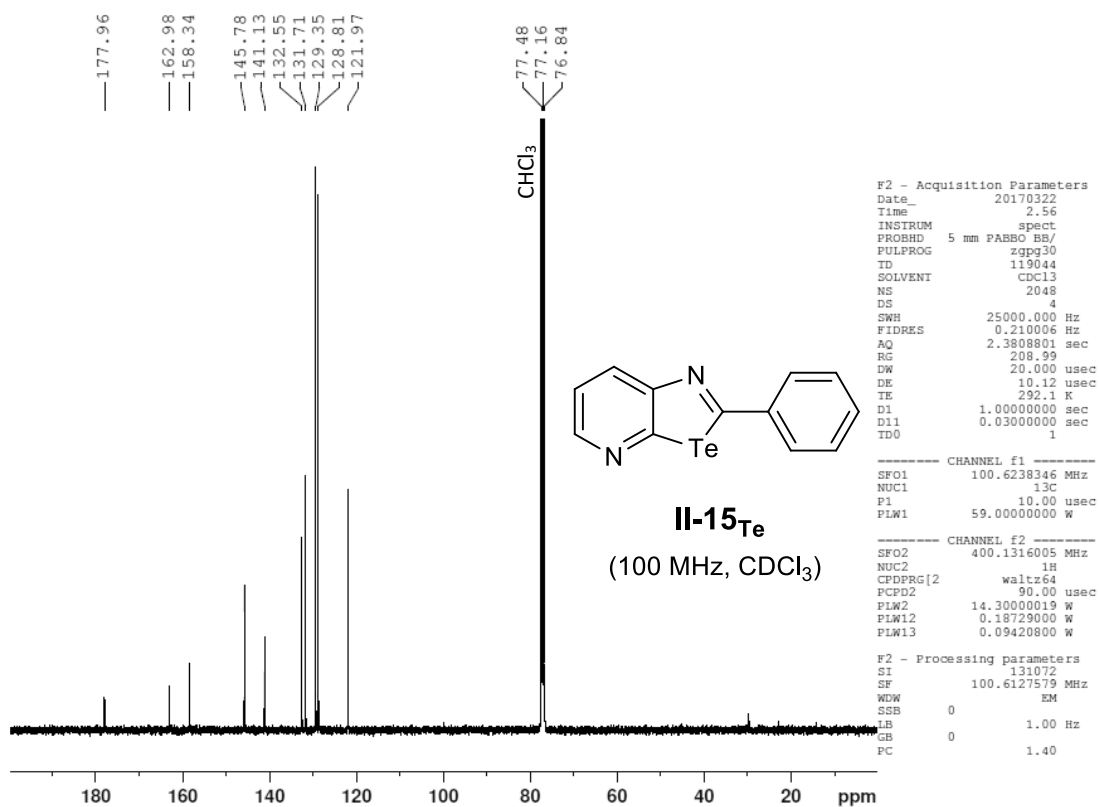
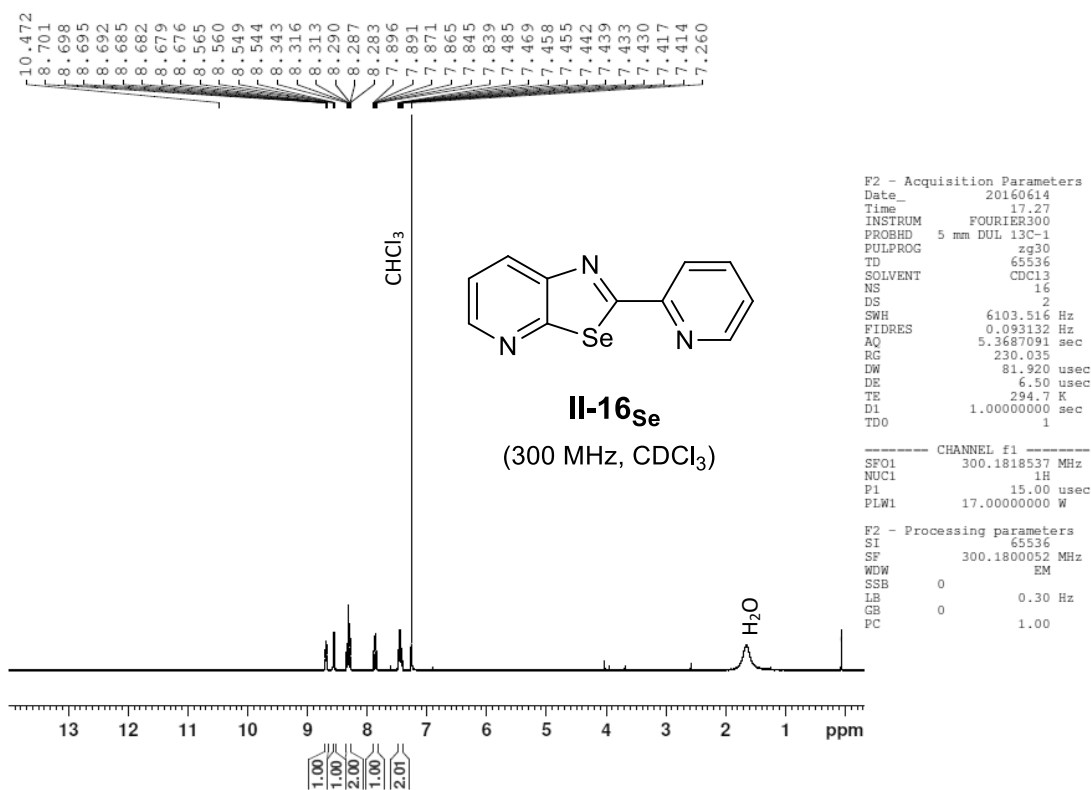
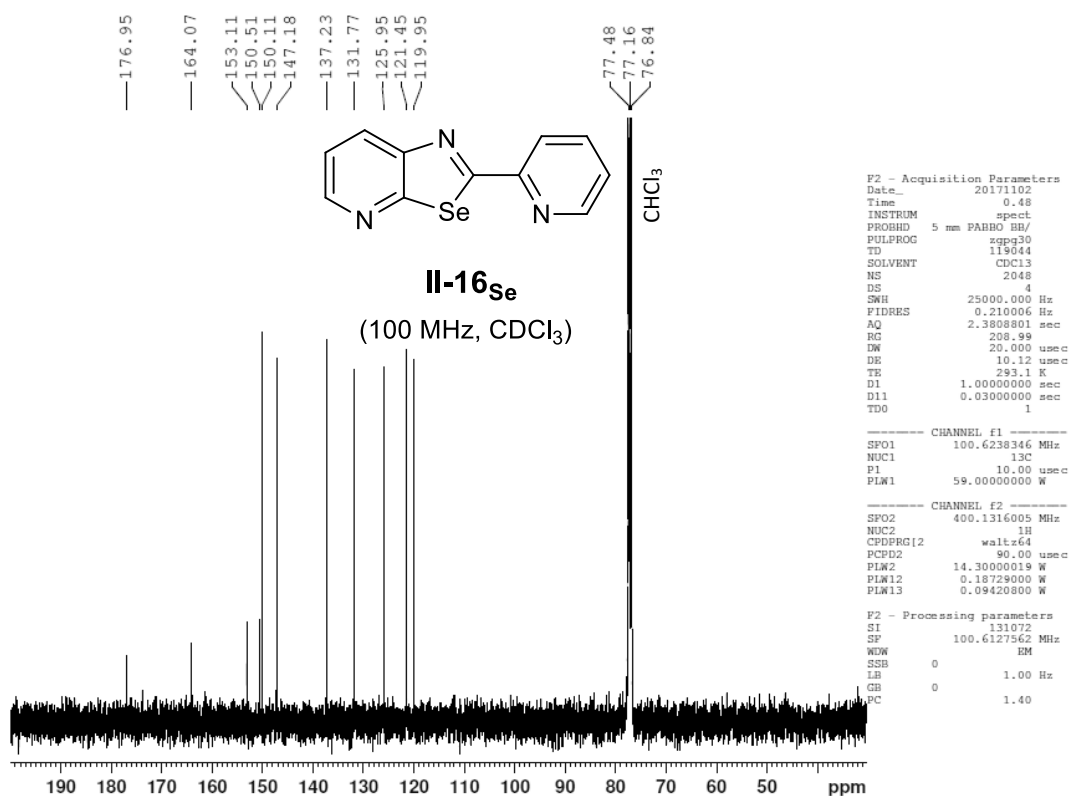
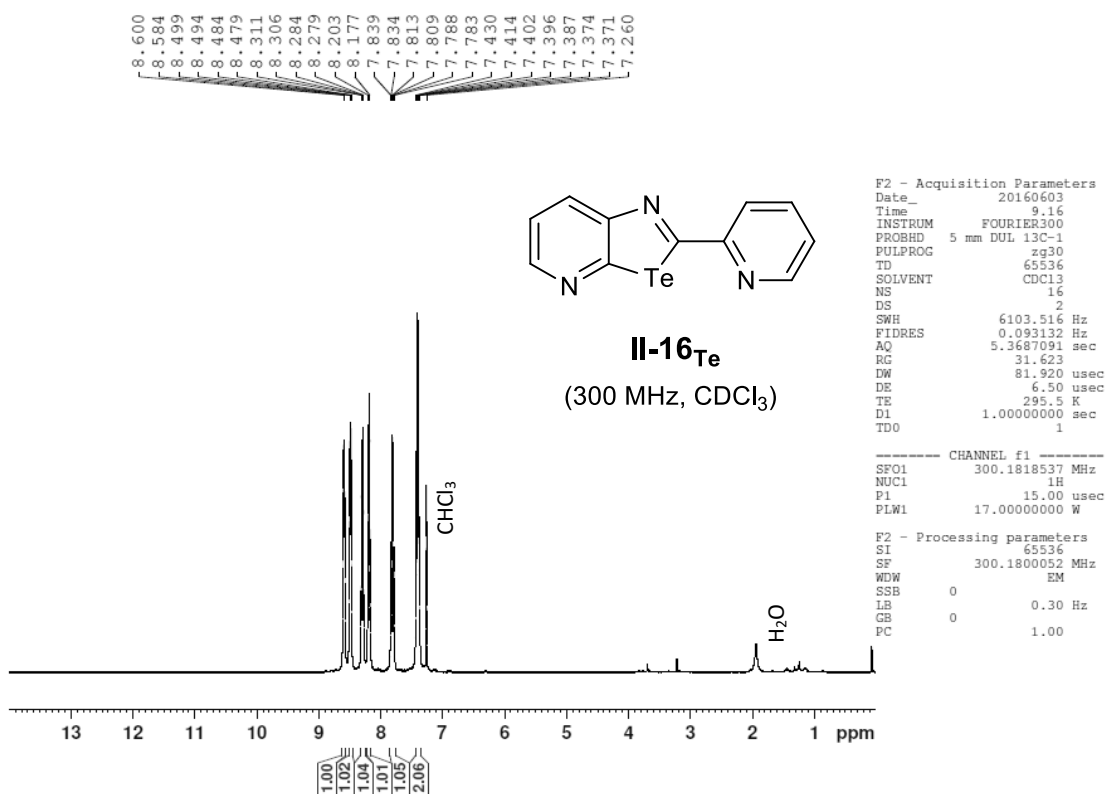
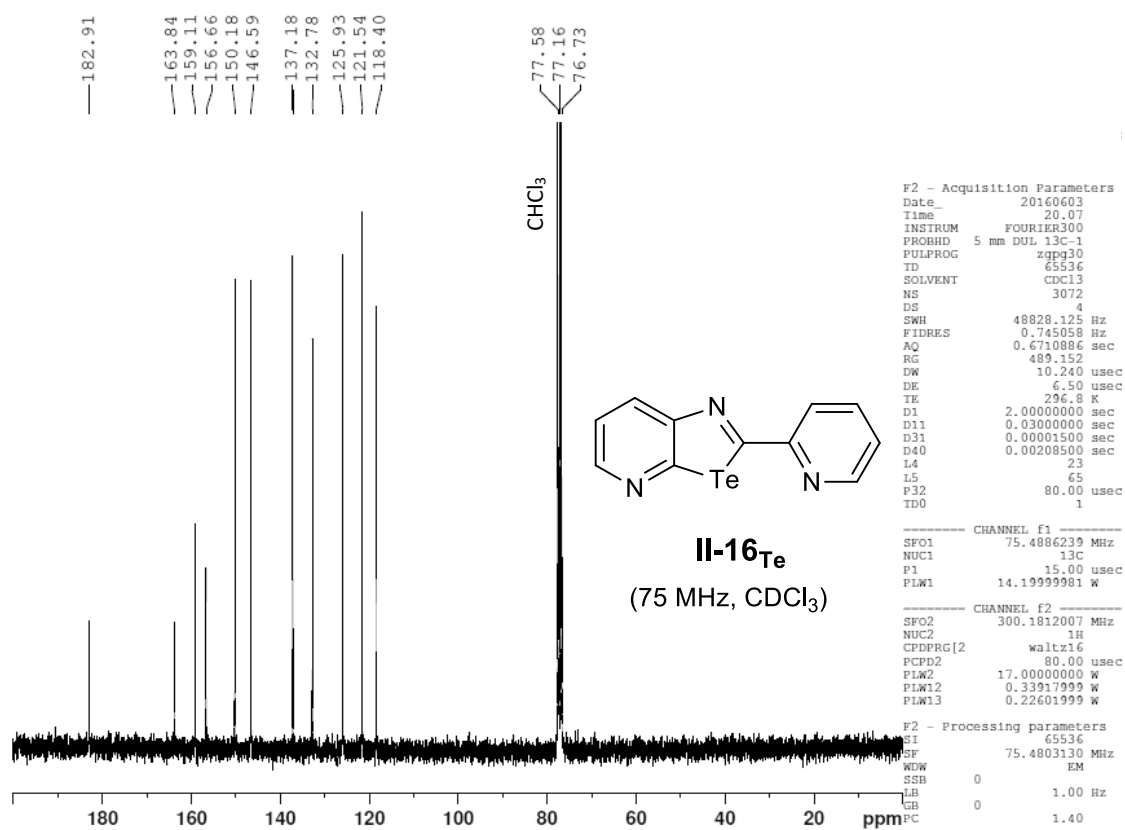
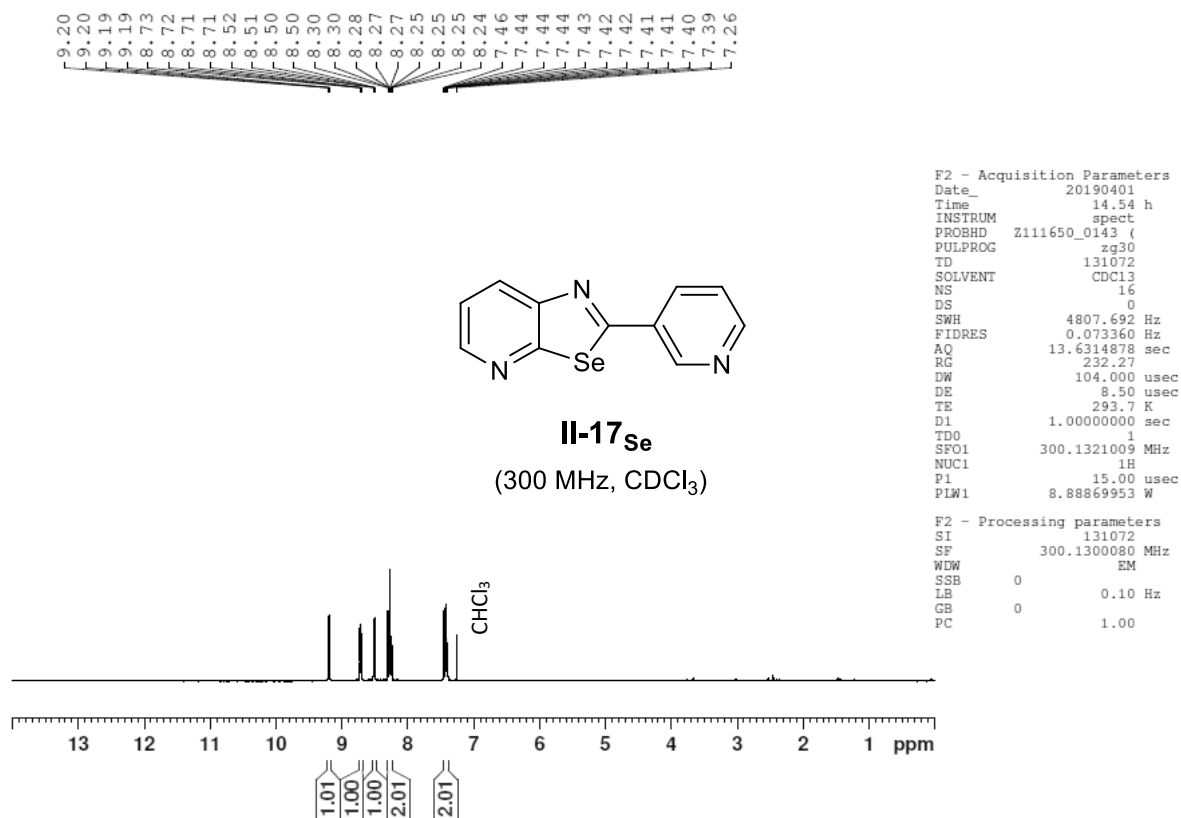


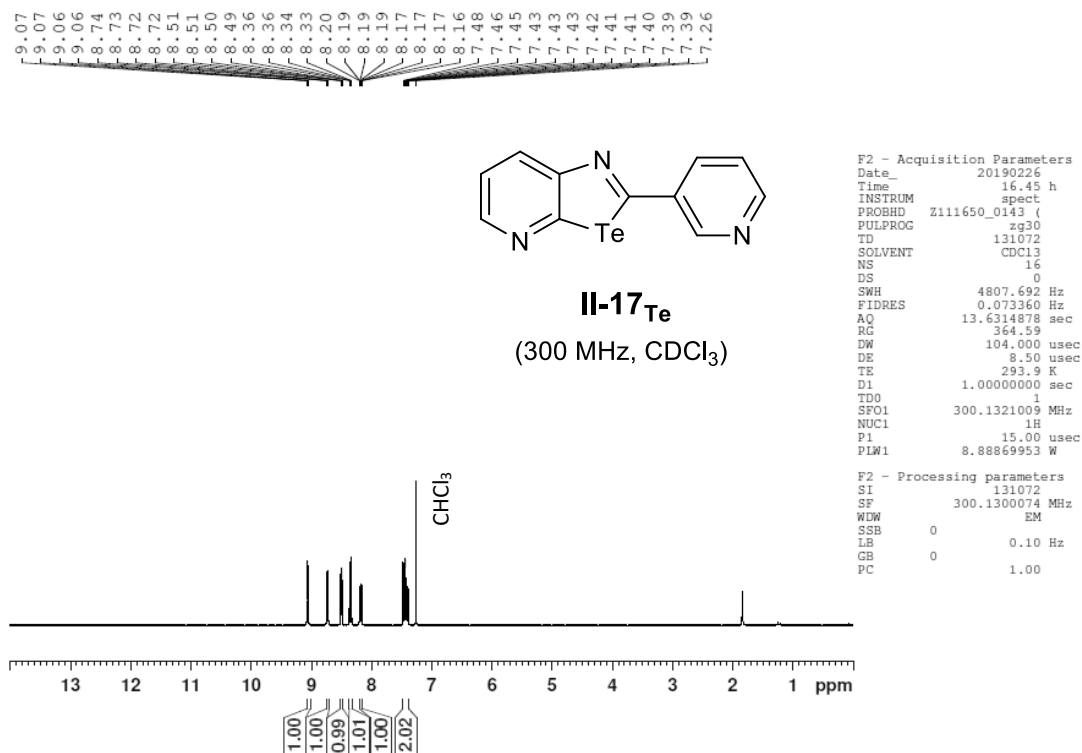
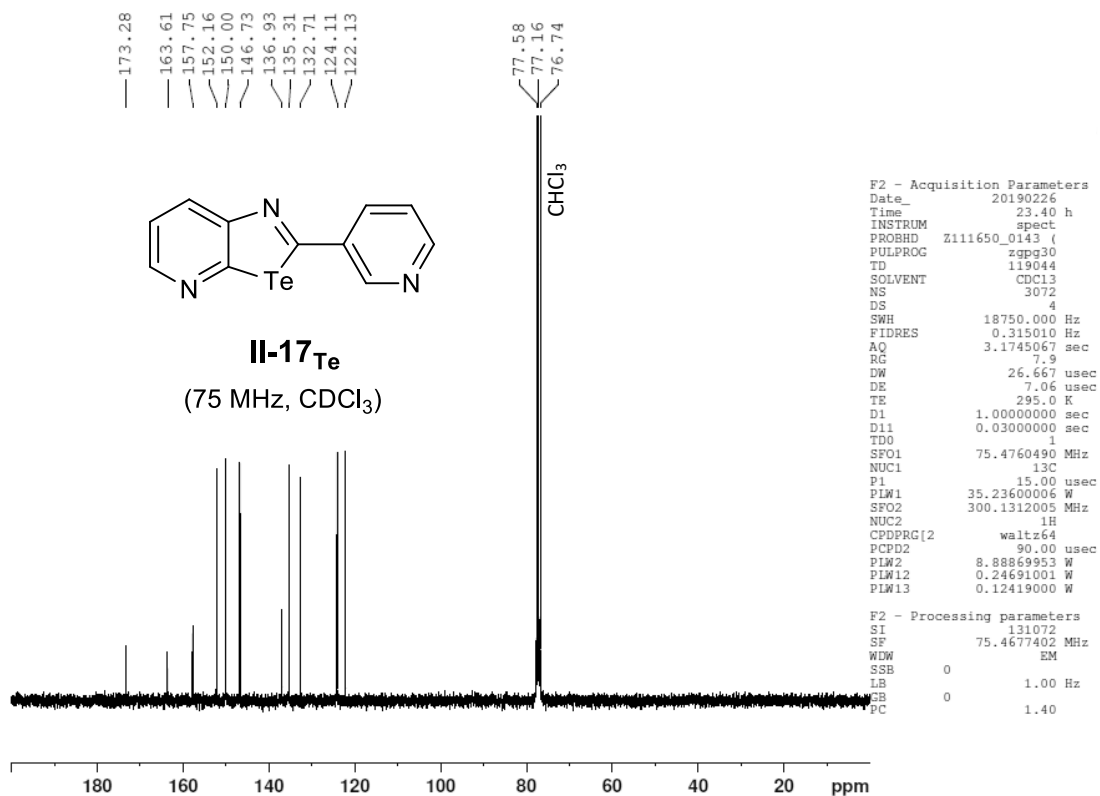
Figure VI - 46: 400 MHz  $^1\text{H}$ -NMR in  $\text{CDCl}_3$  of molecule **II-15<sub>Se</sub>**.

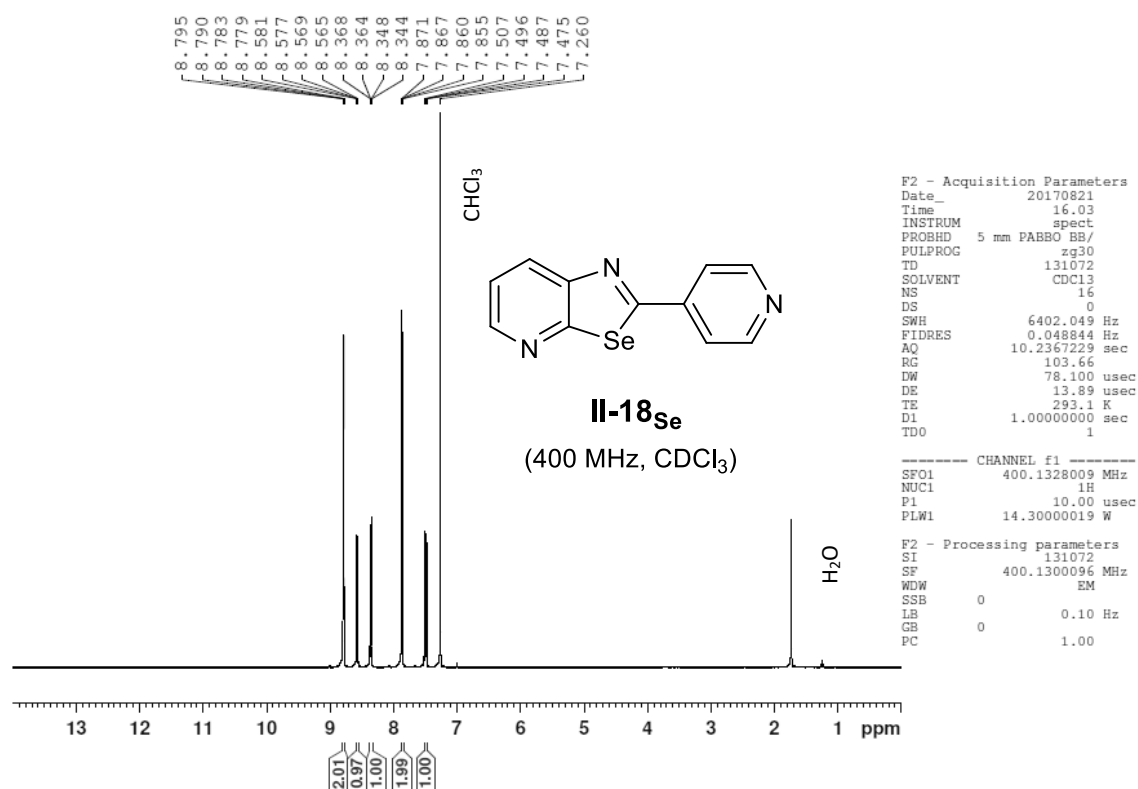
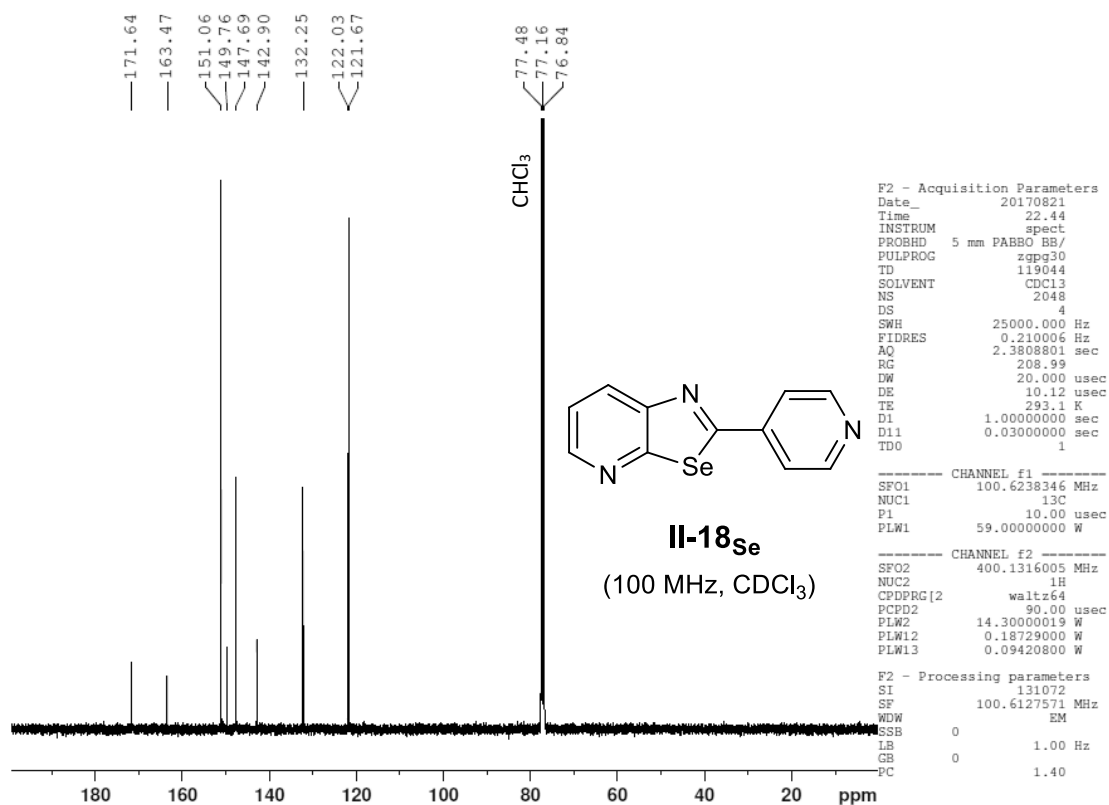
Figure VI - 47: 100 MHz <sup>13</sup>C-NMR in CDCl<sub>3</sub> of molecule **II-15<sub>Se</sub>**.Figure VI - 48: 400 MHz <sup>1</sup>H-NMR in CDCl<sub>3</sub> of molecule **II-15<sub>Te</sub>**.

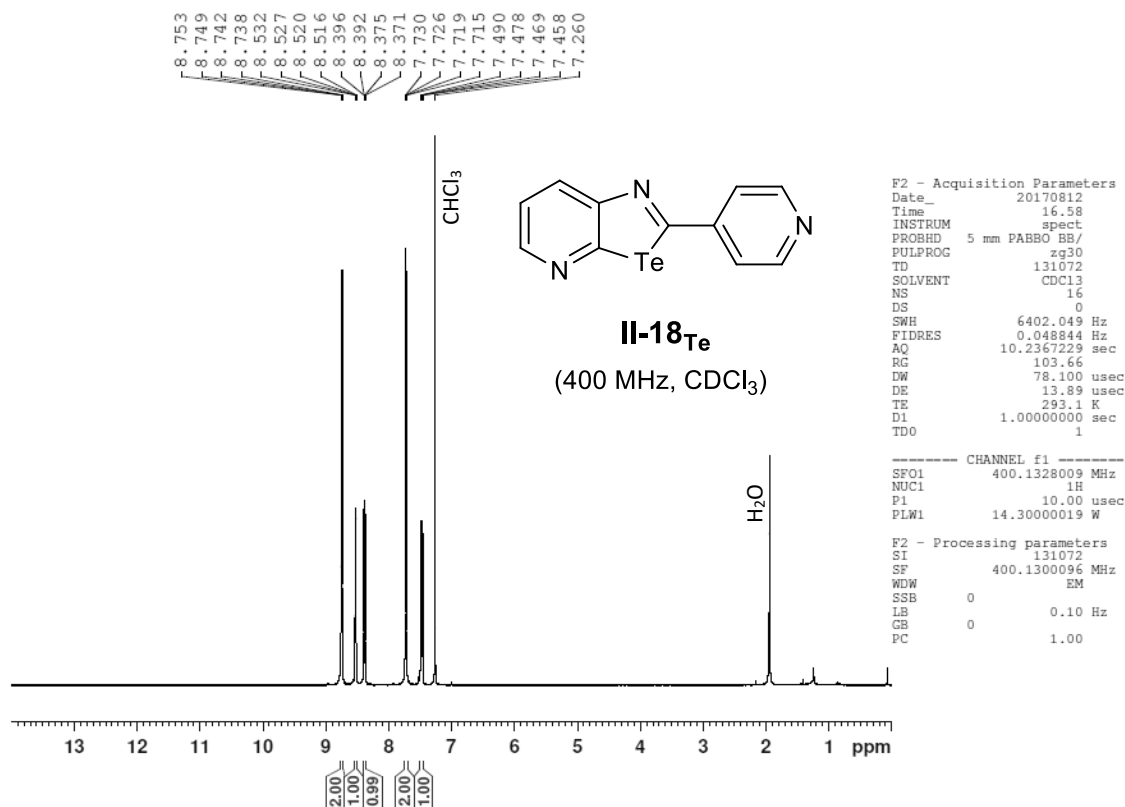
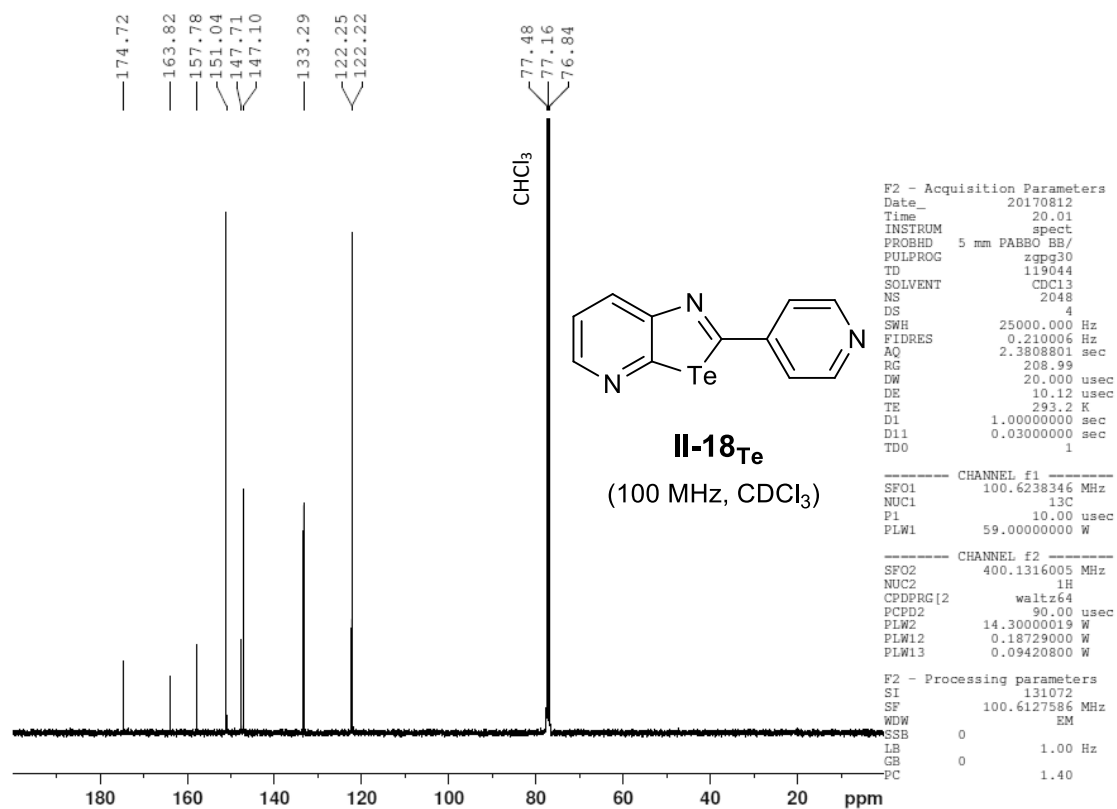
Figure VI - 49: 100 MHz <sup>13</sup>C-NMR in CDCl<sub>3</sub> of molecule **II-15<sub>Te</sub>**.Figure VI - 50: 400 MHz <sup>1</sup>H-NMR in CDCl<sub>3</sub> of molecule **II-16<sub>Se</sub>**.

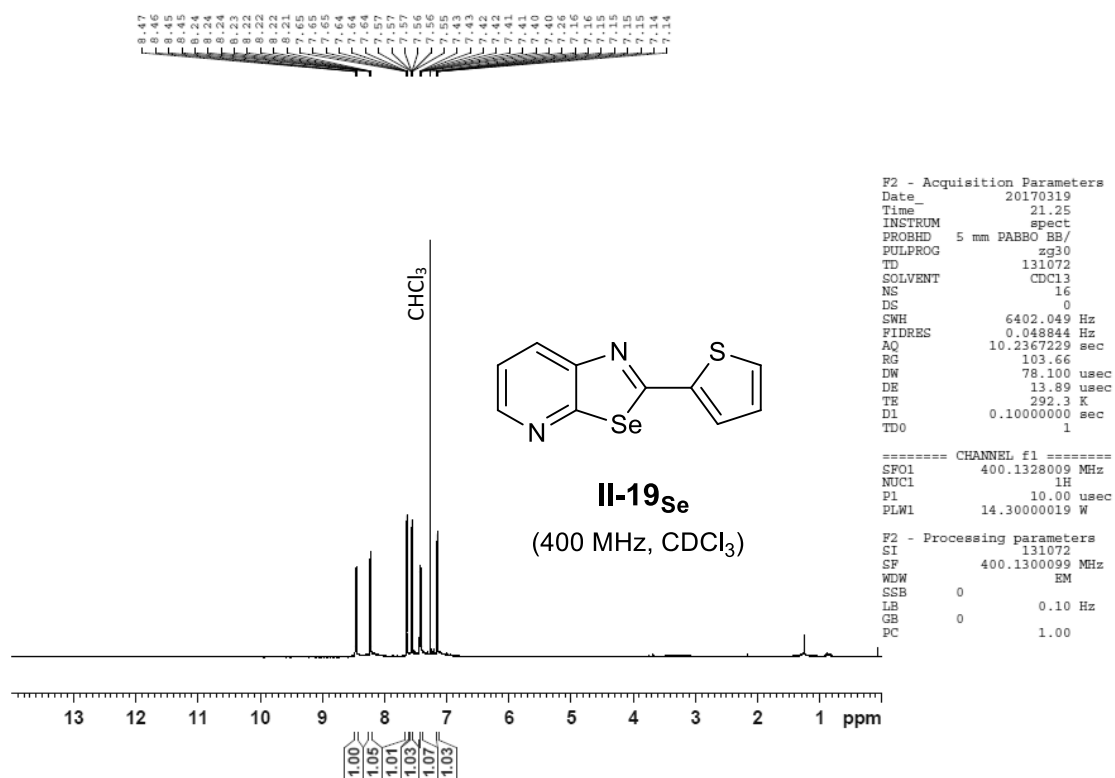
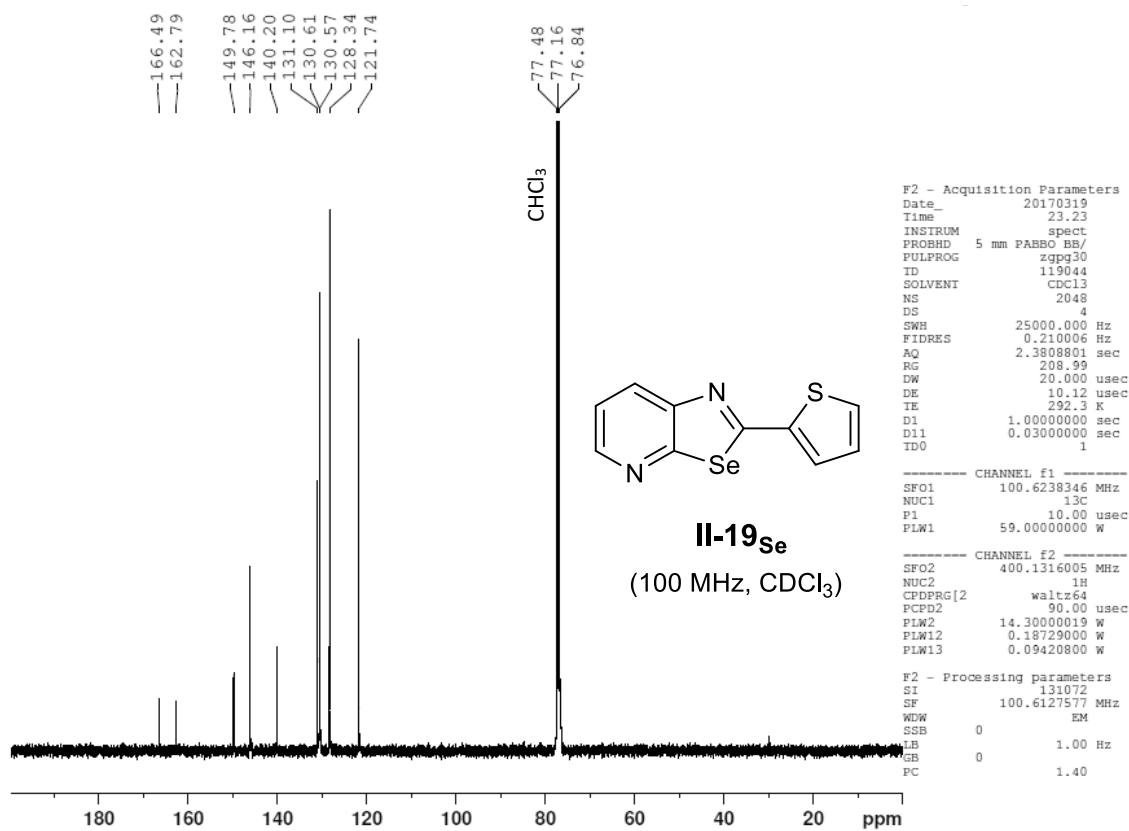
Figure VI - 51: 100 MHz <sup>13</sup>C-NMR in CDCl<sub>3</sub> of molecule **II-16<sub>Se</sub>**.Figure VI - 52: 300 MHz <sup>1</sup>H-NMR in CDCl<sub>3</sub> of molecule **II-16<sub>Te</sub>**.

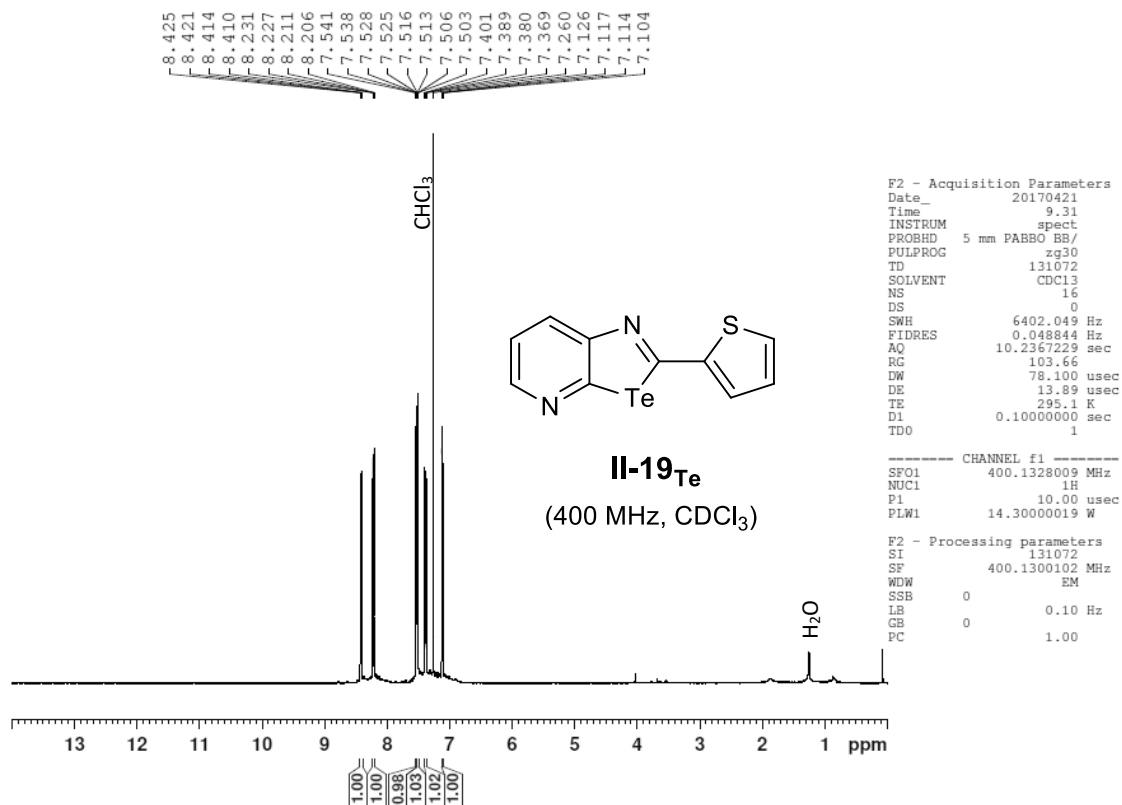
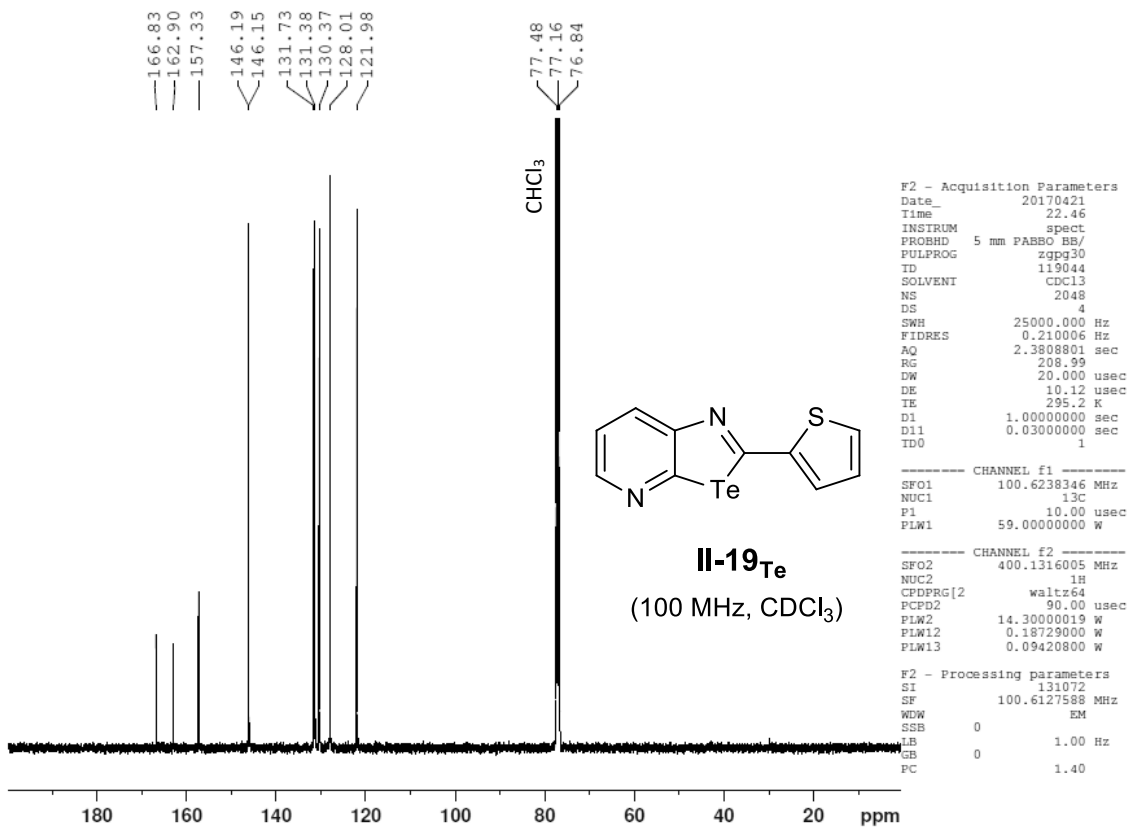
Figure VI - 53: 75 MHz <sup>13</sup>C-NMR in CDCl<sub>3</sub> of molecule II-16<sub>Te</sub>.Figure VI - 54: 300 MHz <sup>1</sup>H-NMR in CDCl<sub>3</sub> of molecule II-17<sub>Se</sub>.

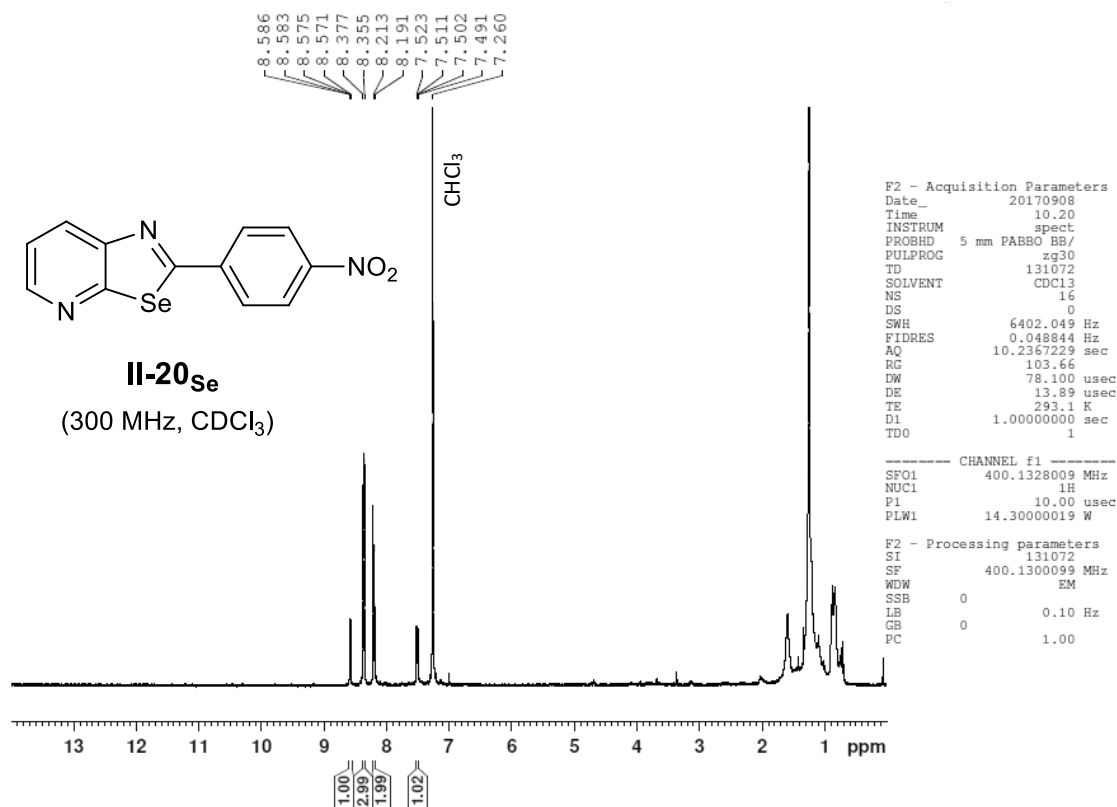
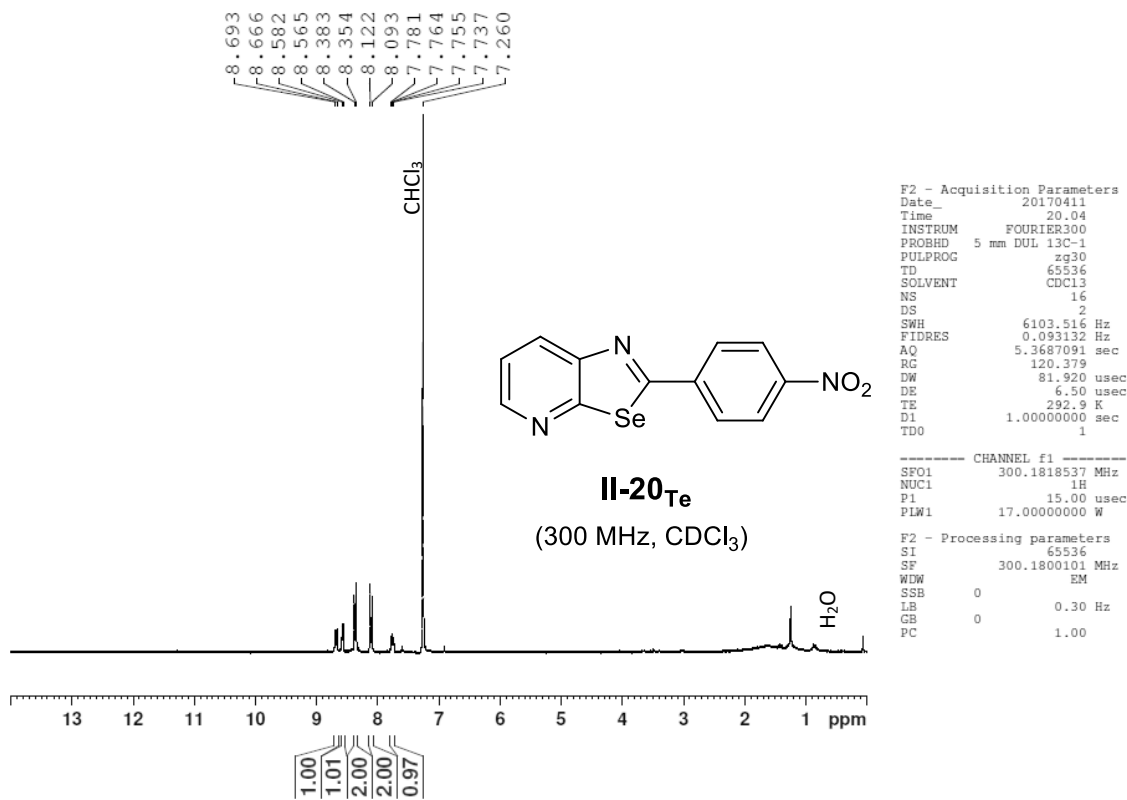
Figure VI - 55: 300 MHz <sup>1</sup>H-NMR in CDCl<sub>3</sub> of molecule II-17<sub>Te</sub>.Figure VI - 56: 75 MHz <sup>13</sup>C-NMR in CDCl<sub>3</sub> of molecule II-17<sub>Te</sub>.

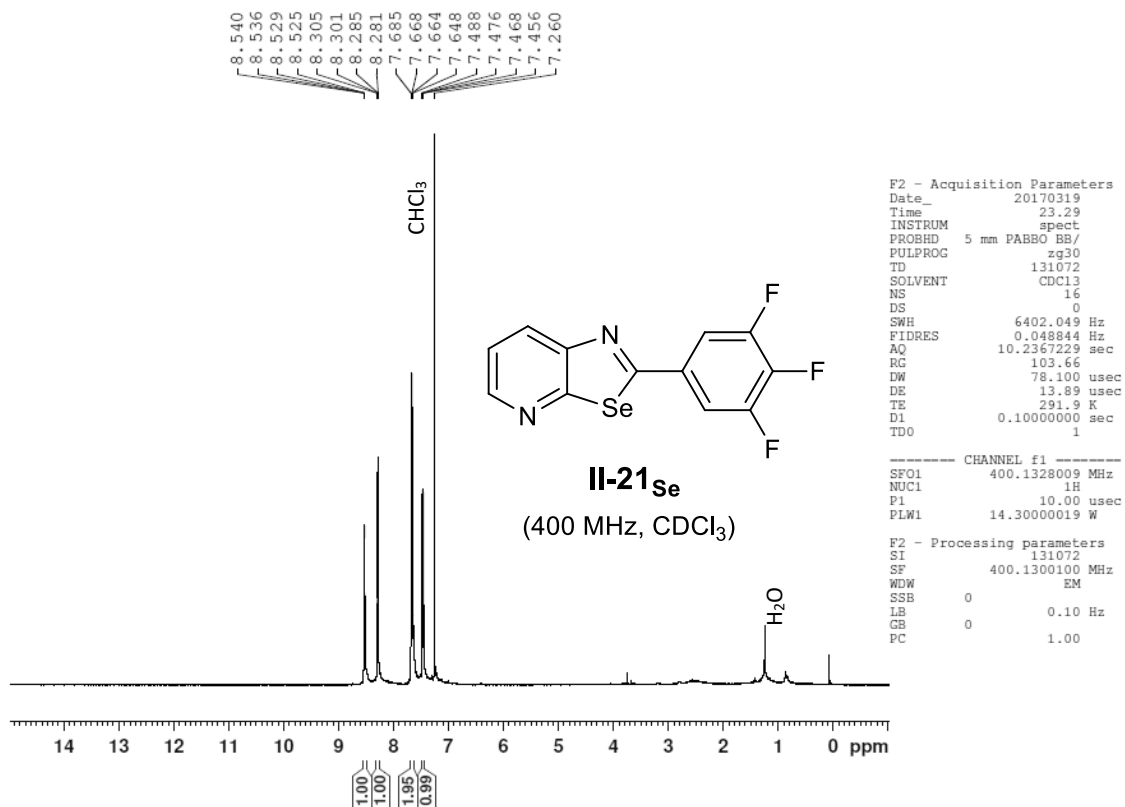
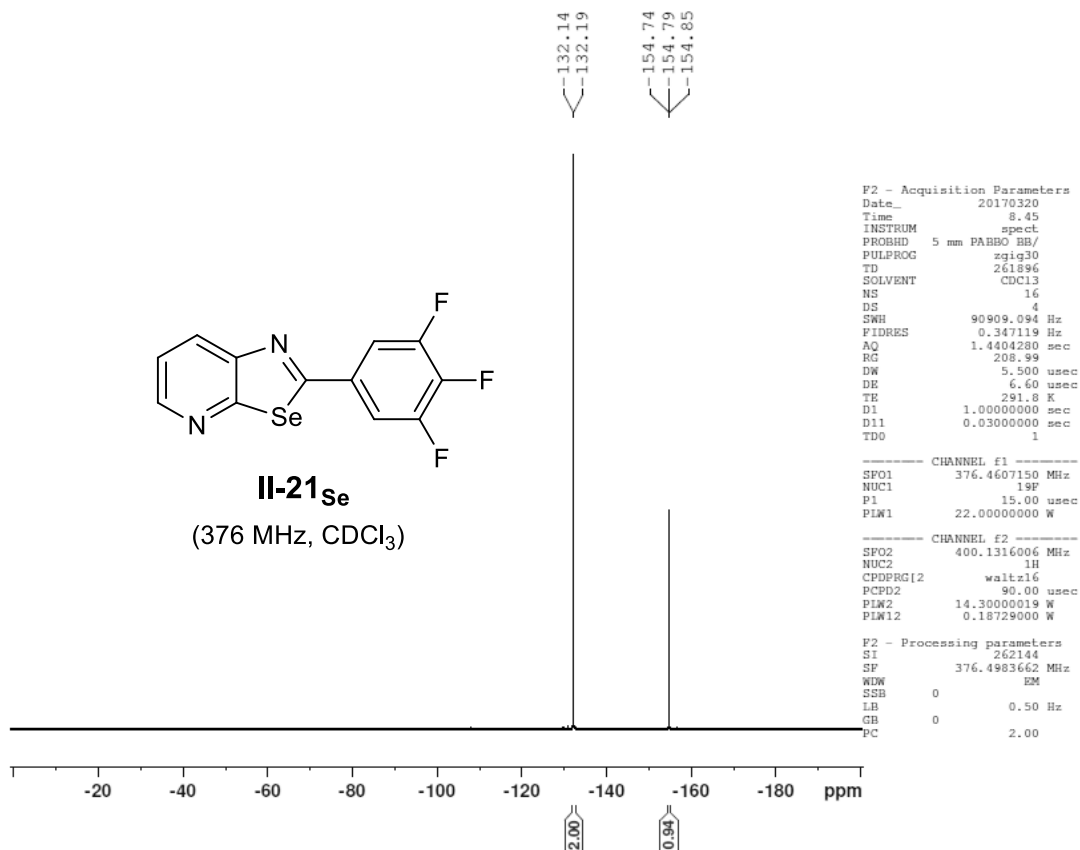
Figure VI - 57: 400 MHz <sup>1</sup>H-NMR in CDCl<sub>3</sub> of molecule **II-18<sub>Se</sub>**.Figure VI - 58: 100 MHz <sup>13</sup>C-NMR in CDCl<sub>3</sub> of molecule **II-18<sub>Se</sub>**.

Figure VI - 59: 400 MHz <sup>1</sup>H-NMR in CDCl<sub>3</sub> of molecule **II-18<sub>Te</sub>**.Figure VI - 60: 100 MHz <sup>13</sup>C-NMR in CDCl<sub>3</sub> of molecule **II-18<sub>Te</sub>**.

Figure VI - 61: 400 MHz <sup>1</sup>H-NMR in CDCl<sub>3</sub> of molecule II-19<sub>Se</sub>.Figure VI - 62: 100 MHz <sup>13</sup>C-NMR in CDCl<sub>3</sub> of molecule II-19<sub>Se</sub>.

Figure VI - 63: 400 MHz <sup>1</sup>H-NMR in CDCl<sub>3</sub> of molecule **II-19<sub>Te</sub>**.Figure VI - 64: 100 MHz <sup>13</sup>C-NMR in CDCl<sub>3</sub> of molecule **II-19<sub>Te</sub>**.

Figure VI - 65: 300 MHz <sup>1</sup>H-NMR in CDCl<sub>3</sub> of molecule II-20<sub>Se</sub>.Figure VI - 66: 300 MHz <sup>1</sup>H-NMR in CDCl<sub>3</sub> of molecule II-20<sub>Se</sub>.

Figure VI - 67: 400 MHz <sup>1</sup>H-NMR in CDCl<sub>3</sub> of molecule **II-21<sub>Se</sub>**.Figure VI - 68: 376 MHz <sup>19</sup>F-NMR in CDCl<sub>3</sub> of molecule **II-21<sub>Se</sub>**.

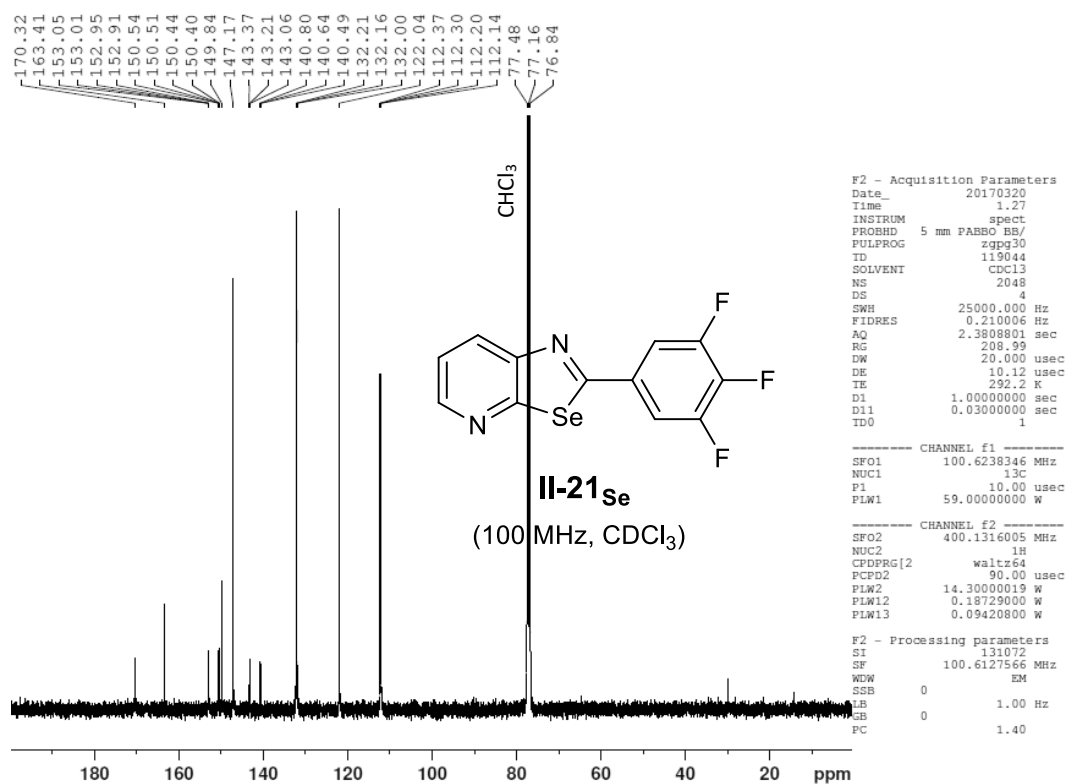


Figure VI - 69: 100 MHz <sup>13</sup>C-NMR in CDCl<sub>3</sub> of molecule **II-21<sub>Se</sub>**. Due to <sup>13</sup>C-<sup>19</sup>F coupling: Peak 151.8 splits into 153.05, 153.01, 152.95, 150.54, 150.51, 150.44 and 150.40; Peak 141.9 splits into 143.37, 143.21, 143.06, 140.80, 140.64 and 140.49; Peak 132.2 splits into 132.21 and 132.16; Peak 112.3 splits into 112.37, 112.30, 112.20 and 112.14.

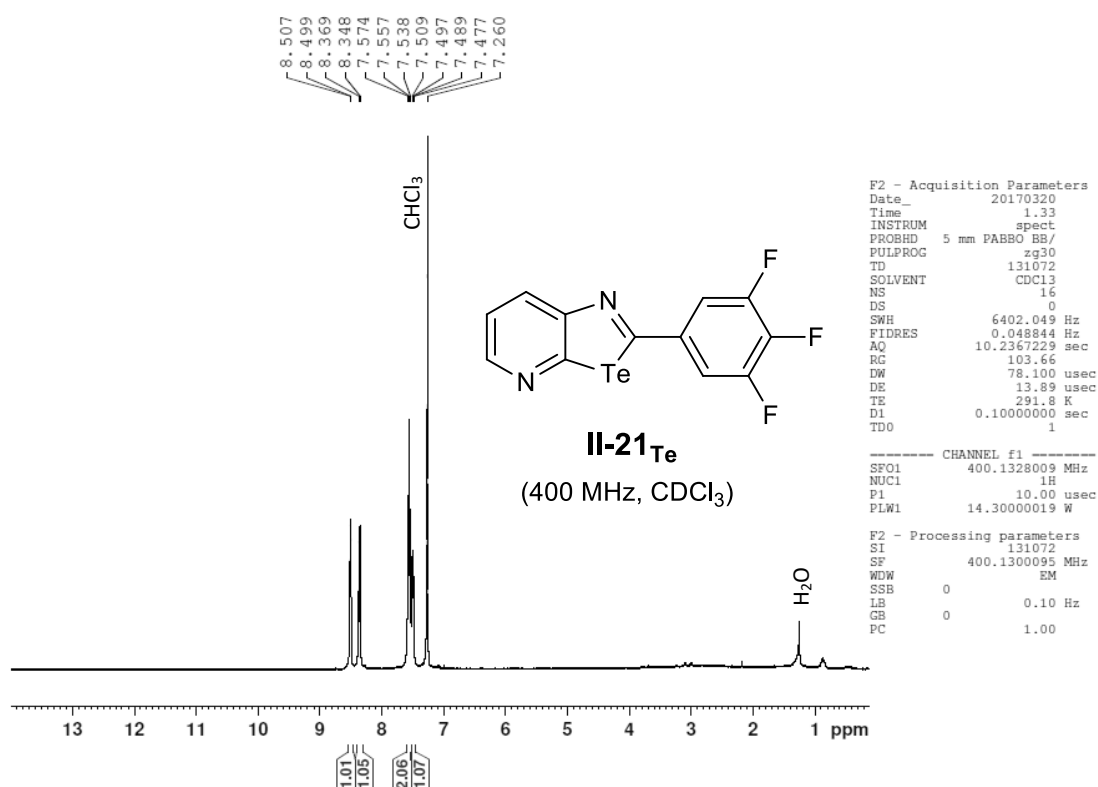
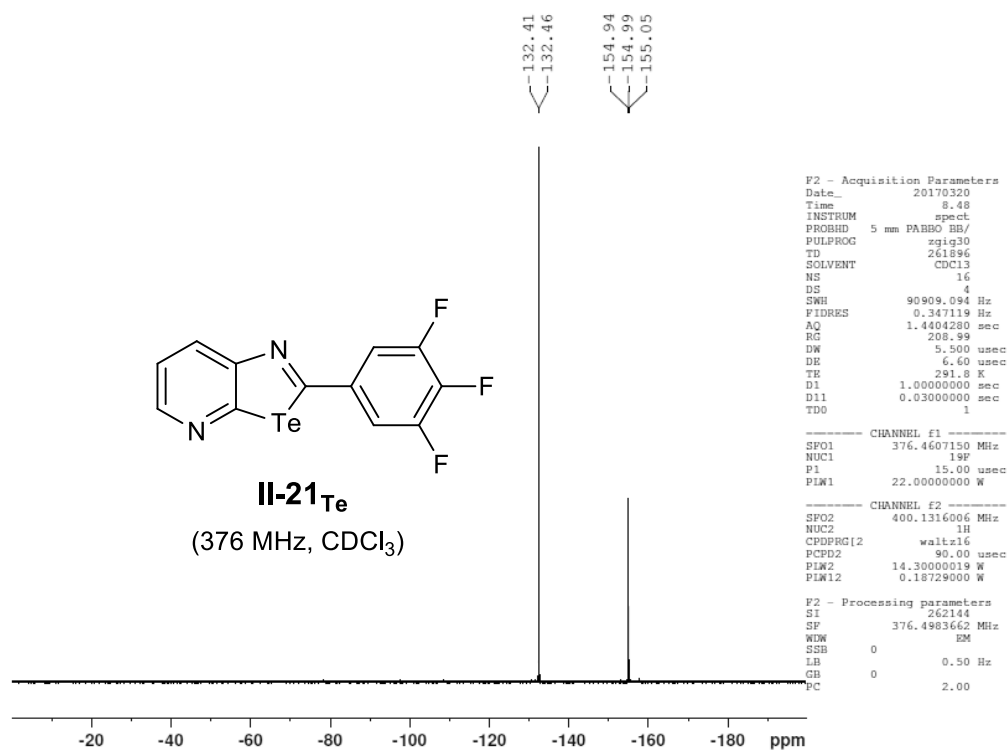
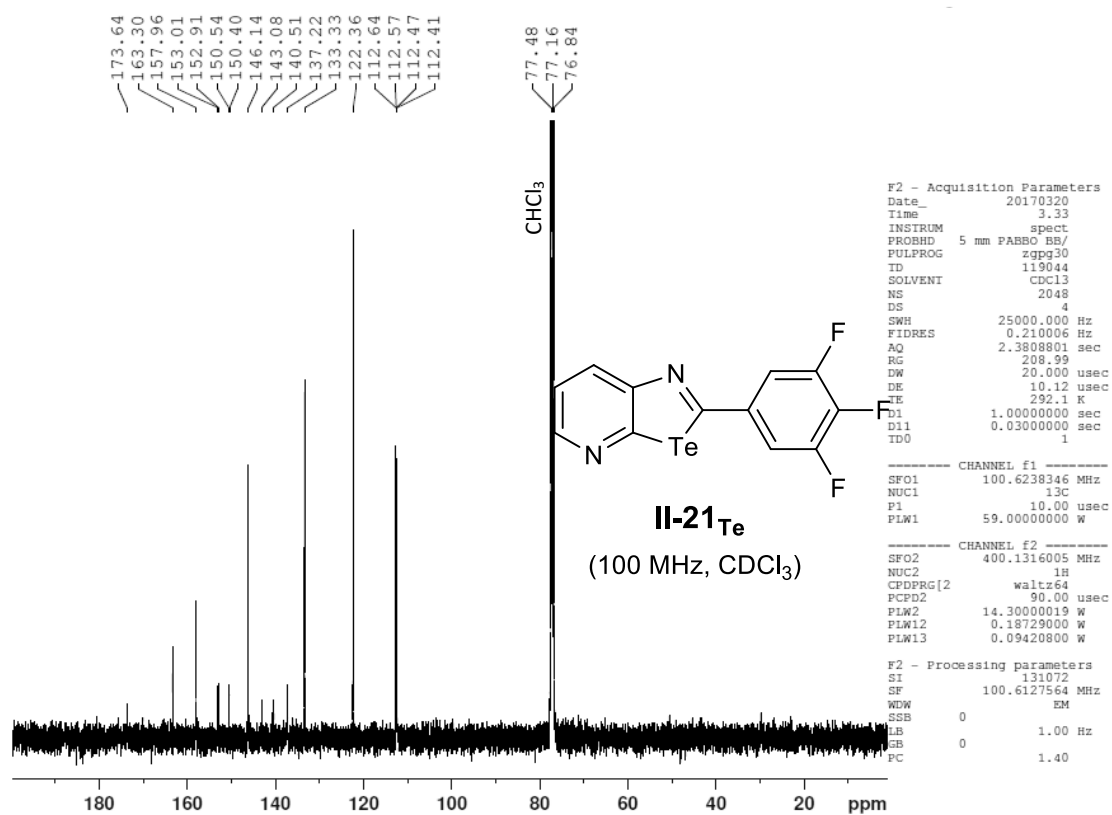
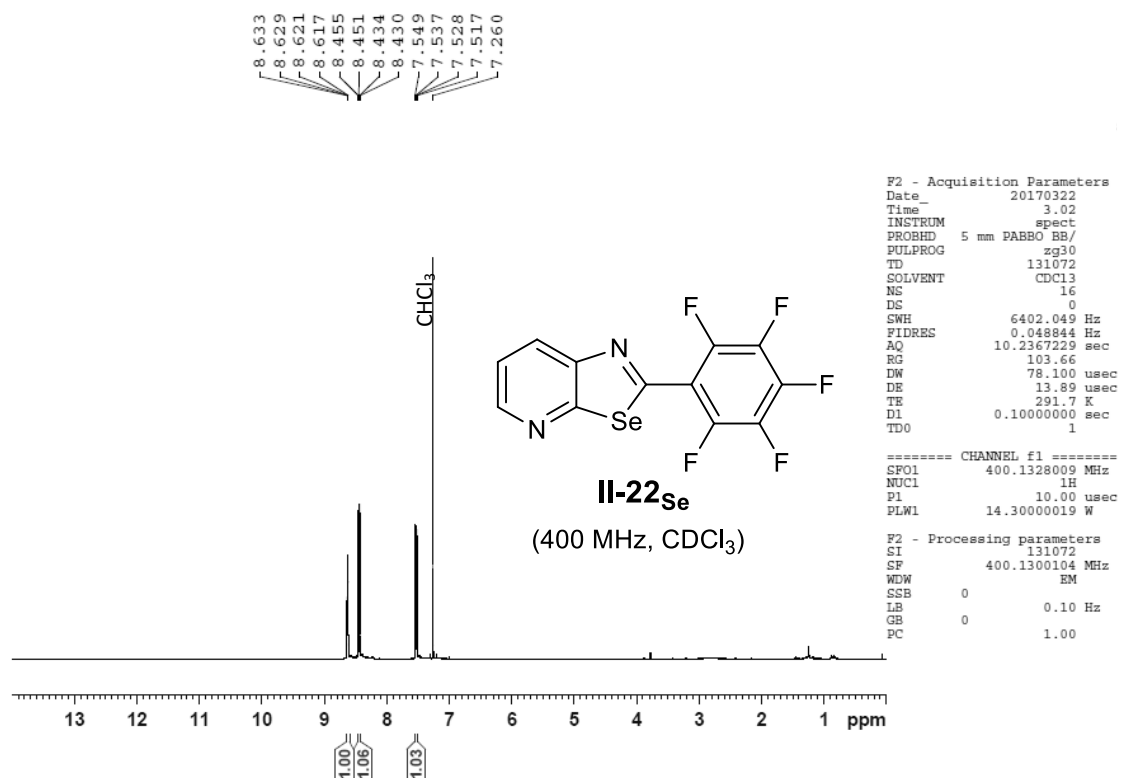
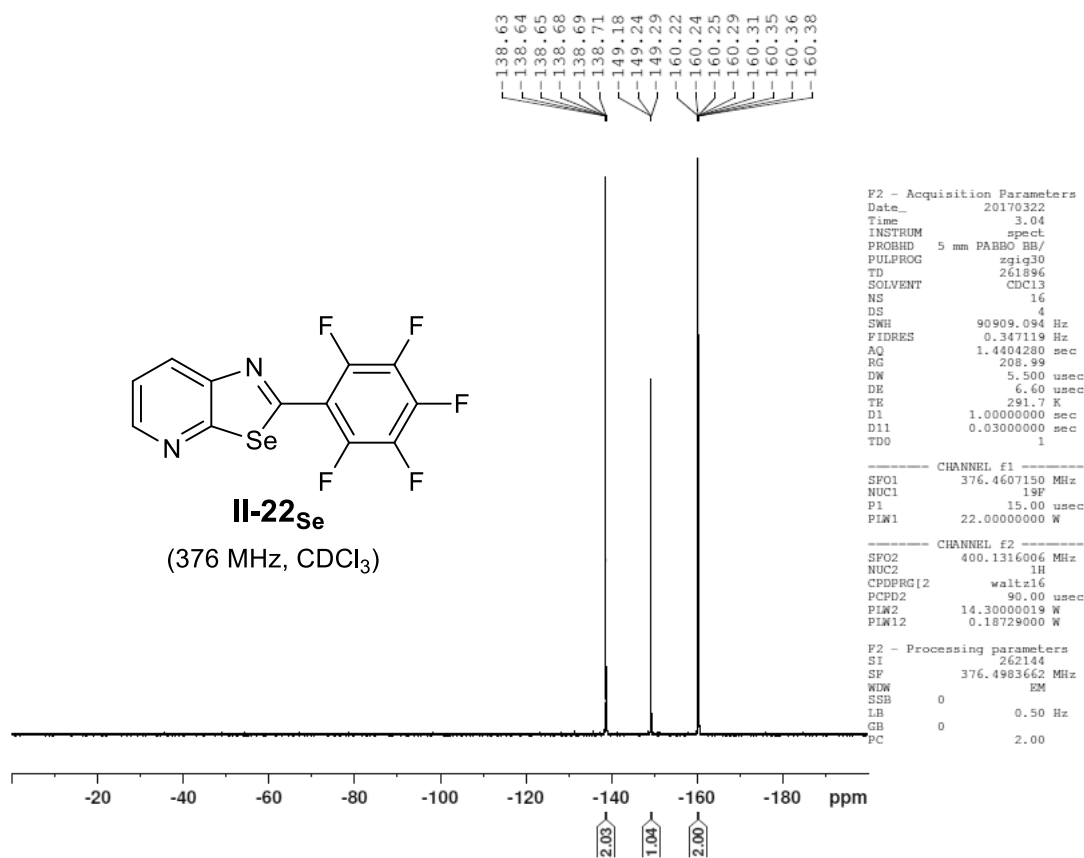


Figure VI - 70: 400 MHz <sup>1</sup>H-NMR in CDCl<sub>3</sub> of molecule **II-21<sub>Te</sub>**.

Figure VI - 71: 376 MHz <sup>19</sup>F-NMR in CDCl<sub>3</sub> of molecule II-21<sub>Te</sub>.Figure VI - 72: 100 MHz <sup>13</sup>C-NMR in CDCl<sub>3</sub> of molecule II-21<sub>Te</sub>. Due to <sup>13</sup>C-<sup>19</sup>F coupling: Peak 151.7 splits into 153.01, 152.91, 150.54 and 150.40; Peak 141.8 splits into 143.08 and 140.51; Peak 112.5 splits into 112.64, 112.57, 112.47 and 112.41.

Figure VI - 73: 400 MHz <sup>1</sup>H-NMR in CDCl<sub>3</sub> of molecule **II-22<sub>se</sub>**.Figure VI - 74: 376 MHz <sup>19</sup>F-NMR in CDCl<sub>3</sub> of molecule **II-22<sub>se</sub>**.

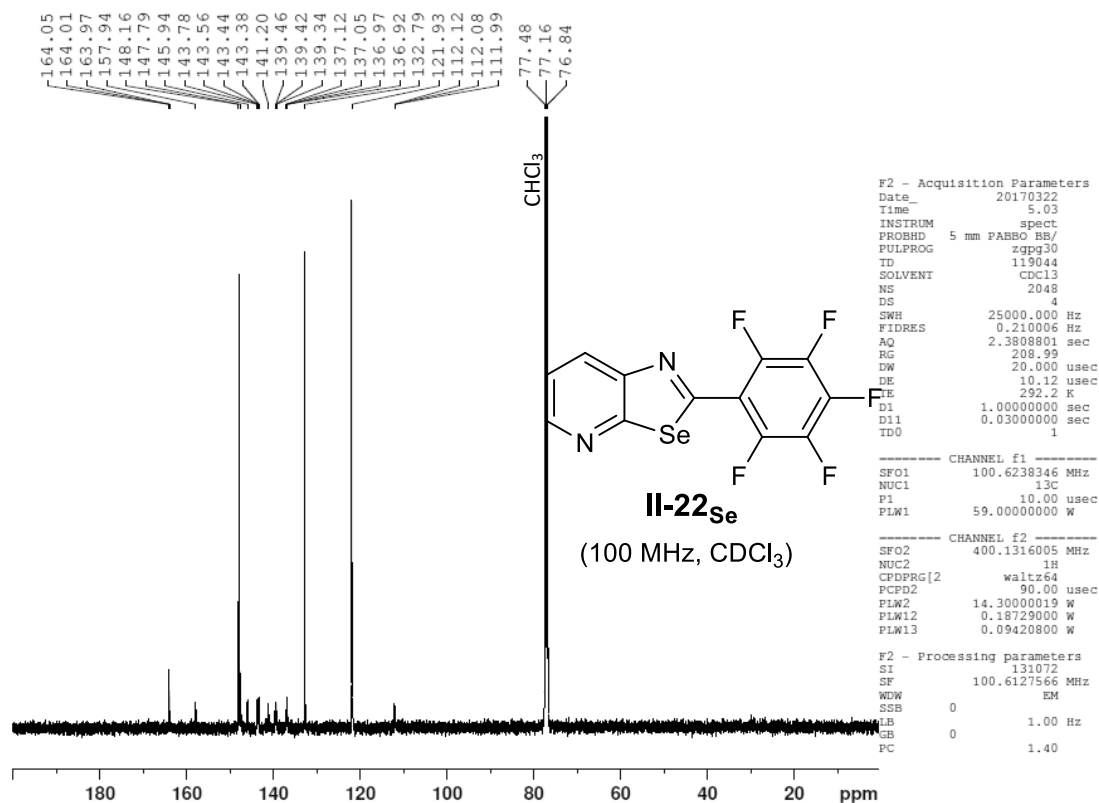


Figure VI - 75: 100 MHz <sup>13</sup>C-NMR in CDCl<sub>3</sub> of molecule II-22<sub>Se</sub>. Due to <sup>13</sup>C-<sup>19</sup>F coupling: Peak 164.0 splits into 164.05, 164.01 and 163.97; Peak 144.7 splits into 145.94, 143.56, 143.44 and 143.38; Peak 142.5 splits into 143.78 and 141.20; Peak 138.3 splits into 139.46, 139.42, 139.34, 137.12, 137.05, 136.97 and 136.92.

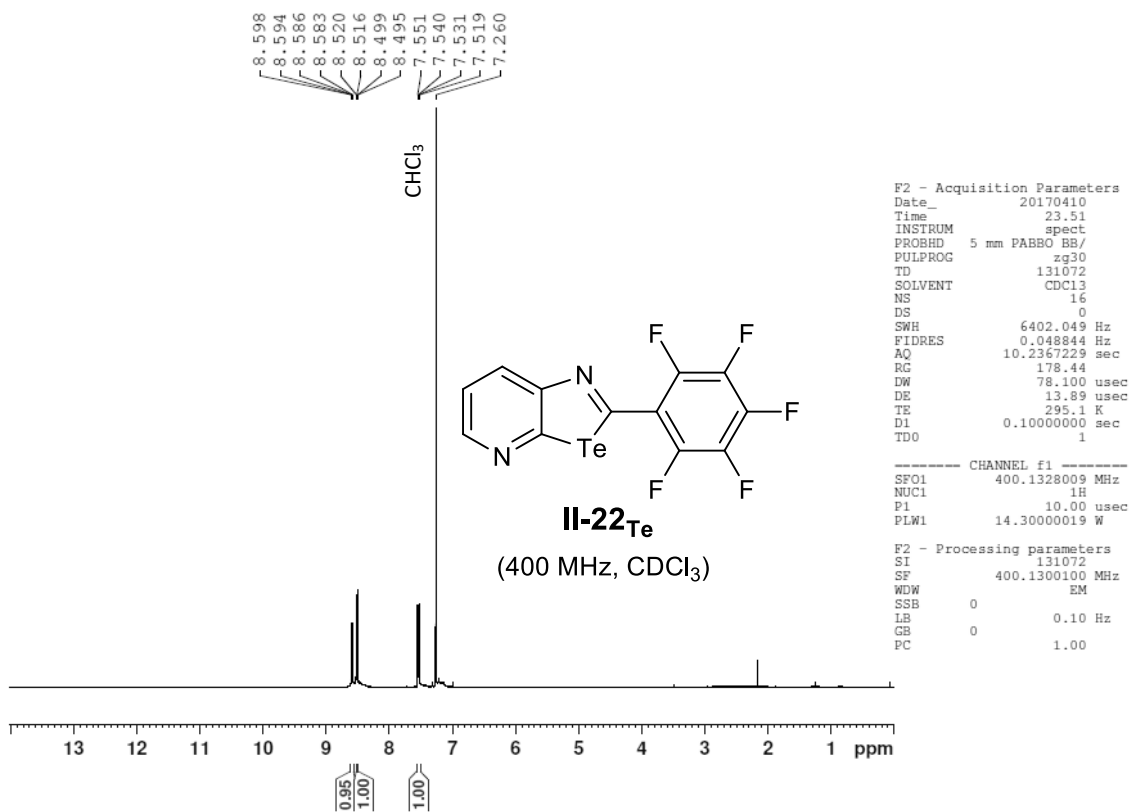
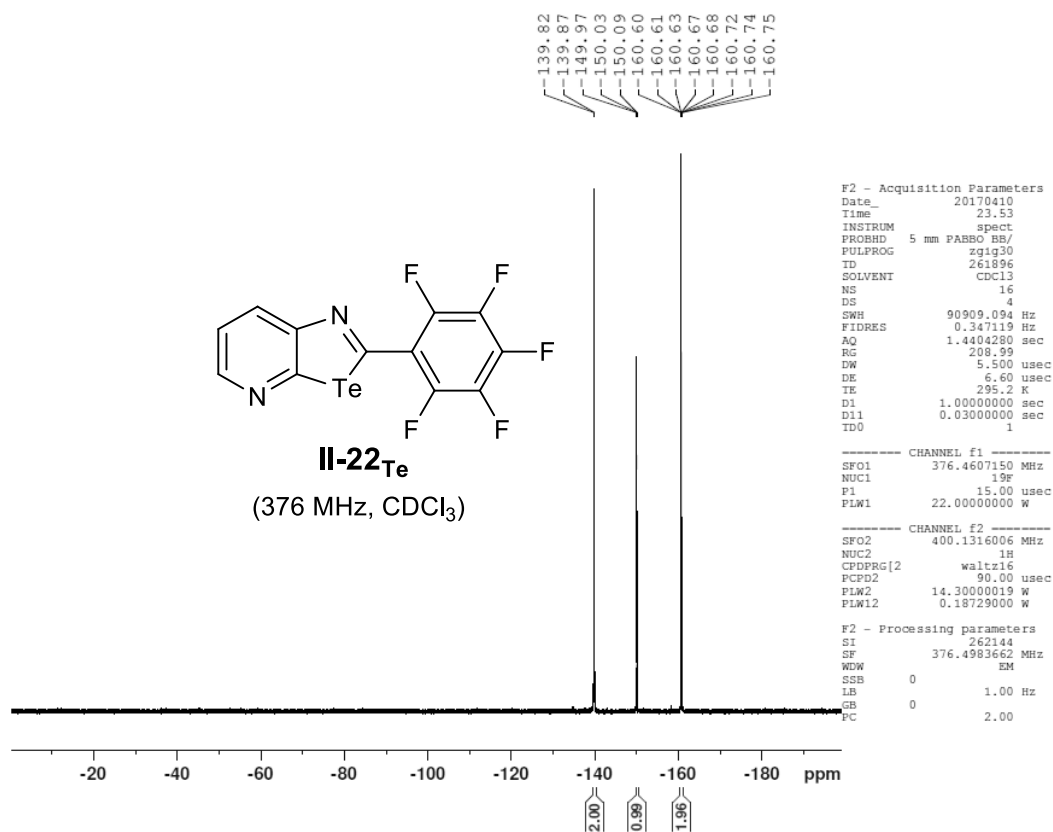
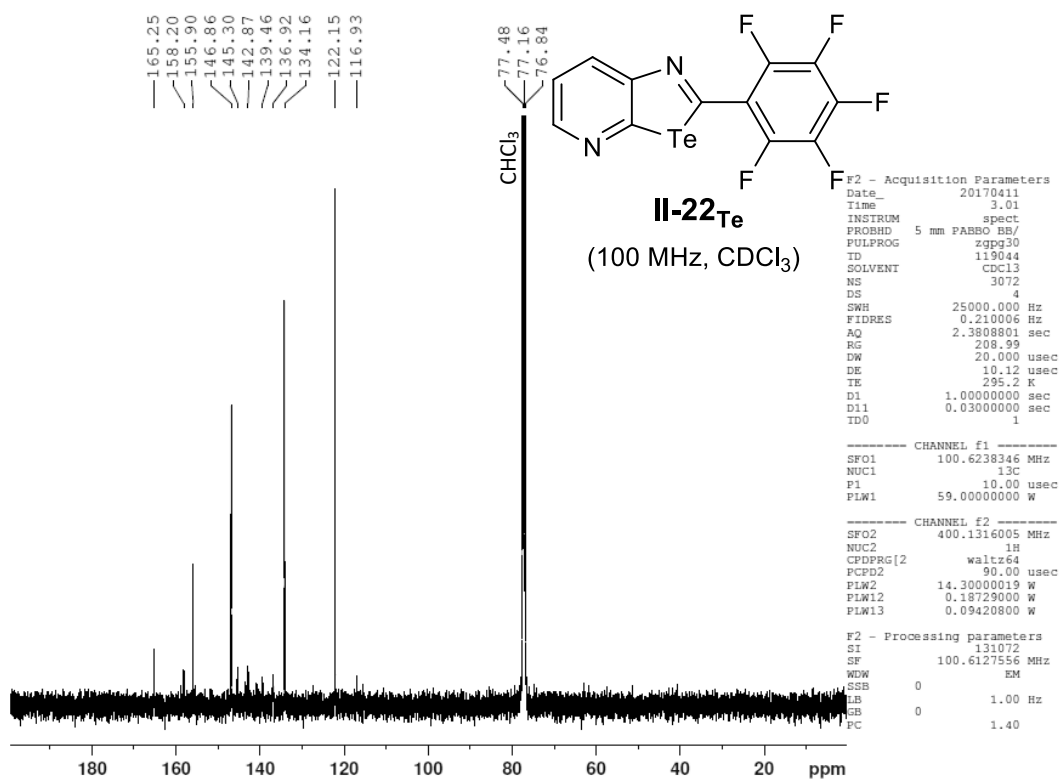
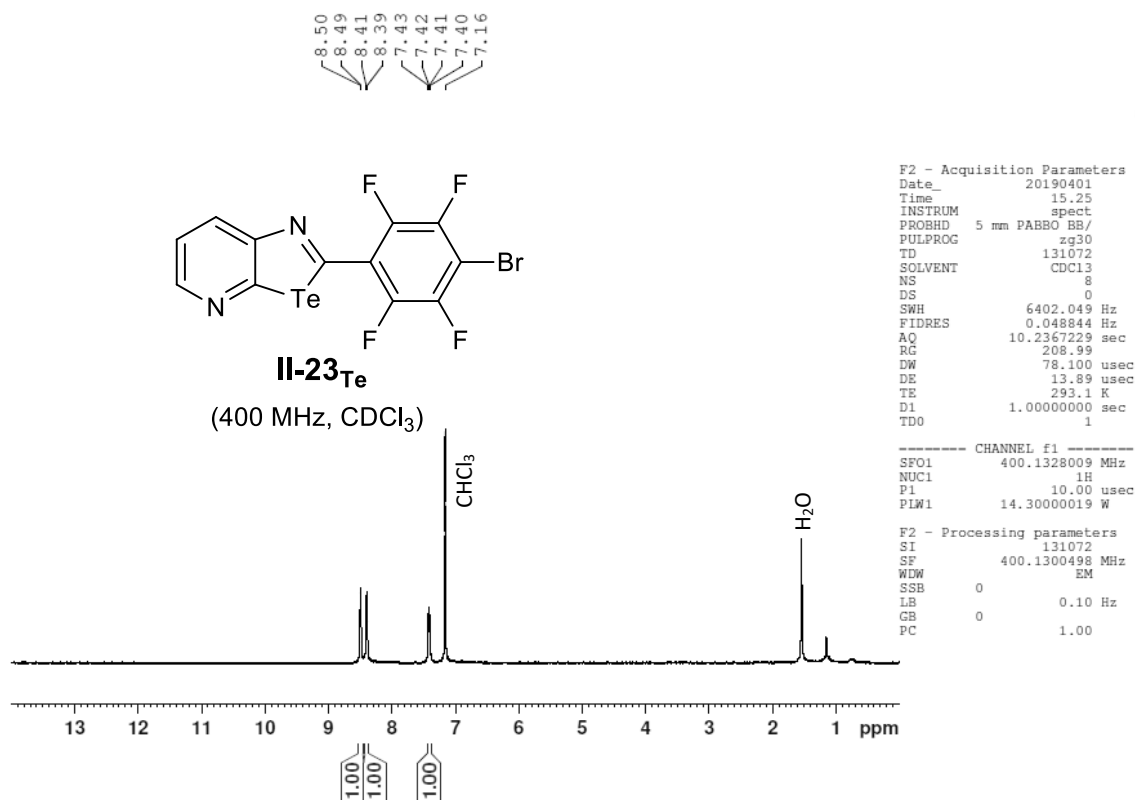
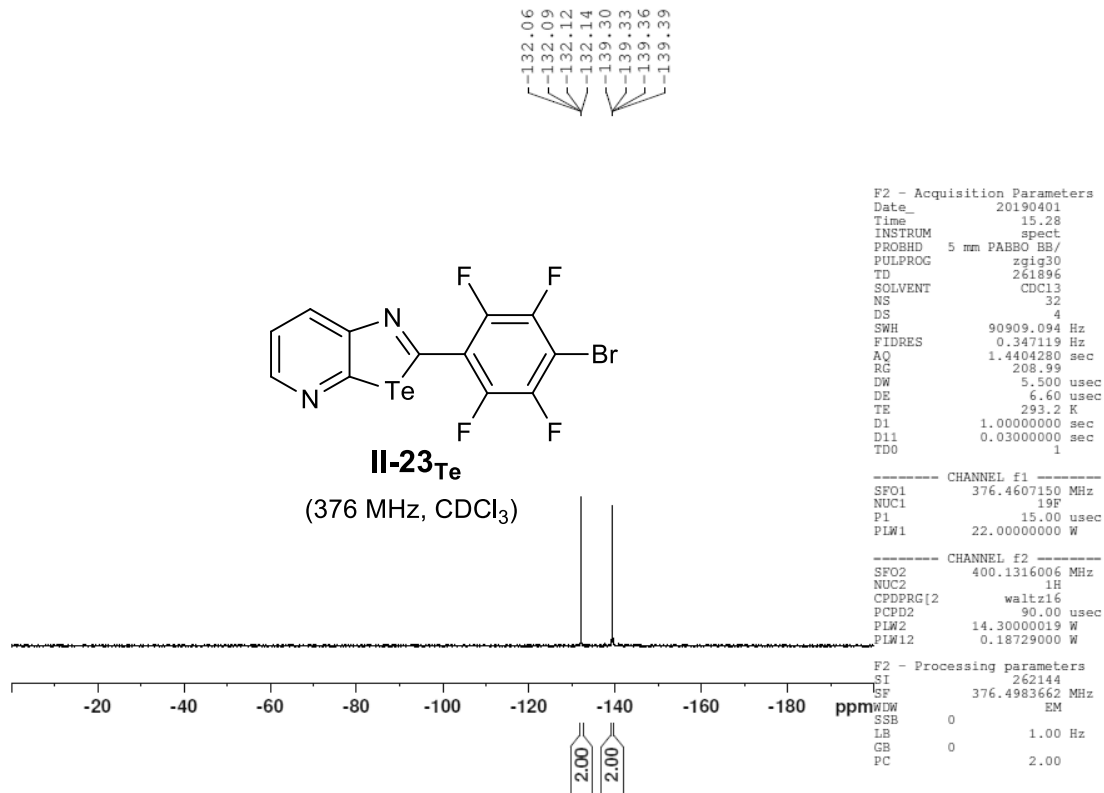


Figure VI - 76: 400 MHz <sup>1</sup>H-NMR in CDCl<sub>3</sub> of molecule II-22<sub>Te</sub>.

Figure VI - 77: 376 MHz <sup>19</sup>F-NMR in CDCl<sub>3</sub> of molecule II-22<sub>Te</sub>.Figure VI - 78: 100 MHz <sup>13</sup>C-NMR in CDCl<sub>3</sub> of molecule II-22<sub>Te</sub>. Due to <sup>13</sup>C-<sup>19</sup>F coupling: Peak 144.0 splits into 146.86 and 145.30; Peak 142.2 splits into 142.87 and 139.46; 138.2 splits into 140.89 and 136.

Figure VI - 79: 400 MHz <sup>1</sup>H-NMR in CDCl<sub>3</sub> of molecule **II-23<sub>Te</sub>**.Figure VI - 80: 376 MHz <sup>19</sup>F-NMR in CDCl<sub>3</sub> of molecule **II-23<sub>Te</sub>**.

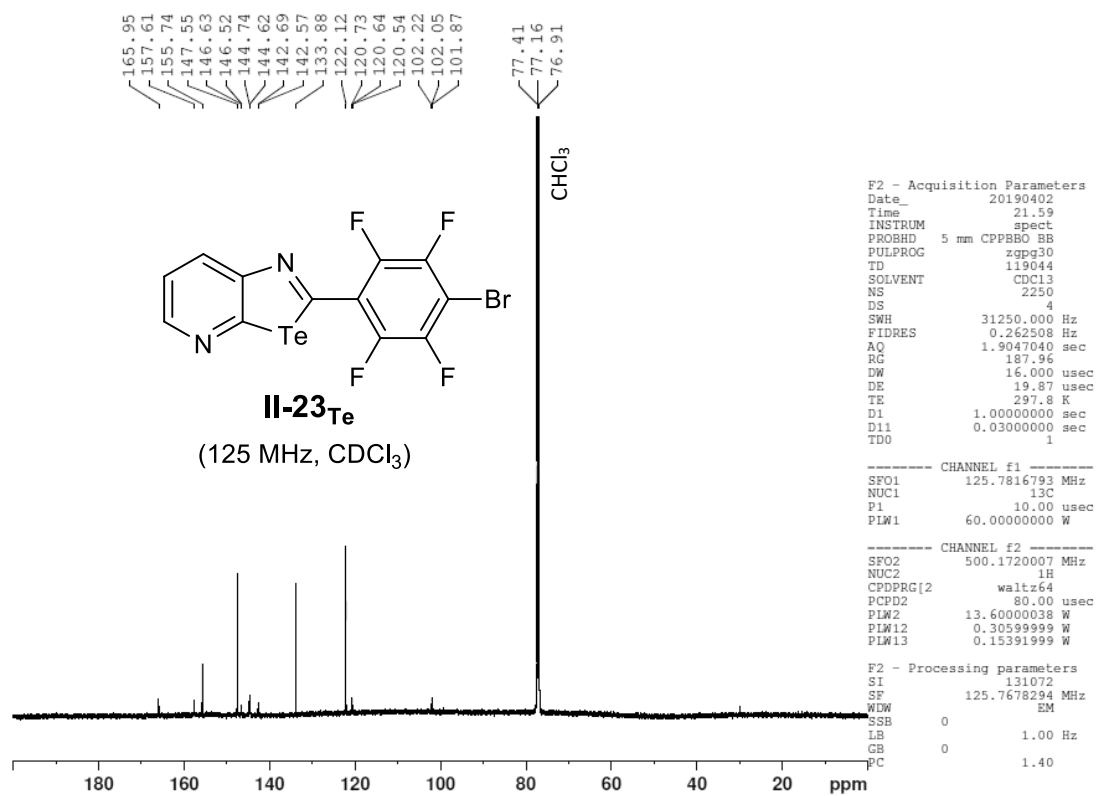


Figure VI - 81: 125 MHz <sup>13</sup>C-NMR in CDCl<sub>3</sub> of molecule II-23<sub>Te</sub>. Due to <sup>13</sup>C-<sup>19</sup>F coupling: Peak 145.7 splits into 146.63, 146.52 and 144.374; Peak 143.7 splits into 144.74, 142.69 and 142.57.

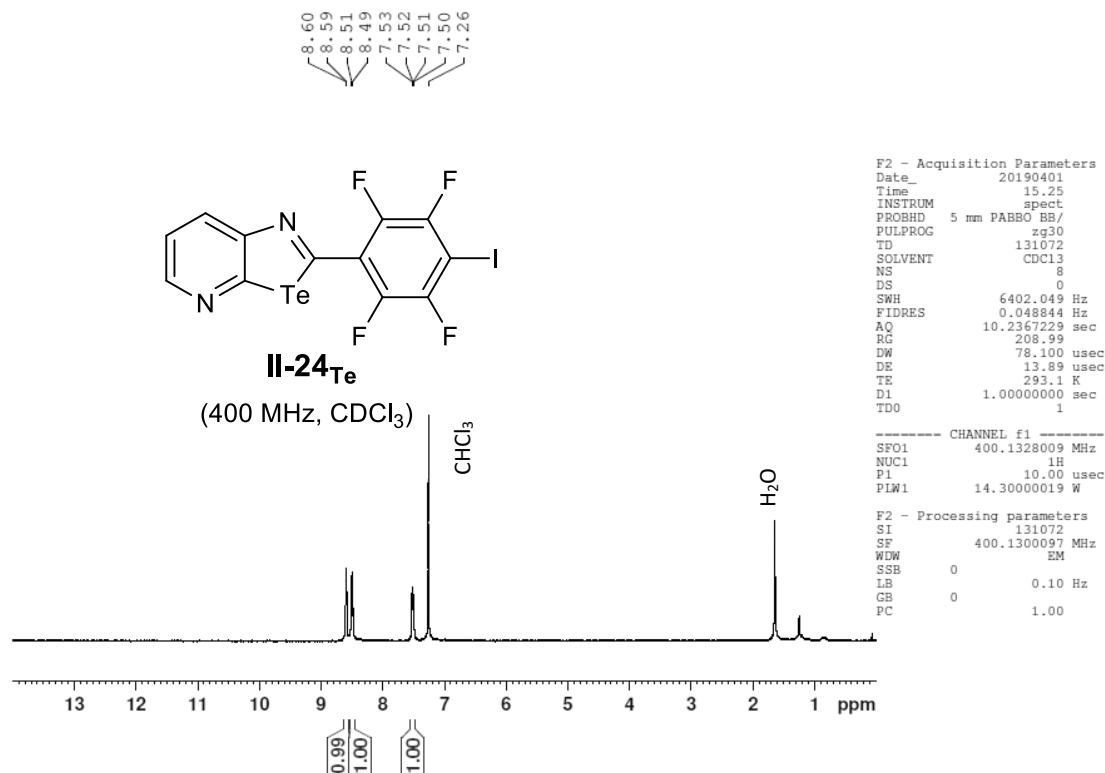
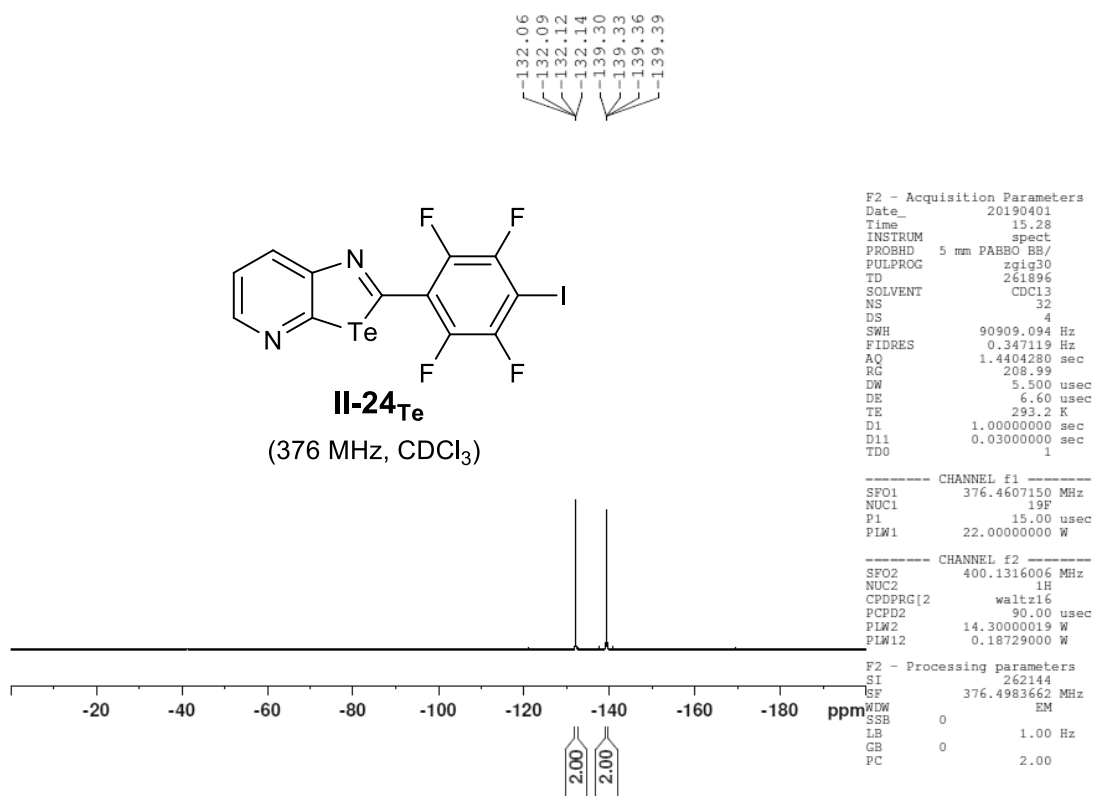
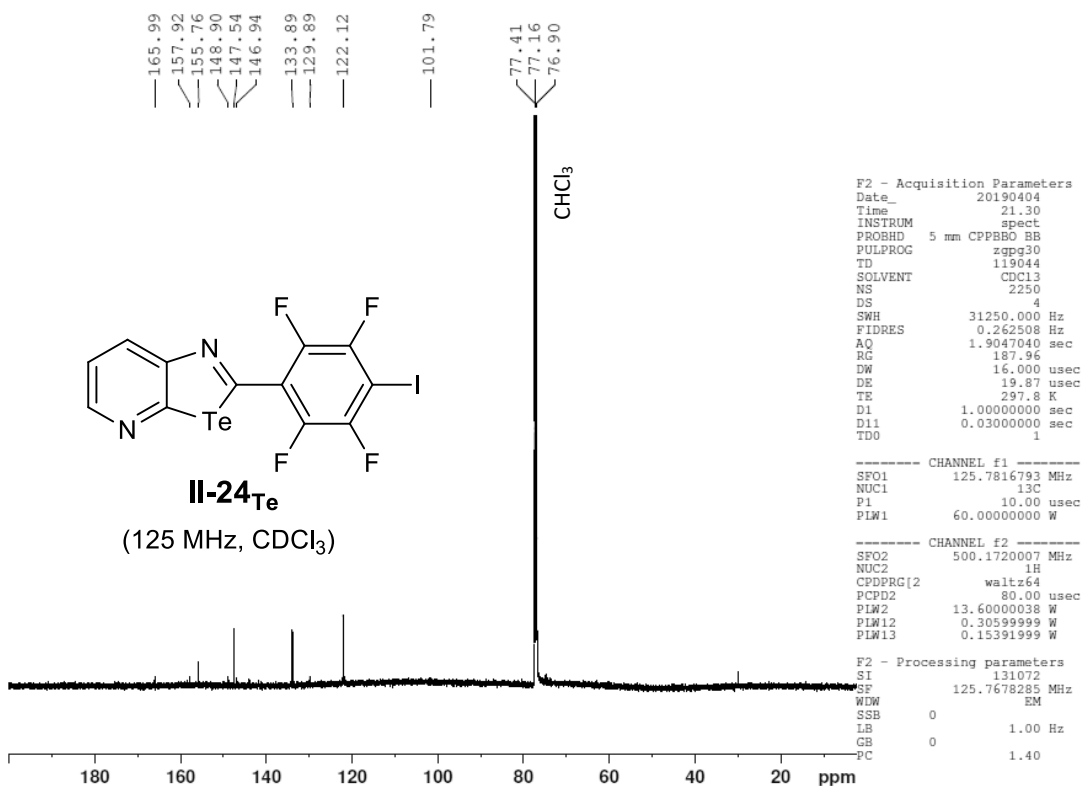
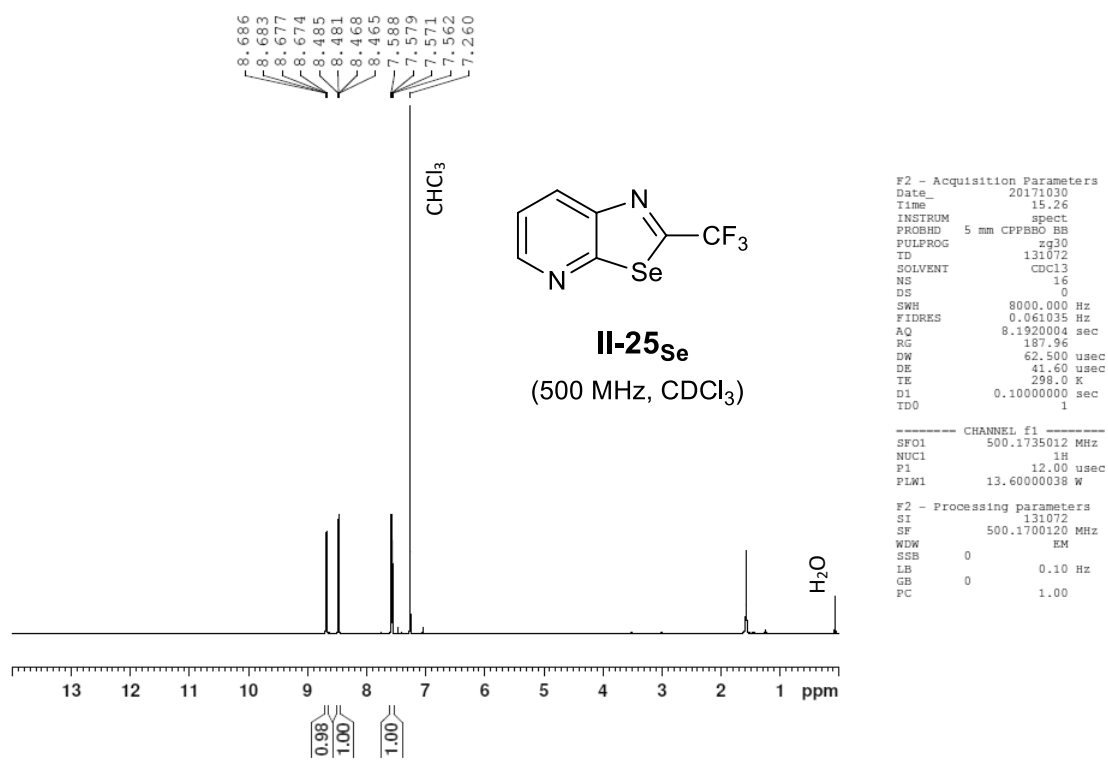
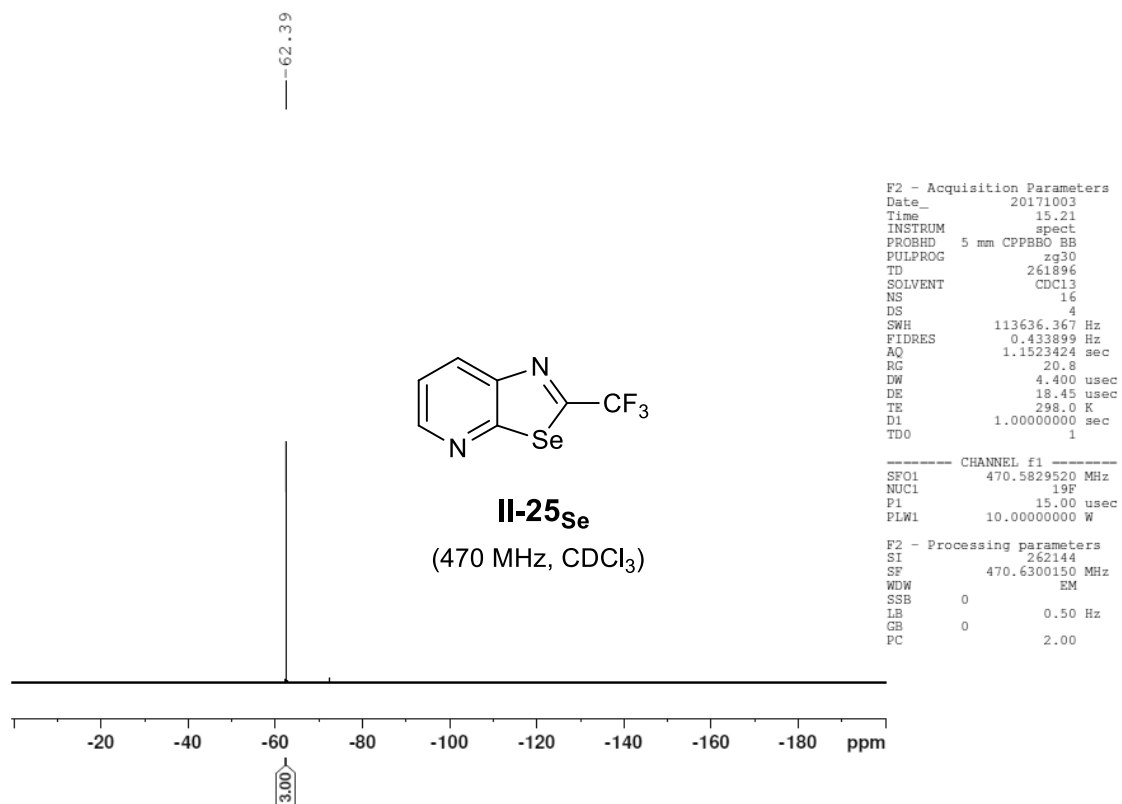


Figure VI - 82: 400 MHz <sup>1</sup>H-NMR in CDCl<sub>3</sub> of molecule II-24<sub>Te</sub>.

Figure VI - 83: 376 MHz <sup>19</sup>F-NMR in CDCl<sub>3</sub> of molecule II-24<sub>Te</sub>.Figure VI - 84: 125 MHz <sup>13</sup>C-NMR in CDCl<sub>3</sub> of molecule II-24<sub>Te</sub>. Due to <sup>13</sup>C-<sup>19</sup>F coupling: Peak 147.9 splits into 148.89 and 146.94; Peak 142.9 splits into 143.94 and 141.88.

Figure VI - 85: 500 MHz <sup>1</sup>H-NMR in CDCl<sub>3</sub> of molecule **II-25<sub>Se</sub>**.Figure VI - 86: 470 MHz <sup>19</sup>F-NMR in CDCl<sub>3</sub> of molecule **II-25<sub>Se</sub>**.

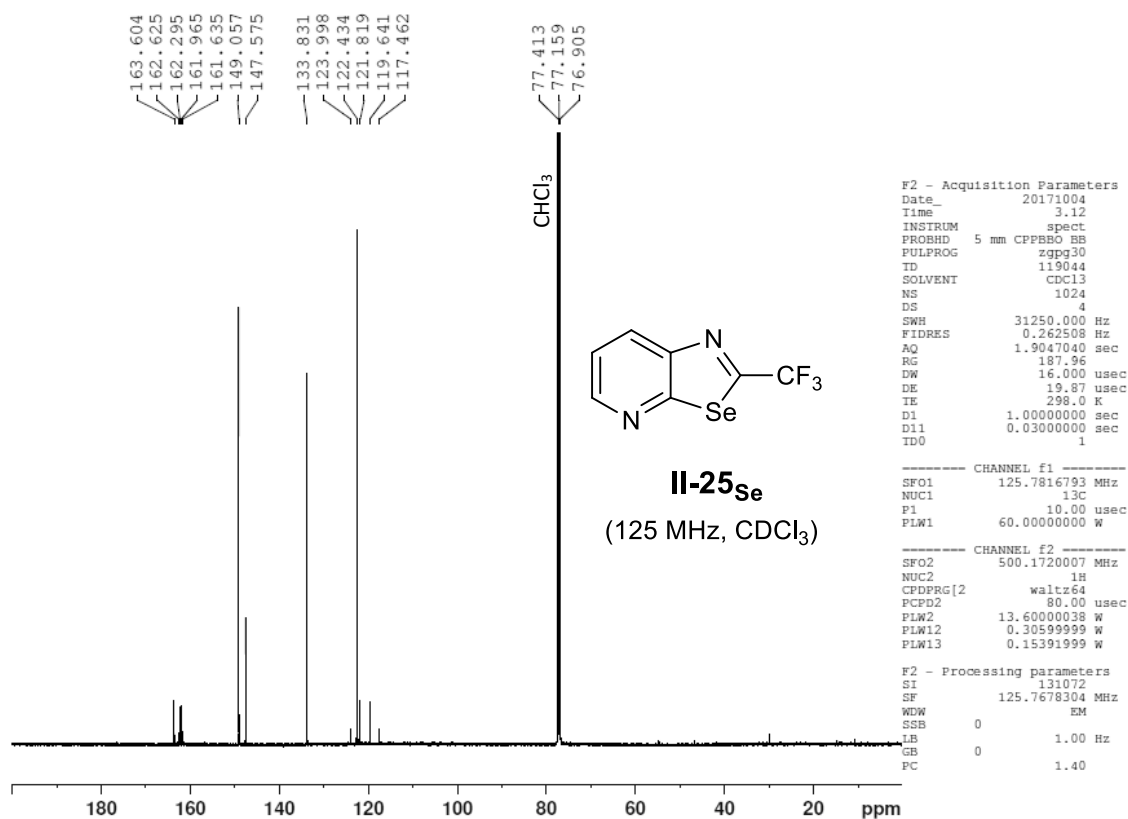


Figure VI - 87: 125 MHz <sup>13</sup>C-NMR in CDCl<sub>3</sub> of molecule II-25<sub>Se</sub>. Due to <sup>13</sup>C-<sup>19</sup>F coupling: Peak 162.1 splits into 162.63, 162.30, 161.97 and 161.58; Peak 120.7 splits into 124.0, 121.82, 119.64 and 117.46.

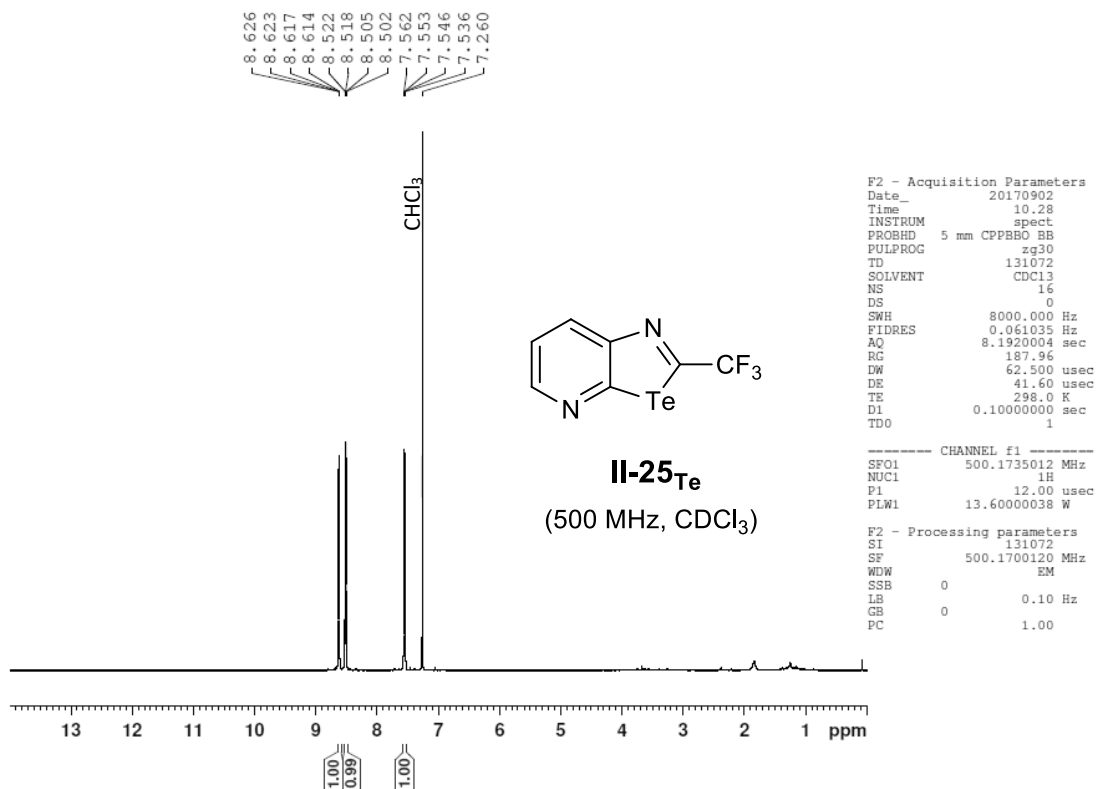
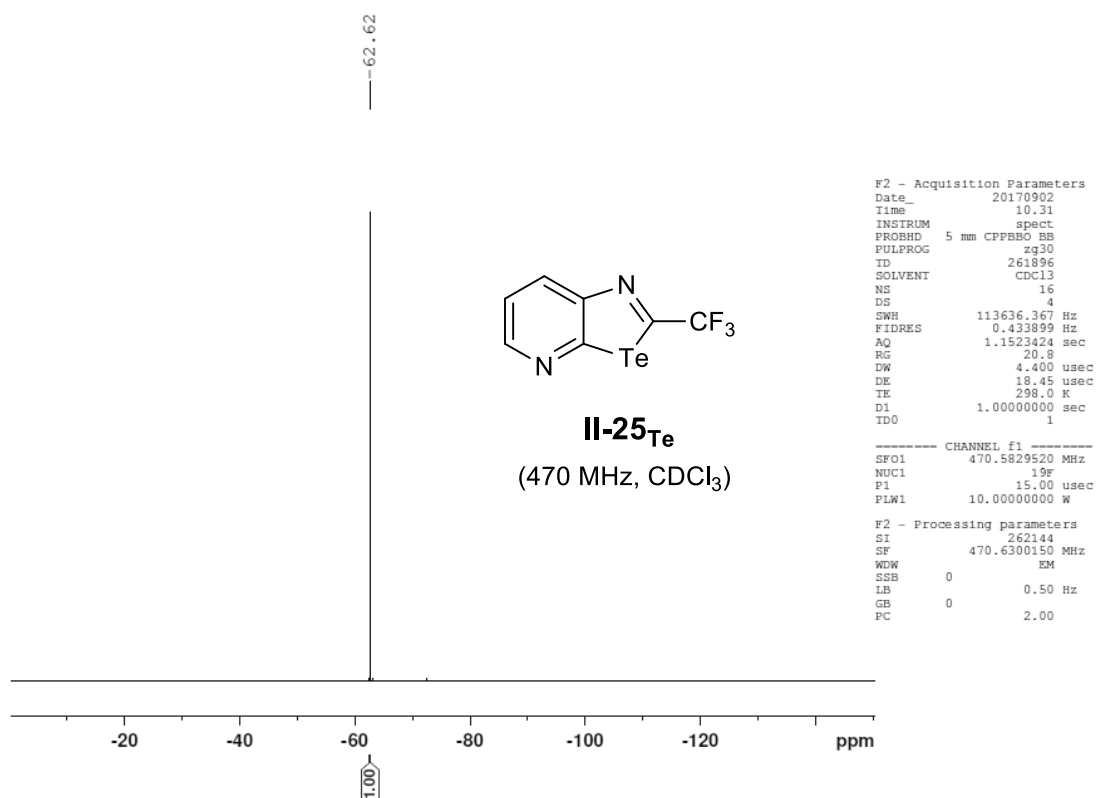
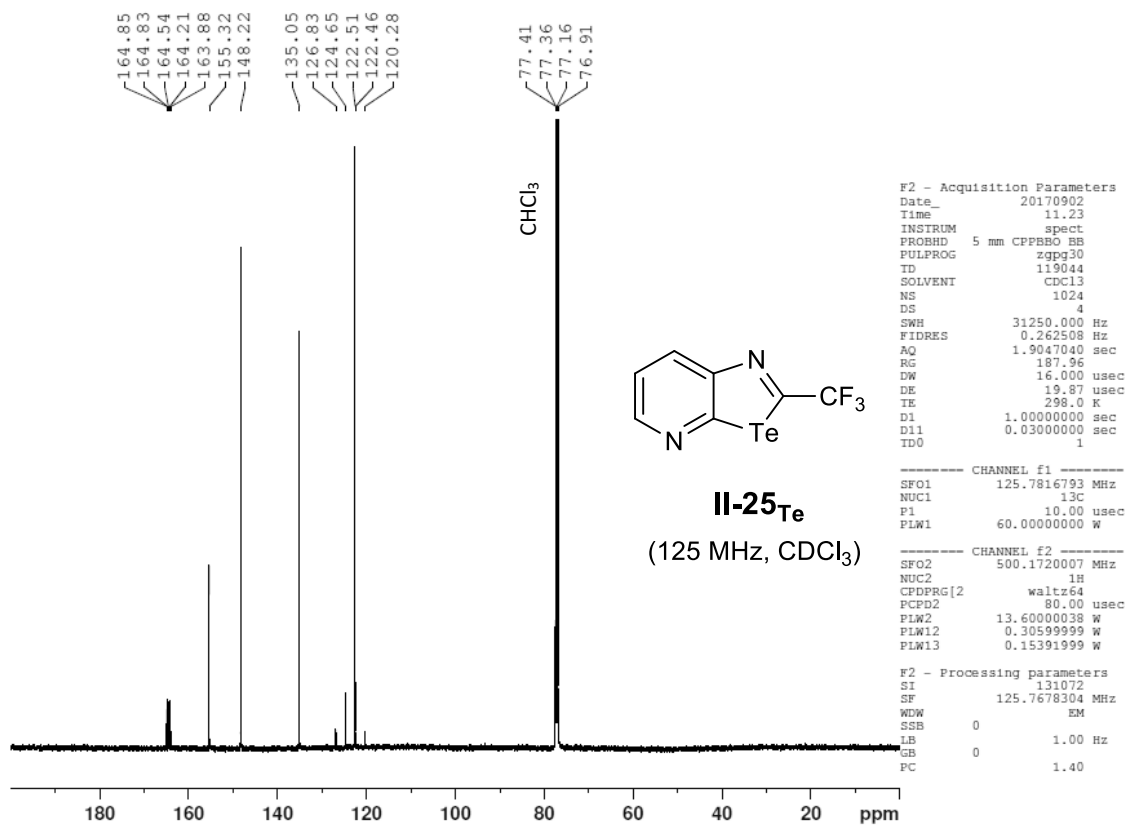
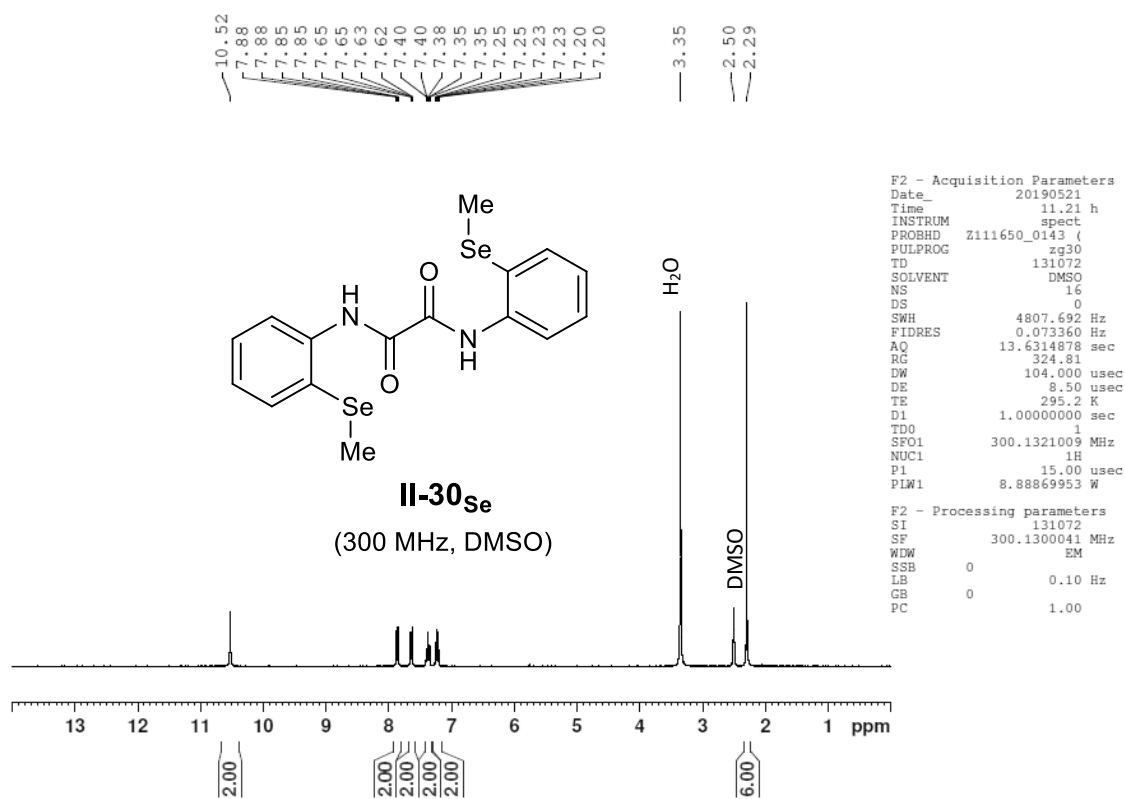
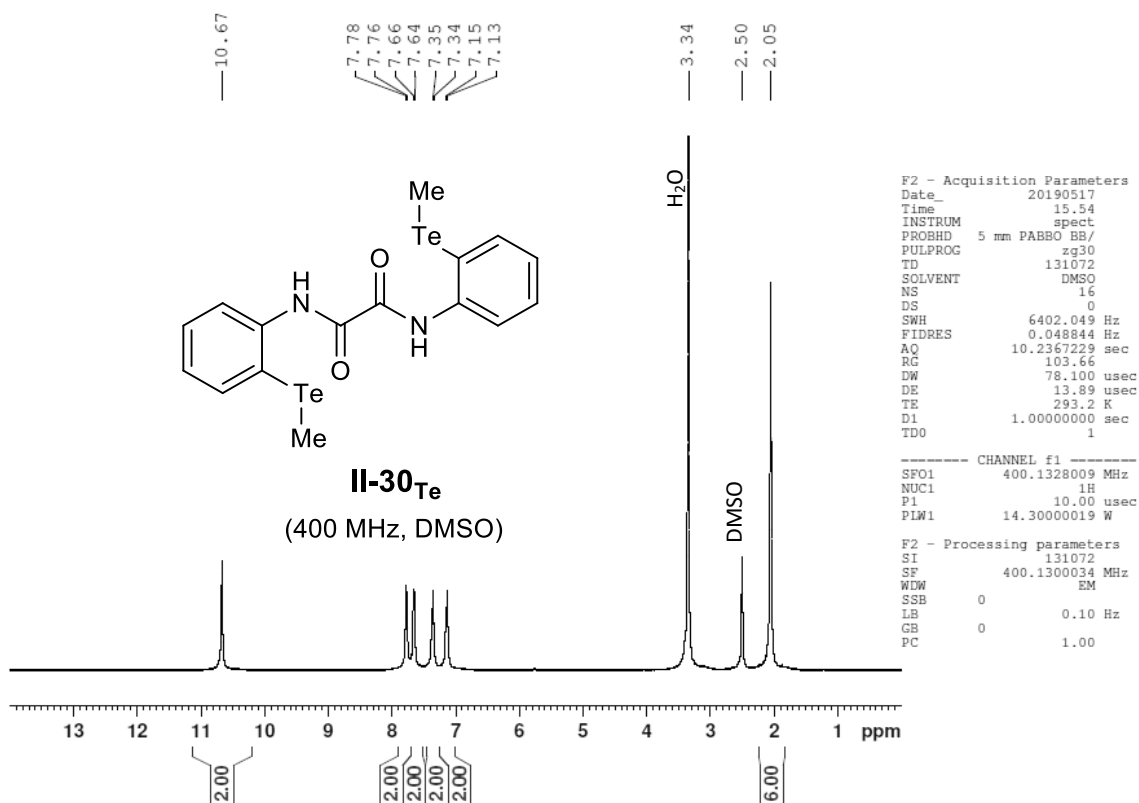
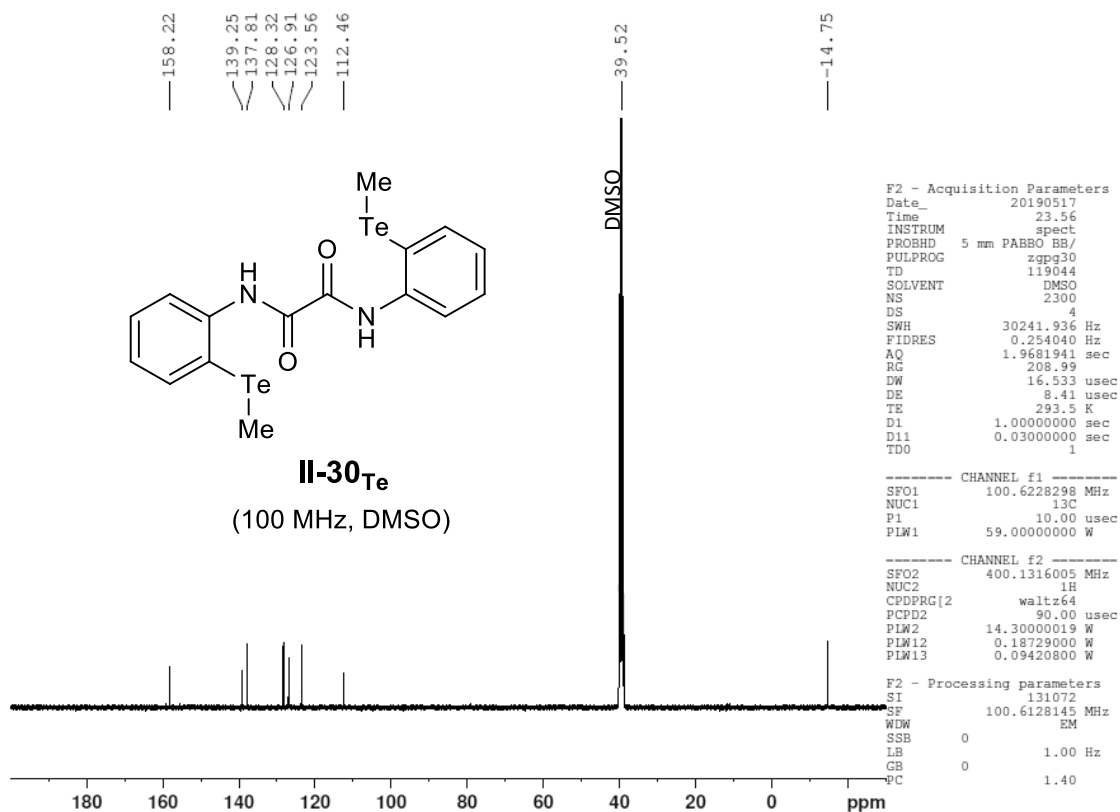
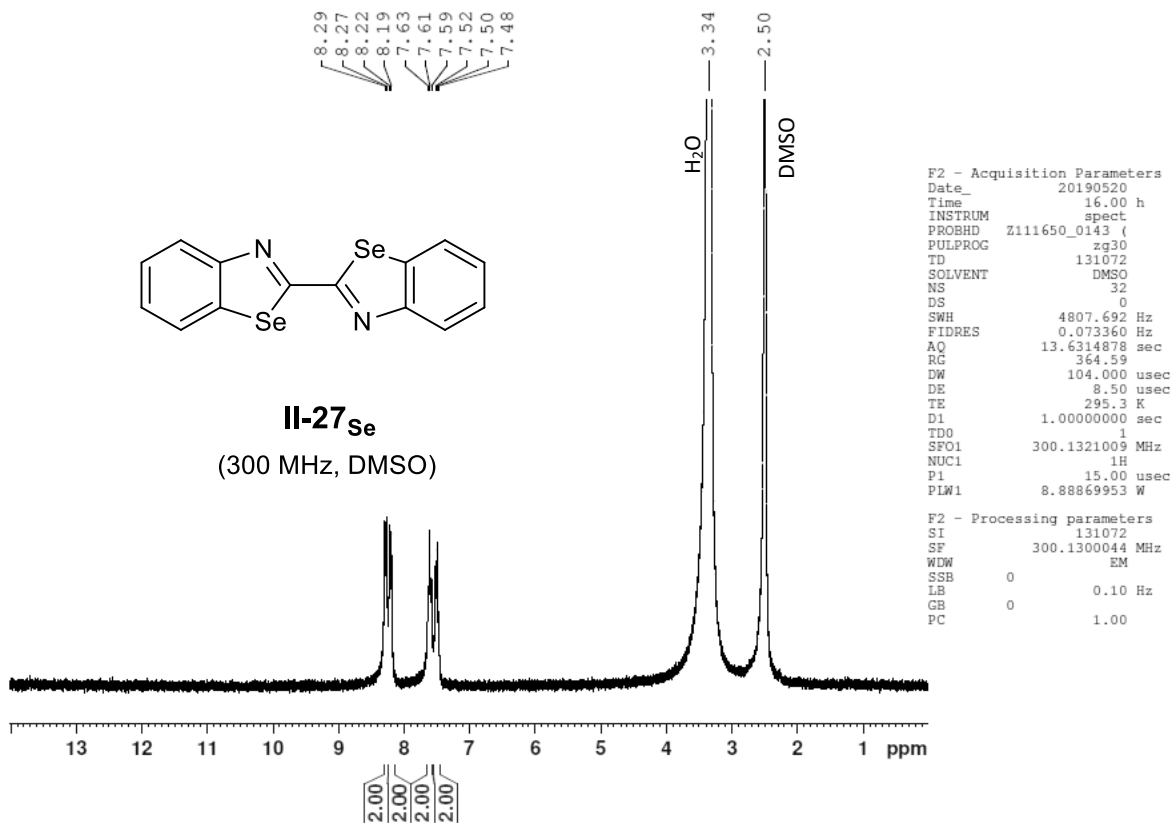
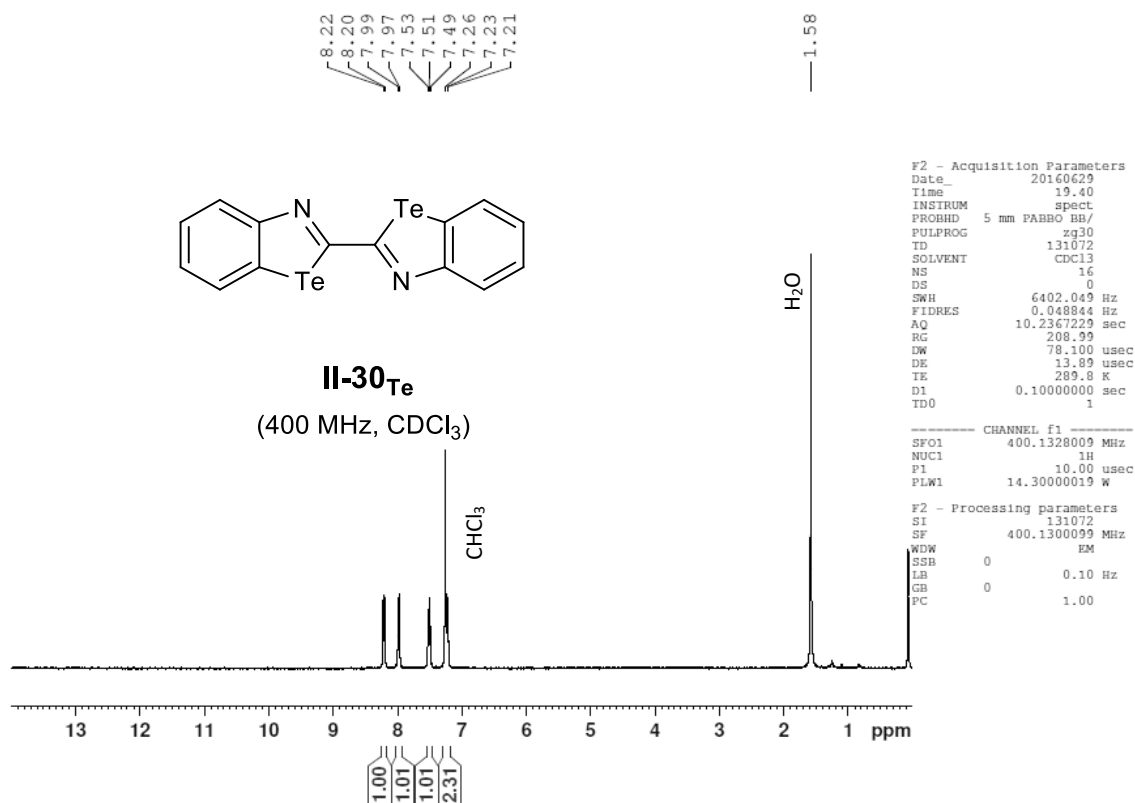
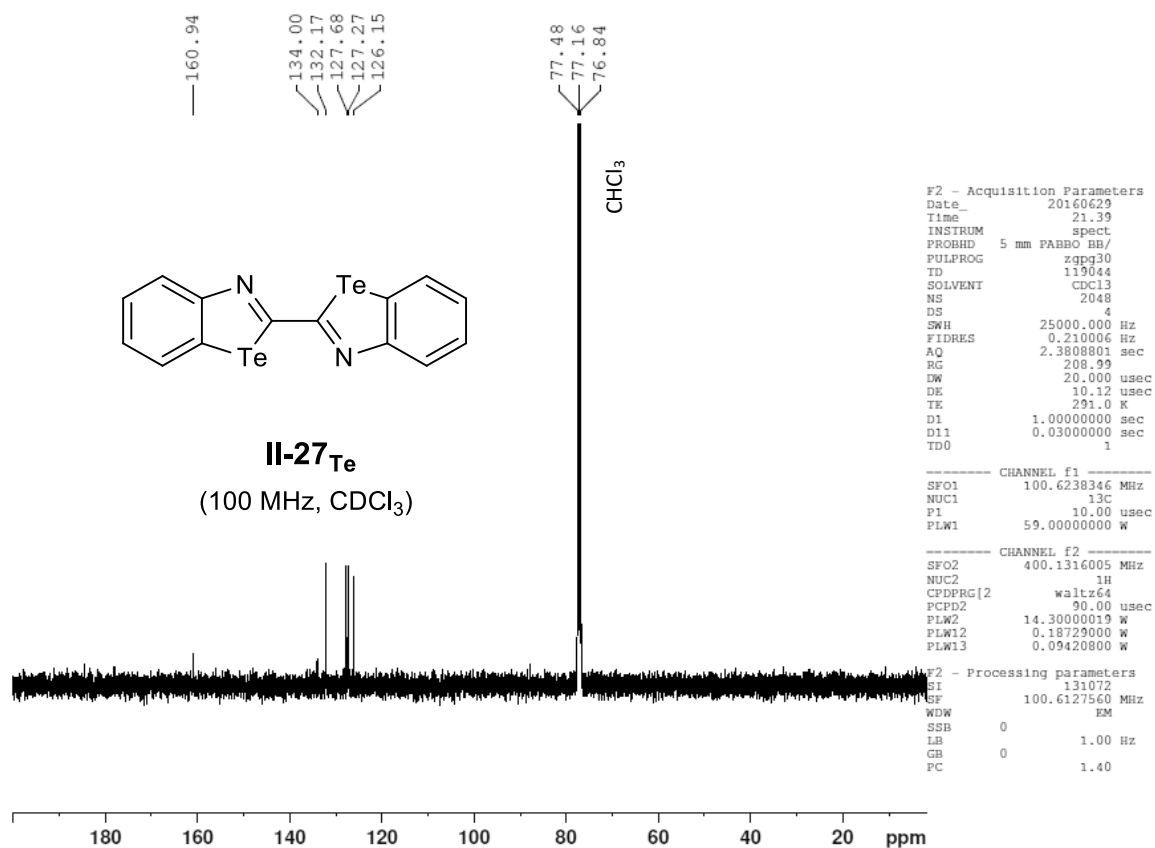


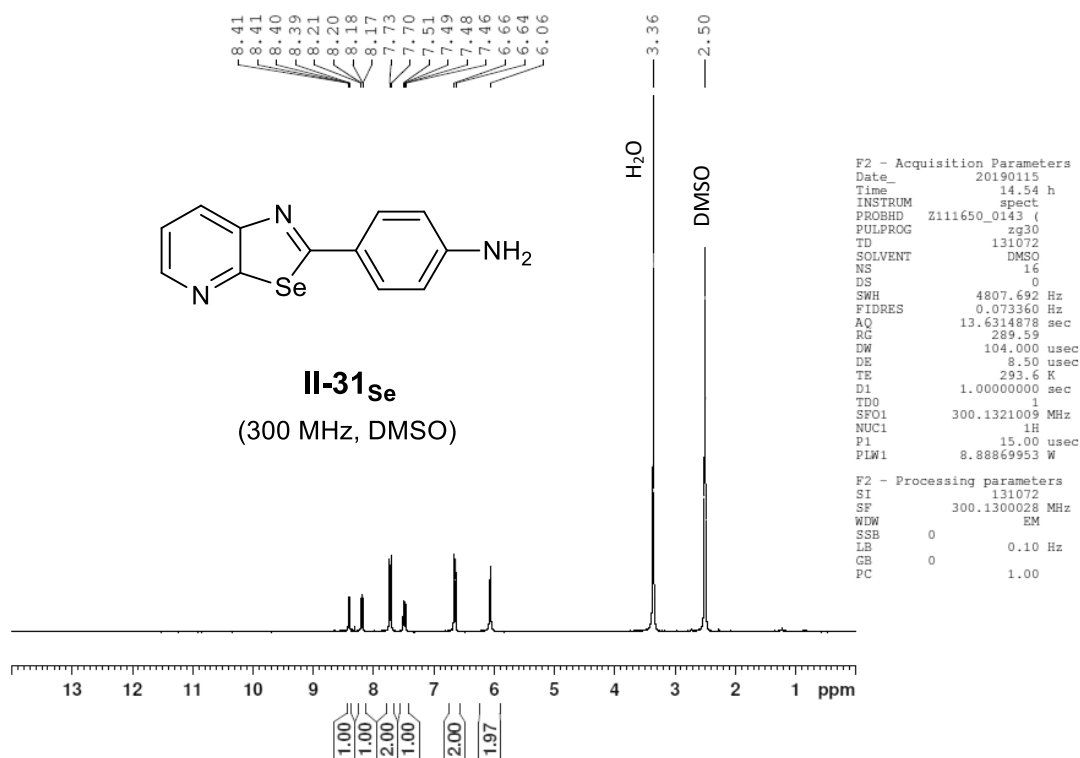
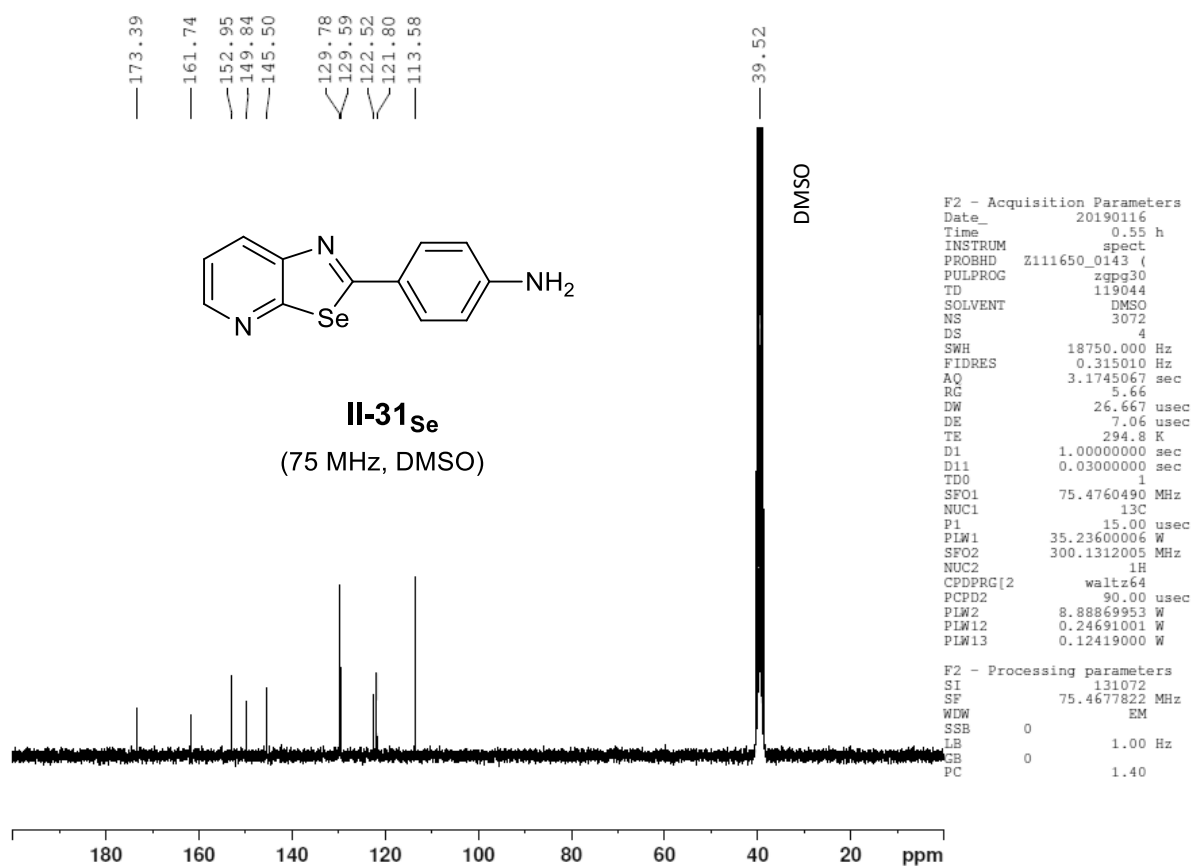
Figure VI - 88: 500 MHz <sup>1</sup>H-NMR in CDCl<sub>3</sub> of molecule II-25<sub>Te</sub>.

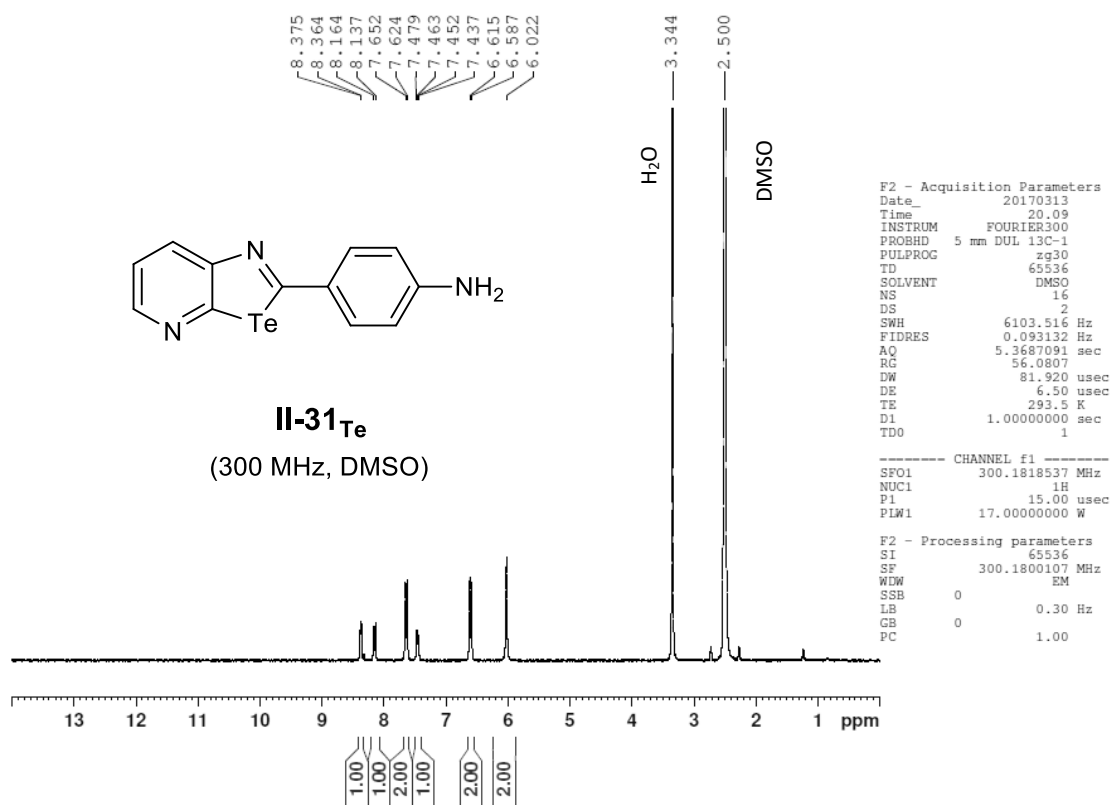
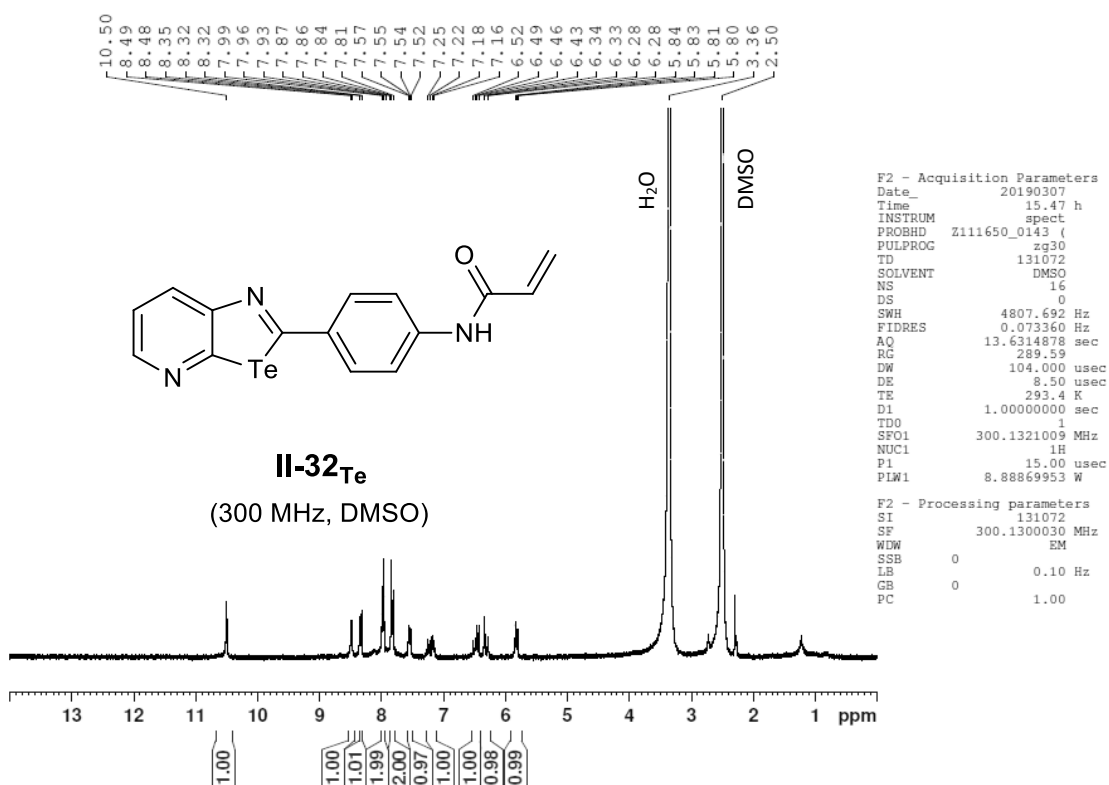
Figure VI - 89: 470 MHz <sup>19</sup>F-NMR in CDCl<sub>3</sub> of molecule II-25<sub>Te</sub>.Figure VI - 90: 125 MHz <sup>13</sup>C-NMR in CDCl<sub>3</sub> of molecule II-25<sub>Te</sub>. Due to <sup>13</sup>C-<sup>19</sup>F coupling: Peak 164.4 splits into 164.83, 164.54, 164.21 and 163.88; Peak 123.6 splits into 126.83, 124.65, 122.46 and 120.8.

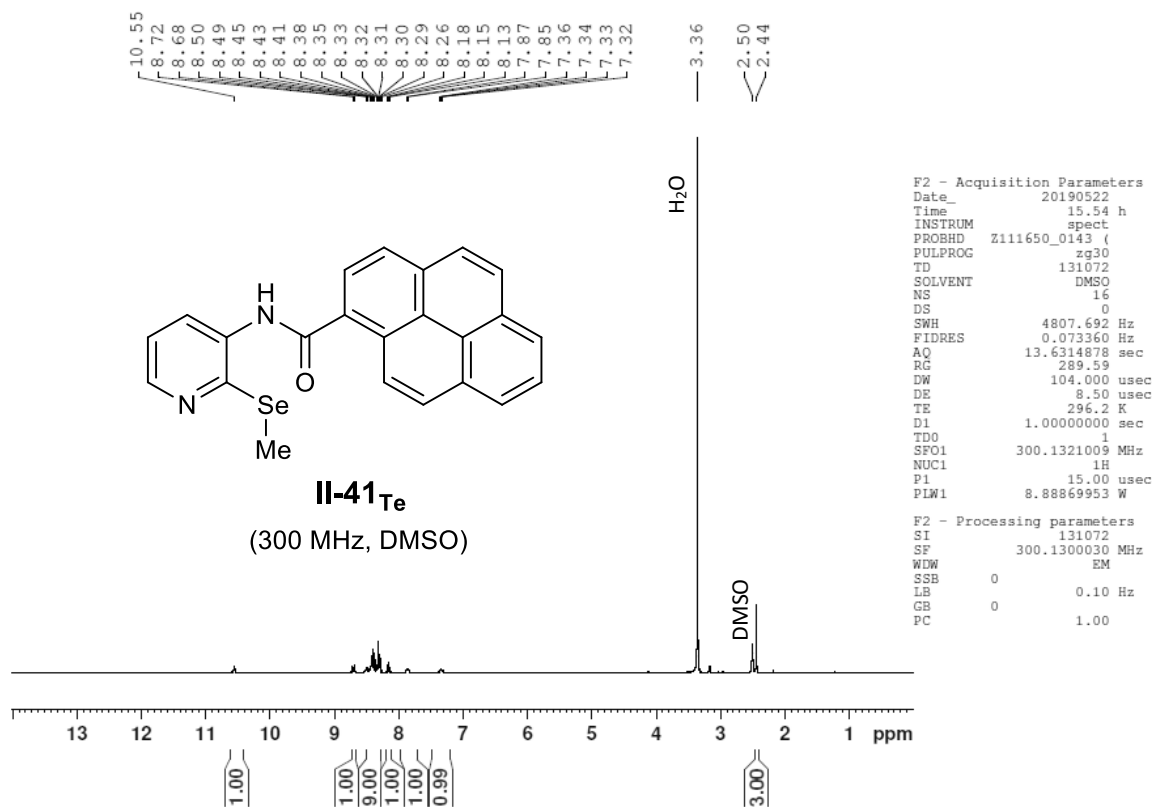
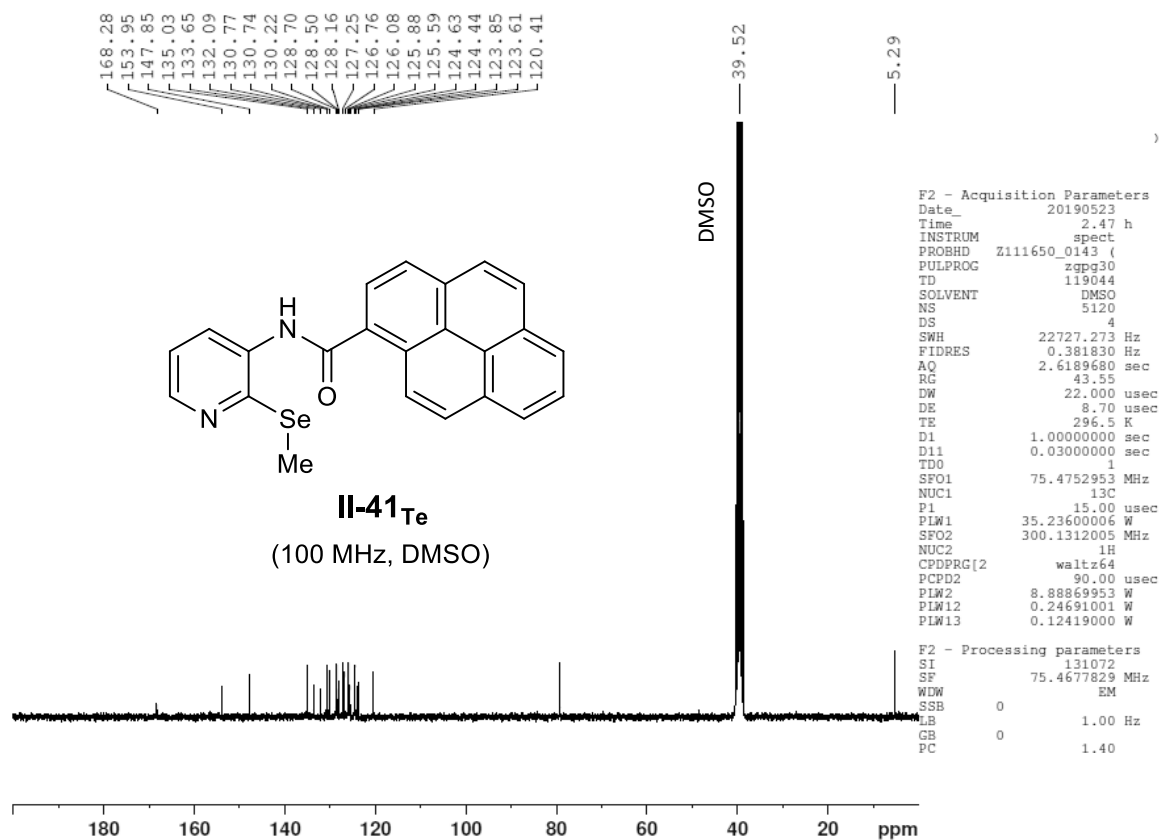
Figure VI - 91: 300 MHz <sup>1</sup>H-NMR in DMSO of molecule II-30<sub>Se</sub>.Figure VI - 92: 400 MHz <sup>1</sup>H-NMR in DMSO of molecule II-30<sub>Te</sub>.

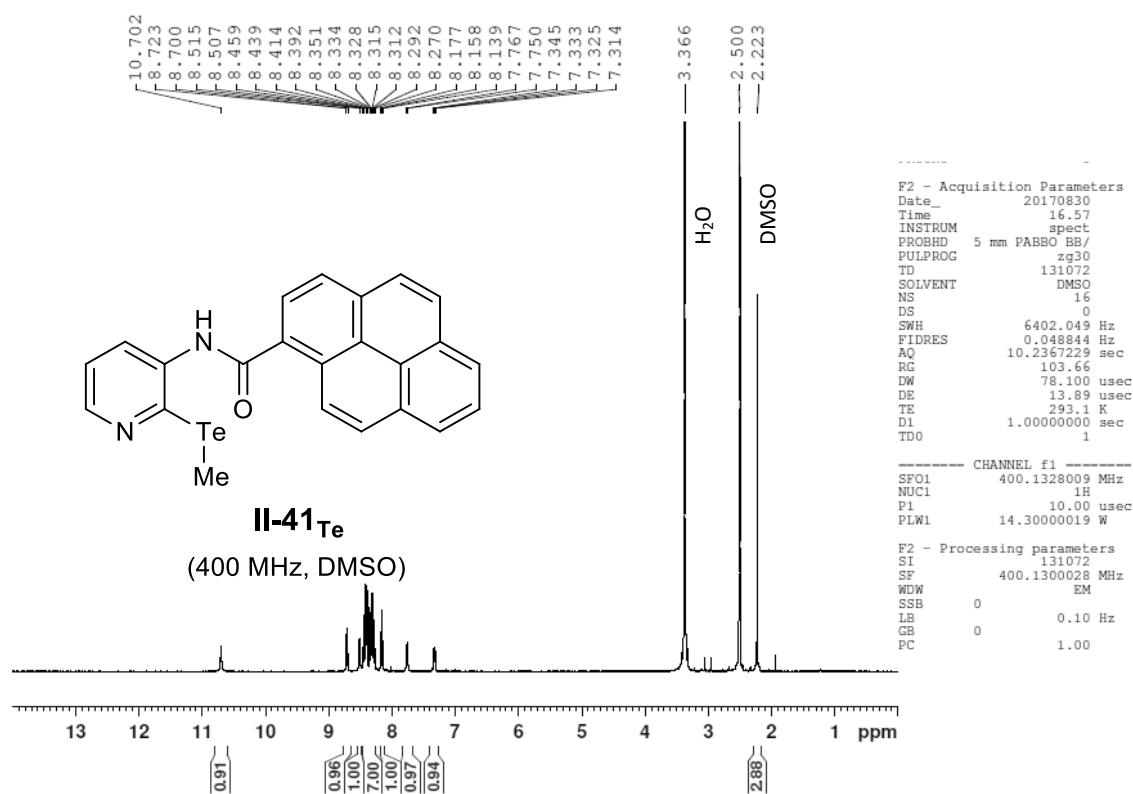
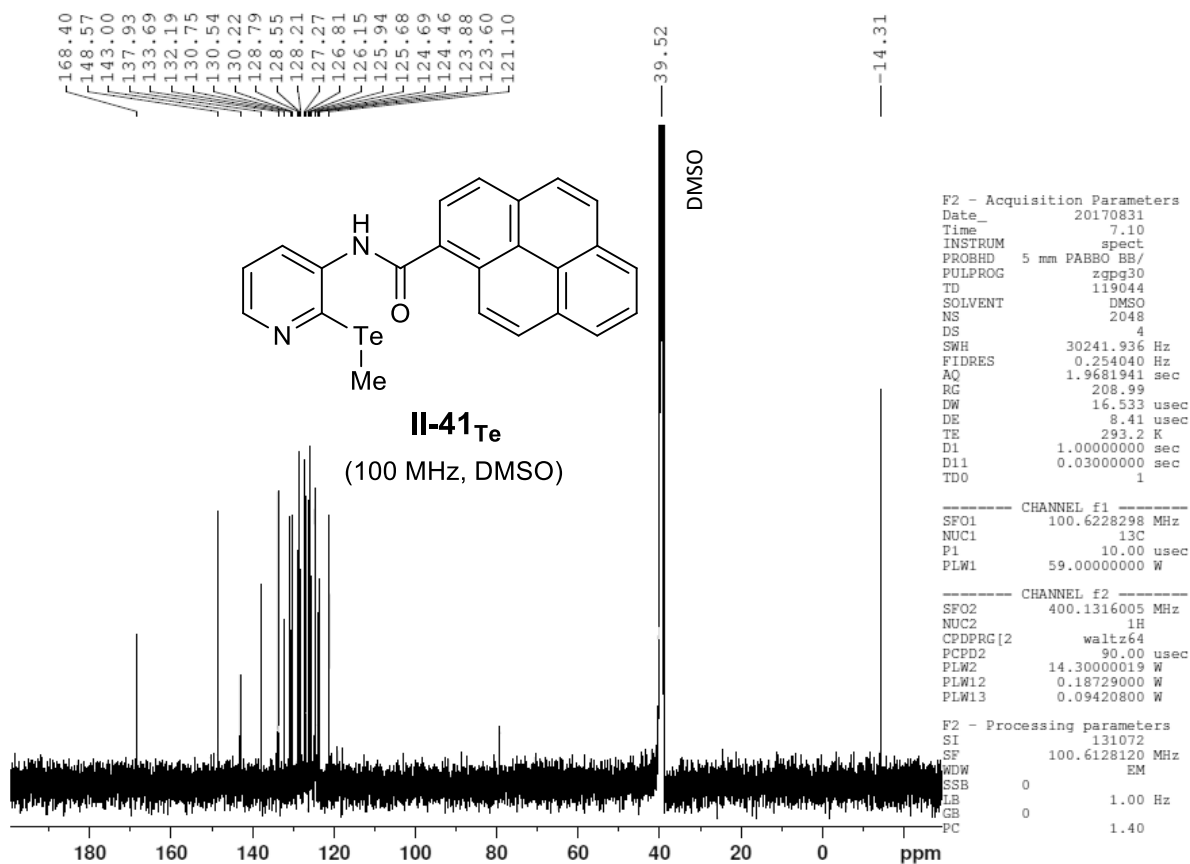
Figure VI - 93: 100 MHz <sup>13</sup>C-NMR in DMSO of molecule II-30<sub>Te</sub>.Figure VI - 94: 300 MHz <sup>1</sup>H-NMR in DMSO of molecule II-30<sub>Se</sub>.

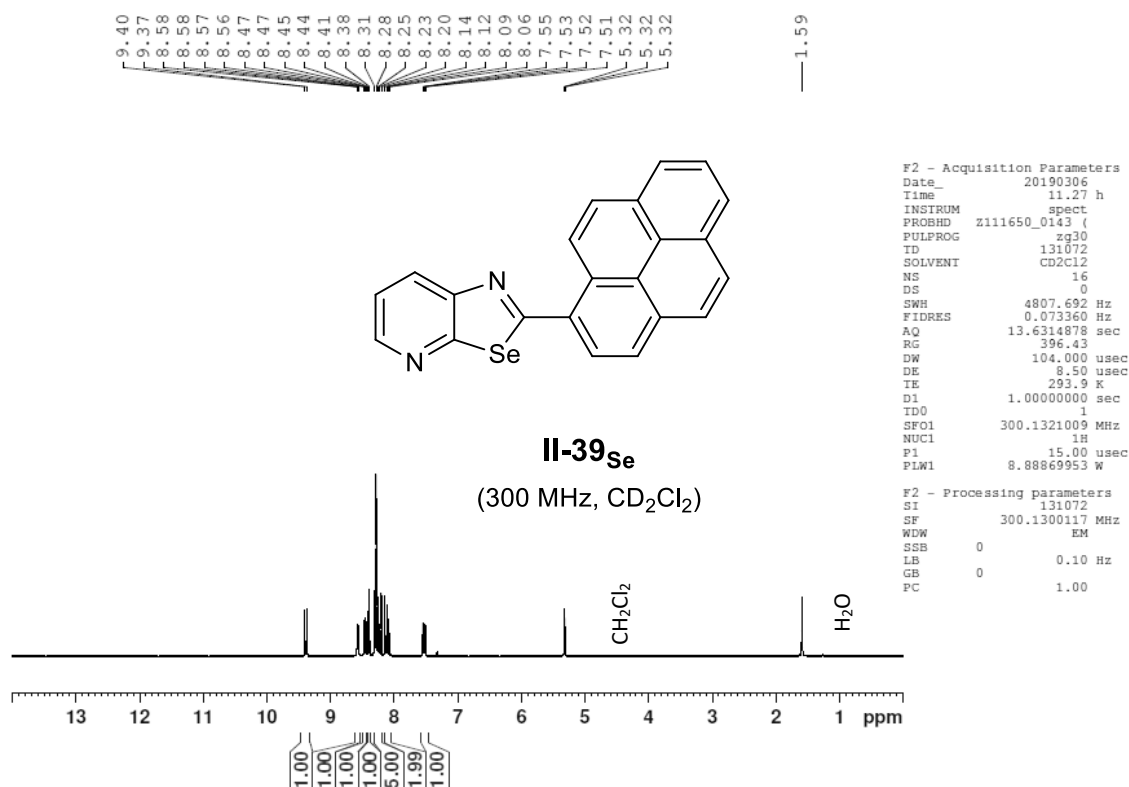
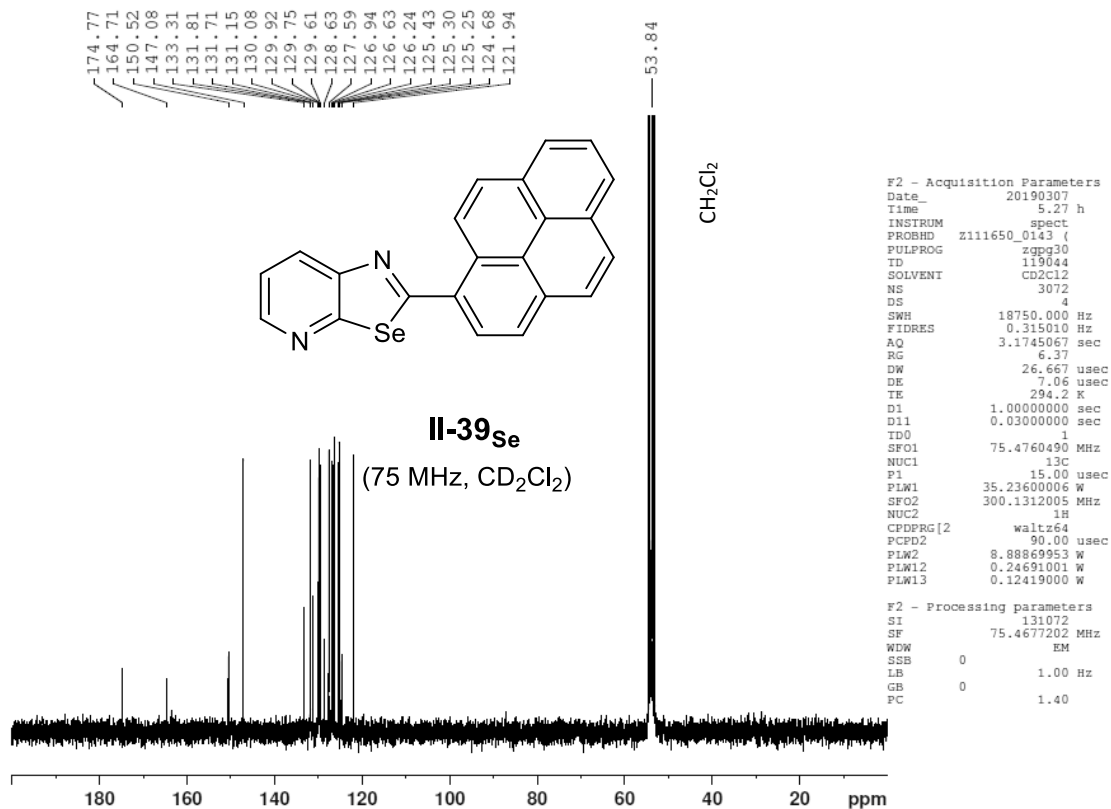
Figure VI - 95: 400 MHz <sup>1</sup>H-NMR in CDCl<sub>3</sub> of molecule II-27<sub>Te</sub>.Figure VI - 96: 100 MHz <sup>13</sup>C-NMR in CDCl<sub>3</sub> of molecule II-27<sub>Te</sub>.

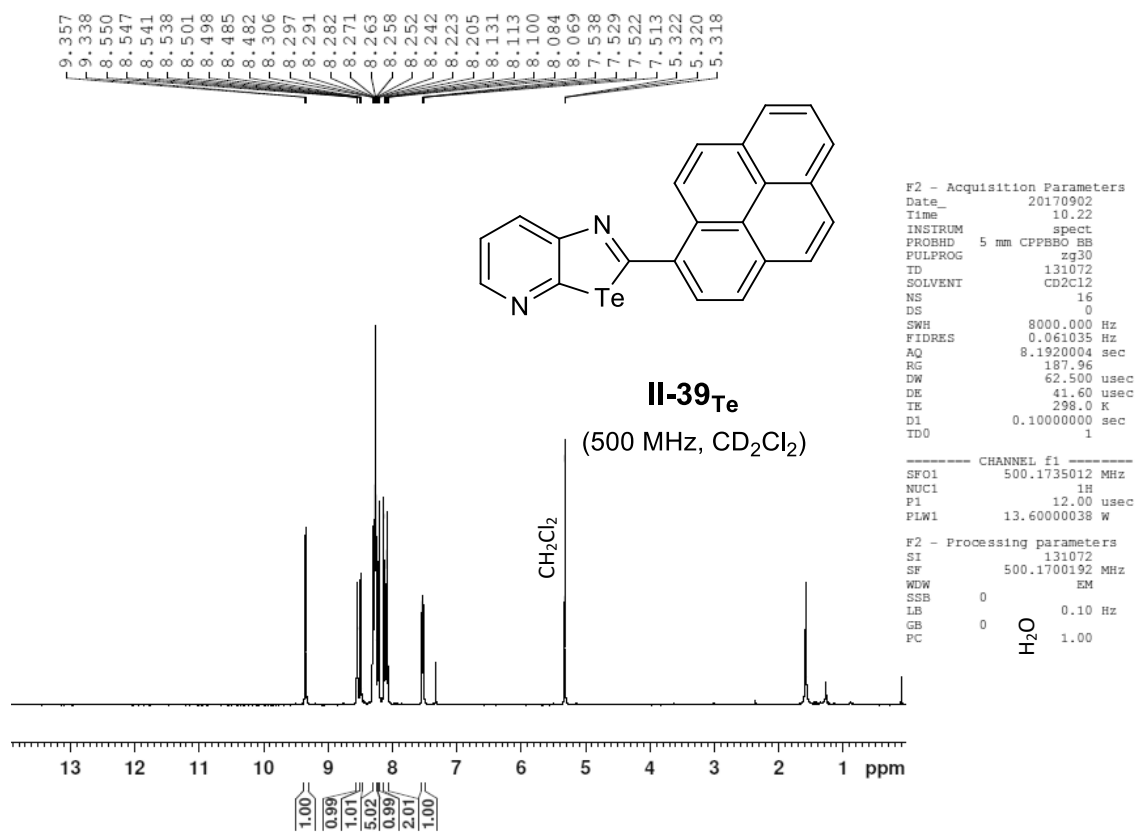
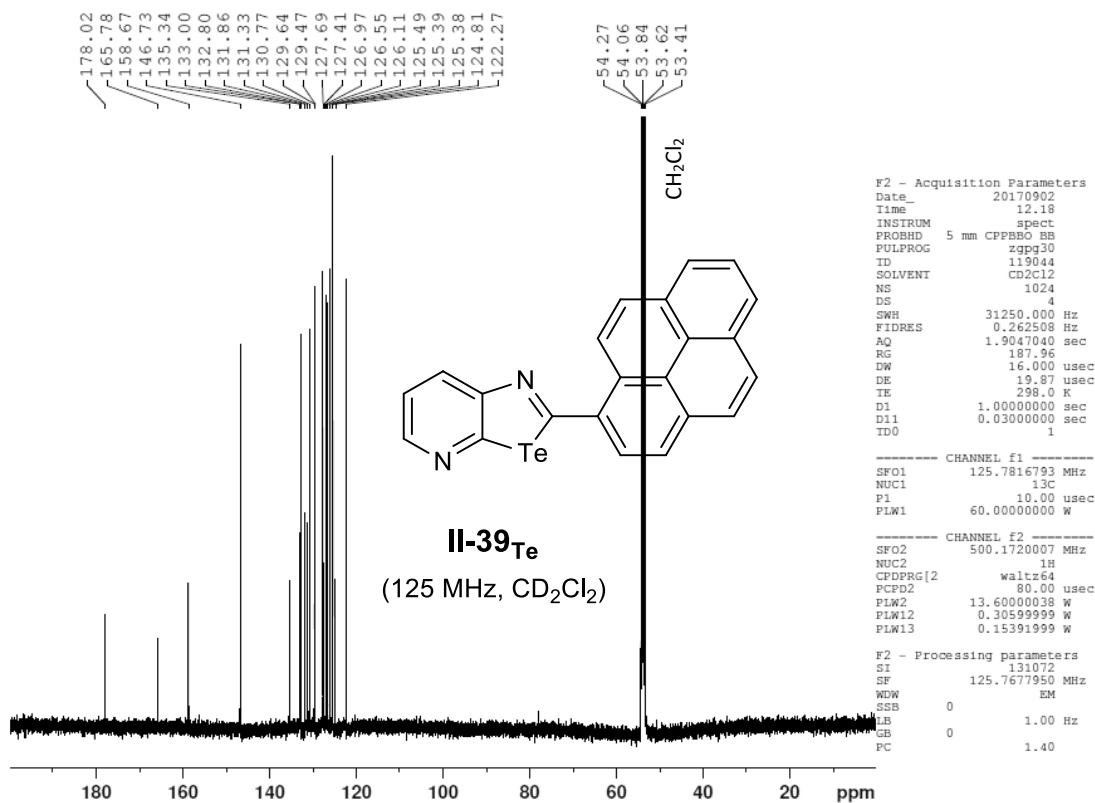
Figure VI - 97: 300 MHz <sup>1</sup>H-NMR in DMSO of molecule II-31<sub>Se</sub>.Figure VI - 98: 300 MHz <sup>13</sup>C-NMR in DMSO of molecule II-31<sub>Se</sub>.

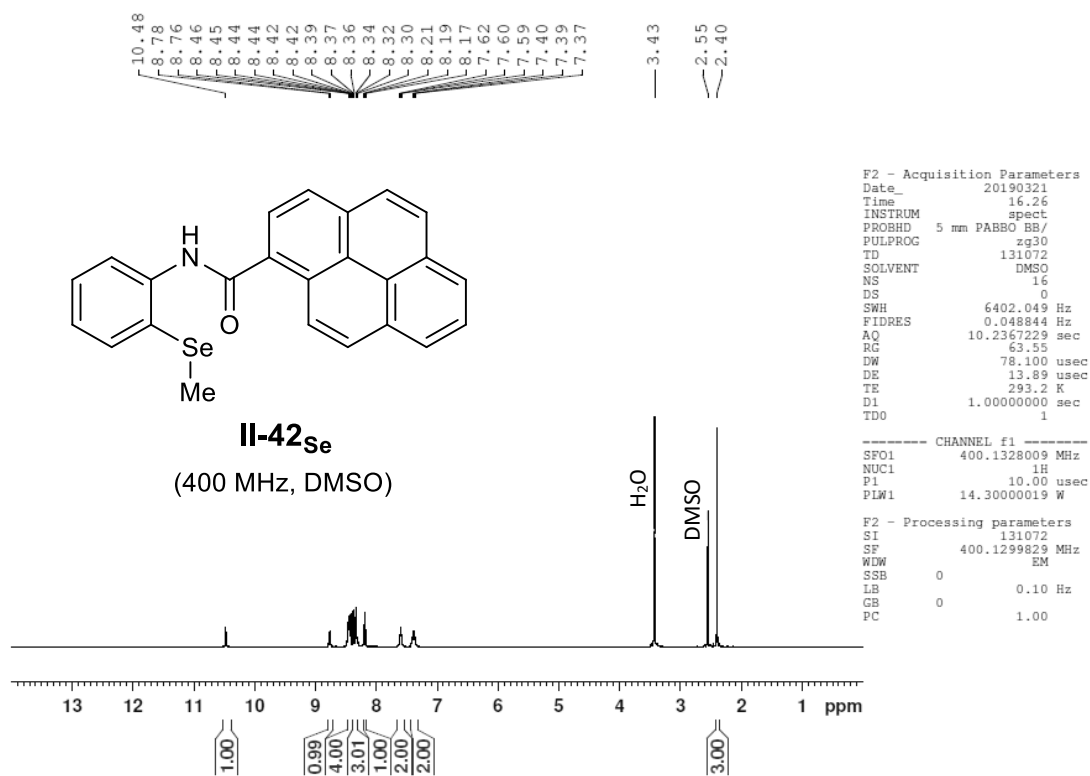
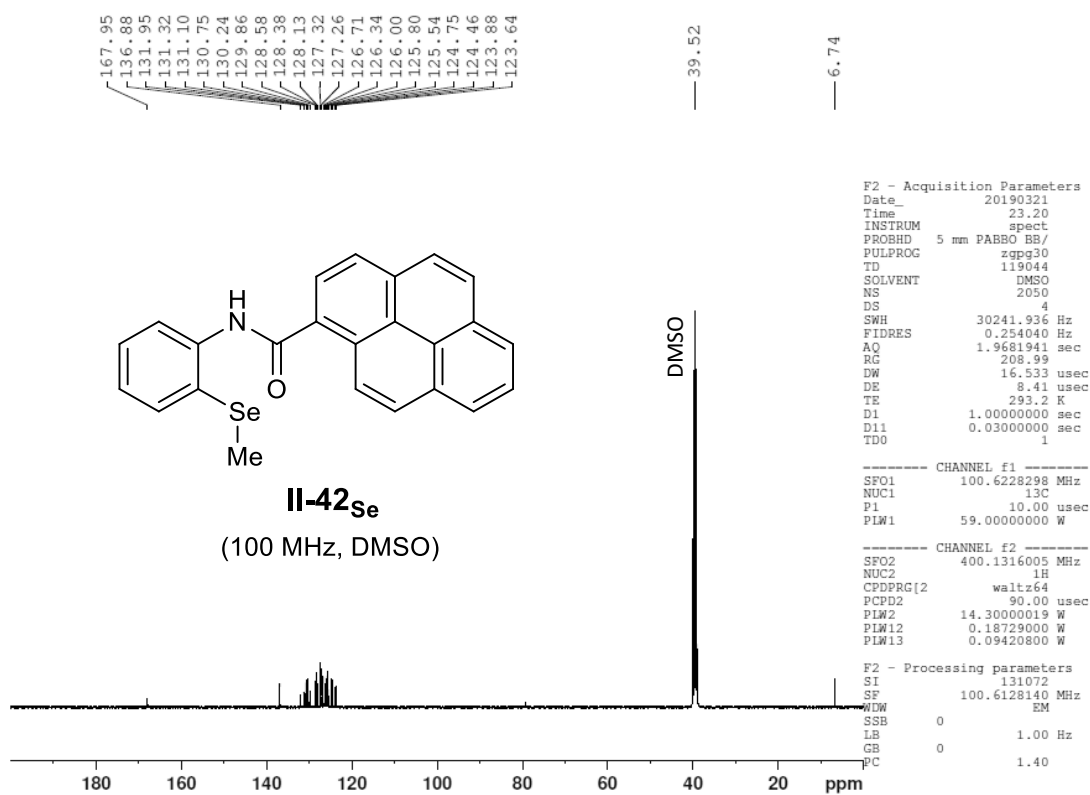
Figure VI - 99: 300 MHz <sup>1</sup>H-NMR in DMSO of molecule II-31<sub>Te</sub>.Figure VI - 100: 300 MHz <sup>1</sup>H-NMR in DMSO of molecule II-32<sub>Te</sub>.

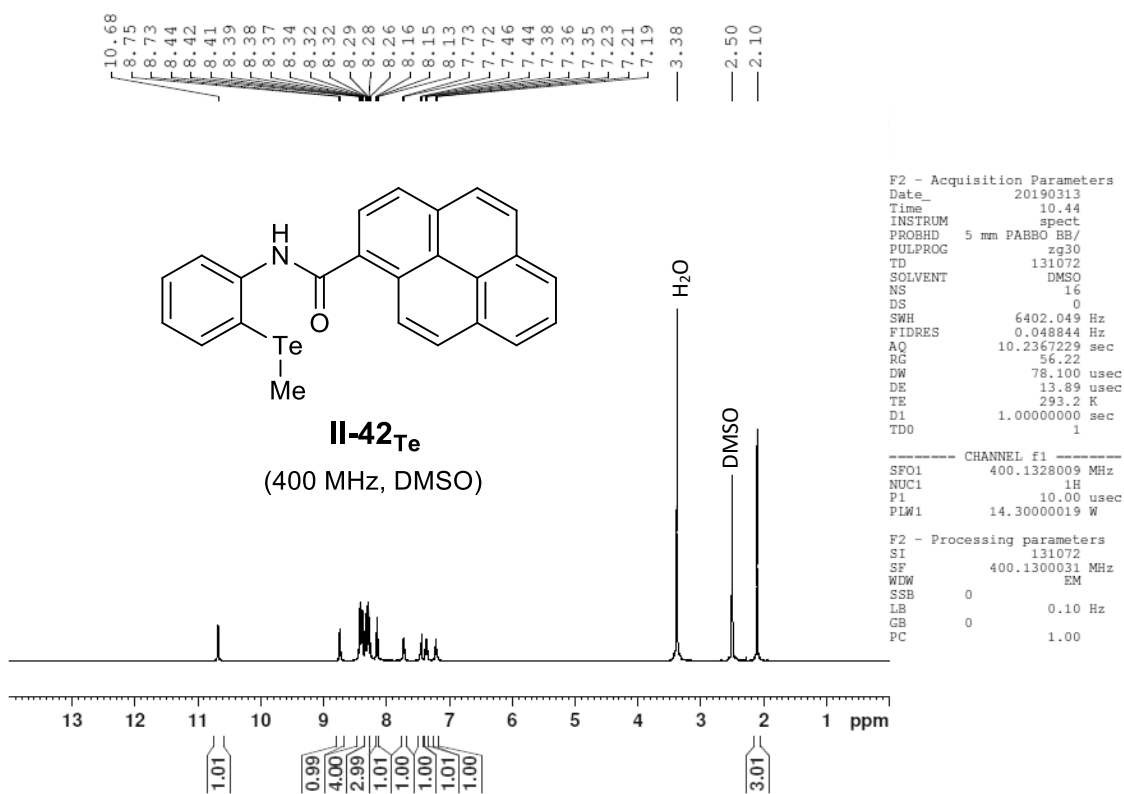
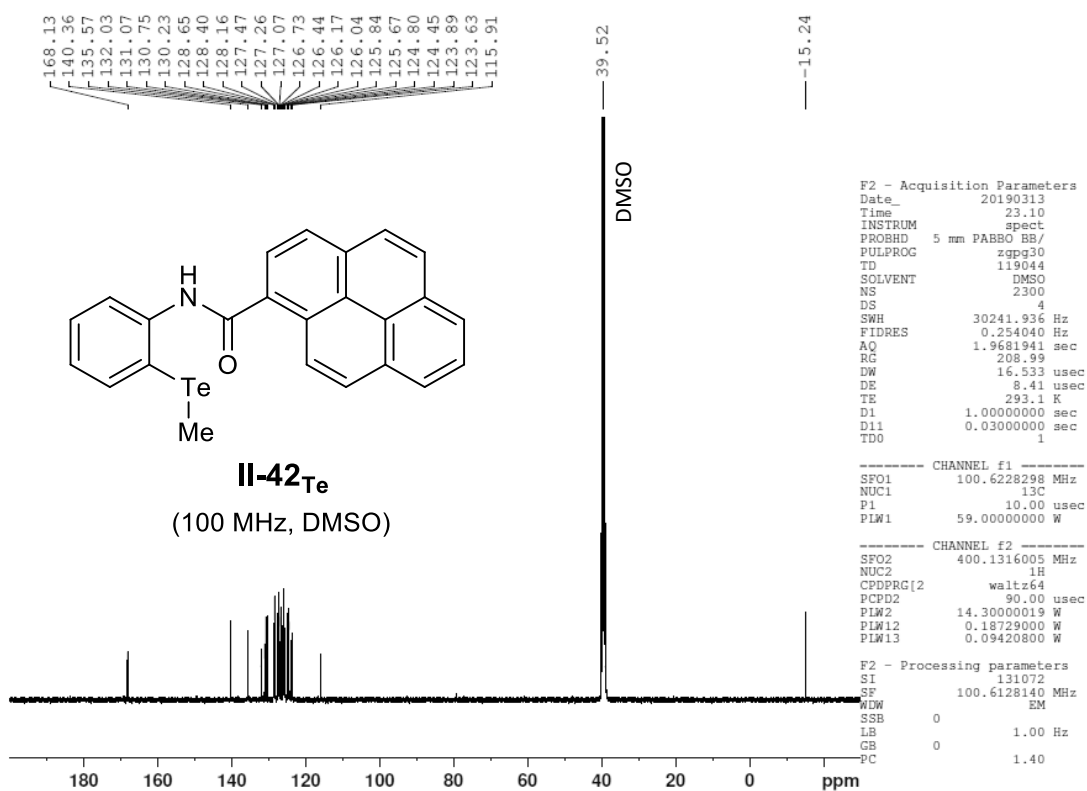
Figure VI - 101: 300 MHz  $^1\text{H}$ -NMR in DMSO of molecule **II-41<sub>Se</sub>**.Figure VI - 102: 100 MHz  $^{13}\text{C}$ -NMR in DMSO of molecule **II-41<sub>Se</sub>**.

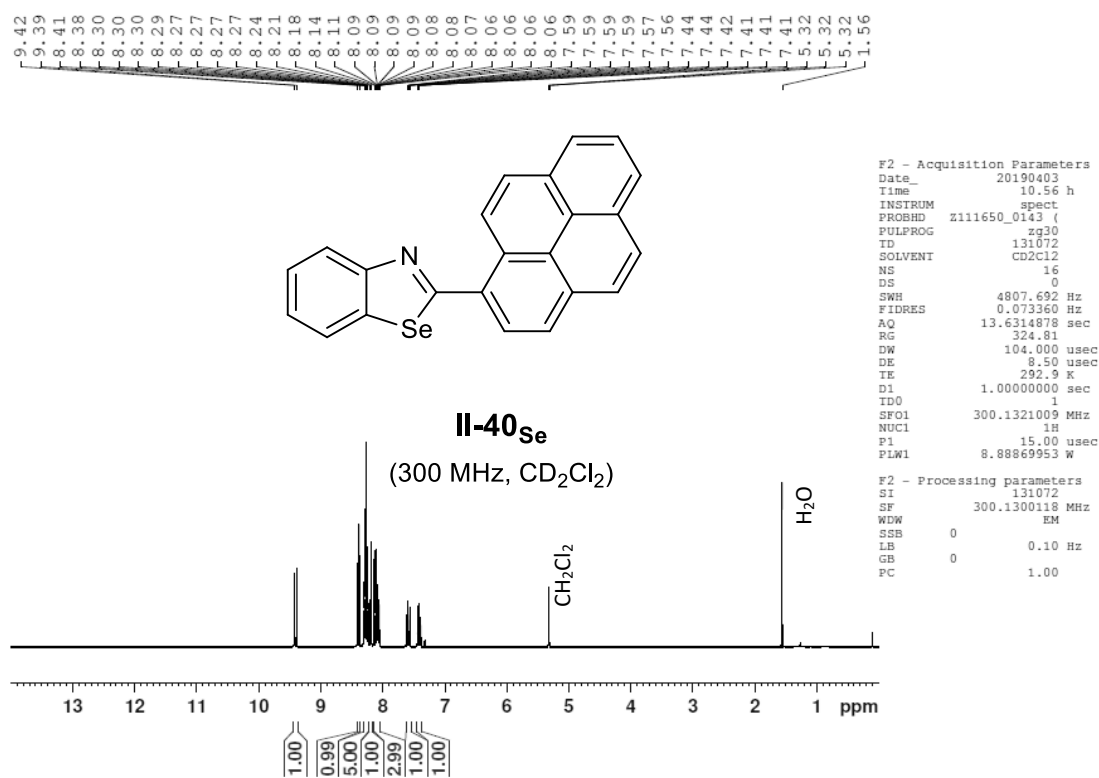
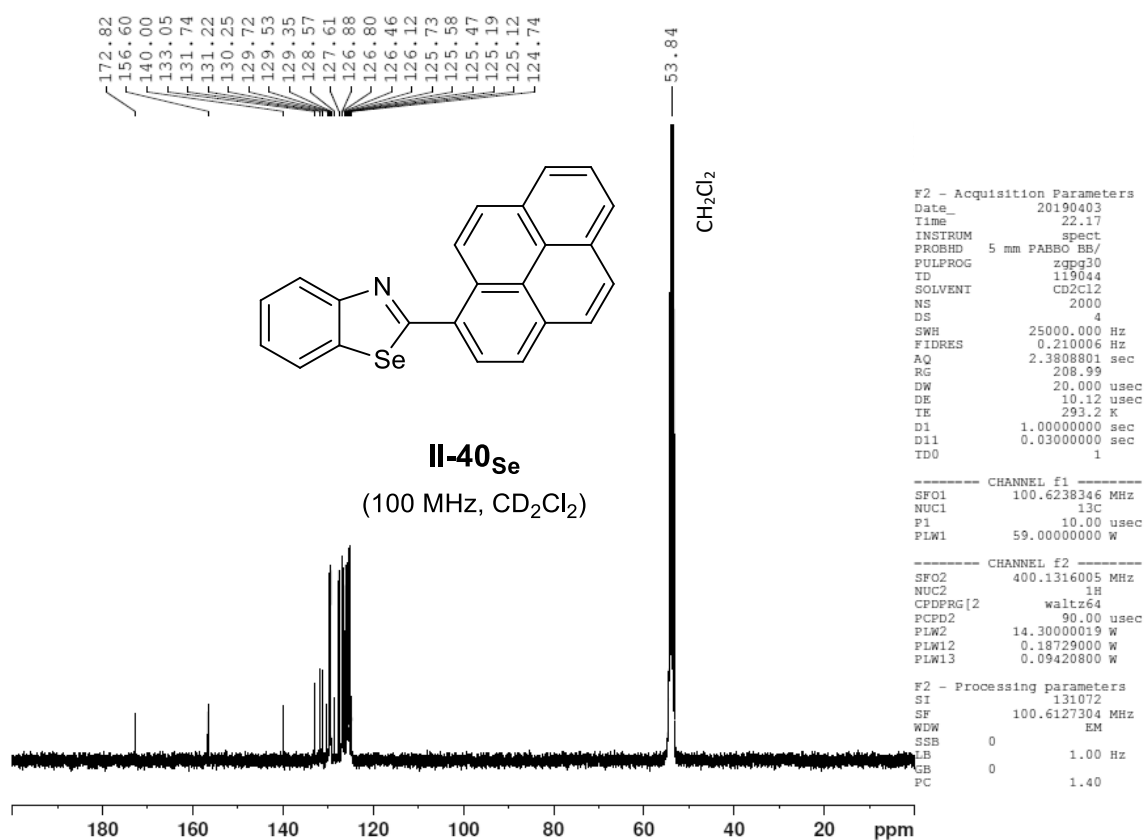
Figure VI - 103: 400 MHz <sup>1</sup>H-NMR in DMSO of molecule II-41<sub>Te</sub>.Figure VI - 104: 100 MHz <sup>13</sup>C-NMR in DMSO of molecule II-41<sub>Te</sub>.

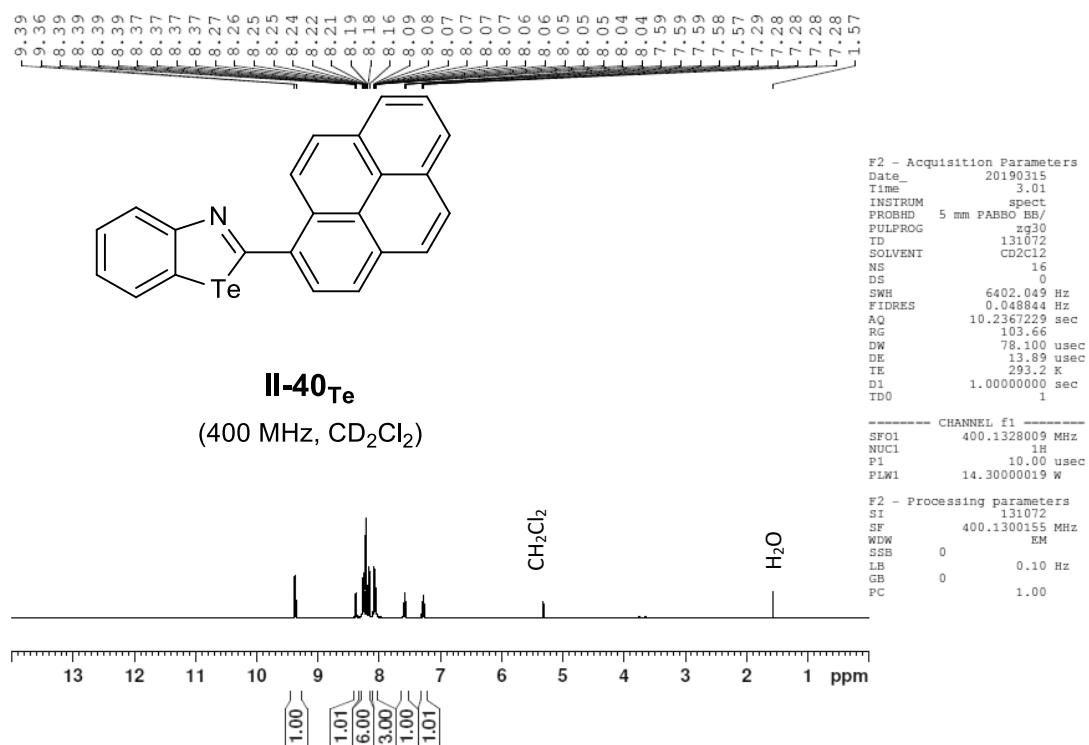
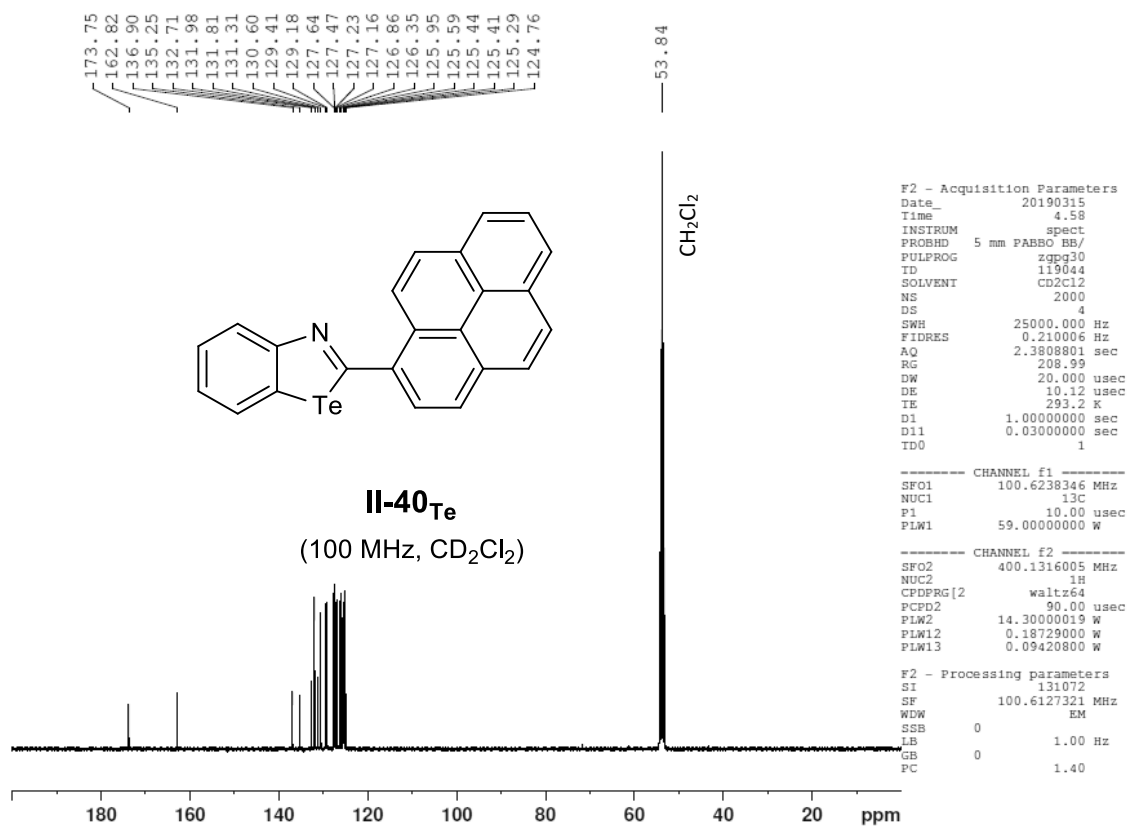
Figure VI - 105: 400 MHz <sup>1</sup>H-NMR in CD<sub>2</sub>Cl<sub>2</sub> of molecule II-39<sub>Se</sub>.Figure VI - 106: 75 MHz <sup>13</sup>C-NMR in CD<sub>2</sub>Cl<sub>2</sub> of molecule II-39<sub>Se</sub>.

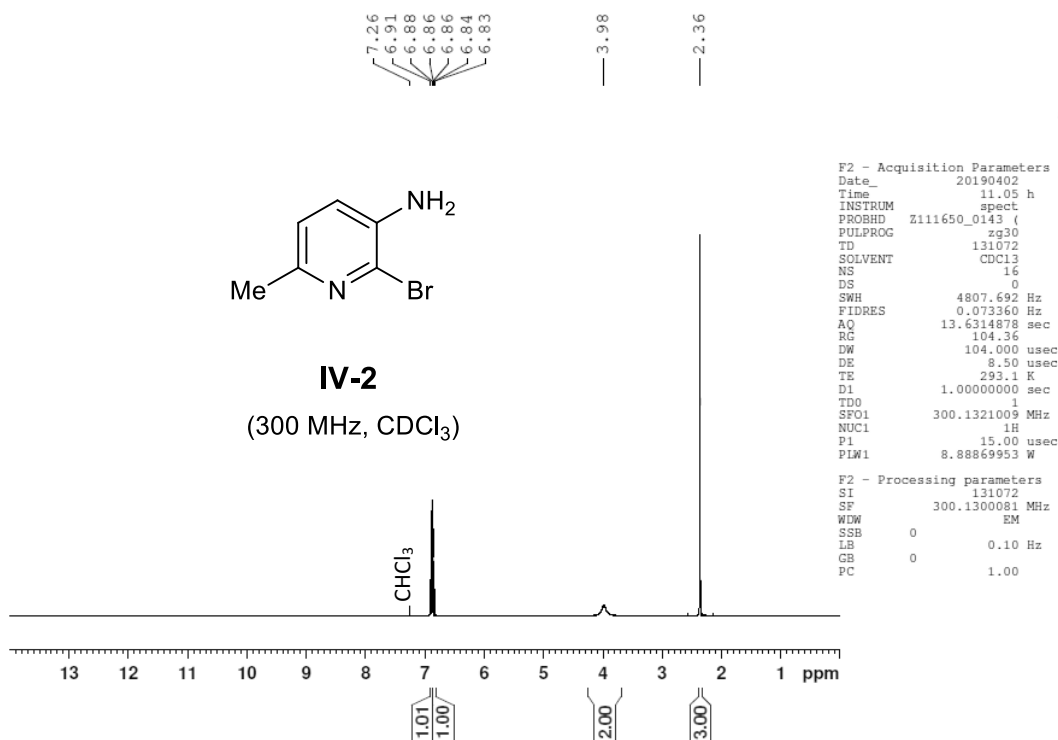
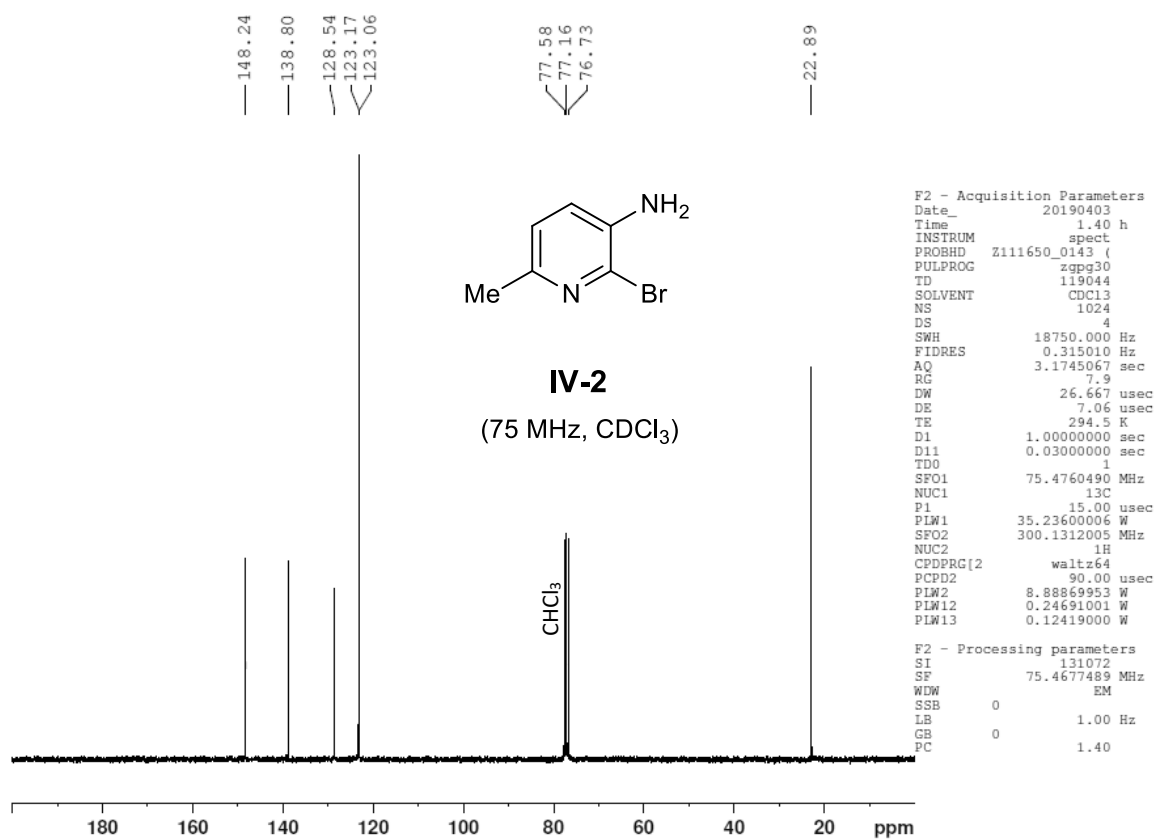
Figure VI - 107: 400 MHz <sup>1</sup>H-NMR in CD<sub>2</sub>Cl<sub>2</sub> of molecule **II-39<sub>Te</sub>**.Figure VI - 108: 125 MHz <sup>13</sup>C-NMR in CD<sub>2</sub>Cl<sub>2</sub> of molecule **II-39<sub>Te</sub>**.

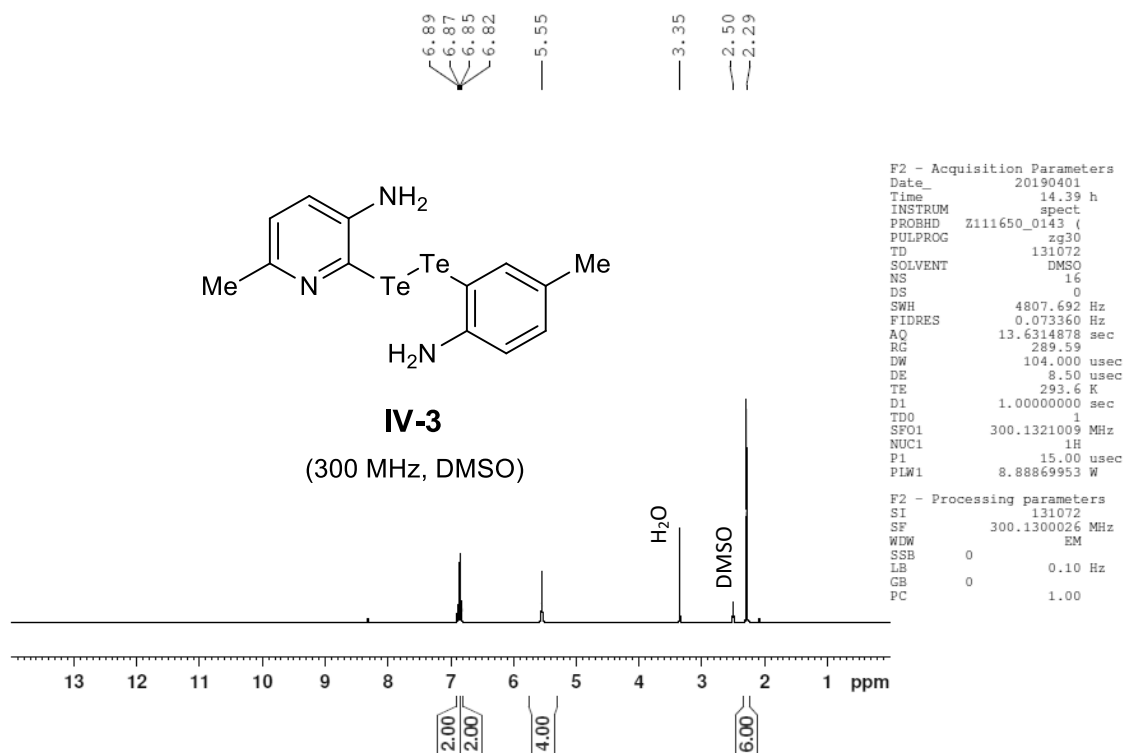
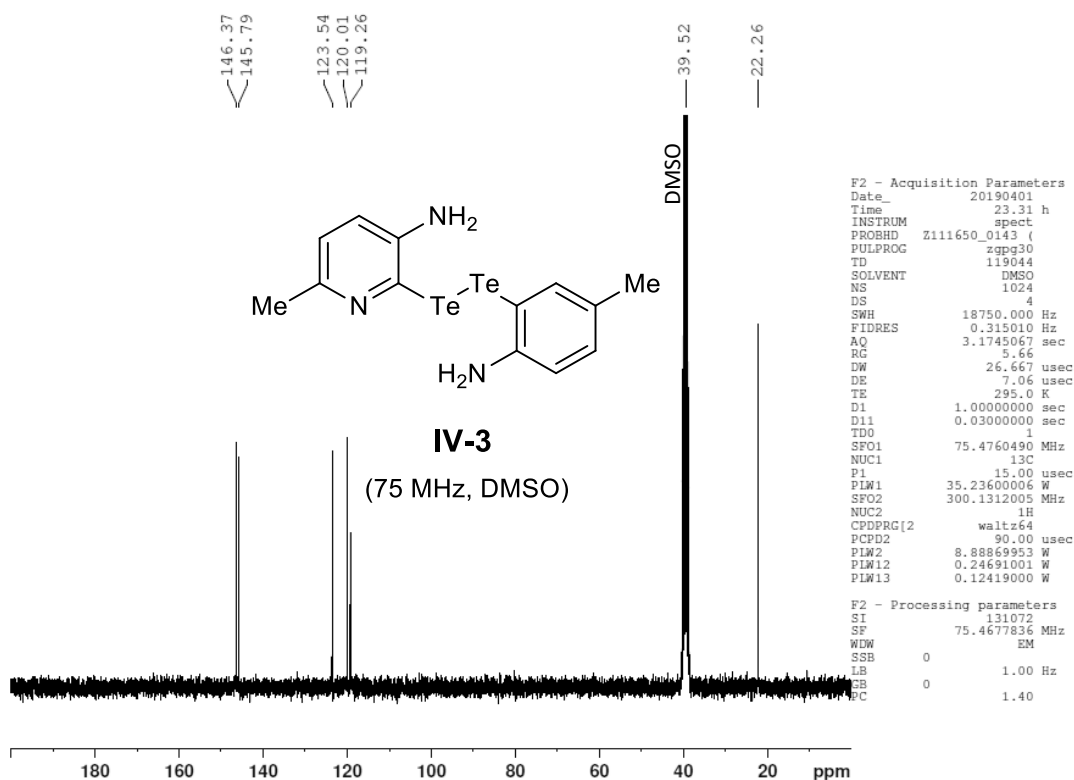
Figure VI - 109: 400 MHz <sup>1</sup>H-NMR in DMSO of molecule II-42<sub>Se</sub>.Figure VI - 110: 100 MHz <sup>13</sup>C-NMR in DMSO of molecule II-42<sub>Se</sub>.

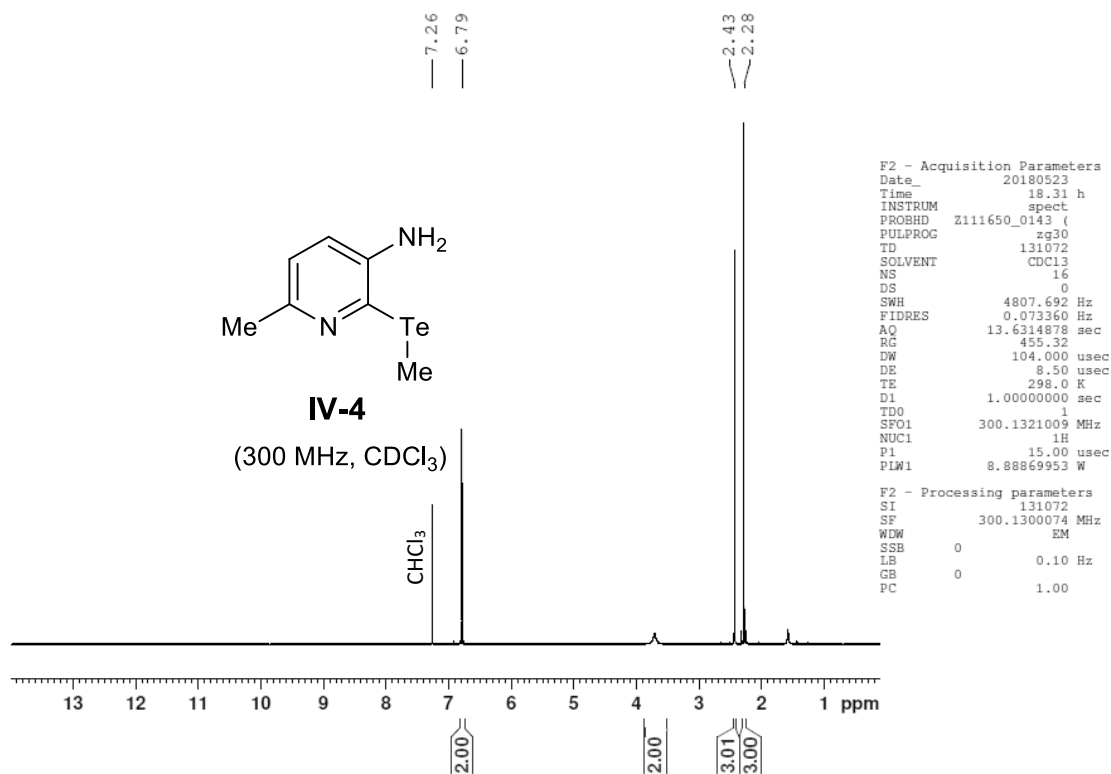
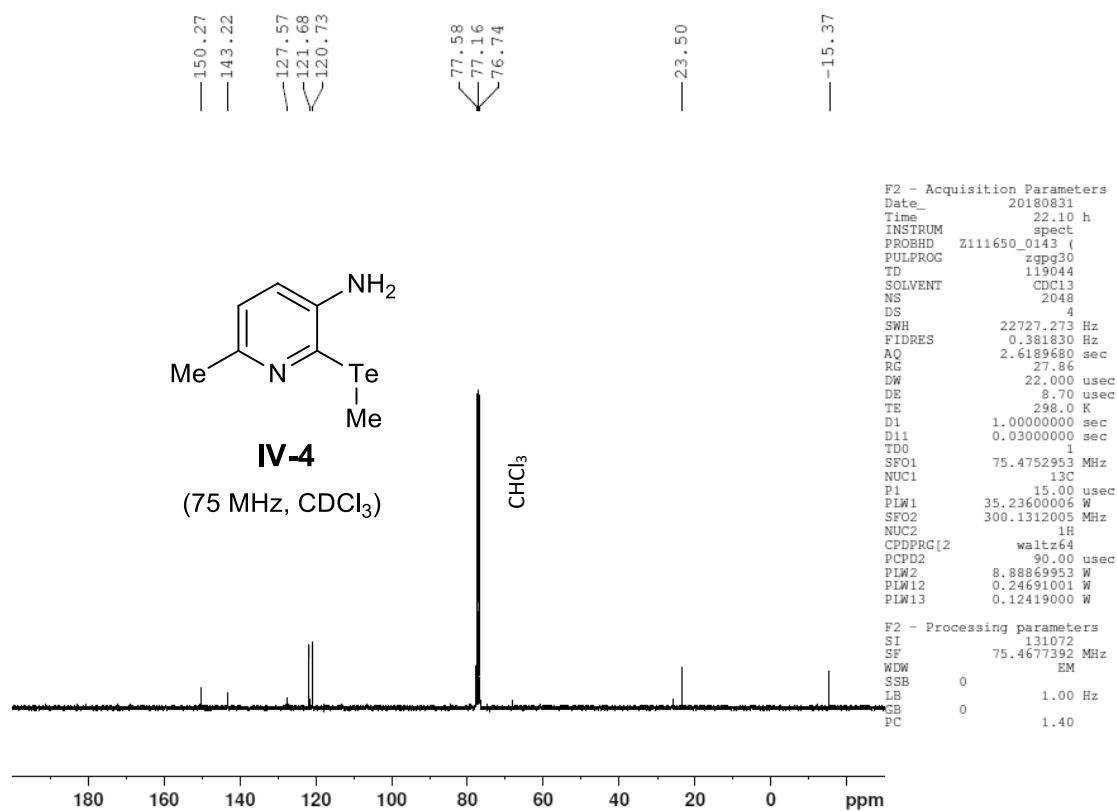
Figure VI - 111: 400 MHz <sup>1</sup>H-NMR in DMSO of molecule II-42<sub>Se</sub>.Figure VI - 112: 100 MHz <sup>13</sup>C-NMR in DMSO of molecule II-42<sub>Te</sub>.

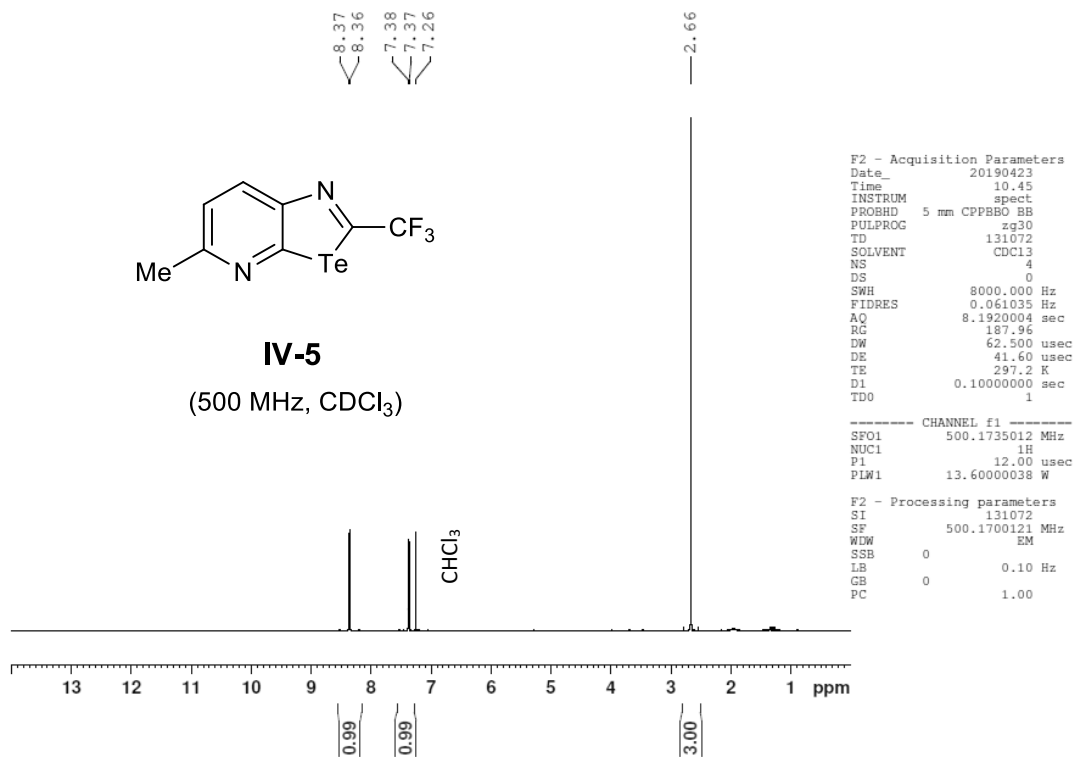
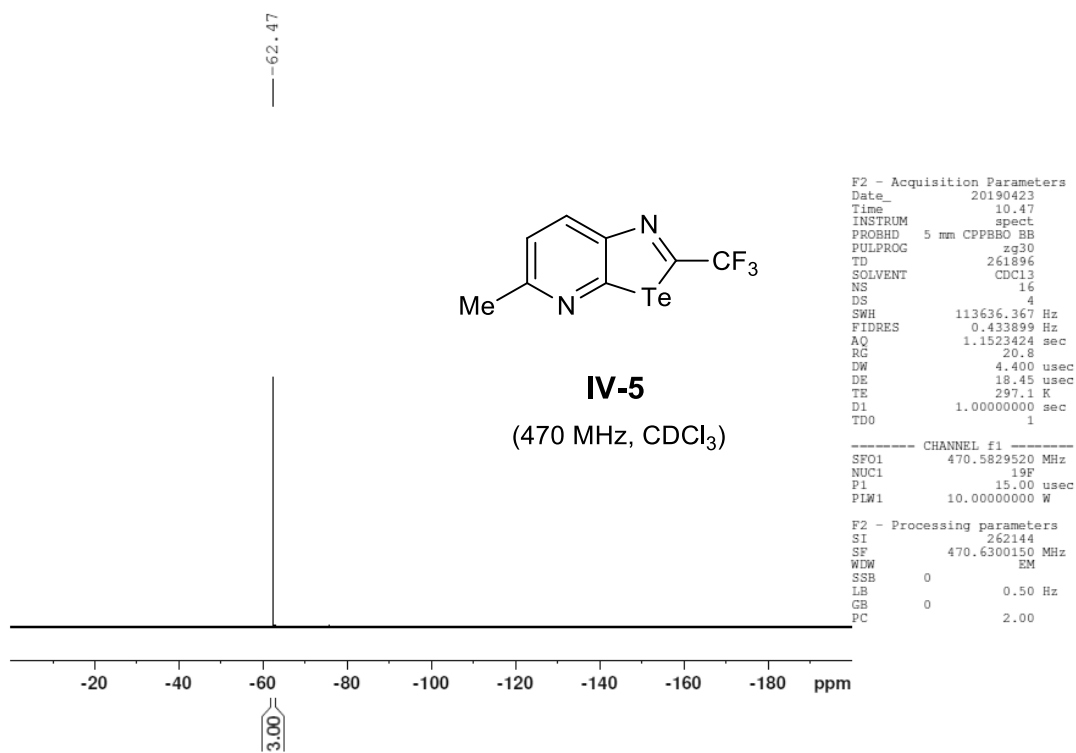
Figure VI - 113: 400 MHz <sup>1</sup>H-NMR in CD<sub>2</sub>Cl<sub>2</sub> of molecule **II-40<sub>Se</sub>**.Figure VI - 114: 100 MHz <sup>13</sup>C-NMR in CD<sub>2</sub>Cl<sub>2</sub> of molecule **II-40<sub>Se</sub>**.

Figure VI - 115: 400 MHz <sup>1</sup>H-NMR in CD<sub>2</sub>Cl<sub>2</sub> of molecule II-40<sub>Te</sub>.Figure VI - 116: 100 MHz <sup>13</sup>C-NMR in CD<sub>2</sub>Cl<sub>2</sub> of molecule II-40<sub>Te</sub>.

Figure VI - 117: 300 MHz <sup>1</sup>H-NMR in CDCl<sub>3</sub> of molecule IV-2.Figure VI - 118: 75 MHz <sup>13</sup>C-NMR in CDCl<sub>3</sub> of molecule IV-2.

Figure VI - 119: 300 MHz  $^1\text{H}$ -NMR in DMSO of molecule IV-3.Figure VI - 120: 75 MHz  $^{13}\text{C}$ -NMR in DMSO of molecule IV-4.

Figure VI - 121: 300 MHz <sup>1</sup>H-NMR in CDCl<sub>3</sub> of molecule IV-4.Figure VI - 122: 300 MHz <sup>13</sup>C-NMR in CDCl<sub>3</sub> of molecule IV-4.

Figure VI - 123: 500 MHz <sup>1</sup>H-NMR in CDCl<sub>3</sub> of molecule IV-5.Figure VI - 124: 470 MHz <sup>19</sup>F-NMR in CDCl<sub>3</sub> of molecule IV-5.

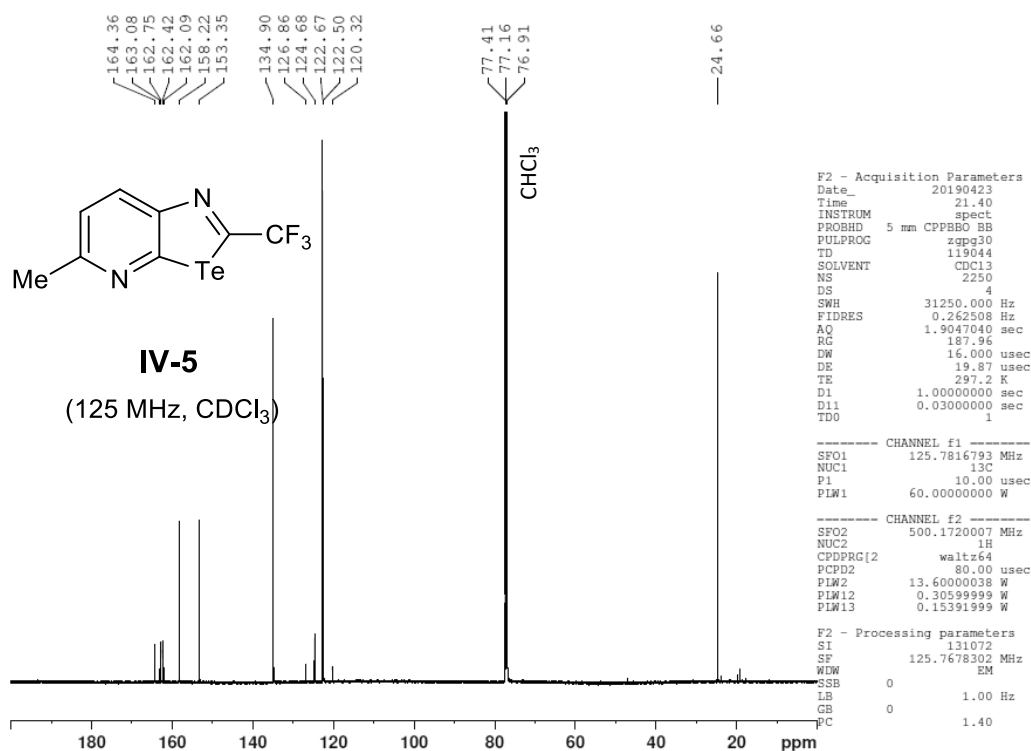


Figure VI - 125: 125 MHz <sup>13</sup>C-NMR in CDCl<sub>3</sub> of molecule IV-5. Due to <sup>13</sup>C-<sup>19</sup>F coupling: Peak 162.6 splits into 163.08, 163.45, 162.75 and 162.42; Peak 123.6 splits into 126.86, 124.68, 122.50 and 120.32.

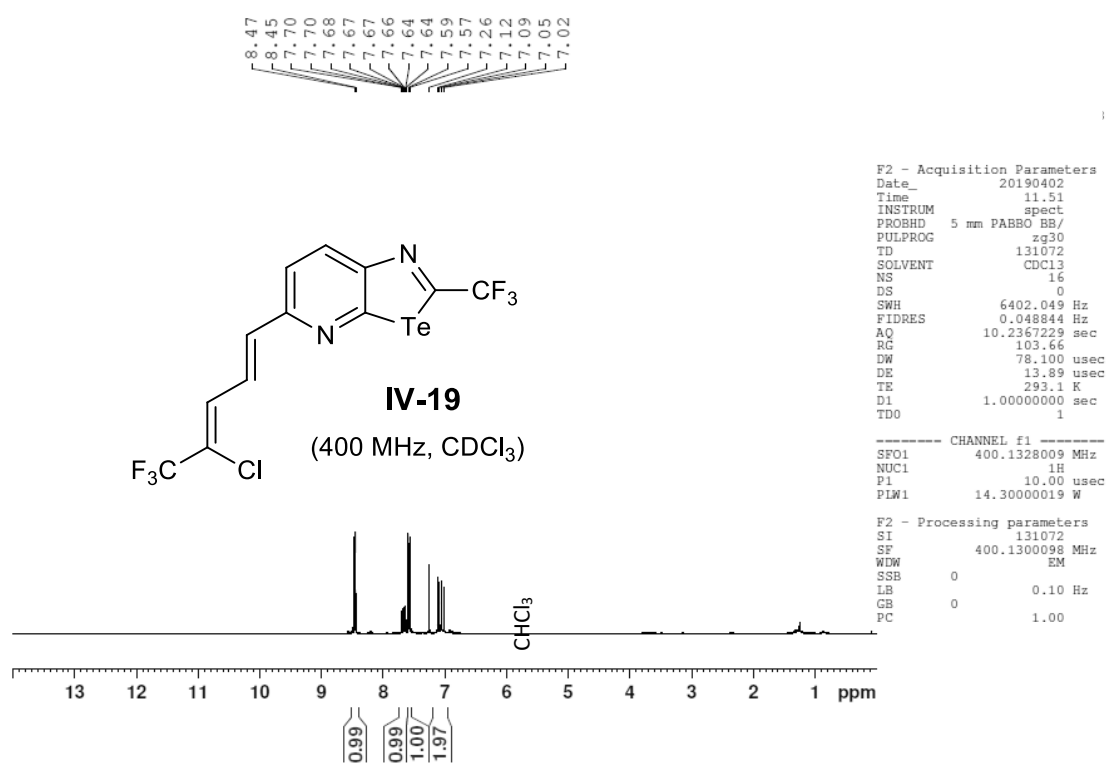
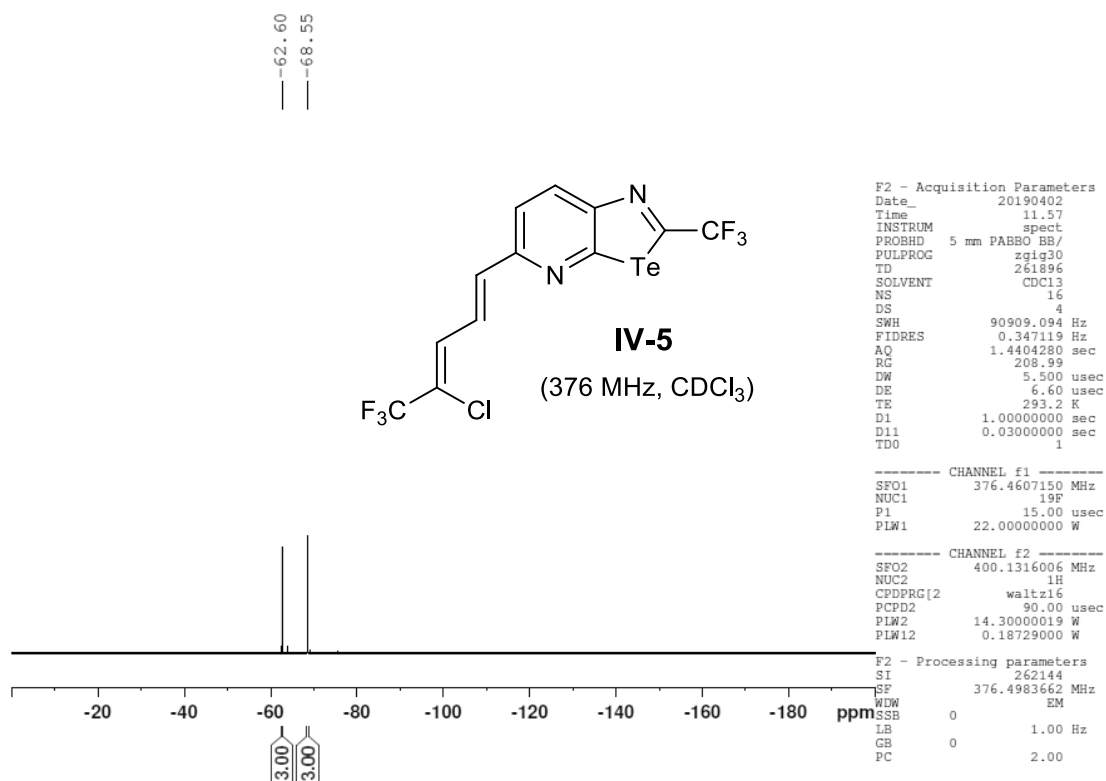
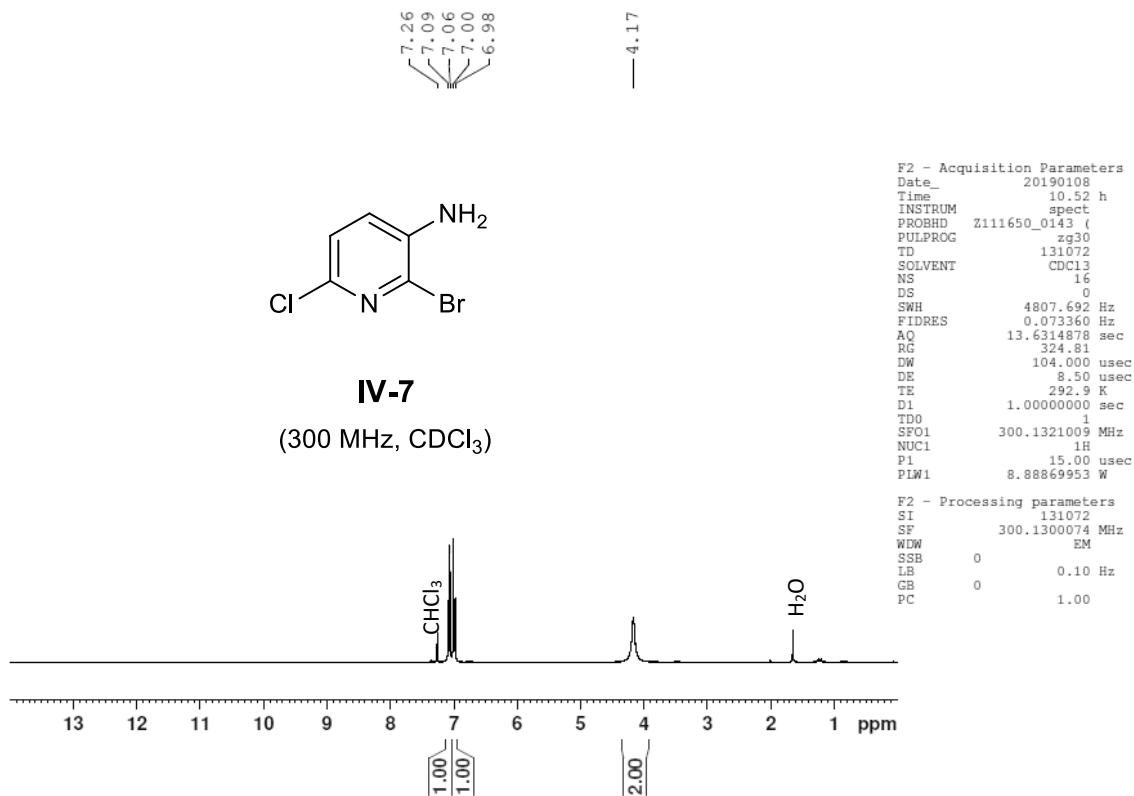
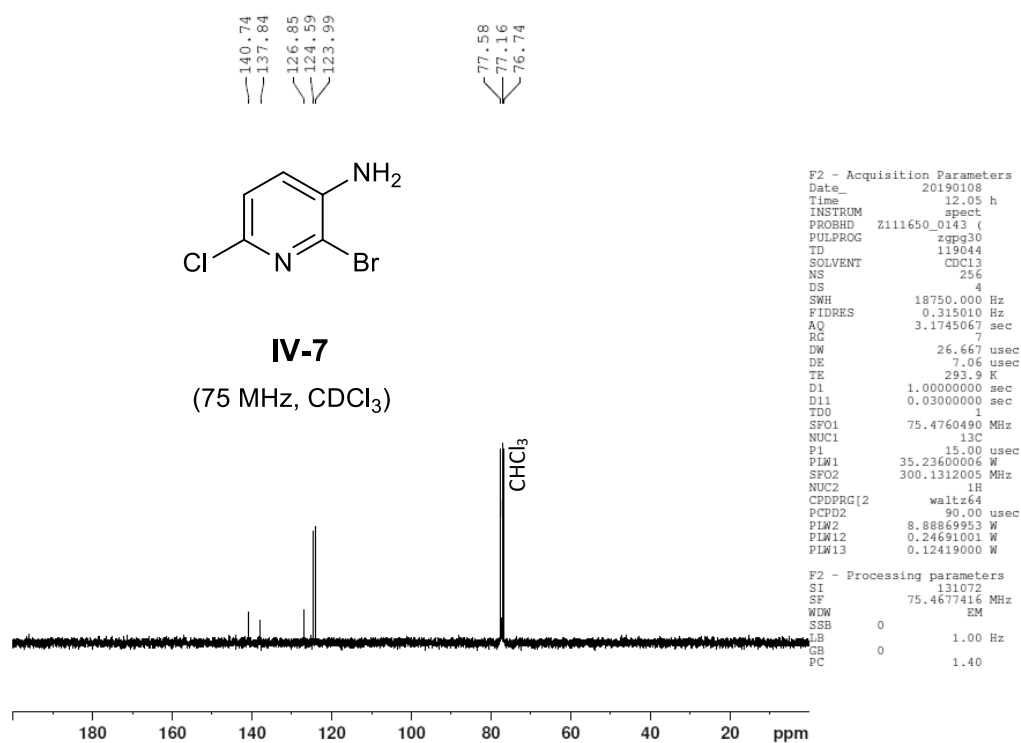
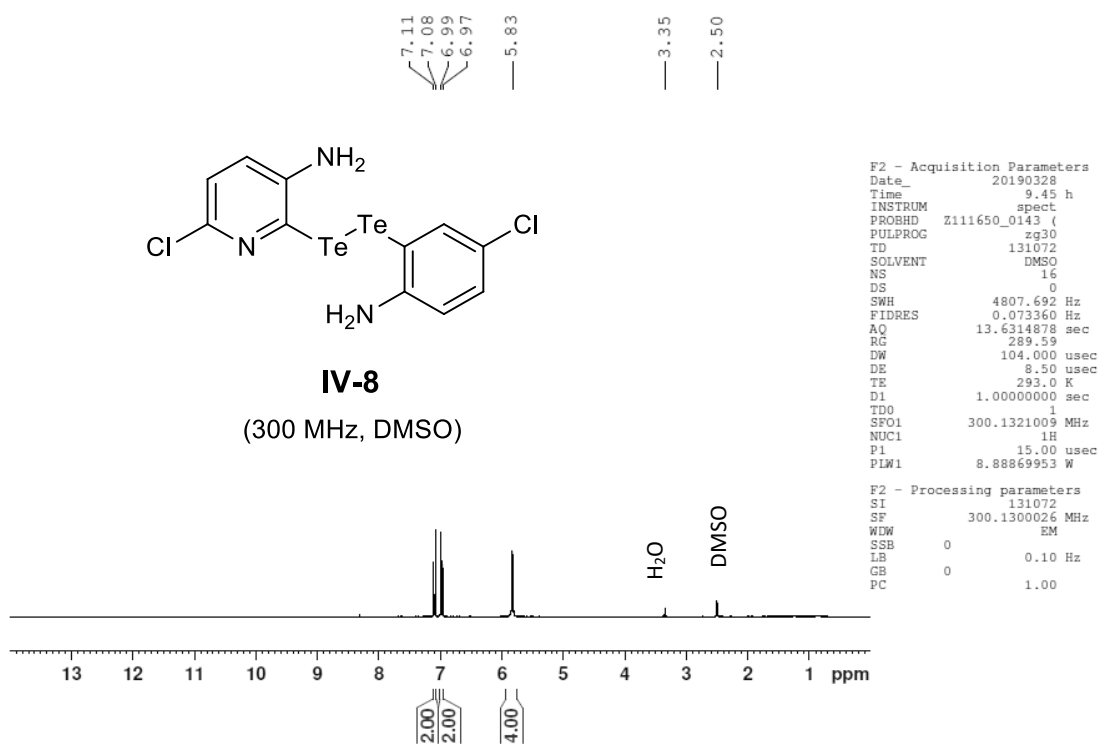
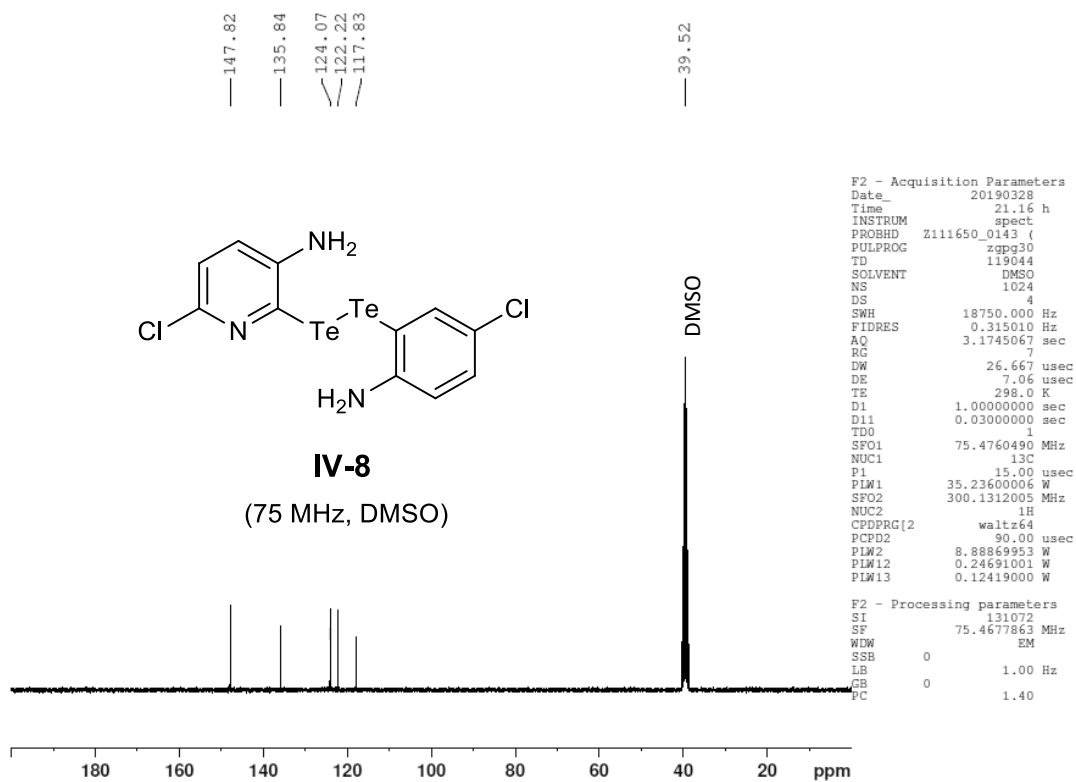
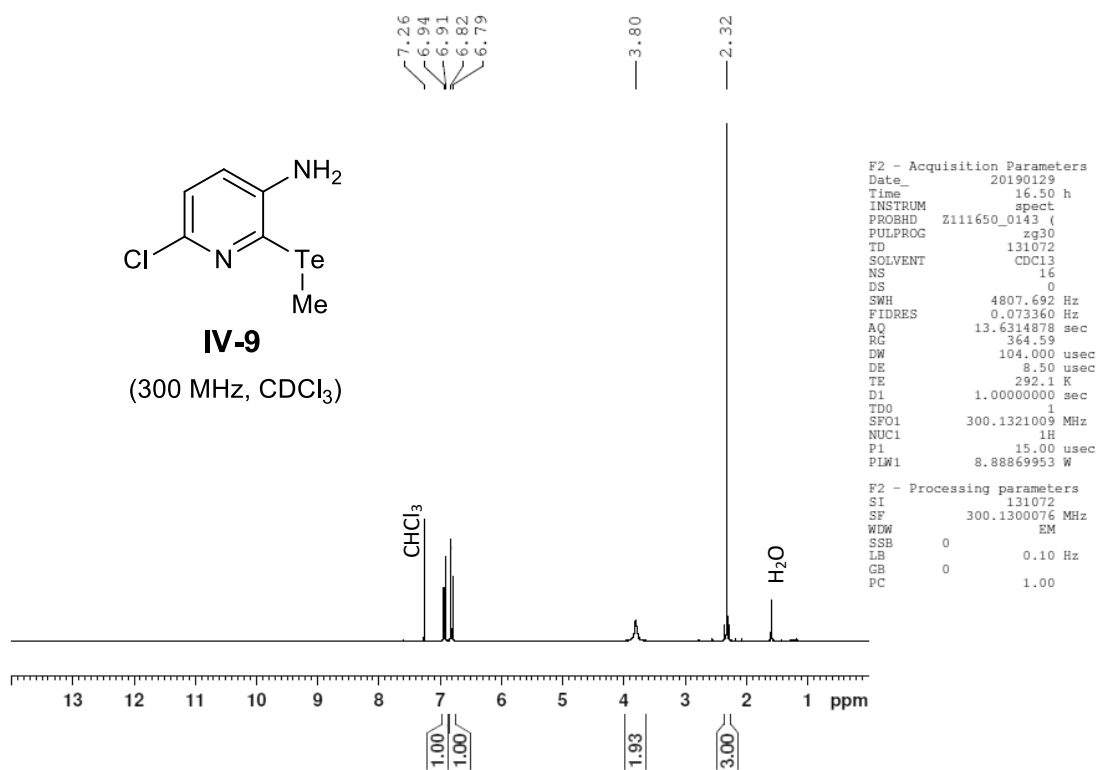
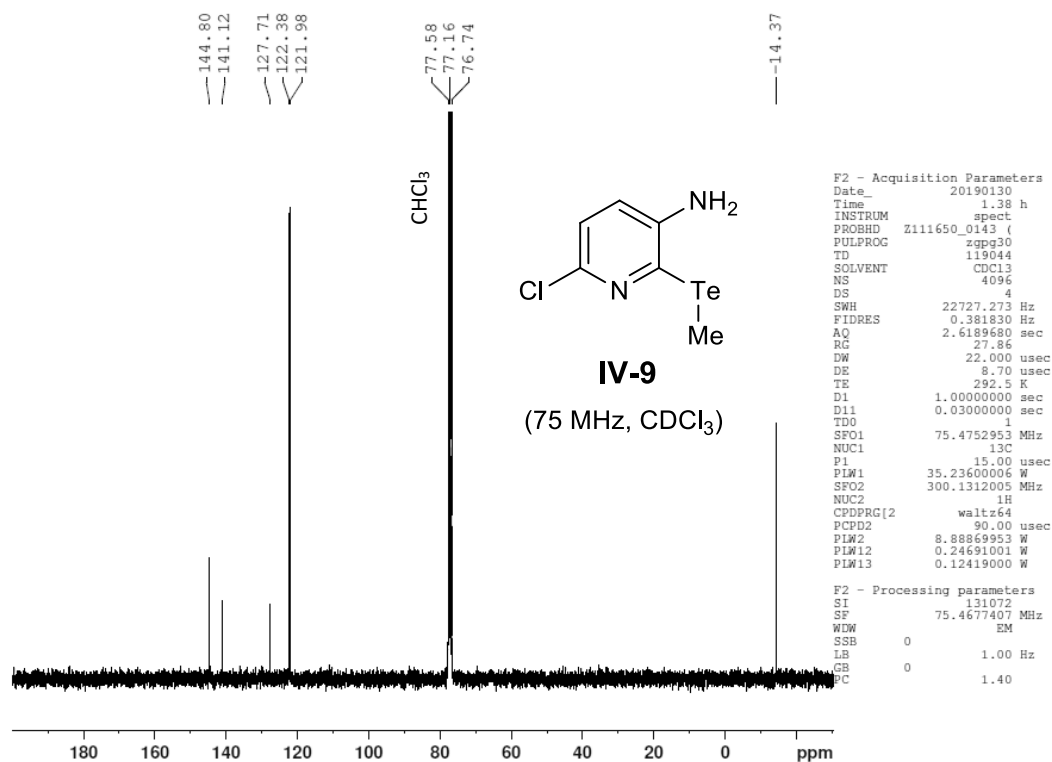
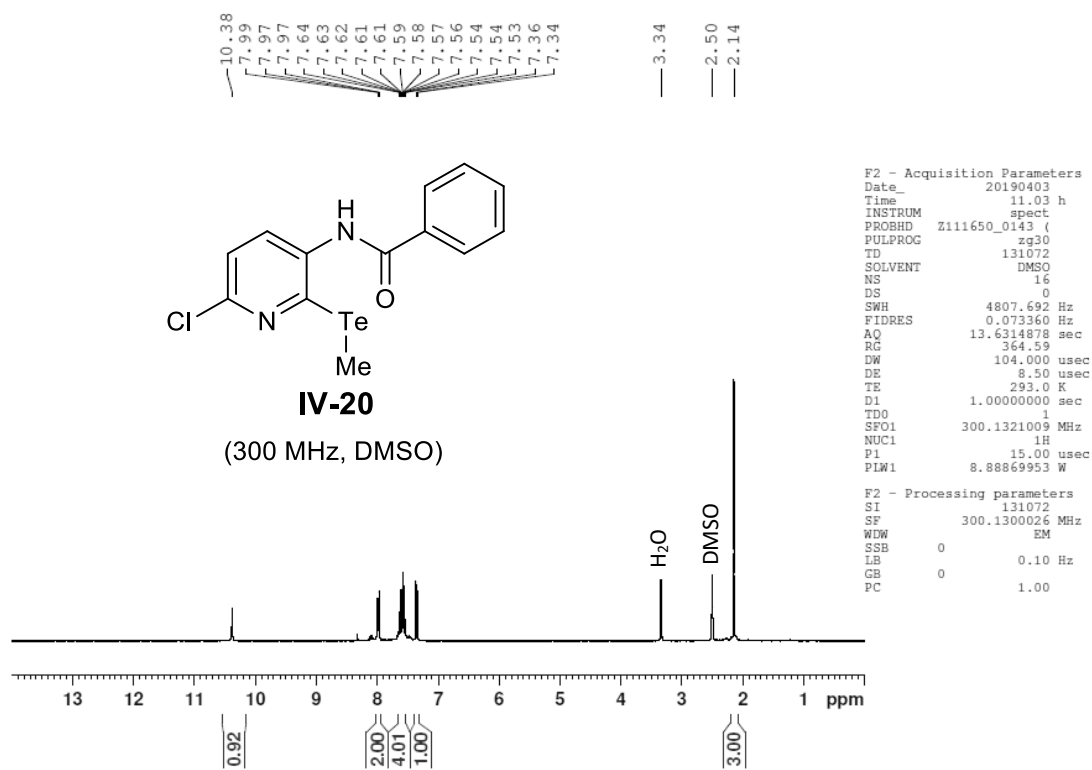


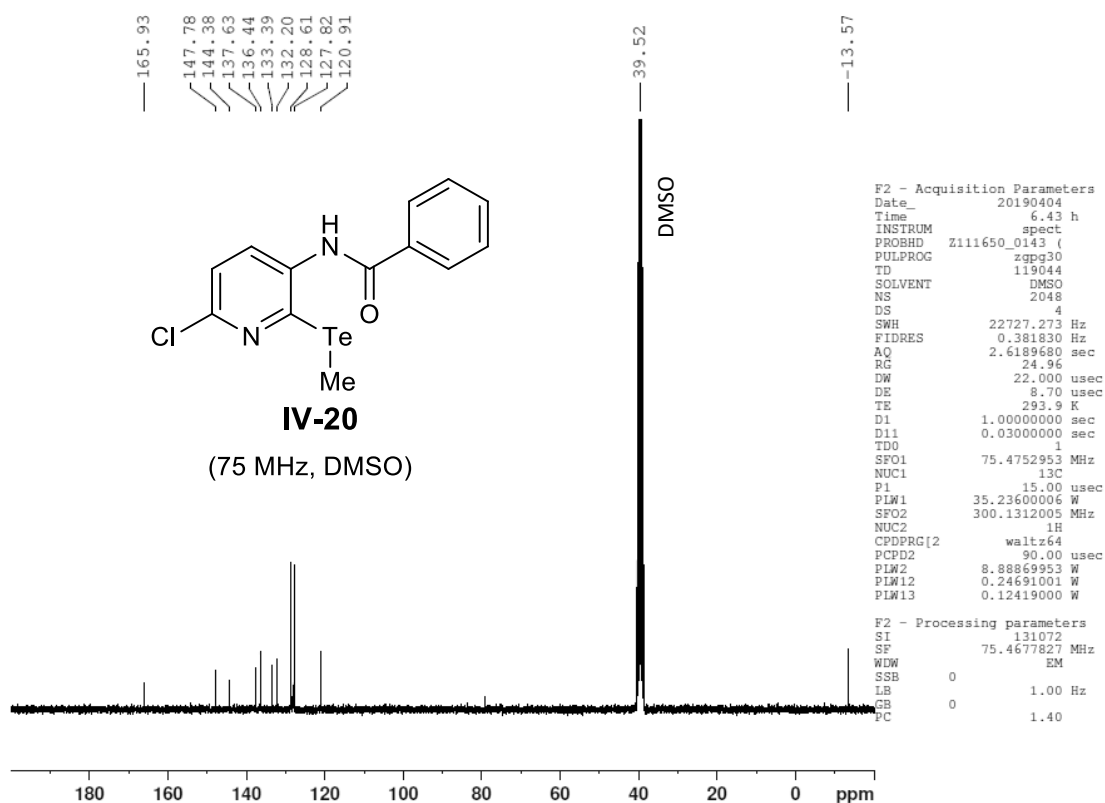
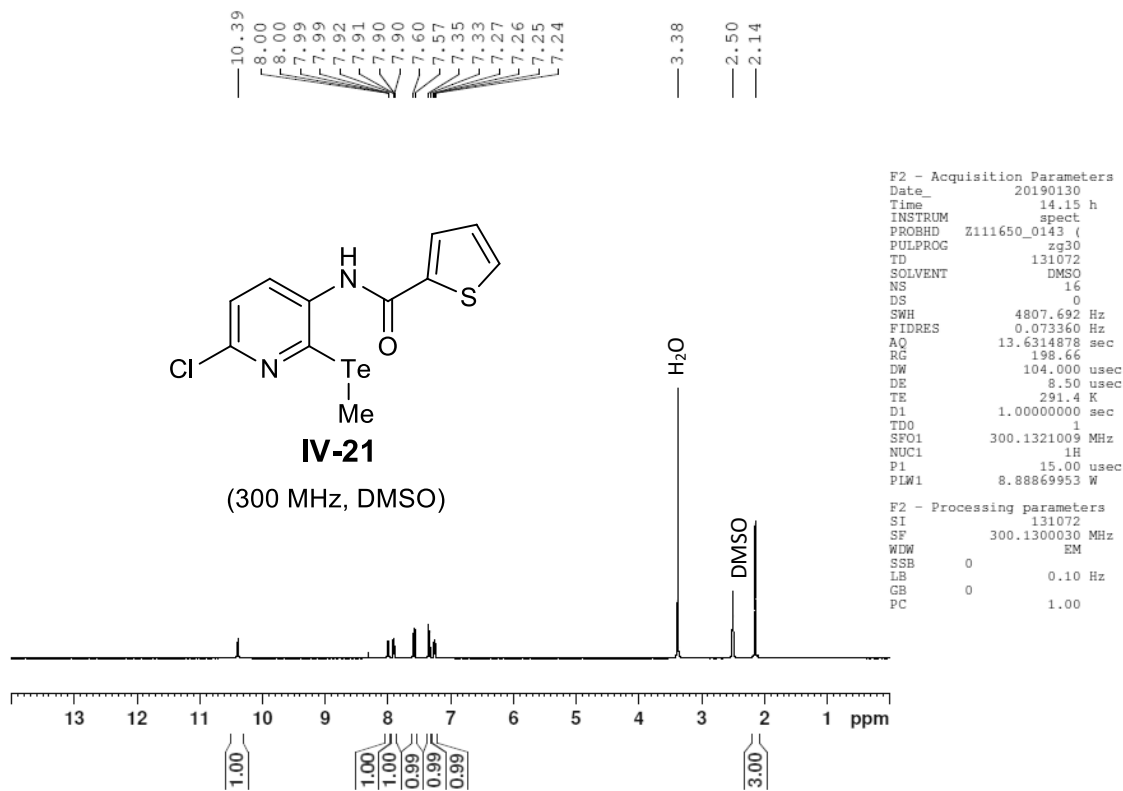
Figure VI - 126: 400 MHz <sup>1</sup>H-NMR in CDCl<sub>3</sub> of molecule IV-19.

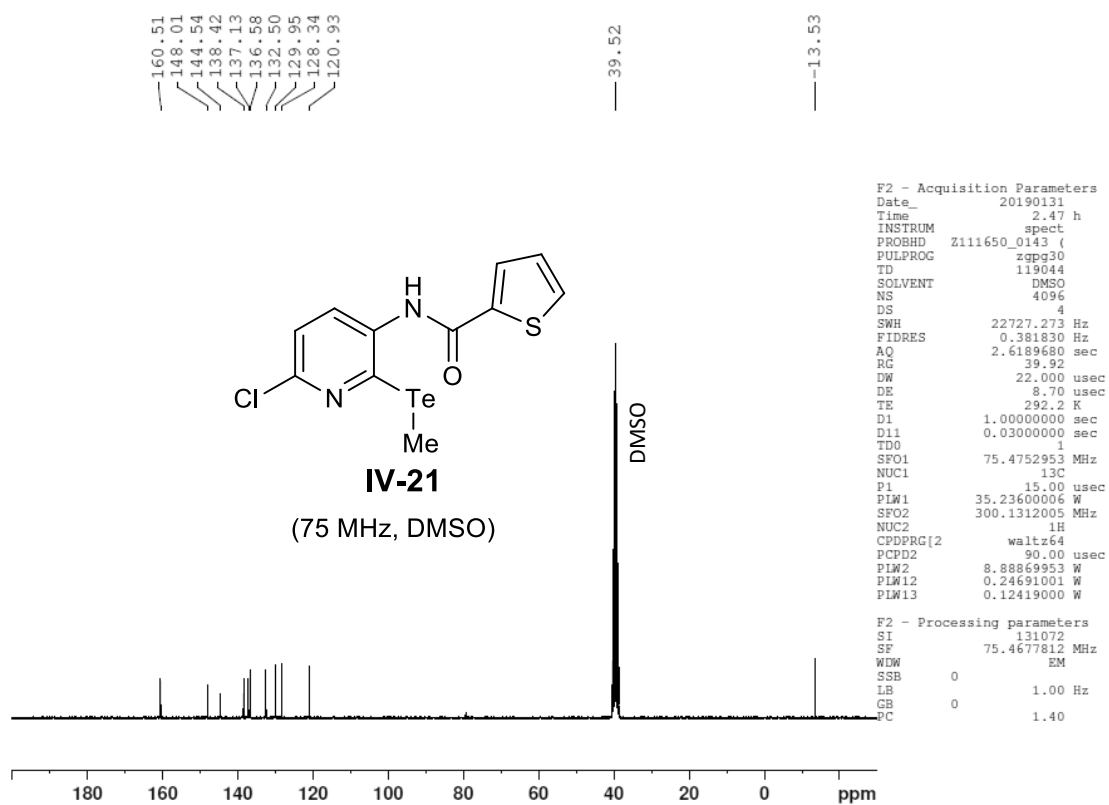
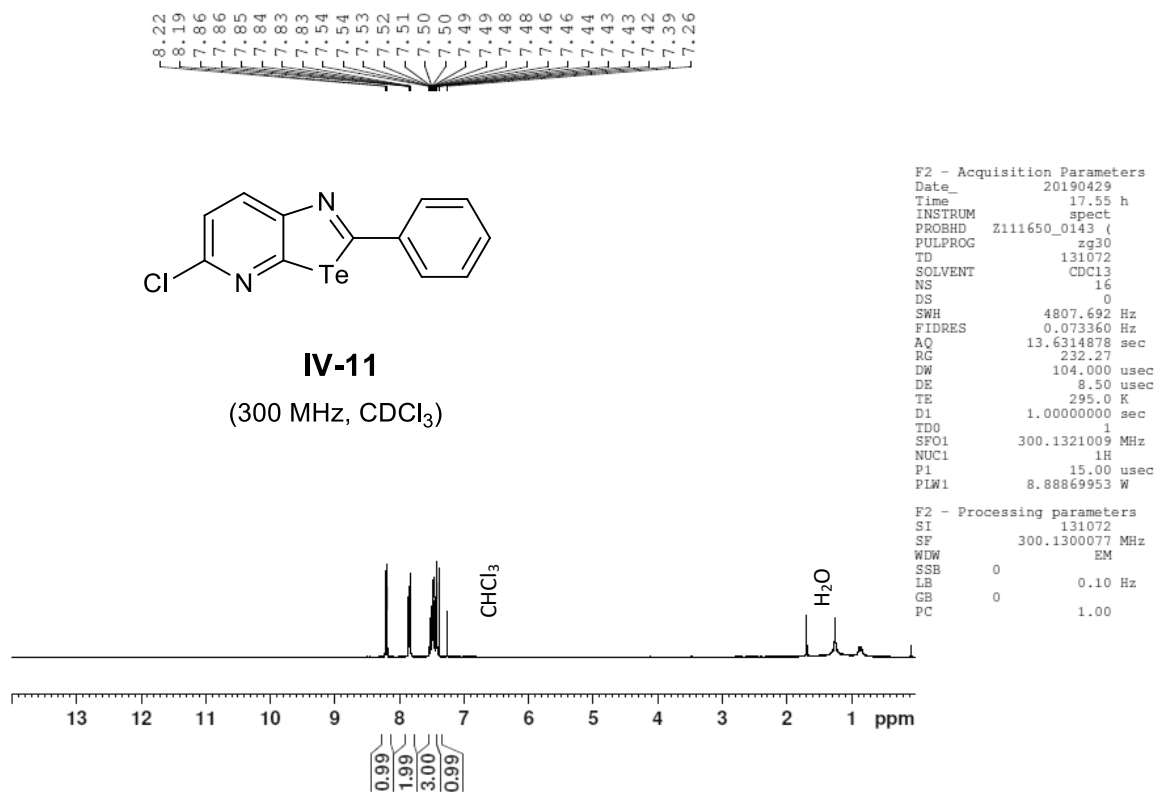
Figure VI - 127: 376 MHz <sup>19</sup>F-NMR in CDCl<sub>3</sub> of molecule IV-19.Figure VI - 128: 300 MHz <sup>1</sup>H-NMR in CDCl<sub>3</sub> of molecule IV-7.

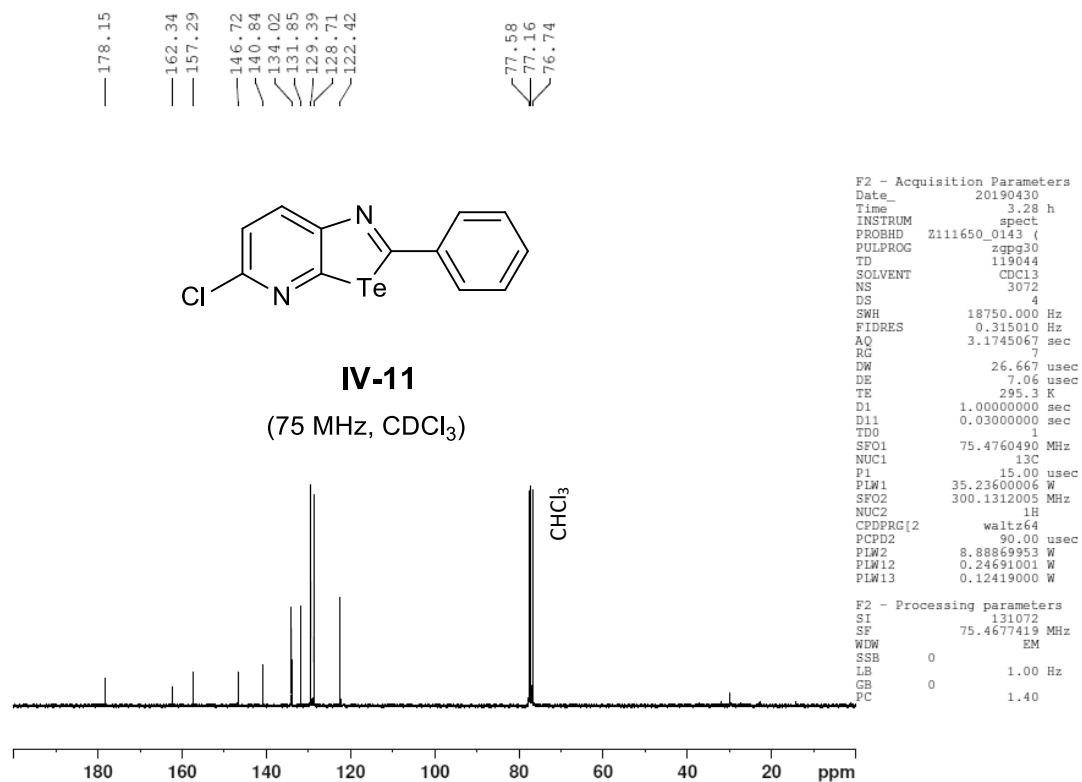
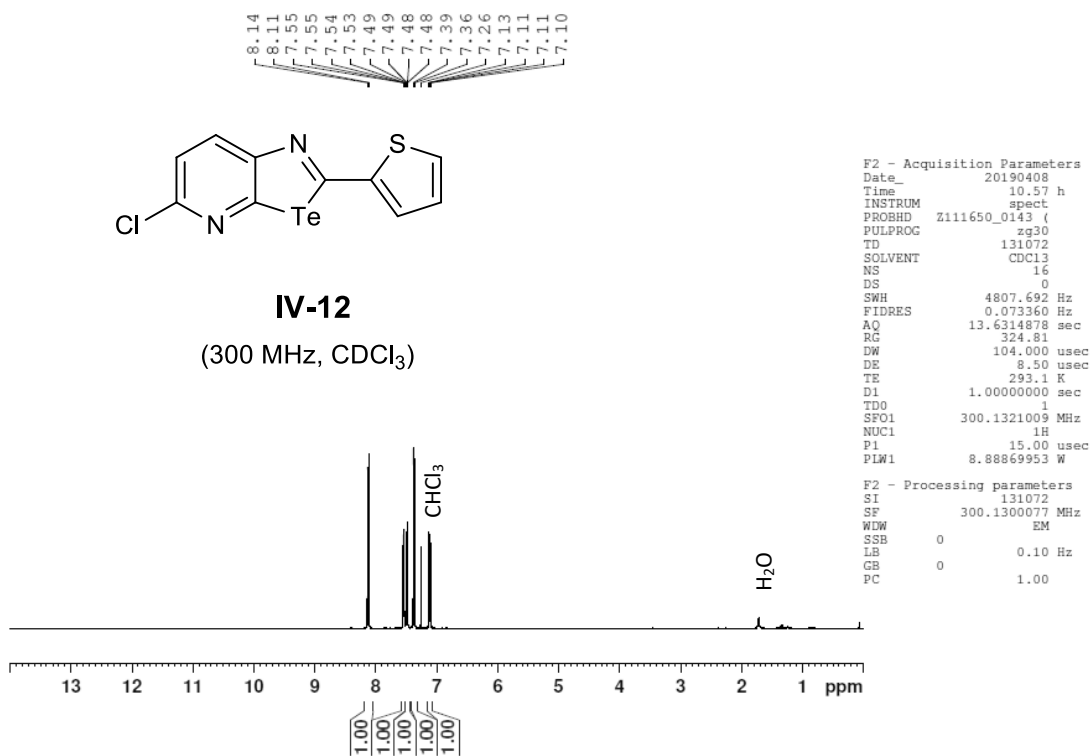
Figure VI - 129: 75 MHz <sup>13</sup>C-NMR in CDCl<sub>3</sub> of molecule IV-7.Figure VI - 130: 300 MHz <sup>1</sup>H-NMR in DMSO of molecule IV-8.

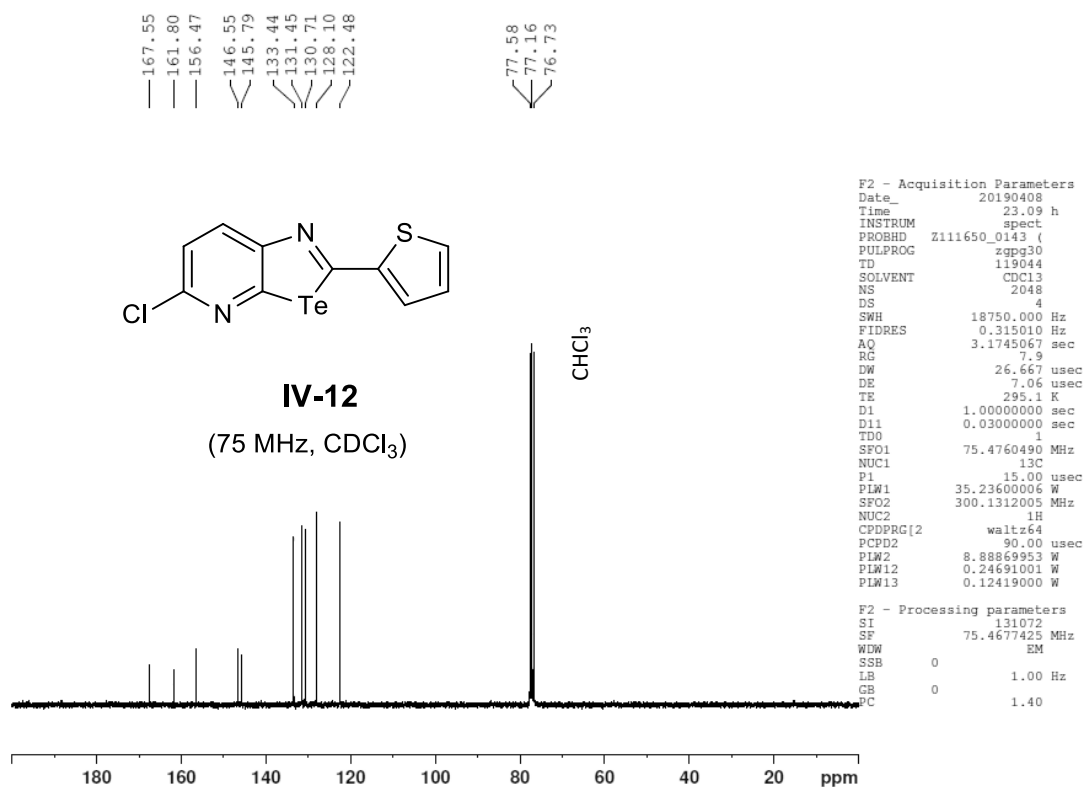
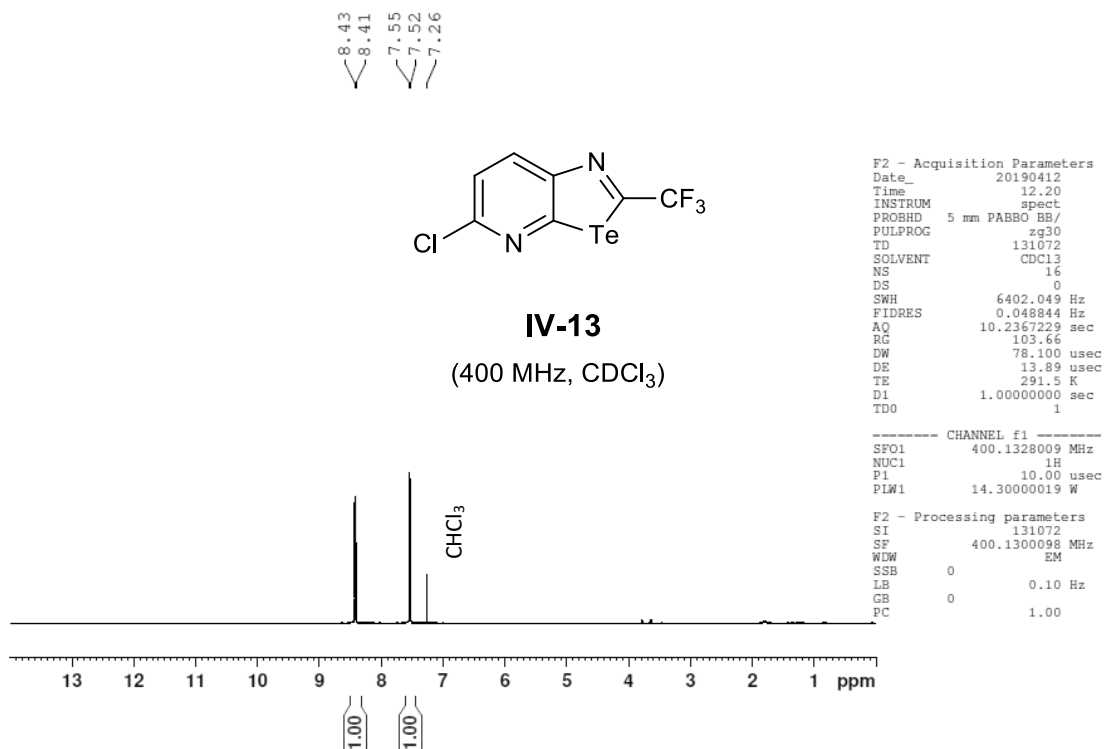
Figure VI - 131: 300 MHz  $^1\text{H}$ -NMR in DMSO of molecule IV-8.Figure VI - 132: 300 MHz  $^1\text{H}$ -NMR in  $\text{CDCl}_3$  of molecule IV-9.

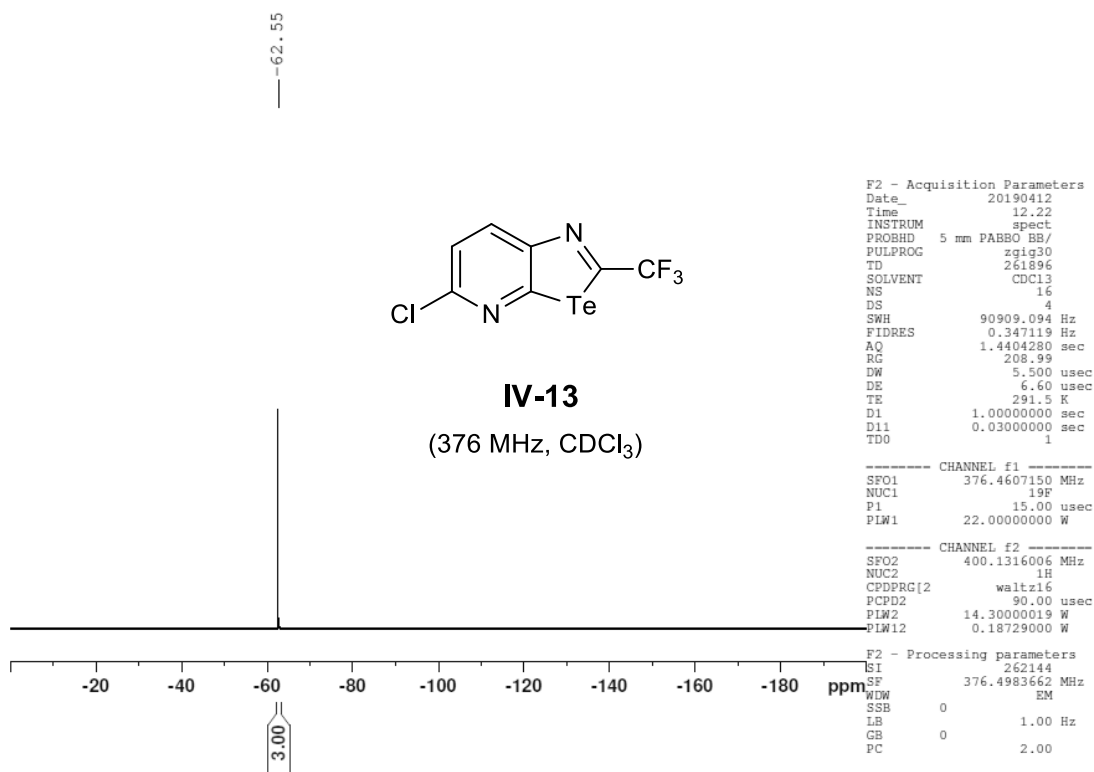
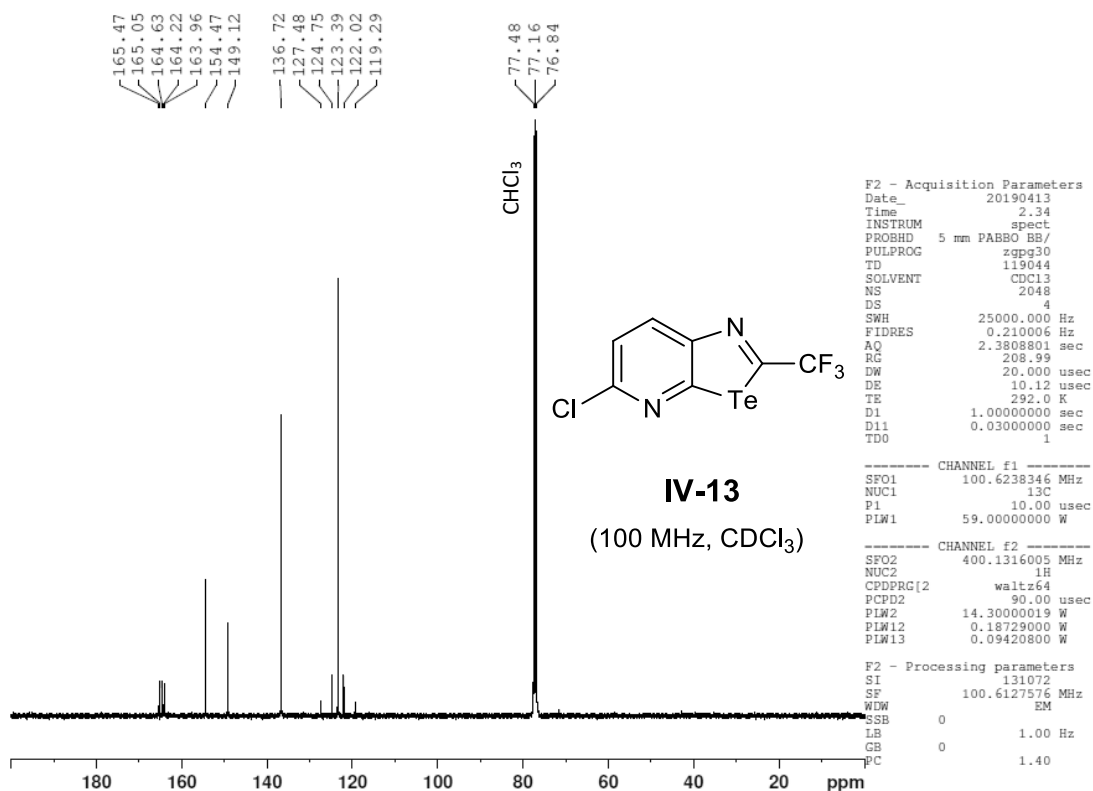
Figure VI - 133: 75 MHz <sup>13</sup>C-NMR in CDCl<sub>3</sub> of molecule IV-9.Figure VI - 134: 300 MHz <sup>1</sup>H-NMR in DMSO of molecule IV-20.

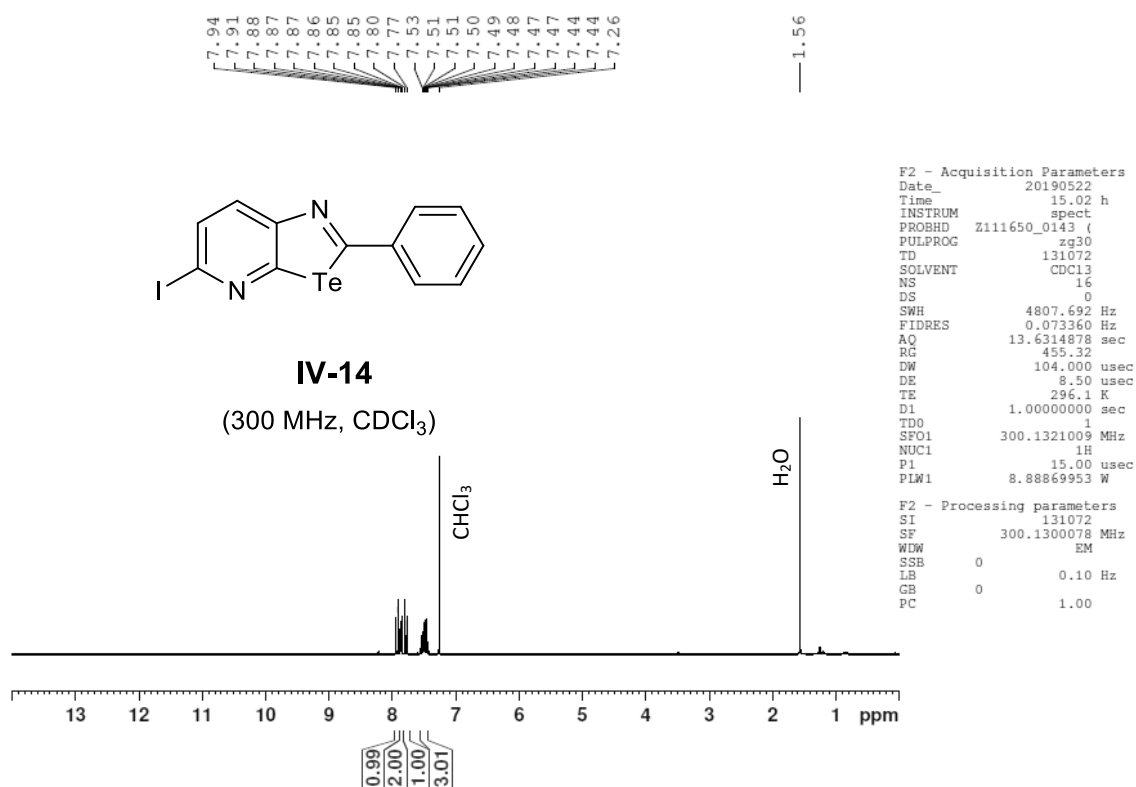
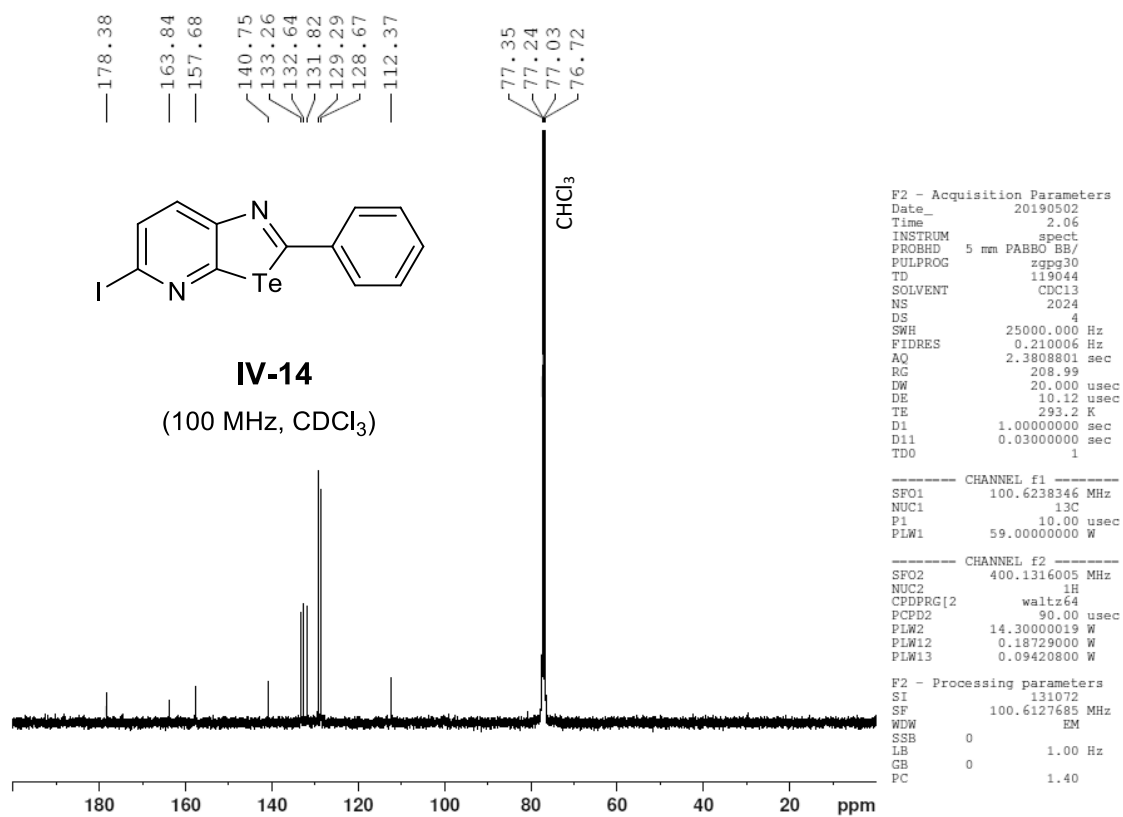
Figure VI - 135: 75 MHz  $^{13}\text{C}$ -NMR in DMSO of molecule IV-20.Figure VI - 136: 300 MHz  $^1\text{H}$ -NMR in DMSO of molecule IV-21.

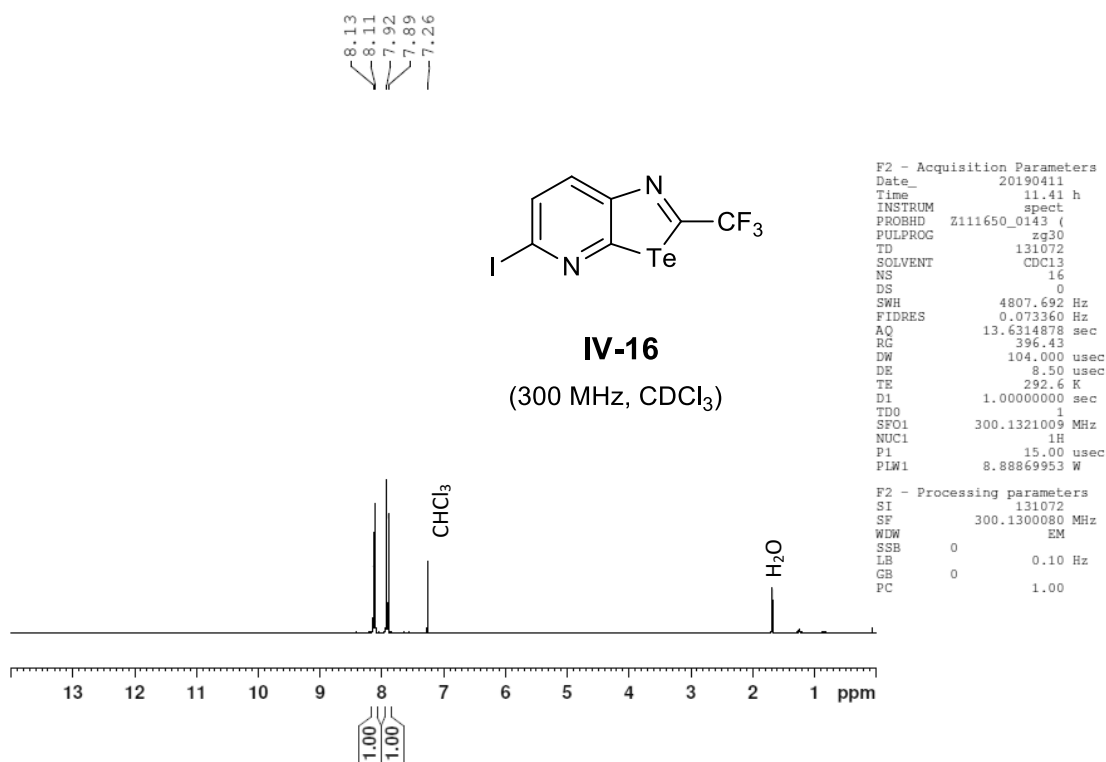
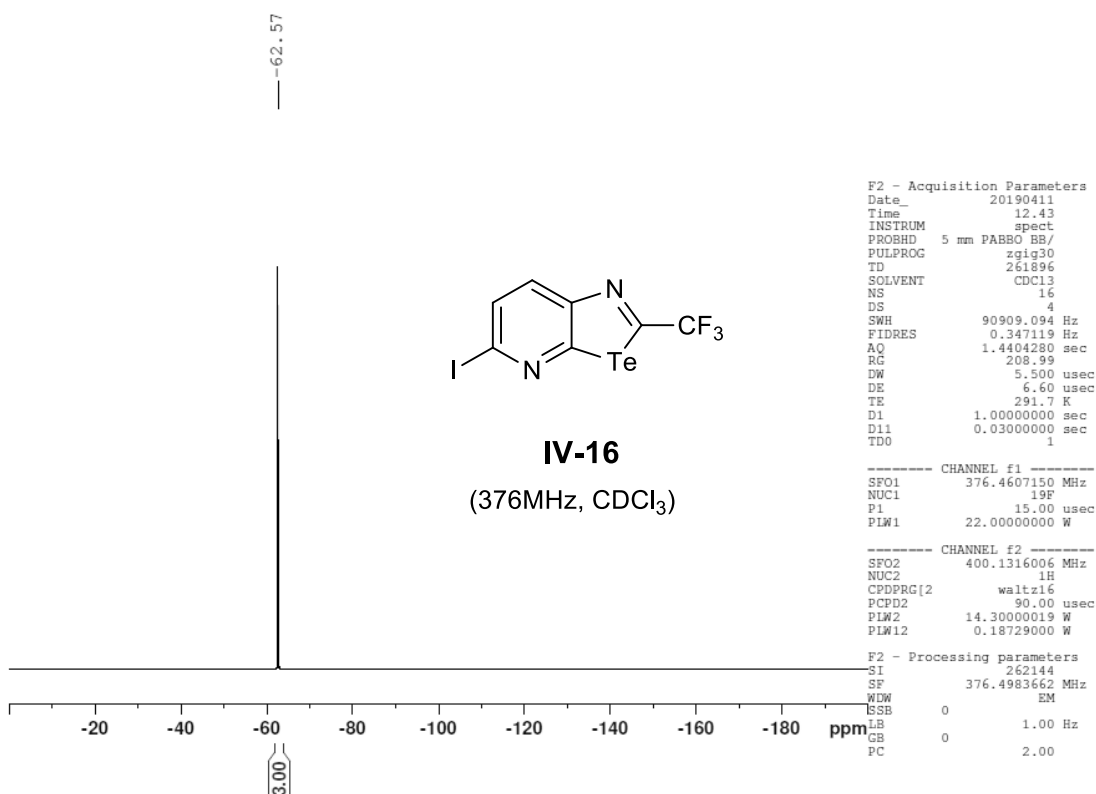
Figure VI - 137: 75 MHz  $^{13}\text{C}$ -NMR in DMSO of molecule IV-21.Figure VI - 138: 300 MHz  $^1\text{H}$ -NMR in  $\text{CDCl}_3$  of molecule IV-11.

Figure VI - 139: 75 MHz <sup>13</sup>C-NMR in CDCl<sub>3</sub> of molecule IV-11.Figure VI - 140: 300 MHz <sup>1</sup>H-NMR in CDCl<sub>3</sub> of molecule IV-12.

Figure VI - 141: 75 MHz <sup>13</sup>C-NMR in CDCl<sub>3</sub> of molecule IV-12.Figure VI - 142: 400 MHz <sup>1</sup>H-NMR in CDCl<sub>3</sub> of molecule IV-13.

Figure VI - 143: 376 MHz <sup>19</sup>F-NMR in CDCl<sub>3</sub> of molecule IV-13.Figure VI - 144: 100 MHz <sup>13</sup>C-NMR in CDCl<sub>3</sub> of molecule IV-13. Due to <sup>13</sup>C-<sup>19</sup>F coupling: Peak 164.8 splits into 165.47, 165.05, 164.63 and 164.22; Peak 123.2 splits into 127.48, 124.75, 122.02 and 119.29.

Figure VI - 145: 300 MHz <sup>1</sup>H-NMR in CDCl<sub>3</sub> of molecule IV-14.Figure VI - 146: 100 MHz <sup>13</sup>C-NMR in CDCl<sub>3</sub> of molecule IV-14.

Figure VI - 147: 300 MHz <sup>1</sup>H-NMR in CDCl<sub>3</sub> of molecule IV-16.Figure VI - 148: 376 MHz <sup>19</sup>F-NMR in CDCl<sub>3</sub> of molecule IV-16.

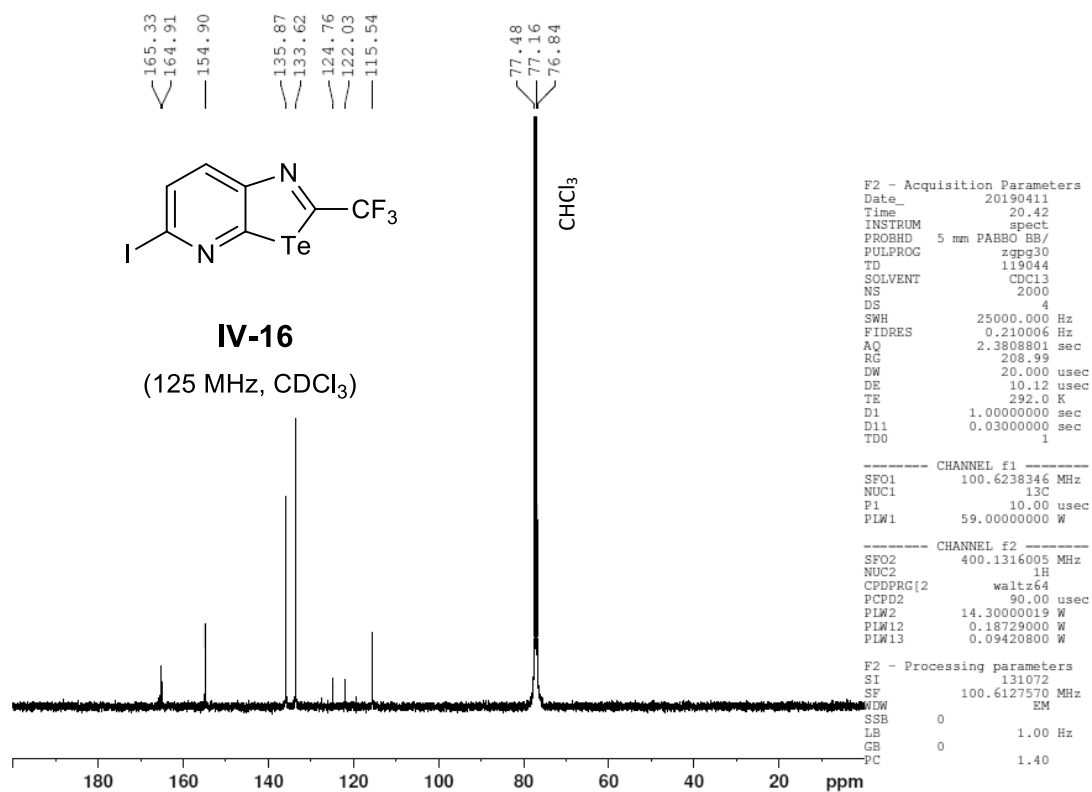


Figure VI - 149: 125 MHz <sup>13</sup>C-NMR in CDCl<sub>3</sub> of molecule **IV-16**. Due to <sup>13</sup>C-<sup>19</sup>F coupling: Peak 165.1 splits into 165.33 and 164.91; Peak 123.4 splits into 124.76 and 122.03.

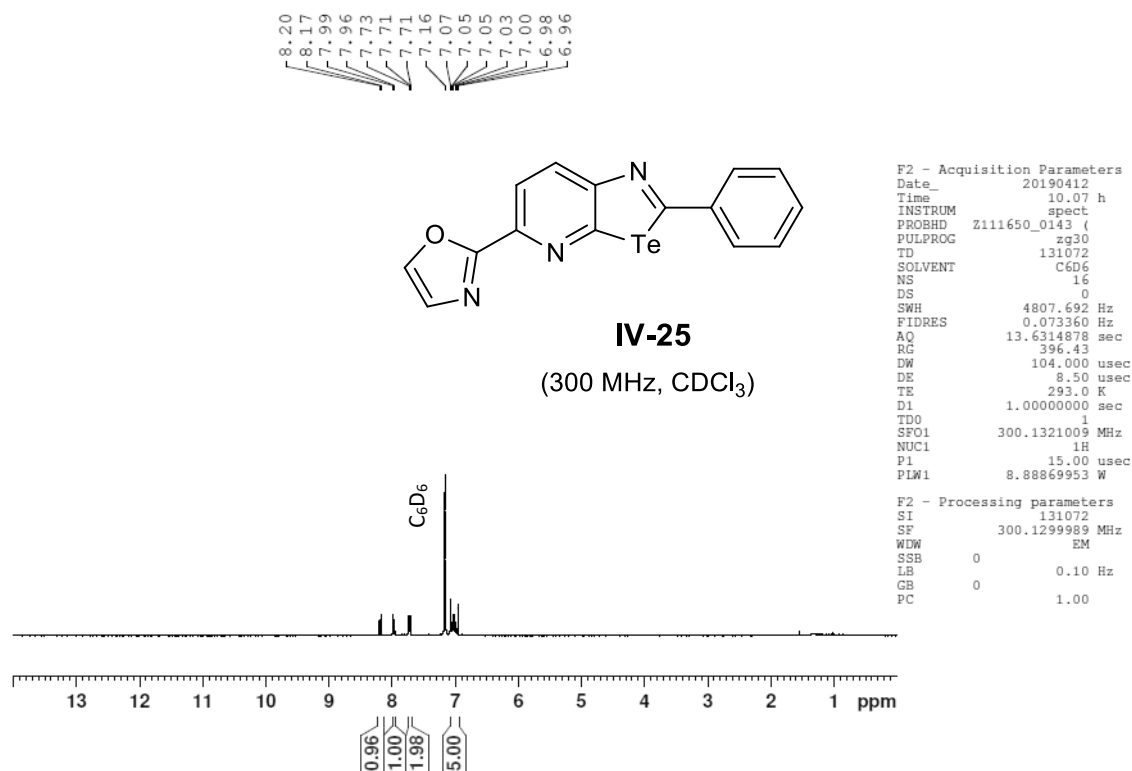
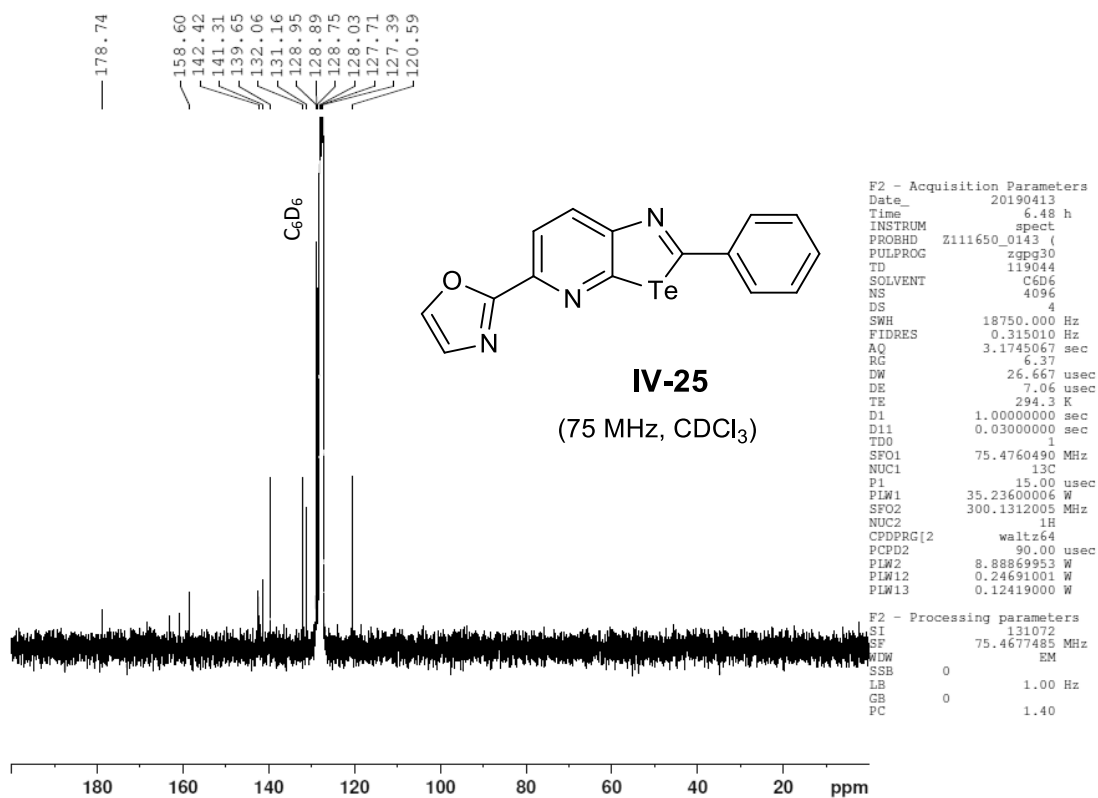
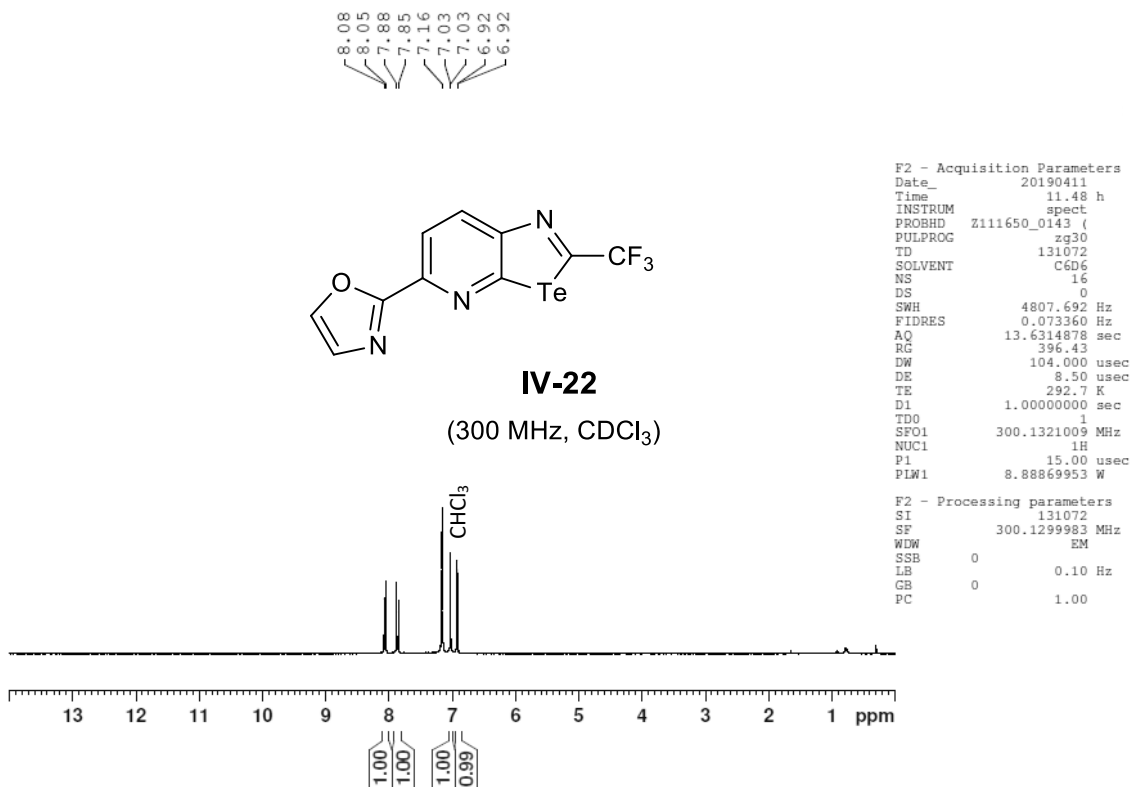
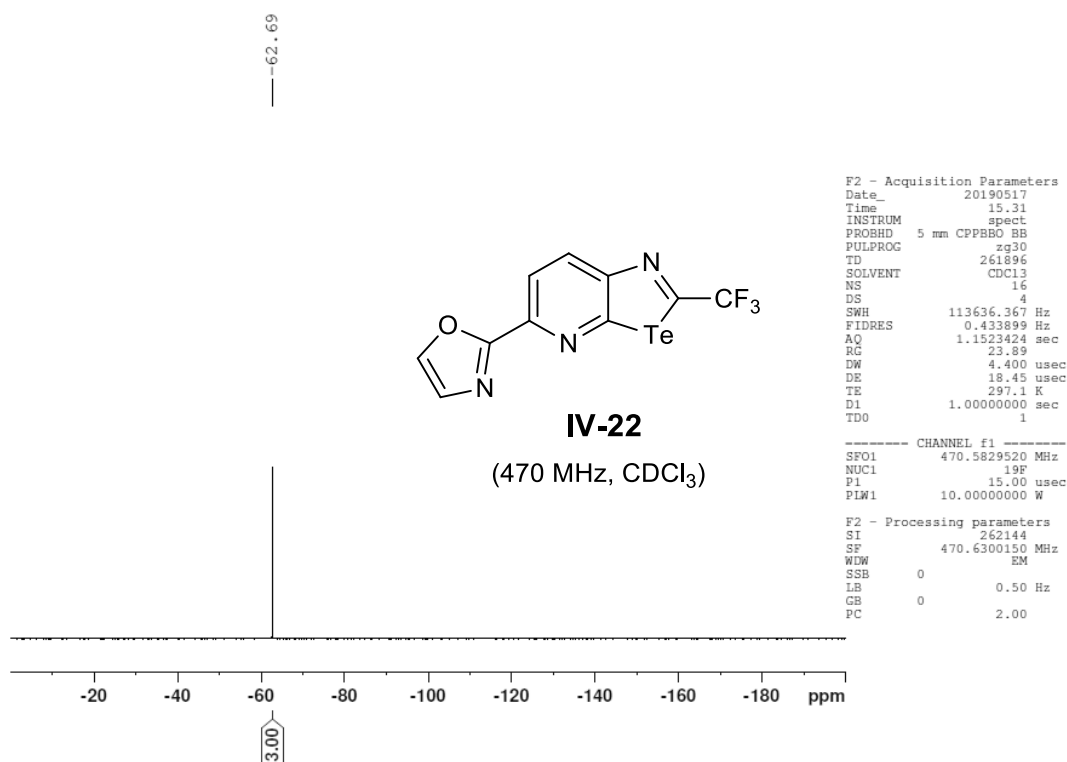
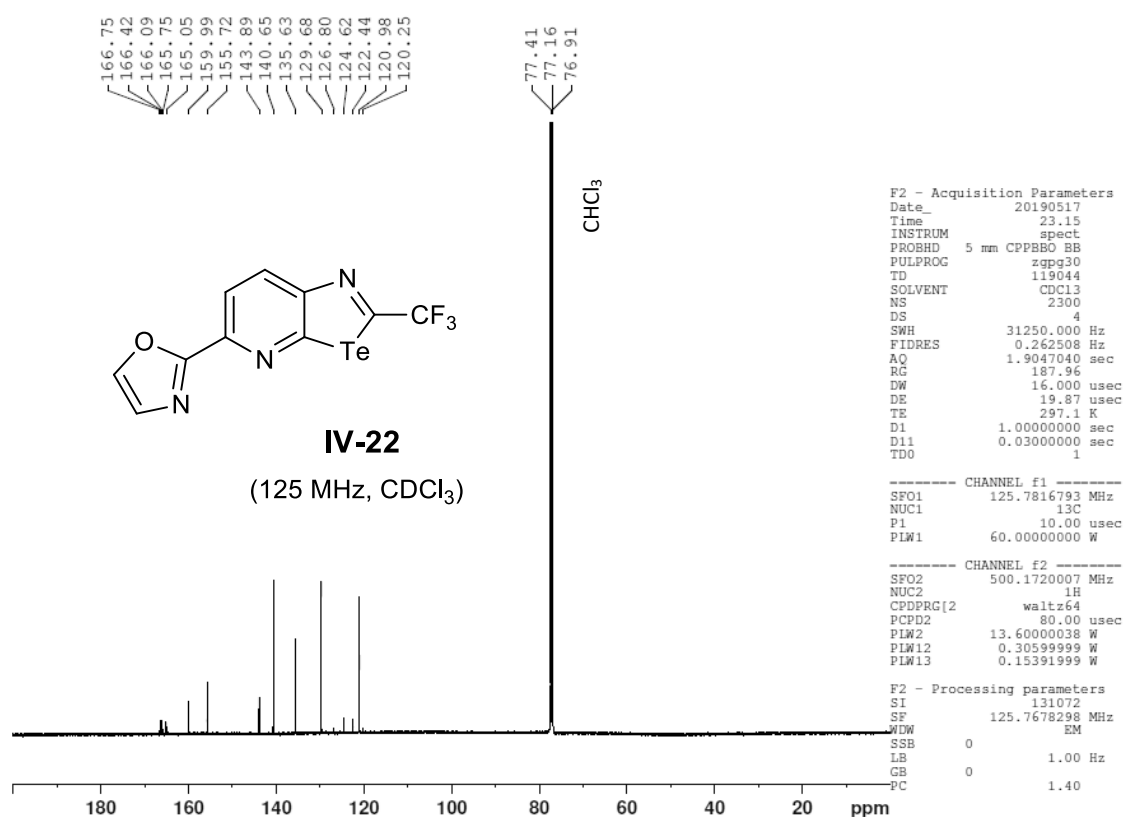


Figure VI - 150: 300 MHz <sup>1</sup>H-NMR in C<sub>6</sub>D<sub>6</sub> of molecule **IV-25**.

Figure VI - 151: 75 MHz <sup>13</sup>C-NMR in C<sub>6</sub>D<sub>6</sub> of molecule IV-25.Figure VI - 152: 300 MHz <sup>1</sup>H-NMR in CDCl<sub>3</sub> of molecule IV-22.

Figure VI - 153: 470 MHz <sup>19</sup>F-NMR in CDCl<sub>3</sub> of molecule IV-22.Figure VI - 154: 125 MHz <sup>13</sup>C-NMR in CDCl<sub>3</sub> of molecule IV-22. Due to <sup>13</sup>C-<sup>19</sup>F coupling: Peak 166.3 splits into 166.75, 166.42, 166.09 and 165.75; Peak 123.5 splits into 126.80, 124.62, 122.44 and 120.25.

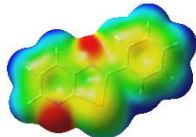
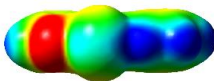
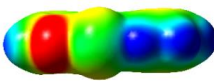
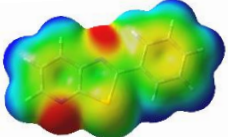
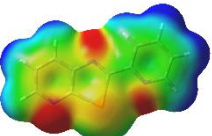
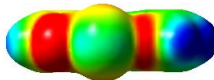
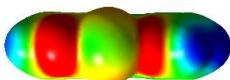
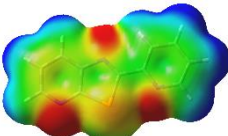
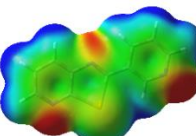
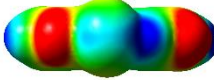
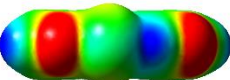
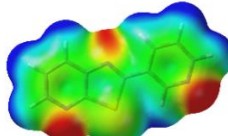
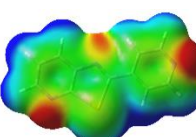
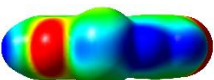
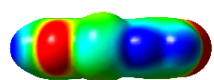
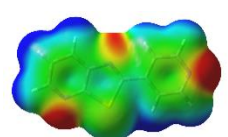
## VI – 4 Calculations

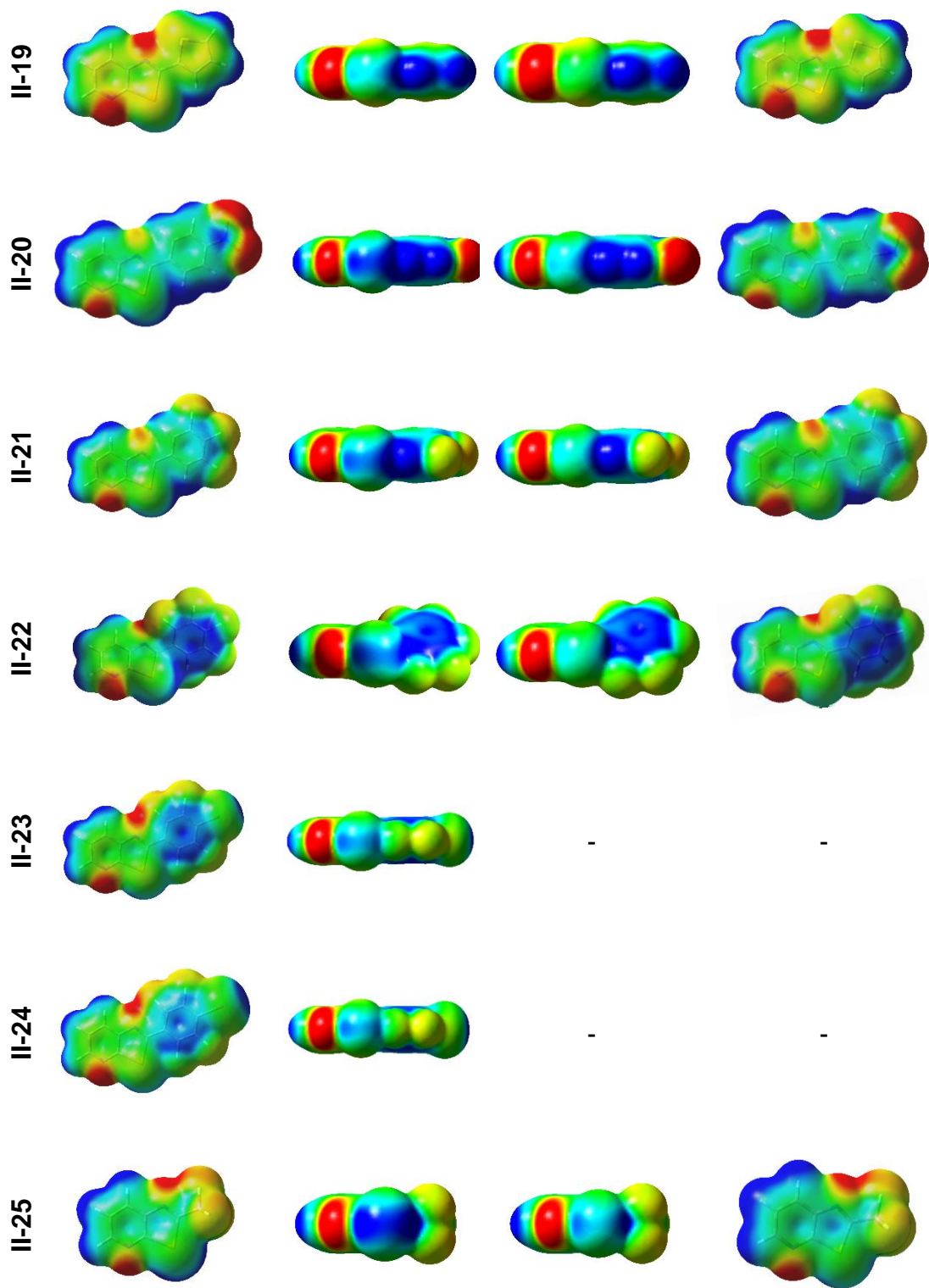
### VI – 4.1 General remarks

**Calculations** were carried out using Gaussian 09 including the D01 revision.<sup>[14]</sup> Geometries optimizations were firstly carried out at B97-D3/LanL2DZ level of theory and frontier orbitals were obtained at the same level.<sup>[15-17]</sup> Then structures were optimized again at B97-D3/Def2-TZVP level of theory and electrostatic surface potential were created at the same level.<sup>[18, 19]</sup> ESP surfaces were mapped on the van der Waals surface of molecules up to an electron density of 0.001 electron.bohr<sup>-3</sup>.  $V_{s,max}$  were determined with a classical method.<sup>[20]</sup> Frontier orbitals images were obtained using the Avogadro software and ESP figures with Gaussview4.

### VI – 4.2 Electrostatic surface potential

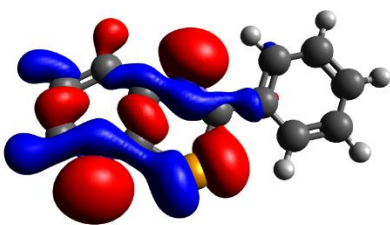
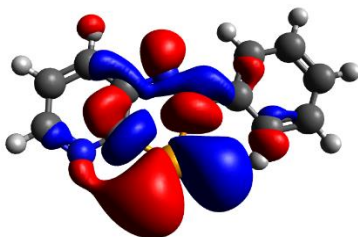
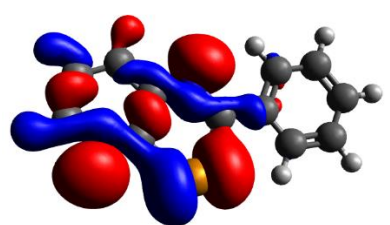
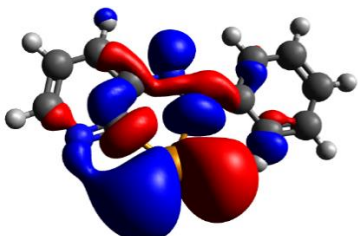
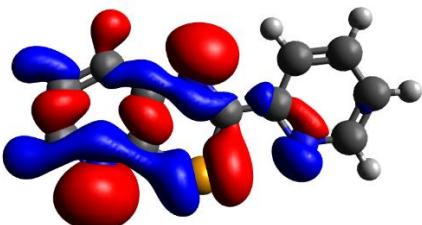
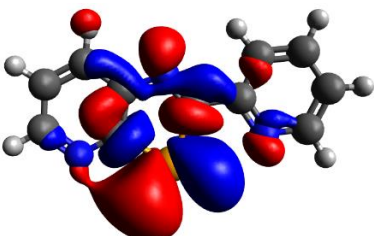
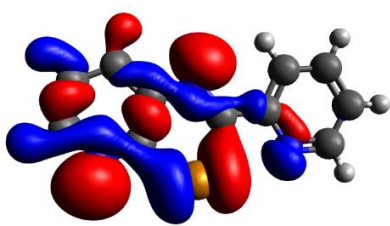
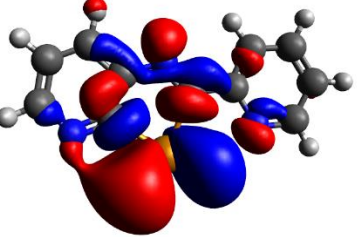
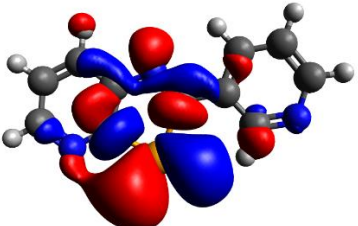
Table VI - 1: ESP maps.

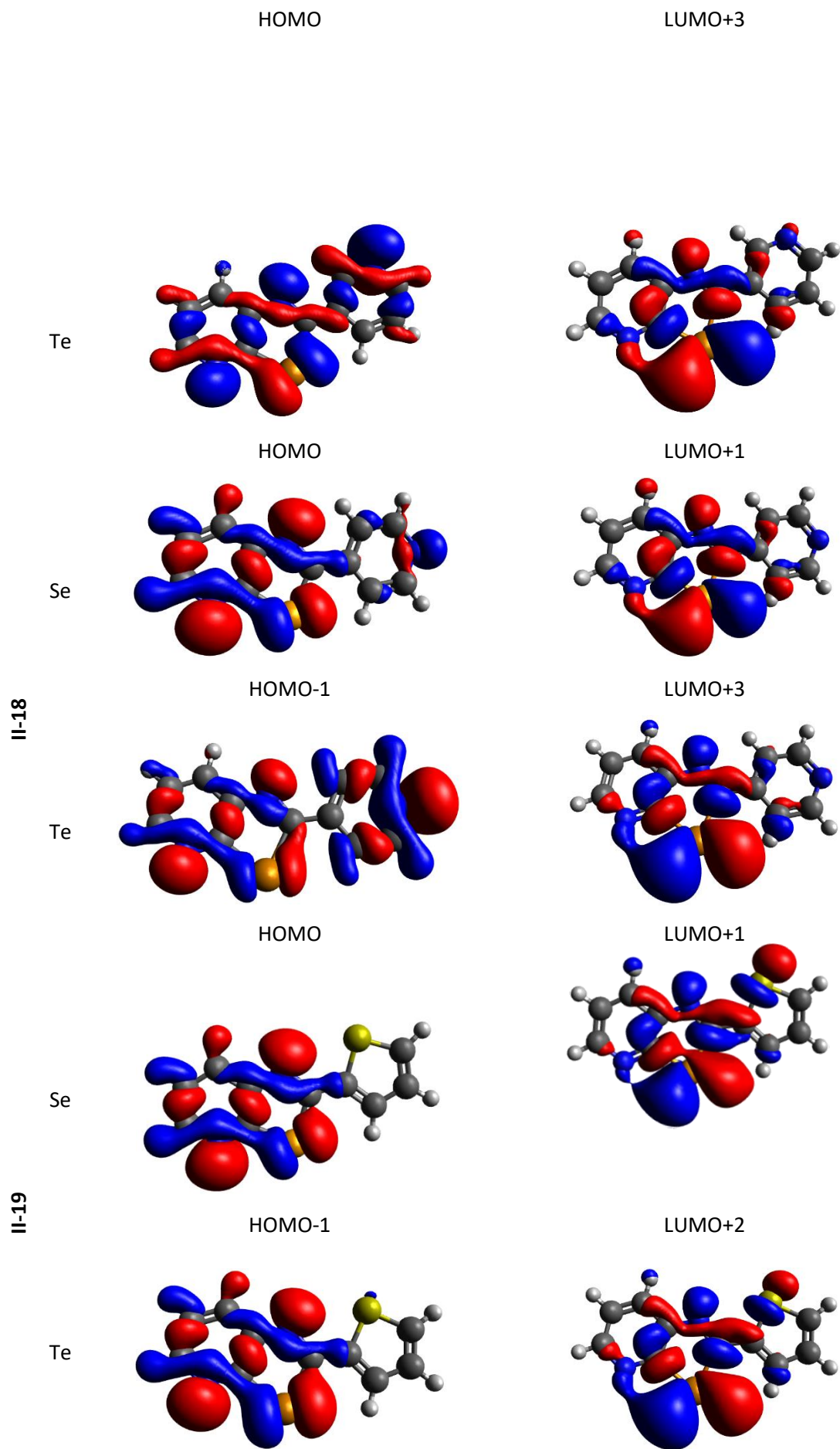
	Te		Se	
	Top view	Side view	Side view	Top view
II-15				
II-16				
II-17				
II-18				

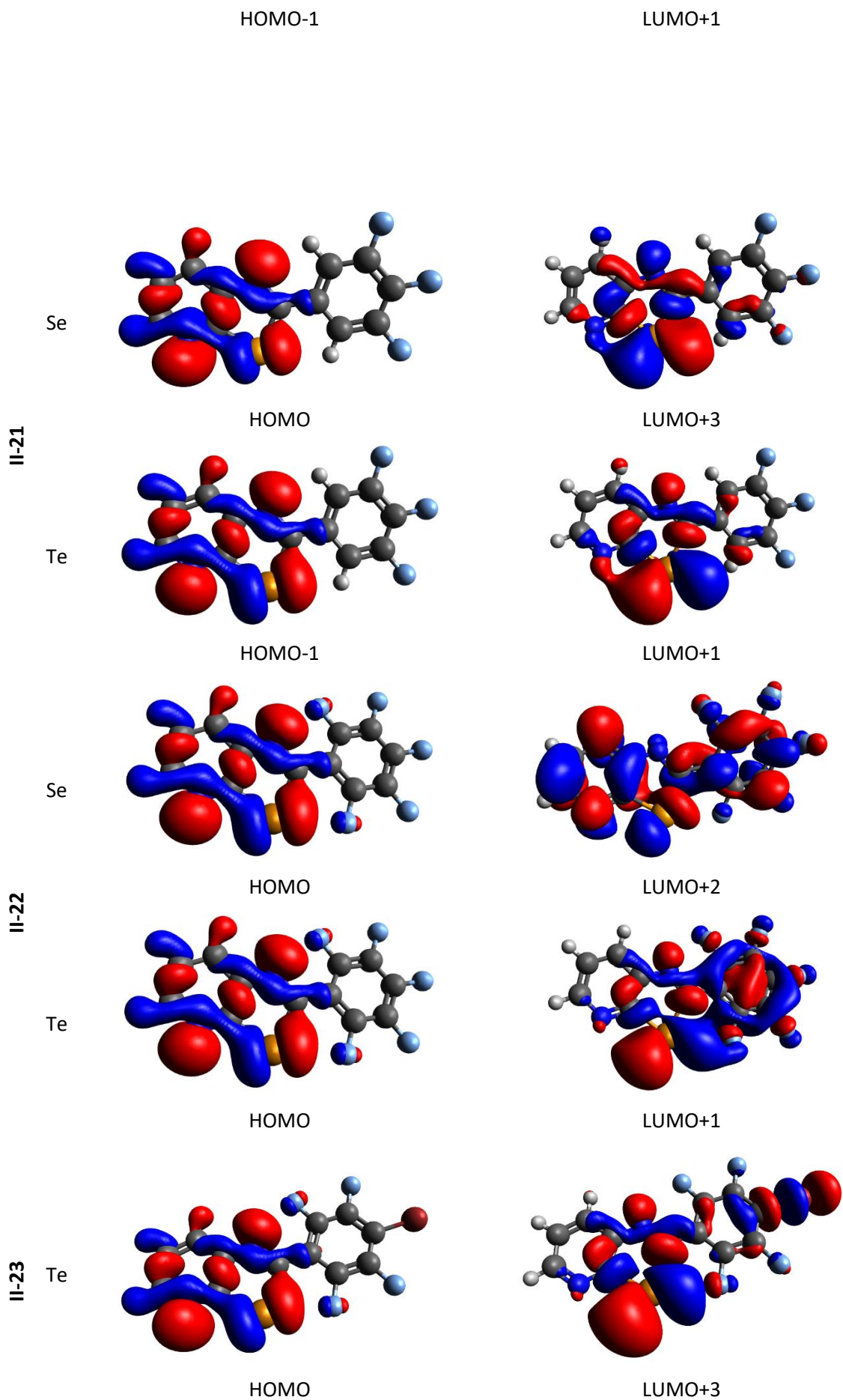


## VI – 4.3 Frontier orbitals

Table VI - 2: Representation of  $n$  and  $\sigma^*$  orbitals.

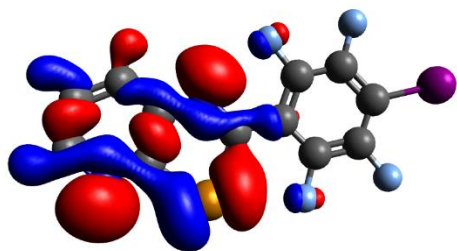
E	$n$	$\sigma^*$
Se		
II-15	HOMO-1	LUMO+3
Te		
	HOMO-1	LUMO+3
Se		
II-16	HOMO	LUMO+4
Te		
	HOMO	LUMO+3
II-17	Se	



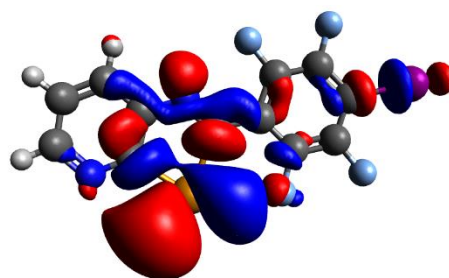


II-24

Te

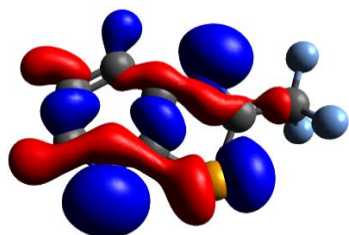


HOMO

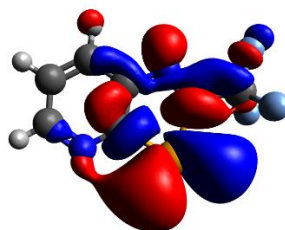


LUMO+2

Se



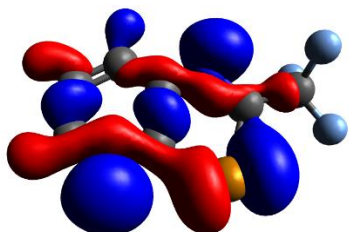
HOMO



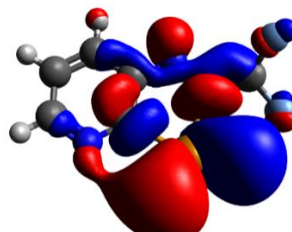
LUMO+2

II-25

Te



HOMO



LUMO+1

---

## VI – 5 Crystal data and structure refinement

Table VI - 3: Crystal data and structure refinement for II-15<sub>Se</sub> (1584376).

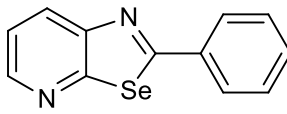
	<b>Crystal data</b>	
Empirical formula	C <sub>12</sub> H <sub>8</sub> N <sub>2</sub> Se	
Formula weight	259.16	
Crystal system	Orthorhombic	
Space group	P n a 2 <sub>1</sub>	
Unit cell dimensions	a = 11.7340(6) Å	α = 90°.
	b = 5.5228(4) Å	β = 90°.
	c = 15.1199(11) Å	γ = 90°.
Volume	979.84(11) Å <sup>3</sup>	
Z	4	
Density (calculated)	1.757 Mg/m <sup>3</sup>	
Absorption coefficient	3.793 mm <sup>-1</sup>	
F(000)	512	
Crystal size	0.486 x 0.162 x 0.120 mm <sup>3</sup>	
	<b>Data Collection</b>	
Temperature	150(2) K	
Wavelength	0.71073 Å	
Theta range for data collection	3.725 to 29.577°.	
Index ranges	-10<=h<=16, -7<=k<=5, -19<=l<=12	
Reflections collected	2991	
Independent reflections	1831 [R(int) = 0.0255]	
Completeness to theta = 25.242°	99.8 %	
	<b>Refinement</b>	
Absorption correction	Gaussian	
Max. and min. transmission	1.000 and 0.872	
Refinement method	Full-matrix least-squares on F <sup>2</sup>	
Data / restraints / parameters	1831 / 1 / 136	
Goodness-of-fit on F <sup>2</sup>	0.798	
Final R indices [I>2sigma(I)]	R1 = 0.0253, wR2 = 0.0610	
R indices (all data)	R1 = 0.0286, wR2 = 0.0642	
Absolute structure parameter	0.001(12)	
Extinction coefficient	n/a	
Largest diff. peak and hole	0.281 and -0.602 e.Å <sup>-3</sup>	

Table VI - 4: Crystal data and structure refinement for II-15<sub>Te</sub> (1584372).

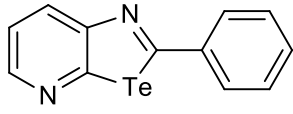
	<b>Crystal data</b>	
Empirical formula	C <sub>12</sub> H <sub>8</sub> N <sub>2</sub> Te	
Formula weight	307.80	
Crystal system	Monoclinic	
Space group	P 2/c	
Unit cell dimensions	a = 12.2429(10) Å	α = 90°.
	b = 6.7691(3) Å	β = 115.913(11)°.
	c = 13.8924(13) Å	γ = 90°.
Volume	1035.56(16) Å <sup>3</sup>	
Z	4	
Density (calculated)	1.974 Mg/m <sup>3</sup>	
Absorption coefficient	2.836 mm <sup>-1</sup>	
F(000)	584	
Crystal size	0.194 x 0.153 x 0.074 mm <sup>3</sup>	
	<b>Data Collection</b>	
Temperature	150(2) K	
Wavelength	0.71073 Å	
Theta range for data collection	2.952 to 29.775°.	
Index ranges	-15 ≤ h ≤ 16, -6 ≤ k ≤ 9, -18 ≤ l ≤ 11	
Reflections collected	3807	
Independent reflections	2198 [R(int) = 0.0185]	
Completeness to theta = 25.242°	96.5 %	
	<b>Refinement</b>	
Absorption correction	Gaussian	
Max. and min. transmission	1.000 and 0.829	
Refinement method	Full-matrix least-squares on F <sup>2</sup>	
Data / restraints / parameters	2198 / 0 / 137	
Goodness-of-fit on F <sup>2</sup>	1.357	
Final R indices [I > 2σ(I)]	R1 = 0.0500, wR2 = 0.1224	
R indices (all data)	R1 = 0.0533, wR2 = 0.1239	
Extinction coefficient	n/a	
Largest diff. peak and hole	2.212 and -1.587 e.Å <sup>-3</sup>	

Table VI - 5: Crystal data and structure refinement for II-16<sub>Se</sub> (1584366).

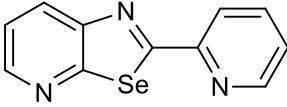
		<b>Crystal data</b>	
Empirical formula		C <sub>11</sub> H <sub>7</sub> N <sub>3</sub> Se	
Formula weight		260.16	
Crystal system		Monoclinic	<b>II-16<sub>Se</sub></b>
Space group		P 2 <sub>1</sub> /n	
Unit cell dimensions		a = 3.8531(7) Å	α = 90°.
		b = 15.461(3) Å	β = 90.609(15)°.
		c = 16.315(2) Å	γ = 90°.
Volume		971.9(3) Å <sup>3</sup>	
Z		4	
Density (calculated)		1.778 Mg/m <sup>3</sup>	
Absorption coefficient		3.827 mm <sup>-1</sup>	
F(000)		512	
Crystal size		0.319 x 0.046 x 0.026 mm <sup>3</sup>	
		<b>Data Collection</b>	
Temperature		150(2) K	
Wavelength		0.71073 Å	
Theta range for data collection		3.631 to 29.477°.	
Index ranges		-4<=h<=5, -19<=k<=11, -16<=l<=22	
Reflections collected		3500	
Independent reflections		2013 [R(int) = 0.0624]	
Completeness to theta = 25.242°		99.7 %	
		<b>Refinement</b>	
Absorption correction		Gaussian	
Max. and min. transmission		0.998 and 0.987	
Refinement method		Full-matrix least-squares on F <sup>2</sup>	
Data / restraints / parameters		2013 / 0 / 137	
Goodness-of-fit on F <sup>2</sup>		1.048	
Final R indices [I>2sigma(I)]		R1 = 0.0863, wR2 = 0.2067	
R indices (all data)		R1 = 0.1463, wR2 = 0.2559	
Extinction coefficient		n/a	
Largest diff. peak and hole		2.803 and -0.866 e.Å <sup>-3</sup>	

Table VI - 6: Crystal data and structure refinement for II-16<sub>Te</sub> (1584370).

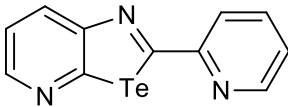
	<b>Crystal data</b>	
Empirical formula	C <sub>11</sub> H <sub>7</sub> N <sub>3</sub> Te	
Formula weight	308.80	
Crystal system	Monoclinic	<b>II-16<sub>Te</sub></b>
Space group	P 2 <sub>1</sub> /c	
Unit cell dimensions	a = 6.8231(6) Å	α = 90°.
	b = 12.1223(10) Å	β = 93.365(7)°.
	c = 12.2071(9) Å	γ = 90°.
Volume	1007.93(14) Å <sup>3</sup>	
Z	4	
Density (calculated)	2.035 Mg/m <sup>3</sup>	
Absorption coefficient	2.917 mm <sup>-1</sup>	
F(000)	584	
Crystal size	0.484 x 0.277 x 0.147 mm <sup>3</sup>	
	<b>Data Collection</b>	
Temperature	150(2) K	
Wavelength	0.71073 Å	
Theta range for data collection	3.344 to 29.853°.	
Index ranges	-8 ≤ h ≤ 9, -16 ≤ k ≤ 16, -16 ≤ l ≤ 10	
Reflections collected	5500	
Independent reflections	2429 [R(int) = 0.0362]	
Completeness to theta = 25.242°	99.8 %	
	<b>Refinement</b>	
Absorption correction	Gaussian	
Max. and min. transmission	0.997 and 0.992	
Refinement method	Full-matrix least-squares on F <sup>2</sup>	
Data / restraints / parameters	2429 / 0 / 136	
Goodness-of-fit on F <sup>2</sup>	1.093	
Final R indices [I > 2σ(I)]	R1 = 0.0371, wR2 = 0.0704	
R indices (all data)	R1 = 0.0542, wR2 = 0.0847	
Extinction coefficient	n/a	
Largest diff. peak and hole	1.405 and -1.677 e.Å <sup>-3</sup>	

Table VI - 7: Crystal data and structure refinement for II-17<sub>Se</sub> (1954222).

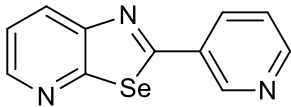
	<b>Crystal data</b>	
Empirical formula	C <sub>11</sub> H <sub>7</sub> N <sub>3</sub> Se	
Formula weight	260.16	
Crystal system	Orthorhombic	
Space group	P n a 2 <sub>1</sub>	
Unit cell dimensions	a = 11.6387(6) Å	α = 90°.
	b = 5.6404(3) Å	β = 90°.
	c = 14.4020(8) Å	γ = 90°.
Volume	945.45(9) Å <sup>3</sup>	
Z	4	
Density (calculated)	1.828 Mg/m <sup>3</sup>	
Absorption coefficient	3.935 mm <sup>-1</sup>	
F(000)	512	
Crystal size	0.221 x 0.137 x 0.078 mm <sup>3</sup>	
	<b>Data Collection</b>	
Temperature	150(2) K	
Wavelength	0.71073 Å	
Theta range for data collection	3.501 to 29.508°.	
Index ranges	-12<=h<=15, -5<=k<=7, -18<=l<=19	
Reflections collected	4106	
Independent reflections	2037 [R(int) = 0.0277]	
Completeness to theta = 25.242°	99.9 %	
	<b>Refinement</b>	
Absorption correction	Gaussian	
Max. and min. transmission	0.989 and 0.720	
Refinement method	Full-matrix least-squares on F <sup>2</sup>	
Data / restraints / parameters	2037 / 1 / 136	
Goodness-of-fit on F <sup>2</sup>	1.033	
Final R indices [I>2sigma(I)]	R1 = 0.0306, wR2 = 0.0606	
R indices (all data)	R1 = 0.0385, wR2 = 0.0662	
Absolute structure parameter	-0.042(13)	
Extinction coefficient	n/a	
Largest diff. peak and hole	0.469 and -0.552 e.Å <sup>-3</sup>	

Table VI - 8: Crystal data and structure refinement for II-17<sub>Te</sub> (1954221).

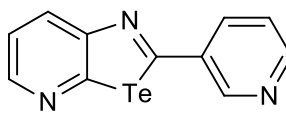
	<b>Crystal data</b>	
Empirical formula	C <sub>11</sub> H <sub>7</sub> N <sub>3</sub> Te	
Formula weight	308.80	
Crystal system	Monoclinic	
Space group	P 21/c	
Unit cell dimensions	a = 6.3049(4) Å	α = 90°.
	b = 13.4115(10) Å	β = 97.734(6)°.
	c = 12.1571(8) Å	γ = 90°.
Volume	1018.63(12) Å <sup>3</sup>	
Z	4	
Density (calculated)	2.014 Mg/m <sup>3</sup>	
Absorption coefficient	2.886 mm <sup>-1</sup>	
F(000)	584	
Crystal size	0.241 x 0.080 x 0.042 mm <sup>3</sup>	
	<b>Data Collection</b>	
Temperature	150(2) K	
Wavelength	0.71073 Å	
Theta range for data collection	3.038 to 29.486°.	
Index ranges	-6 ≤ h ≤ 8, -18 ≤ k ≤ 16, -15 ≤ l ≤ 10	
Reflections collected	4840	
Independent reflections	2435 [R(int) = 0.0327]	
Completeness to theta = 25.242°	99.9 %	
	<b>Refinement</b>	
Absorption correction	Gaussian	
Max. and min. transmission	1.000 and 0.857	
Refinement method	Full-matrix least-squares on F <sup>2</sup>	
Data / restraints / parameters	2435 / 0 / 136	
Goodness-of-fit on F <sup>2</sup>	1.066	
Final R indices [I > 2σ(I)]	R1 = 0.0306, wR2 = 0.0482	
R indices (all data)	R1 = 0.0457, wR2 = 0.0557	
Extinction coefficient	n/a	
Largest diff. peak and hole	1.040 and -0.834 e.Å <sup>-3</sup>	

Table VI - 9: Crystal data and structure refinement for II-18<sub>Se</sub> (1584369).

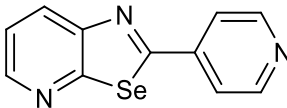
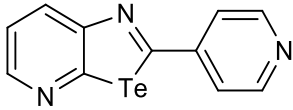
Empirical formula	C <sub>11</sub> H <sub>7</sub> N <sub>3</sub> Se	
Formula weight	260.16	
Crystal system	Monoclinic	<b>II-18<sub>Se</sub></b>
Space group	P 2 <sub>1</sub> /c	
Unit cell dimensions	a = 13.3783(10) Å	α = 90°.
	b = 6.1146(3) Å	β = 99.195(5)°.
	c = 11.8397(6) Å	γ = 90°.
Volume	956.08(10) Å <sup>3</sup>	
Z	4	
Density (calculated)	1.807 Mg/m <sup>3</sup>	
Absorption coefficient	3.891 mm <sup>-1</sup>	
F(000)	512	
Crystal size	0.171 x 0.077 x 0.038 mm <sup>3</sup>	
<b>Data collection</b>		
Temperature	150(2) K	
Wavelength	0.71073 Å	
Theta range for data collection	3.085 to 29.710°.	
Index ranges	-18 ≤ h ≤ 12, -6 ≤ k ≤ 8, -15 ≤ l ≤ 16	
Reflections collected	4590	
Independent reflections	2243 [R(int) = 0.0275]	
Completeness to theta = 25.242°	98.9 %	
<b>Refinement</b>		
Absorption correction	Gaussian	
Max. and min. transmission	1.000 and 0.518	
Refinement method	Full-matrix least-squares on F <sup>2</sup>	
Data / restraints / parameters	2243 / 0 / 136	
Goodness-of-fit on F <sup>2</sup>	1.077	
Final R indices [I > 2σ(I)]	R1 = 0.0324, wR2 = 0.0615	
R indices (all data)	R1 = 0.0466, wR2 = 0.0670	
Extinction coefficient	n/a	
Largest diff. peak and hole	0.469 and -0.584 e.Å <sup>-3</sup>	

Table VI - 10: Crystal data and structure refinement for II-18<sub>Te</sub> (1584371).

	<b>Crystal data</b>	
Empirical formula	C <sub>11</sub> H <sub>7</sub> N <sub>3</sub> Te	
Formula weight	308.80	
Crystal system	Triclinic	
Space group	P -1	
Unit cell dimensions	a = 6.5793(6) Å	α = 77.417(7)°.
	b = 7.3427(6) Å	β = 74.097(8)°.
	c = 11.4381(9) Å	γ = 67.579(8)°.
Volume	487.24(8) Å <sup>3</sup>	
Z	2	
Density (calculated)	2.105 Mg/m <sup>3</sup>	
Absorption coefficient	3.017 mm <sup>-1</sup>	
F(000)	292	
	<b>Data collection</b>	
Temperature	150(2) K	
Wavelength	0.71073 Å	
Crystal size	0.174 x 0.121 x 0.077 mm <sup>3</sup>	
Theta range for data collection	3.026 to 29.579°.	
Index ranges	-9 ≤ h ≤ 9, -7 ≤ k ≤ 9, -15 ≤ l ≤ 15	
Reflections collected	3823	
Independent reflections	2289 [R(int) = 0.0327]	
	<b>Refinement</b>	
Absorption correction	Gaussian	
Max. and min. transmission	1.000 and 0.870	
Completeness to theta = 25.242°	99.9 %	
Refinement method	Full-matrix least-squares on F <sup>2</sup>	
Data / restraints / parameters	2289 / 0 / 136	
Goodness-of-fit on F <sup>2</sup>	1.045	
Final R indices [I > 2σ(I)]	R1 = 0.0394, wR2 = 0.0741	
R indices (all data)	R1 = 0.0506, wR2 = 0.0807	
Extinction coefficient	n/a	
Largest diff. peak and hole	0.979 and -1.089 e.Å <sup>-3</sup>	

**Table VI - 11:** Crystal data and structure refinement for **II-19<sub>Se</sub>** (1584203).

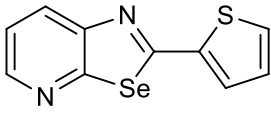
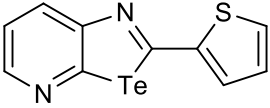
	<b>Crystal data</b>	
Empirical formula	C <sub>10</sub> H <sub>6</sub> N <sub>2</sub> S Se	<b>II-19<sub>Se</sub></b>
Formula weight	265.19	
Crystal system	Monoclinic	
Space group	P 2 <sub>1</sub> /c	
Unit cell dimensions	a = 14.4301(13) Å	α = 90°.
	b = 5.9265(4) Å	β = 109.531(9)°.
	c = 11.7897(8) Å	γ = 90°.
Volume	950.24(13) Å <sup>3</sup>	
Z	4	
Density (calculated)	1.854 Mg/m <sup>3</sup>	
Absorption coefficient	4.125 mm <sup>-1</sup>	
F(000)	520	
Crystal size	0.186 x 0.064 x 0.037 mm <sup>3</sup>	
	<b>Data collection</b>	
Temperature	150(2) K	
Wavelength	0.71073 Å	
Theta range for data collection	2.996 to 29.653°.	
Index ranges	-20 ≤ h ≤ 12, -5 ≤ k ≤ 7, -13 ≤ l ≤ 15	
Reflections collected	4231	
Independent reflections	2231 [R(int) = 0.0569]	
Completeness to theta = 25.242°	99.9 %	
	<b>Refinement</b>	
Absorption correction	Gaussian	
Max. and min. transmission	1.000 and 0.955	
Refinement method	Full-matrix least-squares on F <sup>2</sup>	
Data / restraints / parameters	2231 / 665 / 254	
Goodness-of-fit on F <sup>2</sup>	1.296	
Final R indices [I > 2σ(I)]	R1 = 0.0761, wR2 = 0.1323	
R indices (all data)	R1 = 0.1047, wR2 = 0.1419	
Extinction coefficient	n/a	
Largest diff. peak and hole	0.585 and -0.949 e.Å <sup>-3</sup>	

Table VI - 12: Crystal data and structure refinement for II-19<sub>Te</sub> (1584374).

	<b>Crystal data</b>	
Empirical formula	C <sub>10</sub> H <sub>6</sub> N <sub>2</sub> S Te	
Formula weight	313.83	
Crystal system	Monoclinic	
Space group	I 2/a	
Unit cell dimensions	a = 14.3756(12) Å b = 6.4236(6) Å c = 22.864(2) Å	α = 90° β = 104.867(10)° γ = 90°
Volume	2040.6(3) Å <sup>3</sup>	
Z	9	
Density (calculated)	2.298 Mg/m <sup>3</sup>	
Absorption coefficient	27.662 mm <sup>-1</sup>	
F(000)	1332	
Crystal size	0.156 x 0.095 x 0.085 mm <sup>3</sup>	
	<b>Data collection</b>	
Temperature	150(2) K	
Wavelength	1.54184 Å	
Theta range for data collection	4.001 to 74.074°	
Index ranges	-17 ≤ h ≤ 11, -6 ≤ k ≤ 7, -23 ≤ l ≤ 27	
Reflections collected	3410	
Independent reflections	1981 [R(int) = 0.0361]	
Completeness to theta = 67.684°	99.4 %	
	<b>Refinement</b>	
Absorption correction	Gaussian	
Max. and min. transmission	0.996 and 0.992	
Refinement method	Full-matrix least-squares on F <sup>2</sup>	
Data / restraints / parameters	1981 / 0 / 127	
Goodness-of-fit on F <sup>2</sup>	1.046	
Final R indices [I > 2σ(I)]	R1 = 0.0559, wR2 = 0.1467	
R indices (all data)	R1 = 0.0623, wR2 = 0.1572	
Extinction coefficient	n/a	
Largest diff. peak and hole	2.313 and -1.924 e.Å <sup>-3</sup>	

**Table VI - 13:** Crystal data and structure refinement for **II-21<sub>Se</sub>** (1584204).

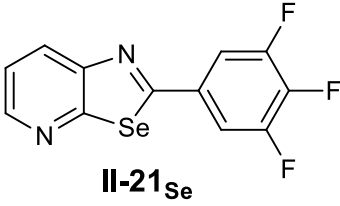
Empirical formula	<b>Crystal data</b> C <sub>24</sub> H <sub>10</sub> F <sub>6</sub> N <sub>4</sub> Se <sub>2</sub>	 <p style="text-align: center;"><b>II-21<sub>Se</sub></b></p>	
Formula weight	626.28		
Crystal system	Monoclinic		
Space group	P 2 <sub>1</sub> /c		
Unit cell dimensions	a = 12.1370(8)Å b = 12.1884(7)Å c = 7.2345(5)Å		α = 90°. β = 98.366(6)°. γ = 90°.
Volume	1058.82(12)Å <sup>3</sup>		
Z	4		
Density (calculated)	1.964 Mg/m <sup>3</sup>		
Absorption coefficient	3.568 mm <sup>-1</sup>		
F(000)	608		
	<b>Data collection</b>		
Temperature	150(2) K		
Wavelength	0.71073 Å		
Crystal size	0.232 x 0.056 x 0.048 mm <sup>3</sup>		
Theta range for data collection	3.7370 to 28.7680°.		
Index ranges	-15<=h<=15, -11<=k<=16, -7<=l<=10		
Reflections collected	5109		
Independent reflections	2525 [R(int) = 0.0424]		
Completeness to theta = 25.242°	99.9 %		
	<b>Refinement</b>		
Refinement method	Full-matrix least-squares on F <sup>2</sup>		
Data / restraints / parameters	2525 / 570 / 326		
Goodness-of-fit on F <sup>2</sup>	1.207		
Final R indices [I>2σ(I)]	R1 = 0.0882, wR2 = 0.2067		
R indices (all data)	R1 = 0.1032, wR2 = 0.2142		
Extinction coefficient	n/a		
Largest diff. peak and hole	1.137 and -1.324 e.Å <sup>-3</sup>		

Table VI - 14: Crystal data and structure refinement for II-21<sub>Te</sub> (1584377).

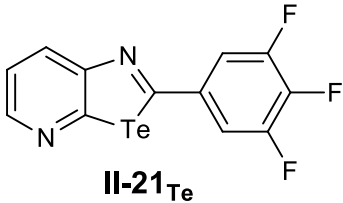
Empirical formula	C <sub>12</sub> H <sub>5</sub> F <sub>3</sub> N <sub>2</sub> Te	 <p style="text-align: center;"><b>II-21<sub>Te</sub></b></p>
Formula weight	361.78	
Crystal system	Triclinic	
Space group	P -1	
Unit cell dimensions	a = 6.7428(6) Å	α = 79.247(6)°.
	b = 7.3273(6) Å	β = 77.062(7)°.
	c = 11.8662(8) Å	γ = 72.221(8)°.
Volume	539.66(8) Å <sup>3</sup>	
Z	2	
Density (calculated)	2.226 Mg/m <sup>3</sup>	
Absorption coefficient	2.778 mm <sup>-1</sup>	
F(000)	340	
Crystal size	0.151 x 0.066 x 0.052 mm <sup>3</sup>	
<b>Data collection</b>		
Temperature	150(2) K	
Wavelength	0.71073 Å	
Theta range for data collection	2.943 to 29.624°.	
Index ranges	-8<=h<=8, -9<=k<=7, -16<=l<=15	
Reflections collected	4299	
Independent reflections	2524 [R(int) = 0.0276]	
Completeness to theta = 25.242°	99.9 %	
<b>Refinement</b>		
Absorption correction	Gaussian	
Max. and min. transmission	1.000 and 0.926	
Refinement method	Full-matrix least-squares on F <sup>2</sup>	
Data / restraints / parameters	2524 / 0 / 163	
Goodness-of-fit on F <sup>2</sup>	1.047	
Final R indices [I>2sigma(I)]	R1 = 0.0338, wR2 = 0.0513	
R indices (all data)	R1 = 0.0457, wR2 = 0.0569	
Extinction coefficient	n/a	
Largest diff. peak and hole	0.598 and -0.617 e.Å <sup>-3</sup>	

Table VI - 15: Crystal data and structure refinement for II-22<sub>Se</sub> (1584378).

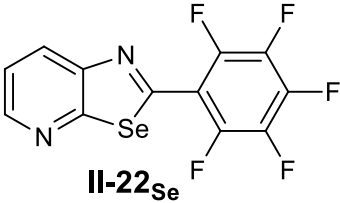
Empirical formula	C <sub>12</sub> H <sub>3</sub> F <sub>5</sub> N <sub>2</sub> Se	 <p style="text-align: center;"><b>II-22<sub>Se</sub></b></p>	
Formula weight	349.12		
Crystal system	Monoclinic		
Space group	P 2 <sub>1</sub> /c		
Unit cell dimensions	a = 10.4047(10) Å		α = 90°.
	b = 4.6117(4) Å		β = 90.488(8)°.
	c = 22.6734(19) Å		γ = 90°.
Volume	1087.91(17) Å <sup>3</sup>		
Z	5		
Density (calculated)	2.664 Mg/m <sup>3</sup>		
Absorption coefficient	4.388 mm <sup>-1</sup>		
F(000)	840		
Crystal size	0.421 x 0.079 x 0.031 mm <sup>3</sup>		
<b>Data collection</b>			
Temperature	150(2) K		
Wavelength	0.71073 Å		
Theta range for data collection	3.595 to 29.537°.		
Index ranges	-14<=h<=13, -6<=k<=4, -31<=l<=23		
Reflections collected	4673		
Independent reflections	2525 [R(int) = 0.0521]		
Completeness to theta = 25.242°	99.7 %		
<b>Refinement</b>			
Absorption correction	Gaussian		
Max. and min. transmission	1.000 and 0.761		
Refinement method	Full-matrix least-squares on F <sup>2</sup>		
Data / restraints / parameters	2525 / 0 / 181		
Goodness-of-fit on F <sup>2</sup>	1.053		
Final R indices [I>2sigma(I)]	R1 = 0.0617, wR2 = 0.1453		
R indices (all data)	R1 = 0.0924, wR2 = 0.1692		
Extinction coefficient	n/a		
Largest diff. peak and hole	0.975 and -1.112 e.Å <sup>-3</sup>		

Table VI - 16: Crystal data and structure refinement for II-22<sub>Se</sub> (1584367).

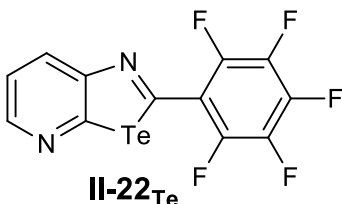
Empirical formula	C <sub>12</sub> H <sub>3</sub> F <sub>5</sub> N <sub>2</sub> Te	 <p style="text-align: center;"><b>II-22<sub>Te</sub></b></p>
Formula weight	397.76	
Crystal system	Monoclinic	
Space group	P 2 <sub>1</sub> /c	
Unit cell dimensions	a = 10.8545(8) Å	α = 90°.
	b = 4.5188(4) Å	β = 91.006(7)°.
	c = 22.8774(17) Å	γ = 90°.
Volume	1121.95(15) Å <sup>3</sup>	
Z	5	
Density (calculated)	2.944 Mg/m <sup>3</sup>	
Absorption coefficient	3.385 mm <sup>-1</sup>	
F(000)	930	
Crystal size	0.653 x 0.114 x 0.022 mm <sup>3</sup>	
<b>Data Collection</b>		
Temperature	150(2) K	
Wavelength	0.71073 Å	
Theta range for data collection	3.563 to 29.700°.	
Index ranges	-14 ≤ h ≤ 9, -5 ≤ k ≤ 6, -31 ≤ l ≤ 31	
Reflections collected	5090	
Independent reflections	2650 [R(int) = 0.0436]	
Completeness to theta = 25.242°	99.8 %	
<b>Refinement</b>		
Absorption correction	Gaussian	
Max. and min. transmission	0.999 and 0.981	
Refinement method	Full-matrix least-squares on F <sup>2</sup>	
Data / restraints / parameters	2650 / 0 / 181	
Goodness-of-fit on F <sup>2</sup>	0.983	
Final R indices [I > 2σ(I)]	R1 = 0.0425, wR2 = 0.0782	
R indices (all data)	R1 = 0.0692, wR2 = 0.0905	
Extinction coefficient	n/a	
Largest diff. peak and hole	1.021 and -0.751 e.Å <sup>-3</sup>	

Table VI - 17: Crystal data and structure refinement for II-23<sub>Te</sub> (1954224).

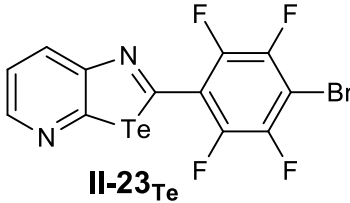
	<b>Crystal data</b>	
Empirical formula	C <sub>12</sub> H <sub>3</sub> Br F <sub>4</sub> N <sub>2</sub> Te	
Formula weight	458.67	
Crystal system	Monoclinic	
Space group	P 2 <sub>1</sub> /c	
Unit cell dimensions	a = 11.5479(14) Å	α = 90°.
	b = 4.5624(6) Å	β = 92.754(11)°.
	c = 22.376(3) Å	γ = 90°.
Volume	1177.6(2) Å <sup>3</sup>	
Z	4	
Density (calculated)	2.587 Mg/m <sup>3</sup>	
Absorption coefficient	5.960 mm <sup>-1</sup>	
F(000)	848	
Crystal size	0.623 x 0.075 x 0.023 mm <sup>3</sup>	
	<b>Data Collection</b>	
Temperature	150(2) K	
Wavelength	0.71073 Å	
Theta range for data collection	3.533 to 29.765°.	
Index ranges	-11<=h<=16, -4<=k<=6, -29<=l<=29	
Reflections collected	5673	
Independent reflections	2842 [R(int) = 0.0322]	
Completeness to theta = 25.242°	99.8 %	
	<b>Refinement</b>	
Absorption correction	Gaussian	
Max. and min. transmission	1.000 and 0.887	
Refinement method	Full-matrix least-squares on F <sup>2</sup>	
Data / restraints / parameters	2842 / 0 / 181	
Goodness-of-fit on F <sup>2</sup>	1.035	
Final R indices [I>2sigma(I)]	R1 = 0.0319, wR2 = 0.0627	
R indices (all data)	R1 = 0.0434, wR2 = 0.0679	
Extinction coefficient	n/a	
Largest diff. peak and hole	0.751 and -0.995 e.Å <sup>-3</sup>	

Table VI - 18: Crystal data and structure refinement for **II-24<sub>Te</sub>** (1954223).

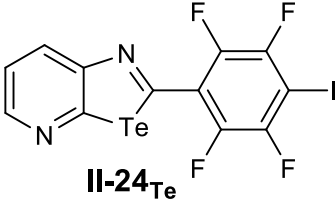
Empirical formula	$C_{12}H_3F_4IN_2Te$	 <p style="text-align: center;"><b>II-24<sub>Te</sub></b></p>	
Formula weight	505.66		
Crystal system	Monoclinic		
Space group	$P 2_1/c$		
Unit cell dimensions	$a = 9.0513(4) \text{ \AA}$		$\alpha = 90^\circ$
	$b = 19.3504(9) \text{ \AA}$		$\beta = 103.087(5)^\circ$
	$c = 14.8691(8) \text{ \AA}$		$\gamma = 90^\circ$
Volume	$2536.6(2) \text{ \AA}^3$		
Z	8		
Density (calculated)	$2.648 \text{ Mg/m}^3$		
Absorption coefficient	$4.817 \text{ mm}^{-1}$		
F(000)	1840		
Crystal size	$0.681 \times 0.290 \times 0.207 \text{ mm}^3$		
<b>Data Collection</b>			
Temperature	150(2) K		
Wavelength	$0.71073 \text{ \AA}$		
Theta range for data collection	$3.379$ to $29.722^\circ$		
Index ranges	$-12 \leq h \leq 9$ , $-25 \leq k \leq 26$ , $-20 \leq l \leq 19$		
Reflections collected	13576		
Independent reflections	6031 [R(int) = 0.0380]		
Completeness to theta = $25.242^\circ$	99.7 %		
<b>Refinement</b>			
Absorption correction	Gaussian		
Max. and min. transmission	1.000 and 0.524		
Refinement method	Full-matrix least-squares on $F^2$		
Data / restraints / parameters	6031 / 0 / 361		
Goodness-of-fit on $F^2$	1.035		
Final R indices [ $I > 2\sigma(I)$ ]	R1 = 0.0350, wR2 = 0.0773		
R indices (all data)	R1 = 0.0498, wR2 = 0.0874		
Extinction coefficient	n/a		
Largest diff. peak and hole	0.958 and $-1.466 \text{ e.\AA}^{-3}$		

Table VI - 19: Crystal data and structure refinement for II-25<sub>Se</sub> (1584368).

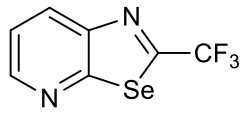
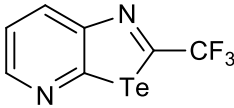
Empirical formula	C <sub>7</sub> H <sub>3</sub> F <sub>3</sub> N <sub>2</sub> Se	
Formula weight	251.07	
Crystal system	Triclinic	<b>II-25<sub>Se</sub></b>
Space group	P -1	
Unit cell dimensions	a = 5.3964(4) Å b = 7.8741(5) Å c = 9.7525(7) Å	α = 81.764(6)°. β = 81.290(6)°. γ = 76.381(6)°.
Volume	395.60(5) Å <sup>3</sup>	
Z	2	
Density (calculated)	2.108 Mg/m <sup>3</sup>	
Absorption coefficient	4.745 mm <sup>-1</sup>	
F(000)	240	
Crystal size	0.223 x 0.054 x 0.049 mm <sup>3</sup>	
<b>Data Collection</b>		
Temperature	150(2) K	
Wavelength	0.71073 Å	
Theta range for data collection	3.228 to 29.633°.	
Index ranges	-5<=h<=7, -9<=k<=10, -12<=l<=11	
Reflections collected	3155	
Independent reflections	1854 [R(int) = 0.0313]	
Completeness to theta = 25.242°	99.9 %	
<b>Refinement</b>		
Absorption correction	Gaussian	
Max. and min. transmission	1.000 and 0.750	
Refinement method	Full-matrix least-squares on F <sup>2</sup>	
Data / restraints / parameters	1854 / 42 / 146	
Goodness-of-fit on F <sup>2</sup>	1.063	
Final R indices [I>2sigma(I)]	R1 = 0.0367, wR2 = 0.0560	
R indices (all data)	R1 = 0.0510, wR2 = 0.0618	
Extinction coefficient	n/a	
Largest diff. peak and hole	0.470 and -0.481 e.Å <sup>-3</sup>	

Table VI - 20: Crystal data and structure refinement for II-25<sub>Te</sub> (1584375).

Empirical formula	C <sub>7</sub> H <sub>3</sub> F <sub>3</sub> N <sub>2</sub> Te	
Formula weight	299.71	
Crystal system	Triclinic	<b>II-25<sub>Te</sub></b>
Space group	P -1	
Unit cell dimensions	a = 9.1200(7) Å b = 9.8379(8) Å c = 10.3447(7) Å	α = 105.380(7)° β = 101.891(6)° γ = 102.649(7)°
Volume	838.07(12) Å <sup>3</sup>	
Z	4	
Density (calculated)	2.375 Mg/m <sup>3</sup>	
Absorption coefficient	3.549 mm <sup>-1</sup>	
F(000)	552	
Crystal size	0.214 x 0.083 x 0.053 mm <sup>3</sup>	
<b>Data collection</b>		
Temperature	150(2) K	
Wavelength	0.71073 Å	
Theta range for data collection	3.449 to 29.899°	
Index ranges	-9 ≤ h ≤ 11, -13 ≤ k ≤ 12, -12 ≤ l ≤ 14	
Reflections collected	7066	
Independent reflections	3927 [R(int) = 0.0321]	
Completeness to theta = 25.242°	99.8 %	
<b>Refinement</b>		
Absorption correction	Gaussian	
Max. and min. transmission	1.000 and 0.900	
Refinement method	Full-matrix least-squares on F <sup>2</sup>	
Data / restraints / parameters	3927 / 0 / 235	
Goodness-of-fit on F <sup>2</sup>	1.061	
Final R indices [I > 2σ(I)]	R1 = 0.0446, wR2 = 0.1028	
R indices (all data)	R1 = 0.0654, wR2 = 0.1202	
Extinction coefficient	n/a	
Largest diff. peak and hole	1.810 and -1.726 e.Å <sup>-3</sup>	

**Table VI - 21:** Crystal data and structure refinement for **II-27<sub>Se</sub>** (1954286).

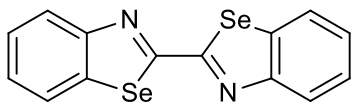
Empirical formula	<b>Crystal data</b> C <sub>14</sub> H <sub>8</sub> N <sub>2</sub> Se <sub>2</sub>	
Formula weight	362.14	<b>II-27<sub>Se</sub></b>
Crystal system	Monoclinic	
Space group	P 2 <sub>1</sub> /c	
Unit cell dimensions	a = 9.0647(10) Å b = 6.0347(5) Å c = 11.5964(10) Å	α = 90°. β = 110.681(11)°. γ = 90°.
Volume	593.48(10) Å <sup>3</sup>	
Z	2	
Density (calculated)	2.027 Mg/m <sup>3</sup>	
Absorption coefficient	6.209 mm <sup>-1</sup>	
F(000)	348	
Crystal size	0.423 x 0.124 x 0.044 mm <sup>3</sup>	
	<b>Data collection</b>	
Temperature	293(2) K	
Wavelength	0.71073 Å	
Theta range for data collection	3.675 to 29.623°.	
Index ranges	-12 ≤ h ≤ 12, -8 ≤ k ≤ 8, -12 ≤ l ≤ 15	
Reflections collected	2879	
Independent reflections	1406 [R(int) = 0.0432]	
Completeness to theta = 25.242°	99.8 %	
	<b>Refinement</b>	
Absorption correction	Gaussian	
Max. and min. transmission	0.994 and 0.976	
Refinement method	Full-matrix least-squares on F <sup>2</sup>	
Data / restraints / parameters	1406 / 0 / 98	
Goodness-of-fit on F <sup>2</sup>	1.069	
Final R indices [I > 2σ(I)]	R1 = 0.0428, wR2 = 0.0872	
R indices (all data)	R1 = 0.0547, wR2 = 0.0961	
Extinction coefficient	n/a	
Largest diff. peak and hole	1.163 and -1.367 e.Å <sup>-3</sup>	

Table VI - 22: Crystal data and structure refinement for II-27<sub>Te</sub> (1954287).

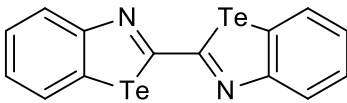
	<b>Crystal data</b>	
Empirical formula	C <sub>14</sub> H <sub>8</sub> N <sub>2</sub> Te <sub>2</sub>	
Formula weight	459.42	
Crystal system	Orthorhombic	<b>II-27<sub>Te</sub></b>
Space group	P b c a	
Unit cell dimensions	a = 11.5651(4) Å	α = 90°.
	b = 11.9277(5) Å	β = 90°.
	c = 18.6397(11) Å	γ = 90°.
Volume	2571.3(2) Å <sup>3</sup>	
Z	8	
Density (calculated)	2.374 Mg/m <sup>3</sup>	
Absorption coefficient	4.519 mm <sup>-1</sup>	
F(000)	1680	
Crystal size	0.441 x 0.416 x 0.076 mm <sup>3</sup>	
	<b>Data collection</b>	
Temperature	296(2) K	
Wavelength	0.71073 Å	
Theta range for data collection	3.416 to 29.782°.	
Index ranges	-15 ≤ h ≤ 11, -15 ≤ k ≤ 16, -25 ≤ l ≤ 19	
Reflections collected	11288	
Independent reflections	3246 [R(int) = 0.0539]	
Completeness to theta = 25.242°	99.7 %	
	<b>Refinement</b>	
Refinement method	Full-matrix least-squares on F <sup>2</sup>	
Data / restraints / parameters	3246 / 0 / 163	
Goodness-of-fit on F <sup>2</sup>	1.121	
Final R indices [I > 2σ(I)]	R1 = 0.0468, wR2 = 0.1061	
R indices (all data)	R1 = 0.0760, wR2 = 0.1296	
Extinction coefficient	n/a	
Largest diff. peak and hole	1.656 and -1.409 e.Å <sup>-3</sup>	

Table VI - 23: Crystal data and structure refinement for II-32<sub>Te</sub> (1954288).

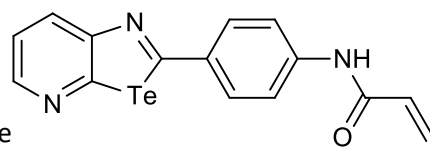
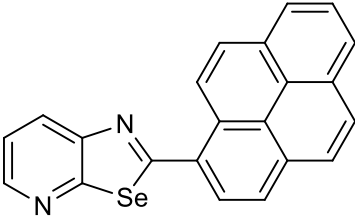
		 <p style="text-align: center;"><b>II-32<sub>Te</sub></b></p>
<b>Crystal data</b>		
Empirical formula	C <sub>15</sub> H <sub>11</sub> N <sub>3</sub> O Te	
Formula weight	376.87	
Crystal system	Tetragonal	
Space group	I 4 <sub>1</sub> /a	
Unit cell dimensions	a = 19.6512(7) Å	α = 90°.
	b = 19.6512(7) Å	β = 90°.
	c = 15.8856(12) Å	γ = 90°.
Volume	6134.5(6) Å <sup>3</sup>	
Z	16	
Density (calculated)	1.632 Mg/m <sup>3</sup>	
Absorption coefficient	1.938 mm <sup>-1</sup>	
F(000)	2912	
Crystal size	0.226 x 0.194 x 0.121 mm <sup>3</sup>	
	<b>Data collection</b>	
Temperature	150(2) K	
Wavelength	0.71073 Å	
Theta range for data collection	2.932 to 29.767°.	
Index ranges	-20 ≤ h ≤ 25, -25 ≤ k ≤ 12, -22 ≤ l ≤ 15	
Reflections collected	9116	
Independent reflections	3715 [R(int) = 0.0406]	
Completeness to theta = 25.242°	99.8 %	
	<b>Refinement</b>	
Absorption correction	Gaussian	
Max. and min. transmission	1.000 and 0.797	
Refinement method	Full-matrix least-squares on F <sup>2</sup>	
Data / restraints / parameters	3715 / 1 / 181	
Goodness-of-fit on F <sup>2</sup>	1.090	
Final R indices [I > 2σ(I)]	R1 = 0.0683, wR2 = 0.1893	
R indices (all data)	R1 = 0.1133, wR2 = 0.2274	
Extinction coefficient	n/a	
Largest diff. peak and hole	1.902 and -1.012 e.Å <sup>-3</sup>	

Table VI - 24: Crystal data and structure refinement for II-39<sub>Se</sub> (1954289).

	<b>Crystal data</b>	
Empirical formula	C <sub>22</sub> H <sub>12</sub> N <sub>2</sub> Se	
Formula weight	219.03	
Crystal system	Orthorhombic	
Space group	P c a 2 <sub>1</sub>	<b>II-39<sub>Se</sub></b>
Unit cell dimensions	a = 16.5064(12) Å	α = 90°.
	b = 3.8412(3) Å	β = 90°.
	c = 24.029(2) Å	γ = 90°.
Volume	1523.5(2) Å <sup>3</sup>	
Z	7	
Density (calculated)	1.671 Mg/m <sup>3</sup>	
Absorption coefficient	2.470 mm <sup>-1</sup>	
F(000)	768	
	<b>Data collection</b>	
Crystal size	0.211 x 0.046 x 0.026 mm <sup>3</sup>	
Temperature	150(2) K	
Wavelength	0.71073 Å	
Theta range for data collection	2.994 to 29.818°.	
Index ranges	-22 ≤ h ≤ 14, -3 ≤ k ≤ 4, -25 ≤ l ≤ 31	
Reflections collected	4932	
Independent reflections	3076 [R(int) = 0.0342]	
Completeness to theta = 25.242°	99.8 %	
	<b>Refinement</b>	
Absorption correction	Gaussian	
Max. and min. transmission	1.000 and 0.939	
Refinement method	Full-matrix least-squares on F <sup>2</sup>	
Data / restraints / parameters	3076 / 1 / 226	
Goodness-of-fit on F <sup>2</sup>	1.023	
Final R indices [I > 2σ(I)]	R1 = 0.0454, wR2 = 0.0939	
R indices (all data)	R1 = 0.0631, wR2 = 0.1023	
Absolute structure parameter	0.367(9)	
Extinction coefficient	n/a	
Largest diff. peak and hole	0.442 and -0.437 e.Å <sup>-3</sup>	

**Table VI - 25:** Crystal data and structure refinement for **II-39<sub>Te</sub>** (15844373).

Empirical formula

Formula weight

Crystal system

Space group

Unit cell dimensions

Volume

Z

Density (calculated)

Absorption coefficient

Temperature

Wavelength

F(000)

Crystal size

Theta range for data collection

Index ranges

Reflections collected

Independent reflections

Completeness to theta = 25.242°

Absorption correction

Max. and min. transmission

Refinement method

Data / restraints / parameters

Goodness-of-fit on F<sup>2</sup>Final R indices [*I* > 2σ(*I*)]

R indices (all data)

Extinction coefficient

Largest diff. peak and hole

**Crystal data**C<sub>22</sub> H<sub>12</sub> N<sub>2</sub> Te

431.94

Monoclinic

P 2<sub>1</sub>/c

a = 22.3299(15) Å

b = 4.6587(2) Å

c = 15.5840(8) Å

1547.25(15) Å<sup>3</sup>

4

1.854 Mg/m<sup>3</sup>1.928 mm<sup>-1</sup>**Data collection**

150(2) K

0.71073 Å

840

0.586 x 0.139 x 0.086 mm<sup>3</sup>

3.159 to 29.609°.

-20 ≤ h ≤ 28, -4 ≤ k ≤ 6, -21 ≤ l ≤ 16

6922

3652 [R(int) = 0.0364]

99.8 %

**Refinement**

Gaussian

1.000 and 0.676

Full-matrix least-squares on F<sup>2</sup>

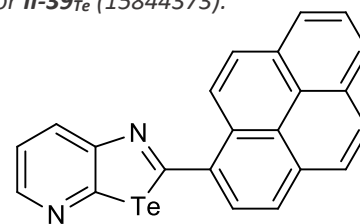
3652 / 0 / 226

1.011

R1 = 0.0338, wR2 = 0.0657

R1 = 0.0485, wR2 = 0.0716

n/a

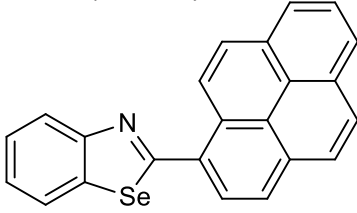
0.575 and -0.819 e.Å<sup>-3</sup>**II-39<sub>Te</sub>**

α = 90°.

β = 107.369(6)°.

γ = 90°.

Table VI - 26: Crystal data and structure refinement for II-40<sub>Se</sub> (1954291).

	<b>Crystal data</b>		
Empirical formula	C <sub>23</sub> H <sub>13</sub> N Se		
Formula weight	382.30		
Crystal system	Monoclinic		
Space group	P 2 <sub>1</sub> /c		
Unit cell dimensions	a = 25.6107(5) Å		α = 90°.
	b = 3.86960(10) Å		β = 108.348(3)°.
	c = 16.4786(4) Å		γ = 90°.
Volume	1550.06(7) Å <sup>3</sup>		
Z	4		
Density (calculated)	1.638 Mg/m <sup>3</sup>		
Absorption coefficient	3.290 mm <sup>-1</sup>		
F(000)	768		
	<b>Data collection</b>		
Temperature	150(2) K		
Wavelength	1.54184 Å		
Crystal size	0.380 x 0.122 x 0.038 mm <sup>3</sup>		
Theta range for data collection	3.637 to 74.067°.		
Index ranges	-31 ≤ h ≤ 31, -4 ≤ k ≤ 4, -20 ≤ l ≤ 19		
Reflections collected	29069		
Independent reflections	3124 [R(int) = 0.0626]		
Completeness to theta = 67.684°	100.0 %		
	<b>Refinement</b>		
Absorption correction	Gaussian		
Max. and min. transmission	1.000 and 0.720		
Refinement method	Full-matrix least-squares on F <sup>2</sup>		
Data / restraints / parameters	3124 / 0 / 227		
Goodness-of-fit on F <sup>2</sup>	1.168		
Final R indices [I > 2σ(I)]	R1 = 0.0855, wR2 = 0.2532		
R indices (all data)	R1 = 0.0858, wR2 = 0.2543		
Extinction coefficient	n/a		
Largest diff. peak and hole	1.363 and -2.131 e.Å <sup>-3</sup>		

**Table VI - 27:** Crystal data and structure refinement for **II-40<sub>Te</sub>** (15844390).

Empirical formula

Formula weight

Crystal system

Space group

Unit cell dimensions

Volume

Z

Density (calculated)

Absorption coefficient

F(000)

Temperature

Wavelength

Crystal size

Theta range for data collection

Index ranges

Reflections collected

Independent reflections

Completeness to theta = 25.242°

Absorption correction

Max. and min. transmission

Refinement method

Data / restraints / parameters

Goodness-of-fit on F<sup>2</sup>Final R indices [*I* > 2σ(*I*)]

R indices (all data)

Extinction coefficient

Largest diff. peak and hole

**Crystal data**C<sub>23</sub> H<sub>13</sub> N Te

430.94

Orthorhombic

P b c a

a = 14.7257(5) Å

b = 10.7315(4) Å

c = 20.7441(7) Å

3278.2(2) Å<sup>3</sup>

8

1.746 Mg/m<sup>3</sup>1.819 mm<sup>-1</sup>

1680

**Data collection**

150(2) K

0.71073 Å

0.316 x 0.149 x 0.118 mm<sup>3</sup>

3.356 to 29.586°.

-11 ≤ h ≤ 19, -14 ≤ k ≤ 9, -27 ≤ l ≤ 27

14284

4066 [R(int) = 0.0305]

99.8 %

**Refinement**

Gaussian

1.000 and 0.682

Full-matrix least-squares on F<sup>2</sup>

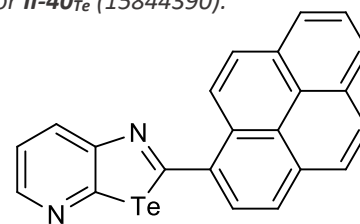
4066 / 0 / 226

1.042

R1 = 0.0288, wR2 = 0.0625

R1 = 0.0407, wR2 = 0.0703

n/a

0.673 and -0.633 e.Å<sup>-3</sup>**II-40<sub>Te</sub>**

α = 90°.

β = 90°.

γ = 90°.

Table IV - 28: Crystal data and structure refinement for  $(III-1Te)_2 \cdot HDFIO$  (1584205).

<b>Crystal data</b>	
Empirical formula	2 C <sub>11</sub> H <sub>7</sub> N <sub>3</sub> Te · C <sub>8</sub> F <sub>16</sub> I <sub>2</sub>
Formula weight	1271.47
Crystal system	Triclinic
Space group	P -1
Unit cell dimensions	a = 14.5778(5) Å                      α = 90.369(2)°. b = 15.5849(3) Å                      β = 108.326(3)°. c = 17.8089(5) Å                      γ = 107.116(2)°.
Volume	3648.84(19) Å <sup>3</sup>
Z	4
Density (calculated)	2.315 Mg/m <sup>3</sup>
Absorption coefficient	3.407 mm <sup>-1</sup>
F(000)	2360
Crystal size	0.347 x 0.118 x 0.053 mm <sup>3</sup>
<b>Data collection</b>	
Temperature	150(2) K
Wavelength	0.71073 Å
Theta range for data collection	2.930 to 29.914°.
Index ranges	-19 ≤ h ≤ 19, -21 ≤ k ≤ 19, -23 ≤ l ≤ 24
Reflections collected	42051
Independent reflections	17492 [R(int) = 0.0430]
Completeness to theta = 25.242°	99.9 %
<b>Refinement</b>	
Absorption correction	Gaussian
Max. and min. transmission	0.999 and 0.997
Refinement method	Full-matrix least-squares on F <sup>2</sup>
Data / restraints / parameters	17492 / 734 / 1244
Goodness-of-fit on F <sup>2</sup>	1.039
Final R indices [I > 2σ(I)]	R1 = 0.0496, wR2 = 0.0920
R indices (all data)	R1 = 0.0780, wR2 = 0.1083
Extinction coefficient	n/a
Largest diff. peak and hole	1.670 and -1.587 e.Å <sup>-3</sup>

Table VI - 29: Crystal data and structure refinement for  $(\text{III-1Te})_2 \cdot \text{DITFB}$  (1954225).

<b>Crystal data</b>	
Empirical formula	$\text{C}_{11} \text{H}_7 \text{N}_3 \text{Te} \cdot 0.5 \text{C}_6 \text{F}_4 \text{I}_2$
Formula weight	508.73
Crystal system	Triclinic
Space group	P -1
Unit cell dimensions	$a = 6.4432(5) \text{ \AA}$ $\alpha = 100.833(6)^\circ$ $b = 9.3098(7) \text{ \AA}$ $\beta = 96.613(6)^\circ$ $c = 12.7311(9) \text{ \AA}$ $\gamma = 103.000(6)^\circ$
Volume	$720.88(10) \text{ \AA}^3$
Z	2
Density (calculated)	$2.344 \text{ Mg/m}^3$
Absorption coefficient	$4.220 \text{ mm}^{-1}$
F(000)	470
Crystal size	$0.500 \times 0.145 \times 0.093 \text{ mm}^3$
<b>Data collection</b>	
Temperature	150(2) K
Wavelength	$0.71073 \text{ \AA}$
Theta range for data collection	$3.116$ to $29.711^\circ$
Index ranges	$-6 \leq h \leq 8$ , $-10 \leq k \leq 11$ , $-17 \leq l \leq 12$
Reflections collected	5610
Independent reflections	3392 [R(int) = 0.0243]
Completeness to theta = $25.242^\circ$	99.9 %
<b>Refinement</b>	
Absorption correction	Gaussian
Max. and min. transmission	1.000 and 0.747
Refinement method	Full-matrix least-squares on $F^2$
Data / restraints / parameters	3392 / 0 / 190
Goodness-of-fit on $F^2$	1.018
Final R indices [ $I > 2\sigma(I)$ ]	$R1 = 0.0310$ , $wR2 = 0.0582$
R indices (all data)	$R1 = 0.0441$ , $wR2 = 0.0654$
Extinction coefficient	n/a
Largest diff. peak and hole	$0.809$ and $-0.879 \text{ e.\AA}^{-3}$

Table VI - 30: Crystal data and structure refinement for III-1<sub>Te</sub>•DITFB (1954226).

<b>Crystal data</b>	
Empirical formula	C <sub>11</sub> H <sub>7</sub> N <sub>3</sub> Te . C <sub>6</sub> F <sub>4</sub> I <sub>2</sub>
Formula weight	710.66
Crystal system	Monoclinic
Space group	P 21/n
Unit cell dimensions	a = 8.2302(2) Å                      α = 90°. b = 7.7527(2) Å                      β = 90.211(2)°. c = 29.1565(7) Å                     γ = 90°.
Volume	1860.35(8) Å <sup>3</sup>
Z	4
Density (calculated)	2.537 Mg/m <sup>3</sup>
Absorption coefficient	4.963 mm <sup>-1</sup>
F(000)	1296
<b>Data collection</b>	
Crystal size	0.391 x 0.241 x 0.094 mm <sup>3</sup>
Temperature	150(2) K
Wavelength	0.71073 Å
Theta range for data collection	3.361 to 29.843°.
Index ranges	-10<=h<=11, -10<=k<=10, -38<=l<=39
Reflections collected	30735
Independent reflections	4906 [R(int) = 0.0463]
Completeness to theta = 25.242°	99.8 %
<b>Refinement</b>	
Absorption correction	Gaussian
Max. and min. transmission	1.000 and 0.499
Refinement method	Full-matrix least-squares on F <sup>2</sup>
Data / restraints / parameters	4906 / 0 / 244
Goodness-of-fit on F <sup>2</sup>	1.121
Final R indices [I>2sigma(I)]	R1 = 0.0301, wR2 = 0.0554
R indices (all data)	R1 = 0.0401, wR2 = 0.0595
Extinction coefficient	n/a
Largest diff. peak and hole	0.696 and -0.741 e.Å <sup>-3</sup>

**Table VI - 31:** Crystal data and structure refinement for *III-1Te•(DITFB)<sub>2</sub>* (1954227).

<b>Crystal data</b>	
Empirical formula	C <sub>11</sub> H <sub>7</sub> N <sub>3</sub> Te . 2 C <sub>6</sub> F <sub>4</sub> I <sub>2</sub>
Formula weight	1112.52
Crystal system	Triclinic
Space group	P -1
Unit cell dimensions	a = 4.2386(2) Å                      α = 75.012(3)°. b = 15.7217(6) Å                     β = 89.349(3)°. c = 21.3799(7) Å                     γ = 84.936(4)°.
Volume	1370.78(10) Å <sup>3</sup>
Z	2
Density (calculated)	2.695 Mg/m <sup>3</sup>
Absorption coefficient	5.664 mm <sup>-1</sup>
F(000)	1004
Crystal size	0.277 x 0.075 x 0.043 mm <sup>3</sup>
<b>Data collection</b>	
Temperature	150(2) K
Wavelength	0.71073 Å
Theta range for data collection	2.959 to 29.869°.
Index ranges	-5<=h<=5, -19<=k<=21, -25<=l<=28
Reflections collected	13650
Independent reflections	6611 [R(int) = 0.0313]
Completeness to theta = 25.242°	99.7 %
<b>Refinement</b>	
Absorption correction	Gaussian
Max. and min. transmission	1.000 and 0.799
Refinement method	Full-matrix least-squares on F <sup>2</sup>
Data / restraints / parameters	6611 / 0 / 352
Goodness-of-fit on F <sup>2</sup>	1.040
Final R indices [I>2sigma(I)]	R1 = 0.0360, wR2 = 0.0551
R indices (all data)	R1 = 0.0566, wR2 = 0.0622
Extinction coefficient	n/a
Largest diff. peak and hole	0.852 and -1.039 e.Å <sup>-3</sup>

Table VI - 32: Crystal data and structure refinement for (III-2Te)<sub>2</sub>•DITFB (1955118).

<b>Crystal data</b>	
Empirical formula	C <sub>11</sub> H <sub>7</sub> N <sub>3</sub> Te . 0.5 C <sub>6</sub> F <sub>4</sub> I <sub>2</sub>
Formula weight	509.73
Crystal system	Monoclinic
Space group	P 21/n
Unit cell dimensions	a = 15.330(2) Å                      α = 90°. b = 4.6082(6) Å                      β = 104.529(12)°. c = 21.030(3) Å                      γ = 90°.
Volume	1438.1(3) Å <sup>3</sup>
Z	4
Density (calculated)	2.354 Mg/m <sup>3</sup>
Absorption coefficient	4.232 mm <sup>-1</sup>
F(000)	940
Crystal size	0.308 x 0.063 x 0.054 mm <sup>3</sup>
<b>Data collection</b>	
Temperature	150(2) K
Wavelength	0.71073 Å
Theta range for data collection	3.601 to 29.713°.
Index ranges	-18<=h<=16, -5<=k<=6, -27<=l<=17
Reflections collected	6833
Independent reflections	3314 [R(int) = 0.0565]
Completeness to theta = 25.242°	97.4 %
<b>Refinement</b>	
Absorption correction	Gaussian
Max. and min. transmission	1.000 and 0.625
Refinement method	Full-matrix least-squares on F <sup>2</sup>
Data / restraints / parameters	3314 / 709 / 326
Goodness-of-fit on F <sup>2</sup>	1.108
Final R indices [I>2sigma(I)]	R1 = 0.0741, wR2 = 0.1569
R indices (all data)	R1 = 0.1239, wR2 = 0.1915
Extinction coefficient	n/a
Largest diff. peak and hole	1.870 and -2.478 e.Å <sup>-3</sup>

Table VI - 33: Crystal data and structure refinement for  $(III-3_{Te})_2 \bullet HDFIO$  (1954228).

<b>Crystal data</b>	
Empirical formula	2 C <sub>12</sub> H <sub>8</sub> N <sub>2</sub> Te · C <sub>8</sub> F <sub>16</sub> I <sub>2</sub>
Formula weight	1269.49
Temperature	150(2) K
Space group	P -1
Unit cell dimensions	a = 7.4276(4) Å                      α = 81.685(5)°. b = 14.6567(8) Å                     β = 85.132(5)°. c = 17.4866(11) Å                    γ = 79.882(5)°.
Volume	1850.90(19) Å <sup>3</sup>
Z	2
Density (calculated)	2.278 Mg/m <sup>3</sup>
Absorption coefficient	3.356 mm <sup>-1</sup>
F(000)	1180
Crystal size	0.413 x 0.235 x 0.115 mm <sup>3</sup>
<b>Data collection</b>	
Wavelength	0.71073 Å
Crystal system	Triclinic
Theta range for data collection	2.912 to 29.935°.
Index ranges	-10<=h<=10, -14<=k<=20, -23<=l<=22
Reflections collected	18260
Independent reflections	8843 [R(int) = 0.0314]
Completeness to theta = 25.242°	99.9 %
<b>Refinement</b>	
Absorption correction	Gaussian
Max. and min. transmission	1.000 and 0.767
Refinement method	Full-matrix least-squares on F <sup>2</sup>
Data / restraints / parameters	8843 / 0 / 505
Goodness-of-fit on F <sup>2</sup>	1.068
Final R indices [I>2sigma(I)]	R1 = 0.0413, wR2 = 0.0830
R indices (all data)	R1 = 0.0647, wR2 = 0.1001
Extinction coefficient	n/a
Largest diff. peak and hole	1.979 and -1.054 e.Å <sup>-3</sup>

Table VI - 34: Crystal data and structure refinement for  $(\text{III-3Te})_2 \cdot \text{DITFB}$  (1954235).

<b>Crystal data</b>	
Empirical formula	$\text{C}_{12} \text{H}_8 \text{N}_2 \text{Te} \cdot 0.5 \text{C}_6 \text{F}_4 \text{I}_2$
Formula weight	508.73
Temperature	150(2) K
Space group	P -1
Unit cell dimensions	$a = 6.4432(5) \text{ \AA}$ $\alpha = 100.833(6)^\circ$ . $b = 9.3098(7) \text{ \AA}$ $\beta = 96.613(6)^\circ$ . $c = 12.7311(9) \text{ \AA}$ $\gamma = 103.000(6)^\circ$ .
Volume	$720.88(10) \text{ \AA}^3$
Z	2
Density (calculated)	$2.344 \text{ Mg/m}^3$
Absorption coefficient	$4.220 \text{ mm}^{-1}$
F(000)	470
Crystal size	$0.500 \times 0.145 \times 0.093 \text{ mm}^3$
<b>Data collection</b>	
Wavelength	$0.71073 \text{ \AA}$
Crystal system	Triclinic
Theta range for data collection	$3.116$ to $29.711^\circ$ .
Index ranges	$-6 \leq h \leq 8$ , $-10 \leq k \leq 11$ , $-17 \leq l \leq 12$
Reflections collected	5610
Independent reflections	3392 [R(int) = 0.0243]
Completeness to theta = $25.242^\circ$	99.9 %
<b>Refinement</b>	
Absorption correction	Gaussian
Max. and min. transmission	1.000 and 0.747
Refinement method	Full-matrix least-squares on $F^2$
Data / restraints / parameters	3392 / 0 / 190
Goodness-of-fit on $F^2$	1.018
Final R indices [ $I > 2\sigma(I)$ ]	$R1 = 0.0310$ , $wR2 = 0.0582$
R indices (all data)	$R1 = 0.0441$ , $wR2 = 0.0654$
Extinction coefficient	n/a
Largest diff. peak and hole	$0.809$ and $-0.879 \text{ e. \AA}^{-3}$

Table VI - 35: Crystal data and structure refinement for  $(III-1_{se})_2 \bullet DITFB$  (1954220).

<b>Crystal data</b>	
Empirical formula	2 C <sub>11</sub> H <sub>7</sub> N <sub>3</sub> Se · C <sub>6</sub> F <sub>4</sub> I <sub>2</sub>
Formula weight	922.17
Crystal system	Triclinic
Space group	P -1
Unit cell dimensions	a = 10.2008(5) Å      α = 105.628(4)° b = 11.6341(5) Å      β = 105.072(4)° c = 12.7627(6) Å      γ = 95.204(4)°
Volume	1387.26(12) Å <sup>3</sup>
Z	2
Density (calculated)	2.208 Mg/m <sup>3</sup>
Absorption coefficient	4.950 mm <sup>-1</sup>
F(000)	868
Crystal size	0.300 x 0.126 x 0.094 mm <sup>3</sup>
<b>Data collection</b>	
Temperature	150(2) K
Wavelength	0.71073 Å
Theta range for data collection	2.893 to 29.903°
Index ranges	-10<=h<=14, -15<=k<=15, -17<=l<=15
Reflections collected	10137
Independent reflections	6357 [R(int) = 0.0381]
Completeness to theta = 25.242°	98.3 %
<b>Refinement</b>	
Absorption correction	Gaussian
Max. and min. transmission	1.000 and 0.491
Refinement method	Full-matrix least-squares on F <sup>2</sup>
Data / restraints / parameters	6357 / 0 / 379
Goodness-of-fit on F <sup>2</sup>	0.999
Final R indices [I>2sigma(I)]	R1 = 0.0370, wR2 = 0.0615
R indices (all data)	R1 = 0.0585, wR2 = 0.0766
Extinction coefficient	n/a
Largest diff. peak and hole	0.978 and -1.256 e.Å <sup>-3</sup>

Table VI - 36: Crystal data and structure refinement for III-2<sub>Se</sub>•(DITFB)<sub>3</sub> (1954229).

<b>Crystal data</b>	
Empirical formula	C <sub>11</sub> H <sub>7</sub> N <sub>3</sub> Se . 2 C <sub>6</sub> F <sub>4</sub> I <sub>2</sub>
Formula weight	1063.88
Crystal system	Triclinic
Space group	P -1
Unit cell dimensions	a = 4.1629(2) Å                      α = 73.523(4)°. b = 16.0529(8) Å                     β = 88.733(4)°. c = 21.3057(10) Å                    γ = 85.225(4)°.
Volume	1360.58(12) Å <sup>3</sup>
Z	2
Density (calculated)	2.597 Mg/m <sup>3</sup>
Absorption coefficient	5.993 mm <sup>-1</sup>
F(000)	968
<b>Data collection</b>	
Crystal size	0.785 x 0.058 x 0.041 mm <sup>3</sup>
Temperature	150(2) K
Wavelength	0.71073 Å
Theta range for data collection	2.909 to 29.882°.
Index ranges	-3<=h<=5, -22<=k<=22, -29<=l<=28
Reflections collected	12031
Independent reflections	6317 [R(int) = 0.0397]
Completeness to theta = 25.242°	98.6 %
<b>Refinement</b>	
Absorption correction	Gaussian
Max. and min. transmission	1.000 and 0.649
Refinement method	Full-matrix least-squares on F <sup>2</sup>
Data / restraints / parameters	6317 / 0 / 352
Goodness-of-fit on F <sup>2</sup>	1.022
Final R indices [I>2sigma(I)]	R1 = 0.0418, wR2 = 0.0792
R indices (all data)	R1 = 0.0643, wR2 = 0.0948
Extinction coefficient	n/a
Largest diff. peak and hole	1.635 and -1.602 e.Å <sup>-3</sup>

Table VI - 37: Crystal data and structure refinement for (III-5)<sub>2</sub>•DABCO (1954231).

<b>Crystal data</b>	
Empirical formula	2 C <sub>12</sub> H <sub>3</sub> F <sub>4</sub> I N <sub>2</sub> Te . C <sub>6</sub> H <sub>12</sub> N <sub>2</sub>
Formula weight	1123.50
Temperature	150(2) K
Wavelength	0.71073 Å
Crystal system	Monoclinic
Space group	P 21/n
Unit cell dimensions	a = 10.8213(7) Å                      α = 90°. b = 23.5156(11) Å                     β = 112.285(8)°. c = 13.7951(10) Å                    γ = 90°.
Volume	3248.2(4) Å <sup>3</sup>
Z	4
Density (calculated)	2.297 Mg/m <sup>3</sup>
Absorption coefficient	3.776 mm <sup>-1</sup>
F(000)	2088
Crystal size	0.314 x 0.099 x 0.037 mm <sup>3</sup>
Theta range for data collection	3.486 to 29.602°.
Index ranges	-14<=h<=13, -26<=k<=31, -17<=l<=10
Reflections collected	11043
Independent reflections	6890 [R(int) = 0.0259]
Completeness to theta = 25.242°	92.3 %
Refinement method	Full-matrix least-squares on F <sup>2</sup>
Data / restraints / parameters	6890 / 0 / 433
Goodness-of-fit on F <sup>2</sup>	1.210
Final R indices [I>2sigma(I)]	R1 = 0.0584, wR2 = 0.1208
R indices (all data)	R1 = 0.0688, wR2 = 0.1262
Extinction coefficient	n/a
Largest diff. peak and hole	3.603 and -1.210 e.Å <sup>-3</sup>

Table VI - 38: Crystal data and structure refinement for (III-5)<sub>2</sub>•DABCO (1954232).

<b>Crystal data</b>	
Empirical formula	2 C <sub>12</sub> H <sub>3</sub> F <sub>4</sub> I N <sub>2</sub> Te . C <sub>6</sub> H <sub>12</sub> N <sub>2</sub>
Formula weight	1123.50
Temperature	150(2) K
Wavelength	0.71073 Å
Crystal system	Monoclinic
Space group	P 2 <sub>1</sub> /n
Unit cell dimensions	a = 11.1253(5) Å                      a = 90°. b = 14.5815(7) Å                      b = 97.586(4)°. c = 20.1277(8) Å                      g = 90°.
Volume	3236.6(3) Å <sup>3</sup>
Z	4
Density (calculated)	2.306 Mg/m <sup>3</sup>
Absorption coefficient	3.790 mm <sup>-1</sup>
F(000)	2088
Crystal size	0.145 x 0.106 x 0.042 mm <sup>3</sup>
Theta range for data collection	3.350 to 29.814°.
Index ranges	-14<=h<=13, -20<=k<=19, -26<=l<=27
Reflections collected	20127
Independent reflections	7807 [R(int) = 0.0282]
Completeness to theta = 25.242°	99.8 %
Absorption correction	Gaussian
Max. and min. transmission	1.000 and 0.940
Refinement method	Full-matrix least-squares on F <sup>2</sup>
Data / restraints / parameters	7807 / 0 / 433
Goodness-of-fit on F <sup>2</sup>	1.052
Final R indices [I>2sigma(I)]	R1 = 0.0297, wR2 = 0.0664
R indices (all data)	R1 = 0.0389, wR2 = 0.0708
Extinction coefficient	n/a
Largest diff. peak and hole	1.058 and -1.080 e.Å <sup>-3</sup>

Table VI - 39: Crystal data and structure refinement for III-5•DABCO (1954233).

<b>Crystal data</b>	
Empirical formula	C <sub>12</sub> H <sub>3</sub> F <sub>4</sub> I N <sub>2</sub> Te · C <sub>6</sub> H <sub>12</sub> N <sub>2</sub>
Formula weight	617.84
Crystal system	Triclinic
Space group	P -1
Unit cell dimensions	a = 8.9769(5) Å                      α = 100.758(5)°. b = 10.3694(7) Å                     β = 96.805(5)°. c = 11.7598(8) Å                     γ = 111.616(6)°.
Volume	978.55(12) Å <sup>3</sup>
Z	2
Density (calculated)	2.097 Mg/m <sup>3</sup>
Absorption coefficient	3.146 mm <sup>-1</sup>
F(000)	584
<b>Data collection</b>	
Crystal size	0.234 x 0.119 x 0.060 mm <sup>3</sup>
Temperature	150(2) K
Wavelength	0.71073 Å
Theta range for data collection	3.363 to 29.904°.
Index ranges	-11<=h<=12, -13<=k<=14, -15<=l<=16
Reflections collected	8199
Independent reflections	4658 [R(int) = 0.0335]
Completeness to theta = 25.242°	99.7 %
<b>Refinement</b>	
Absorption correction	Gaussian
Max. and min. transmission	0.835 and 0.263
Refinement method	Full-matrix least-squares on F <sup>2</sup>
Data / restraints / parameters	4658 / 0 / 253
Goodness-of-fit on F <sup>2</sup>	1.076
Final R indices [I>2sigma(I)]	R1 = 0.0399, wR2 = 0.0805
R indices (all data)	R1 = 0.0646, wR2 = 0.0950
Extinction coefficient	n/a
Largest diff. peak and hole	1.204 and -1.163 e.Å <sup>-3</sup>

Table VI - 40: Crystal data and structure refinement for III-1<sub>Te</sub>•III-5 (1954234).

<b>Crystal data</b>	
Empirical formula	C <sub>12</sub> H <sub>3</sub> F <sub>4</sub> N <sub>2</sub> Te I . C <sub>11</sub> H <sub>7</sub> N <sub>3</sub> Te
Formula weight	814.46
Crystal system	Monoclinic
Space group	P 2 <sub>1</sub> /n
Unit cell dimensions	a = 7.4490(3) Å                      α = 90° b = 12.8417(3) Å                     β = 91.419° c = 23.3811(7) Å                    γ = 90
Volume	2235.90(12) Å <sup>3</sup>
Z	4
Density (calculated)	2.420 Mg/m <sup>3</sup>
Absorption coefficient	3.672 mm <sup>-1</sup>
F(000)	1504.0
<b>Data collection</b>	
Crystal size	0.093 x 0.014 x 0.014mm <sup>3</sup>
Temperature	100(2) K
Wavelength	0.6889 Å
Theta range for data collection	1.689° to 25.376°
Index ranges	-9<=h<=9, -15<=k<=15, -19<=l<=29
Reflections collected	7563
Independent reflections	4458
Completeness to theta = 25.242°	99.6%
<b>Refinement</b>	
Absorption correction	Multi-scan
Max. and min. transmission	1.00000 and 0.80406
Refinement method	Full-matrix least-squares on F <sup>2</sup>
Data / restraints / parameters	7563 / 0 / 316
Goodness-of-fit on F <sup>2</sup>	1.025
Final R indices [I>2sigma(I)]	R1 = 0.1179, wR2 = 0.2721
R indices (all data)	R1 = 0.1483, wR2 = 0.2874
Extinction coefficient	n/a
Largest diff. peak and hole	4.984 and -2.340 e.Å <sup>-3</sup>

Table VI - 41: Crystal data and structure refinement for IV-5<sub>e</sub> (1954271).

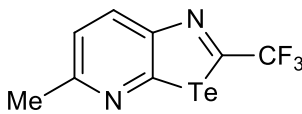
	<b>Crystal data</b>	
Empirical formula	C <sub>8</sub> H <sub>5</sub> F <sub>3</sub> N <sub>2</sub> Te	
Formula weight	313.74	
Crystal system	Monoclinic	
Space group	P 2 <sub>1</sub> /m	
Unit cell dimensions	a = 6.2430(5) Å b = 7.0585(7) Å c = 10.5317(8) Å	α = 90°. β = 97.461(7)°. γ = 90°.
Volume	460.16(7) Å <sup>3</sup>	
Z	2	
Density (calculated)	2.264 Mg/m <sup>3</sup>	
Absorption coefficient	3.237 mm <sup>-1</sup>	
F(000)	292	
Crystal size	0.241 x 0.118 x 0.033 mm <sup>3</sup>	
	<b>Data collection</b>	
Temperature	150(2) K	
Wavelength	0.71073 Å	
Theta range for data collection	3.484 to 29.493°.	
Index ranges	-8<=h<=5, -9<=k<=8, -14<=l<=12	
Reflections collected	2129	
Independent reflections	1163 [R(int) = 0.0242]	
Completeness to theta = 25.242°	99.8 %	
	<b>Refinement</b>	
Absorption correction	Gaussian	
Max. and min. transmission	1.000 and 0.825	
Refinement method	Full-matrix least-squares on F <sup>2</sup>	
Data / restraints / parameters	1163 / 0 / 82	
Goodness-of-fit on F <sup>2</sup>	1.054	
Final R indices [I>2sigma(I)]	R1 = 0.0294, wR2 = 0.0599	
R indices (all data)	R1 = 0.0328, wR2 = 0.0635	
Extinction coefficient	n/a	
Largest diff. peak and hole	0.666 and -0.981 e.Å <sup>-3</sup>	

Table VI - 42: Crystal data and structure refinement for IV-19 (1954272).

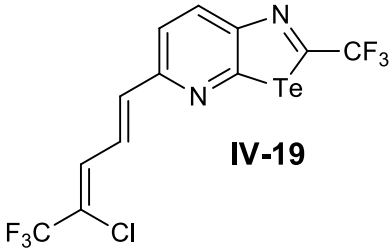
	<b>Crystal data</b>	
Empirical formula	C <sub>12</sub> H <sub>5</sub> Cl F <sub>6</sub> N <sub>2</sub> Te	
Formula weight	454.23	
Crystal system	Triclinic	
Space group	P -1	
Unit cell dimensions	a = 5.8122(3) Å	α = 82.248(7)°.
	b = 10.8654(9) Å	β = 81.714(6)°.
	c = 11.5535(10) Å	γ = 89.841(6)°.
Volume	715.31(9) Å <sup>3</sup>	
Z	2	
Density (calculated)	2.109 Mg/m <sup>3</sup>	
Absorption coefficient	2.328 mm <sup>-1</sup>	
F(000)	428	
Crystal size	0.577 x 0.180 x 0.126 mm <sup>3</sup>	
	<b>Data collection</b>	
Temperature	150(2) K	
Wavelength	0.71073 Å	
Theta range for data collection	3.543 to 29.867°.	
Index ranges	-7<=h<=7, -15<=k<=14, -10<=l<=14	
Reflections collected	5495	
Independent reflections	3368 [R(int) = 0.0255]	
Completeness to theta = 25.242°	99.8 %	
	<b>Refinement</b>	
Absorption correction	Gaussian	
Max. and min. transmission	1.000 and 0.825	
Refinement method	Full-matrix least-squares on F <sup>2</sup>	
Data / restraints / parameters	3368 / 0 / 200	
Goodness-of-fit on F <sup>2</sup>	1.095	
Final R indices [I>2sigma(I)]	R1 = 0.0584, wR2 = 0.1455	
R indices (all data)	R1 = 0.0823, wR2 = 0.1659	
Extinction coefficient	n/a	
Largest diff. peak and hole	2.028 and -0.610 e.Å <sup>-3</sup>	

Table VI - 43: Crystal data and structure refinement for IV-13 (1954273).

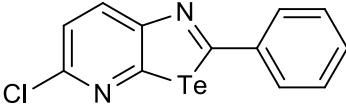
Empirical formula	C <sub>12</sub> H <sub>7</sub> Cl N <sub>2</sub> Te	 <p style="text-align: center;"><b>IV-13</b></p>	
Formula weight	342.25		
Crystal system	Orthorhombic		
Space group	P b c a		
Unit cell dimensions	a = 12.4328(6) Å		α = 90°.
	b = 8.4466(5) Å		β = 90°.
	c = 21.1948(16) Å		γ = 90°.
Volume	2225.8(2) Å <sup>3</sup>		
Z	8		
Density (calculated)	2.043 Mg/m <sup>3</sup>		
Absorption coefficient	2.882 mm <sup>-1</sup>		
F(000)	1296		
Crystal size	0.439 x 0.049 x 0.044 mm <sup>3</sup>		
<b>Data collection</b>			
Temperature	150(2) K		
Wavelength	0.71073 Å		
Theta range for data collection	3.493 to 29.648°.		
Index ranges	-17<=h<=11, -11<=k<=9, -28<=l<=19		
Reflections collected	7941		
Independent reflections	2620 [R(int) = 0.0312]		
Completeness to theta = 25.242°	97.2 %		
<b>Refinement</b>			
Absorption correction	multi-scan		
Max. and min. transmission	1.00000 and 0.66818		
Refinement method	Full-matrix least-squares on F <sup>2</sup>		
Data / restraints / parameters	2620 / 0 / 145		
Goodness-of-fit on F <sup>2</sup>	1.091		
Final R indices [I>2sigma(I)]	R1 = 0.0290, wR2 = 0.0558		
R indices (all data)	R1 = 0.0459, wR2 = 0.0664		
Extinction coefficient	n/a		
Largest diff. peak and hole	1.067 and -0.953 e.Å <sup>-3</sup>		

Table VI - 44. Crystal data and structure refinement for IV-12 (1954278).

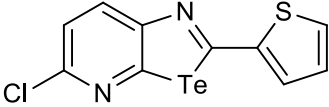
		<b>Crystal data</b>		
Empirical formula		C <sub>10</sub> H <sub>5</sub> Cl N <sub>2</sub> S Te	 <p style="text-align: center;"><b>IV-12</b></p>	
Formula weight		348.27		
Crystal system		Monoclinic		
Space group		P 2 <sub>1</sub> /c		
Unit cell dimensions		a = 11.0278(5) Å		α = 90°.
		b = 18.0069(8) Å		β = 104.168(5)°.
		c = 11.1423(5) Å		γ = 90°.
Volume		2145.30(17) Å <sup>3</sup>		
Z		8		
Density (calculated)		2.157 Mg/m <sup>3</sup>		
Absorption coefficient		3.180 mm <sup>-1</sup>		
F(000)		1312		
Crystal size		0.333 x 0.255 x 0.178 mm <sup>3</sup>		
		<b>Data collection</b>		
Temperature		150(2) K		
Wavelength		0.71073 Å		
Theta range for data collection		3.751 to 29.792°.		
Index ranges		-13<=h<=15, -18<=k<=24, -15<=l<=10		
Reflections collected		10688		
Independent reflections		5177 [R(int) = 0.0278]		
Completeness to theta = 25.242°		99.8 %		
		<b>Refinement</b>		
Absorption correction		Gaussian		
Max. and min. transmission		1.000 and 0.758		
Refinement method		Full-matrix least-squares on F <sup>2</sup>		
Data / restraints / parameters		5177 / 0 / 271		
Goodness-of-fit on F2		1.058		
Final R indices [I>2sigma(I)]		R1 = 0.0319, wR2 = 0.0554		
R indices (all data)		R1 = 0.0475, wR2 = 0.0646		
Extinction coefficient		n/a		
Largest diff. peak and hole		0.701 and -0.710 e.Å <sup>-3</sup>		

Table IV - 45: Crystal data and structure refinement for IV-13 (1954275).

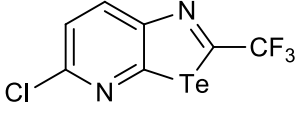
Empirical formula	C <sub>7</sub> H <sub>2</sub> Cl F <sub>3</sub> N <sub>2</sub> Te	
Formula weight	334.16	
Crystal system	Monoclinic	<b>IV-13</b>
Space group	P 2 <sub>1</sub> /m	
Unit cell dimensions	a = 6.1992(4) Å	α = 90°.
	b = 6.9684(6) Å	β = 95.722(7)°.
	c = 10.4885(9) Å	γ = 90°.
Volume	450.83(6) Å <sup>3</sup>	
Z	2	
Density (calculated)	2.462 Mg/m <sup>3</sup>	
Absorption coefficient	3.599 mm <sup>-1</sup>	
F(000)	308	
Crystal size	0.124 x 0.092 x 0.050 mm <sup>3</sup>	
	<b>Data collection</b>	
Temperature	293(2) K	
Wavelength	0.71073 Å	
Theta range for data collection	3.303 to 29.580°.	
Index ranges	-8 ≤ h ≤ 8, -9 ≤ k ≤ 9, -13 ≤ l ≤ 13	
Reflections collected	4037	
Independent reflections	1229 [R(int) = 0.0371]	
Completeness to theta = 25.242°	99.9 %	
	<b>Refinement</b>	
Absorption correction	Gaussian	
Max. and min. transmission	0.840 and 0.595	
Refinement method	Full-matrix least-squares on F <sup>2</sup>	
Data / restraints / parameters	1229 / 430 / 150	
Goodness-of-fit on F <sup>2</sup>	1.113	
Final R indices [I > 2σ(I)]	R1 = 0.0309, wR2 = 0.0483	
R indices (all data)	R1 = 0.0427, wR2 = 0.0532	
Extinction coefficient	n/a	
Largest diff. peak and hole	0.728 and -0.806 e.Å <sup>-3</sup>	

Table IV - 46: Crystal data and structure refinement for IV-14 (1954274).

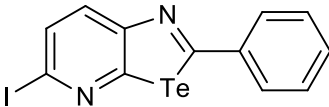
	<b>Crystal data</b>	
Empirical formula	C <sub>12</sub> H <sub>7</sub> I N <sub>2</sub> Te	
Formula weight	433.70	
Crystal system	Monoclinic	<b>IV-14</b>
Space group	P 2 <sub>1</sub> /c	
Unit cell dimensions	a = 12.5510(6) Å	α = 90°.
	b = 8.2204(5) Å	β = 104.881(6)°.
	c = 23.8900(14) Å	γ = 90°.
Volume	2382.2(2) Å <sup>3</sup>	
Z	8	
Density (calculated)	2.419 Mg/m <sup>3</sup>	
Absorption coefficient	5.061 mm <sup>-1</sup>	
F(000)	1584	
Crystal size	0.599 x 0.060 x 0.036 mm <sup>3</sup>	
	<b>Data collection</b>	
Temperature	150(2) K	
Wavelength	0.71073 Å	
Theta range for data collection	3.359 to 29.660°.	
Index ranges	-17<=h<=17, -10<=k<=10, -32<=l<=33	
Reflections collected	13008	
Independent reflections	5678 [R(int) = 0.0380]	
Completeness to theta = 25.242°	99.7 %	
	<b>Refinement</b>	
Absorption correction	Gaussian	
Max. and min. transmission	0.840 and 0.595	
Refinement method	Full-matrix least-squares on F <sup>2</sup>	
Data / restraints / parameters	5678 / 0 / 289	
Goodness-of-fit on F2	1.072	
Final R indices [I>2sigma(I)]	R1 = 0.0387, wR2 = 0.0794	
R indices (all data)	R1 = 0.0604, wR2 = 0.0940	
Extinction coefficient	n/a	
Largest diff. peak and hole	1.083 and -1.355 e.Å <sup>-3</sup>	

Table VI - 47: Crystal data and structure refinement for IV-16 (1954276).

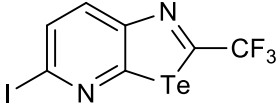
Empirical formula	C <sub>7</sub> H <sub>2</sub> F <sub>3</sub> I N <sub>2</sub> Te	
Formula weight	425.61	
Crystal system	Monoclinic	<b>IV-16</b>
Space group	C 2/c	
Unit cell dimensions	a = 19.4935(10) Å	α = 90°.
	b = 4.5147(4) Å	β = 98.020(6)°.
	c = 22.524(2) Å	γ = 90°.
Volume	1962.9(3) Å <sup>3</sup>	
Z	8	
Density (calculated)	2.880 Mg/m <sup>3</sup>	
Absorption coefficient	6.181 mm <sup>-1</sup>	
F(000)	1520	
Crystal size	0.192 x 0.091 x 0.066 mm <sup>3</sup>	
<b>Data collection</b>		
Temperature	150(2) K	
Wavelength	0.71073 Å	
Theta range for data collection	3.654 to 29.465°.	
Index ranges	-26<=h<=16, -6<=k<=4, -31<=l<=29	
Reflections collected	4346	
Independent reflections	2313 [R(int) = 0.0220]	
Completeness to theta = 25.242°	99.8 %	
<b>Refinement</b>		
Absorption correction	Gaussian	
Max. and min. transmission	1.000 and 0.938	
Refinement method	Full-matrix least-squares on F <sup>2</sup>	
Data / restraints / parameters	2313 / 0 / 127	
Goodness-of-fit on F <sup>2</sup>	1.148	
Final R indices [I>2sigma(I)]	R1 = 0.0421, wR2 = 0.0930	
R indices (all data)	R1 = 0.0539, wR2 = 0.1020	
Extinction coefficient	n/a	
Largest diff. peak and hole	2.188 and -1.443 e.Å <sup>-3</sup>	

Table VI - 48: Crystal data and structure refinement for IV-25 (1954277).

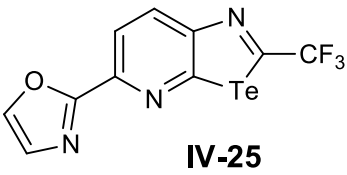
		<b>Crystal data</b>		
Empirical formula		C <sub>10</sub> H <sub>4</sub> F <sub>3</sub> N <sub>3</sub> O Te	 <p style="text-align: center;"><b>IV-25</b></p>	
Formula weight		366.76		
Crystal system		Orthorhombic		
Space group		P n m a		
Unit cell dimensions		a = 26.0295(14) Å		$\alpha = 90^\circ$ .
		b = 6.6541(5) Å		$\beta = 90^\circ$ .
		c = 6.2290(3) Å		$\gamma = 90^\circ$ .
Volume		1078.88(11) Å <sup>3</sup>		
Z		4		
Density (calculated)		2.258 Mg/m <sup>3</sup>		
Absorption coefficient		2.789 mm <sup>-1</sup>		
F(000)		688		
Crystal size		0.233 x 0.046 x 0.039 mm <sup>3</sup>		
		<b>Data collection</b>		
Temperature		150(2) K		
Wavelength		0.71073 Å		
Theta range for data collection		3.363 to 29.727°.		
Index ranges		-34<=h<=35, -6<=k<=8, -6<=l<=8		
Reflections collected		4463		
Independent reflections		1452 [R(int) = 0.0408]		
Completeness to theta = 25.242°		99.8 %		
		<b>Refinement</b>		
Absorption correction		Semi-empirical from equivalents		
Max. and min. transmission		1.00000 and 0.47820		
Refinement method		Full-matrix least-squares on F <sup>2</sup>		
Data / restraints / parameters		1452 / 0 / 106		
Goodness-of-fit on F2		1.106		
Final R indices [I>2sigma(I)]		R1 = 0.0374, wR2 = 0.0755		
R indices (all data)		R1 = 0.0521, wR2 = 0.0856		
Extinction coefficient		n/a		
Largest diff. peak and hole		0.894 and -0.878 e.Å <sup>-3</sup>		

Table VI - 49: Crystal data and structure refinement for IV-5•PhCOOH (1954280).

<b>Crystal data</b>	
Empirical formula	C <sub>8</sub> H <sub>5</sub> F <sub>3</sub> N <sub>2</sub> Te · C <sub>7</sub> H <sub>6</sub> O <sub>2</sub>
Formula weight	435.86
Crystal system	Monoclinic
Space group	P 2 <sub>1</sub> /n
Unit cell dimensions	a = 6.7627(9) Å      α = 90°. b = 11.8632(10) Å     β = 90.30°. c = 19.313(3) Å        γ = 90°.
Volume	1549.4(3) Å <sup>3</sup>
Z	4
Density (calculated)	1.868 Mg/m <sup>3</sup>
Absorption coefficient	1.962 mm <sup>-1</sup>
F(000)	840
Crystal size	0.248 x 0.037 x 0.023 mm <sup>3</sup>
<b>Data collection</b>	
Temperature	150(2) K
Wavelength	0.71073 Å
Theta range for data collection	3.435 to 29.890°.
Index ranges	-8<=h<=9, -14<=k<=15, -24<=l<=15
Reflections collected	7593
Independent reflections	3724 [R(int) = 0.0404]
Completeness to theta = 25.242°	99.6 %
<b>Refinement</b>	
Absorption correction	Gaussian
Max. and min. transmission	1.000 and 0.863
Refinement method	Full-matrix least-squares on F <sup>2</sup>
Data / restraints / parameters	3724 / 0 / 208
Goodness-of-fit on F2	1.214
Final R indices [I>2sigma(I)]	R1 = 0.0855, wR2 = 0.1780
R indices (all data)	R1 = 0.1216, wR2 = 0.1956
Extinction coefficient	n/a
Largest diff. peak and hole	1.603 and -1.517 e.Å <sup>-3</sup>

Table VI - 50: Crystal data and structure refinement for IV-5•Isoquinolinone (1954279).

<b>Crystal data</b>	
Empirical formula	C <sub>8</sub> H <sub>5</sub> F <sub>3</sub> N <sub>2</sub> Te . C <sub>9</sub> H <sub>7</sub> N O
Formula weight	458.90
Crystal system	Monoclinic
Space group	P 2 <sub>1</sub> /c
Unit cell dimensions	a = 16.6595(12) Å      α = 90°. b = 5.6280(5) Å      β = 114.564(10)°. c = 19.3960(16) Å      γ = 90°.
Volume	1654.0(3) Å <sup>3</sup>
Z	4
Density (calculated)	1.843 Mg/m <sup>3</sup>
Absorption coefficient	1.840 mm <sup>-1</sup>
F(000)	888
Crystal size	0.300 x 0.064 x 0.018 mm <sup>3</sup>
<b>Data collection</b>	
Temperature	150(2) K
Wavelength	0.71073 Å
Theta range for data collection	3.723 to 29.492°.
Index ranges	-20<=h<=22, -7<=k<=7, -26<=l<=23
Reflections collected	8380
Independent reflections	3927 [R(int) = 0.0327]
Completeness to theta = 25.242°	99.8 %
<b>Refinement</b>	
Absorption correction	Gaussian
Max. and min. transmission	1.000 and 0.781
Refinement method	Full-matrix least-squares on F <sup>2</sup>
Data / restraints / parameters	3927 / 0 / 226
Goodness-of-fit on F2	1.104
Final R indices [I>2sigma(I)]	R1 = 0.0359, wR2 = 0.0647
R indices (all data)	R1 = 0.0516, wR2 = 0.0728
Extinction coefficient	n/a
Largest diff. peak and hole	1.250 and -0.700 e.Å <sup>-3</sup>

## VI – 6 References

- [1] A. T. CrysAlisPro, Version 1.171.37.33 (release 27-03-2014 CrysAlis171 .NET).
- [2] G. M. Sheldrick, *SHELX-2013: Program for the Solution of Crystal Structures* **2013**, University of Göttingen.
- [3] G. M. Sheldrick, *SHELX-2018: Program for the Solution of Crystal Structures* **2018**, University of Göttingen.
- [4] W. Lin, L. Chen, P. Knochel, 'Preparation of Functionalized 3,4-Pyridynes via 2-Magnesiated Diaryl Sulfonates', *Tetrahedron* **2007**, *63*, 2787-2797.
- [5] H.-S. Lin, L. A. Paquette, 'A Convenient Method for Determining the Concentration of Grignard Reagents', *Synth. Commun.* **1994**, *24*, 2503-2506.
- [6] Kuldip K. Bhasin, V. Arora, Thomas M. Klapötke, M.-J. Crawford, 'One-Pot Synthesis of Pyridyltellurium Derivatives from a Reaction with Isopropylmagnesium Chloride and X-ray Crystal Structures of Various Pyridyl Ditellurides', *Eur. J. Inorg. Chem.* **2004**, *2004*, 4781-4788.
- [7] A. Inoue, K. Kitagawa, H. Shinokubo, K. Oshima, 'Selective Halogen–Magnesium Exchange Reaction via Organomagnesium Ate Complex', *J. Org. Chem.* **2001**, *66*, 4333-4339.
- [8] O. Dumele, N. Trapp, F. Diederich, 'Halogen Bonding Molecular Capsules', *Angew. Chem. Int. Ed.* **2015**, *54*, 12339-12344.
- [9] G. Monzón, I. Tirota, P. Knochel, 'The Ortho and Meta Magnesiumation of Functionalized Anilines and Amino-Substituted Pyridines and Pyrazines at Room Temperature', *Angew. Chem. Int. Ed.* **2012**, *51*, 10624-10627.
- [10] W. Cho, H. J. Lee, G. Choi, S. Choi, M. Oh, 'Dual Changes in Conformation and Optical Properties of Fluorophores within a Metal–Organic Framework during Framework Construction and Associated Sensing Event', *J. Am. Chem. Soc.* **2014**, *136*, 12201-12204.
- [11] A. D. Dunn, A. Currie, L. E. Hayes, 'Bromination of Pyridines. II. Bromination of Aminopicolines', *J. Prakt. Chem.* **1989**, *331*, 369-374.
- [12] A. C. Bissember, M. G. Banwell, 'Microwave-Assisted Trans-Halogenation Reactions of Various Chloro-, Bromo-, Trifluoromethanesulfonyloxy- and Nonfluorobutanesulfonyloxy-Substituted Quinolines, Isoquinolines, and Pyridines Leading to the Corresponding Iodinated Heterocycles', *J. Org. Chem.* **2009**, *74*, 4893-4895.
- [13] G. Piersanti, L. Giorgi, F. Bartocchini, G. Tarzia, P. Minetti, G. Gallo, F. Giorgi, M. Castorina, O. Ghirardi, P. Carminati, 'Synthesis of Benzo[1,2-d;3,4-d']diimidazole and 1H-pyrazolo[4,3-b]pyridine as Putative A2A Receptor Antagonists', *Org. Biomol. Chem.* **2007**, *5*, 2567-2571.
- [14] G. W. T. M. J. Frisch, H. B. Schlegel, G. E. Scuseria, M. A. Robb, J. R. Cheeseman, G. Scalmani, V. Barone, B. Mennucci, G. A. Petersson, H. Nakatsuji, M. Caricato, X. Li, H. P. Hratchian, A. F. Izmaylov, J. Bloino, G. Zheng, J. L. Sonnenberg, M. Hada, M. Ehara, K. Toyota, R. Fukuda, J. Hasegawa, M. Ishida, T. Nakajima, Y. Honda, O. Kitao, H. Nakai, T. Vreven, J. A. Montgomery Jr., J. E. Peralta, F. Ogliaro, M. J. Bearpark, J. Heyd, E. N. Brothers, K. N. Kudin, V. N. Staroverov, R. Kobayashi, J. Normand, K. Raghavachari, A. P. Rendell, J. C. Burant, S. S. Iyengar, J. Tomasi, M. Cossi, N. Rega, N. J. Millam, M. Klene, J. E. Knox, J. B. Cross, V. Bakken, C. Adamo, J. Jaramillo, R. Gomperts, R. E. Stratmann, O. Yazyev, A. J. Austin, R. Cammi, C. Pomelli, J. W. Ochterski, R. L. Martin, K. Morokuma, V. G. Zakrzewski, G. A. Voth, P. Salvador, J. J. Dannenberg, S. Dapprich, A. D. Daniels, Ö. Farkas, J. B. Foresman, J. V. Ortiz, J. Cioslowski, D. J. Fox, *Gaussian, Inc., Wallingford, CT*.
- [15] S. Grimme, S. Ehrlich, L. Goerigk, 'Effect of the Damping Function in Dispersion Corrected Density Functional Theory', *J. Comput. Chem.* **2011**, *32*, 1456-1465.
- [16] P. J. Hay, W. R. Wadt, 'Ab Initio Effective Core Potentials for Molecular Calculations. Potentials for the Transition Metal Atoms Sc to Hg', *J. Chem. Phys.* **1985**, *82*, 270-283.
- [17] A. F. Cozzolino, I. Vargas-Baca, S. Mansour, A. H. Mahmoudkhani, 'The Nature of the Supramolecular Association of 1,2,5-Chalcogenadiazoles', *J. Am. Chem. Soc.* **2005**, *127*, 3184-3190.

- [18] F. Weigend, R. Ahlrichs, 'Balanced Basis Sets of Split Valence, Triple Zeta Valence and Quadruple Zeta Valence Quality for H to Rn: Design and Assessment of Accuracy', *Phys. Chem. Chem. Phys.* **2005**, *7*, 3297-3305.
- [19] G. E. Garrett, G. L. Gibson, R. N. Straus, D. S. Seferos, M. S. Taylor, 'Chalcogen Bonding in Solution: Interactions of Benzotelluradiazoles with Anionic and Uncharged Lewis Bases', *J. Am. Chem. Soc.* **2015**, *137*, 4126-4133.
- [20] P. Politzer, J. S. Murray, T. Clark, 'Halogen Bonding and Other  $\sigma$ -Hole Interactions: a Perspective', *Phys. Chem. Chem. Phys.* **2013**, *15*, 11178-11189.

